Optimization of High Data Rate Ground to Satellite Links Pre-compensated by Adaptive Optics

Perrine Lognoné

INSTITUT POLYTECHNIQUE DE PARIS

NNT : 2023IPPAT041

Thèse de doctorat

Optimization of High Data Rate Ground to Satellite Links Pre-compensated by Adaptive Optics

Thèse de doctorat de l'Institut Polytechnique de Paris
préparée à Télécom Paris

École doctorale n°626 École doctorale de l'Institut Polytechnique de Paris (ED IP Paris)
Spécialité de doctorat : Réseaux, informations et communications

Thèse présentée et soutenue à Palaiseau, le 13/12/2023, par

PERRINE LOGNONÉ

Composition du Jury :

Eleni Diamanti Professor, Sorbonne Université (LIP6)	Présidente/Examinatrice
Aniceto Belmonte Professor, Technical University of Catalonia (Department of Signal Theory and Communications)	Rapporteur
Christophe Peucheret Professor, Université de Rennes 1 (FOTON)	Rapporteur
James Osborn Professor Associate, Durham University (CfAI)	Examinateur
Ramon Mata Calvo System engineer, European Space Agency (ESA)	Examinateur
Ghaya Rekaya Professor, Télécom Paris (COMELEC)	Directrice de thèse
Jean-Marc Conan Research engineer, ONERA	Co-directeur de thèse
Bouchra Benammar Research engineer, Centre National d'Etudes Spatiales (CNES)	Invité, corresp. CNES

To my friends, family and to life

Acknowledgements/Remerciements

C'est donc pour introduire ce manuscrit de thèse qu'il me fallait avoir quelques mots pour clore ces trois années de thèse. Il y a trois ans, le premier octobre 2020, nous nous retrouvions à l'ONERA, masqués, en pleine période de COVID-19, Alix, Pablo, Valentina, Nicolas, Émile et moi-même, prêt à percer les mystères de la turbulence atmosphérique et de la haute résolution angulaire. Trois, ans plus tard, nous voila tous docteurs, et quel chemin parcouru ! À cette occasion, j'aimerais remercier toutes les personnes sans qui l'obtention de mon doctorat n'aurait pas été possible, et qui ont participé à rendre ce chemin unique.

J'aimerais commencer par remercier ma directrice et mon directeur de thèse, Ghaya Rekaya et Jean-Marc Conan. Je vous remercie pour tous ces savoirs que vous m'avez transmis, qu'ils soient scientifiques, méthodologiques ou de l'ordre du savoir-être. Ce fut un réel plaisir d'apprendre et de travailler avec vous. Je voudrais également vous remercier d'avoir eu l'idée de ce sujet de thèse, qui m'a permis d'allier trois sujets scientifiques me tenant à cœur lors de mon master : les communications numériques, l'optique et le spatial. D'un point de vue plus personnel, vous avez toujours su être à l'écoute et vous rendre disponible. Vous m'avez tous les deux accompagnée dans les hauts de la thèse, comme dans les moments difficiles. Je vous remercie encore pour tout et espère que cette thèse sera le début d'une longue collaboration.

Je remercie également Bouchra Benammar ainsi qu'Hugo Méric, mes correspondants CNES, et plus largement le CNES, pour les conseils et les réunions aux discussions enrichissantes. Je les remercie aussi de leur confiance qu'ils m'ont donné dans la réalisation de mes travaux de thèse.

Je remercie aussi mon Jury et mes rapporteurs, pour avoir accepté de lire et de juger de mes travaux.

Durant cette thèse, j'ai eu la chance de travailler dans deux laboratoires d'accueil, l'équipe HRA de l'ONERA et l'équipe COMNUM de Télécom. Je me sens très chanceuse d'avoir pu évoluer dans ces deux environnements, et apprendre de ces deux équipes aux spécialités différentes. Ainsi, commençant par l'ONERA, j'aimerais remercier l'équipe HRA dans sa globalité. Je remercie aussi Jean-Marc et Nicolas de m'avoir donnée l'opportunité de participer aux essais FEEDELIO, ainsi qu'Aurélie, Cyril, Joseph et Caroline, de m'avoir formée à la participation à ces essais. Je remercie également l'équipe COMNUM à télécom, pour ces réunions enrichissantes. Merci également à Ghaya, Michelle, Philippe et Robert de m'avoir donné l'opportunité d'enseigner. Pour terminer sur le plan professionnel, je remercie également MIMOPT, et en particulier Akram et Rami, qui m'ont aidée à mettre en valeur les résultats MMSE en effectuant les simulations de communication E2E (qui ont dû faire chauffer les ordinateurs).

D'un point de vue plus personnel, je remercie tous les doctorants, de HRA et de COMNUM/COMELEC, qui sont maintenant des amis, toujours là pour amener de la bonne humeur au labo, même dans les moments les plus stressants. Côté HRA, je remercie donc:

Alix, Pablo, Valentina, Emile, Nicolas, Yann L, Pierre, Inès, Eve, Timothée, Mahawa, Lucas, Léa, Hiyam, Yann LT, Hugo J, Elyes et les petits nouveaux, Alberto, Mathieu, Hugo, Florian. Merci pour ces sessions de mots croisés, ces séances d'escalade, les moments bubble tea, les sorties bar à jeux et autres. Aussi un special thanks à Laurie, notre maman des thésards, qui a toujours su nous aider et nous conseiller dans tous moments. J'aimerais aussi en particulier remercier Alix, et aussi Pablo et Émile et Valentina, la team des 3A. Je remercie aussi tous les doctorants de l'équipe COMNUM et plus largement les doctorants COMELEC. Je remercie en particulier Thomas, Joana, Aymen, Ibrahim, Abdelaziz, Julien, Peter, Hyunah, Razi, Isaia, Mohannad, Sara, Pierre, Francesco.

Et comme ce manuscrit de thèse n'aurait pu exister sans moments hors du labo, je remercie tous mes amis pour leur soutien et tous ces moments partagés qui m'ont permis de déconnecter du travail. Je remercie en particulier mes amis de la team supop: Yann, Elo, Lucas, Anouk, Célia, Cerise, Am, Raph, Matal, Magui, Jérem, Félix, Arnaud, mes amis de prépa Arthur, Hippo, Victor, Tristan, Tristan, Alice, Sarah, Nicolas, François, Vincent, et aussi je remercie Tanguy et Gaetan. Je remercie aussi mes colocs du 106, Marta, Juli, Nico, Antoine et Pépé, de m'avoir accompagnée durant cette fin de thèse et en particulier pendant la période de rédaction.

Pour terminer, j'aimerais remercier ma famille, dont certains ont fait le déplacement pour assister à ma soutenance de thèse. Je vous remercie d'avoir été là et je remercie en particulier mes parents d'avoir été d'un soutien inconditionnel dans mes choix d'orientation.

Pour terminer, j'aimerais remercier toutes les personnes qui, depuis m'ont enfance, m'ont donné le goût de la physique. Je pense à mon professeur de maths de Lycée, Mr Briand, m'ayant parlé pour la première fois de supoptique dans mon lycée Lannionnais, à mon professeur de physique de prépa Mr. Jahier, qui a su donner vie aux électrons pour nous expliquer de manière dynamique et pédagogique la physique atomique, à mes différents maîtres de stage, Denis Battarel de Sodern, qui m'a fait découvrir les communications optiques spatiales à travers mon stage de césure, à Nicolas Leroy, Patrice Hello, David Corre et Sarah Antier qui m'ont fait découvrir la vie de laboratoire et plus largement le domaine de la recherche, et finalement Antonin Billaud et Olivier Pinel qui m'ont initié aux FSO durant le stage précédant la thèse.

Merci à tous !

Contents

List of Figures

List of Tables

Introduction (English)

Context

In our increasingly interconnected world, the need for robust and reliable communication systems has never been more critical. Whether it's for global internet access, disaster response, or weather forecasting, satellite networks have emerged as indispensable tools that bridge the gaps in our terrestrial infrastructure. To address the global internet's need and mitigate the digital divide stemming from the lack of terrestrial network infrastructure, satellite networks offer a flexible and complementary solution.

For a seamless integration between satellite and terrestrial networks, it is required to establish reliable communication links between Earth and satellites that can support high data rates. This transmission can be achieved thanks to radio-frequency (RF) communication systems, already in operation. However, satellite RF communications are reaching their limits, due to the conjunction of the RF intrinsic throughput limitations and the RF spectrum congestion. To overcome these RF system limitations, ground-space optical links emerge as an appealing solution that can unlock higher achievable data rates while ensuring secure connections and freeing operators from frequency allocation constraints.

Challenges

Unlike radio-frequency links, optical links enable communication at very high data rates, as high as hundreds of terabits per second over a single point-to-point link. However, the reliability of high data rate free-space optical links is compromised by atmospheric disturbances. When an optical beam traverses the turbulent atmosphere, it undergoes phase and amplitude distortions, resulting in random fluctuations of the signal received by the optical receiver. These flux random attenuations introduce errors and ultimately affect the link reliability.

To mitigate the signal attenuation caused by atmospheric turbulence, phase correction techniques, such as adaptive optics, have been proposed. These systems operate by measuring and correcting the phase perturbation of the incoming beam in real-time. Their effectiveness has been demonstrated for satellite-to-ground (downlink) corrections, significantly reducing the flux fluctuations received by the ground optical system.

In this thesis, we focus on the ground-to-GEO satellite link (uplink). In this scenario, the adaptive optics (AO) correction is used to pre-distort the phase of the beam before its emission towards the satellite. Currently, it is foreseen to use the downlink AO correction to pre-compensate the uplink beam. However, due to the presence of a point-ahead angle (PAA) that separates the downlink and uplink optical paths, the encountered phase perturbations differ, and such a pre-compensation is suboptimal. Consequently, the optical signal coupled onboard the satellite still experiences long and deep attenuation, thereby degrading the communication link's reliability. This sets the stage for the central problem

addressed in this thesis:

How can we ensure reliable communication at high data rates over the pre-compensated ground-to-GEO satellite optical fading channel?

Optical and digital solutions can address this issue. We list in the following the current available solutions from the literature.

The impact of the fades on the communication channel is to drastically limit the theoretical transmission data-rate of the link, that is, the channel capacity. A first solution is to improve the channel capacity by improving the channel statistics. This can be done by improving the pre-compensation of the link. In 1996, Tyson introduced the concept of using a beacon on the optical axis at PAA, in order to measure the phase perturbation more relevant for the uplink pre-compensation [1]. Either a slave satellite or a laser guide star (LGS) can provide this beacon. While the slave satellite solution has never been implemented, laser guide star systems, leveraging the developments from the astronomy domain, are currently under implementation to demonstrate its potential to mitigate uplink signal fluctuations. However, it is not yet possible to measure the tip tilt and focus at PAA on the LGS beacon [2, 3]. Currently, the most mature technique that has been demonstrated experimentally is the technique that we will call 'classical pre-compensation', applying the downlink AO correction for pre-compensation of the uplink. Additionally, the accurate pre-compensation of the tip and tilt is shown to be crucial to reduce the signal fadings onboard the satellite [4]. Hence, whether the considered system is aided or not by a LGS, there is still a need to improve the uplink tip and tilt correction.

On the other hand, the communication link reliability can be optimized using digital signal processing techniques. These techniques involve the use of coding and interleaving techniques to average the channel fadings. To be efficient, these techniques need to be tailored to the channel. Current developments involve the design of long channel interleavers to match the channel coherence time [5], with interleaver duration above 70 ms to ensure reliability in strong turbulence cases. In the RF wireless domain, that also faces fading channels, the classical method to improve the communication reliability is to exploit channel diversity. In both cases, a fine knowledge of the channel model is required to design adapted and optimal coding schemes. These models are currently available thanks to numerical end-to-end simulation. However, there is not yet a statistical channel model of the AO ground to GEO pre-compensated link.

Methodology

In this thesis, we aim at improving the uplink channel statistics, therefore the telecommunication performance of the link, by optimizing the pre-compensation phase at point ahead angle. Also, to allow future digital optimization of the link, a second objective is to provide accurate models to link the complex field spatial disturbances to the scalar coupled flux, in the presence of relatively large phase residuals.

To achieve these goals, we use all along the thesis a principle that is at the very essence of the pre-compensation method: **the reciprocity principle**. Originally proposed and theoretically demonstrated by Shapiro [6], the reciprocity principle was exploited later to model ground-to-space optical links in [7–9]. This powerful formalism will be used in this thesis to:

- provide an analytical general model of the ground to GEO satellite pre-compensation phase error. This model will be used to characterize the AO pre-compensation performance for diverse atmospheric conditions, ground station geometries and type of AO correction.

- design and improve flexible numerical models to compute the impact of the phase error on the coupled flux.

- and provide the analytical framework to optimize the pre-compensation phase error.

The reciprocity principle also offers a new point of view to analyze the relationship between the phase error and the coupled flux statistics. Using this principle allows leveraging the developments made for downlink modeling and developments related to anisoplanatism in the astronomy domain.

Structure of the manuscript

In **chapter 1**, we explain the motivation for implementing optical feeder links. We describe the optical point to point link and its components, to emphasize on the technological drivers of the system. Finally, we present the telecommunication chain to identify the key elements impacting the data-rate and the link reliability. This performance is shown to depend on the optical system design and atmospheric turbulence conditions.

In **chapter 2**, we describe the channel model and the physical phenomenon ruling the signal random attenuation. We describe the theory and tools allowing to model and characterize the optical beam propagation through atmospheric turbulence, without AO correction. We also describe the AO system and explain its impact on the coupled flux, in both downlink and uplink scenarios. We present the tools and formalism from the literature to evaluate the impact of the AO correction on the flux coupled to a single mode fiber. Finally, we present the fading mitigation techniques existing in the literature.

In **chapter 3**, we propose to use a reciprocal point of view to model the uplink channel and its AO partial correction. We explain the reciprocity principle, and validate the principle experimentally and numerically. We propose a general formalism to model the phase error, and use it to characterize state of the art pre-compensation methods. Thanks to this formalism, we explain and refine pseudo-analytical models from the literature. Finally, we illustrate the strength of this formalism by evaluating parametrically the reciprocal uplink pre-compensated channel for different OGS geometries and turbulence conditions.

In **chapter 4**, we present the main contribution of this thesis work, that is, the construction of a MMSE phase estimator at point ahead angle using phase and log-amplitude measurements. This approach is a generalization of Whiteley's work on phase estimation based on phase only measurements [10]. In this chapter, we develop the MMSE estimator general formalism for any measurements. We apply Whiteley's approach to the ground to GEO link geometry and prove that phase only measurements are not sufficient to reduce the pre-compensation error in the considered scenario. Therefore, we present the new estimator relying on phase and log-amplitude measurements and explore the gain and limitation brought by this method.

In **chapter 5**, we propose an analytical framework to jointly model the pre-compensation residual phase spatio-temporal properties. Thanks to this formalism, we model the impact of the AO loop delay on the pre-compensation phase error. We also propose a second phase estimator constructed from phase and log-amplitude past measurements. This estimator is shown to rely on priors on the wind profile. As the wind profile priors are strong in the LEO satellite case, we explore the efficiency of this estimator in this scenario. We question the ability to estimate the LEO pre-compensation phase at PAA using only the satellite slew rate deterministic priors.

In **chapter 6**, we introduce two new estimators, both relying on phase and log-amplitude spatial measurements and statistical priors collected from two different OGS designs. The first estimator exploits a multi-receiver OGS geometry, with one or several

additional apertures in the direction of the PAA. We extend the estimator analytical formalism in order to account for these measurements on several apertures. Secondly, we propose to combine measurements from a laser guide star system and from the downlink beam, to estimate the tip tilt and focus at point-ahead angle. We then assess and discuss the performance of both strategies.

Finally, **chapter 7** aims at evaluating the telecom performance of each estimator, with respect to state-of-the-art methods, and to develop the channel statistical model with the reciprocal point of view. We synthesize the performance of the different estimators and evaluate their impact on the channel capacity. We assess the estimator impact on the telecom performance with an E2E transmission. Finally, we develop a novel strategy to develop a statistical model of the coupled flux statistics impaired by pre-compensation phase errors.

Thesis publications and contributions

Peer-review publications

- Lognoné, P., Conan, J.-M., Rekaya, G., and Védrenne, N. (2023). Phase estimation at the point-ahead angle for AO pre-compensated ground to GEO satellite telecoms. Optics Express, 31(3), 3441-3458.

- Lognoné, P., Conan, J.-M., Rekaya, G., Paillier, L., and Védrenne, N. (2023). Two-aperture measurements for GEO-feeder adaptive optics pre-compensation optimization. Optics Letters, 48(17), 4550-4553.

- [To be submitted] Lognoné, P., Rekaya, G., Montmerle-Bonnefois, A., Paillier, L., and Conan, J.-M. (2023). GEO Feeder uplinks: tip-tilt-focus estimation at point ahead aided by joint measurement of on-axis phase and amplitude and LGS off-axis phase high-orders [Invited paper, MDPI Photonics]

- [To be submitted] Conan, J.-M., Petit, C., Robles, P., Lognoné, P. (2023). Turbulence temporal prediction performance assessment for adaptive optics: application to LEO satellite observation and communication links.

Conference publications

- Lognoné, P., Montmerle-Bonnefois, A., Conan, J.-M., Paillier, L., Petit, C., B. Lim, C., Meimon, S., Montri, J., Sauvage J.-F. and Védrenne, N. (2022, March). New results from the 2021 feedelio experiment-a focus on reciprocity. In 2022 IEEE International Conference on Space Optical Systems and Applications (ICSOS) (pp. 261-266). IEEE.

- P. Lognoné, J.-M. Conan, L. Paillier, N. Védrenne, and G. Rekaya, "Channel Model of a Ground to Satellite Optical Link Pre-compensated by Adaptive Optics," in Optica Advanced Photonics Congress 2022, Technical Digest Series (Optica Publishing Group, 2022), paper SpTu3G.3.

- P. Lognoné, J.-M. Conan, G. Rekaya, L. Paillier, N. Védrenne, "Optimisation of the pre-compensation phase for GEO-feeder optical uplinks," Proc. SPIE 12413, Free-Space Laser Communications XXXV, 1241314 (15 March 2023); https://doi.org/10.1117/12.2648898

- P. Lognoné, J.-M. Conan, G. Rekaya, L. Paillier and N. Védrenne, "Multi-Aperture Ground Receiver to Enhance Adaptive Optics Corrected GEO-Feeder Uplinks," 2023 IEEE International Conference on Acoustics, Speech, and Signal Processing Workshops (ICASSPW), Rhodes Island, Greece, 2023, pp. 1-5, doi: 10.1109/ICASSPW59220.2023.10193470.

Workshops

- P. Lognoné, G. Rekaya, A. Montmerle-Bonnefois, L. Paillier, J.-M. Conan, (COAT-2023). GEO Feeder uplinks: tip-tilt-focus estimation at PAA aided by on-axis phase and amplitude sensing and LGS off-axis high-order measurements.

CHAPTER 1

Ground to space optical links in the space telecom network

Contents

1.1 Context: Space network for a globalized internet

1.1.1 Motivations

Studies from the last decades show that access to broadband internet is an important vector of socio-economical development. As highlighted in the figure 1.1 from the **Global connectivity report 2022** [11], produced by the international telecommunication union (ITU), human development is highly correlated to internet usage. Unfortunately, we also observe

today a connectivity gap in the world, comprising a gap in coverage and a gap in broadband access. The broadband access disparities in the case of Europe are illustrated in figure 1.2. These disparities can be explained by the lack of terrestrial fiber infrastructures that allows to access to broadband internet. Indeed, nowadays, more than 99% of the intercontinental data traffic pass through the submarine network. Isolated regions, such as islands or remote regions where it is expensive, or difficult, because of geographical topography, to install optical fiber links still remain poorly connected to this global network. The implementation of a space based internet network can participate in closing this digital divide.

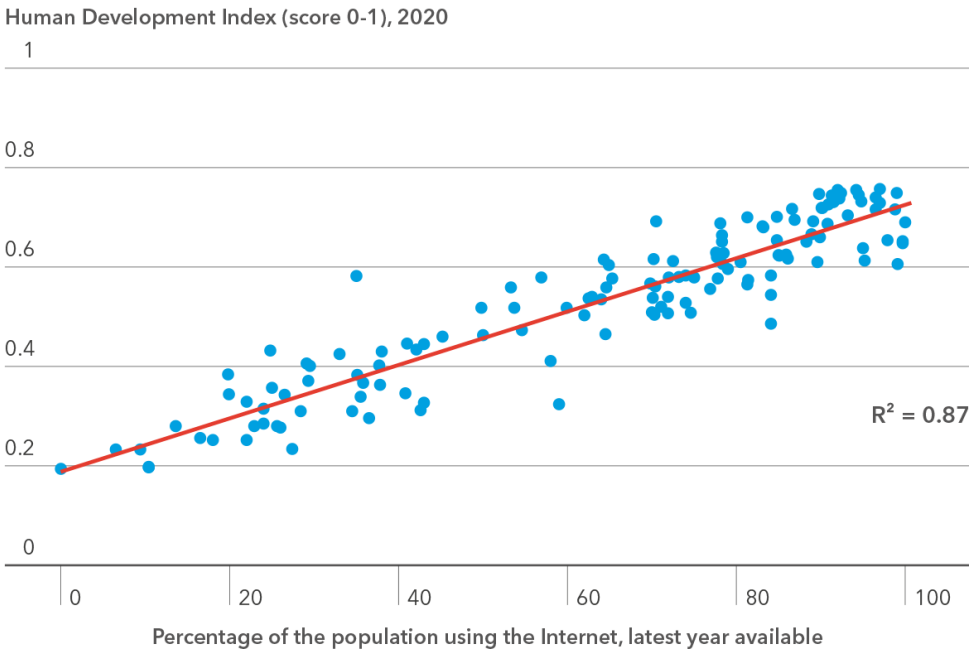

Figure 1.1: Connectivity and human development.
Source: Global connectivity report 2022, ITU and UNDP.

Beyond connecting the unconnected, implementing a space based network can participate to meet the growing demand in data transfer that has not stopped growing in the internet era. By complementing the terrestrial fiber network, the space network is foreseen to offload the terrestrial existing network, allowing to increase the global network capacity.

Satellite based communications already exist and have proved their efficiency for various services, such as TV broadcast or phone/internet access, in isolated areas. However, in most cases, satellites are conceived as standalone communication systems, rarely included in a telecommunication network [12]. For implementing a global internet, there is a need for integrating the space network to the terrestrial network, by transforming satellites in nodes of the network compatible with the terrestrial transmission.

Moreover, including satellite communications in the network offers interesting properties such as network flexibility and resiliency, and intrinsic security. These characteristics are useful to manage the data traffic but also make the network more robust, and secure. It allows communicating in case of crisis (war or natural disaster). We can cite the example of the operations of the association **Télécom sans frontières**, that installs emergency communication centers (antennas and modem for satellite communications) for local and international humanitarian actors during humanitarian crisis [13].

Establishing such space internet networks is nowadays limited by the congestion of the radio-frequency spectrum, whose available frequencies are increasingly rare. Using optical

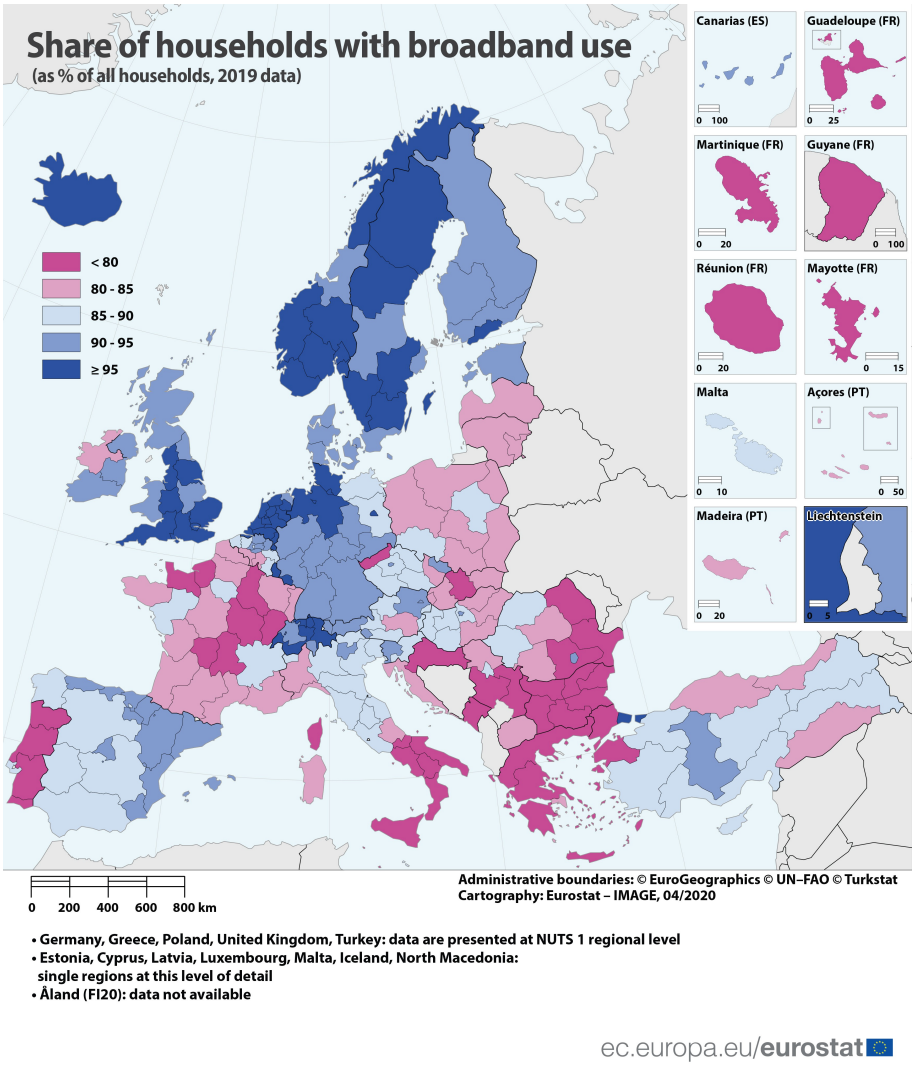

Figure 1.2: Broadband internet access in Europe in 2019.
Source: ec.europa.eu/eurostat

technologies is a solution to overcome this spectrum allocation limitation, while offering very high data rate that are naturally available due to the high optical carrier frequency.

To conclude, a space based telecommunication network integrated to the terrestrial network would allow increasing the global internet coverage and the global network capacity. These networks, can benefit from free space optical links between the earth and satellites to overcome the radio-frequencies data-rate and allocation limitations, while ensuring the connection between the space and terrestrial network. These satellite optical links will be a complementary solution to current radio satellite communications.

1.1.2 Space Optical Network architecture

A satellite network is defined as a set of low-earth orbit (LEO), medium earth orbit (MEO) and geostationary earth orbit (GEO) satellites, located at 500-1200 km, 5000-20000 km and 36000 km above the earth surface, respectively. These satellites are considered as nodes of the network in a mesh topology. The assets from different orbits are combined to take advantage of the visibility of the satellites in higher orbits (such as GEO) and the low latency offered by LEO satellites. These latencies are reported in table 1.1 compared with the latency of intercontinental fiber links issued from [14]. These latencies are determinant for the role of each node in the network, as well as the type of service that can be provided through the satellite network.

Type	Terrestrial					
Link	Europe	North America	Transatlantic	Transpacific	Au to UK	Au to US
Latency	14 ms	30 ms	71 ms	106 ms	244 ms	152 ms
Type	Satellite (roundtrip)					
Link	LEO		MEO		GEO	
Latency	18.4 ms		93.5 ms		272.2 ms	

Table 1.1: Table of the latency encountered 1) for terrestrial fiber links, for links in different regions of the world, 2) Roundtrip satellite links, in function of the satellite orbit.

Service with respect to the link nature

In this network, given the latency constraints, LEO satellites are the closest nodes from the users, whereas GEO satellites are the closest nodes from the core terrestrial network. The data can either transit from the ground to a GEO to a LEO to the ground, or from the ground to a LEO satellite and to the ground. The path taken by the data will depend on the service delivered. This service is determined by the capacity and latency constraints. These services are illustrated in figure 1.3, issued from [15], depicting what kind of link support what service function of the latency and capacity offered by each type of link. Capacity starving application such as streaming or data transfer of earth observation instruments, or less-latency constrained application (such as text messages) can benefit from links with a

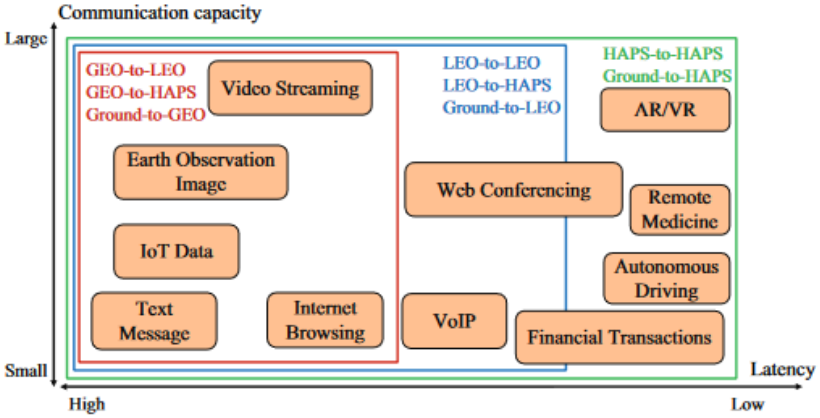

Figure 1.3: Type of service, function of the capacity and latency constraints.
Source: [15]

GEO satellite. However, application relying on ultra-low latencies (VR, Remote healthcare ...) cannot rely either on LEO or GEO communication and need nodes much closer to the user. In the article of [15], it is foreseen to be operated by HAPS (high altitude platform systems). However, it can be operated as well by mobile wireless networks. In this case, as explained in [16], the satellite network can still play a role by connecting the mobile edge cloud to the core network through the satellite network.

Network architecture

The space network is envisioned as a backhaul network, defined as a transmission network between the core network and the edge of the network, close to the users. Therefore, the global architecture is an umbrella architecture. The data is transmitted from the core terrestrial network to the GEO satellite. Thanks to its wide visibility, the GEO satellite aims at relaying the data from the core network to LEO satellites, themselves relaying the data toward the earth.

In this architecture, we can find different types of links, that bidirectionally connect the ground to the satellites and the satellite between themselves. These links can be either optical or radio-frequency links. Figure 1.4 illustrate the links that can be found in this network, with optical links represented in red and radio-frequency links in blue. Optical links are foreseen to be feeder links because of the large capacity offered by optical technologies. These links are mostly considered connecting the GEO satellites to the earth, in order to interconnect the core terrestrial network to the space network. The links between the GEO satellite and other satellites (GEO/LEO/MEO) can be either optical inter-satellite links (OISL) or radio-frequency links. The downlink from the LEO satellite to the ground can also be either optical or RF. Indeed, we can find in the literature several concepts of networks, as the one proposed in [15], considering only optical links for ground-GEO, GEO-ground and GEO-GEO links and radio frequency links for the other segments of the network. Another concept is proposed in the framework of the HYDRON project from ESA [12, 17]. In their proposed architecture, optical links are also foreseen to be implemented for GEO-LEO, LEO-LEO and LEO-ground/ground-LEO links. However, the implementation of such network concept still relies on needed technologies developments necessary to make optical communications more mature and reliable, especially to enable ground to LEO optical links.

The two above described networks are still in the stage of propositions. Still, optical networks design remains an active field of research, as mentioned in [18]. To enable such

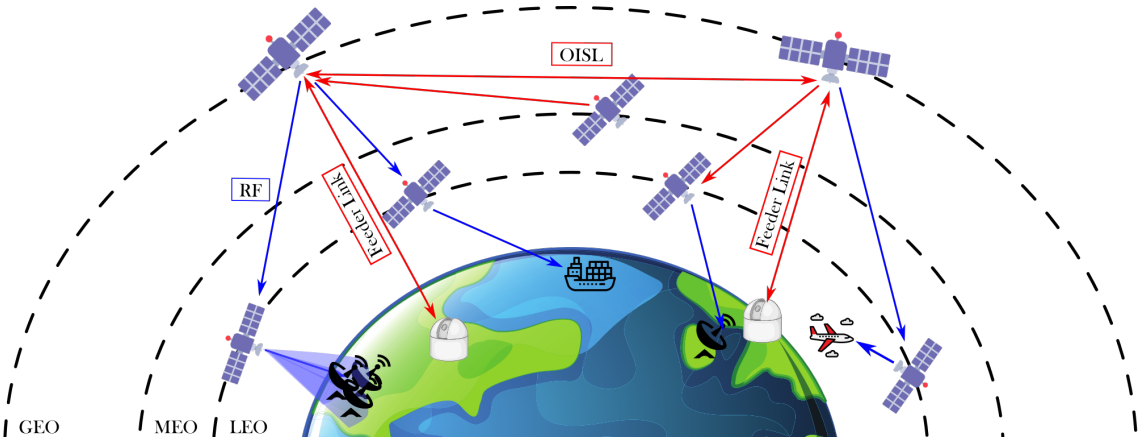

Figure 1.4: Schematic of a satellite optical network

network, the main challenges are: the network optimization, the channel modeling for performance optimization, the pointing tracking and acquisition (PAT) management and automation, and the hardware development that will enable to both increase the optical links' robustness and decrease the systems cost. In this thesis, we focus our study on the optical GEO-Feeder link and on its ability to reliably transmit data at very high data rates.

1.1.3 Optical Feeder link: opportunities and challenges with respect to RF.

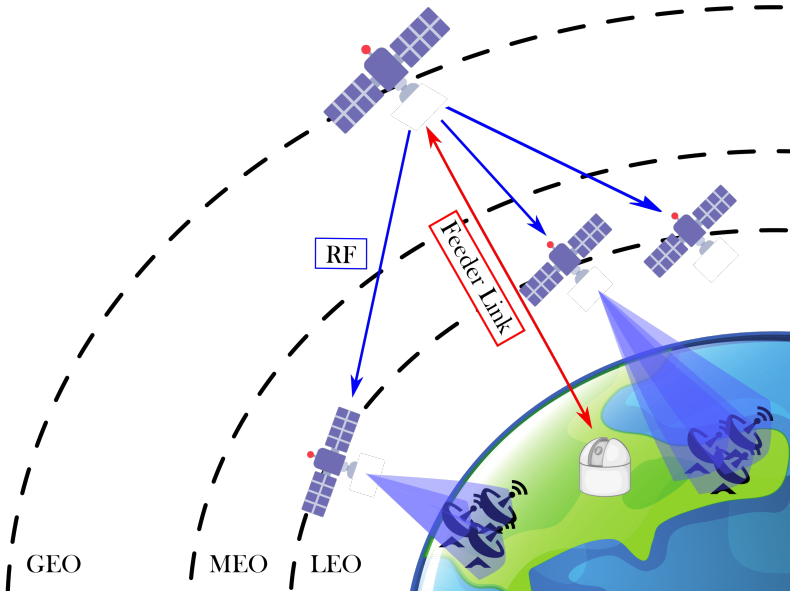

Figure 1.5: Zoom on the GEO-Feeder link.

Due to the GEO satellite role in the network, the link between the earth and the satellite needs to be very capacitive. Optical technologies can allow reaching these high data rates. However, free space optical technologies are less mature than RF communication systems and still face technical challenges that need to be solved. In order to be a long-term viable solution for operators, the development should aim at maximizing the optical data rate while decreasing the cost of the deployed system.

In the following, we compare RF and optical satellite communication and identify the challenge to address in each case.

Opportunities

We list below the different advantages of using optical frequencies for very high throughput satellite (VHTS) links, as explained in [19] from the **INMARSAT** satellite operator point of view.

Capacity. In the radio frequency domain, three main frequency bands are considered to be used for VHTS, at different levels of technology maturity: the Ka-band, the Q/V band and the W band. These bands are illustrated among the whole spectrum in figure 1.6.

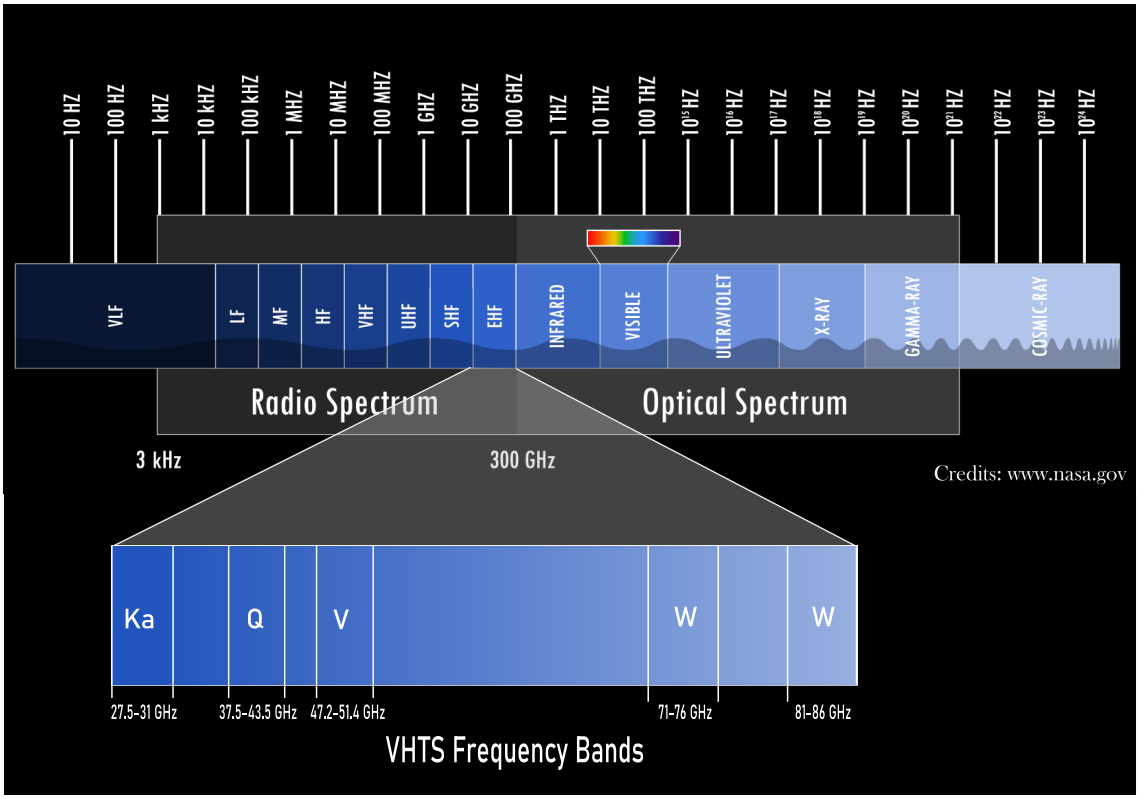

Figure 1.6: Electromagnetic spectrum, with an emphasis on VHTS frequency bands distribution. Source: www.nasa.gov (modified).

- **The Ka-band** is located in the 27.5-31GHz radio-frequency range. However, due to regulations, only 2.5 GHz of bandwidth per polarization is available, i.e., 5Ghz in total. It is the more mature RF technology for high-throughput satellites, with currently more than 60 satellites in orbit. The latest HTS satellites launched, and their capabilities, are reported in table 1.2. The best performance is achieved by **KONNECT VHTS**, an EUTELSAT satellite launched in 2022 reaching a total throughput of 500 Gbps.
- **The Q/V band** is located in the 37.5-43.5 GHz and the 47.2-51.4 GHz frequency range, with 5GHz available bandwidth per polarization, i.e., 10 GHz in total per gateway. This technology is at the demonstration stage, as shown in the QV-Feed ESA project [20, 21].
- **The W band** is located in the 71-76 GHz and 81-86 GHz frequency range, with 5GHz available bandwidth per polarization, i.e., 10 GHz in total per gateway. This

Satellite	Viasat 2	KONNECT	SES-17	KONNECT VHTS
Company	Viasat	Eutelsat	SES	Eutelsat
Launch year	2018	2020	2021	2022
Coverage area	America	Africa, Europe	America	Europe
Band	Ka	Ka	Ka	Ka
Data rate	300 Gbps	75 Gbps	400 Gbps	500 Gbps

Table 1.2: Example of radio high throughput GEO satellites.

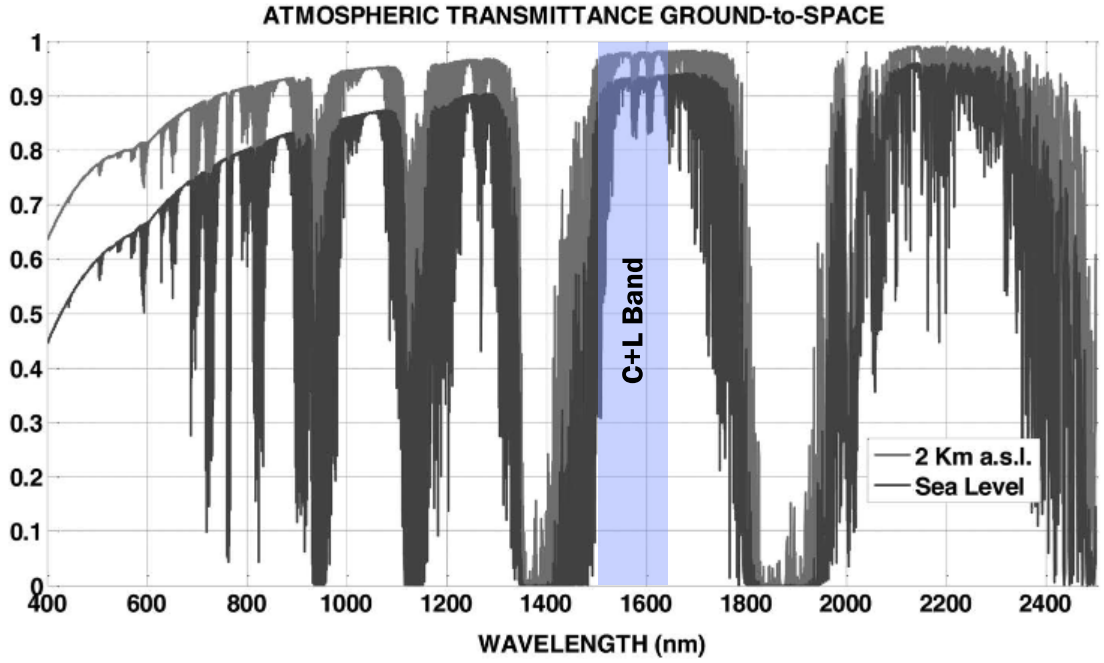

Figure 1.7: Atmospheric transmittance function of the wavelength.
Source: [25]

technology is even more immature than Q/V band technologies. A first demonstration was done in 2021 [22] within the scope of the W-Cube project funded by ESA [23, 24].

In comparison, two frequency bands are envisioned to be used for free-space optical communications, due to the atmospheric transmission window, as illustrated in 1.7. Historically, the band around 1064 nm was envisioned to be used due to the existence of high power lasers at this wavelength. It is used for the EDRS system and the Alphasat satellite payload [26]. However, most of scientific and industrial community turned today towards the 1550 nm wavelengths, in order to take advantage of off-the-shelf telecommunication components developed at this wavelength for terrestrial fiber communications. It is envisioned to use the commonly called C (1530-1565 nm) and L (1565-1625 nm) bands [27]. The C and L bands offers 5 THz and 14 THz bandwidth, respectively. This band is as well illustrated in figure 1.7. We can observe that the C+L bandwidth is smaller than the total transmission window. It is indeed limited by the amplifier bandwidth. Considering the wavelength multiplexing recommendations from ITU, the useful bandwidth is 1 THz wide [19]. Overall, even using only the useful C band, the optical bandwidth is 100 to 200 times greater than the RF bandwidth.

Regulation. The Ka-band is already used by other users in space or on earth, therefore, we observe a congestion of the spectrum at these frequencies. It is however not the case for the Q/V and W bands [19]. In comparison, the optical spectrum is completely unregulated. Indeed, the low optical beam divergence prevent the beams to interfere. We note that this low beam divergence also brings inherent security to the link.

Ground segment. To use Ka-band at its full potential and reach hundreds of Gbps transmission, it is needed to use at least 50 gateways on earth. This number of gateways decreases to around 20 for Q/V and W bands. However, these frequency bands are more

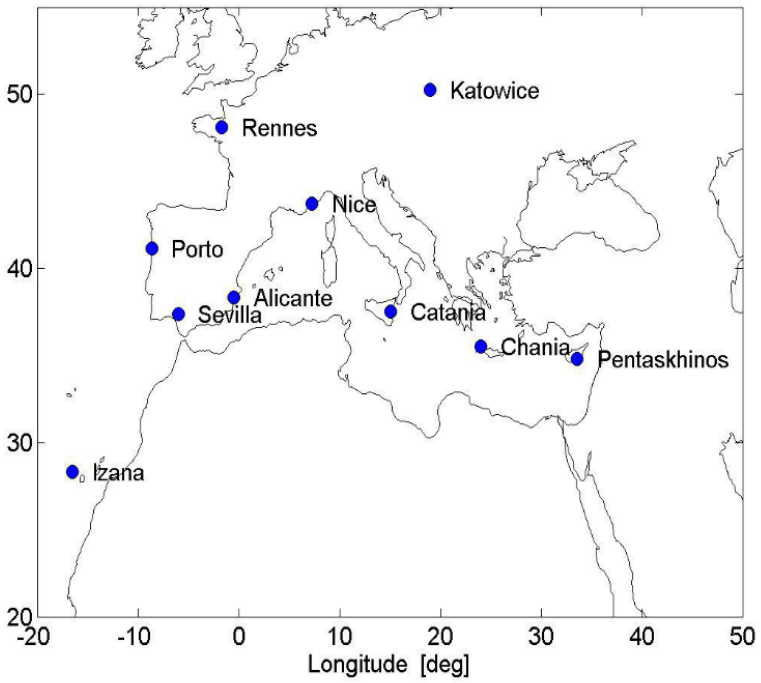

Figure 1.8: Example of site locations for an OGS network providing 99.9% link availability. Source:[28]

sensitive to atmospheric effects and weather. Therefore, there is a need for dynamic ground segment management and scheduling.

Concerning optical links, there is a potential of transmitting Tbps of data with only one point-to-point link, reducing greatly the number of optical gateway. However, due to the very high sensitivity to clouds and atmospheric effects (especially turbulence) of optical links, we still need a network of optical gateways on the ground to ensure the transmission with high reliability. It was shown in [28, 29] that a network from 5 to 10 OGS in the European region was sufficient to ensure 99.98% link availability. Such network architecture is illustrated in figure 1.8.

Challenges

Optical links show great potential in achieving very high capacities, in a secure unlicensed way, requiring smaller network of stations. However, as mentioned above, this OGS network is still necessary due to the weather and atmospheric effects impairing the optical link. To use satellite optical communication links at their full potential, several challenges still need to be addressed to enable optical Feeder link technologies and ensure its reliability. In particular, the question of atmospheric turbulence mitigation needs to be solved (either by digital, physical techniques or including turbulence link availability in network scheduling and sizing).

In this thesis, we focus on the mitigation of the atmospheric turbulence effects that impairs optical GEO-Feeder uplinks. To comprehensively explain how atmospheric turbulence affects the optical flux coupled aboard the satellite and the digital signal transmission quality, we start by describing the point to point link and its main building blocks, in order to highlight the technological drivers.

1.2 Point to point optical link

Due to the low beam divergence, the ground to GEO link is a point-to-point link, on the contrary to radio link that can be a broadcast link. This is a bidirectional high data rate link that uses several WDM channels both in up and down.

In the following, we describe the complete system, starting by the bidirectional link geometry. Then, we describe the current envisioned design for the ground stations and the satellite payloads.

1.2.1 Bidirectional optical link

1.2.1.1 System geometry

The GEO satellite is located on the geostationary orbit, at 35786 km above the earth surface, on the equator latitude. The longitude position depends on the considered satellite. In this study, we consider the optical ground station to be located at European latitudes. Therefore, the optical link with the satellite is at a 30° elevation.

From this link geometry, we can compute the effective distance of the satellite to the OGS on the line of sight (LOS) [30]. Denoting ϵ_0 the elevation angle, R_E the earth radius, H_o the orbit height and d_{sat} the satellite distance to the OGS, all represented on figure 1.9, we can show that:

$$d_{sat} = R_E \left[\sqrt{\left(\frac{H_o + R_E}{R_E} \right)^2 - cos^2(\epsilon_0)} - sin(\epsilon_0) \right] \tag{1.1}$$

where $r = H_o + R_E$ on the figure. Applying this equation, we find a satellite distance of $d_{sat} = 38611$ km.

The same reasoning can be applied to the calculation of the thickness of the atmospheric layer along the line of sight. At zenith angle (90°), the thickness of atmosphere with significant impact on optical field is equal to 20 km. Therefore, by applying Eq. 1.1, we find an atmospheric layer on the line of sight thick of 40 km.

Having described the different distance parameters, we describe the overall bidirectional link geometry in figure 1.10. The GEO satellite emits a laser beam that propagates through approximately 38000 km in space (in the void) before reaching the atmosphere. There, it propagates through 40 km of atmosphere before reaching the OGS. From the uplink perspective (from the earth to the satellite), we need to point ahead of the downlink

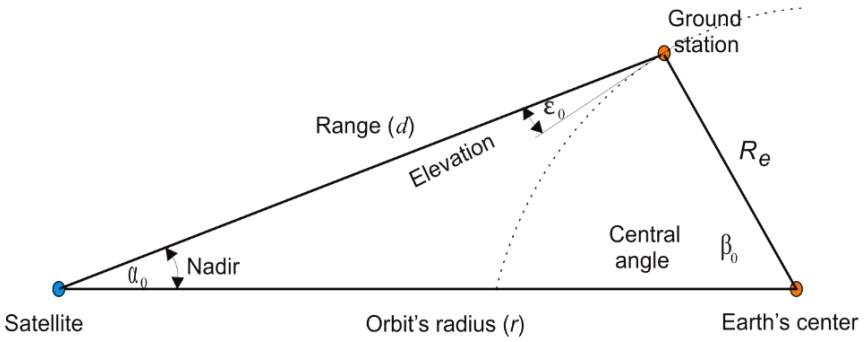

Figure 1.9: Schematic of the system geometry, to compute the distances on the line of sight. Source:[30].

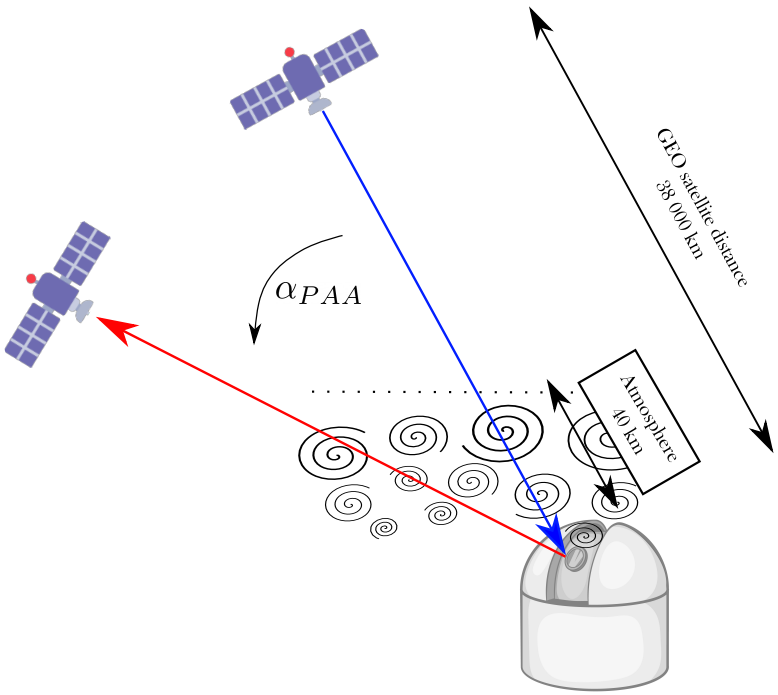

Figure 1.10: Schematic of the bidirectional optical link geometry between the GEO satellite and the OGS. The downlink is depicted in blue, the uplink is depicted in red.

because of the angle separating the downlink and the uplink due to the earth rotation, called the point-ahead angle.

Point-ahead angle

Since we operate with geostationary satellites, they consistently remain positioned directly over the same spot on Earth. The point-ahead angle arises due to the Earth's rotation while the satellite-to-ground and ground-to-satellite beam propagation occurs. This phenomenon occurs because the time taken by the beam to traverse these distances is no longer insignificant, amounting to approximately 2.4 milliseconds.

The point-ahead angle is defined as follows:

$$\alpha_{PAA} = \frac{2V_{sat,\perp}}{c} \tag{1.2}$$

where $V_{sat,\perp}$ is the transverse speed of the satellite in the OGS referential [31, 32]. The value considered at European latitudes, considered in this study, is a point-ahead angle of **18.5 µrad**. This angular separation will play a major role in the quality of the correction of the beam disturbances by the atmosphere.

In the following, we describe separately the downlink and uplink, and the effect of the atmosphere on both beams, qualitatively.

1.2.1.2 Downlink

The downlink beam is described in figure 1.11. The GEO satellite emits a laser beam from its orbit. In the satellite plane, this beam is a Gaussian mode. After propagating through $\sim$ 38000 km of void, the beam enters the atmosphere. At the entry of the atmosphere,

because of the beam divergence, the optical beam can be considered as a plane wave (with respect to the OGS telescope diameter size). The beam propagates through 40 km of atmosphere and reaches the OGS telescope pupil. At the entrance of the pupil, the phase and amplitude of the beam are distorted due to the atmospheric turbulence, as depicted in B. in the figure 1.11. Afterward, it goes through the optical system. The system can be equipped with a phase correction system (called adaptive optics system). In this case, the phase and amplitude are represented in C. in the pupil plane. The last step is to inject the light toward a single mode fiber, located in the focal plane of the telescope. The obtained diffraction pattern at the focal plane is represented in E and F. The coupled light is then sent toward the telecommunication receiver.

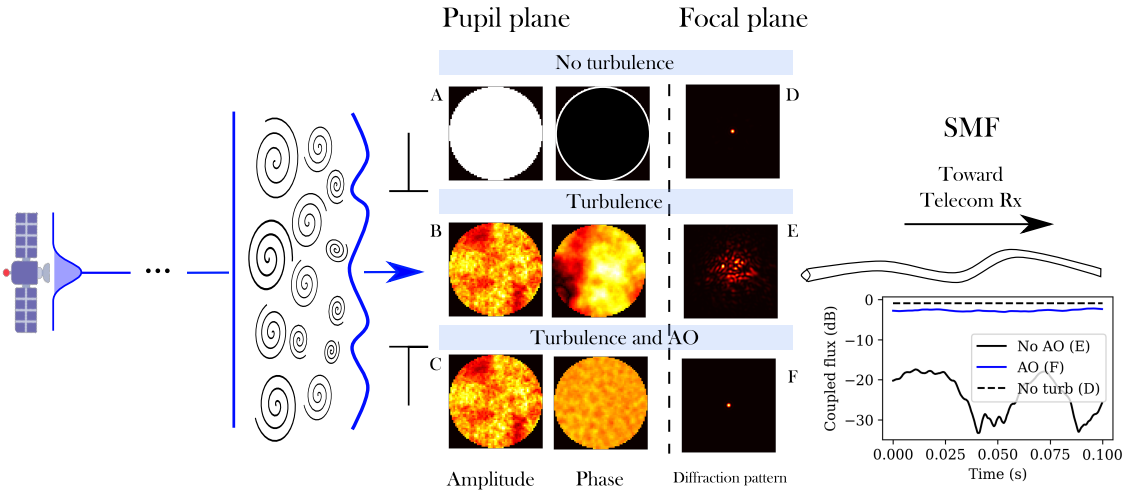

Figure 1.11: Schematic of the downlink propagation through the atmosphere, with the received complex field represented for three scenarios both in the pupil and focal planes: no turbulence, turbulence without and with AO correction.

To understand how atmospheric turbulence impacts the received signal, we comment on the diffraction pattern in the different cases. We observe a severe degradation when the beam is affected by turbulence without adaptive optics correction. These distortions induce heavy fluctuations of the coupled flux into the SMF. When using an adaptive optics system, by correcting the phase of the incoming beam, the shape of the diffraction pattern is improved, getting closer to the "no turbulence" diffraction pattern in D. Therefore, there are no or few coupled flux fluctuations in the SMF anymore. The need to couple the signal into a single mode fiber, is to amplify the signal after reception before the digital signal processing stage.

1.2.1.3 Uplink

In the uplink scenario, a laser mode is sent ahead of the downlink optical axis. As described in figure 1.12.A., if there is no turbulence, the emitted laser Gaussian mode goes through the pupil and, after the 38000 km of propagation, is received in the satellite plane. In this case, we observe a diffraction pattern in the satellite plane much larger than the satellite telescope aperture size, due to the beam divergence.

In real transmission, the atmospheric layer, close to the ground, distorts the wavefront of the beam, as described in figure 1.12.B. Therefore, after the propagation through the free space (or void), the issued diffraction pattern in the satellite plane is a speckled pattern whose speckles' size are very large with respect to the satellite telescope entrance pupil. This speckle pattern fluctuates in time and in space. We can decouple the spatial effects

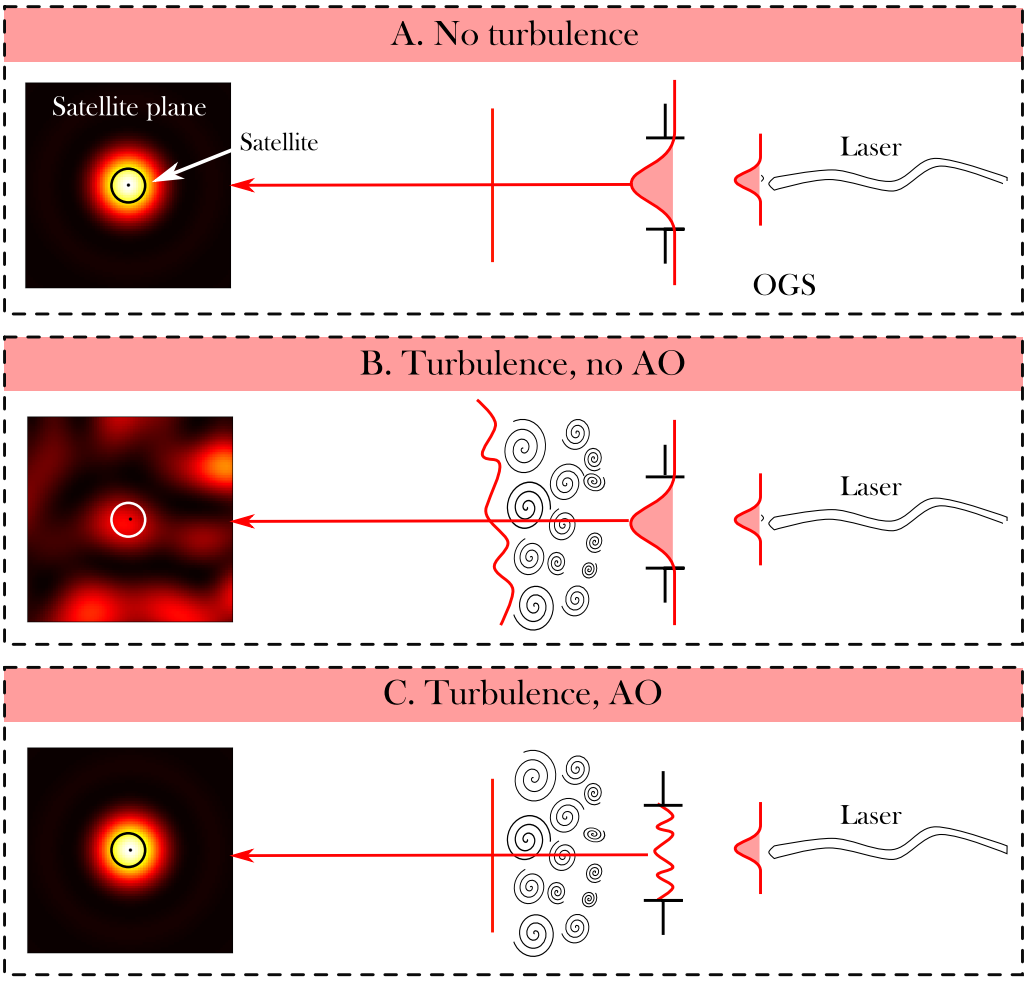

Figure 1.12: Schematic of the uplink propagation through the atmosphere, with the received diffraction pattern obtained in the satellite plane represented for three scenarios both in the pupil and focal planes: no turbulence, turbulence without and with AO correction.

impacting this diffraction pattern as the beam wander and the scintillation effects. The beam wander refers to the displacement of the instantaneous pattern barycenter in the satellite plane, whereas the scintillation effect refers to the speckles' spatial arrangement variation within the spot. This pattern spatio-temporal fluctuations induce the fluctuation of the coupled flux aboard the satellite.

As for the downlink, we can apply phase correction with adaptive optics system, to mitigate the atmospheric turbulence effects, as described in figure 1.12.C. In the uplink case, as the turbulence is concentrated close to the ground, the phase correction has to to be done at the OGS. Applying a phase distortion to the beam before its propagation is called **pre-compensation**. If the phase correction fits the turbulence phase perturbation encountered by the beam, the beam phase is supposed to be plane at the exit of the turbulence. Therefore, the expected diffraction pattern in the satellite plane would be the large Airy pattern described in figure 1.12.A. However, if the pre-compensation is not accurate, the diffraction pattern still experiences beam wander and scintillation. Hence, the coupled flux aboard the satellite still fluctuates. The techniques to choose the pre-compensation phase of the uplink beam will be discussed in the section. 2.5.

1.2.2 Optical ground stations

In this section, we describe the different blocks at the OGS, in order to identify the critical elements that need to be tailored in our study. A block diagram of the OGS is depicted in figure 1.13. It is composed of an optical system, and a telecommunication transceiver/receiver (Tx/Rx). The optical system is composed of a telescope and an adaptive optics system, to collect and apply a phase correction on the received or emitted beam. The telecommunication Tx/Rx is composed of a digital Tx/Rx, that encodes or decodes the information signal, and an optical Tx/Rx, that either maps the information signal to the emitted laser beam (in Tx), or detects and maps the optical signal to an information signal in reception. Additionally, OGS are equipped with weather and turbulence monitoring modules to evaluate the link availability.

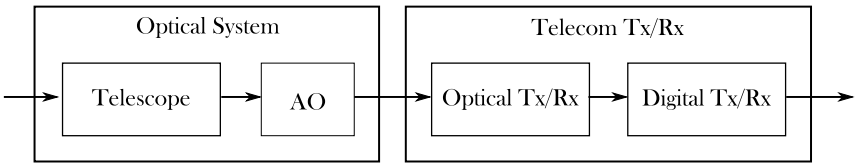

Figure 1.13: Block diagram of the OGS main components (downlink point of view).

The main drivers of this emission/reception chain will be the telescope diameter size, the adaptive optics parameters (such as the number of corrected modes and the correction frequency) and, in the case of the uplink, the emitted power. Digital telecommunication module comes back to design digital signal processing and coding algorithm matching the free-space optical channel properties and the system requirements. Indeed, on the ground, this system can benefit from many power and memory resources, as well as state-of the art components developed for terrestrial fiber communication systems.

Telescope diameter. For the telescope diameter design, the sizing factor is the power link budget. Due to the large distance of the GEO satellite, the link budget is very constrained by the geometrical losses [33]. These losses are induced by the beam divergence, proportional to the inverse of the square diameter. This is also known in the telecom domain as antenna gains [34, 35]. The larger is the ground aperture, the smaller are the geometrical losses. However, the larger is the telescope aperture, the larger are the phase disturbance and the coupled flux fluctuation. Therefore, there is a trade-off to find in order to optimize the link budget. The current diameter envisioned are in the order of ~ 60 cm. This diameter dimensioning constraint can be put in perspective with other type of links, such as LEO links and QKD links. For LEO links, as the satellite is much closer to the earth, geometrical losses are much smaller and the power link budget is less constrained. Therefore, the OGS system can be designed with smaller telescope diameters. However, for QKD links, as it is by nature a photon starved link, much bigger telescopes are foreseen to collect as many photons as possible, within the $+1$ m range [36, 37].

Adaptive optics system. The AO system sizing consists in dimensioning the number of turbulent phase spatial frequency that the system can correct (number of correction modes) and the correction speed. Both of these elements are sized with respect to the telescope diameter and the turbulence conditions of the OGS site. This system dimensioning will be detailed in section 2.7.

Power source. In the uplink point of view, there is a need to emit powerful laser sig-

(a) Credits: IQOQI Vienna, Austrian Academy of Sciences (b) Credits: NASA

Figure 1.14: Example of existing OGS. (a) ESA OGS, Tenerife. (b) OGS-2, Hawaii.

nal in order to satisfy the power link budget. This led to the development of High Power Optical Amplifiers (HPOA) [38], that cumulates several amplification stages to reach a 50 W power emission. In order to reach the 100 W class power amplifier, coherent beam combining technologies are required.

Optical bench Finally, the optical bench needs to be optimized, in order to reduce aberrations induced by the optical components. It is also needed to shape the emitted laser beam in order to account for the central osculation for large emission diameters.

As GEO-Feeder link enters in it demonstration phase, several OGS are already designed, in construction or even in activity. We give the main properties of the OGS designs from the literature in table 1.3.

An example of the FEELINGS optical ground station is given 1.15, with its main characteristics. It is the future ONERA's OGS. In the following of this work, we will consider the parameters associated to FEELING's design, i.e., a 60 cm diameter, a 50 W power emission and a monostatic scheme. Monostatic means the uplink and downlink are received and emitted through the same telescope aperture.

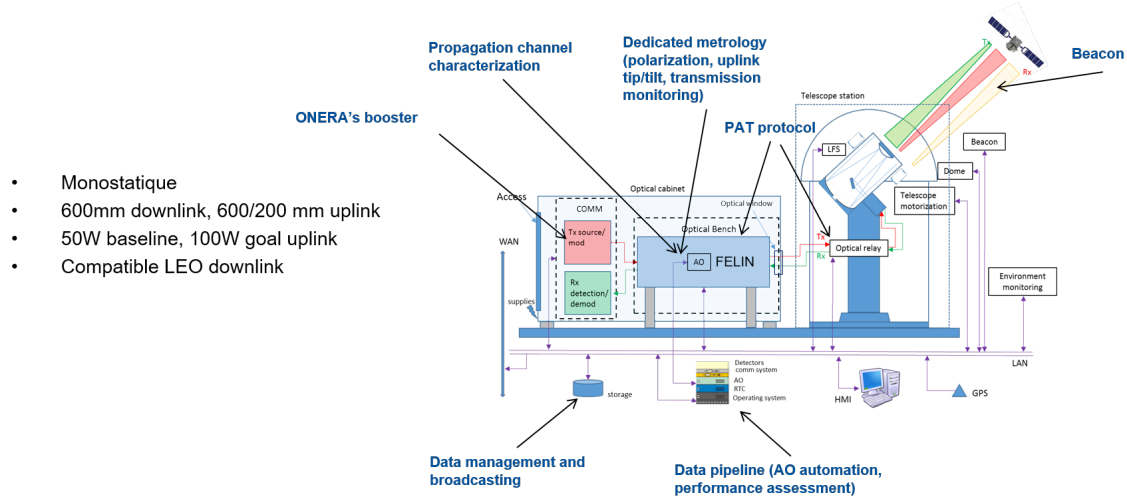

Figure 1.15: Feelings optical ground station scheme and main properties [46].

Name	Location	Owner	λ (µm)	Rx Ø	Tx Ø	Power	AO	In use	Reference
OGS-1	Table Mountain (USA)	NASA	1.55	1 m	1 m	10 W	×	×	[39]
OGS-2	Hawaii (USA)	NASA	1.55	60 cm	15 cm	5.4 W	×	×	[40]
LCOT	Greenbelt (USA)	NASA	1.55	70 cm	70/15 cm	4×20 W	×	×	[41]
ESA OGS	Tenerife (Spain)	ESA	1.064	1 m	20 cm	50 W	×	×	[42]
			1.55						[43]
Okinawa OGS	Okinawa (Japan)	NICT	1.55	1 m	1 m	×		×	[44]
Name	Munich (Germany)	DLR		80 cm	80 cm		×	×	[45]
FEELINGS	Fauga (France)	ONERA	1.55	60 cm	60 cm	50W	×		[46]
FROGS	Calerne (France)	CNES	1.55	50 cm	50 cm	20W	×		[47]
A-OGS/M-OGS	Zimmerwald (Switzerland)	ADS	1.55	80 cm	20 cm	5W	×		[47]

Table 1.3: Table of current and in construction OGS properties.

1.2.3 Satellite payload

The satellite payload is composed of an optical system to collect the light, and of a telecommunication Tx/Rx module. However, there is a particularity in the GEO satellite payload architecture that needs to be underlined. As mentioned in section 1.1.2, the GEO satellite aims at relaying data from the optical feeder link to RF users. Therefore, there is a need to convert the data issued from the optical signal to the radio-frequency signal. Three possible architectures are studied: analog transparent, digital transparent and regenerative [19, 48–50].

Analog transparent architecture

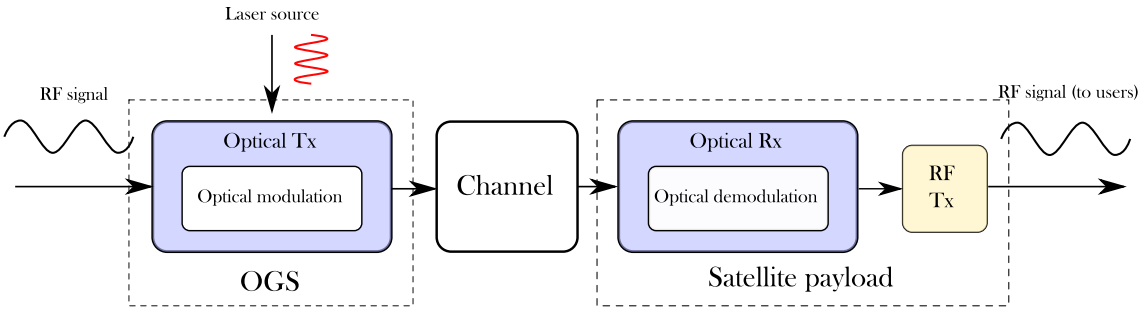

Figure 1.16: Scheme of the analog transparent architecture (at the OGS and onboard the satellite).

A simplified scheme of the analog transparent architecture is depicted in figure 1.16. In this architecture, the RF signal to be transmitted to users modulates directly the optical carrier at the OGS. The modulated optical signal is sent through the channel and demodulated onboard the satellite. Then, the recovered RF signal is sent toward the RF users. This technique is known as RF over FSO [51, 52]. The advantage of this technique is to decrease the satellite payload complexity. However, there is no reliability mechanisms protecting the signal against the distortions of the optical beam by the turbulence (i.e., no channel coding). This technique requires therefore either very high power amplifiers on the ground, either physical fading mitigation techniques.

Digital transparent architecture

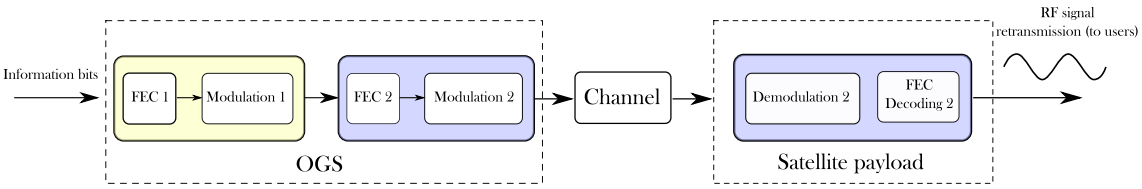

Figure 1.17: Scheme of the digital transparent architecture (at the OGS and onboard the satellite). The processing in the RF domain is depicted in yellow and in the optical domain in blue.

A simplified scheme of the digital transparent architecture is depicted in figure 1.17. In this scheme, the information to transmit to the user is encoded with a first FEC (FEC 1) and modulated in the radio-frequency domain (modulation 1). This encoded RF signal is then digitized and encoded with a second FEC (FEC 2) and the optical signal is modulated (modulation 2) before its emission through the channel. This second FEC protects the bits against the free-space optical optical channel distrubances. In reception, the optical signal

is demodulated and decoded. The output bitstream, that is composed of the digitization bits of the RF frame, is then converted to a RF signal, then relayed to the users.

It is called transparent because there is no decoding of the information message onboard the satellite. The consequence is that, to encode the same information message, the frames are longer, due to the two encoding stages. However, it requires less processing onboard the satellite.

Digital regenerative architecture

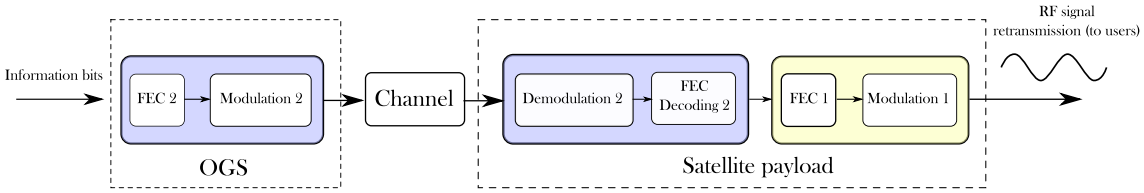

Figure 1.18: Scheme of the regenerative architecture (at the OGS and onboard the satellite). The processing in the optical domain is depicted in blue and in the RF domain in yellow.

The last option is the digital regenerative scheme. A simplified scheme of this architecture is depicted in figure 1.18. In this scheme, the original bit-stream carrying the information is encoded by the FEC 2 and mapped to the optical signal at the OGS (without transiting through the RF domain) before its emission through the channel. Onboard the satellite, the optical signal is demodulated and decoded. The decoded bits are the message information bits. These bits are then encoded by the FEC 1 and mapped to the RF signal before its emission toward the users.

While this scheme benefits from an enhanced performance against fadings, it comes at the cost of significantly increased satellite processing complexity. Furthermore, the ability to adapt to new RF transmission standards is lost in this scheme [50].

We underline that the FEC coding and modulation part protecting the information against the optical channel disturbances are common to the digital transparent and the regenerative architecture. Hence, in this work we consider the transmission chain starting from the FEC encoding 2 to FEC decoding 2 onboard the satellite, as described in blue in figures 1.17 and 1.18.

Experimental payloads

Current flying payloads aim at demonstrating the feasibility of a bidirectional high data rate optical link. Therefore, at this stage, the conversion of the optical frames to RF frames is not yet implemented. In the GEO orbit, we can cite the following satellites hosting optical payloads: Alphasat (ESA – equipped with LCT terminals [42, 53]), the LCRD optical payload onboard the STPSat-6 satellite (NASA [54]) and LUCAS payload (NICT and JAXA [44]). Most of these payloads were originally used to perform inter-satellite optical links, and are now used to perform ground-to-GEO channel characterization.

We focus our attention on the last payload sent in the GEO orbit, the TELEO payload, designed by Airbus and sent onboard the Badr-8 satellite in May 2023 [47, 55]. This payload aim at demonstrating high data rate bidirectional optical links. It is designed to receive 3 optical channels: one to demodulate OOK-modulated optical signals at 10 Gbps, a second for redundancy and a third to demonstrate RF over optics technologies. It is also designed to emit a two levels coherent modulated optical downlink.

1.3 Telecommunication transmission chain

In this thesis, we explore the ability to reliably transmit data at very high data rates from the ground to a GEO satellite thanks to optical signals. It is therefore important to define what is the reliability and what are the achievable data-rates. From a telecommunication point of view, we define the reliability as the ability to transmit information bits with an error probability that tends to 0. Threshold as low as 10^{-12} are generally considered, after FEC decoding. Concerning the data-rate, it needs to be higher than 1 Tbps. The ability to reliably reach this data rate is strongly related to the optical channel properties and the optimization of the digital and optical transmission chain.

In this section, we define the system error-probability function of the data-rate and the overall system properties (including the channel properties). Therefore, we describe the different blocks of the optical telecommunication transmission chain. The following description is general and common to all optical communication systems. However, we will illustrate it with the chosen parameters for optical GEO-Feeder links.

1.3.1 Transmission chain

A telecommunication system is composed of a transceiver and a receiver processing the signal in the digital and optical domain. The processing operations in the digital domain protect the data against channel distortions and shape the data into an electrical signal so as to maximize data-rate and bandwidth efficiency, while minimizing the bit error probability in reception. The processing operations in the optical domain map the electrical signal carrying the information to the optical carrier. We start our description by considering a one subcarrier system.

Figure 1.19 illustrates the transmission chain of the telecom system. The input bits are encoded using a FEC encoder and mapped to an electrical baseband signal. This signal modulates the emitted laser beam, which is amplified before its emission through the channel. When reaching the satellite aperture, the received optical beam is coupled to a single-mode fiber. After a pre-amplification stage, the optical signal is detected and demodulated. The resulting electrical signal, affected by channel distortions and noise, is sampled in the digital domain, and mapped to the symbols finite set. Finally, the associated bit-stream is decoded. We describe each blocks in the following.

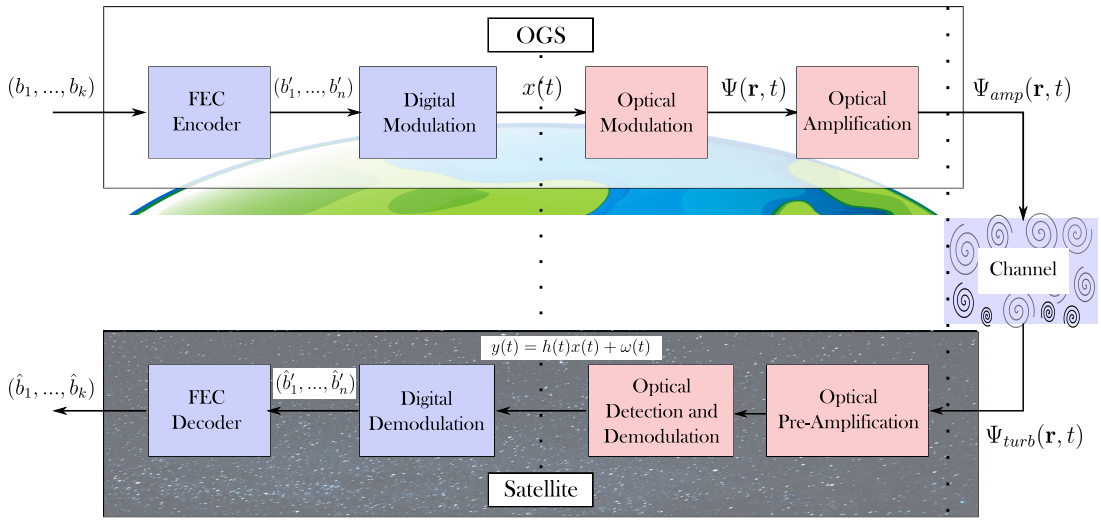

Figure 1.19: Telecommunication chain of the ground to satellite link. The blocks in blue depicts the operation in the digital domain and, in red, in the optical domain.

1.3.2 Forward error correction

The aim of the FEC encoder is to protect the bit stream against the channel induced errors, by adding bit redundancy. The FEC encoder is defined as a linear application f that maps an input bit-stream of k elements into a bit-stream of n elements, as:

$$\begin{aligned} f: \quad \mathcal{X}^k &\rightarrow \mathcal{C} \in \mathcal{X}^n \\ (b_1, ..., b_k) &\mapsto (b'_1, ..., b'_n) \end{aligned}$$

where $\mathcal{X} = \{0, 1\}$ and $\mathcal{X}^k$, resp $\mathcal{X}^n$, are the ensembles of k, resp n, bits taking their values in $\mathcal{X}$. $\mathcal{C}$ that is included in $\mathcal{X}^n$, is the finite set of codewords of the considered code. The code is characterized by k, the code dimension and n the code length. The code rate is $r_c = k/n$.

Famous FEC codes that proved to be very efficient and achieving the theoretical transmission limits of the channel are LDPC codes [56]. These codes are characterized by a sparse parity check matrix, limiting the decoding complexity. These codes are very efficient to correct noisy channel impairments. One other famous type of FEC codes are the cyclic codes, including the BCH and Reed-Solomon codes, that are more suited to correct burst errors. In order to be robust to these two types of channel distortions, we use a concatenation of an inner code and an outer code separated by an interleaver. An interleaver is a permutation operator. An example of the serial combination of an inner code and an outer code is given in figure 1.20.

Figure 1.20: Illustration of the serial FEC concatenation scheme.

This serial FEC concatenation scheme is the one recommended in satellite communication, in the DVBS2 format [57]. The DVBS2 format is a norm standardizing the whole communication chain. The encoding and decoding schemes are a BCH code followed by an interleaver and an LDPC code. In a recent publication, another coding scheme was proposed, called ARA-LDPC and photograph-based raptor like codes [58]. The advantages of these new codes is to decrease the LDPC encoding/decoding hardware complexity, at very high data rates.

1.3.3 Digital modulation

To transform the input encoded bit-stream $(b'_1, \ldots, b'_n)$ into a continuous-time signal, it is first necessary to map the bits into discrete symbols $(s_1, \ldots, s_l)$ where $s_l \in \mathcal{C}$. These symbols are then mapped into levels of signal amplitude a_l. This process is known as digital modulation.

The set of symbols, referred to as the constellation, can be either real or complex-valued. The number of elements in $\mathcal{C}$ depends on the number of optical wave states (both phase and amplitude states) used to transmit the information. It also determines the number of bits mapped to one symbol, which is $\log_2(M)$ bits per symbol, where M is the constellation size.

For instance, the on-off keying (OOK) constellation, which is an amplitude modulation with two levels of amplitude, maps one bit to one symbol. It encodes a '0' as an amplitude of 0 and a '1' as an amplitude of A. An illustration of this constellation is provided in Figure 1.21a. There are higher-level amplitude constellations, such as amplitude shift

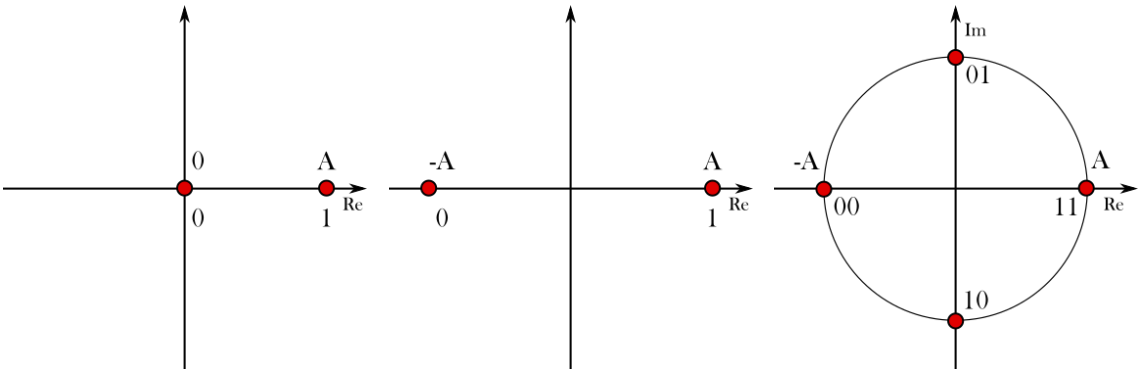

(a) OOK (b) BPSK (c) QPSK

Figure 1.21: Example of usual real and complex constellations.

keying (ASK). Figures 1.21b and 1.21c depict complex constellations with 2 and 4 levels, respectively, where the real and imaginary parts of the symbol values are plotted in a 2D plane.

The advantage of using high order modulations is to increase the spectral efficiency, that is defined as the number of bits per second per unit of used bandwidth: $\eta = D_b/B$, where D_b is the binary data rate and B the signal bandwidth.

The constellation is also characterized by its average symbol energy E_s. Assuming a constellation whose symbols follow a uniform distribution (meaning that they have the same probability of occurrence), this energy is equal to:

$$E_s = \frac{1}{M}\sum_{i=1}^{M} a_i^2 \tag{1.3}$$

and $E_b = E_s/\log_2(M)$.

New fields of telecommunications research focuses on the constellation shaping using new methods such as the constellation probabilistic shaping to optimize the data rate (not considering a uniform distribution for the symbol occurrences) or geometry shaping to optimize the power efficiency of the system (optimizing the distance between the symbols) [59].

These symbols are then mapped into an electrical signal, that is called the **baseband signal** $x(t)$. This signal will modulate the laser. It is a continuous signal that has a given frequency bandwidth, relative to the symbol period T_s. A step of pulse shaping is needed in order to optimize the baseband signal bandwidth occupation. Classically, the baseband bandwidth is equal to $B_b = \frac{1}{T_s}$ Hz, and $B_m = \frac{2}{T_s}$ Hz when modulated around a carrier. The symbol-rate R_s of the modulated signal is equal to $R_s = B_m/2$ and the data-rate R_d is equal to $R_d = R_s\log_2(M)$ bit/s.

1.3.4 Optical modulation

The baseband signal $x(t)$ modulates the laser, which is the carrier of the information signal. We distinguish two types of optical modulation: intensity modulation and coherent modulation (modulating the signal in phase and amplitude), that can be achieved either by direct or external modulation.

Intensity modulation is commonly achieved through direct modulation, which involves modulating the laser intensity with a time-varying voltage. An example of direct modulation is on-off keying (OOK) modulation, where two signal intensities are used to transmit

information (intensity 0 and intensity I). This scheme offers a low-cost and low-complexity modulation approach. However, the modulation rate is limited by the laser itself, which has an incompressible response time.

Coherent modulation involves modulating the laser in both phase and amplitude. This is achieved by separating the real and imaginary parts of the baseband signal and modulating two lasers in phase and quadrature. Typically, this is accomplished using an external modulator, such as a Mach-Zehnder modulator, which enables higher modulation rates compared to the direct modulation scheme. The two beams are then recombined to produce the output laser beam. Coherent modulation schemes allow for higher data rates and offer the advantage of increased detection sensitivity, thereby reducing symbol detection errors due to an increased Euclidean distance between the symbols.

1.3.5 Optical amplification

Once modulated, the complex field $\Psi(\mathbf{r}, t)$ goes through a high power amplification stage. A high power attenuation is needed to balance the losses due to the satellite distance. The amplifiers, called HPOA for "High Power Optical Amplifiers", rely on several stages of amplification based on erbium doped fiber amplifier (EDFA) technologies, and optical beams coherent combination. Nowadays, 10 to 80 W amplifiers have been demonstrated [60], with the objective to reach a 100 W amplification [38].

1.3.6 Channel

The modulated and amplified beam goes through the optical assembly (optical bench and telescope) and is then emitted through the atmospheric channel. This beam is then distorted in phase and amplitude during its propagation through the channel. After propagation towards the satellite, we denote $\Psi_{turb}(\mathbf{r}, t)$ the perturbed complex field in the satellite plane. In this plane, because of the beam divergence, the beam pattern is much bigger than the satellite telescope aperture. Therefore, only a small portion of the beam is coupled to the satellite optical system and then to a single mode fiber. The received signal is a complex scalar $\Omega_{turb}(t)$. The distortions of the complex coupled flux $\Omega_{turb}(t)$ induced by its propagation through the atmosphere will be described in chapter 2.

1.3.7 Optical demodulation and detection

After its coupling to the optical system, the optical signal needs to be demodulated and detected. In the case of incoherent modulation, it is only necessary to detect the amplitude level to demodulate the signal, whereas for coherent schemes, it is necessary to retrieve the real and imaginary part of the signal to access the phase and amplitude information of the output symbol. Therefore, we can distinguish two families of detection techniques: direct detection and coherent detection. They differ in the use or not of a local laser oscillator in the detection scheme. This step will add noise to the received continuous time baseband signal $y(t)$. The details of these schemes architectures can be found in [61].

It is common to add a pre-amplification stage before the signal detection, in order to reach the detection threshold. It is done onboard the satellite with low-noise optical amplifiers (LNOA). This amplification stage adds noise to the signal, known as amplified spontaneous emission (ASE) noise. In presence of amplification, the optical SNR can be defined as [62]:

$$OSNR = \frac{P_{out}}{P_{ASE}} = \frac{gP_{in}}{2n_{sp}hfB_o(g-1)} \tag{1.4}$$

where g is the amplifier gain, n_{sp} is the spontaneous emission factor of the amplifier, h is the Planck's constant, f the optical signal center frequency assumed to be equal to 193.4 THz, and B_o the optical channel bandwidth in Hz. Defining the spontaneous emission factor function of the noise figure (NF) as $n_{sp} = 0.5F\frac{g}{g-1}$, we can write the optical SNR on the reference bandwidth of 12.5 GHz as:

$$OSNR_{dB} = 58 + P_{dBm,in} - NF_{dB} \tag{1.5}$$

where the $NF = 10\log_{10}(F)$, and $F = SNR_{in}/SNR_{out}$. The factor 58 results from the constants of the equation: $10\log_{10}(hfB_o * 1\text{mW})$. If computing the OSNR on an optical bandwidth different from the reference bandwidth, it stands:

$$OSNR_{dB} = 58 + P_{in} - NF_{dB} - 10\log_{10}\left(\frac{B_m}{12.5 \times 10^{-9}}\right) \tag{1.6}$$

where the optical signal bandwidth $B_m = 2R_s$, where R_s is the symbol rate.

When the signal is dominated by amplification noise, it is common to approximate the electrical SNR to the OSNR (reference).

1.3.8 Digital demodulation

Once the baseband signal is recovered, it is converted from the analog domain to the digital domain and is discretized. The obtained discrete samples y_k are mapped to one of the symbols of the symbol's alphabet, and the symbols unmapped to the encoded bits. The signal discrete samples can be expressed for a given time index t_k as:

$$y_k = h_k s_k + \omega_k \tag{1.7}$$

where s_k is the information symbol, h_k is a complex scalar modeling the channel impairment, and ω_k is an additive white Gaussian noise. The sample is mapped to the symbol minimizing the Euclidean distance between y_k and the constellation symbols. This minimization uses the knowledge of the noise and channel properties. We denote the detected symbol $\hat{s}_k$, that is defined as:

$$\hat{s}_k = \text{argmin}_{s_k \in \mathcal{C}^M} \|y_k - h_k s_k\|^2 \tag{1.8}$$

An example of the received symbols for a specific signal-to-noise ratio is given in figure 1.22, for a QPSK constellation. On the left, the received symbols show a high SNR, and we

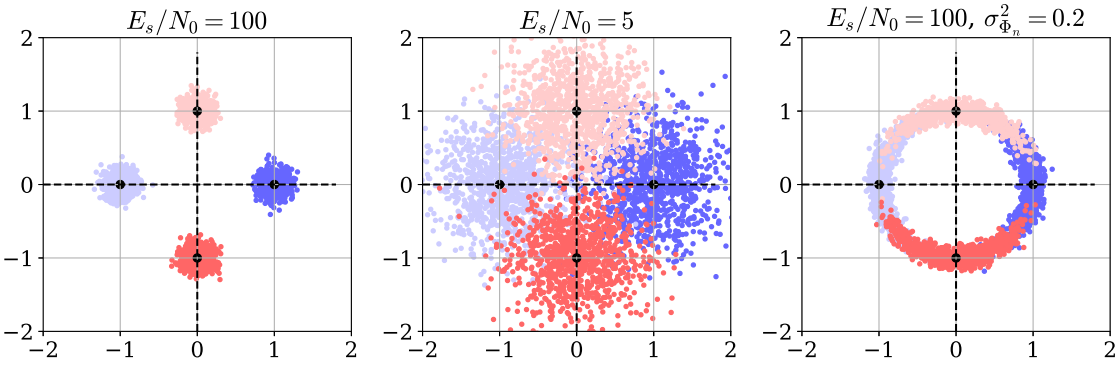

Figure 1.22: Example of a noisy QPSK with AWGN (left, center) and AWGN + Gaussian phase noise (right)

observe that there is no ambiguity to map the received symbols to constellation symbols. In the center, we illustrate a case with a low SNR. We observe that we can no more distinguish the four constellation points. The last case on the right is a case affected by phase noise that makes the constellation rotating.

We highlight that this optimal detection requires knowing the channel state h_k at the receiver side. As the channel variation, characterized by the channel coherence time T_c, is very slow with respect to the symbol duration T_s, this channel state can be estimated using pilot symbols.

To characterize the quality of transmission, we can derive the bit error rate (BER). The BER is equal in the case of an OOK modulation and a BPSK modulation to:

$$P_{e,OOK}(E_b/N_0) = Q\left(\sqrt{\frac{E_b}{N_0}}\right) \tag{1.9}$$

$$P_{e,BPSK}(E_b/N_0) = Q\left(\sqrt{\frac{2E_b}{N_0}}\right) \tag{1.10}$$

where E_b is the bit energy and $N_0/2$ the noise variance. We note the gain in sensitivity obtained in the BPSK case. In the case of an attenuated channel, the BER becomes (in the OOK case, for instance):

$$P_{e,h}(E_b/N_0) = \mathbb{E}_H\left[P_e(h^2 E_b/N_0)\right] \tag{1.11}$$

Commonly, we evaluate the system performance without FEC, and we observe the achieved gain at a pre-FEC bit error rate (BER) threshold, which is used to be around 10^{-3} [63]. Therefore, in our study, we aim at optimizing the pre-FEC BER.

1.3.9 Balance between reliability and high data rate

We defined the reliability evaluation factor as the pre-FEC BER, that depends on the SNR. We also showed that the SNR, that is equivalent to the OSNR if the dominant noise is the ASE noise, depends on the signal bandwidth, therefore on the symbol rate. Hence, a compromise needs to be found between high data rate and reliability. The data-rate of the system is defined as follows.

Considering a one subcarrier system, the information data-rate is defined as follows:

$$R_{total}(\text{bit/s}) = R_{s,channel} * \eta * r_c \tag{1.12}$$

where $R_{s,channel}$ is the baud rate for one channel, $\eta = \log_2(M)$ is the modulation format spectral efficiency and r_c the code rate.

Additionally, to increase the throughput and take advantage of the large optical bandwidth, it is common to transmit the information over several optical wavelengths. This technique is called wavelength division multiplexing (WDM). The throughput will be multiplied by the number of wavelengths considered. Another degree of freedom that can be used is the light polarization. It is possible to encode data on the two distinct polarization of the optical wave, therefore multiplying by two the throughput. In the article [27], a transmission over the C+L band is considered, yielding to 300 channels, each at 33 Gbaud/s (baud rate is the symbol rate). We highlight that in this article, power constraints due to eye safety limits are considered, with a total maximum power that can be transmitted of 300 W. This power is distributed over the different wavelengths. They also consider using the two optical polarizations.

Using WDM and dual-polarization techniques, the total data-rate writes as:

$$R_{total}(\text{bit/s}) = R_{s,channel} * \eta * N_{WDM} * N_{polar} * r_c \tag{1.13}$$

where we added the factor N_{WDM}, the number of wavelength channels used and N_{polar}, the number of polarizations.

1.4 Conclusion

In this chapter we presented the principle of a satellite telecommunication relying on optical communication links. We showed that optical technologies offer great potential to reach the high data-rates required to operate a satellite internet network. However, we could highlight constraints on the optical links related to the link nature and geometry that are: sensitivity to presence of clouds, and the power constraints due to the atmospheric turbulence and the large distance of the link with a GEO satellite, inducing large geometrical losses.

From the uplink perspective, at the ground station, the main drivers are the telescope aperture size, the power available to emit the uplink, and the type of AO correction. It is also highlighted that the optical correction needs to be located at the OGS, as the turbulence is located close to the ground.

Onboard the satellite, an architecture needs to be chosen in order to convert the optical frames into RF frames, while protecting the encapsulated RF frames against the optical channel distortions. As the uplink channel suffers from large distortions due to atmospheric turbulence, the analog transparent scheme is not appropriate as it does not protect the optical signal with coding. We choose in the following to consider either a digital transparent scheme or a regenerative scheme, both relying on a FEC protection against the optical channel disturbances. Additionally, a second constraint is that the power and memory resources onboard the satellite are limited. The design of digital signal processing algorithms will need to account for this constraint.

We also described the telecommunication transmission chain, in order to identify the metric to optimize to design a high data-rate optical link. The BER is shown to depend on the signal SNR, depending itself on the received power onboard the satellite and the symbol rate. In the following, we describe the physical phenomenons affecting the optical beam propagation through the atmosphere in order to develop the channel model and model the received power onboard the satellite.

CHAPTER 2

Free space optical channel characterization and modeling

Contents

Previously, we described the motivations for implementing a satellite optical network relying on high data rate optical links, and described the telecommunication transmission chain. We highlighted that the reliability of a data-rate optical link strongly depends on the channel statistics. For ground to GEO satellite optical links, atmospheric turbulence impairs the channel. In this chapter, we describe the physical phenomenons that govern the optical beam propagation in the atmosphere, therefore inducing the coupled flux fluctuations onboard the satellite. We both describe the disturbances affecting the downlink and the uplink, as we will later use downlink models to model the reciprocal uplink. We also describe the impact of an adaptive optics correction on the coupled flux fades mitigation.

Therefore, we start in section 2.1 by presenting the channel model and the physical effects that impair the optical beam propagation. These effects show to induce both constant and random attenuations of the coupled flux onboard the satellite. Afterward, we focus on the random attenuation factor of the channel model, that is also referred to as **the coupled flux**, whose fluctuations are induced by the atmospheric turbulence. In section 2.2, we describe the atmospheric turbulence phenomenon and its statistical characterization. In section 2.3, we present the statistical models that describe the optical propagation through atmospheric turbulence in the weak perturbation regime, applied to plane waves propagation, and existing models that characterize the uplink resulting intensity fluctuations in the satellite plane. Finally, we present the coupled flux equation that is, both for the uplink and downlink, the core equation that describes the amount of the received power that will be coupled to the optical system. In section 2.4, we describe the adaptive optics system and the impact of applying an AO correction on the coupled flux. We present the concept of uplink AO pre-compensation in section 2.5, and describe the anisoplanatic phase error that impairs the uplink pre-compensation in the presence of a point-ahead angle and its impact on the coupled flux onboard the satellite. We present state-of-the-art physical and digital fading mitigation techniques in section 2.6. We conclude by presenting in 2.7 the scenarios and the main objectives of this thesis.

2.1 Free space optical channel model

The atmospheric impaired optical channel model can be described as:

$$y(t) = h(t)\exp(i\phi_\Omega(t))x(t) + \omega(t) \tag{2.1}$$

where $h(t)$ is the square modulus of the complex coupled flux, $\phi_\Omega(t)$ is the argument of the complex coupling (not to be confused with the spatial phase of the turbulent beam $\Phi(\mathbf{r}, t)$), $x(t)$ is the electrical baseband signal containing the information, $y(t)$ the received electrical signal, and $\omega(t)$ is the AWGN noise related to the detection.

The channel is characterized by an attenuation term $h(t)$ or $|h(t)|^2$ in the case of an intensity modulation which is composed of **static losses** (not varying with respect to the coherence time of the channel) and **dynamic losses**. The dynamic losses are induced by the turbulence perturbation of the optical beam, whose coherence time T_c is greater than the symbol time T_s. The resulting channel attenuation is expressed as:

$$|h(t)|^2 = P_{Tx} \underbrace{L_{abs} L_{geom} L_{pointing} a_{Tx} a_{Rx}}_{\text{Static losses}} \underbrace{L_{turb}(t)}_{\text{Dynamic losses}} \tag{2.2}$$

usually expresses in dBs as $10\log_{10}(h(t))$, and where P_{Tx} is the emitted power, whose value is taken as 50 W. We indicate an exponent 'dB' on the losses terms when expressed in dB.

Considering the phase noise induced by the turbulence, it was shown in [61] that it was equivalent to the piston term in the downlink case and its evolution was relatively

slow compared to the laser phase noise and the coupled flux variations. In the following, we neglect this phase noise and assume a perfect phase synchronization in reception. We explain the origin and typical values of the static losses of the channel attenuation as follows.

Atmosphere molecular absorption: L_{abs}

The propagation through the atmosphere induces absorption and diffusion on the air molecules of the optical power. Another term of losses can be added due to the presence of thin clouds. Following [33], L_{abs}^{dB} can be set to 8 dB. we consider an 8 dB loss for these two contributions.

Geometrical losses: L_{geom}

The geometrical losses are the losses induced by the beam divergence. Indeed, the collected energy is only a small amount of the energy sent due to the small size of the aperture receiver with respect to the beam footprint pattern in the satellite plane. This term can also be seen as the multiplication of the more classically used antenna gains and propagation losses. Therefore, we can express the geometrical losses:

$$L_{geom} = G_{Tx} G_{Rx} a_{fsp} \tag{2.3}$$

where the antenna gains are:

$$G_{Tx/Rx} = g_{Tx/Rx} \left(\frac{\pi D_{Tx/Rx}}{\lambda} \right)^2 \tag{2.4}$$

and the propagation loss is:

$$a_{atmo} = \left(\frac{\lambda}{4\pi L_{sol-sat}} \right)^2 \tag{2.5}$$

where $D_{Tx/Rx}$ is the aperture diameter in emission or reception, λ is the communication wavelength, and $L_{sol-sat}$ is the distance from the ground to the satellite on the line of sight. Additionally, $g_{Tx/Rx}$ is a loss term induced by the mode mismatch between a plane wave and the single mode fiber Gaussian mode. It is equal to $g_{Tx/Rx} = 0.81$ for an optimized waist of the Gaussian mode taken as $\omega_0 = D/2.2$, for an unobscured pupil.

Transmitter, receiver and pointing losses: a_{Tx}, a_{Rx}, $L_{pointing}$

It is necessary to consider losses resulting from imperfections like aberrations and reflections in the optical elements comprising both the transmitter and the receiver. Losses can also occur due to the imperfect assembly of these components, which are referred to as a_{Tx} and a_{Rx} for the transmitter and receiver, respectively. In [25], these losses are estimated to $a_{Tx}^{dB} = a_{Rx}^{dB}$=-3 dB. Additionally, losses from pointing inaccuracies have to be taken into account. These losses are estimated to be equal to $L_{pointing}^{dB}$=-2 dBs [64].

The last term of the channel losses, denoted $L_{turb}(t)$, corresponds to the losses induced by atmospheric turbulence. This term varies in time with respect to the other losses. Its coherence time is comprised between the 1 and 10 ms (depending on the use or not of an AO correction). These losses are due to the phase and amplitude perturbations of the optical complex field during its propagation through the atmosphere. We describe the physical phenomenon and modeling tools allowing to characterize this coefficient in the following section.

2.2 Characterization of the atmospheric turbulence

2.2.1 Turbulent atmosphere description

The Earth's atmosphere consists of a gas blend exposed to solar radiation and radiative transfer from the ground. Wind-induced shearing generates turbulent air movements, characterized by chaotic flow and the formation of eddies. These eddies structure with characteristic sizes of several tens to hundreds of meters (defining the external scale L_0 of the phenomenon's formation) gradually break down into smaller structures, reaching a scale of a few millimeters (internal scale l_0), before dissipating due to viscosity. The range between these two scales is referred to as the inertial range. This evolution of the eddies is referred to as the theory of the energy cascade, and was developed by Kolmogorov during his elaboration of an atmospheric turbulent model [65].

These eddies lead to the mixing of air masses with different temperatures. However, the local refractive index of the air $n(\vec{r})$ is a function of the local temperature and pressure. This refractive index influences the length of the optical path traversed by an electromagnetic wave propagating through the atmosphere. These refractive index fluctuations will impact the properties of the propagated optical complex field through the atmospheric turbulence.

2.2.2 Refractive index fluctuations statistical description

The statistical description of the refractive index fluctuations is developed in the literature. A first description is given using the covariance function:

$$B_{\Delta n}(\vec{\rho}, h) = \langle \Delta n(\vec{r}, h) \Delta n(\vec{r} + \vec{\rho}, h) \rangle \tag{2.6}$$

where $\Delta n(\vec{r}, h) = n(\vec{r}, h) - n_{mean}$ and $\vec{r}$ and $\vec{\rho}$ are 2D spatial vectors on the plane at height h. However, within the [65] model, this covariance function diverge for $\vec{\rho} = 0$. An alternative is to describe the statistics thanks to the structure function of the refractive index fluctuations that is defined as the variance of the fluctuation difference between two point separated by $\vec{\rho}$:

$$D_{\Delta n}(\vec{\rho}, h) = \left\langle (\Delta n(\vec{r}, h) - \Delta n(\vec{r} + \vec{\rho}, h))^2 \right\rangle \tag{2.7}$$

[66] and [67] showed that this structure function could be expressed within the inertial range ($L_0 < \rho < l_0$) as:

$$D_n(\vec{\rho}, h) = C_n^2(h) \rho^{\frac{2}{3}} \tag{2.8}$$

where $C_n^2(h)$ is defined as the refractive index structure constant at height h. This structure function is isotropic, no longer depending on $\vec{\rho}$ but on $\rho = |\vec{\rho}|$.

Another way to describe the refractive index fluctuations statistics is through its power spectral density (PSD), which is a tool commonly used in the characterization of random processes. This PSD is obtained by using the Wiener-Khinchine theorem [68], by computing the Fourier transform of the covariance function. This refractive index fluctuations PSD, called Kolmogorov spectrum, is expressed as:

$$W_n(\vec{f}, h) = 0.033(2\pi)^{-\frac{2}{3}} C_n^2(h) f^{-\frac{11}{3}} \tag{2.9}$$

where $\vec{f}$ is the spatial frequencies vector (m^{-1}), and $f = |\vec{f}|$. This PSD is defined for $\frac{1}{L_0} < f < \frac{1}{l_0}$, still in the inertial range. To obtain a spectrum representative for all the frequencies, a novel model was proposed by Von Karman, called the Von Karman spectrum:

$$W_n(\vec{f}, h) = 0.033(2\pi)^{-\frac{2}{3}} C_n^2(h) (f^2 + \frac{1}{L_0})^{-\frac{11}{6}} e^{\left(-\frac{2\pi l_0}{5.91 f}\right)^2} \tag{2.10}$$

introducing the two cutoff frequencies, $1/L_0$ and $1/l_0$.

2.2.3 Refractive index structure constant : C_n^2

As highlighted in section 2.2.2, the statistics of the refractive index fluctuations depends on the refractive index structure constant $C_n^2(h)$. This constant characterizes the turbulence strength distribution along the line of sight. Its knowledge is essential to characterize the optical properties of the optical perturbed field, such as scintillation or anisoplanatism. The scintillation depicts the fluctuation of the amplitude of the complex field, whereas the anisoplanatism characterize the angular decorrelation of the phase of a complex beam. This constant will vary with meteorological conditions as well as orographic parameters (terrain character and surface topography) [69, 70].

C_n^2 profile metrology

Several instruments and techniques allows measuring C_n^2 profiles. The different techniques involve using thermal probes, Doppler shift [71, 72] or optical measurements. We emphasize on the techniques using optical measurements. These measurements give access to the C_n^2 profile, as the turbulence fluctuations impair the phase and the amplitude of optical complex fields. Several methods were developed to estimate the profile thanks to phase (or more particularly, slopes on a wavefront sensor) and amplitude fluctuation measurements, separately or combined. These instruments can use several sources or single sources. Example of these instruments are given in [73] and reference therein. The developments in this thesis, are partly inspired from the concept of these instruments, as we will exploit phase and log-amplitude measurements from a single source on one or more apertures to estimate the phase off-axis.

C_n^2 profile modeling

Models have been proposed in the literature to describe the mean profile of C_n^2 as a function of the altitude. The most commonly used in the literature is the Hufnagel-Valley C_n^2 profile [74–76], which is a parametric semi-empirical model derived from averages of profile databases.

In this thesis, we don't use Hufnagel-Valley profiles, but in-house profiles named **MOSPAR**. The principle of construction of the MOSPAR profiles is given in section 2.7.

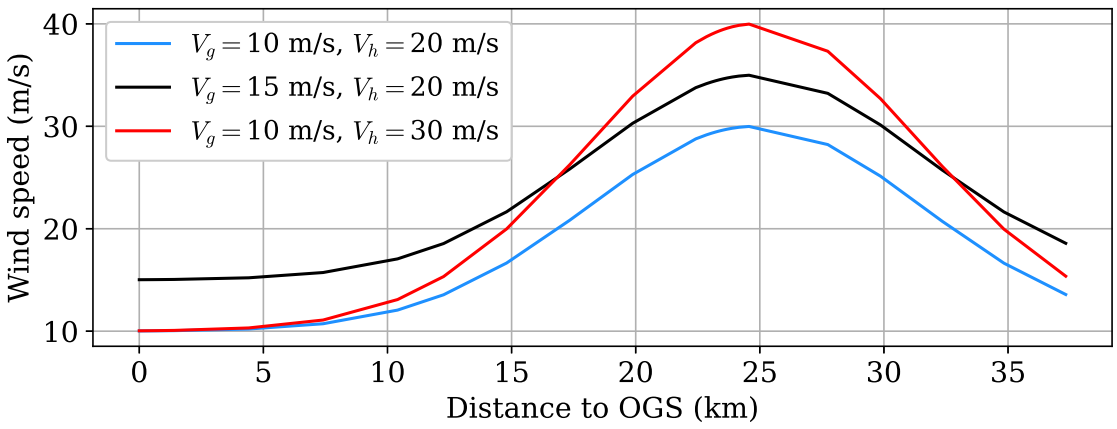

Figure 2.1: Illustration of the Bufton wind profiles for three couples of (v_g, v_t).

2.2.3.1 Wind modeling

We assume the wind to follow the Bufton model [77], defined as:

$$v(z) = v_g + v_t * exp(-\left[\frac{zcos(\zeta) - h_t}{L_t}\right]^2) \tag{2.11}$$

where z is the distance to the OGS on the line of sight, v_g the wind speed at the ground or low altitude, v_t the wind speed at tropopause, h_t the height of the tropopause, L_t the thickness of the tropopause layer and ζ the zenith angle of the observation. We specify that all along the thesis, z will stand for the distance to the OGS on the LOS while h stands for the height at zenith. The wind profile is illustrated in figure 2.1 for a ground wind speed of 10 m/s and a tropopause wind speed of 20 m/s.

2.2.4 Turbulence characterization

Either modeled or measured, the C_n^2 turbulence profile allows characterizing the optical effects due to the turbulence.

2.2.4.1 Fried parameter

An essential parameter when studying the effects of atmospheric turbulence on the propagation of light waves is the Fried parameter r_0 [78]. r_0 is defined as an equivalent diameter that sets the resolution limit of the telescope caused by turbulence. r_0 reflects the overall strength of turbulence in the various atmospheric layers encountered along a specific line of sight. In the case of a plane wave and considering a Kolmogorov spectrum, it can be expressed as follows:

$$r_0 = \left[0.423\left(\frac{2\pi}{\lambda}\right)^2 \int_0^{z_{max}} C_n^2(h(z))dz\right]^{-\frac{3}{5}} \tag{2.12}$$

where we assume the C_n^2 profile to be measured at zenith. We also refer to r_0 as the coherence length of the turbulence.

2.2.4.2 Turbulence coherence time

In the same way, we can describe the coherence time of the turbulence, called τ_0. It is defined such that:

$$\mathbb{E}[[\Phi(\vec{r},t) - \Phi(\vec{r},t+\tau_0)]^2] = 1 \text{ rad}^2 \tag{2.13}$$

where $\Phi(\vec{r},t)$ depicts the phase fluctuations. This constant is developed by Roddier [79] as:

$$\tau_0 = 0.314\frac{r_0}{\overline{V}}, \tag{2.14}$$

where $\overline{V}$ is the averaged wind defined as:

$$\overline{V} = \left[\frac{\int_0^{z_{max}} \left|\vec{V}(h(z))\right|^{\frac{5}{3}} C_n^2(h(z))dz}{\int_0^{z_{max}} C_n^2(h(z))dz}\right]^{\frac{3}{5}} \tag{2.15}$$

2.2.4.3 Anisoplanatic angle

A last parameter, that will be of the utmost importance in our analysis, is the anisoplanatic angle. This parameter characterizes the angular decorrelation of the turbulence. It is defined by Fried [80] such that:

$$\mathbb{E}[[\Phi(\vec{r},t,\theta_0)-\Phi(\vec{r},t,0)]^2]=1 \text{ rad}^2 \tag{2.16}$$

It results from this definition that:

$$\theta_0=\left[2.91\left(\frac{2\pi}{\lambda}\right)^2\int_0^{z_{max}} z^{5/3}C_n^2(h(z))dz\right]^{-3/5} \tag{2.17}$$

It is shown in this equation that it only depend on the C_n^2 profile and the height, giving a large weight to the high altitude layers.

And can be expressed function of r_0 [81] as:

$$\theta_0=\frac{r_0}{\overline{h}} \tag{2.18}$$

where $\overline{h}$ is defined analogly to $\overline{V}$:

$$\overline{h}=\left[\frac{\int_0^{z_{max}} h^{\frac{5}{3}}C_n^2(h(z))dz}{\int_0^{z_{max}} C_n^2(h(z))dz}\right]^{\frac{3}{5}} \tag{2.19}$$

2.3 Optical propagation through the atmosphere modeling

The optical wave propagation through the atmosphere is impaired by the atmospheric turbulence, and, especially, by the local fluctuations of the refractive index. In the aim to describe the fluctuation of the turbulent complex field, several models were developed in the literature. Analytical models are developed given some approximations on the perturbations, such as weak perturbations. However, to study the complex field behavior out of this regime, we need to rely on numerical models, such as the phase-screen propagation method. In this section, we intend to explain and derive these models, starting from the wave propagation equation, in order to recall each hypothesis made for the considered regime.

2.3.1 Wave propagation equation

2.3.1.1 Helmholtz equation

We consider a monochromatic electromagnetic (EM) field $\mathbf{E}(\mathbf{r})$, which is a random complex field. This EM random field, traveling through a dielectric medium (air), is ruled by Maxwell's equations. Under the assumptions that the turbulent atmosphere is isotropic and that the refractive index fluctuations evolve more rapidly than the optical wave's period, it can be demonstrated that the evolution of $\mathbf{E}(\mathbf{r})$ follows Helmholtz's propagation equation [82]:

$$\nabla^2\mathbf{E}(\mathbf{r})+k_0^2n(\mathbf{r})^2\mathbf{E}(\mathbf{r})+2\nabla(\mathbf{E}(\mathbf{r})\cdot\nabla(log(n(\mathbf{r})))=0 \tag{2.20}$$

where $\mathbf{r}$ is the spatial vector coordinates, $k_0=2\pi/\lambda$ the wave vector, where λ is the field wavelength, and $n(\mathbf{r})$ the local refraction index at location $\mathbf{r}$.

The term $2\nabla(\mathbf{E}(\mathbf{r})\cdot\nabla(log(n(\mathbf{r}))))$ is related to the wave polarization states variations. In the range of visible and infrared wavelength, that we consider for the communication

link, this term can be neglected, since the wavelength λ is significantly smaller than the variation scale of the refractive index [83]. Consequently, a simplified wave equation is adopted:

$$\nabla^2\mathbf{E}(\mathbf{r}) + k_0^2 n(\mathbf{r})^2\mathbf{E}(\mathbf{r}) = 0 \tag{2.21}$$

2.3.1.2 Parabolic equation method

The parabolic equation can be used to solve the Helmholtz reduced equation. Assuming that the EM field is an almost plane wave propagating in the $\vec{e}_z$ direction, we can express the amplitude of the scalar field as:

$$E(\mathbf{r}) = A_0\Psi(\mathbf{r})e^{ikz} \tag{2.22}$$

where $\Psi(\mathbf{r})$ is the complex amplitude of the deviation from a perfectly plane wave $\exp(ikz)$, and A_0 denoting the unperturbed amplitude. The average refractive index over time, characterizing the medium through which the wave propagates, is denoted as $\langle n(\mathbf{r})\rangle$. Consequently, the wave number can be expressed as $k = \langle n(\mathbf{r})\rangle k_0$. Thus, by injecting Eq. 2.22 in Eq. 2.21, the complex amplitude $\psi(\mathbf{r})$ is a solution to the simplified wave equation:

$$\nabla^2\Psi(\mathbf{r}) + 2ik\frac{\partial\Psi(\mathbf{r})}{\partial z} + k_0^2\left(n(\mathbf{r})^2 - \langle n(\mathbf{r})\rangle^2\right)\Psi(\mathbf{r}) = 0 \tag{2.23}$$

The parabolic assumption consists in assuming $\left|\frac{\partial^2\Psi(\mathbf{r})}{\partial^2 z}\right| \ll \left|k\frac{\partial\Psi(\mathbf{r})}{\partial z}\right|$. This assumption is true when the diffraction effects affecting the complex amplitude $\Psi(\mathbf{r})$ vary slowly compared to z. Additionally, we assume that the refraction index fluctuations are small, i.e. $n_1(\mathbf{r}) \ll 1$, where $n(\mathbf{r}) = \langle n(\mathbf{r})\rangle + n_1(\mathbf{r})$. Applying both assumptions, we obtain the following Helmholtz parabolic equation:

$$\nabla_T^2\Psi(\mathbf{r}) + 2ik\frac{\partial\Psi(\mathbf{r})}{\partial z} + k_0^2 n_1(\mathbf{r})\langle n(\mathbf{r})\rangle\Psi(\mathbf{r}) = 0 \tag{2.24}$$

where $\nabla_T^2 = (\frac{\partial^2}{\partial^2 x} + \frac{\partial^2}{\partial^2 y})$ is the transverse Laplacian operator.

The Helmholtz equation is a partial differential equation with coefficients that vary spatially. It cannot be solved analytically in the general case. However, it is possible to solve it analytically by assuming weak phase perturbations. This method is known as the Rytov approximation method. Beyond this regime of weak perturbations, it is possible to solve locally the equation under some assumptions [84]. This local resolution is the principle on which relies end-to-end numerical simulations.

2.3.2 Phase screen propagation model

The phase screen propagation model relies on two principles: the discretization of the turbulent volume and the alternance of propagation steps and application of the turbulent phase perturbation to the complex field. The thickness d of the discretized turbulent layers needs to be sufficiently thin to allow neglecting the diffraction effects within the layer, and sufficiently large to allow the different layers to be decorrelated. Figure. 2.2 depicts this phase screen discretization.

The first step is the propagation in the void. This is computed by solving the wave equation for the free-space propagation. Using the parabolic approximation, it results that:

$$\Psi(x,y,z+d) = \Psi(x,y,z+d) * \frac{e^{ikd}}{i\lambda d}e^{\frac{ik(x^2+y^2)}{2d}} = \Psi(x,y,z+d) * F_d(x,y) \tag{2.25}$$

where, $F_d(x,y)$ is the Fresnel operator and $*$ denotes the convolution operator.

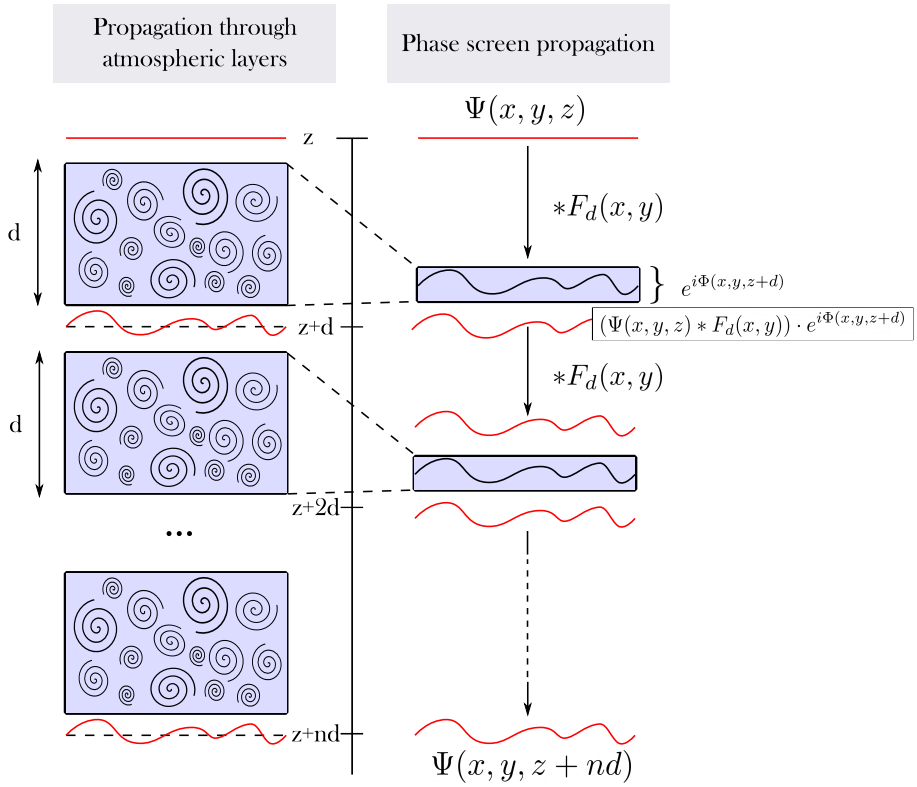

Figure 2.2: Schematic of the phase-screen propagation method principle. On the left, discretization of the turbulent volume, on the right, method illustration.

Within a layer, the refractive index variation is modeled by introducing a simple phase shift term, denoted by Φ. This phase shift term accounts for the path difference encountered by the optical wave as it passes through d, and is used to model the refractive index heterogeneity within the layer. The computation of this phase shift term relies on the near-field approximation. It is expressed as:

$$\Phi(x, y, z + d) = k_0 \int_z^{z+d} n_1(x, y, h)dh \tag{2.26}$$

Finally, the propagation through one layer of thickness d is modeled as:

$$\Psi(x, y, z + d) = (\Psi(x, y, z + d) * F_d(x, y)) \cdot e^{i\Phi(x,y,z+d)} \tag{2.27}$$

An illustration of this propagation modeling is also proposed in figure 2.2.

This principle can be generalized to an arbitrary number of phase-screens. Therefore, it results that the turbulent complex field is modeled as a succession of phase perturbations induced by the multiplication of the field by the phase-screen perturbation, followed by phase and amplitude perturbation induced by the propagation in free space [85–87].

Numerical modeling tool: Turandot

This modeling approach is at the origin of numerical models, such as the code PILOT that became later TURANDOT, the ONERA in house end-to-end (E2E) modeling tool. This code, validated on experimental data [88, 89] in a LEO downlink case, applies the

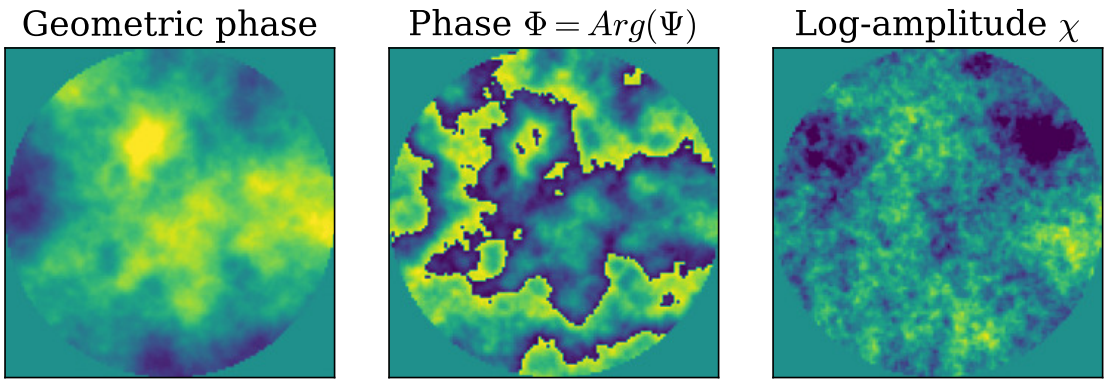

Figure 2.3: Illustration of TURANDOT output. From the left to the right: geometric phase, diffractive phase (argument of the complex field), and log-amplitude (logarithm of the module of the complex field).

phase-screen propagation modeling approach and allows computing downlink and uplink propagations through the atmosphere. An illustration of a resulting complex field phase and amplitude obtained with this code is given in figure 2.3 for a downlink case.

This tool also allows modeling the impact of the turbulence temporal effects on the propagated complex field. This temporal relies on the Taylor's frozen turbulence hypothesis [90]. This hypothesis states that, if the wavefront characteristic evolution time is negligible with respect to its translation due to the wind, thus, we can convert temporal statistics into spatial statistics. The refractive index can therefore be expressed as:

$$n(\mathbf{r}, t) = n\left(\mathbf{r} - V_{\perp}(\mathbf{r})t\right) \tag{2.28}$$

where $V_{\perp}(\mathbf{r})$ is the transverse wind at position $\mathbf{r}$.

Therefore, the temporal effects in the TURANDOT tool are generated by the translation of the turbulence layers according to a wind profile that is generating according to the Bufton model described in section 2.2.3.1.

2.3.3 Weak perturbations regime

As mentioned in section 2.3.1, the Helmholtz equation can be analytically solved if the amplitude of the field perturbations are small. The most known approximation used in the literature is the Rytov approximation [82], that relies on a linearization of the wave equation.

2.3.3.1 Rytov approximation

In the Rytov approximation model, the complex field is modeled as:

$$E(\mathbf{r}) = e^{\psi_0(\mathbf{r}) + \psi(\mathbf{r})} \tag{2.29}$$

where $E_0(\mathbf{r}) = e^{\psi_0(\mathbf{r})}$ is the unperturbed EM field.

We define $\delta n(\mathbf{r}) = \frac{n_1(\mathbf{r})}{<n(\mathbf{r})>}$. The Rytov approximation consists in assuming $\delta n(\mathbf{r}) \ll 1$ and that the complex field spatial fluctuations are small with respect to k_0. Therefore, by injecting Eq. 2.29 in Eq. 2.21, we can show that [82, 91, 92]:

$$\nabla^2\psi(\mathbf{r}) + 2\nabla\psi_0(\mathbf{r})\nabla\psi(\mathbf{r}) + 2k_0^2\left\langle n(\mathbf{r})\right\rangle \delta n(\mathbf{r}) = 0 \tag{2.30}$$

and can be analytically solved. For these conditions to be verified, the refractive index fluctuations need to be small, which is always verified in the atmosphere. The second constraint is more restrictive, as it limits the amplitude of the perturbation that affects the complex field.

The solution of this equation is:

$$\psi(\mathbf{r}) = \frac{k_0^2}{2\pi E_0(\mathbf{r})} \int_V dr' \delta n(\mathbf{r}') E_0(\mathbf{r}') \frac{exp(ik_0|\mathbf{r}-\mathbf{r}'|)}{|\mathbf{r}-\mathbf{r}'|} \tag{2.31}$$

2.3.3.2 Phase and log-amplitude analytical expressions

The complex perturbed amplitude of the field $\psi(\mathbf{r})$ can be decomposed as:

$$\psi(\mathbf{r}) = \chi(\mathbf{r}) + i\phi(\mathbf{r}) \tag{2.32}$$

where the real part $\chi(\mathbf{r})$, so called log-amplitude, depicts the logarithm of the field amplitude fluctuations, whereas the imaginary part $\phi(\mathbf{r})$, is the perturbed phase of the field. These two quantities can be developed as [82, 93]:

$$\phi(\mathbf{r}) = \frac{k_0^2}{2\pi} \int_0^L \frac{dz}{L-z} \int_{-\infty}^{\infty} d\mathbf{r}' n_1(\mathbf{r}', z) \sin(k_0 \frac{|\mathbf{r}-\mathbf{r}'|^2}{2(L-z)}) \tag{2.33}$$

$$\chi(\mathbf{r}) = \frac{k_0^2}{2\pi} \int_0^L \frac{dz}{L-z} \int_{-\infty}^{\infty} d\mathbf{r}' n_1(\mathbf{r}', z) \cos(k_0 \frac{|\mathbf{r}-\mathbf{r}'|^2}{2(L-z)}) \tag{2.34}$$

Power spectrum densities

From Eq. 2.31, we derive the power spectral densities of the phase and log-amplitude [81]:

$$W_\phi(\mathbf{f}) = k_0^2 \int_0^L W_{\Delta_{n,h}}(f) \cos^2(\pi h \lambda f^2) dh \tag{2.35}$$

$$W_\chi(\mathbf{f}) = k_0^2 \int_0^L W_{\Delta_{n,h}}(f) \sin^2(\pi h \lambda f^2) dh \tag{2.36}$$

where $W_{\Delta_{n,h}}$ is the Von Karman spectrum given in Eq. 2.9.

Variance of the phase and log-amplitude

By integration of the power spectral densities, we can compute the phase and log-amplitude variances:

$$\sigma_\phi^2 = k_0^2 \int_0^L \int_0^\infty 2\pi f W_{\Delta n,h} \cos^2(\pi h \lambda f^2) df dh \tag{2.37}$$

$$\sigma_\chi^2 = k_0^2 \int_0^L \int_0^\infty 2\pi f W_{\Delta n,h} \sin^2(\pi h \lambda f^2) df dh \tag{2.38}$$

Due to the weighting term $\sin^2(\pi h \lambda f^2)$, it can be shown that the σ_χ^2 integral expression converges for both Von Karman and Kolmogorov. Indeed, it acts has a high-pass filter (whereas the $\cos^2(\pi h \lambda f^2)$ term from the phase term acts as a low-pass filter). This means that the outer scale from the Von Karman spectrum has little impact the σ_χ^2 computation. Therefore, a simplified expression, called Rytov variance, can be developed:

$$\sigma_{\chi^R}^2 = 0.5631 k_0^{7/6} \int_0^L C_n^2(z) z^{5/6} dz \tag{2.39}$$

[92] showed that the Rytov approximation was valid while $\sigma^2_{\chi_R} < 0.3$.

A last quantity that can be derived from these equations is the complex field irradiance I (also known as scintillation). By defining $I = \Psi\Psi^* = e^{2\chi}$, it is shown that the normalized of the field intensity equals to:

$$\sigma_I^2 = \frac{\langle I^2 \rangle}{\langle I \rangle^2} - 1 = \exp(4\sigma_\chi^2) - 1 \tag{2.40}$$

Under the approximation of the weak perturbations' regime, it results that $\sigma_I^2 \approx 4\sigma_\chi^2$ (by linearization of the exponential).

2.3.3.3 Statistical distribution of ϕ and χ

From the derived equations 2.33, it appears that, both phase and log-amplitude can be considered as a weighted sum of the refractive index fluctuation random variable. As this random variable is a centered Gaussian variable, like many natural phenomenons, the phase and log-amplitude, as sums of Gaussian random variables are also Gaussian variables, whose variances are equal to σ_Φ^2 and σ_χ^2, respectively.

The irradiance random variable I probability density function can also be characterized. As $I = e^{2\chi}$, it follows a log-normal probability law [94], whose probability density function is:

$$f_I(I) = \frac{1}{2\sqrt{2\pi} I \sigma_\chi} \exp\left(- \frac{\left(\log\left(\frac{I}{I_0}\right) - 2\langle\chi\rangle \right)^2}{8\sigma_\chi^2} \right) \tag{2.41}$$

where $\langle\chi\rangle = -\sigma_\chi^2$ in order to ensure energy conservation [78].

However, this characterization of the scintillation is limited to the weak perturbation regime. In the strong perturbation regime, the log-amplitude variance is shown to saturate (figure?), whereas the Rytov variance infinitely increases.

Moreover, this description does not include the pupil effects (both on the phase and the log-amplitude). In the log-amplitude case, the pupil averages the log-amplitude fluctuations. It can be characterized by the following variance [95, 96]:

$$\sigma^2_{\chi_{Ap}} = 5.20 R_{tel}^{5/3} k_0^2 \int_0^L dz C_n^2(z) \int_0^\infty dk k^{-14/3} J_1(k)^2 \sin^2\left(\frac{zk^2}{2k_0^2 R_{tel}^2}\right) \tag{2.42}$$

where R_{tel} is the telescope radius, $J_1(k)$ is the Bessel function of first order, and k is the angular frequency.

In the following, we will adopt a modal formalism that allows to characterize the phase perturbations on the pupil.

2.3.4 Zernike modal characterization of the turbulence

2.3.4.1 Zernike modal formalism

In order to characterize and analyze the phase distortions within the pupil of the telescope, it is convenient to express the phase disturbances in the Zernike orthonormal basis, whose support is circular.

The Zernike polynomial basis is an orthonormal basis on the unit disk, whose polynomials are defined for a given index $i \in 1, N_{max}$:

$$Z_i(\mathbf{r}) = R_n^m(\mathbf{r})\Theta_n^m(\theta) \tag{2.43}$$

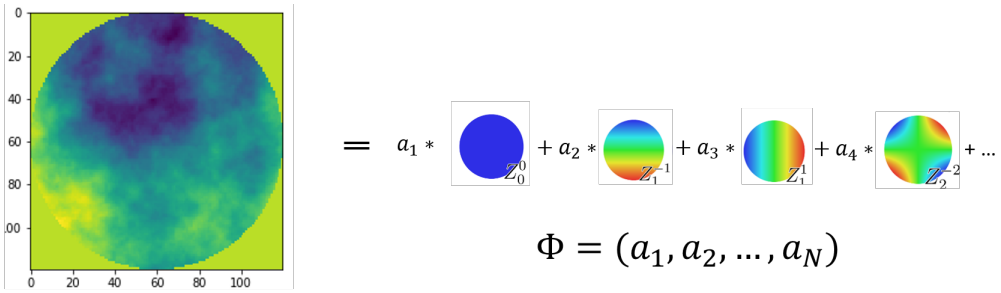

Figure 2.4: Illustration of the phase modal decomposition onto the Zernike polynomial basis.

where $R_n^m(\mathbf{r})$ and $\Theta_n^m(\theta)$ can be found in [97], and where n is the radial order and m the azimuthal order. We also define the index i, the Noll index, that is a function of n and m and orders the polynomials [97].

The Zernike polynomials have the following properties over the pupil:

$$\langle Z_i(\mathbf{r}), Z_j(\mathbf{r})\rangle = \frac{1}{S}\int_S Z_i(\mathbf{r})Z_j^*(\mathbf{r})d\mathbf{r} = \delta_{ij}. \tag{2.44}$$

2.3.4.2 Turbulence modal characterization

The turbulent phase can be expanded onto the Zernike polynomial basis, allowing its characterization through the vectors of projections $\mathbf{\Phi} = [a_1, ..., a_N]^T$. The phase expansion is computed as:

$$\Phi(\mathbf{r}, t) = \sum_{i=1}^{N} a_i Z_i(\mathbf{r}) \tag{2.45}$$

and we can express the projections a_i as:

$$a_i = \langle \Phi(\mathbf{r}, t), Z_i(\mathbf{r})\rangle = \frac{1}{S}\int_S \Phi(\mathbf{r}, t)Z_i(\mathbf{r})d\mathbf{r}. \tag{2.46}$$

These coefficients allow to statistically characterize the phase. Indeed, Noll [97] gives a simple expression to characterize the following modal covariance, for a Kolmogorov spectrum (i.e., $L_0 = +\infty$ and $l_0 = 0$):

$$\langle a_i a_j\rangle = 3.90\sqrt{(n_1+1)(n_2+1)}(-1)^{(n_1+n_2-2m_1)/2}\delta_{m_1 m_2}\left(\frac{D}{r_0}\right)^{\frac{5}{3}}\int_0^\infty k^{-\frac{14}{3}}J_{n_1+1}(k)J_{n_2+1}(k)dk \tag{2.47}$$

where D is the diameter of the pupil (support of Zernike polynomials), the functions $J_l(k)$ are the Bessel functions of order l, n_1 and m_1 (resp. n_2 and m_2 are the radial and azimuthal orders of polynomial i (resp. j).

The logarithm of the absolute value of the turbulent coefficients covariance matrix is depicted in figure 2.5. We observe that the matrix is not diagonal, presenting phase modal inter-correlations (whose value is nevertheless weak compared to the modes variance). We also note that the second diagonal is a diagonal of anti-correlations, that is only observable by taking the absolute value of the matrix in the log-scale.

Due to the orthonormality property of the Zernike polynomial basis, we can compute the phase variance as:

$$\sigma_\Phi^2 = \sum_{i=2}^{\infty}\langle a_i^2\rangle \tag{2.48}$$

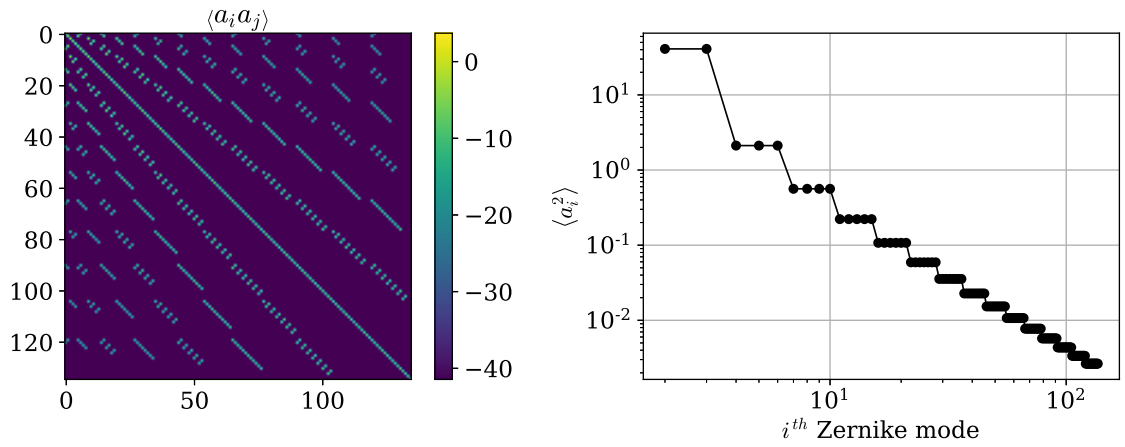

Figure 2.5: On the left: absolute value of the covariance matrix of the turbulent Zernike modal projections. On the right, Zernike modal phase variances function of the Zernike mode. The second diagonal is a diagonal of anti-correlations that only appears by taking the matrix absolute value

where the indexes are taken as Noll indexes. The sum is therefore agnostic of the Piston term.

These results can also be obtained with a Von Karman spectrum, that transforms Eq. 2.47 in:

$$\langle a_i a_j \rangle = 3.90\sqrt{(n_1+1)(n_2+1)}(-1)^{(n_1+n_2-2m_1)/2}\delta_{m_1 m_2}\left(\frac{D}{r_0}\right)^{\frac{5}{3}} \int_0^\infty k^{-\frac{14}{3}} J_{n_1+1}(k) J_{n_2+1}(k)\left(1+\left(\frac{2\pi R_{tel}}{L_0 k}\right)^2\right)^{-11/6} dk \quad (2.49)$$

The influence of the outer scale is depicted in figure 2.6, computed for an outer scale of 5 (red) and 20 m (blue). We observe that the outer scale impacts mostly the low order modes. Additionally, the larger is the outer scale and the higher is the phase variance.

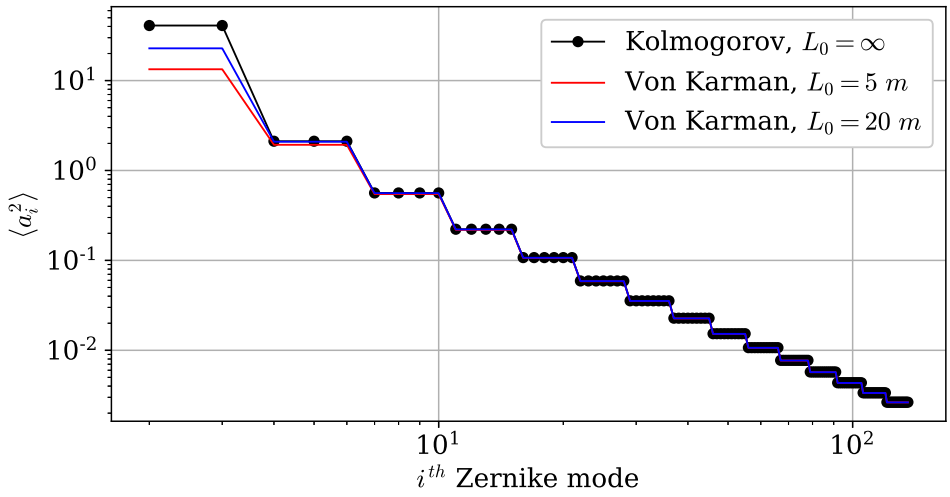

Figure 2.6: Turbulent modal phase variance function of the Zernike mode, for different outer scales.

2.3.5 Uplink point of view

2.3.5.1 Emitted Gaussian mode definition

As described in section 1.2.1.3, the emitted wave from the optical ground station is the Gaussian mode TEM_{00} from the laser. To be accurate, the emitted mode from the pupil is a Gaussian mode truncated by the telescope aperture. However, in uplink models, for simplification, the truncature is neglected. The analytical expression of this Gaussian mode is [98]:

$$E_0(\mathbf{r}, z) = \frac{\omega_0}{\omega(z)} \exp\left(-\left(\frac{|\mathbf{r}|^2}{\omega^2(z)} + \frac{ik_0|\mathbf{r}|^2}{2R(z)}\right)\right) \tag{2.50}$$

In this equation, $\omega(z)$ is the beam radius at $1/e$ (waist) defined as:

$$\omega(z) = \sqrt{\omega_0^2\left(1 + \left(\frac{z}{Z_R}\right)^2\right)} \tag{2.51}$$

where $Z_R = \frac{\pi\omega_0^2}{\lambda}$ is the Rayleigh distance, and ω_0 is the waist of the laser at $z = 0$, and $R(z)$ is the curvature radius defined as:

$$R(z) = z\left(1 + \left(\frac{Z_R}{z}\right)^2\right) \tag{2.52}$$

This expression tends toward $\lim_{z\to\infty} \omega(z) = \frac{\lambda z}{\pi\omega_0}$, which gives the beam divergence in the far field. For instance, in the GEO satellite case, $\omega(d_{sat}) = 68$ m at the wavelength of 1.55 µrad, for a waist equal to $\omega_0 = D/2.2$, that is an optimized waist value.

2.3.5.2 Gaussian beam propagation modeling

As depicted in section 2.3.2 in the plane wave case, this Gaussian beam propagation through atmospheric turbulence can be either modeled thanks to the phase-screen propagation E2E model, or statistically characterized thanks to perturbative approaches (i.e., Rytov model).

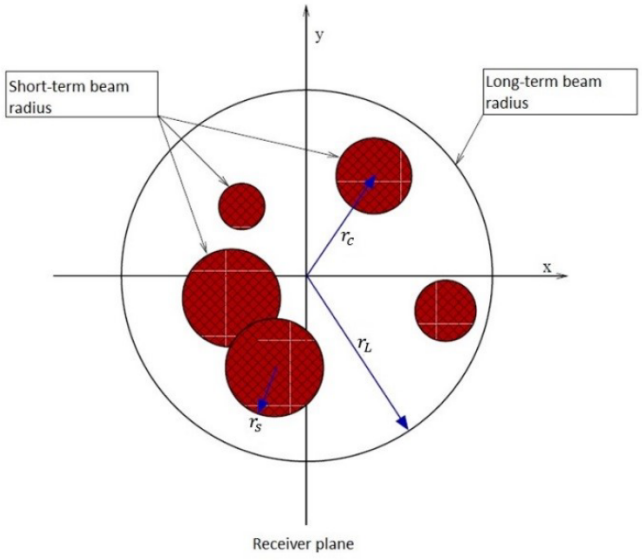

Figure 2.7: Physical disturbances of the Gaussian propagated beam. r_c denotes the deviation distance to the center, r_L the long term beam radius, and r_s the short-term beam radius. Source: [99].

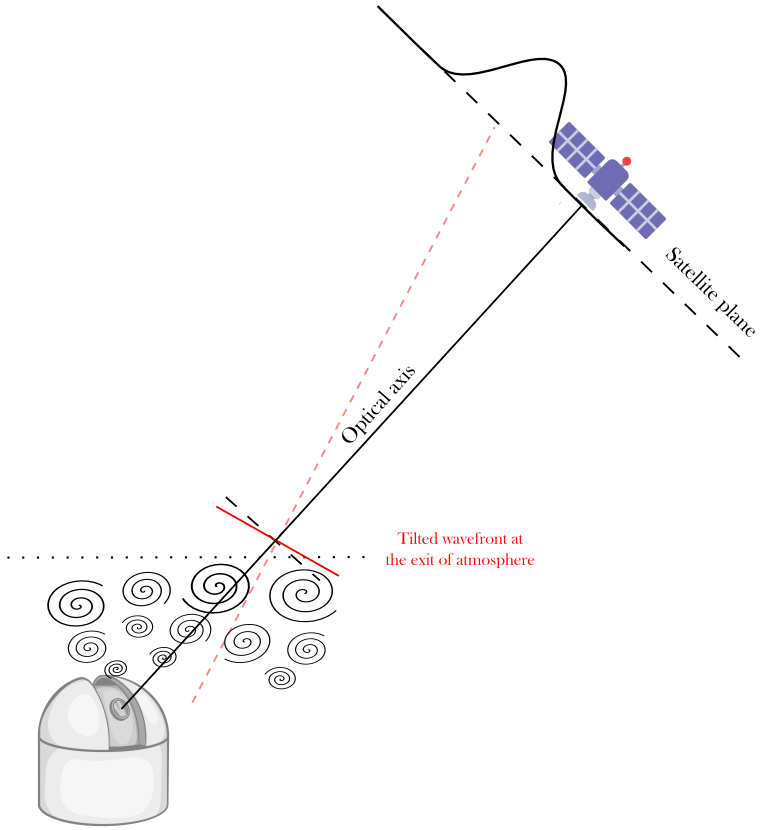

Figure 2.8: Illustration of the beam wander effect.

Through the results obtained thanks to E2E models, it is observed that two major effects impact the diffraction pattern in the satellite plane: beam spreading and beam wander. These two effects are depicted in figure 2.7.

Beam spreading. The beam spreading in the satellite plane describes the widening of the diffraction pattern in the satellite plane, due to turbulence (mostly high frequency turbulence components). The consequence of such a spreading is an energy spread, inducing a decreased amount of flux collected by the satellite.

Beam wander. The beam wander effect describes the beam diffraction pattern barycenter deviation from the center of the optical axis, in the satellite plane. This effect is related to the low frequency phase disturbances induced by the atmosphere, so-called tip and tilt aberrations. Indeed, as depicted in figure 2.8, the atmosphere layer close to the OGS pupil acts as a prism. At the exit of the atmosphere, the beam wavefront can be tilted (the strength of the tip-tilt depends on the turbulence strength). Hence, the far field pattern of this aberrated beam is shifted in the satellite plane.

The beam structure in the satellite plane is statistically characterized in the literature. Three parameters are worth being underlined to model the above effects [92], which are, the beam deviation with respect to the optical axis center r_c, the diffraction pattern long exposure radius r_L (related to the beam spreading effect described earlier), and the width of the short exposure diffraction pattern r_s. The relation between this three radius is:

$$\langle r_L^2 \rangle = \langle r_s^2 \rangle + \langle r_c^2 \rangle \tag{2.53}$$

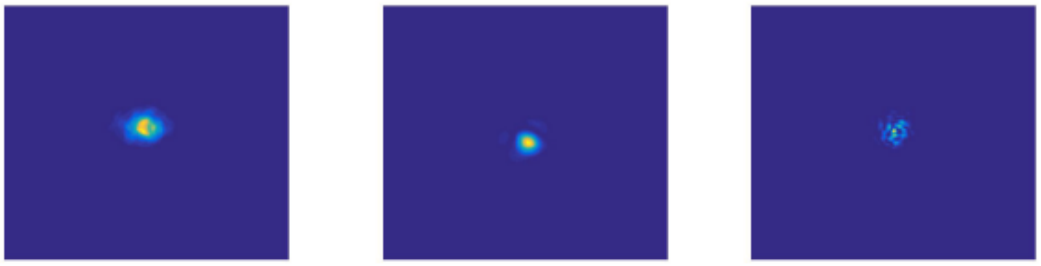

(a) $w_0/r_0 \ll 1$ (b) $w_0/r_0 \approx 1$ (c) $w_0/r_0 \gg 1$

Figure 2.9: Illustration of the beam pattern in the satellite plane in the three turbulent regimes. Source: [100]

where the long-exposure radius is developed by Fante as:

$$\langle r_L^2 \rangle = \left(\frac{L\lambda}{\pi\omega_0}\right)^2 + \omega_0^2 + 8.8\left(\frac{L\lambda}{\pi r_0}\right)^2 \tag{2.54}$$

where L is the satellite distance to the OGS. The first two terms of the equation are related to the diffraction limited pattern width in the satellite plane, and the last term to the beam spreading induced by the expansion of the diffraction pattern width due to the turbulence.

Finally, the beam deviation with respect to the center (the proper beam wander parameter), is computed as:

$$\langle r_c^2 \rangle = \frac{18.2L^2}{k_0^2 r_0^{5/3} \omega_0^{1/3}} \tag{2.55}$$

Three turbulence regimes are highlighted and studied in the thesis of [100]: $w_0 >> r_0$, $w_0 \approx r_0$ and $w_0 << r_0$. We synthesize below the impact on the scintillation pattern:

- $w_0 << r_0$: weak perturbations regime

In this regime, when the emitted waist is smaller than the Fried parameter r_0, we only observe beam spreading in the satellite plane and no beam wander.

Models in the weak perturbations' regime have been developed by Andrews [101]. In this article, the intensity fluctuation I still follows a log-normal law. The novelty of this article is to develop the intensity moments on and off-axis to take into account the Gaussian beam propagation and the pointing errors.

The result of the moments are given by:

$$\langle I(r,L) \rangle = \frac{\omega_0^2}{\omega_e^2} \exp\left(-2r^2/\omega_e^2\right) \tag{2.56}$$

where ω_e is the effective spot size for the uplink channel in the satellite plane, whose expression is given in the article. Here, the spatial mean intensity is approximated by a spatial beam profile.

The intensity variance is given by the concatenation of the on axis contribution and the off-axis contribution:

$$\sigma_I^2(r,L) = \sigma_I^2(0,L) + \sigma_{I,r}^2(r,L) \tag{2.57}$$

Both quantities are computed thanks to the spatial moments of the perturbed field in the Rytov approximation, using the perturbative approach.

- $w_0 \approx r_0$: beam wander regime

In this regime, the beam pattern in the satellite plane is dominated by the beam wander and discrepancies appear with respect to results obtained with the Rytov theory. It was questioned in the scientific community if the Rytov approximation accounted or not this effect, and if it had to be added on top of Rytov developments. Two main families of uplink models arose.

The first family of uplink models develop the on-axis scintillation as:

$$I(0,0,L) = I_s I_{BW} \tag{2.58}$$

where I_s is the Rytov scintillation contribution and I_{BW} is the beam wander contribution. From this first hypothesis, two models were developed. The first one, by [98], assumes that the scintillation has a Gaussian profile with a maximum equal to the on-axis scintillation contribution $I(0,0,L)$, that is independent of the beam wander. It results that:

$$I(0,0,L) = I(0,0,L)\exp\left(-2\frac{\delta x^2 + \delta y^2}{\omega_{ST}^2}\right) \tag{2.59}$$

where δx and δy are the laser spot deviation from the center. In his article, he details the moment of the I (mean and variance). However, he does not develop a closed form model of the PDF of I. The beam wander term statistical distribution was developed in [102, 103] as a beta distribution such that:

$$P_{I_{BW}}(I_{BW}) = \frac{1}{2\alpha} I_{BW}^{\frac{1}{2\alpha}-1} \tag{2.60}$$

where $\alpha = < r_c^2 > /\omega_{ST}(L)$. [102] also developed the complete PDF of I, in weak, moderate and strong turbulence affected by beam wander.

Similarly, Dios in [104] develops a model, accounting this time for a scintillation term depending on the beam wander, as:

$$I(0,0,L) = I(\delta x, \delta y, L)\exp\left(-2\frac{\delta x^2 + \delta y^2}{\omega_{ST}^2}\right) \tag{2.61}$$

The second family of models are the LOT models (low-order turbulence), consisting in analytically computing the aberrated field on its first phase Zernike modes. The original LOT model was developed by Baker [103]. It was later extended by Camboulives for AO pre-compensated uplinks in the W-PLOT model [105].

- $w_0 >> r_0$: strong perturbation regime

In this regime, the spatial coherence of the beam is lost in the satellite plane. Therefore, it was proposed to model the irradiance fluctuations with the Gamma-Gamma model [106]. This model, widely used for horizontal links, assumes that the intensity results from the multiplication of intensity resulting from diffractive effects induced by small eddies ,I_d, and the intensity resulting from diffractive effects induced by large eddies, I_r. Finally, expressing I as:

$$I = I_r I_d \tag{2.62}$$

where I_r and I_d follows Gamma distribution and are assumed statistically independent, the probability density function of I is computed as:

$$p(I) = 2\frac{(\alpha\beta)^{\frac{\alpha+\beta}{2}}}{\Gamma(\alpha)\Gamma(\beta)} I^{\frac{\alpha+\beta}{2}-1} K_{\alpha-\beta}(2\sqrt{\alpha\beta I}), \quad I > 0 \tag{2.63}$$

where α and β are deduced from the scintillation index and beam parameter ().

However, empirical description.

2.3.6 Coupling to an optical system

Previously, we described the punctual field phase and amplitude fluctuations. However, the metric of interest for telecommunications, regardless of the link direction (up or down), is the coupled flux. It is defined as the overlap integral between the turbulent complex field and the receiver mode, typically a Gaussian mode from a single mode fiber.

The complex coupling of the received mode Ψ_1 to the reception mode Ψ_2 is expressed as:

$$\Omega(t) = \frac{\iint \Psi_1(\mathbf{r},t)\Psi_2^*(\mathbf{r},t)d^2r}{\sqrt{\iint |\Psi_1(\mathbf{r},t)|^2 \, d^2r \cdot \iint |\Psi_2(\mathbf{r},t)|^2 \, d^2r}} \tag{2.64}$$

which is the normalized overlap integral between the two modes.

We define the coupling efficiency as the square modulus of the complex coupling:

$$\rho(t) = |\Omega(t)|^2 \tag{2.65}$$

$$\phi_\Omega(t) = \arg(\Omega(t)) \tag{2.66}$$

where we also defined the argument of the complex coupling $\phi_\Omega(t)$. This quantity corresponds to the so-called phase noise and is of interest if we want to consider coherent modulation formats.

Finally, the coupled flux is defined as:

$$f(t) = \rho(t) \iint |\Psi_1(\mathbf{r},t)|^2 \, d^2r \tag{2.67}$$

which is the coupling efficiency multiplied by the energy collected by the reception aperture.

2.3.6.1 Downlink case

In the downlink case, we express the received mode as the turbulent complex field cropped by the telescope aperture in the pupil plane. Therefore, we can express the received mode as:

$$\Psi_{1,down}(\mathbf{r},t) = A_0 \cdot \exp(\chi_{turb,down}(\mathbf{r},t) + i\Phi_{turb,down}(\mathbf{r},t))P(\mathbf{r}) \tag{2.68}$$

where $P(\mathbf{r})$ is the pupil mask function.

In this case, the receiver mode $\Psi_{2,down}(\mathbf{r},t)$ is a fiber Gaussian mode whose waist is adjusted in order to optimize the coupling with an unperturbed optical field.

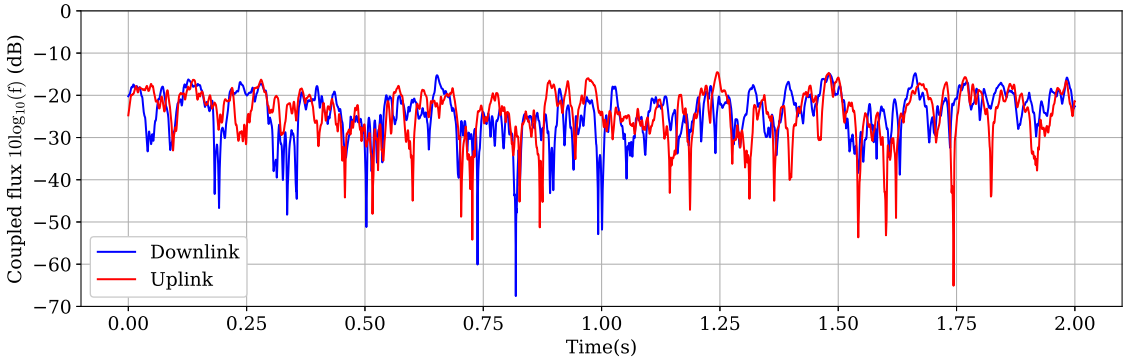

Figure 2.10: Coupled flux time-series for an optical downlink (blue) and an optical uplink (red), for a 60 cm OGS telescope Tx/Rx at 1550 nm, and for turbulence conditions characterized by $r_0 = 4$ cm, $\theta_0 = 6.8$ µrad and $\sigma_\chi^2 = 0.08$.

An illustration of the coupled flux behavior, computed from E2E turbulent fields, is given in blue in figure 2.10. We observe large coupling fluctuations, with losses reaching -70 dBs in the considered scenario.

2.3.6.2 Uplink case

In the uplink case, the received turbulent mode after propagation Ψ_1 in the satellite plane is coupled to the satellite Rx mode, Ψ_2 which is also a Gaussian mode. However, given the size of the satellite telescope entrance pupil compared to the diffraction pattern size (in the order of hundred of meters), the complex field received by the telescope in the pupil plane is considered uniform in phase and amplitude. Ψ_2 is therefore modeled as a Dirac.

An illustration of the uplink coupled flux is given in red in figure 2.10, showing heavy signal fluctuations.

We will see later in chapter 3 that, when no AO correction is applied, the uplink coupled flux statistics are actually identical to the downlink coupled flux statistics. This can be observed in figure 2.11 where is depicted the coupled flux (up and down) probability density function and cumulative density function. We observe that these functions are identical in the two cases.

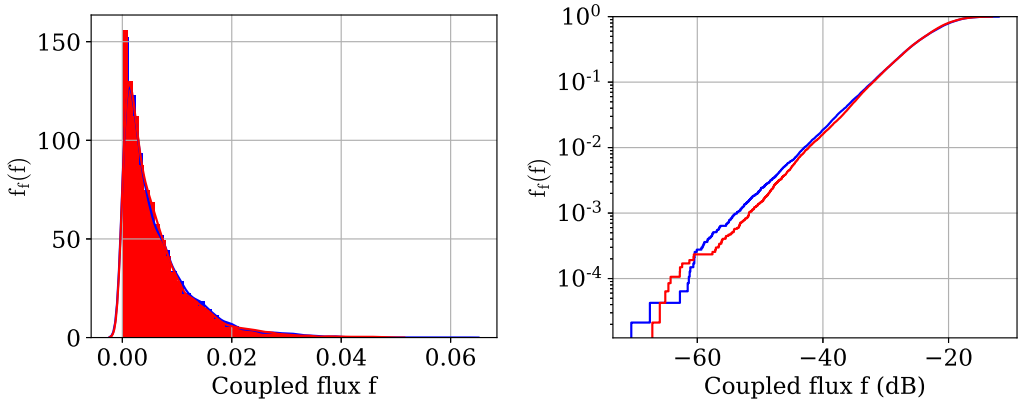

(a) PDF (b) CDF

Figure 2.11: Uplink (red) and downlink (blue) coupled flux without AO correction, in the turbulence case MOSPAR 9090 30°, for 60 cm OGS Tx/Rx diameter D=60cm.

A last observation is that, either in the uplink or downlink case, the coupled flux attenuation is huge, with a mean attenuation of -20 dB. It is therefore mandatory to use adaptive optics in order to enhance the coupled flux statistics (up and down).

2.4 Impact of the adaptive optics correction

In order to mitigate the coupled flux attenuations, a solution is to use an adaptive optics system that will correct the wavefront perturbations of the optical complex field. Adaptive optics is particularly foreseen in the GEO case, due to the severe link budget constraints induced by the satellite distance. Indeed, most of the OGS depicted in section 1.2.2 envision to use such a system for the first GEO feeder link demonstrations.

2.4.1 Context: Astronomy heritage

Adaptive optics systems are widely used in the field of astronomy, leading to many system developments. Indeed, it is at stake in the astronomy field to ensure reaching the diffraction limit of the telescopes in order to improve the spatial resolution, therefore allowing to observe smaller and smaller space objects, located far away from our galaxy, informing us about the physics of our universe. Optical communications can benefit from these developments undertaken for many years in the astronomy field. While some design issues are common, it is worth underlining differences in the performance requirements that will influence the AO system design for telecom applications:

- Performance criterion

Astronomical imaging and optical communication differs in the performance criterion used to characterize the system. Astronomy imaging uses time averaged metrics such as the long exposure Strehl ratio, based on the phase residual variance, whereas in optical communication, we will be interested in the instantaneous performance and statistics such as quantiles of the signal and time statistics, in order to ensure the continuity of the communication.

Indeed, in astronomy, in order to capture the desired information (image of a quasi-static object), the systems have to use long exposure detection, because of the low SNR induced by the variable brightness of astronomical objects. In telecommunications, the detection frequency has to be very high ($>$ of the baud rate, i.e., the symbol rate of the signal). In this case, there is no issue of SNR, due to the high flux provided by the laser beam (with respect to star irradiance). This long exposure versus short exposure character will change the nature of the models used to characterize the field and the performance of the system.

- Receiver nature

Before reaching a photoelectric detector, the beam goes through an optical system in the telecommunication case. Therefore, to compute the complex coupling of the beam to the SMF, we need to consider the complex field, either in the pupil plane, satellite plane or focal plane. On the reverse, in astronomy, the physical quantity of interest is the point-spread function which is already the square modulus of the diffraction pattern in the focal plane. This PSF is well studied in long-exposure[107, 108], less for short exposure, even if some works considered this case [109]. Considering a short exposure complex diffraction pattern, the closest field of astronomy that we could find is stellar interferometry, that uses this complex field analysis to compute the complex visibilities.

- OGS and link properties

A major difference between the nighttime astronomy and the telecommunication field are the diameter sizes used for the telescopes. In astronomy, it is at stake to use big telescope aperture in order to increase the system resolution (accompanied by very complex AO

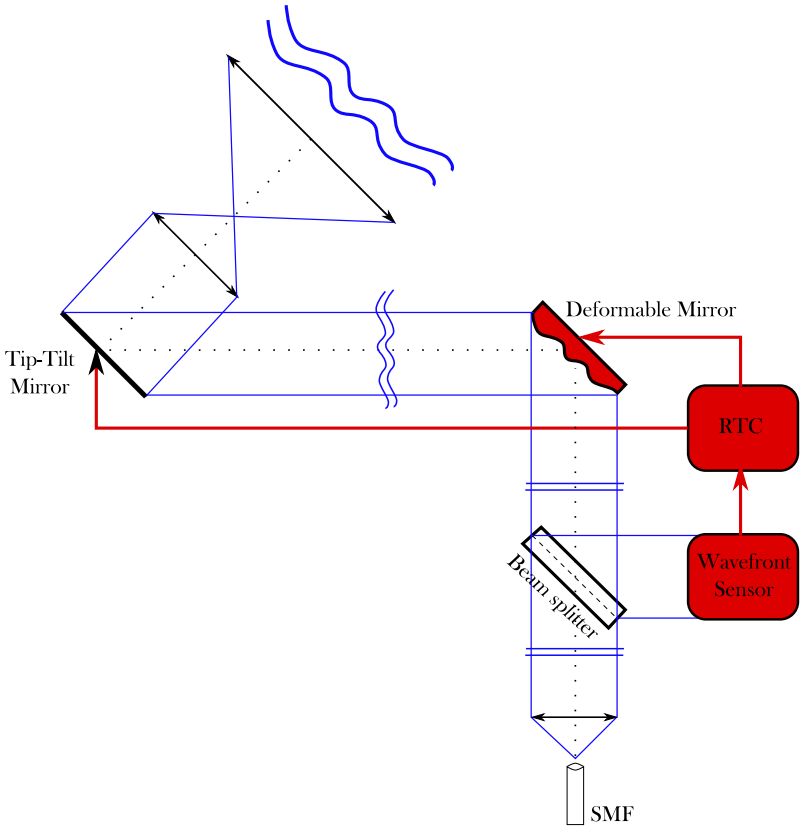

Figure 2.12: Schematic of an adaptive optics system in closed loop in a telecommunication downlink configuration. The optical rays and wavefront are depicted in blue. The elements composing the AO system are colored in red.

systems), and to collect as many photons as possible. In the telecom field, depending on the considered link, this diameter requirements are relaxed, and are constrained by link budgets. The range of considered telescope aperture diameters goes from 10 to around 1 m. A second requirement is the price and commercial availability of the telescopes. This limits the size of the telescope aperture.

- Turbulence conditions

In the astronomy field, most of the observation occurs during the night. For the telecommunication links, the system needs to work 24h/7d. Therefore, the links are expected to work under more challenging turbulence conditions.

2.4.2 Adaptive optics system description

2.4.2.1 System overview

An adaptive optics system is a closed loop system that corrects in real time the wavefront distortions of an incoming disturbed optical beam. This system is depicted in figure 2.12 in the case of a downlink incoming beam. To perform the correction, this system is composed of a deformable mirror that corrects the wavefront, a wavefront sensor, that senses the residual phase perturbations, and a real-time controller that computes the next command to apply to the deformable mirror. After the beam correction by the deformable mirror, a part of the signal is sent toward the wavefront sensor and the other part, which is the useful part of the signal, is sent toward a single mode fiber. The operation of these different elements is described below.

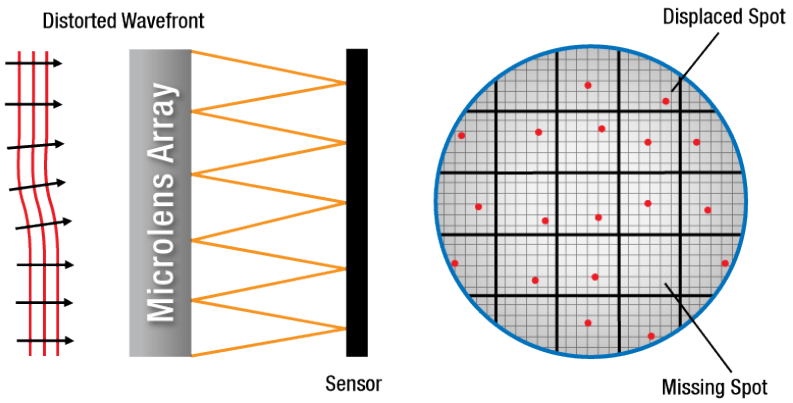

Figure 2.13: Illustration of the working principles of a Shack-Hartmann Wavefront sensor. Source: www.thorlabs.com

2.4.2.2 Wavefront sensor

One of the most frequently employed wavefront sensors (WFS) is the Shack-Hartmann WFS [110, 111]. This sensor operates within the pupil plane, employing sub-pupils to sample the pupil. Each sub-pupil provides local information about the wavefront, as described in figure 2.13. The Shack-Hartmann WFS determines the local slope of the wavefront by analyzing the barycenter displacement in the sub-pupil, induced by the wavefront sampled local tilt. Another commonly used WFS is the pyramidal WFS, introduced by [112] and further developed by [113]. The pyramidal WFS exploit Fourier theory principle to analyze the wavefront. However, the focus in this work will primarily be on the Shack-Hartmann WFS, given its widespread usage in adaptive optics.

The WFS does not provide directly a phase measurement, but a vector of slopes measurement. Afterward, the phase needs to be reconstructed by the RTC. The model of the slopes measurement vector y_{mes} is:

$$y_{mes} = D\Phi_{res} + b \tag{2.69}$$

where D is the linear operator characterizing the WFS, Φ_{res} the residual phase to reconstruct and b is the noise vector. In the weak perturbation regime, this noise is composed with photon noise and detection noise.

In the following of this study, we assume being in the high SNR regime and therefore, we neglect the measurement noise induced by the WFS.

2.4.2.3 Deformable mirror

The deformable mirror physically corrects the beam wavefront. An overview of the DM technologies is established in [114]. To explain the principle, we will consider a DM using an optical membrane and actuators. In practice, the actuators receive a command from the RTC that contains a command increment to update the mirror's shape. By application of this command, the actuators modify the shape of the membrane accordingly.

We define the phase after correction as:

$$\Phi_{res}(\mathbf{r}, t) = \Phi_{turb}(\mathbf{r}, t) - \Phi_{corr}(\mathbf{r}, t) \tag{2.70}$$

where $\Phi_{turb}(\mathbf{r}, t)$ is the distorted wavefront of the incoming beam and $\Phi_{corr}(\mathbf{r}, t)$ is the correction applied by the DM.

2.4.2.4 Real-Time Controller: reconstruction and control

The role of the real-time controller is to compute the command to control the DM given the received WFS measurements. To achieve an optimal correction, it is necessary not only to spatially reconstruct the phase from the wavefront sensor measurements but also to manage the temporal aspects related to the control loop, particularly issues such as system bandwidth, loop stability, and control optimization of the commands to be applied to the deformable mirrors. In a first approximation, spatial and temporal problems can be decoupled, although there are connections between them, and defining an optimal control requires a comprehensive approach to the problem [115].

We describe the temporal effects affecting the AO loop dynamics in the following. Due to the time of measurements acquisition and computation time of the new command, a delay arises between the measurement and correction instants. This time delay is illustrated on figure 2.14, where y_n depicts the measurements and u_n the command at the instant nT, where T depicts the frame duration. It is expressed as a multiple of the loop frequency $f_{samp} = 1/T$. In the following, we will assume an AO loop delay of two frames. Other aspect of the loop design such as the design of AO control laws will be neglected in the rest of this thesis.

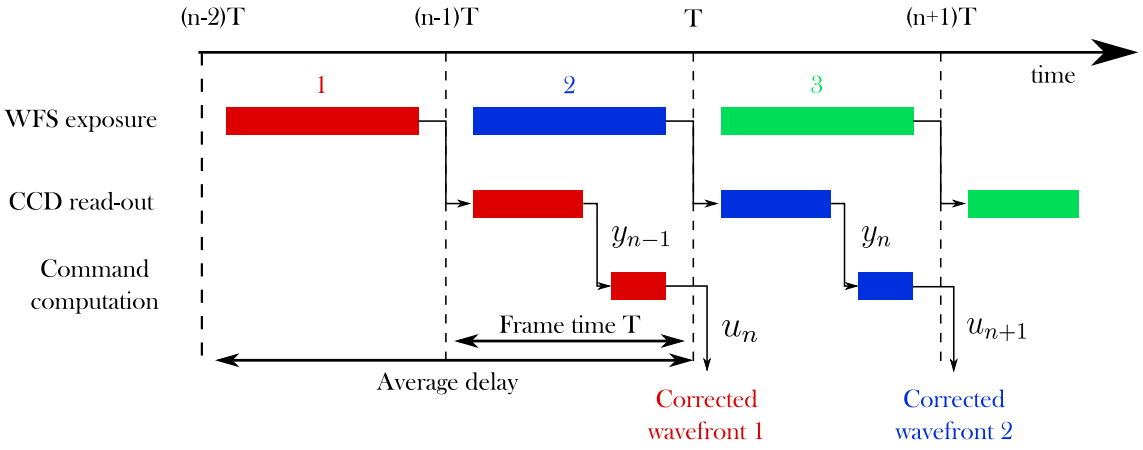

Figure 2.14: Chronogram of an AO correction

2.4.3 Adaptive optics error budget

The phase correction of the adaptive optics system described above is intrinsically not perfect due to system aspects. We can highlight sources of errors that will contribute to what we call: the adaptive optics error budget. This error budget is characterized by the phase residual variance after correction, which is expressed as:

$$\sigma^2_{\Phi_{res}} = \sigma^2_{Fitting} + \sigma^2_{Aliasing} + \sigma^2_{Tempo} + \sigma^2_{Others} \tag{2.71}$$

The different sources of contributions of residual phase variance are depicted below.

Fitting. The fitting error results from the finite spatial resolution of the measurements and of the correction. Indeed, due to the finite number of sub-pupils and actuators, it is only possible to measure and correct the phase on a limited number of modes. This residual phase variance term affects therefore the high frequencies of the residual phase.

Aliasing. Because the Shack-Hartmann wavefront sensor samples the wavefront using a limited number of sub-pupils, high spatial frequencies are poorly sampled and partially

folds upon the measured lower frequencies. This results in a bias that propagates towards the AO correction, generating an aliasing residual error on the corrected modes. This error is commonly modeled as a portion of the fitting error.

Temporal error. The temporal error is induced by the adaptive optics loop delay. As explained in section 2.4.2.4, the measurement acquisition time and the computation time of the command by the RTC induces a delay between the instant of measurement of the perturbation and the instant of phase correction. Therefore, because the turbulence evolves with time, this delay of correction induces a phase error. This error affects all the corrected modes. In the following, we will consider a 2 frames loop delay, which is equal to $\delta t = 2/f_{samp}$, where f_{samp} is the sampling frequency of the AO loop.

Others. There are other sources of phase error due for instance to calibration errors, static aberrations induced by the optical bench, vibrations, or measurement noise from the WFS. These errors will be neglected in the following. A last, but not least, error that can be encountered in an adaptive optics system is the anisoplanatism error. This error occurs when the direction of the beam sensed is different from the direction of the beam that has to be corrected. It is of major interest in large field of view astronomy. In the telecommunication domain, there is no anisoplanatism in the downlink correction. However, we will see that it is a major contributor to the phase error of pre-compensated uplinks.

2.4.4 Impact of the correction on the coupled flux

2.4.4.1 Downlink coupled flux after AO correction

In the downlink case, when an AO correction is applied, the coupling equation from Eq. 2.64 transforms as:

$$\Omega_{down,AO}(t) = \frac{\iint \Psi_{corr}(\mathbf{r},t) M_0^*(\mathbf{r}) d^2r}{\sqrt{\iint |\Psi_{corr}(\mathbf{r},t)|^2 \, d^2r \cdot \iint |M_0(\mathbf{r})|^2 \, d^2r}} \tag{2.72}$$

where Ψ_{corr} is the downlink corrected field that is expressed as $\Psi_{corr}(\mathbf{r},t) = A_0 \exp(\chi(\mathbf{r},t) + j\Phi_{res}(\mathbf{r},t))$, and $M_0(\mathbf{r})$ is the fiber Gaussian mode.

It can be either numerically modeled thanks to E2E simulation, followed by a numerical AO simulator, that emulates dynamically the AO correction, as described in section 2.3.2, or using simplified models that exploit the statistics of the residual phase after propagation and AO correction budget [89]. The principle of this simplified model will be described in chapter 3.

The downlink coupled flux with adaptive optics correction has also been statistically characterized in the work of Lucien Canuet [116]. This model will be described in details in chapter 7. It lies on an approximation of the overlap integral that stands in the residual phase regime. This model, whilst having the advantage to characterize the coupled flux statistics function of the residual phase variances, has no closed form expression. It was later shown, in the work of Klotz [117], that the Gumbel law was a very good fit for the downlink coupled flux corrected by AO.

2.4.4.2 AO pre-compensation for uplink

To compensate for uplink phase error, the technique envisioned is to pre-compensate on the ground the uplink beam before its emission with a given correction. This pre-compensation

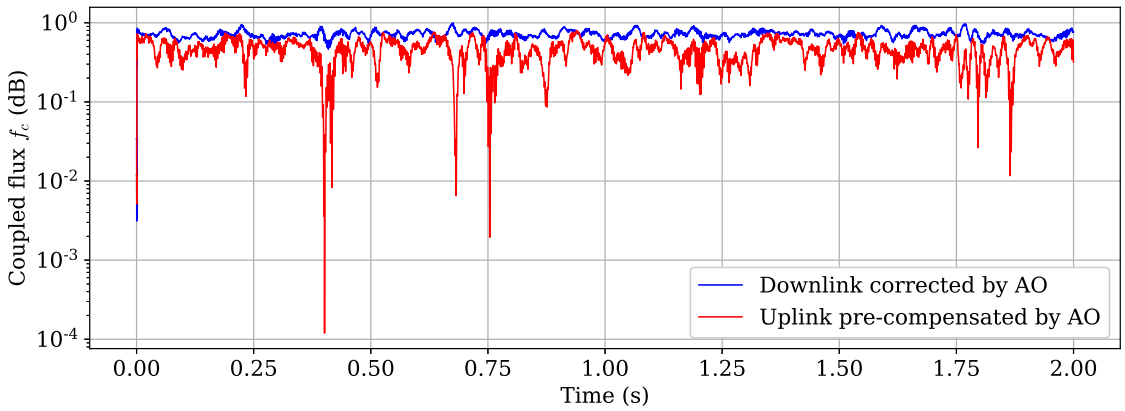

Figure 2.15: Illustration of the downlink (blue) and uplink (red) coupled flux after adaptive optics correction, in the turbulence case MOSPAR 9090 at 30° elevation, for an OGS aperture diameter $D = 60\ cm$.

technique relies on the point reciprocity principle [118]. This principle will be detailed in section 3.2.1 of chapter 3. The ideal AO correction would be obtained by sensing a beacon propagating from space to the ground on the uplink axis. The GEO-Feeder link is bidirectional, but the only beacon that can be used for sensing is the downlink, that is separated from the uplink by the point-ahead angle, as mentionned in section 1.2.1. Therefore, the phase perturbations encountered by the two beams are not the same. We will refer to this phase error as anisoplanatism. The value of the pre-compensation phase error depends on the turbulence angular decorrelation, described by the anisoplanatic angle θ_0, given in section 2.2.4.3.

This technique, that consists in using the downlink beam correction to pre-compensate the uplink, is the more mature technique. We call it **Classical pre-compensation**. However, due to the pre-compensation error, the coupled flux aboard the satellite still suffers from long and deep fades. An illustration of the coupled flux obtained with the E2E simulation of an AO pre-compensated is depicted in figure 2.15 in red, compared with the downlink corrected link in blue.

To our knowledge, there is no analytical model yet to describe this coupled flux behavior. It is therefore mostly studied thanks to numerical simulations. In the following, we review the literature studying the anisoplanatic phenomenon as well as its impact on the coupled flux applied to GEO-Feeder links.

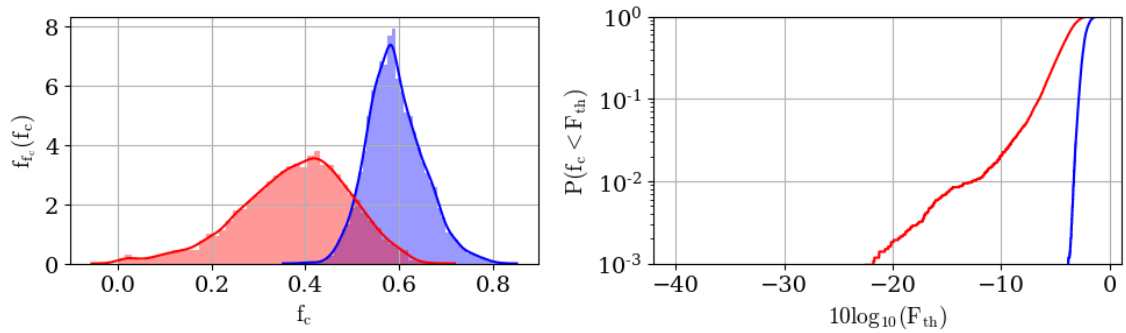

Figure 2.16: Statistics of the AO corrected downlink (blue) and uplink (red). On the left: PDF. On the right: CDF.

2.5 Point ahead anisoplanatism : uplink partial AO correction

2.5.1 Anisoplanatism in the literature

The anisoplanatism effect has been studied for a long time for astronomy purposes. Indeed, for wide field of view imaging, it is necessary to correct for the anisoplanatism error with AO systems or to account for this error in deconvolution algorithms. This led to several models for the characterization of the phase anisoplanatism.

2.5.1.1 Anisoplanatic phase error

A first characterization of the anisoplanatic phase error is given by Fried [80] as:

$$\sigma^2_{\Phi,aniso}(\theta) = (\theta/\theta_0)^{5/3} \tag{2.73}$$

where θ_0 is the anisoplanatic angle given in Eq.2.5. However, this expression is a punctual characterization and does not include the pupil effects in the error computation. It was shown to be pessimistic when characterizing the anisoplanatism error over finite apertures [119].

A more accurate description of the phase error induced by the anisoplanatism was given in a modal formalism by Chassat [120]. The associated formulas will be given and analyzed in Chapter 3. We compare the anisoplanatic phase variance by Fried and the one of Chassat in figure 2.17. In this figure, the Fried error is represented in black, and the Chassat anisoplanatic error in blue/green, function of the angular decorrelation, for an anisoplanatic angle $\theta_0 = 6.83$ µrad. This figure confirms that the Fried expression overestimate the anisoplanatic error, and that this error depends strongly on the aperture diameter.

An example of the anisoplanatic modal spectrum is given in figure 2.18, compared with the turbulent modal spectrum without correction. In this figure, we observe that the anisoplanatic error induces strong low order phase residual (especially tip and tilt).

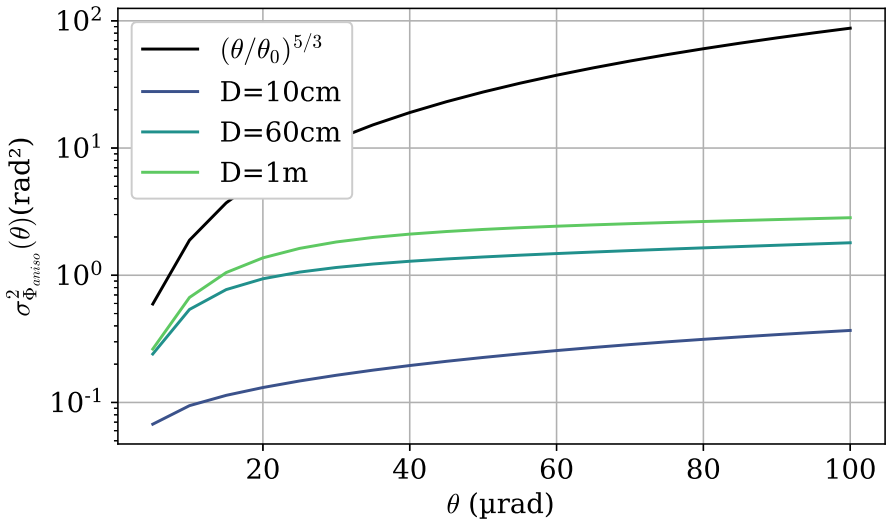

Figure 2.17: Comparison between the phase variance by Fried and the phase variance by Chassat, function of the angular separation θ, for the following integrated parameters: $\theta_0 = 6.83$ µrad,$r_0 = 4.1$ cm, $\sigma^2_\chi = 0.08$.

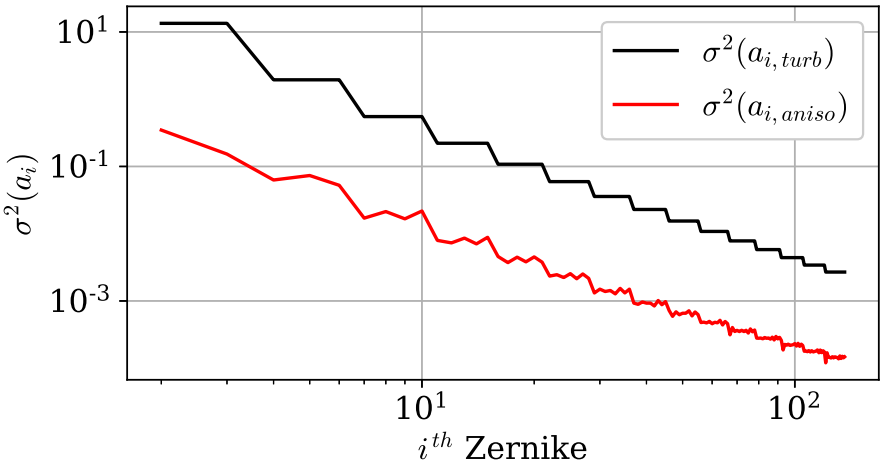

Figure 2.18: Modal phase variance of the turbulent wavefront in black, and the anisoplanatic wavefront in red.

2.5.1.2 Impact in the focal plane

The impact of the anisoplanatic phase error on the point spread function in the focal plane have been studied for astronomy purposes. It was shown in [121] that the long exposure optical transfer function (OTF) (averaged over a given time slot) is asymmetric. It results that the long-exposure PSF is elongated. An example of this elongation is given in figure 2.19, in the center. Considering now the short exposure anisoplanatic PSF, it is shown to present a non-symmetric halo and coherent pic whose barycenter is shifted. All these effects are induced by the energetic low-order modes phase residuals. A characterization of the moments of the short-exposure PSF was undertaken in [109].

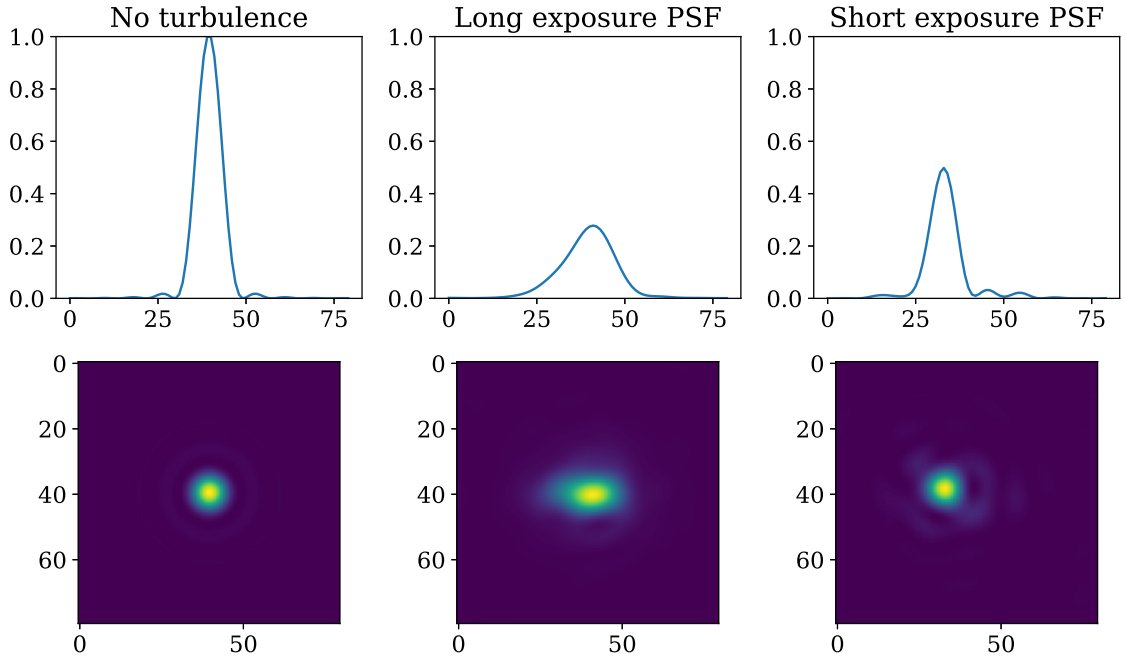

Figure 2.19: Anisoplanatic PSF compared to an Airy pattern. On the left: Airy pattern (PSF with perfect plane phase), center: Long exposure anisoplanatic PSF (averaged on 0.1 s), right: short exposure anisoplanatic PSF. Top: centered slice, bottom: image in the focal plane.

2.5.1.3 Impact in the satellite plane

In the case of the AO pre-compensated uplink suffering from anisoplanatic phase error, there is no analytical model in the literature describing the impact of this partial AO correction on the far-field pattern in the satellite plane, neither on the coupled flux aboard the satellite. We can though find a characterization of the moments of the pre-compensated anisoplanatic uplink beam in [122]. Further investigation have been done by Tyson in [1] that performs an analysis of the fade statistics, and later a BER analysis of an uplink pre-compensated beam, under perfect AO correction [123]. In this article, Tyson assumes the irradiance in the satellite plane to be ruled by the Gamma-Gamma distribution, and computes the probability law parameters function of the fully turbulent parameters filtered by the AO correction transfer function. However, as mentioned, he assumes a perfect AO correction of the N first AO modes, and therefore, do not consider anisoplanatic phase residuals. This perfect AO correction can be applied only if an off-axis measurement beacon is provided. He mentions that such a beacon could be provided by a slave satellite or a laser guide star. However, the practical implementation of a slave satellite has not been demonstrated, and the laser guide stars systems still suffers from tip tilt and focus indetermination, that are strong contributors to the signal fades.

Therefore, most of the characterizations made in the literature of finer statistics of the AO pre-compensated uplink impacted by anisoplanatism relies on numerical simulation or experimental studies.

2.5.2 Experimental studies of PAA anisoplanatism for GEO feeder links

We sum-up in this section the main findings from experimental demonstrations of AO pre-compensated uplinks. Up-to-date, we can cite several on-bench or in the field experimental demonstrations of AO pre-compensated uplinks relying on classical pre-compensation. An overview of these experiments is given in [124].

The first in lab AO pre-compensation representative of GEO-Feeder uplinks, with a dynamic AO correction, have been performed by the Fraunhofer Institute [125]. In this work, a tip-tilt off-axis pre-compensation have been performed for different values of angular separation. They evaluated the achievable Strehl ratios associated to the different angles. The Strehl ratio was shown to be improved with respect to an uncompensated link. This lab experiment was followed by on the field experimental tests, firstly on 494 m, and then on a 1 km link [126, 127]. Once again, these experiments assessed for the improvement of the coupled flux statistics thanks to the AO pre-compensation under angular decorrelation, with respect to uncompensated links.

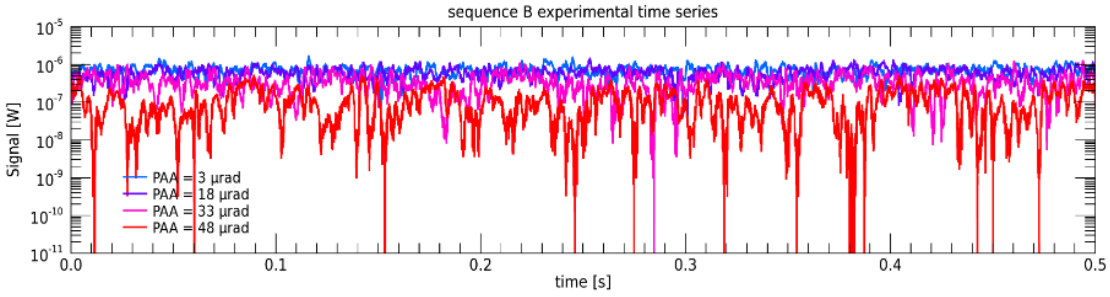

Figure 2.20: Illustration of time-series of the pre-compensated FEEDELIO uplink, function of the angular decorrelation[89]

In 2019, another field experiment was performed jointly by TNO and the DLR [128] on a 10 km slant path elevation line of sight. They proved that despite the point-ahead angle, a tip-tilt pre-compensation improved by 4.5 dB the coupled flux, with an additional 1.5 dB gain with 16 AO modes.

Finally, ONERA demonstrated AO pre-compensation in a 13 km slant path experiment in representative GEO Feeder turbulence conditions. The project, called FEEDELIO (funded by ESA), led to two campaigns and many results, including time-series, still exploring the performance of the AO correction with respect to turbulence conditions and angular decorrelations [89, 129, 130]. The statistics of coupled flux obtained have also been exploited in order to validate ONERA in-house numerical models. An example of the time-series function of the angular separation is given in figure 2.20, where we can clearly observe the degradation of the coupled flux statistics with the increasing PAA. Other results from the FEEDELIO experiment, in particular reciprocity results, will be given in chapter 3.

To conclude, all these demonstrations participated in proving the viability and efficiency of AO pre-compensation for satellite GEO-Feeder uplinks. However, it also demonstrated that the classical pre-compensation is very impaired in severe turbulence angular decorrelation conditions, resulting in a fading channel.

2.6 Fading mitigation techniques

We can find several methods in the literature to deal with communication over fading channels. On the one hand, physical techniques are developed to limit the atmospheric impact on the optical beam propagation, by improving the channel statistics. On the other hand, digital signal processing techniques have been developed in the framework of RF communications to combat the channel fadings.

2.6.1 Optical methods

The channel statistics can be improved following the techniques listed below:

Small emission aperture systems

The first option is to decrease the diameter of the emitter. It has the effect to reduce the impact of the atmosphere on the optical propagation. It is equivalent to a reduction of the D/r_0 ratio. This solution limits the coupling losses due to phase disturbances. It is however more sensitive to losses induced by amplitude fluctuations and also leads to greater geometrical losses due to a greater beam divergence. Therefore, given the tight constraints of the GEO Feeder link power budget, induced by the large satellite distance, having a small diameter is not an adapted solution. Using a small emission aperture diameter can however be suitable for LEO uplinks that are less constrained by the link budget.

Multi-aperture systems

Multi-aperture systems are designed to use several small apertures, therefore taking advantage of the small aperture fading averaging property described above while combining more power thanks to the increased number of emitter. Additionally, as the emitted beams propagate through different optical paths, they do not encounter the same turbulence perturbations, hence not the same signal fluctuations. This allows to average the received power onboard the satellite. However, this sum needs to be incoherent to prevent from destructive interferences along the path. This scheme is already implemented in systems

as in the LLCD [131], but operates at very low data rates. A study by Conan showed that for a fixed emitted power in a ground to GEO scheme, AO pre-compensated links were still more advantageous than multi-aperture schemes [132]. Further details on multi-aperture OGS schemes will be provided in chapter 6.

The multi aperture transmission scheme is an active field of research. A solution was proposed by Fuchs in order to be able to use this scheme with coherent modulation schemes [133].

Adaptive optics pre-compensation optimization

The last solution that would allow using wider telescopes, hence limiting geometrical losses, is to use an optimized AO phase pre-compensation. The more accurate AO pre-compensation would be provided by a downlink beacon propagated at PAA. As mentioned by Tyson, this measurement beacon could be provided by an LGS or a slave satellite. However, the slave satellite implementation has not yet been demonstrated and the LGS solution does not yet allow for sensing the tip tilt and focus, that are crucial modes to correct to limit the signal attenuations. A more comprehensive explication of these state-of-the art methods issues will be given in chapter 4. In addition, chapter 4, chapter 5 and chapter 6 of this thesis tackles the pre-compensation phase optimization at point-ahead angle.

2.6.2 Telecommunication fading channel mitigation techniques

Fading mitigation techniques have been developed in the wireless RF communication domain. However, these techniques need to be tailored to the physical channel properties. The main fading mitigation technique is the one exploiting diversity that is explained as follows.

Diversity principle

The principle of diversity is to exploit parallel independent channels in order to send combinations of information, and therefore, average the channel fadings and increase the transmission rate. Several parallel channels can be considered using different degrees of freedom: frequency or wavelength, the time, the space, polarization, or the modes. Diversity methods are widely used in wireless radio communication, hindered by multipath transmission, and in optical fiber communication in order to maximize data-rates.

Diversity for ground to satellite links

To exploit diversity in ground to satellite links, there is a need to identify uncorrelated parallel channels.

Frequency diversity. As the turbulence is achromatic, it is not possible to use parallel frequency channels, as they are affected the same. However, as stated in [134], in presence of scattering due to the presence of fog or thin clouds, the coherence bandwidth of the channel increases up to 1-100 THz [135].

Spatial diversity. Spatial uncorrelated channels could be considered. Indeed, if the emitter or receiver are separated by a distance exceeding the beam coherence length, the beams emitted through this spatially separated channels will be uncorrelated. These distance belongs to the 2-30 cm range at the telecom wavelengths [136]. Moreover, this distance decreases as the turbulence strength increases, which makes this scheme suitable and feasible to protect the communication link to strong atmospheric disturbances. Classically, this scheme can be applied with several emitters and/or receivers. However, in the

case of the ground to satellite link, given the size of the diffraction pattern in the satellite plane ($\sim$ 100 m), receiver diversity is not applicable. The scheme of multi-emitter diversity is called multi-input single-output (MISO).

Temporal diversity. The last degree of freedom that can be exploited to find parallel uncorrelated channels is the time. To use temporal diversity, the duration separating the symbols needs to exceed the coherence time of the channel, T_c, that is typically in the order of 0.1-10 ms (depending on if the link is AO corrected or not). The typical operation that exploits the diversity is the interleaving process, that permutes the order of read-out of the encoded bits or symbols, in order to spread the errors induced by the fading channel and allow for the FEC decoding.

Others. Other type of diversity can be found considering optical fiber links, such as modal or polarization diversity. However, in the case of FSO links, there is no way to distinguish different modes at the Rx onboard the satellite and both polarization are affected the same by the turbulence.

The article [134] illustrates the use of coding diversity to improve the throughput for ground to GEO Feeder links. They propose a space-time block coding scheme and a multi-beams, multi-λ coding scheme that are shown to be quasi-orthogonal full rate codes. The full-rate property means that for one degree of freedom used, one symbol is sent. For instance, if using a 2 Rx space-time code, the full rate property indicates that for each time-slot, a combination of 2 symbols will be sent. The orthogonality property ensures a transmission without inter-symbol interference in reception.

2.7 Thesis scenario

2.7.1 OGS and satellite properties

Throughout this study, if not specified, we consider the OGS parameters presented in Tab. 2.1. In some sections, parametric studies will be undertaken, the geometry will be specified in these cases.

OGS Parameters	
Elevation	30°
α_{PAA}	18.5 µrad
λ	1550 nm
$\text{D}_{\text{telescope}}$	60 cm
AO Parameters	
N_{AO}	136

Table 2.1: OGS and AO general parameters.

The chosen configuration is characterized by a large aperture that limits the geometrical losses induced by the beam divergence, but results in increased wavefront perturbations in the telescope aperture, and thus requires a good quality AO system [8]. During the thesis, we will study different telescope emission apertures. However, when not specified, the telescope aperture diameter is set to 60 cm, which is in accordance with the current OGS designs [137–139]. In this scheme, the anisoplanatic error due to the angular decorrelation of the turbulence is larger, thus there is a greater interest in improving the correction at PAA. We consider a Feeder-link with a GEO satellite at 30° elevation, corresponding to a point-ahead angle of 18.5 µrad. It is a plausible scenario for a link between a GEO satellite

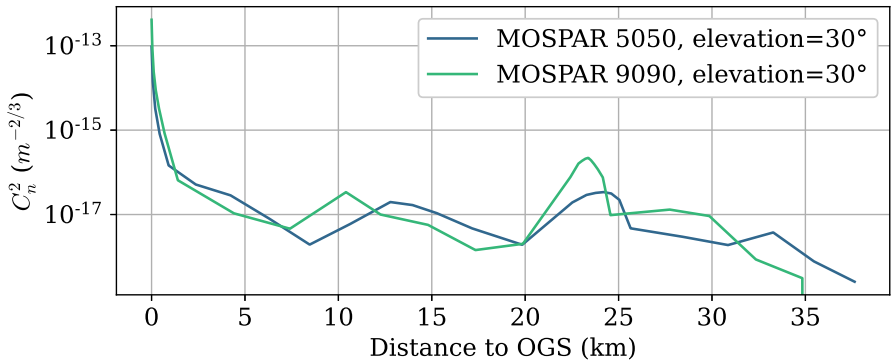

Figure 2.21: Illustration of the MOSPAR profiles 5050 and 9090 at 30° elevation. The distance to the OGS is plotted function of the turbulence strength.

and an OGS in Europe [140]. The considered wavelength is 1550 nm to benefit from off-the-shelf telecom components and of low atmospheric attenuation. Concerning the AO parameters, we consider a high quality correction with a number of correction modes as high as $N_{AO} = 136$ (n_r=15), in accordance with current OGS AO systems [138, 141, 142].

2.7.2 Atmospheric conditions

We consider statistically representative atmospheric C_n^2 profiles. These profiles, called MOSPAR-XY, are composite profiles constructed thanks to astronomical site measurement databases [143, 144]. The construction of these profiles is detailed in [33, 145]. X and Y are thresholds on the statistical distributions of the anisoplanatic angle θ_0, describing the turbulence angular decorrelation, and the Fried parameter r_0, corresponding to the strength of the phase perturbation. For example, the MOSPAR-9090 is a profile whose θ_0 is chosen $P(x > \theta_0) = 0.9$ and r_0 is chosen $P(y > r_0) = 0.9$ according to on-site measurements.

To illustrate and evaluate the performance of the estimator, we choose a strong turbulence case MOSPAR-9090 as depicted in Fig. 2.21. We also explore a set of different strengths of θ_0 and r_0 with all combinations of thresholds $(X, Y) \in \{50, 60, 70, 80, 90\} \times \{50, 60, 70, 80, 90\}$. An example of the explored integrated parameters values with respect to their XY thresholds applied in the profile construction are given in Tab. 2.2. We underline that at fixed threshold X, respectively Y, the value of θ_0, respectively r_0, barely varies.

Parameter \Threshold	5050	6060	7070	8080	9090	9999
r_0 (cm)	7.8	6.8	5.8	4.9	4.1	2.9
θ_0 (µrad)	11.3	10.2	9.2	8.2	6.8	4.82
σ_χ^2	0.035	0.043	0.046	0.060	0.080	0.136

Table 2.2: Table of the integrated parameters for different XY thresholds considered in the construction of a C_n^2 profile computed for a wavelength of 1550 nm and for a 30° elevation.

Considering the wind properties, we assume a Bufton wind profile with the following parameters: $v_g = 10\ m/s$ and $v_t = 20\ m/s$.

2.7.3 Link budget

The overall link budget before turbulence losses is given in table 2.3. We consider the total static losses induced by the combination of pointing losses, absorption losses, system losses, antenna gains and free space propagation losses given in 2.1. Therefore, before turbulence losses, assuming a 50 W emitted power, the received power onboard the satellite is equal to -25 dBm.

Additionally, we compute the link margin assuming a 25 Gbps OOK transmission. After pre-amplification onboard the satellite, considering a LNOA amplifier with a noise figure $NF = 4$ dB, as specified in section from chapter 1, the OSNR equals 28.9 dB, measured on the optical bandwidth of 12.5 GHz. The SNR at 25 Gbps therefore equals to 25.8 dB. Considering the required SNR to reach a BER=10^{-3} for an OOK modulation and an additive 3 dB link margin, the total link margin before turbulence losses equals 12.8 dB. We will use this threshold in the next chapters to study the telecommunication link availability, when adding the turbulence disturbances.

Contribution	Value	unit
P_{Tx}	47	dBm
G_{Tx}	120.8	dB
G_{Rx}	113.1	dB
a_{fsp}	-290	dB
L_{abs}	-8	dB
a_{Tx}	-3	dB
a_{Rx}	-3	dB
$L_{pointing}$	-2	dB
Received power before turbulence losses	-25.1	dBm
Noise figure	4	dB
OSNR before turbulence	15.9	dB
SNR before turbulence at 25 Gbps	25.9	dB
Required SNR for BER 10^{-3} (OOK)	10	dB
link margin	3	dB
Total margin before turbulence	12.9	dB

Table 2.3: Link budget for an emission aperture of diameter 60 cm, a 25 cm receiver aperture diameter, for a communication link at 1.55 µm with a GEO satellite at 30° elevation.

2.8 Conclusion and thesis objectives

In this chapter, we presented the channel model. This channel model is shown to be affected by constant losses, and random losses induced by the turbulence impact on the optical beam propagation. We detailed the models used in the literature to characterize the atmospheric induced coupled flux fluctuations, both for the uplink and downlink case. We emphasized on the impact of adaptive optics systems on the mitigation of the coupled flux fluctuations. We described, in the uplink case, the impact on the coupled flux of an AO pre-compensation suffering from anisoplanatic errors. Finally, we exposed the system and atmospheric scenario that will be considered all along this thesis.

To tackle the main issue of this thesis, that is to explore new methods to evaluate and optimize the AO pre-compensated telecommunication link, we present in the next chapter the methods and numerical tools used to characterize the performance of AO pre-compensations and their impact on the coupled flux onboard the satellite.

CHAPTER 3

Reciprocal Modeling of the ground to space optical channel pre-compensated by adaptive optics

Contents

3.1 Introduction

In Chapter 2, we presented numerical tools to simulate AO pre-compensated ground-to-GEO links. These tools are E2E tools, relying on the uplink propagation of a pre-compensated Gaussian beam. However, such tools do not allow for analyzing the pre-compensation phase error at the origin of the uplink beam perturbation in the satellite plane, and to link this phase error to these perturbations. Additionally, we showed that

there is no analytical model allowing to model the coupled flux onboard the satellite while accounting for the uplink beam pre-compensation.

In this chapter, our aim is not only to use the reciprocity principle for computing the pre-compensation phase, but also as a modeling tool for characterizing the coupled flux onboard the satellite. As mentioned in chapter 2, in section 2.5, the point reciprocity principle is already employed for calculating the pre-compensation phase of the uplink. Building upon the pioneering work of Shapiro [6], which demonstrates that reciprocity also applies to the coupled flux, we develop tools to model the pre-compensated uplink coupled flux. While relatively recent in the literature, these reciprocal tools are not new and are already utilized in pseudo-analytic models, such as SAOST [8, 89] (an ONERA in-house modal-based pseudo-analytic model) and FAST [9] (an approach based on Fourier analysis). In this chapter, we aim to present the principles of these tools and how to employ them as a fast analysis tool for assessing pre-compensated uplink performance. We also enhanced the existing tool.

Therefore, we begin this chapter in section 3.2 by presenting and demonstrating the theoretical reciprocity principle applied to the ground-to-GEO link, relying on Shapiro's work. We also provide an experimental demonstration of the AO pre-compensated link reciprocity and demonstrate this principle using E2E numerical simulation. This also serves as an opportunity to introduce the developed E2E reciprocal simulation tool developed during the thesis, allowing for more efficient computation of uplink time-series and more flexible time-series analysis. Secondly, in section 3.3 we present a general formalism to express the pre-compensation phase error, in a modal formalism. We illustrate this formalism on state-of-the-art pre-compensation methods. We also provide the formulas from the literature allowing to compute the phase error statistics, that are the modal phase angular covariances. In section 3.4, we present the principle of reciprocity-based pseudo-analytical tools that allow for the fast computation of numerous coupled flux occurrences for any phase pre-compensation. We also highlight the improvements made to this model within the scope of this thesis. Finally, in section 3.5, we apply the reciprocity-based tools to the AO pre-compensated uplink (both E2E for a time analysis and pseudo-analytical models for a statistically representative parametric analysis), which is corrected by the "classical pre-compensation" relying on downlink beam phase correction, and the LGS based correction.

3.2 Reciprocal channel modeling approach

3.2.1 Reciprocity principle

Point reciprocity principle has been proven in the literature since 1971 [118, 146], and is the principle on which relies the laser guide star approach. The point reciprocity principle states that the spatial impulse function of the turbulence $h(\mathbf{r}', \mathbf{r})$ (Green function) that is used to compute the beam propagation from a plane $\mathcal{A}_0$ to a plane $\mathcal{A}_L$ is the same as the one characterizing the beam propagation from plane $\mathcal{A}_L$ to $\mathcal{A}_0$. This impulse function is a function of $\mathbf{r}$, the transverse spatial coordinates in the plane at $z = 0$, denoted $\mathcal{A}_0$, and $\mathbf{r}'$ the transverse spatial coordinates in the plane at $z = L$, denoted $\mathcal{A}_L$. Hence, the complex field Ψ_L^{Rx} resulting from the propagation of the field Ψ_0^{Tx} from $z = 0$ to $z = L$ and the complex field Ψ_0^{Rx} resulting from the propagation of the field Ψ_L^{Tx} from $z = L$ to

$z = 0$, can both be computed thanks to the same impulse response $h(\mathbf{r}', \mathbf{r})$ as:

$$\Psi_L^{Rx}(\mathbf{r}') = \int_{\mathcal{A}_0} h(\mathbf{r}', \mathbf{r}) \Psi_0^{Tx}(\mathbf{r}) d\mathbf{r} \tag{3.1}$$

$$\Psi_0^{Rx}(\mathbf{r}) = \int_{\mathcal{A}_L} h(\mathbf{r}', \mathbf{r}) \Psi_L^{Tx}(\mathbf{r}') d\mathbf{r}'. \tag{3.2}$$

Shapiro and Puryear, in their seminal work [147], proposed to extend this principle to power transfer reciprocity applied to communication systems. They propose in this article a general and theoretical proof of this power transfer reciprocity, that they finally apply to power transfer in the far field. Whilst some assumptions are made to develop this formalism, it is shown in the article to be valid for most FSO communication links.

This principle is used by Shapiro and Puryear in order to access channel information in [148]. Additionally, Robert and Conan propose in [149] to apply this principle to model ground to satellite links in the context of frequency transfer, and theoretically demonstrates its applicability to the ground to satellite link geometry. It is further extended to ground-to-GEO communication links in [8].

In the following, we aim at synthesizing, from Shapiro and Puryear's work, the proof, and assumptions of the power transfer reciprocity principle in the general case. Afterward, following the work of Conan, we develop the theoretical demonstration in the ground to satellite case.

3.2.1.1 General theoretical principle

Shapiro and Puryear develop in their article [6] a general formalism to express the coupled power reciprocity. They consider systems with or without adaptive optics pre-compensation. Figure 3.1 depicts the mono-axial considered scheme with AO compensation on both sides of the communication link. The system is composed of four planes:

- $\mathcal{F}_0$ the focal plane of the optical system located at $z = 0$, whose transverse coordinates are denoted $\mathbf{r}_f$,
- $\mathcal{A}_0$ the pupil plane of the optical system located at $z = 0$, whose transverse coordinates are denoted $\mathbf{r}$,
- $\mathcal{A}_L$ the pupil plane of the optical system located at $z = L$, whose transverse coordinates are denoted $\mathbf{r}'$,
- $\mathcal{F}_L$ the pupil plane of the optical system located at $z = L$, whose transverse coordinates are denoted $\mathbf{r}'_f$.

In the system at $z = 0$, a Gaussian single mode is emitted in the focal plane $\mathcal{F}_0$, at $z = 0$, collimated, sent through the diplexer and through the AO system in the pupil plane $\mathcal{A}_0$. The complex field propagates through the turbulence and reach the second optical system at $z = L$. It goes through a second AO system in the pupil plane $\mathcal{A}_L$, and is then focused to the focal plane $\mathcal{F}_L$ where it is coupled to the receiver mode, which is the Gaussian mode of the single mode fiber. Reciprocally, at $z = L$ a Gaussian mode is emitted through a single mode fiber in the focal plane $\mathcal{F}_L$, is collimated and compensated by the AO system in $\mathcal{A}_L$, and propagates on the same optical axis, toward the optical system at $z = 0$. In this system, it is compensated by the AO system in the pupil plane $\mathcal{A}_0$, and focused through the focal plane $\mathcal{F}_0$ to the receiver mode that is the Gaussian mode of the single mode fiber.

In the following, we develop the received optical power received at both ends of the system, before demonstrating the equality of their coupling efficiency. To make these developments, we assume the turbulence to be frozen, meaning that the propagation time

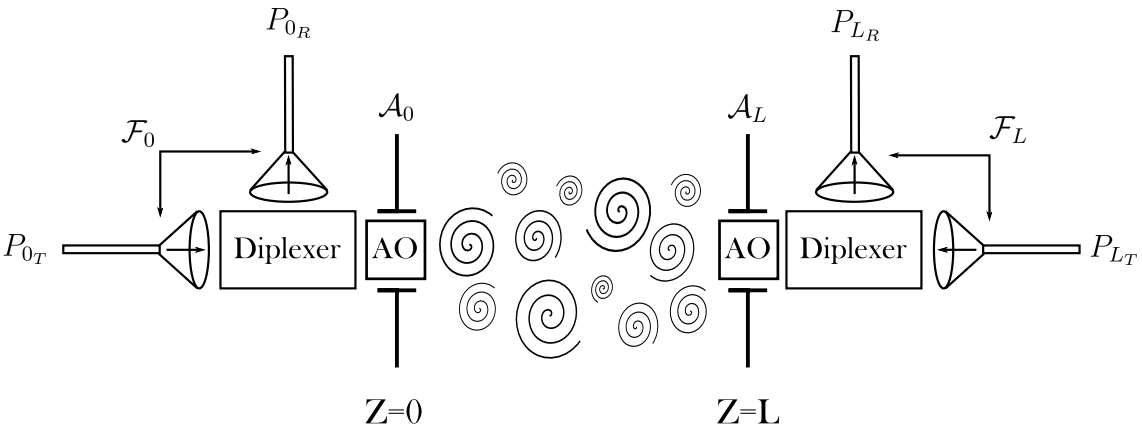

Figure 3.1: Reciprocity general scheme with adaptive optics system [6]

L/c is assumed to be smaller than the turbulence evolution characteristic time. Therefore, the following developments are made at fixed instant t. To simplify the reciprocity demonstration, we demonstrate the coupling reciprocity computed in the planes $\mathcal{A}_0$ and $\mathcal{A}_L$, as it is widely known that the coupling in the pupil plane equals to the pupil in the focal plane.

Forward path coupling efficiency

Let the emitted power from the optical system at $z = 0$ be:

$$P_{0_T} = \int_{\mathcal{F}_0} d\mathbf{r} \left|\Psi^{Tx}_{\mathcal{A}_0}(\mathbf{r})\right|^2 \tag{3.3}$$

where $\Psi^{Tx}_{\mathcal{A}_0}(\mathbf{r})$ is the emitted Gaussian mode in the pupil plane $\mathcal{A}_0$:

$$\Psi^{Tx}_{\mathcal{A}_0}(\mathbf{r}) = \sqrt{P_{0_T}}\xi(\mathbf{r}) \tag{3.4}$$

where $\xi(\mathbf{r})$ is the mode of the SMF of unitary energy. The coupled power into the Gaussian mode $\xi(\mathbf{r}'_f)$ of the SMF in the pupil plane of the optical system at distance $z = L$, $\mathcal{A}_L$, can be expressed as:

$$P_{L_R} = \left|\int_{\mathcal{A}_L} d\mathbf{r}' \Psi^{Rx}_{\mathcal{A}_L}(\mathbf{r}')\xi^*(\mathbf{r}')\right|^2 \tag{3.5}$$

where $\Psi^{Rx}_{\mathcal{A}_L}(\mathbf{r})$ is the complex turbulent field in the pupil plane after propagation, and $\exp(-i\Phi_L(\mathbf{r}'))$ is the phase compensation applied in L. In a model of a system without AO, this term is equal to 0. The received field in the pupil plane $\Psi^{Rx}_{\mathcal{A}_L}(\mathbf{r}')$ is expressed as:

$$\Psi^{Rx}_{\mathcal{A}_L}(\mathbf{r}') = \int_{\mathcal{A}_0} d\mathbf{r}\Psi^{Tx}_{\mathcal{A}_0}(\mathbf{r})e^{i\Phi_0(\mathbf{r})}h(\mathbf{r}',\mathbf{r})e^{-i\Phi_L(\mathbf{r}')} = \int_{\mathcal{A}_0} d\mathbf{r}e^{i\Phi_0(\mathbf{r})}h(\mathbf{r}',\mathbf{r})e^{-i\Phi_L(\mathbf{r}')}\sqrt{P_{0_T}}\xi(\mathbf{r}) \tag{3.6}$$

where $h(\mathbf{r}',\mathbf{r})$ is the spatial impulse response of the considered atmospheric state from $z = 0$ to $z = L$, $\Phi_0(\mathbf{r})$ is the phase compensation applied in $z = 0$, that equals to 0 if there is no compensation.

Return path power

Reciprocally, we express the coupled power from the emitted mode from $\mathcal{A}_L$ from the optical system in $z = L$ to the mode at $\mathcal{A}_0$ in the optical system at $z = 0$.

The emitted power is expressed as:

$$P_{L_T} = \int_{\mathcal{A}_L} d\mathbf{r}' \left|\Psi^{Tx}_{\mathcal{A}_L}(\mathbf{r}')\right|^2, \tag{3.7}$$

where $\Psi^{Tx}_{\mathcal{A}_L}(\mathbf{r}'_f)$ is the emitted Gaussian mode:

$$\Psi^{Tx}_{\mathcal{A}_L}(\mathbf{r}') = \sqrt{P_{L_T}}\xi(\mathbf{r}') \tag{3.8}$$

The coupled power in the fiber, in the pupil plane $\mathcal{A}_0$, can be expressed as:

$$P_{0_R} = \left|\int_{\mathcal{A}_0} d\mathbf{r}\Psi^{Rx}_{\mathcal{A}_0}(\mathbf{r})\xi^*(\mathbf{r})\right|^2 \tag{3.9}$$

where the complex turbulent field $\Psi^{Rx}_{\mathcal{A}_0}(\mathbf{r})$ in the pupil plane is defined as:

$$\Psi^{Rx}_{\mathcal{A}_0}(\mathbf{r}) = \int_{\mathcal{A}_L} d\mathbf{r}' e^{i\Phi_0(\mathbf{r})}h(\mathbf{r}',\mathbf{r})e^{-i\Phi_L(\mathbf{r}')}\psi^{Tx}_{\mathcal{A}_L}(\mathbf{r}') = \int_{\mathcal{A}_L} d\mathbf{r}' e^{i\Phi_0(\mathbf{r})}h(\mathbf{r}',\mathbf{r})e^{-i\Phi_L(\mathbf{r}')}\sqrt{P_{L_T}}\xi(\mathbf{r}') \tag{3.10}$$

where $h(\mathbf{r}',\mathbf{r})$ is the spatial impulse response of the considered atmospheric state from $z = L$ to $z = 0$, $\Phi_0(\mathbf{r})$ is the phase compensation applied in $z = 0$ and $\Phi_L(\mathbf{r})$ the phase compensation applied in $z = L$.

Reciprocity proof

The reciprocal criterion is defined as:

$$\rho_L = \frac{P_{L_R}}{P_{0_T}} = \frac{P_{0_R}}{P_{L_T}} = \rho_0 \tag{3.11}$$

which holds for the normalized coupling efficiency on both sides of the system.

It is possible to develop both coupling efficiency as:

$$\rho_L = \frac{P_{L_R}}{P_{0_T}} = \left|\int_{\mathcal{A}_L} d\mathbf{r}' \int_{\mathcal{A}_0} d\mathbf{r}\xi(\mathbf{r})e^{i\Phi_0(\mathbf{r})}h(\mathbf{r}',\mathbf{r})e^{-i\Phi_L(\mathbf{r})}\xi^*(\mathbf{r}')\right|^2 \tag{3.12}$$

and

$$\rho_0 = \frac{P_{0_R}}{P_{L_T}} = \left|\int_{\mathcal{A}_0} d\mathbf{r} \int_{\mathcal{A}_L} d\mathbf{r}'\xi(\mathbf{r}')e^{-i\Phi_L(\mathbf{r}')}h(\mathbf{r}',\mathbf{r})e^{i\Phi_0(\mathbf{r}')}\xi^*(\mathbf{r})\right|^2 \tag{3.13}$$

.

By assuming that the Gaussian single modes are real-valued, i.e., that $\xi^* = \xi$, we can express both coupling efficiency as:

$$\rho_L = \frac{P_{L_R}}{P_{0_T}} = \left|\int_{\mathcal{A}_L} d\mathbf{r}' \int_{\mathcal{A}_0} d\mathbf{r}\xi(\mathbf{r})e^{i\Phi_0(\mathbf{r})}h(\mathbf{r}',\mathbf{r})e^{-i\Phi_L(\mathbf{r})}\right|^2 \tag{3.14}$$

and

$$\rho_0 = \frac{P_{0_R}}{P_{L_T}} = \left|\int_{\mathcal{A}_0} d\mathbf{r} \int_{\mathcal{A}_L} d\mathbf{r}'\xi(\mathbf{r}')e^{-i\Phi_L(\mathbf{r}')}h(\mathbf{r}',\mathbf{r})e^{i\Phi_0(\mathbf{r}')}\xi(\mathbf{r})\right|^2 \tag{3.15}$$

Therefore, the equality becomes trivial, and the coupling efficiency reciprocity principle is proven.

This formalism is shown to be very powerful, as it doesn't make any assumption on the turbulence regime or distribution along the line of sight. It doesn't assume any properties either on the AO corrections applied to the system, except that the the AO correction

applied to the incoming or emitting beam is the same on both sides. In the same way, the formalism is given for a symmetrical system, however, the reciprocity principle holds for asymmetrical systems (with different geometries at $z = 0$ and $z = L$, for instance, different pupil sizes, or AO at only one side). The only symmetry that has to be kept is the symmetry between the Tx and Rx mode at each ends of the system. The ground-to-GEO satellite system architecture allows us to illustrate this system asymmetry.

Applications of the reciprocity principle

This principle is used in the part 2 article of Puryear and Shapiro [148] in order to use the channel state information in a perfect reciprocal scheme, to optimize the communication system, in an optimal scheme and a suboptimal scheme, that allows to reduce the complexity of the digital system.

It is furthermore specified by Shapiro that the reciprocity can not directly be used to optimize optical uplink (ground to satellite) telecommunication systems, because it shows only partial reciprocity. Indeed, in this case, the reciprocity is broken by the point-ahead angle separating the uplink from downlink path. The mono-axial property of the system is lost.

However, this principle can still be used in the framework of ground to satellite telecommunication links analysis. Indeed, as showed in the article [8, 149], the reciprocity principle can be used to model the uplink coupled flux. This allows to simplify the uplink modeling as a a downlink modeling. This is convenient, especially if we want to study the performance of an adaptive optics system correction for the uplink, as downlink modeling tools are very well-developed.

3.2.1.2 Application to the ground to GEO case

We apply the reciprocity principle to model the ground to satellite link. This is of interest to model the impact of an imperfect AO correction, hindered by anisoplanatism, as it eases the expression of the phase correction error, and allows working with downlink models that are well-developed in the literature.

A scheme of the considered system is depicted in figure 3.2. We consider the uplink on the axis at PAA depicted in red and a virtual downlink, in blue, that are emitted and received through the same fiber, and propagates on the same optical axis, through the same turbulent volume. The downlink is denoted as 'virtual', as it does not really exist and is used only for modeling purposes.

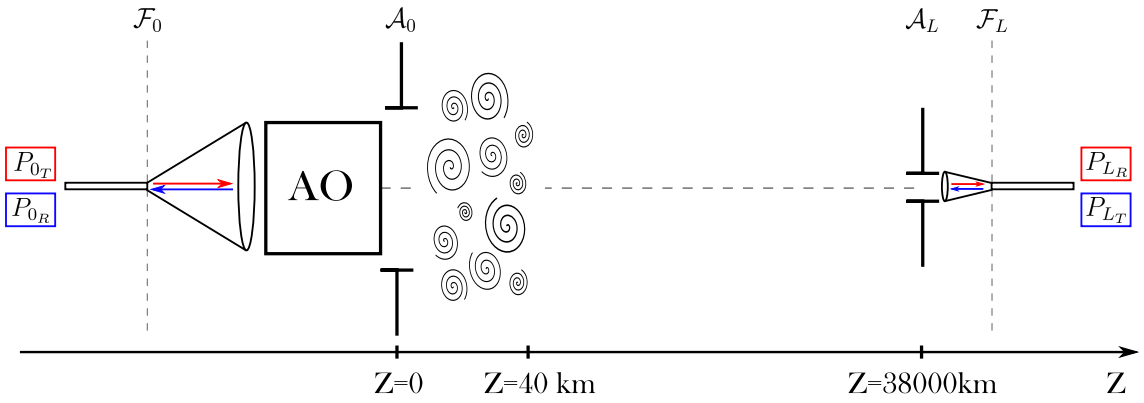

Figure 3.2: Reciprocity scheme of a ground to satellite optical link with adaptive optics correction. The uplink is depicted in red, and the downlink in blue.

In this case, several system asymmetries can be underlined between the OGS and the satellite system: the entrance pupil sizes are different, the turbulence is located close to the ground (close to the OGS pupil) and there is only one AO system at the OGS. However, the reciprocity principle still applies, as the general principle does not assume anything on the turbulence distribution on the line of sight, nor on the system assymetries at both ends of the link. The system depicted in figure 3.2 is therefore a particular case of the general scheme presented in figure 3.1, in section 3.2.1.1.

Therefore, we can write the following equality:

$$\mathrm{f}_{\mathrm{pre-compensated,OGS}\rightarrow\mathrm{satellite}}(\alpha_{\mathrm{PAA}}) = \mathrm{f}_{\mathrm{compensated,satellite}\rightarrow\mathrm{OGS}}(\alpha_{\mathrm{PAA}}). \tag{3.16}$$

meaning that the coupled flux of the pre-compensated uplink propagated from the ground to the satellite is equal to the coupled flux of the reception mode of the satellite back-propagated to the ground, and corrected by the adaptive optics system.

We highlight that the propose scheme in figure 3.2 could also apply to the on-axis downlink, with the true downlink in blue and a virtual uplink in red. Hence, both on-axis and off-axis channels are independently reciprocal. However, the true uplink and the true downlink are not reciprocal because of the point ahead angle, both being associated to two different green functions. Consequently, the optimal AO correction for both links is different. We will use the virtual reciprocal uplink to assess the performance, keeping in mind that the AO correction can only be inferred from the true downlink.

Also, as the downlink and uplink are only partially reciprocal, the downlink channel state information cannot be used for the communication system optimization in the same way as in a completely reciprocal scheme.

3.2.2 Reciprocity experimental demonstrations

The coupling reciprocity principle have been several times demonstrated in the literature. During my thesis, I had the opportunity to participate in the FEEDELIO experimental campaign (by ONERA), and the first reciprocity experimental demonstration of an AO pre-compensated link in a GEO-Feeder configuration. This experiment led to a conference contribution [150], whose main findings are summarized in this section.

3.2.2.1 State-of the art

The reciprocity principle, has been largely demonstrated in the framework of free space optics (FSO) horizontal links [151, 152], with the motivation to obtain real-time knowledge on the telecommunication channel state (see [153] and references therein). However, to our knowledge, it has not been demonstrated in an asymmetrical system configuration equipped with AO, as in the FEEDELIO demonstration.

3.2.2.2 Experiment overview

The aim of the FEEDELIO experiment was to demonstrate the effectiveness of an AO pre-compensated optical link in improving the telecom link budget in presence of point-ahead angle (PAA) induced anisoplanatism in conditions representative of a GEO-Feeder link. It was also the opportunity to demonstrate the reciprocity principle in a ground to satellite link emulated configuration, testing the principle in a mono-axial configuration.

The experiment took place in Tenerife, Canary Island, hosted at the ESA premises. A two-week first measurement campaign occurred in April 2019 and a two-week second measurement campaign took place in October 2021 in order to gather additional data. The

optical link was established between ESA's optical ground station (OGS) dome and the top of the mount Teide on a 13.2 km 5° elevation slant path [154].

Figure 3.3: Illustration of the Feedelio line of sight. The OGS is located at the GTB (ground terminal breadboard) and the satellite emulator at the STB (satellite terminal breadboard).

To emulate the GEO-Feeder link, two terminals were designed :

- The satellite terminal breadboard (STB) to emulate the satellite.

  This terminal is composed of two modules, one on-axis and the other off-axis as to emulate PAA, on the top of the mount Teide as depicted in Fig. 3.3. In the frame of this reciprocity experiment, we will focus on the on-axis module. It provides the reference downlink beacon at 1550 nm and is also equipped with a receiver to allow for the reciprocity experiment. The entrance pupil has a small 1.8 mm diameter and the receiver is a low noise PIN 20 kHz photodiode.

- The ground terminal breadboard (GTB) to emulate the OGS.

  The GTB is composed of a 35 cm diameter commercial telescope and an optical bench that receives the downlink beacon, performs the AO correction on the downlink and pre-compensates the uplink. The uplink optical path is equipped with a point ahead mirror (PAM). The downlink signal is coupled to a single mode fiber (SMF) after the AO system. The signal is then detected by a low noise PIN 20 kHz photodiode.

This AO system is composed of an Alpao 95-17 deformable mirror (DM), a wavefront sensor (WFS) equipped with a Raptor Owl HS camera and a Shakti real-time computer. The WFS has 8×8 sub-apertures, the DM has 11×11 actuators, and the AO system runs at 1.5 kHz with a 2.3 frames delay. More details on the AO loop performance can be found in [155].

3.2.2.3 Reciprocity experiment

Aim, set-up, and data acquisition protocol

The reciprocity experiment aimed at demonstrating the coupling flux reciprocity in a GEO-Feeder like scheme, equipped with an AO system. To that end, an AO corrected bidirectional link was established between the on-axis STB module and the GTB module. The measurement protocol consisted in simultaneously acquiring the AO corrected downlink

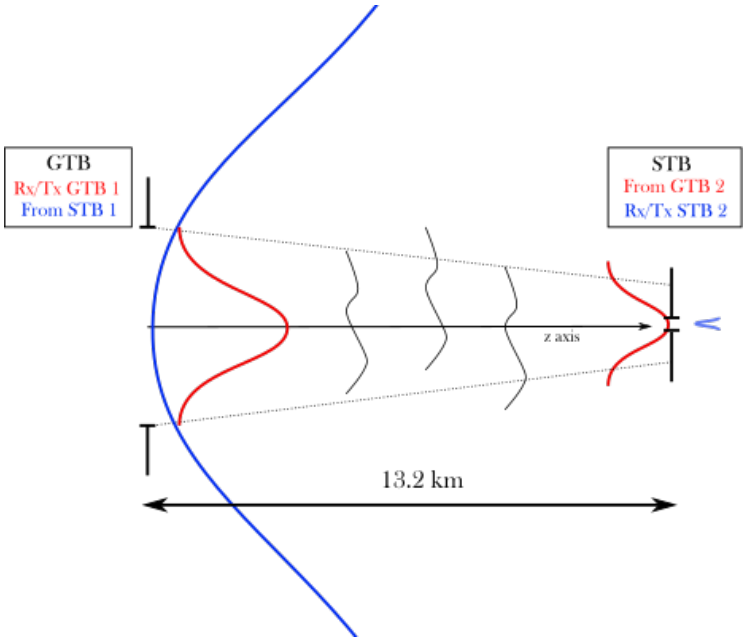

Figure 3.4: Reciprocity scheme in the FEEDELIO geometry taking account of the finite distance of the line of sight. On the left in the GTB plane, the red mode is the Rx/Tx mode of the GTB and the blue mode is the one received from the STB. On the right, in the STB plane, the blue mode is the Rx/Tx mode of the STB and the red mode is the received mode from the GTB. We specify that the Tx mode from STB after propagation, in the GTB plane (in blue), is a wide Gaussian-like mode of which we represent only the top.

signal in the GTB and pre-compensated on-axis uplink signal in the STB. Three types of AO corrections (Tip-Tilt, 9 modes, full-correction) are applied for each acquisition and each sub-acquisition is 10 s long. We recall that the sampling frequency of the PIN photodiodes is 20 kHz.

As scheme of the experiment principle is depicted in figure 3.4. The uplink is depicted in red and is focused on the GEO satellite target. This is possible as the Rayleigh distance is equal to 18 km, which is larger than the distance of the GTB from the STB. The downlink mode is depicted in blue and diverges toward the GTB. In this scheme, the reciprocity principle still applies, as the emission and reception modes are the same on both sides of the link.

Reciprocity performance metric

To evaluate the reciprocity of the coupled flux time series f_{STB} and f_{GTB}, we compute the Pearson correlation coefficient (PCC) [156] which is defined as :

$$PCC_{f_{STB},f_{GTB}} = \frac{COV(f_{STB}, f_{GTB})}{\sigma_{f_{STB}} \sigma_{f_{GTB}}} \tag{3.17}$$

Because the STB and GTB acquisitions are not fully synchronized, it is necessary to compute the coefficient over a rolling window to find its maximum and thus find the time-shift between the two series, as shown in Fig. 3.6. We chose a 180000 samples sliding window (over 200000 samples).

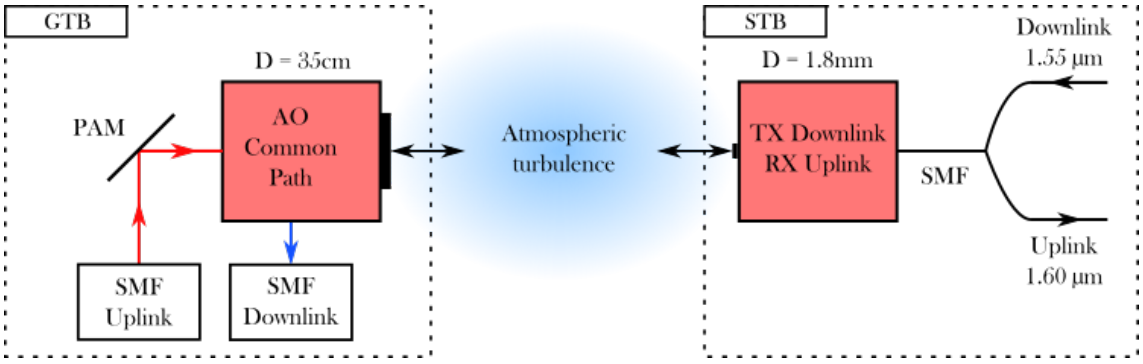

Figure 3.5: Block diagram of the system. The black arrows represent the common path. The red arrows correspond to the uplink non common path after the mode emission and the blue arrows to the non common path of the downlink before coupling into a SMF.

Upgrade of the reciprocity set-up

First measurements were done during the first campaign reaching 85% of signal correlation. Part of this correlation loss may be explained by the original set-up, composed with two different Rx/Tx pupils separated by 1.9 µrad angular distance on the STB module, hence leading to residual PAA anisoplanatism.

It was chosen to upgrade the experimental set-up for the second campaign so as to obtain a truly mono-axial scheme by means of a dedicated coupling system on-board the STB module, as shown in the STB part of Fig. 3.5.

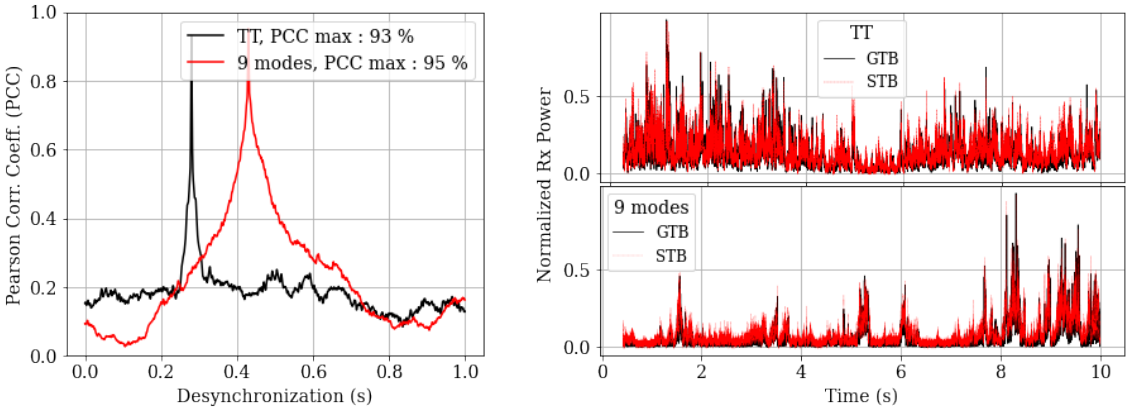

Figure 3.6: On the left the PCC computed for a given desynchronization between the uplink and downlink acquisition, on the right the normalized and synchronized Rx and Tx power for the Tip-Tilt corrected signal and the 9 modes corrected signal. These results were obtained for the following integrated parameters : Fried parameter $r_0 = 8$ cm and the Rytov variance of the log-amplitude $\sigma_\chi^2 = 0.15$.

Thanks to this new set-up, correlation results up to 95% were obtained. These results are presented in Fig. 3.6. The best correlation coefficient of 95% is obtained for the 9 modes correction, and the Tip-Tilt only correction gives a 93% correlation. We notice in this result a high latency between the two signals (0.5 s). This is due to the experimental architecture implying a variable desynchronization between the two time series acquisition. Computing the PCC is therefore a way to re-synchronize the two time series during the post-processing.

Origin of the decorrelation

We identified the source of decorrelation as the results of mispointing errors and non-common path aberrations (NCPAs) that were identified, during the calibration, on the bench between the uplink and downlink optical path. Figure 3.5 depicts these two paths at the GTB. We validated thanks to numerical simulation the hypothesis that NCPAs and mispointing errors hindered the coupled flux reciprocity. These results can be found in the article [150].

3.2.3 Reciprocal End-to-End numerical tool

We demonstrated theoretically and experimentally the reciprocity in the ground to GEO configuration with adaptive optics correction. We will finally use this principle to develop numerical tools to model and analyze the phase error induced by the bidirectional link non mono-axial property, and the associated coupled flux. In the following, we present an adaptation of the E2E wave propagation tool TURANDOT, that allows us to study the reciprocal uplink channel.

3.2.3.1 Principle

We consider the bidirectional ground-GEO system depicted in figure 3.7. In this scheme, the downlink is located at the angular reference $\alpha = 0$ and emits a Gaussian beam, that can be considered as a plane wave when it enters the atmosphere. After propagation through the atmosphere, it reaches the OGS pupil and goes through the adaptive optics system, where the wavefront is corrected. The classical uplink is emitted from the OGS, is pre-compensated by the AO system with the same correction as the downlink, and is emitted in the point-ahead angle direction.

In the proposed numerical simulation tool, we consider a reciprocal uplink, that is represented in the figure in red, that is an off-axis downlink beam. Therefore, the principle of the reciprocal E2E tool, uses the same principle as the classical TURANDOT simulator defined in 2.3.2, but propagating simultaneously two downlink beams separated by an angle α_{PAA}, corrected by an adaptive optics system at the OGS.

Finally, the complex coupling is obtained by numerically computing the overlap integral between the reciprocal uplink field, corrected by AO, and the Gaussian mode of reception.

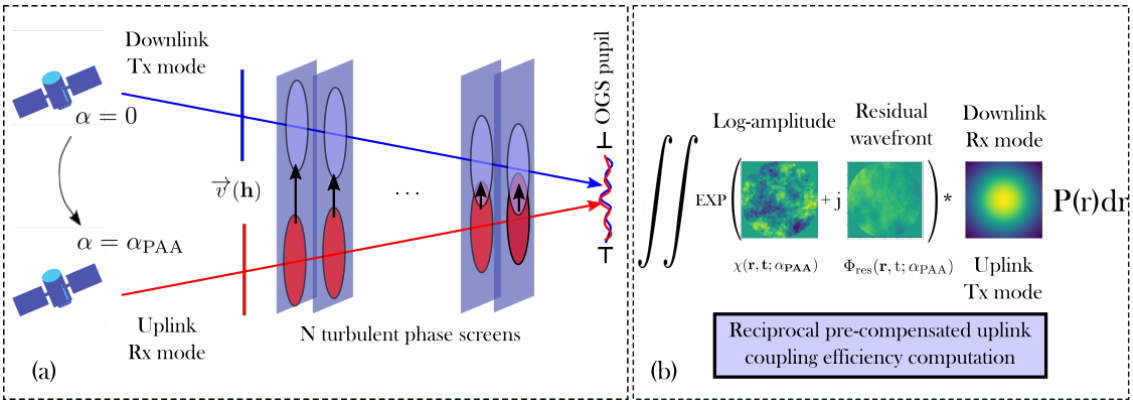

Figure 3.7: Schematic of the principle of the reciprocal E2E wave optics simulator. The optical downlink is depicted in blue, the reciprocal uplink in red. (a) depicts the propagation step. (b) depicts the wavefront correction and coupling step.

In the following, we explain how is computed the phase correction, and validate the reciprocal approach thanks to data obtained from the true uplink.

3.2.3.2 Reciprocal residual wavefront

We provide details on the phase error terms we consider and explain how we computed these phase errors on the complex fields obtained from the reciprocal E2E simulator.

AO simplified model

We adopt a simplified AO correction, based on a correction in the Zernike space, that accounts for anisoplanatism, fitting and temporal error. Therefore, we do not account for all the errors related to a real AO system. However, as the anisoplanatism is the dominant error term, this approximation is justified.

Residual phase computation for the classical pre-compensation.

The residual phase is expressed as:

$$\Phi_{res}(\mathbf{r}) = \Phi(\alpha_{PAA}, \mathbf{r}, t) - \Phi_{corr}(\mathbf{r}, t) \tag{3.18}$$

where $\Phi(\alpha_{PAA}, \mathbf{r}, t)$ is the reciprocal uplink phase corresponding to the downlink beam propagating at PAA, and $\Phi_{corr}(\mathbf{r}, t)$ is the correction phase that is applied by the AO system.

The correction phase has to take into account the errors mentioned above. We model these errors as follows:

- Anisoplanatism

The anisoplanatism is induced by the correction of the phase at PAA by the phase measured on-axis ($\alpha = 0$). Therefore, the anisoplanatic correction phase is modeled as:

$$\Phi_{corr}(\mathbf{r}, t) = \Phi(0, \mathbf{r}, t) \tag{3.19}$$

- AO correction limited number of modes

The AO system can measure and correct a limited number of modes that we denote N_{AO}. The correction of this limited number of modes will induce fitting error on the corrected wavefront. To account for this limited resolution, we express the correction phase, that is the downlink phase, as follows:

$$\Phi_{corr}(\mathbf{r}, t) = \sum_{i=2}^{N_{AO}} a_i^0(t) Z_i(\mathbf{r}) \tag{3.20}$$

where $\{a_i^0(t)\}_i$ is the set of Zernike coefficients of the on-axis correction phase onto the Zernike polynomial basis, summed until N_{AO}.

- Temporal error

The temporal error is induced by the AO loop delay. We simulate this temporal error by shifting the correction phase by the number of discrete samples equivalent to the AO loop delay. For an AO loop sampling frequency of $f_{s,data} = f_{s,AO} = 1/\Delta t$, and a frame delay $N = 2$, the correction phase is hence expressed ad:

$$\Phi_{corr}(\mathbf{r}, t) = \sum_{i=2}^{N_{AO}} a_i^0(t - N\Delta t) Z_i(\mathbf{r}) \tag{3.21}$$

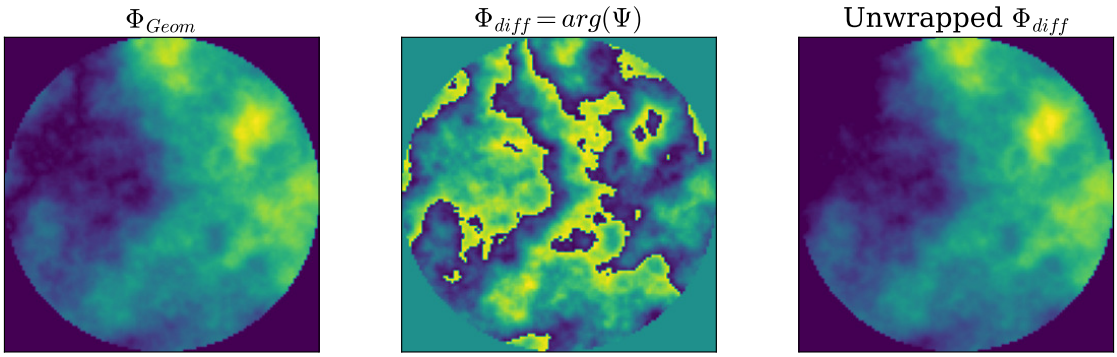

Figure 3.8: Illustration of the unwrapping method.

which is also the correction phase accounting for anisoplanatism, finite resolution of the DM and the AO loop delay.

To compute the correction phase from the downlink on-axis complex field, it is needed to unwrap the phase to compute the correction phase, as it requires expanding the phase onto the Zernike polynomial basis. Indeed, to have an accurate correction, we want to account for the phase issued from the complex field, that includes the results of diffractive effects on the phase. We denote this phase term as: $\Phi_{diff} = \arg \Psi$. However, only computing the argument of the complex field results in a phase modulo 2π. To unwrap the phase, we use the geometrical phase provided by the E2E simulator for each sample. The geometrical phase Φ_{geom}, is the sum of the phase screens cropped by the pupil at the instant t. We apply the following method:

$$\Phi_{diff}(\mathbf{r}) = \Phi_{geom}(\mathbf{r}) + \Delta\Phi(\mathbf{r}) \tag{3.22}$$

where

$$\Delta\Phi(\mathbf{r}) = \arg\left(\Psi(\mathbf{r}) \cdot \exp\left(-i\Phi_{geom}(\mathbf{r})\right)\right) = \arg\left(\exp\left(i(\Phi_{diff}(\mathbf{r}) - \Phi_{geom}(\mathbf{r}))\right)\right) \tag{3.23}$$

Therefore, by using the complex field and the associate geometrical phase, we can compute the diffractive phase. However, this method is valid under the assumption that diffractive effects' contribution $\Delta\Phi(\mathbf{r})$ are lower than 2π. Figure 3.8 illustrate the results obtained with this method.

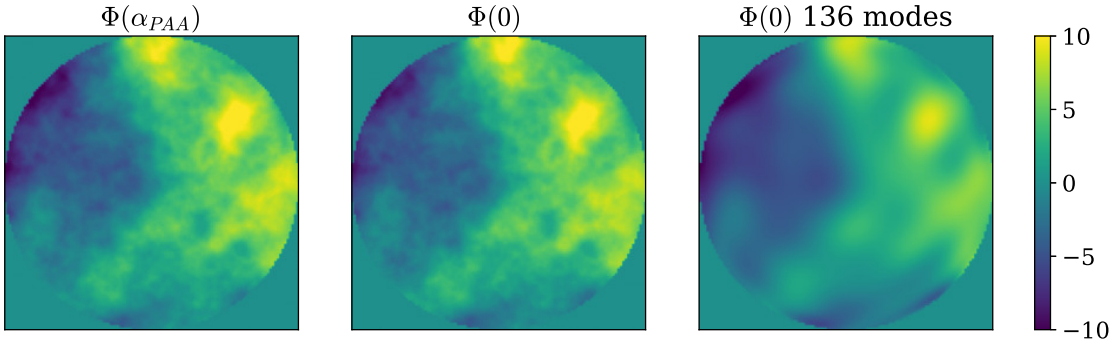

Figure 3.9: Illustration of the reconstructed correction phase.

This unwrapping method will also be useful to analyze turbulent modal phase variances from the E2E data, in order to validate theoretical formulas.

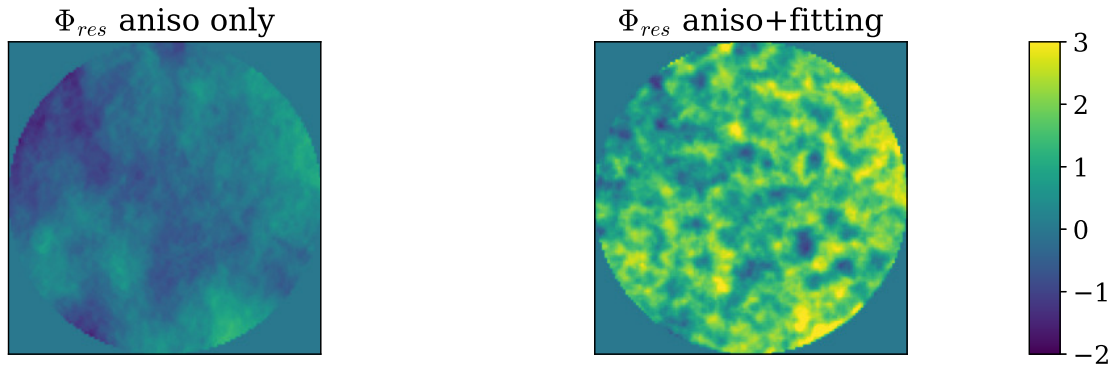

Figure 3.10: Illustration of the residual phase when considering: on the left, only anisoplanatism error, on the right, anisoplanatism and fitting errors.

We finally illustrate the correction phase from Eq. 3.21, in figure 3.9. We show the unwrapped phase at point-ahead angle on the left, the phase on-axis in the center and the reconstructed phase on-axis on 136 modes on the right. We observe that the high spatial frequencies of the correction phase have been filtered. We also observe that the off-axis and on-axis phase do not seem very different. However, when analyzing the residual phase, depicted in figure 3.10, this phase difference is highlighted. Indeed, this figure depicts the residual phase accounting only for the anisoplanatic error on the left, and anisoplanatism and fitting on the right. The residual phase "aniso only" shows low frequency residuals, whereas the correction phase "aniso+fitting" shows additional energetic high frequency residuals. These high frequency residuals seem anormally enegretic. This can be due to the Gibbs effect, that is a sampling effect. In both cases, the phase range is smaller than the initial phase range in figure 3.9.

3.2.3.3 Reciprocal coupling validation

After the correction of the reciprocal uplink, i.e., the application of the phase correction described above, we proceed with the calculation of the numerical overlap integral in order to obtain the reciprocal coupled flux.

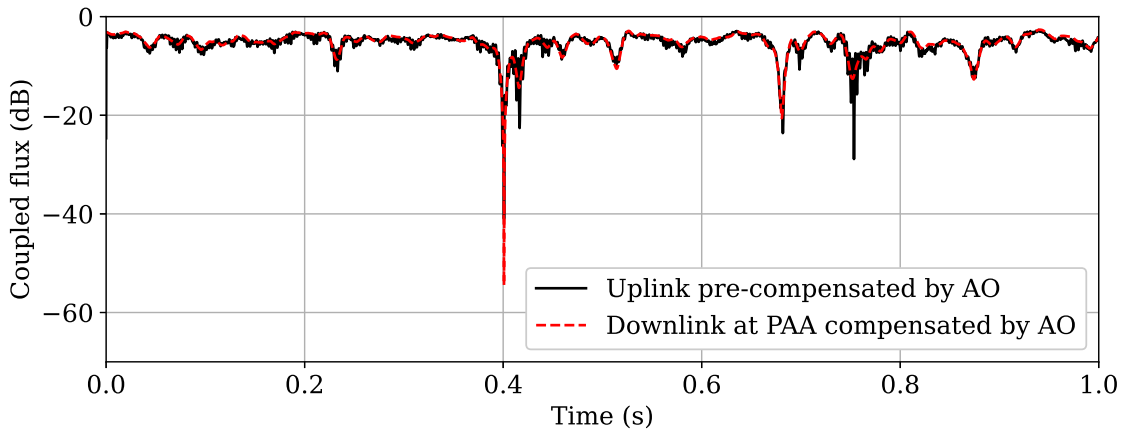

Figure 3.11: Coupled flux time-series of a simulated conventional pre-compensated uplink (black) compared to the uplink reciprocal coupled flux obtained with the reciprocal simulation tool and idealized AO correction (red).

Figure 3.11 depicts the comparison between the AO pre-compensated uplink (propagated from the OGS to the satellite with an AO correction computed from AOST simulator, described in section 2.3.2) and the reciprocal coupled flux obtained from the downlink beam off-axis, corrected using the simplified AO correction , described in section 3.2.3.2.

The Pearson correlation coefficient between the two time-series is 90%. It is not identical, but the coupled flux fluctuations and fades behavior are sufficiently identical to allow us to use this model for our analysis. Additionally, the discrepancies between the two time-series are most likely due to the difference between the two AO corrections. Better results can be expected by still using a reciprocal propagation scheme and an adaptive optics simulator, including all the errors from the AO system, hence providing a more realistic AO correction.

3.2.3.4 Advantages and limits of the reciprocal E2E simulation tool

From these developments, we can highlight several advantages of using the reciprocal E2E simulation tool. The first advantage is the possibility to generate a database of complex fields on-axis and off-axis, that can be reused infinitely to compute the coupled flux, for any phase correction we want to apply (simplified AO or E2E AO simulated dynamic correction thanks to numerical tools as AOST). On the reverse, the classical E2E propagation uplink tool requires to re-propagate the pre-compensated field each time we want to test a new AO correction. This property is useful to test different AO corrections (classical, LGS, other), or to optimize AO control laws. Secondly, the reciprocal tool is less memory-consuming (and therefore time-consuming) than a classical wave optics uplink propagation tool. Indeed, the classical uplink propagation requires big phase screens to take into account the divergence of the uplink beam. In this scheme, we only need screens of the same dimensions as for the downlink.

The principal limit of the proposed approach is related to the computation time. Even if this duration is reduced with respect to classical uplink propagation tools, computing 2s of data still takes around one day of computation. This time-consuming limitation makes this tool proper for static link design and analysis. However, it cannot be used for dynamic optimization of systems (optical or digital). It also means that it takes a very long simulation time to have statistically representative datasets.

In the following, we first present an analytical formalism based on the reciprocity to study the pre-compensation phase error in a general formalism, valid for any phase correction linear with the measurements. Afterward, we use this phase model in a reciprocity based pseudo-analytical approach, to fastly model statistically representative samples of the coupled flux.

3.3 Reciprocal phase error general formalism

We use the reciprocity principle to express the pre-compensation phase error in presence of anisoplanatism and present a phase error general formalism, that aims at providing a theoretical characterization of the pre-compensation phase error for any phase correction linear with the measurements. This analytical phase model will provide a fast tool allowing to study the pre-compensation phase error. It will also serve the fast pseudo-analytical model tool development that will be described in section 3.4.

3.3.1 Definitions and notations

We use the Zernike modal formalism in order to characterize the phase. The spatial phase obtained on the axis α over the pupil is therefore expressed in a vector form as:

$$\mathbf{\Phi}_\alpha(t) = \left[a_2^\alpha(t), ..., a_N^\alpha(t)\right]^T \tag{3.24}$$

where $\forall i$, $a_i(t)$ are the phase Zernike projections at the instant t and N is the Noll index of the last Zernike mode used in the decomposition.

To accurately represent the phase and its correction, we define two subsets:

- the Zernike subset from 2 to N_{AO}, that describes the phase corrected by the adaptive optics system. N_{AO} is the maximum number of the modes that can be measured and corrected by the AO system.
- the Zernike subset from 2 to N_{max}, that describes the phase to correct at point-ahead angle. N_{max} is the maximum number of modes used in the phase representation, in order to have an accurate representation of the phase.

As we will characterize the phase statistics, we define the modal angular covariance matrix of the physical quantities $\mathbf{X}_{\alpha_1}$ and $\mathbf{X}_{\alpha_2}$, separated by an angle $\Delta\alpha$ as:

$$\mathbf{\Gamma}_{\mathbf{X}}(\Delta\alpha) = \mathbb{E}[\mathbf{X}_{\alpha_1}\mathbf{X}_{\alpha_2}^T] \tag{3.25}$$

where $\Delta\alpha = \alpha_2 - \alpha_1$. We give a general description as we will later characterize covariances between different physical quantities. This expression becomes an autocovariance when $\Delta\alpha = 0$. and the modal cross-covariance matrix between the physical quantity $\mathbf{X}_{\alpha_1}$ and $\mathbf{Y}_{\alpha_2}$, separated by an angle $\Delta\alpha$ as:

$$\mathbf{\Gamma}_{\mathbf{XY}}(\Delta\alpha) = \mathbb{E}[\mathbf{X}_{\alpha_1}\mathbf{Y}_{\alpha_2}^T] \tag{3.26}$$

where $\mathbf{X}_{\alpha_1}$ and $\mathbf{Y}_{\alpha_2}$ are supposed to be centered random vectors.

3.3.2 General phase error formalism

We use the reciprocal formalism to explicit the wavefront perturbations at PAA that are corrected by the AO pre-compensation. This allows to evaluate the AO correction performance by computing the reciprocal off-axis residual wavefront:

$$\mathbf{\Phi_{res}} \triangleq \mathbf{\Phi_{PAA}} - \hat{\mathbf{\Phi}}_{\mathbf{PAA}}, \tag{3.27}$$

the difference between the phase of of the complex field corresponding to the the back-propagation of the reception mode of the satellite in the OGS pupil plane $\mathbf{\Phi_{PAA}} \in \mathbb{R}^{\mathrm{N_{max}}-1}$ and the AO correction phase $\hat{\mathbf{\Phi}}_{\mathbf{PAA}} \in \mathbb{R}^{\mathrm{N_{max}}-1}$, both expressed in the subset of Zernike modes of size $\mathrm{N_{max}}$.

To model the fitting, due to the finite AO correction mode basis, hence impacting the high order modes from $N_{AO}+1$ to N_{max}, we define the correction phase as:

$$\hat{\mathbf{\Phi}}_{\mathbf{PAA}} \triangleq \begin{pmatrix} \hat{\mathbf{\Phi}}_{\mathbf{AO,PAA}} \\ \mathbf{0} \end{pmatrix}, \tag{3.28}$$

where $\hat{\mathbf{\Phi}}_{\mathbf{AO,PAA}} \in \mathbb{R}^{N_{AO}-1}$ is the correction phase on the AO modes subset. The zero terms cover the rest of the representation mode subset from $N_{AO}+1$ to N_{max}.

We develop a general formalism relevant to every AO corrections computed as linear operations with AO measurements. In this aim, we assume the correction phase to result from a linear operation hence with a given reconstructor matrix $\mathbf{R}$ applied to a measurement vector $\mathbf{y}_m$, obtained on the on-axis the downlink beam. The correction phase therefore reads:

$$\hat{\mathbf{\Phi}}_{\mathbf{AO,PAA}} \triangleq \mathbf{R}\mathbf{y}_m. \tag{3.29}$$

The value and dimensions of $\mathbf{R}$ and $\mathbf{y_m}$ depend on the chosen correction method. We assume that all measurements are noise free, since we are in a high flux regime in telecom scenarios.

Under this formalism, we can describe the statistics of the residual phase and show that its covariance matrix is equal to:

$$\mathbf{\Gamma_{res}} \triangleq \mathbb{E}[\mathbf{\Phi_{res}}\mathbf{\Phi_{res}}^{\mathbf{T}}] = \begin{pmatrix} \mathbf{\Gamma}_{\text{aniso}} = [\mathbf{\Gamma}_{\text{AO,res}}]_{2\leq i,k,\leq N_{AO}} & \mathbf{0} \\ \mathbf{0} & \mathbf{\Gamma}_{\text{fitting}} = [\mathbf{\Gamma}_{\Phi\Phi}(0)]_{N_{AO}+1\leq i,k,\leq N_{max}} \end{pmatrix}, \tag{3.30}$$

where we neglect the cross-covariances between the corrected and uncorrected modes, supposedly weak.

We compute the residual phase covariance matrix as:

$$\mathbf{\Gamma_{AO,res}} = \mathbf{\Gamma}_{\Phi\Phi}(0) - \mathbf{R}\mathbf{\Gamma}_{\Phi y_m}(\alpha_{PAA})^T - \mathbf{\Gamma}_{\Phi y_m}(\alpha_{PAA})\mathbf{R}^T + \mathbf{R}\mathbf{\Gamma}_{y_m y_m}(0)\mathbf{R}^T. \tag{3.31}$$

where the value of the covariance matrices and of $\mathbf{R}$ depend on the type of correction chosen, and of the choice of $\mathbf{y}_{mes}$.

Finally, the metrics to evaluate the pre-compensation performance are the overall mean square error (MSE) and the modal MSE, also known as residual phase variances:

$$\text{MSE} = \text{tr}[\mathbf{\Gamma_{res}}] \quad \text{and} \quad \text{MSE}_i = (\mathbf{\Gamma_{res}})_{i,i}, \tag{3.32}$$

where tr is the trace operator and i the i^{th} Zernike mode index.

3.3.3 Phase error in state-of-the art cases

The content of $\mathbf{R}$ and $\mathbf{y}_m$ depends on the type of AO correction and on the assumptions on the AO system. We detail these values for the classical pre-compensation and an LGS aided pre-compensation with the detailed below simplified error budget.

AO system hypothesis

We consider an idealized AO system, therefore, we do not account for errors such as aliasing and the measurement noise. In the first place, we also neglect the temporal error induced by the loop delay, that is negligible compared with the anisoplanatism error. However, temporal error will be considered and modeled in chapter 5. Therefore, the residual phase $\mathbf{\Phi}_{res}$ only suffers from anisoplanatism.

Residual phase covariance matrix

Considering only the anisoplanatic error on the subset of corrected modes, we can specify $\mathbf{R}$ and $\mathbf{y}_m$ for the two principal AO correction from the state of the art: the classical pre-compensation and the LGS aided pre-compensation.

Classical pre-compensation

In this case, the correction phase $\hat{\mathbf{\Phi}}_{\mathbf{AO,PAA}}$ is equal to the downlink beam phase measurement located at $\alpha = 0$. Therefore, $\mathbf{R} = \mathbf{I}_{\mathrm{N_{AO}-1}} \in \mathbb{R}^{\mathrm{N_{AO}-1 \times N_{AO}-1}}$ and $\mathbf{y_m} = (\mathbf{\Phi_0}) \in \mathbb{R}^{\mathrm{N_{AO}-1}}$, where $\mathbf{I}$ denotes the identity matrix. As a result, applying Eq. 3.31, we obtain in this particular case:

$$\mathbf{\Gamma_{AO,res-classical}} = \mathbf{2\Gamma_{\Phi\Phi}(0) - \Gamma_{\Phi\Phi}(\alpha_{PAA}) - \Gamma_{\Phi\Phi}(\alpha_{PAA})^T}. \tag{3.33}$$

LGS aided pre-compensation

In the case of an LGS aided pre-compensation at PAA, as explained in section 2.6, it is yet no proven that the tip tilt and focus can be measured. Therefore, we assume in this scheme that the tip tilt and focus correction is done with the tip tilt and focus on axis beacon. Furthermore, we assume an idealized LGS. Hence, the we assume the LGS high order modes from order 5 to N_{AO} to be perfectly sensed at PAA. Therefore, the matrix $\mathbf{R}$ is still equals to the identity matrix, and $\mathbf{y}_m$ is defined as:

$$\mathbf{y}_{m,LGS} = \left[a_2^0, a_3^0, a_4^0, a_5^{\alpha_{PAA}}, ..., a_{N_{AO}}^{\alpha_{PAA}}\right]^T \tag{3.34}$$

As a result, applying Eq. 3.31, we obtain in this particular case:

$$\mathbf{\Gamma}_{AO,res-LGS} = \begin{bmatrix} [\mathbf{\Gamma_{AO,res-classical}}_{2\leq i\leq 4} & \mathbf{0} \\ \mathbf{0} & \mathbf{0} \end{bmatrix} \in \mathbb{R}^{(N_{AO}-1)\times(N_{AO}-1)}. \tag{3.35}$$

Modal angular covariance terms

Finally, we detail the content of $\mathbf{\Gamma}_{\Phi\Phi}(\Delta\alpha)$. The angular phase covariances have been developed by Chassat [157]. For given indexes i and j, we define the angular covariance term as:

$$\begin{aligned}\mathbb{E}[a_i^0 a_j^\alpha] - \mathbb{E}[a_i^0]\mathbb{E}[a_j^\alpha] = 5.20\mathrm{K_{ij}} \int_0^{\mathrm{L}} \mathrm{dz C_n^2(z)} \int_0^{+\infty} \mathrm{dk k}^{\frac{-14}{3}} \\ \mathrm{J_{n_i+1}(k) J_{n_j+1}(k) cos^2}\left(\frac{\mathrm{zk}^2}{2\mathrm{k_0 R_{tel}^2}}\right)\left(1 + \left(\frac{2\pi \mathrm{R_{tel}}}{\mathrm{L_0 k}}\right)^2\right)^{\frac{-11}{6}} \cdot \\ (\mathrm{S1} \cdot \mathrm{J_{m_1+m_2}}\left(\frac{\mathrm{kd(z,\Delta\alpha)}}{\mathrm{R_{tel}}}\right) + \mathrm{S2} \cdot \mathrm{J_{|m_1-m_2|}}\left(\frac{\mathrm{kd(z,\Delta\alpha)}}{\mathrm{R_{tel}}}\right))\end{aligned} \tag{3.36}$$

where $(\mathrm{n_i}, \mathrm{m_i}), (\mathrm{n_j}, \mathrm{m_j})$ are the radial and azimuthal degrees of the i^{th} and j^{th} Zernike polynomials respectively, z is the distance to the OGS pupil on the line of sight, $\mathrm{R_{tel}}$ is the aperture radius and $\mathrm{k_0} = \frac{2\pi}{\lambda}$ is the wave number. $\mathrm{K_{ij}}$ is defined as:

$$\mathrm{K_{ij}} = \sqrt{(\mathrm{n_i}+1)(\mathrm{n_j}+1)}(-1)^{\frac{\mathrm{n_i}+\mathrm{n_j}-\mathrm{m_i}-\mathrm{m_j}}{2}} \mathrm{R_{tel}^{\frac{5}{3}} k_0^2}, \tag{3.37}$$

$C_n^2(z)$ is the turbulence refractive index structure function at the distance to the pupil z on the line of sight, $J_n(k)$ are the Bessel functions of the first kind of order n. Moreover, $(1+\frac{2\pi R_{tel}}{L_0 k}^2)^{\frac{-11}{6}}$ is the Von Karman term accounting for the turbulence outer scale L_0.

The last part of the equation is the contribution of the angular correlation between the two beam footprints at a given height distant from:

$$d(z, \Delta\alpha) = \Delta\alpha \cdot z, \tag{3.38}$$

where $\Delta\alpha$ is an oriented angle. The distance $d(z, \Delta\alpha)$ between the two beam footprints is illustrated in figure 3.12, on the left.

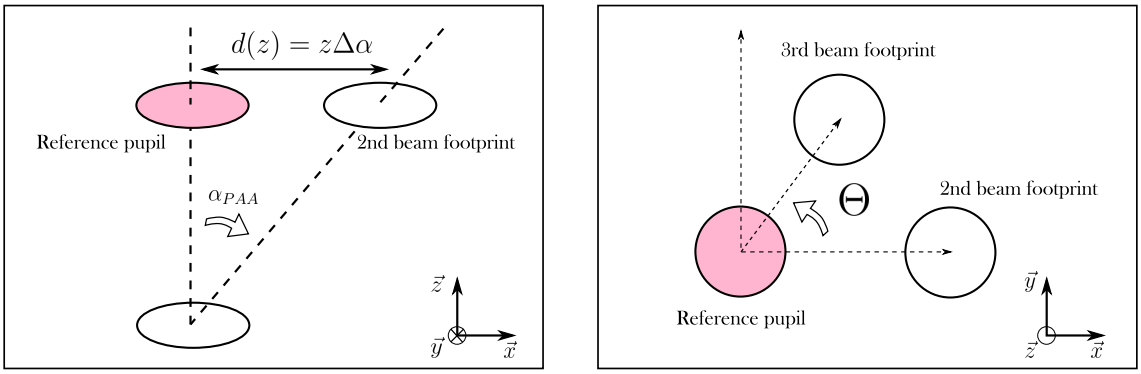

Figure 3.12: Illustration of the beam footprint geometry in two different planes. On the left, illustration of the distance between the beam footprints function of the height and the angle $\Delta\alpha$. On the right, illustration of the relative orientation between the beam footprints, introducing the angle Θ.

S1 and S2 are the geometrical coefficients depicting the relative orientation of the beam footprints that are computed in table 3.1 and table 3.2, function of the angle. In our geometry, $\Theta = 0$. This relative orientation is illustrated on the right of figure 3.12.

S1		$m_i = 0$	$m_i \neq 0$	
			n_i even	n_i odd
$m_j = 0$		1	$\sqrt{2}\cos(m_i\Theta)$	$\sqrt{2}\sin(m_i\Theta)$
$m_j \neq 0$	n_j even	$(-1)^{m_j}\sqrt{2}\cos(m_j\Theta)$	$(-1)^{m_j}\sqrt{2}\cos((m_j+m_i)\Theta)$	$(-1)^{m_j}\sqrt{2}\sin((m_j+m_i)\Theta)$
	n_j odd	$(-1)^{m_j}\sqrt{2}\sin(m_j\Theta)$	$(-1)^{m_j}\sqrt{2}\sin((m_j+m_i)\Theta)$	$(-1)^{m_j+1}\sqrt{2}\cos((m_j+m_i)\Theta)$

Table 3.1: Computation of the S1 term function of the radial order n_j, resp n_i and the azimuthal order m_j,resp m_i and the angle Θ.

S2		$m_i = 0$	$m_i \neq 0$	
			n_i even	n_i odd
$m_j = 0$		0	0	0
$m_j \neq 0$	n_j even	0	$s_{n_i n_j}\cos((m_i - m_j)\Theta)$	$s_{n_i n_j}\sin((m_i - m_j)\Theta)$
	n_j odd	0	$-s_{n_i n_j}\sin((m_i - m_j)\Theta)$	$s_{n_i n_j}\cos((m_i - m_j)\Theta)$

Table 3.2: Computation of the S2 term function of the radial order n_j, resp n_i and the azimuthal order m_j,resp m_i, the angle Θ and the function $s_{n_i n_j} = \text{sign}(m_i - m_j)$.

In the formulas from the work of Chassat, the $\cos^2$ term, that is the term accounting for the diffractive effects on the phase, is neglected. However, we have shown that it is

important to account for this term. Figure 3.13 depicts the modal residual phase variance

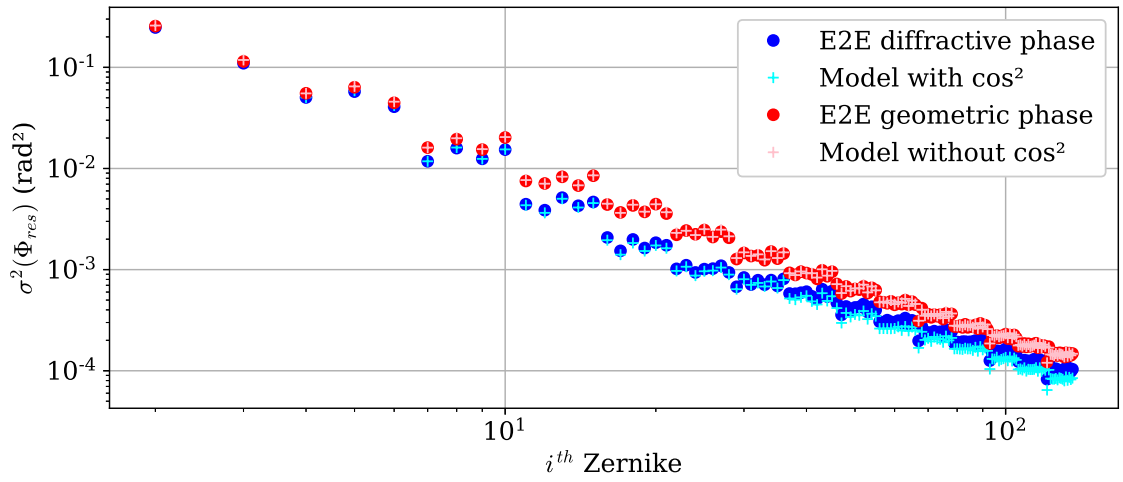

Figure 3.13: Illustration of the residual modal phase variances, computed from E2E data and theoretical, and from the analytical model. The blue and cyan case corresponds to a case comparing the results accounting for diffraction. The red and pink cases do not account for the diffraction and is computed on the geometrical phases (in the E2E case) and without the $\cos^2$ in the analytical case.

function of the Zernike mode number, computed: from E2E data geometrical phases, that are the sum of the phase screens (red dots) compared with the analytical residual phase variances computed without the term $\cos^2$ (pink crosses), and from E2E diffractive phases, computed from the complex field unwrapped phases (blue dots), compared with the analytical residual phase variances computed with the term $\cos^2$ (cyan crosses). We observe a very good accordance between both models and the E2E data.

3.4 Semi-analytical reciprocal channel model

Being able to model the phase statistics allows us to use semi-analytical modeling approaches to simulate the coupled flux, while overcoming the computation time limitation of the E2E model. These simulation techniques have the advantage to suppress the propagation step, which is the time-consuming step in the E2E scheme, by directly considering models of the perturbed complex field in the OGS pupil (in a downlink configuration).

We call semi-analytical modeling the approach relying on the generation of random complex fields thanks to analytical formulas, that are then coupled to a Gaussian mode through a numerical overlap integral. The method to model the phase of the complex field statistics can vary. Fourier's approaches are adopted in [9]. We choose the modal approach as in [8, 116, 158]. However, with respect to the former modal method that considers only the diagonal of the covariance matrix, we developed a formalism that is general to every AO correction linear with the AO measurements which considers the cross-correlations between the modes that are shown to be non-negligible in the classical pre-compensation case [159].

In the following, we will focus on the modal approach, and describe the main properties of the SAOST tool. The model that we will present only models the statistics of the coupled flux. The extension allowing to model temporal time-series have not been developed yet. We will also see that we improved the original SAOST model by taking into account some effects.

3.4.1 Principle

A pseudo-analytic model consists in modeling the statistics of a downlink beam perturbed phase and log-amplitude after propagation in the pupil, that can be derived from analytical formulas, and to couple numerically the obtained field to the single mode fiber Gaussian mode.

We use this approach to model the reciprocal uplink, that is, the downlink at point-ahead angle corrected by adaptive optics. In that aim, we express the random coupled flux of the pre-compensated signal aboard the satellite reciprocally as the coupling, in the OGS aperture, between the given complex field back-propagated from the satellite at PAA, corrected by AO, and the uplink emission Gaussian mode:

$$f_{pre-compensated,OGS\rightarrow satellite}(\alpha_{PAA}) = f_{compensated,satellite\rightarrow OGS}(\alpha_{PAA}). \tag{3.39}$$

Here, f is a random variable as we only study the statistics behavior of the coupling. As this tool does not yet allow for computing time-series of an anisoplanatic link, we consider only the generation of statistically independent sample of coupled flux.

To express f, we assume Φ and χ of the field independent [160]. Therefore, we can consider separately the phase and log-amplitude contributions to the coupling as:

$$f = \rho_\Phi \rho_\chi. \tag{3.40}$$

In the following, we explain how to model these two coupling contributions.

3.4.2 Log-amplitude contribution to the coupling

3.4.2.1 Definition

We assume to be in the weak perturbations' regime. Thus, the log-amplitude contribution ρ_χ can be approximated to the scintillation averaged over the aperture as in [116], also known as power in the bucket (PIB), multiplied by a constant penalty factor $\mathrm{e}^{-\sigma_\chi^2}$ [161, 162], assessing for the mean coupling losses due to the log-amplitude spatial fluctuations over the aperture:

$$\rho_\chi = \mathrm{PIB} \cdot \mathrm{e}^{-\sigma_\chi^2} = \iint |\Psi(\mathbf{r})|^2 \, \mathrm{P}(\mathbf{r}) \mathrm{d}^2\mathrm{r} \cdot \mathrm{e}^{-\sigma_\chi^2}. \tag{3.41}$$

We recall that σ_χ^2 is computed as:

$$\sigma_\chi^2 = 0.5631 k_0^{7/6} \int_0^L C_n^2(z) z^{5/6} dz \tag{3.42}$$

as defined in section 2.3.3.

3.4.2.2 Statistics

Finally, the PIB contribution from Eq. 3.41 can be expressed as $\mathrm{e}^{2\chi_{\mathrm{Ap}}}$, where the aperture-averaged log-amplitude χ_{Ap} follows a normal distribution [116] of variance $\sigma^2_{\chi_{\mathrm{Ap}}}$ and mean $-\sigma^2_{\chi_{\mathrm{Ap}}}$ to ensure energy conservation with $\mathbb{E}[\mathrm{e}^{2\chi_{\mathrm{Ap}}} = 1$. Therefore, ρ_χ follows a log-normal distribution. Therefore, knowing the PIB distribution, mean and variance, we can draw samples from this law.

We also recall from section 2.3.3 the that the formula to compute the log-amplitude variance filtered by the pupil is:

$$\sigma^2_{\chi,Ap} = 5.20\mathrm{K_{ij}} \int_0^{\mathrm{L}} \mathrm{dz} \mathrm{C_n^2(z)} \int_0^{+\infty} \mathrm{dk} \mathrm{k}^{\frac{-14}{3}} \mathrm{J_1(k)^2 sin^2}\left(\frac{\mathrm{zk}^2}{2\mathrm{k_0 R_{tel}^2}}\right)\left(1 + \left(\frac{2\pi \mathrm{R_{tel}}}{\mathrm{L_0 k}}\right)^2\right)^{\frac{-11}{6}} \tag{3.43}$$

We illustrate the results of the PIB draws in figure 3.14, where the PIB distribution issued from the E2E data computation is represented in black, and issued from the draws in red. We observe a good match between the two distributions.

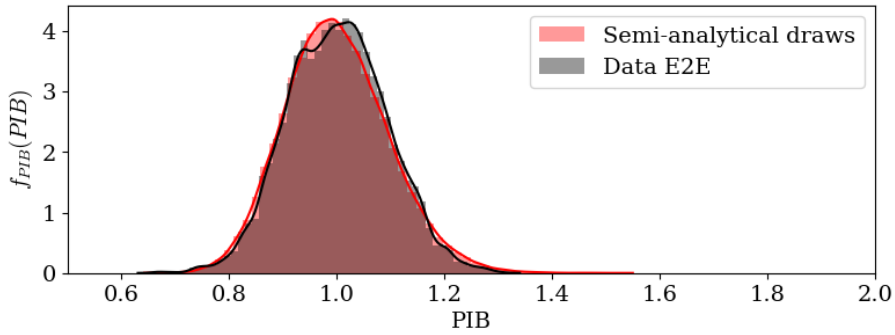

Figure 3.14: Probability density function of the PIB, computed from E2E data in black and issued from the draws in red, in the turbulence case MOSPAR 9090.

3.4.3 Phase contribution to the coupling

3.4.3.1 Definition

The phase contribution is the result of the overlap integral between the field neglecting the log-amplitude fluctuations and the single mode fiber Gaussian mode $\mathrm{M}_0(\mathbf{r})$ [116]:

$$\rho_\Phi = \rho_{\text{compensated,satellite}\rightarrow\text{OGS}} = \left| \frac{\left\langle \mathrm{e}^{\mathrm{j}\Phi_{\text{res}}(\mathbf{r})} | \mathrm{M}_0(\mathbf{r}) \right\rangle_{\mathrm{P}}}{\sqrt{\left\langle \mathrm{e}^{\mathrm{j}\Phi_{\text{res}}(\mathbf{r})} | \mathrm{e}^{\mathrm{j}\Phi_{\text{res}}(\mathbf{r})} \right\rangle_{\mathrm{P}} \left\langle \mathrm{M}_0(\mathbf{r}) | \mathrm{M}_0(\mathbf{r}) \right\rangle_{\mathrm{P}}}} \right|^2 \cdot \exp(-\sigma^2_{\text{super-fitting}}), \tag{3.44}$$

where $\Phi_{\text{res}}(\mathbf{r}) = \sum_{\mathrm{i}=2}^{\mathrm{N}_{\max}} \langle \mathbf{\Phi_{res}} | \mathrm{Z_i}(\mathbf{r}) \rangle \mathrm{Z_i}(\mathbf{r})$ is the residual phase onto the truncated Zernike polynomial basis.

The super-fitting term is defined as:

$$\sigma^2_{super-fitting} = 0.458(n_r + 1)^{-5/3} \left(\frac{D}{r_0} \right)^{5/3} \tag{3.45}$$

developed by [163]. It accounts for the phase non-represented on the basis, where $\mathrm{n_r}$ is the radial order of the last Zernike polynomial of the representation. This result is a variation on the asymptotic development of Noll residual phase variance given in [97]. In practice, we set N_{max} to 496 modes. We illustrate in figure 3.15 the super-fitting phase variance function of the Fried parameter r_0 for a 60 cm diameter case and a maximum number of corrected modes of $N_{max} = 496$. We observe that the super-fitting phase residual is very low for the scenarios considered in the thesis that are depicted as colored stars.

Finally, to express ρ_Φ, we need to define the residual phase and its statistics.

3.4.3.2 Residual phase statistics and coupling computation

To compute the phase occurrences, we characterize the reciprocal phase residual phase after AO correction by applying the methodology presented in section 3.3. This allows to compute the residual phase covariance matrix Γ_{res}. These covariance matrix terms can be calculated thanks to the OGS and atmospheric parameters, in particular the $\mathrm{C_n^2}$ profile

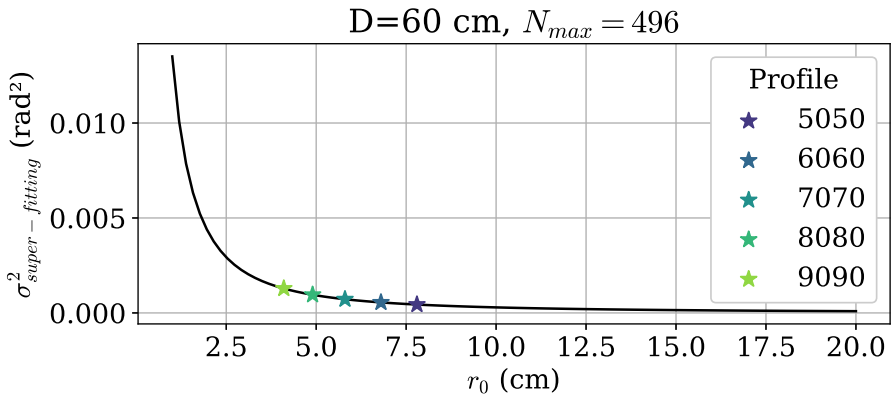

Figure 3.15: Variance of the phase super-fitting function of the Fried parameter r_0, for a diameter of 60 cm and a phase representation on 496 Zernike modes. The stars represent the turbulence conditions encountered in the thesis.

that is supposed to be known, which gives the distribution of the turbulence strength along the line of sight.

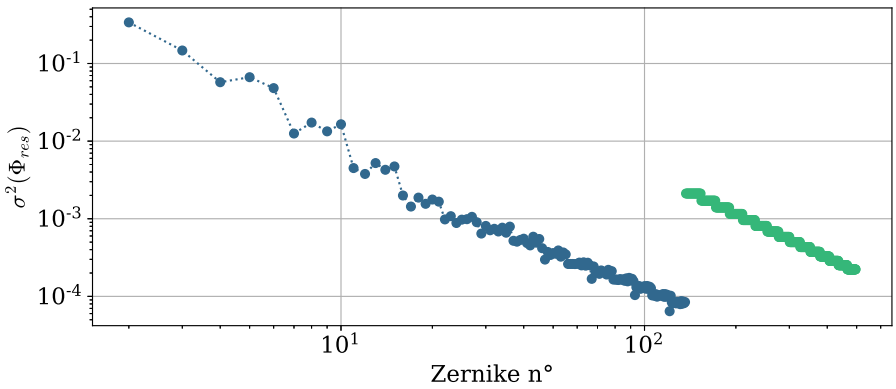

Figure 3.16: Modal residual phase variance function of the Zernike mode, computed in the MOSPAR 9090 case. The blue dots represent the anisoplanatic phase variance, the green dots represent the fitting phase variance.

From the literature, we know that the phase Zernike projections follow a centered normal distribution [164], characterized by the covariance matrix $\mathbf{\Gamma_{res}}$. An example of the diagonal of this covariance matrix is given in figure 3.16, considering the classical pre-compensation scheme affected by anisoplanatism and fitting. Therefore, we can make an arbitrary large number of residual phases draws, synthesize the associated complex fields and compute the numerical overlap integral with the Gaussian mode mentioned above to obtain the coupling phase contribution. The Gaussian mode is represented in the pupil plane and have a waist equal to $\omega_0 = D_{pup}/2.2$, as defined in section 2.1.

Usually, in the SAOST software for instance, the Zernike projections are simply drawn from the diagonal of the covariance matrix $\mathbf{\Gamma_{res}}$. This is a good approximation when the inter-correlation between the Zernike projections are weak. However, we noticed in the anisoplanatic case that we had to account for these inter-correlations to model the coupled flux with accuracy. Therefore, we define:

$$\mathbf{\Gamma_{res}} = \mathbf{P}\mathbf{D_{res}}\mathbf{P}^{-1} \tag{3.46}$$

where $\mathbf{P}$ is the transfer matrix from $\mathbf{\Gamma_{res}}$ to the $\mathbf{D_{res}}$ space, and $\mathbf{D_{res}}$ is a diagonal matrix.

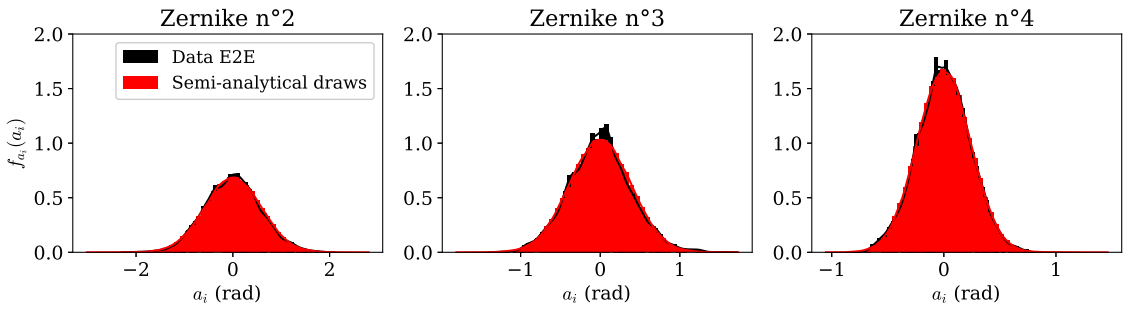

Figure 3.17: Probability density function of the first three Zernike modes, computed from the data in black and issued from the Gaussian draws in red.

Thanks to this diagonal matrix, we draw the samples from the diagonalized space instead of drawing them from the diagonal of the matrix, before back transforming the samples in the $\mathbf{\Gamma_{res}}$ space. In figure 3.17, we show the distribution of the 3 first Zernike modes, computed from the E2E data, compared with the draws taking into account the inter-correlations. We observe a good match between the distributions.

3.4.4 Validation of the pseudo-analytic tool

Finally, we multiply the log-amplitude to the phase coupling contribution to obtain the coupled flux f. We compare the results obtained with the pseudo-analytical model to the coupled flux obtained thanks tot the E2E data.

Figure 3.18 depicts this comparison for two turbulence cases: the MOSPAR 5050 turbulence case and the MOSPAR 9090 turbulence case. We plot both the probability density function and the cumulative density function obtained from the numerical samples. We observe a good match between the E2E data and the semi-analytically computed samples for both turbulence cases. We computed 9400 independent occurrences of E2E data compared with 50000 samples with the semi-analytical tool. We highlight that the time to compute 9400 samples with the E2E model is around one day, whereas it takes less than five minutes to compute the phase covariance matrices and the 50000 semi-analytical samples. The computation of the samples in themselves is around one minute, and the covariance computation is longer due to the numerous integrals to compute. However, this computation could be optimized.

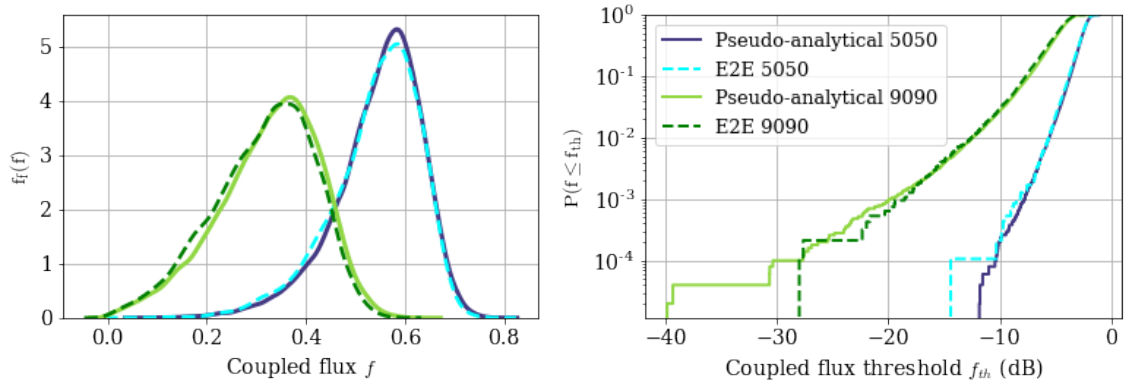

Figure 3.18: Probability density function (left) and cumulative density function (right) of the coupled flux f_c obtained: from E2E data (dashed lines) and from the semi-analytical model (plain lines), for two turbulence cases (MOSPAR 5050 blue, MOSPAR 9090 green).

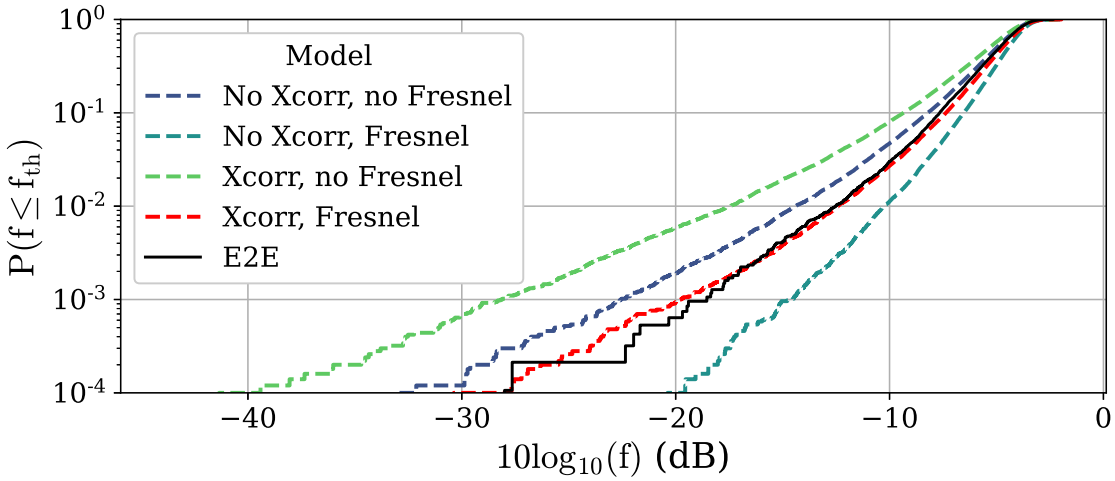

Figure 3.19: Impact on the coupled flux of taking into account (or not) the diffractive term and the inter-correlation, in the four combinations.

Additionally, we plot in figure 3.19 the coupled flux obtained with the semi-analytical model, taking into account or not the Fresnel diffractive term and/or the inter-correlations, compared with the coupled flux obtained from E2E data (in black). We notice that not taking into account one or both of these two effects can lead to discrepancies from the E2E results above 4 dB at probability 10^{-3}. We interpret the impact of the different as follows: not taking into account the Fresnel term leads to more energetic phase variances, as the Fresnel term acts as a low-pass filter. Therefore, computing the coupled flux without accounting for this term is pessimistic, resulting in more frequent fadings than expected. Conversely, not accounting for the cross-correlations leads to an underestimation of the fadings frequency.

3.5 Anisoplanatic channel performance evaluation

In this section, we aim at illustrating the potential of the reciprocal channel modeling numerical tools presented in section 3.2.3, 3.3 and 3.4, while characterizing the optical pre-compensated uplink channel, applying the AO corrections from the state of the art. We will study both the classical pre-compensation and the LGS aided pre-compensation cases described in section 3.3.3.

Indeed, the semi-analytical model allows us to perform parametric evaluations of the channel, thanks to the computation speed of the model. Therefore, we use this model to study the impact of the OGS diameter on the coupled flux statistics. This can be applied to OGS preliminary design, and further be applied to the study of the coupled flux distribution in different turbulence regimes, that are strongly related to the emitted waist diameter (as evoked in [100]) and the level and quality of AO correction. Additionally, studying the temporal characteristics (or fade statistics) of the signal is necessary to have a complete description of the channel, and be able to design communication systems. As this temporal behavior is not yet implemented in the semi-analytical model, we will use the E2E time-series to proceed to this characterization.

Therefore, we present in this section an analysis of the impact of the OGS design on the channel statistics, in the atmospheric conditions MOSPAR 5050 and 9090 that are median and severe turbulence conditions.

3.5.1 System design tool

In order to illustrate the use of reciprocal tools as design tools, we study the channel behavior for different emission aperture diameters. We study the channel in two atmospheric conditions: the MOSPAR 5050 conditions, that is the median turbulence case, and the MOSPAR 9090 case, that is a more extreme and dimensioning turbulence case, with an outer scale L_0 of 5.12 m.

The considered diameters are detailed in table 3.3. We also tune the number of adaptive optics corrected modes, to keep the fitting error roughly constant with the increasing diameter. The associated number of AO modes used in the correction and resulting fitting variance for the MOSPAR 5050 and 9090 cases are also depicted in this table.

Diameter (cm)	10	20	30	40	50	60	70	80	90	100
N_{corr}	21	45	66	91	120	136	171	190	210	231
$\sigma^2_{fit,5050}$ (rad²)	0.04	0.04	0.04	0.04	0.03	0.04	0.03	0.03	0.03	0.03
$\sigma^2_{fit,9090}$ (rad²)	0.12	0.11	0.11	0.11	0.10	0.11	0.10	0.10	0.10	0.10

Table 3.3: Table of the number of AO correction mode function of the diameter to keep the fitting error constant.

3.5.2 Residual phase variance

We analyze the anisoplanatic phase variance for the classical pre-compensation case. In the case of LGS, the result is the same, with the variance of the high-order modes subtracted (from 5 to N_{AO}).

In figure 3.20, we plot, for both atmospheric turbulence cases, the anisoplanatic residual phase variance function of the aperture diameter. The total residual phase variance is depicted in black. We also plot the individual phase variance for the Zernike modes from mode 2 to 10. Each group of modes of the same radial order is plotted in the same color. In both cases, the total anisoplanatic phase variance is shown to increase with the diameter. Additionally, the tip and tilt variances are shown to saturate, while the other mode's variance seems to continue increasing, causing the total variance to increase, which translates the impact of the outer scale L_0.

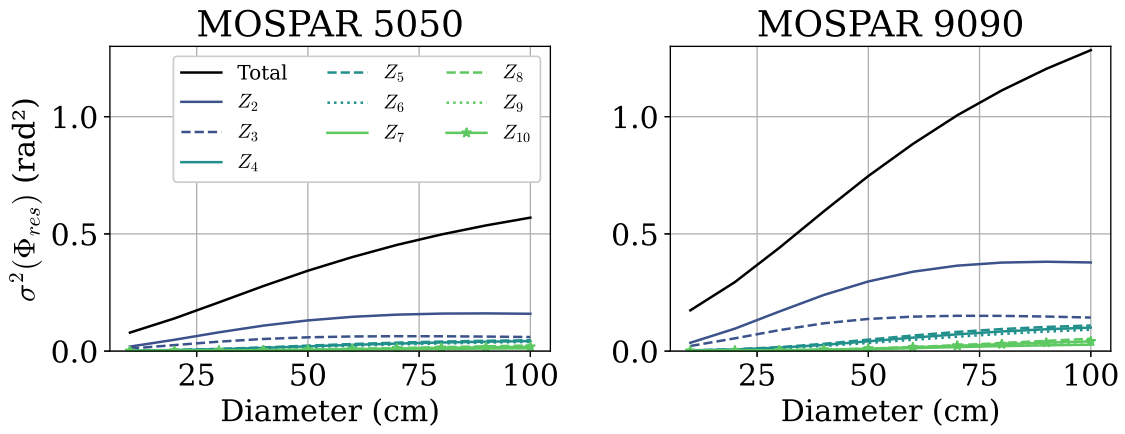

Figure 3.20: Evolution of the total residual phase variance function of the aperture diameter (black) and individual modal phase variance for low order modes (from 2 to 10).

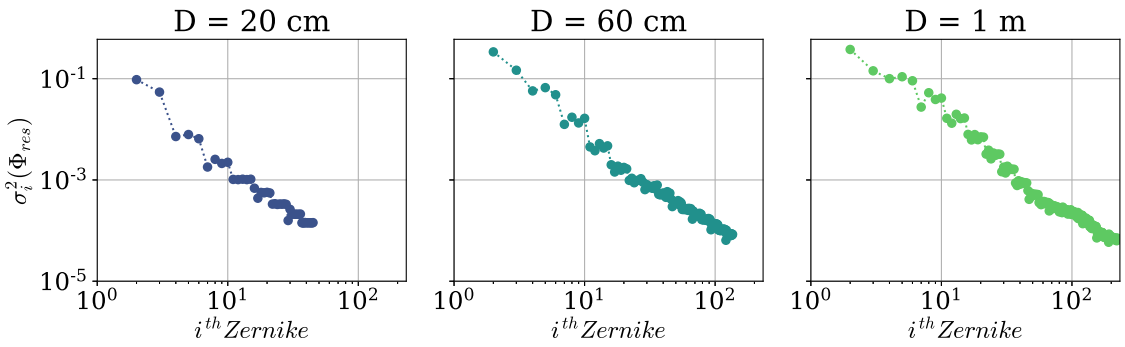

Figure 3.21: Modal residual phase variance function of the Zernike mode number for three different aperture diameters. From the left to the right: 20 cm, 60 cm, 1 m. The considered case is the MOSPAR 9090.

Additionally, we analyze the modal spectrum of the anisoplanatic phase for the turbulence case MOSPAR 9090 in figure 3.21, for three different diameters. Indeed, it is of interest not only analyzing the total phase residual variance, but also analyzing how this energy is distributed along the spatial modes, as it will affect differently the coupling with the Gaussian mode. In this figure, we observe again that as the diameter increases, the low order mode variances increases. It is interesting to notice from the 60 cm and 1 m cases that different cut-off frequencies appears, one in the 60 cm case and 3 in the 1 m case.

3.5.3 Coupled flux statistics

We start by analyzing the coupled flux statistics behavior of f for the different diameters, in order to underline the utility of this tool as a research tool, allowing to intuit the probability law of the coupled flux as a function of the turbulence regime. Then, we proceed to a link budget analysis to determine under which aperture sizes the link budget can be closed for a given availability threshold.

3.5.3.1 Statistics analysis

To analyze the statistical behavior function of the diameter, we computed 50000 samples using the semi-analytical tool in four scenarios: the classical and LGS AO pre-compensation for the MOSPAR 5050 and 9090 cases.

In figure 3.22, we plot the probability density function of the coupled flux function of the coupled flux value and for each aperture diameter, normalized by ρ_0, that is the coupling value for a plane wave. We observe that the signal PDF is right skewed in the small aperture regime, is almost symmetric when the aperture is around 40 cm and finally, ends left skewed with a tail that seems to slide to the left for large apertures. We note that this distribution, by definition, is issued from a mixture of phase contributions to the coupling and log-amplitude contribution to the coupling. To highlight the weighting of each effect in each regime, we separate and plot the two contributions ρ_χ and ρ_Φ separately.

We separate the log-amplitude and phase contributions, ρ_χ and ρ_ϕ, in figure 3.23, to compare their impact on the total coupled flux distribution. In this figure, we plot above the PDF of ρ_χ and below the PDF of ρ_Φ, in the MOSPAR 9090 case. Considering the ρ_χ distribution, we observe that it is a Lognormal distribution (which was expected), hence right-skewed, whose distribution variance decreases as the diameter increases. This is explained by the aperture averaging effect that increases with the diameter. This effect causes the log-amplitude induced flux fluctuations to be reduced as the diameter increases.

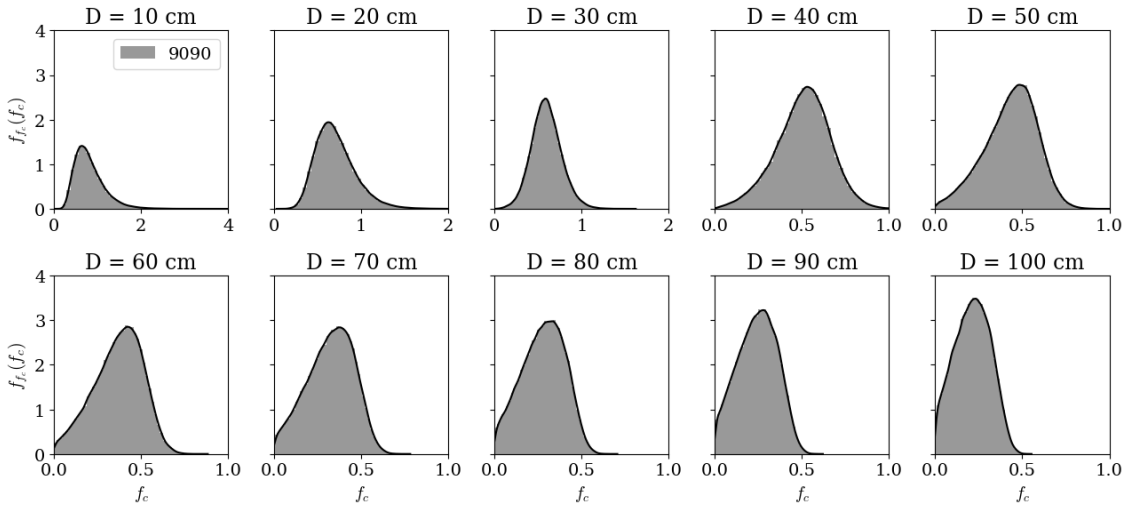

Figure 3.22: PDF of the coupled flux f, for each aperture diameter from 10 cm to 1 m, in the MOSPAR 9090 turbulence case, in the classical pre-compensation case.

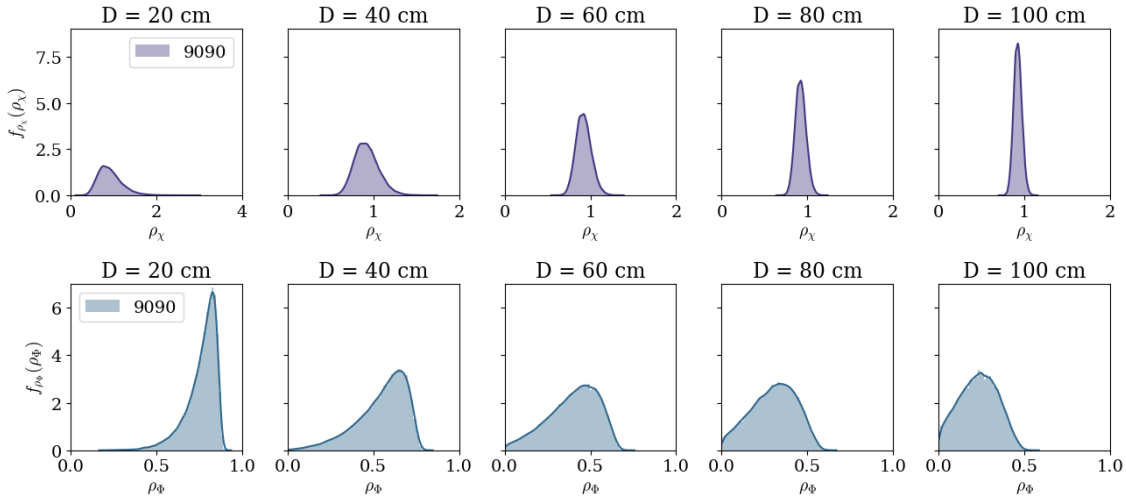

Figure 3.23: Probability density function of ρ_χ above, ρ_ϕ below, for 5 different diameters, in the MOSPAR 9090 case.

Conversely, the phase contribution to the coupling, shows to be a left-skewed distribution, becoming heavier as the diameter increases. Indeed, the ρ_Φ distribution mean decreases and its variance increases with the diameter increasing. We note, in a more subtle analysis, that the variance increases before decreasing for very large diameters.

Therefore, we conclude that we have 3 coupled flux regimes:

- the regime where the log-amplitude fluctuations are dominant and the phase contribution to the coupling is weak, when the aperture is small,
- the regime where the phase contribution to the coupling is dominant and the log-amplitude fluctuations are small, when the aperture is large
- the regime in-between, with balanced phase and log-amplitude effects.

This statistical behavior changing with the aperture size is reminiscent of the turbulence regimes depicted in the chapter 2, in section 2.3.5, depicting 3 regimes of coupling with

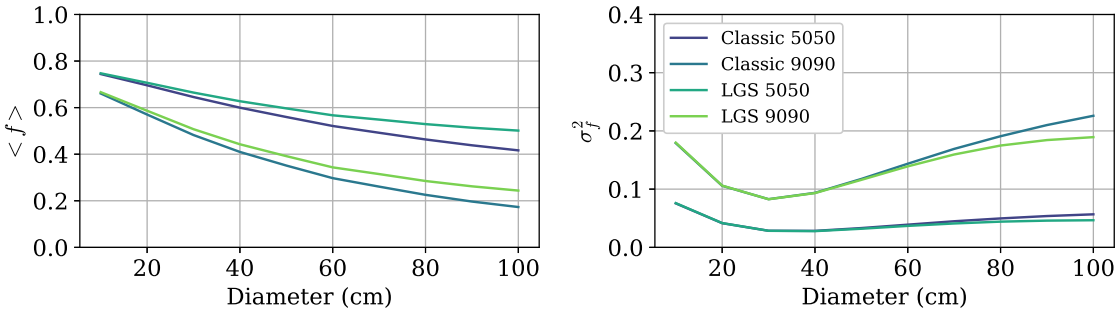

Figure 3.24: Mean coupled flux (left) and coupled flux normalized variance (right), function of the aperture diameter, for the two atmospheric conditions (MOSPAR 5050 and 9090) and the classical and LGS pre-compensation cases.

respect to the parameter ω_0/r_0 - ω_0 being the laser waist in the pupil plane, which is actually a fraction of the diameter. To make an analogy with the considered pre-compensated case, we can recognize two of the three uplink regimes depicted in section 2.3.5: the regime $\omega_0/r_0 << 1$ and the regime $\omega_0/r_0 \approx 1$, that is the beam wander regime. Some differences can although be highlighted. In the depicted uplink coupled flux regimes from section 2.3.5, there is no adaptive optics correction, and no way to distinguish the phase effect from the log-amplitude effects, as these two effects are mixed in the resulting diffraction pattern in the satellite plane. There is also a limited interest in using r_0 to delimit the regimes, as the residual phase depends more on the anisoplanatic property of the turbulence profile than on the turbulence strength. Therefore, we note that using the reciprocal approach allows to decouple the log-amplitude and phase effects, and to add the AO component in the analysis, in a more transparent way than by proceeding to the uplink analysis.

Finally, we comment on the mean coupled flux and normalized variance (sometimes called scintillation index), function of the diameter. We plot, in figure 3.24, the mean value on the left and the normalized variance on the right, for the two turbulence cases and the two pre-compensation cases. We observe that the mean value of the coupled flux decreases with the increase of the diameter, in every case. We observe that the LGS correction also provide a higher mean for both turbulence cases. Commenting on the coupled flux variance, it is shown to reach a minimum in every case for an aperture size around 30 cm. The LGS pre-compensation is also shown to slightly reduce the coupled flux variance in large apertures scenarios.

3.5.3.2 Link availability analysis

To study the telecommunication link availability, we analyze the cumulative density function of the signal, adding the static losses computed in section 2.7.3.

As we vary the diameter of the OGS, we also need to tune the geometrical losses for each diameter scenario. In figure 3.25, we plot the geometrical losses function of the aperture diameter, as well as the resulting additional link margin before turbulence attenuation, for an OOK communication at 25 Gbps for a $BER = 10^{-3}$, computed as in section 2.7.3. We observe a dynamic of almost 18 dB of geometrical losses over the diameter range from 10 cm to 1 m. Analyzing the Link margin before turbulence, we observe that the link budget for an aperture of 10 cm is negative. This means that even without turbulence, the link budget is not closed for a 10 cm emission aperture, for the given emitted power and other static losses. Above 10 cm, the link budget is closed before adding the turbulence losses, and the margin increases with the diameter.

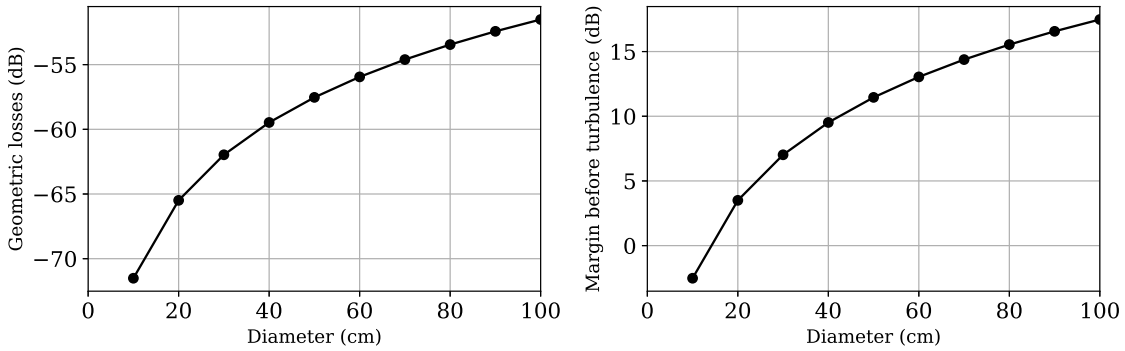

Figure 3.25: On the left: geometrical losses in dB evolution with respect to the aperture diameter. On the right: Associated link margin before turbulence, function of the aperture diameter.

In figure 3.26, we plot the value of the CDF of the normalized coupled flux for different thresholds (10^{-1}, 10^{-2}, 10^{-3}, 10^{-4}, corresponding to 90,99,99.9 and 99.99% of link availability, respectively), in the two atmospheric conditions and the two pre-compensation cases. We also plot the link margin function of the diameter. We depict two zones: above the link margin curve, where the link budget is closed, and below, where it is not. We observe, in the MOSPAR 5050 case (graphs in the first columnn) that the link budget is closed with the maximum availability rate (99.99% from the diameter 30 cm to 1 m), in the LGS case, but only with the rate 99.9% with the classical pre-compensation scheme. If considering the turbulence case, MOSPAR 9090, the link budget is closed from aperture 30 cm to 1 m, with only an availability rate of 90%, for both AO correction cases.

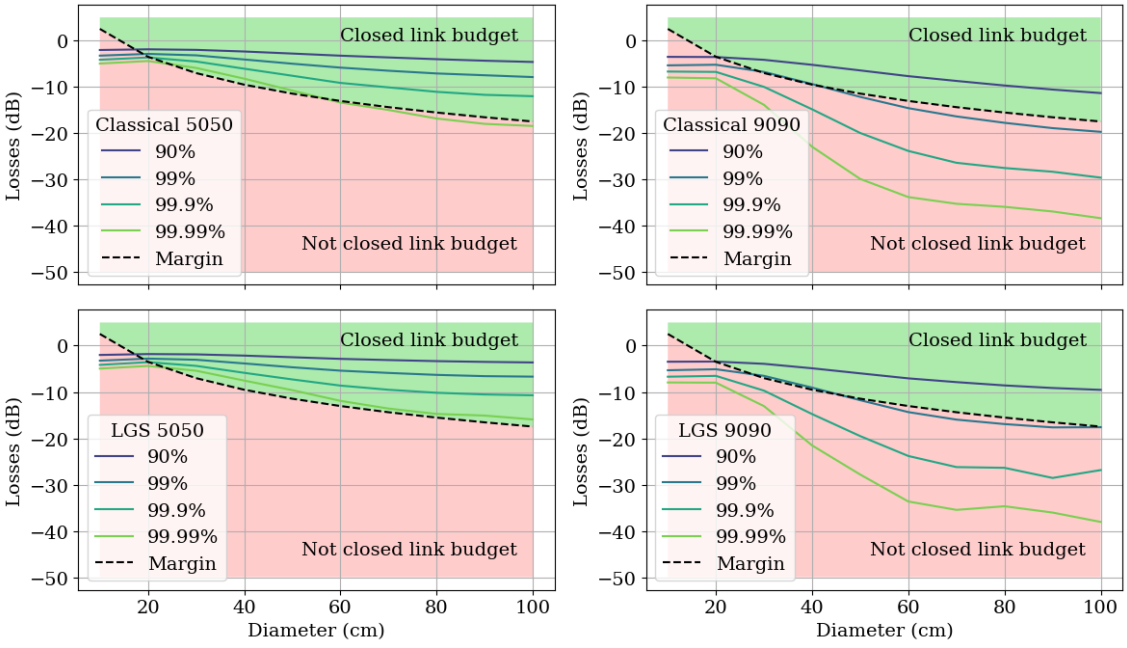

Figure 3.26: CDF at threshold versus the link margin, in the MOSPAR 5050 and 9090 turbulence case, for the classical and LGS aided pre-compensation, depicted for several availability thresholds.

We finally comment the link margin after turbulence, for the given availability thresholds 99% and 99.9%, that are depicted in figure 3.27. Again, a negative link margin means that the link budget is not closed (and is depicted in the red zone in the graph), whereas

a positive link margin indicates a closed link budget (depicted in the green zone). We plot in black the link margin in the MOSPAR 5050 case for the 2 AO corrections, and similarly, in white, the link margin in the MOSPAR 9090 case. The results obtained for the availability threshold 99% is plot on the left and 99.9% on the right. In the MOSPAR 5050 case, we observe a similar behavior for the two threshold and the 2 AO corrections, that is, an increasing link margin with the diameter. However, in the MOSPAR 9090 case, the link budget isn't closed for any case, and we can observe a maximum, that is probably related to the change of regime (between the log-amplitude and phase dominated regimes). A similar behavior is observed in the article of Conan [8].

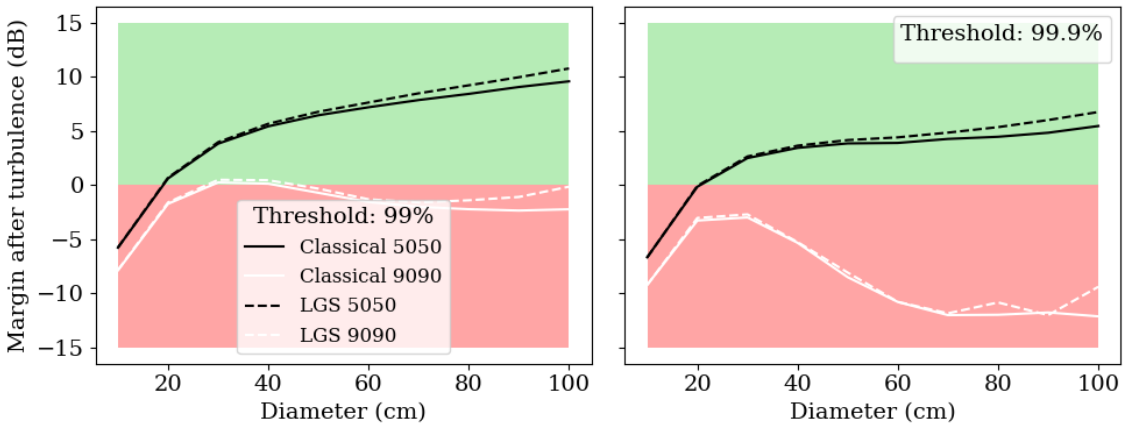

Figure 3.27: Link margin after turbulence, for the availability threshold 99% (left) and 99.9% (right), in the MOSPAR 5050 case (black), and 9090 (white), for the classical AO correction (plain lines) and LGS (dashed lines).

As a conclusion, it seems that in tough atmospheric conditions, there is an availability maximum, that also indicates a change of turbulence regime given the aperture size and AO correction. This is not especially the maximum in milder atmospheric conditions. This optimum is related to a balance between the antenna gains increasing with the diameter size, and the phase induced coupling losses that also increase with the diameter increasing. The same behavior is observed in the LGS case, as the tip and tilt phase errors are the one at the origin of the fadings.

The analysis based on the availability threshold gives a first evaluation of the performance that can be achieved on the telecommunication link, but does not replace the telecom analysis in itself (that will be conducted in chapter 7). This telecom evaluation relies as well on the temporal properties of the coupled flux, that we study in the following.

3.5.4 Temporal statistics

We study the temporal behavior of the coupled flux for three chosen diameters among the ten's: 20 cm, 60 cm and 1 m. We generated 47000 samples time-series thanks to the E2E reciprocal numerical tool, corresponding to 10 s of data.

In figure 3.28, we plot a 2 s coupled flux time-series in the MOSPAR 9090 case, for the classical pre-compensation and the LGS aided pre-compensation. Firstly, we observe a mean value decreasing with the diameter increasing, which was already observed on the statistics analysis in figure 3.24. Secondly, we observe that, as the diameter increases, the fades become deeper and longer. We also note that the fadings are less deep in the LGS case, especially for the large aperture diameters. This is explained by the residual phase high order modes that become very energetic for large aperture cases, and that only

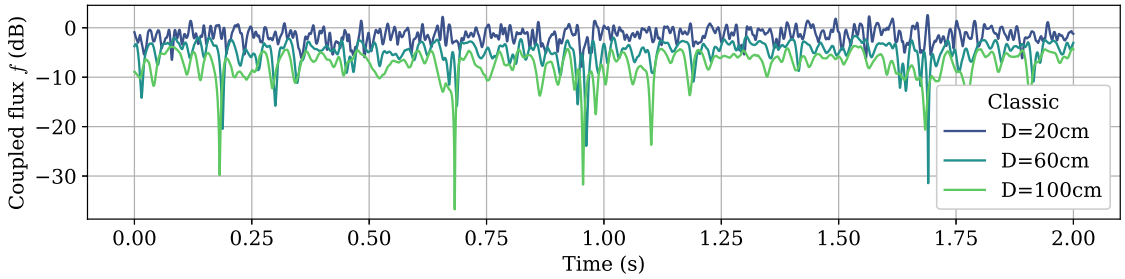

(a) Classical pre-compensation

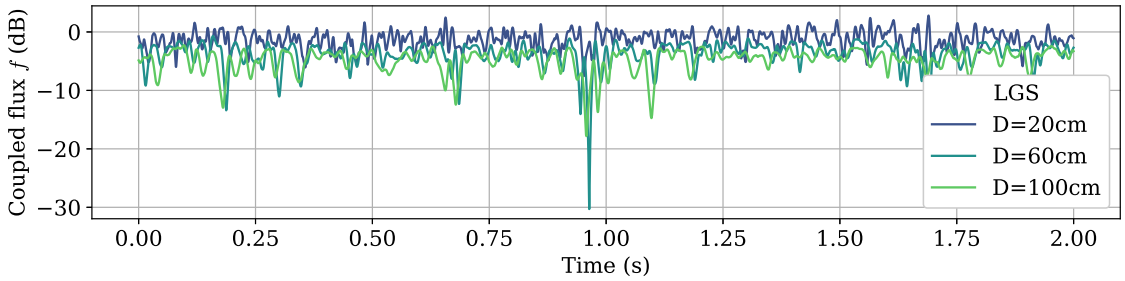

(b) LGS aided pre-compensation

Figure 3.28: 2 s time-series on the MOSPAR 9090 case for an aperture size of 20, 60 and 100 cm.

affects the classical pre-compensation case. These energetic high order modes modify the diffraction pattern shape, hence participating in worsening the fadings. To characterize the fades, we study the time-series autocorrelation functions and fade statistics.

We plot the temporal autocorrelation function (ACF) of the coupled flux function of the lag τ, on the left of figure 3.29, and the coherence time of the channel T_c function of the diameter, on the right. The coherence time corresponds to the time lag width at the ACF half maximum. On the left, we plotted the ACF for 4 different diameters and for both the classical pre-compensation (plain lines) and the LGS pre-compensation (dashed lines). We observe that the ACF width increases with the diameter, and that it is wider for the classical pre-compensation, than for the LGS based correction, except for the 20 cm case, where the two curves are confounded. In this case, the coupling is dominated by log-amplitude effects. This indicates that the phase disturbances are driving the coupling coherence time. Concerning the coherence time of the channel, we compared

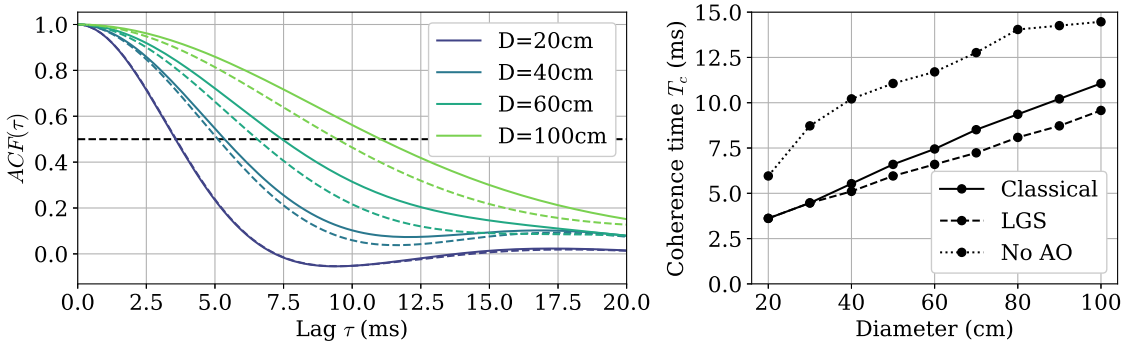

Figure 3.29: Temporal autocorrelation function of the coupled flux f (left) function of the lag τ, and the coherence time function of the diameter (right), for several aperture sizes, and for the classical and LGS AO corrections, in the MOSPAR 9090 turbulence case.

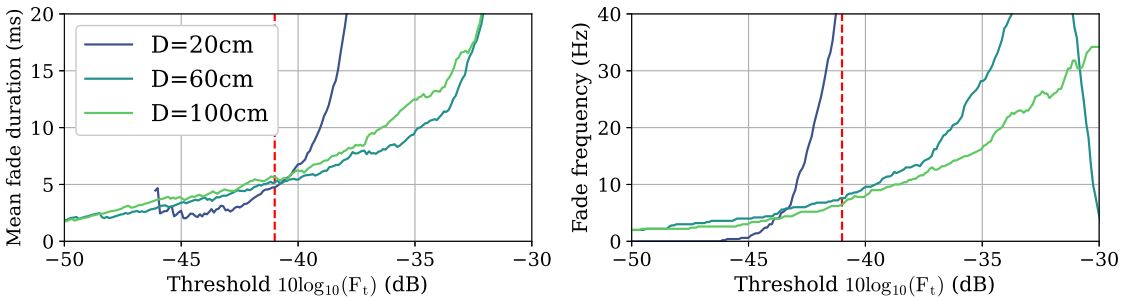

Figure 3.30: Mean fade duration (left) and fade frequency function of the coupled flux threshold (red) for the MOSPAR 9090 case and the classical AO correction.

the 2 correction cases with the uncorrected case. We observe a coherence time increasing with the aperture diameter. Additionally, we observe that, when corrected, the coherence time of the channel is linear with the diameter, and that the coherence time of the LGS corrected case is slightly below the classical corrected case.

However, the ACF is a normalized quantity that does not account for the absolute value of the fades with respect to the detection threshold, depicted in red. Therefore, we study the fade statistics, mainly the mean fade duration, with respect to a given threshold and the fade frequency. We plot in figure 3.30 the mean fade duration and the fade frequency of the coupled flux combined with the total constant losses of the link. We indicate in red the detection threshold, that is equal to -41 dBm (by inversing the relations given in section 2.7.3. We observe that the behavior of the mean fade duration for the 60 and 100 cm apertures is similar, but varies for the 20 cm case. At the detection threshold, the mean fade duration is similar for the three cases (around 6 ms), but the fade frequency differs between the 20 cm case and the 60 and 100 cm cases (more than 40 Hz compared with 10 Hz). This is explained because the detection threshold in the 20 cm case is very close to the signal mean value. Therefore, as it is normal to observe many variations around the mean, the fade frequency of the 20 cm is high.

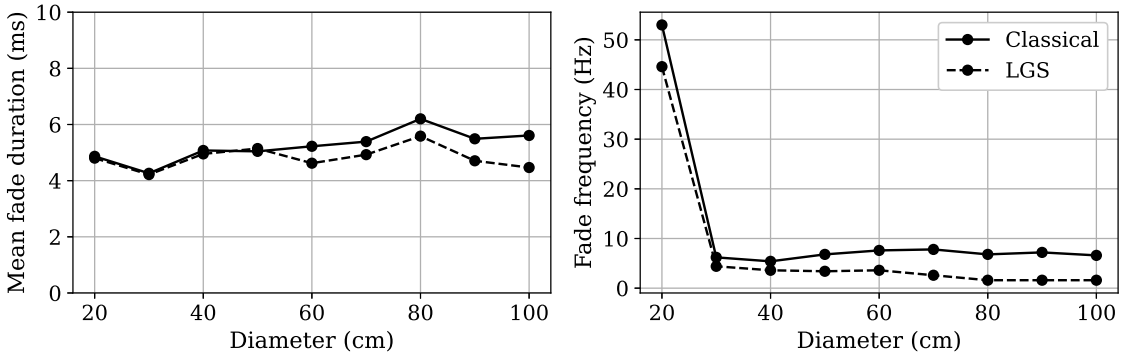

Figure 3.31: Mean fade time and fade frequency at the detection threshold function of the aperture diameter, in the MOSPAR 9090 turbulence case and the classical and LGS AO correction.

We also plot the mean fade time and the fade frequency value at the detection threshold function of the diameter in figure 3.31, for the classical and LGS based AO correction. We observe that the mean fade time is almost the same for all diameters, and almost the same for both pre-compensations, at the exception of large aperture cases whose mean fade duration benefits from the LGS correction. The fade frequency value is stable in the

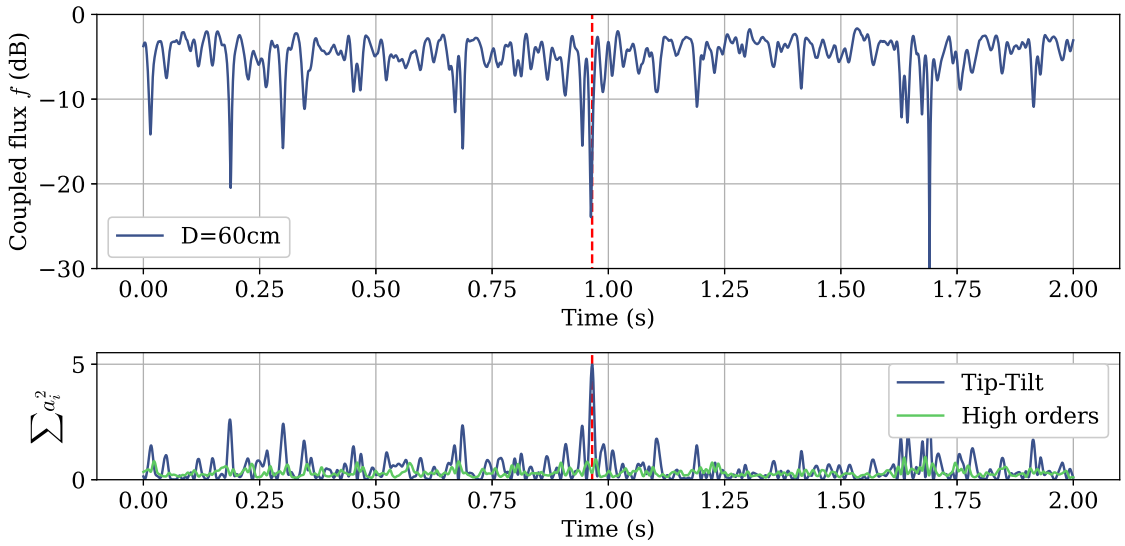

Figure 3.32: Time-series in the 60 cm aperture case (at the top) compared with the instantaneous sum of the square Zernike projections (at the bottom), separated in the sum of the low orders and high orders, in the MOSPAR 9090 turbulence case.

classical correction case starting from 30 cm, while it decreases with the aperture increasing in the LGS correction case. At 20 cm, the high fade frequency value observed was already observed in figure 3.30, and is due to the proximity of the threshold to the received power mean value. This can be explained by the correction of more energetic low order modes (above n=5), that benefits to the signal mean value, therefore reducing the depth of the fades with respect to the detection threshold.

Finally, we aim at analyzing the behavior of the fades with respect to the instantaneous phase variance residuals in figure 3.32. We plot at the top the time-series issued from the 60 cm aperture case, and at the bottom the sum of the square Zernike projections on the low orders (tip and tilt) in blue, and high orders in green. We observe that the dynamic of the square of the tip-tilt value is very high compared with the high order values, and that the tip and tilt value are highly correlated to the occurrences of deep fades.

To conclude, the coherence time of the channel is shown to increase with the diameter, however, this does not imply worst fading statistics. Indeed, the ACF is a normalized value, that does not account for the mean value of the channel. Therefore, it is shown that the fade statistics are equivalent at the detection threshold for the different aperture sizes, with an improvement brought by the LGS that participate in increasing the mean value of the signal.

3.6 Conclusion

Summary

In this chapter, we presented the phase and coupled flux reciprocity principle, and applied it to the pre-compensated ground-to-GEO optical link geometry. We demonstrated the link reciprocity in this geometry thanks to experimental data and numerical data, developing by the same occasion a numerical E2E reciprocal tool, showing interesting properties for studying the uplink coupled flux properties. Indeed, the E2E reciprocal tool reduces the computation time with respect to classical uplink E2E tools, and it provides a complex field database that can be re-used infinitely to test different AO corrections impact on the

coupled flux (ideal corrections or based on numerical AO tools in order to test dynamically AO control laws).

We used this principle to model and characterize the reciprocal phase for any phase correction linear with the measurements, in a modal formalism. We illustrated this formalism for state of the art pre-compensation techniques.

We also used the reciprocity principle to expose the principle of semi-analytical tools for the pre-compensated uplink coupled flux modeling, based on the earlier modal statistical description of the phase error. We showed the limits of the pseudo-analytical models from the literature, and improved the model, taking into account the phase diffractive effects and modal inter-correlation, showing to improve the accuracy of the model with respect to the E2E generated data.

Finally, we illustrated the capabilities of the reciprocal numerical tools (both E2E and pseudo-analytic), by characterizing the ground to GEO link corrected by state of the art AO corrections, in parametric studies. We studied the impact of the aperture diameter and of the atmospheric conditions on the phase error, coupled flux statistics and temporal statistics. It is shown that in mild atmospheric conditions, when the residual phase perturbations are limited, large aperture benefits to the link margin after application of the turbulence dynamic attenuation, improving the SNR onboard the satellite and therefore improving the link reliability, and potentially allowing to consider higher data-rates than the one considered in this first part of the thesis. However, when the turbulence conditions are tougher, the large apertures suffers from heavy phase perturbations, not allowing anymore to close the link budget with a sufficient availability rate. Using an LGS correction improves the performance due to the improvement of the average coupled flux, but does not change the fading nature of the channel. Considering the temporal properties of the channel, the coherence time is shown to increase proportionally with the diameter. Although not optimal, we choose to consider the 60 cm aperture, as we intend later to optimize the pre-compensation phase. This choice allow to take advantage of the reduced geometrical losses while limiting the complexity of the AO system (136 modes of correction), as specified in section 2.7. For this geometry, the system reliability severely decreases with the increase of the turbulence strength. This will lead us to develop new phase corrections to increase the system reliability over the wide variety of turbulence conditions that can be encountered.

Perspectives

From this work, we highlight two categories of perspectives: modeling perspectives and the perspectives related to the link performance.

Modeling perspective:

- Temporal modeling

To our knowledge, there is no model of the modal anisoplanatic phase temporal properties in the literature. Although phase temporal characterization exists in the Fourier formalism [9], developing modal temporal characterization of the phase is also of interest, as the modal characterization of the phase is more appropriate for phase modeling in small apertures (small with respect to the large apertures used in astronomy). Achieving this anisoplanatism modal temporal characterization would allow generating time-correlated series of coupled flux thanks to the pseudo-analytical formalism. Such anisoplanatic phase temporal characterization will be developed in the chapter 5.

- Analytical modeling of the coupled flux

A second perspective is to develop an analytical model of the coupled flux statistics. This would allow understanding and quantifying how the residual phase affects the coupled flux statistics. Indeed, the residual phase and the coupled flux are related by a non-linear operation, that is, the overlap integral. Approximation of this integral exists in case of low phase residual (in the case of the downlink), however, such expression does not exist yet in the case of anisoplanatic residuals. Identifying the coupled flux probability law and associated parameters would allow developing digital processing optimization algorithms. The study of this analytical development will be treated in chapter 7.

Link performance

The second family of perspectives concerns the link performance. Previously, we studied the statistics of the channel with respect to a fixed detection threshold, determined for a communication at a given data-rate and modulation scheme. It was shown, in the chosen design, to lose reliability when the turbulence strength was increasing, due to the phase contribution to the coupling, although the link margin before turbulence was increasing. In order to benefit from this increasing link margin, due to geometrical losses reducing with the diameter increasing, we will first explore methods to improve the coupled flux statistics. Therefore, in chapter 4, chapter 5 and chapter 6, we explore methods to optimize the pre-compensation phase, to reduce the coupled flux statistics and improve the link availability and margin in a wide variety of turbulence. Additionally, it was mentioned that the AO correction applied was idealized. Future work can include the plug of the AO numerical simulator after the reciprocal E2E tool, allowing for a real E2E validation of the link performance. This task and all control related aspects will not be addressed in this thesis.

The second question that can be raised, with respect to the results shown in this chapter, is: how to optimize the telecommunication system performance when the link margin is large with respect to the detection threshold ? Indeed, we've seen, for instance in the MOSPAR 5050 case, that the link margin was large of several dBs, meaning that the SNR onboard the satellite is good. A perspective therefore is to question and design more deeply the communication system to exploit this link margin, by increasing the rate or changing the modulation rate. This topic will be addressed in chapter 7.

CHAPTER 4

MMSE estimator to optimize the pre-compensation phase at point-ahead angle

Contents

Previously, we described the optical channel pre-compensated by adaptive optics and detailed the modeling tools used to study this channel under various turbulence conditions and system geometries. We also examined the performance of the optical channel suffering from anisoplanatism when classical pre-compensation or LGS-based pre-compensation is applied. We demonstrated that the required link budget to achieve high data rates was significantly degraded under moderate to severe atmospheric conditions.

In order to enhance the telecommunication performance of the link, one has two options: designing digital signal processing algorithms that increase the data rate for a given SNR or

using optical techniques to modify the channel itself. As shown in the transmission chain in Figure 4.1, the optical channel consists of two distinct blocks: the adaptive optics system and the atmospheric turbulence. Therefore, the received optical complex field, denoted as ψ_{turb}, and the associated received optical signal, y (which is a function of the coupled flux attenuation f), are affected by the combined effects of turbulence and adaptive optics correction. Turbulence conditions are beyond our control, but it is possible to optimize the adaptive optics correction to enhance the statistics of the coupled flux aboard the satellite. The latter will be the topic of the following chapter.

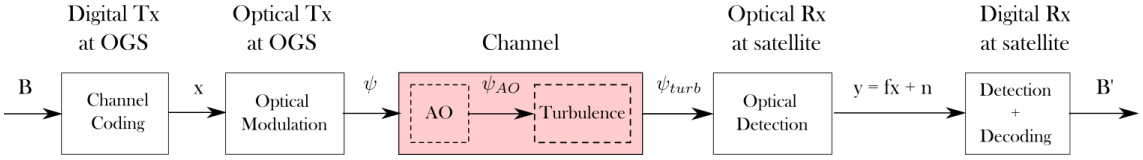

Figure 4.1: Transmission chain of the communication system, with an emphasis on the elements composing the optical channel.

In this chapter, we study a statistical technique to tailor the uplink pre-compensation phase at point-ahead angle. The results presented mainly stem from the article [4], extended to new turbulence regimes to explore the limits of the estimator. We start in section 4.1 by presenting the different state-of-the-art techniques to pre-compensate GEO-Feeder uplinks, with an emphasis on the phase estimation techniques. In section 4.2, we present the phase at point ahead angle estimator studied in this chapter that is a minimum mean square error estimator and develop the general formulas needed for its computation, for any kind of measurements. In section 4.3, we specify the measurements as the downlink phase measurements. This method was already presented in the literature in the work of Whiteley but for different geometries and angular decorrelations. Therefore, we apply this estimator to the GEO-Feeder link geometry and study the gain brought by the estimation. In section 4.4, we present the main contribution of this chapter that is the development of the estimator using the downlink phase and log-amplitude measurements and associated statistical priors. Finally, we study the robustness of the estimator to model errors in section 4.5 and its limits in section 4.6, discussing its applicability in turbulent conditions at the limit of Rytov regime and for strong angular decorrelation regimes.

4.1 State of the art

4.1.1 Optimization of the uplink pre-compensation

In the literature, several concepts were proposed in order to pre-compensate the phase at PAA distortions. We distinguish two families of methods: methods relying on the phase measurements from a downlink beacon at PAA and methods relying on the on-axis downlink phase measurements.

Methods exploiting wavefront at PAA measurements

As the pre-compensation aims at canceling the phase perturbations encountered by the uplink beam at PAA, the optimal adaptive optics correction would be obtained from measurements from a downlink beacon located at PAA, as illustrated in figure 4.2a. In this case, one would obtain downlink like adaptive optics performances as illustrated in figure 4.3 in blue and studied in Lucien Canuet's thesis [165]. In this case, the correction phase would only be degraded by the imperfections of the AO system (temporal delay of

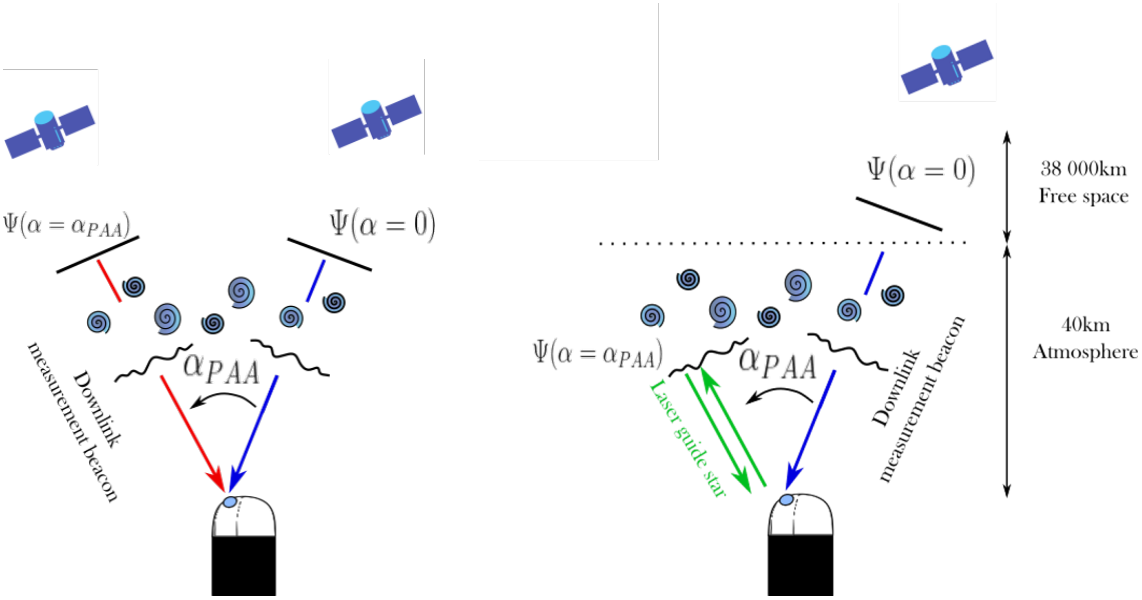

(a) Slave satellite system

(b) Laser guide star system

Figure 4.2: Illustration of systems using a measurement beacon at point-ahead angle as a reference beam for the pre-compensation.

the AO loop, fitting from the finite number of corrected modes, aliasing). To obtain such an off-axis beacon, Tyson in [166] proposed to use a slave satellite that would be located ahead from the geostationary satellite and emitting the downlink laser beam at PAA. This method, apart from being costly, requiring a payload in a second satellite to send in space, is however complex to implement and has not been demonstrated yet. For these reasons, it is preferred to bring most of the system complexity on the ground.

A second solution to obtain this beacon would be to use a laser guide star system, as mentioned in chapter 2. The principle is to excite an atmospheric layer with a laser at the proper wavelength (typically the sodium layer with 589 nm laser) in the direction of interest, and then to measure the wavefront of the back-propagated photons. However, whilst under active scientific investigation [167–170], this method does not allow yet to retrieve the tip tilt and focus [2] which are crucial modes to pre-compensate in order to improve the coupled flux statistics aboard the satellite. Further details on this issue will be given in chapter 6.2. Currently, it is envisionned to correct the tip tilt and focus of the LGS pre-compensated case with the tip tilt and focus measured from the downlink [171].

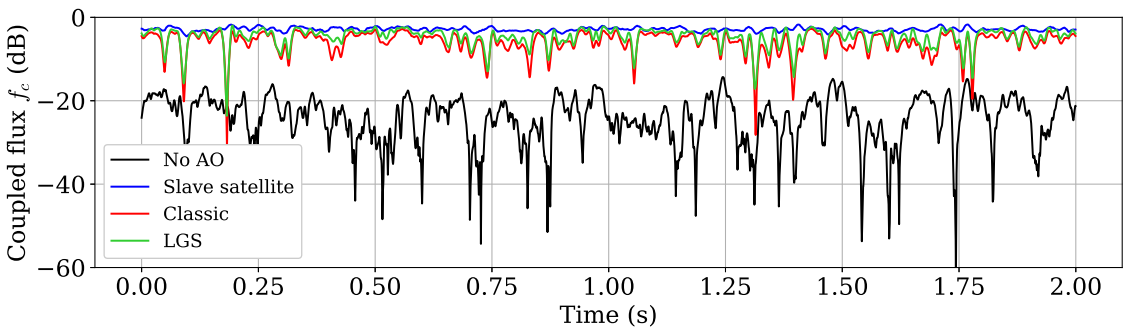

Figure 4.3: Coupled flux time-series for the benchmark pre-compensation cases, in the MOSPAR 9090 conditions, a Tx emission diameter of 60 cm and 136 AO corrected modes.

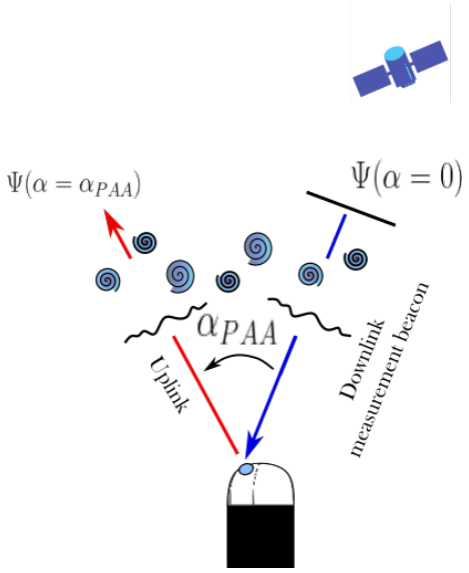

Figure 4.4: Illustration of the classical pre-compensation scheme relying on the downlink beacon measurements.

Such correction would lead to the coupled flux illustrated in green in Fig. 4.3. We can observe that the signal still experience long and deep fades. This is due to the large tip and tilt residuals that are at the origin of the beam wander effect.

Methods exploiting on-axis downlink wavefront measurements

In the absence of systems providing wavefront measurements at point-ahead angle, one can use the measurements obtained from the downlink beacon. The first option is the one described in chapter 2, using the adaptive optics correction computed from the downlink beam measurements to pre-compensate the uplink. This technique is currently the more mature, having led to several field demonstrations, on slant path experiments [89, 127, 128]. In the following, we name this technique the classical pre-compensation technique. As a simplistic description, if the isoplanatic cone is larger than the point-ahead angle, i.e., when the angular decorrelation parameter θ_0 is large, one can expect downlink like performance, as the link becomes quasi-reciprocal. However, if this isoplanatic cone is of the same order or smaller than the point ahead angle, the link reciprocity is lost and the adaptive optics correction performance is degraded. Within these regimes, the optical uplink coupled signal is severely degraded, as illustrated in figure 4.3 in red.

While not being applied to optical telecommunication links, one can find in the literature a concept aiming at reducing the anisoplanatic phase error, that is the concept of angular phase estimation proposed by [10]. The proposed method consists in estimating an off-axis wavefront using on-axis phase measurements and statistical priors. The author applies this method to astronomy, laser projection to airborne platforms and stellar interferometry. This technique would only require measurements already available at the OGS and the knowledge of the turbulence profile.

Based on Whiteley's work, we decide in this chapter to explore angular phase estimation techniques and to apply them to the telecom scenario.

4.1.2 Angular phase estimation methods in the literature

In the literature, one can find several applications requiring to estimate a wavefront off-axis from a measurement beacon. We can cite the field of astronomy where estimating an off-axis wavefront, either for adaptive optics control or for image deconvolution is at stake in order to increase the quality of large field of view images.

This angular phase estimation is usually done thanks to a minimum mean square error estimator (MMSE), as it is an optimal estimator. This estimator becomes linear when it's a priori statistics are Gaussian [172], which is the case for phase a priori. MMSE phase angular estimation have been reported using different formalism to express the phase, that can be modal [173], Fourier based [174] or zonal based [175].

Focusing on the literature using modal MMSE formalism, we report several studies in the literature performing angular phase estimation in this framework. Whiteley in his work, considered for astronomy, and interferometry, a general angular phase estimation formalism [176] to tackle both tip-tilt [177] and multimode [10] AO phase angular estimation relying on phase measurements and priors. We can also report developments in the wide field AO domain using multiple LGS and NGS measurements to estimate off-axis phase of one or multiple objects [173, 178].

We also can find this estimation formalism in the field of temporal phase estimation and predictive control, in order to correct for the temporal error induced by the AO loop delay. This temporal estimation is used to relax the loop frequency in the astronomy domain, but also in the domains implying objects or satellites tracking (both for observation and optical communication). It is shown, in the case of satellite tracking, that such temporal phase estimation approach using several past measurements improve significantly the AO performance [179].

Finally, both angular and temporal phase estimation have been implanted in AO control loops, using control algorithm such as LQG techniques, computing the a priori data-based or model-based. Such AO implantation and priors identification is a topic out of the scope of this thesis.

In this chapter, we will focus on a linear MMSE phase estimation expressed in Zernike modal formalism. We will first develop the general expression of this estimator, for any measurements, before specifying the measurements to downlink on-axis phase measurements, which was the approach of Whiteley. However, the gain on this first method has never been studied for the telecom geometry case. Therefore, we propose to perform this study and to extend this method to other physical quantities that can be sensed from the downlink.

4.2 MMSE phase estimator general formalism

Through this work, we study a modal linear MMSE estimator of the phase at point-ahead angle aided by different measurement vectors. In this aim, we develop in section 4.2.1 the error criterion that we will minimize and give in section 4.2.2 a general formalism for the analytical estimator before specifying the measurement vector in the following sections.

4.2.1 General phase error definition

As described in section 3.3, we define the pre-compensation phase error as the reciprocal phase at PAA corrected by a phase that is linear with measurements, denoted $\mathbf{y}_m$. We recall the expression of this phase error:

$$\boldsymbol{\Phi}_{\mathbf{AO,res}} \triangleq \boldsymbol{\Phi}_{\mathbf{AO,PAA}} - \mathbf{R}\mathbf{y}_{\mathrm{m}}, \tag{4.1}$$

where $\boldsymbol{\Phi}_{\mathbf{AO,PAA}}$ is the modal vector of the phase at point-ahead angle we intend to correct, $\mathbf{R}$ is a general linear operator and $\mathbf{y}_m$ is a measurement vector expressed as well in the modal formalism.

We also recall the general phase error covariance matrix on the subset of AO corrected modes, which is expressed as:

$$\boldsymbol{\Gamma}_{\mathbf{AO,res}} = \boldsymbol{\Gamma}_{\Phi\Phi}(0) - \mathbf{R}\boldsymbol{\Gamma}_{\Phi\mathrm{y_m}}(\alpha_{\mathrm{PAA}})^{\mathrm{T}} - \boldsymbol{\Gamma}_{\Phi\mathrm{y_m}}(\alpha_{\mathrm{PAA}})\mathbf{R}^{\mathrm{T}} + \mathbf{R}\boldsymbol{\Gamma}_{\mathrm{y_m y_m}}(0)\mathbf{R}^{\mathrm{T}}. \tag{4.2}$$

Finally, we recall the metrics to evaluate the pre-compensation performance, that are the overall mean square error (MSE) and the modal MSE:

$$\mathrm{MSE} = \mathrm{tr}[\boldsymbol{\Gamma}_{\mathbf{res}}] \quad \text{and} \quad \mathrm{MSE_i} = (\boldsymbol{\Gamma}_{\mathbf{res}})_{\mathrm{i,i}}, \tag{4.3}$$

where tr is the trace operator and i the i^{th} Zernike mode index.

Previously, in chapter 3, $\mathbf{R}$ was defined as the identity to compute the classical pre-compensation. In this chapter, we aim at optimizing $\mathbf{R}$ given specific measurements in order to minimize the pre-compensation phase error.

4.2.2 General MMSE reconstructor

Here, we aim to optimize the AO correction phase $\hat{\boldsymbol{\Phi}}_{\mathbf{AO,PAA}}$ and compute the associated residual phase covariance matrix $\boldsymbol{\Gamma}_{\mathrm{AO,res}}$. To this end, we use a minimum mean square error (MMSE) method [172] to minimize the residual phase variance. For normal distributed random vectors, the estimator is linear, and the reconstructor $\mathbf{R}$ is given by:

$$\mathbf{R}_{\mathrm{MMSE}} \triangleq \mathrm{argmin}_{\mathbf{R}}\mathrm{tr}(\boldsymbol{\Gamma}_{\mathrm{AO,res}}) = \boldsymbol{\Gamma}_{\Phi\mathrm{y_m}}(\alpha_{\mathrm{PAA}})\boldsymbol{\Gamma}_{\mathrm{y_m y_m}}(0)^{-1} \tag{4.4}$$

and the theoretical associated covariance matrix is, applying Eq. 4.2 and Eq. 4.4:

$$\boldsymbol{\Gamma}_{\mathrm{AO,res-MMSE}} = \boldsymbol{\Gamma}_{\Phi\Phi}(0) - \mathbf{R}_{\mathrm{MMSE}}\boldsymbol{\Gamma}_{\Phi\mathrm{y_m}}(\alpha_{\mathrm{PAA}})^{\mathrm{T}}. \tag{4.5}$$

In the above developments, the statistical priors correspond to the knowledge of the covariance matrices $\boldsymbol{\Gamma}_{\Phi\mathrm{y_m}}(\alpha_{\mathrm{PAA}})$ and $\boldsymbol{\Gamma}_{\mathrm{y_m y_m}}(0)$.

In the following, we will specify different measurement vectors and the associated covariance matrix coefficients in order to compute the reconstructor.

4.3 Prediction at PAA using on-axis phase measurements and priors

We study the modal MMSE phase estimator based on phase measurements and priors depicted by Whiteley [180] to estimate the phase at PAA, this time in the telecom scenario. To define this estimator, we first define the general phase error before developing the estimator.

4.3.1 Theoretical estimator

The MMSE estimation has been introduced in [180] for astronomical applications and was based on a phase measurement:

$$\mathbf{y}_{\mathrm{m}} = [\Phi_0], \tag{4.6}$$

where $\Phi_0 \in \mathbb{R}^{\mathrm{N_{AO}}-1}$ are the on-axis phase measurements expressed in the Zernike modal form. We suppose that the measurement vector is noiseless. By taking this hypothesis, the residual phase error will be a lower bound of the performance we can expect on a real system.

We compute the MMSE estimator $\mathbf{R}_{\mathrm{MMSE}_\Phi}$ as in Eq. 4.4. The two covariance matrices of the estimator can be developed as the matrices below:

$$\mathbf{\Gamma}_{\Phi \mathrm{y_m}}(\alpha_{\mathrm{PAA}}) = \mathbf{\Gamma}_{\Phi\Phi}(\alpha_{\mathrm{PAA}}) \tag{4.7}$$

and,

$$\mathbf{\Gamma}_{\mathrm{y_m y_m}}(0) = \mathbf{\Gamma}_{\Phi\Phi}(0) \tag{4.8}$$

By applying Eq. 4.5, its residual phase covariance matrix is then:

$$\mathbf{\Gamma}_{\mathrm{AO,res-MMSE}_\Phi} = \mathbf{\Gamma}_{\Phi\Phi}(0) - \mathbf{R}_{\mathrm{MMSE},\Phi}\mathbf{\Gamma}_{\Phi\Phi}(\alpha_{\mathrm{PAA}})^{\mathrm{T}}. \tag{4.9}$$

where $\mathbf{\Gamma}_{\Phi\Phi}(\alpha)$ is the phase angular covariance matrix. The analytical expression of the terms of this matrix can be found in the work of Chassat [120], added to the Fresnel term, as detailed in section 3.3.3. The analytical covariance matrices are depicted in Fig. 4.5. We plot the autocovariance of the phase, the phase angular covariance and the two error covariance matrices with or without phase estimation. We note that numerous inter-correlations are excited for every covariance matrix depicted.

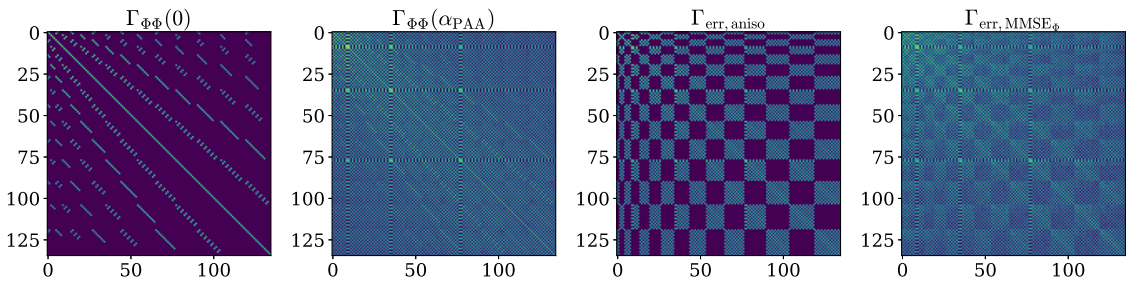

Figure 4.5: From the left to the right: Autocovariance of the phase, angular covariance matrix of the phase, error covariance matrix for the classical pre-compensation case, error covariance matrix for the $MMSE_\Phi$ estimated case.

4.3.2 Residual phase error analysis

Estimator performance

We analyze and compare the residual phase variance given by the classical pre-compensation from section 4.2.1 and the MMSE phase from section 4.3.1 (MMSE_Φ) methods on the strong turbulence case MOSPAR 9090 with an outer scale of 5.12 m. In Fig. 4.6, we plot the modal MSE, i.e., the modal residual phase variance on the AO subset as a function of the mode order. We can see that the MMSE_Φ brings negligible improvement compared to the classical method which suffers from the anisoplanatism error on all the modes with a total MSE of 0.78 rad² in the classical case and 0.77 rad² in the case of the phase estimated with the MMSE_Φ method.

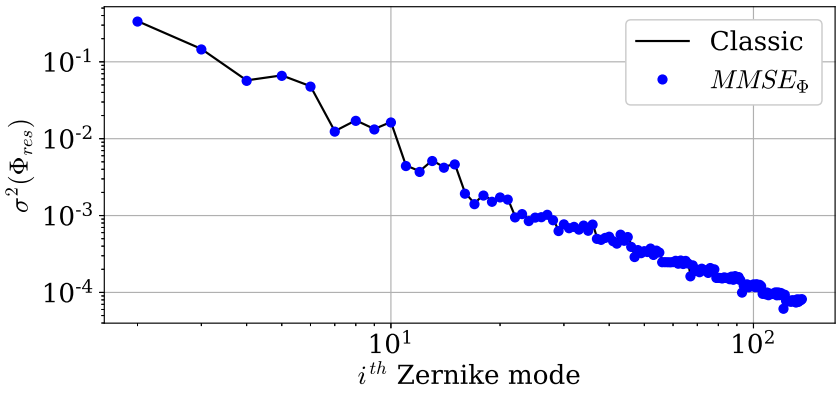

Figure 4.6: Modal residual phase variance for the MOSPAR 9090 turbulence case at 30° elevation and a point-ahead angle of 18.5µrad.

Performance in variable geometry

To understand why there is no gain in the telecom scenario, we explore the estimator performance for different system geometries that can be analog to the one studied in the Whiteley article. In particular, we study the gain for larger point ahead angles and for different telescope diameters. Figure 4.7 depicts the performance for a PAA from 5 to 150 µrad. The absolute value of the total residual phase variance function on the angle is shown on the left, the reduction percentage function of the angle in the center and the modal reduction function of the Zernike mode for extreme cases. We observe that the

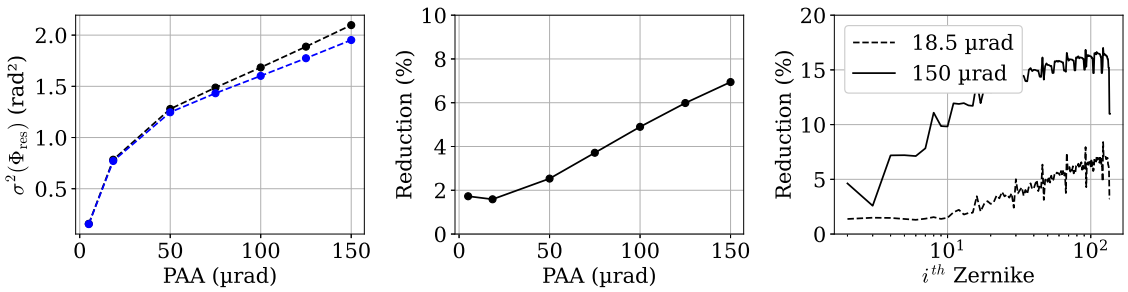

Figure 4.7: Left: residual phase variance function of the point ahead angle for the classical case in black and the $MMSE_\Phi$ case in blue. Center: residual phase variance reduction function of the point-ahead angle. Right: Modal reduction for two angular cases. All the results are computed for the MOSPAR 9090 turbulence case and diameter of 60 cm.

phase only estimator brings gain when the point-ahead angle becomes large. Still, the total reduction percentage at 150 µrad is only equal to 7%, and the residual phase variance absolute is very large (>1rad²). This reduction rate of the mode i is defined as:

$$\text{Reduction}_\text{i} = \frac{\sigma_\text{i}^2(\Phi_{\text{res,classic}}) - \sigma_\text{i}^2(\Phi_{\text{res,MMSE}})}{\sigma_\text{i}^2(\Phi_{\text{res,classic}})}(\%) \tag{4.10}$$

We observe moreover that the gain arises on the high order modes, hence not benefiting in the tip tilt reduction.

We study as well the behavior with respect to the diameter of the telescope. We study the gain of the estimator for systems with a diameter from 10 cm to 1 m, as the case in astronomy concerns mostly the 1 m+ diameters. The point-ahead angle is fixed to 18.5 µrad. Figure 4.8 depicts on the left the absolute residual phase variance for the classical pre-compensation case and the phase estimation method in function of the diameter, at the center the percentage of reduction of the total residual phase variance function of the diameter and on the right the modal reduction for three extreme cases (10 cm, 60 cm and 100 cm diameter). We observe that the bigger gains occurs for small diameters, as well as for the high order modes.

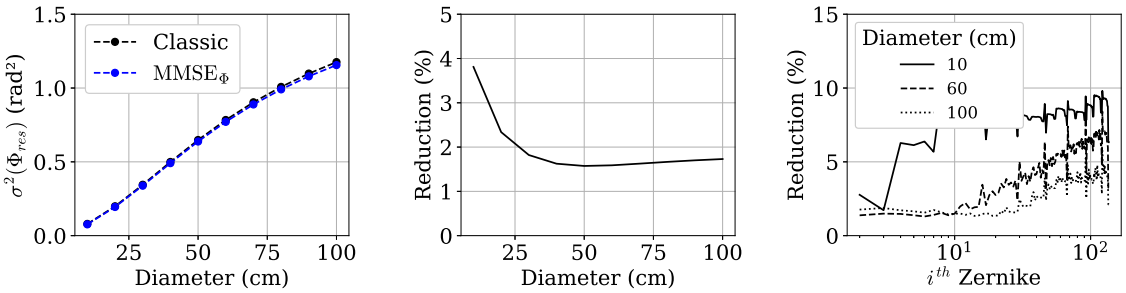

Figure 4.8: Left: residual phase variance function of the ground aperture diameter for the classical case in black and the $MMSE_\Phi$ case in blue. Center: residual phase variance reduction function of the ground aperture diameter. Right: Modal reduction for three ground aperture diameters. All the results are computed for the MOSPAR 9090 turbulence case and diameter of 60 cm.Residual phase varance function

We have observed that the phase estimator brings gain in two specific cases: small aperture diameter and large PAA, when the two beam footprints are significantly separated close to the ground, where turbulence is the strongest. We interpret this gain, which is brought by phase priors, as a consequence of phase information not allowing for the discrimination of the perturbation's height. Consequently, it is dominated by the phase perturbation occurring near the ground. In geometries with rather small PAA, the two beam footprints are almost identical at ground level, resulting in the estimator not providing any gain. However, it starts to bring greater gain when these footprints begin to separate at close to the ground.

To conclude, we proved that the modal MMSE estimator proposed by Whiteley relying on on-axis phase measurements and statistical priors doesn't bring improvement in the telecom scenario geometry. In the following, we will incorporate new measurements available at the optical ground station in the measurement vector in order to improve the phase estimation.

4.4 Prediction at PAA using on-axis Phase and Log-Amplitude measurements and priors

We propose an MMSE estimator based on a measurement of the phase and the log-amplitude and the associated statistical priors. Indeed, the log-amplitude of the complex field still carry information about perturbations occurring in the atmosphere upper layers, where the downlink and uplink beam footprints are the more separated. Adding the log-amplitude information to the phase estimation should thus bring information about the phase perturbations at the origin of anisoplanatism.

4.4.1 Theoretical estimator

4.4.1.1 Covariance matrices specifications

We define the new measurement vector as the following block matrix:

$$\mathbf{y}_{\mathrm{m}} = \begin{bmatrix} \Phi_0^{\mathrm{T}} & \boldsymbol{\chi}_0^{\mathrm{T}} \end{bmatrix}^{\mathrm{T}}, \tag{4.11}$$

where $\mathbf{y}_{\mathrm{m}} \in \mathbb{R}^{2\mathrm{N_{AO}}-1}$. We compute the MMSE estimator $\mathbf{R}_{\mathrm{MMSE}_{\Phi\chi}}$ as in Eq. 4.4. We recall that the phase is expressed in the Zernike modal formalism. Additionally, we express the log-amplitude χ_0 in the Zernike modal formalism. While this is less common, it has already been done in the work of Mahé [70]. Therefore, we denote the log-amplitude vector as:

$$\chi_0^T = \left(b_1, ..., b_{N_{AO}}\right) \tag{4.12}$$

The two covariance matrices of the estimator can be developed as the block matrices below:

$$\boldsymbol{\Gamma}_{\Phi\mathrm{y_m}}(\alpha_{\mathrm{PAA}}) = \begin{bmatrix} \boldsymbol{\Gamma}_{\Phi\Phi}(\alpha_{\mathrm{PAA}}) & \boldsymbol{\Gamma}_{\Phi\chi}(\alpha_{\mathrm{PAA}}) \end{bmatrix} \tag{4.13}$$

and,

$$\boldsymbol{\Gamma}_{\mathrm{y_m y_m}}(0) = \begin{bmatrix} \boldsymbol{\Gamma}_{\Phi\Phi}(0) & \boldsymbol{\Gamma}_{\Phi\chi}(0) \\ \boldsymbol{\Gamma}_{\Phi\chi}(0)^{\mathrm{T}} & \boldsymbol{\Gamma}_{\chi\chi}(0) \end{bmatrix}. \tag{4.14}$$

As in Eq. 4.5, the theoretical associated covariance matrix in this case can be given by:

$$\boldsymbol{\Gamma}_{\mathrm{AO,res-MMSE}_{\Phi\chi}} = \boldsymbol{\Gamma}_{\Phi\Phi}(0) - \mathbf{R}_{\mathrm{MMSE}_{\Phi\chi}} \boldsymbol{\Gamma}_{\Phi\mathrm{y_m}}(\alpha_{\mathrm{PAA}})^{\mathrm{T}}. \tag{4.15}$$

4.4.1.2 Analytical terms of the covariance matrices

The phase and the log-amplitude of the two fields are expressed as vectors in the modal formalism, we can therefore define the angular covariance matrices in the telescope pupil under the following notations:

$$\boldsymbol{\Gamma}_{\Phi\Phi}(\alpha_{\mathrm{PAA}}) \triangleq \left(\mathbb{E}[\mathrm{a_i^0 a_j^{\alpha_{PAA}}}] - \mathbb{E}[\mathrm{a_i^0}]\mathbb{E}[\mathrm{a_j^{\alpha_{PAA}}}]\right)_{2\leq \mathrm{i,j} \leq \mathrm{N_{AO}}} \tag{4.16}$$

$$\boldsymbol{\Gamma}_{\chi\chi}(\alpha_{\mathrm{PAA}}) \triangleq \left(\mathbb{E}[\mathrm{b_i^0 b_j^{\alpha_{PAA}}}] - \mathbb{E}[\mathrm{b_i^0}]\mathbb{E}[\mathrm{b_j^{\alpha_{PAA}}}]\right)_{1\leq \mathrm{i,j} \leq \mathrm{N_{AO}}} \tag{4.17}$$

$$\boldsymbol{\Gamma}_{\Phi\chi}(\alpha_{\mathrm{PAA}}) \triangleq \left(\mathbb{E}[\mathrm{a_i^0 b_j^{\alpha_{PAA}}}] - \mathbb{E}[\mathrm{a_i^0}]\mathbb{E}[\mathrm{b_j^{\alpha_{PAA}}}]\right)_{2\leq \mathrm{i} \leq \mathrm{N_{AO}}, 1\leq \mathrm{j} \leq \mathrm{N_{AO}}} \tag{4.18}$$

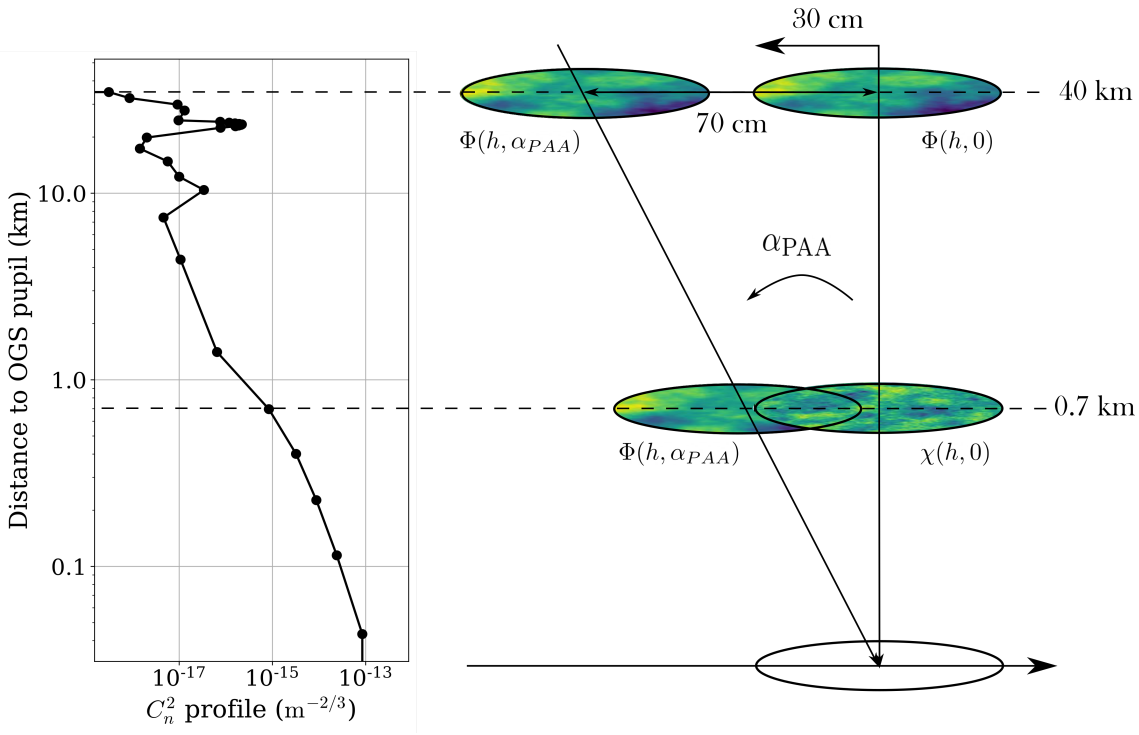

Figure 4.9: Illustration of the beam footprint phase and log-amplitude patterns for different heights, with the C_n^2 weight associated, for a ground aperture of 60 cm.

Let's note that all phase Zernike coefficient distributions are by definition centered, whereas this is not the case for the distribution of the first Zernike coefficient of the log-amplitude, b_1 which mean is equal to the variance of the log-amplitude averaged by the pupil. In the following, we assume knowing $\mathbb{E}[b_1^\alpha]$ from past measurements, allowing to substract the mean of b_1 so as to obtain a centered measurement vector.

We developed the modal phase angular covariance matrix in section 3.3.3. Similarly, the log-amplitude covariance matrix ($\Delta\alpha = 0$) was derived in [96]. We extend and generalize these formulas to derive the angular covariance matrices between the three combinations of phase and log-amplitude. We assume in the following developments to be in the weak perturbations' regime. We only consider the case of beams co-located in the same telescope aperture, as depicted in Fig. 4.9. We denote the matrix coefficients as $(x, y) \in \{(a, a), (a, b), (b, b)\}$:

$$\begin{aligned}\mathbb{E}[x_i^0 y_j^{\alpha_{PAA}}] - \mathbb{E}[x_i^0]\mathbb{E}[y_j^{\alpha_{PAA}}] =& 5.20 K_{ij} \int_0^L dz C_n^2(z) \int_0^{+\infty} dk k^{\frac{-14}{3}} \\ & J_{n_i+1}(k) J_{n_j+1}(k) F_{xy}\left(\frac{zk^2}{2k_0 R_{tel}^2}\right)\left(1 + \frac{2\pi R_{tel}}{L_0 k}^2\right)^{\frac{-11}{6}} \cdot \\ & \left(S1 \cdot J_{m_1+m_2}\left(\frac{kd(z, \Delta\alpha)}{R_{tel}}\right) + S2 \cdot J_{|m_1-m_2|}\left(\frac{kd(z, \Delta\alpha)}{R_{tel}}\right)\right) \quad (4.19)\end{aligned}$$

where we recall the parameters: $(n_i, m_i), (n_j, m_j)$ are the radial and azimuthal degrees of the i^{th} and j^{th} Zernike polynomials respectively, z is the distance to the OGS pupil on the line of sight, R_{tel} is the aperture radius and $k_0 = \frac{2\pi}{\lambda}$ is the wave number. K_{ij} is defined as:

$$K_{ij} = \sqrt{(n_i + 1)(n_j + 1)}(-1)^{\frac{n_i + n_j - m_i - m_j}{2}} R_{tel}^{\frac{5}{3}} k_0^2, \quad (4.20)$$

$C_n^2(z)$ is the turbulence refractive index structure function at the distance to the pupil

z, $J_n(k)$ are the Bessel functions of the first kind of order n. F_{xy} is the Fresnel term discriminating the physical quantities:

$$\begin{aligned} F_{xy} : k \mapsto \cos^2(k) \quad &\text{for (x,y) = (a,a), corresponding to } \mathbf{\Gamma}_{\Phi\Phi}(\Delta\alpha) \\ F_{xy} : k \mapsto \sin^2(k) \quad &\text{for (x,y) = (b,b), corresponding to } \mathbf{\Gamma}_{\chi\chi}(\Delta\alpha) \\ F_{xy} : k \mapsto \sin(k)\cos(k) \quad &\text{for (x,y) = (a,b), corresponding to } \mathbf{\Gamma}_{\Phi\chi}(\Delta\alpha) \end{aligned} , \tag{4.21}$$

where $k = 2\pi f$ is the angular frequency. We recall that we showed in chapter 3 that it was essential to acocunt for the Fresnel term, including for the phase, in order to accurately model the phase behavior. Moreover, $(1 + \frac{2\pi R_{tel}}{L_0 k}^2)^{\frac{-11}{6}}$ is the Von Karman term accounting for the turbulence outer scale L_0. The last part of the equation is the contribution of the angular correlation between the two beam footprints at a given height distant from:

$$d(z, \Delta\alpha) = \Delta\alpha \cdot z, \tag{4.22}$$

where $\Delta\alpha$ is an oriented angle. S1 and S2 are the geometrical coefficients depicting the relative orientation of the beam footprints that are described in section 3.3, in table 3.1 and table 3.2.

We propose an illustration of the beam footprints geometry in figure 4.9. We represent the on-axis beam footprint for different heights (either the phase at 40 km or the log-amplitude at 0.7 km for illustration stake), and the off-axis beam footprint. We can interpret the proposed formula of the summation of the different beam footprints spatial covariances (expressed in modal formalism), weighted by the C_n^2 profile value for a given height.

4.4.2 Performance of the estimator

4.4.2.1 Phase error reduction

To evaluate the estimator gain, we compute the associated modal phase error $\sigma^2(\Phi_{res}$ described in Eq. 3.32, both theoretical and from E2E data.

Figure 4.10a depicts the modal residual phase variance for the classical case in black, being equal to the full anisoplanatic error, compared with the $MMSE_{\Phi\chi}$ estimated case in red. We compare the theoretical phase variances (plain lines) with the variances computed from data (dots). Figure 4.10b depicts the phase variance modal reduction in the theoretical case (plain line) and the reduction computed from the E2E data (dots). Firstly,

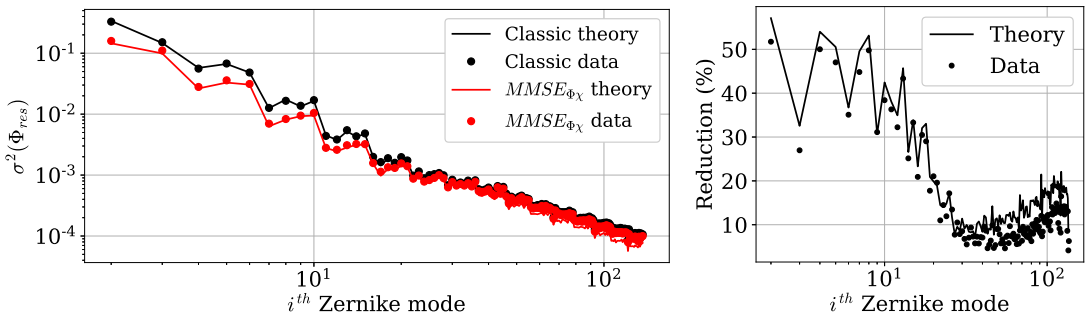

(a) (b)

Figure 4.10: On the left, modal residual phase variance function of the mode number for the classical pre-compensation and the $MMSE_{\Phi\chi}$ estimation method, computed theoretically and from data for the MOSPAR 9090 turbulence case. On the right, modal reduction function of the mode.

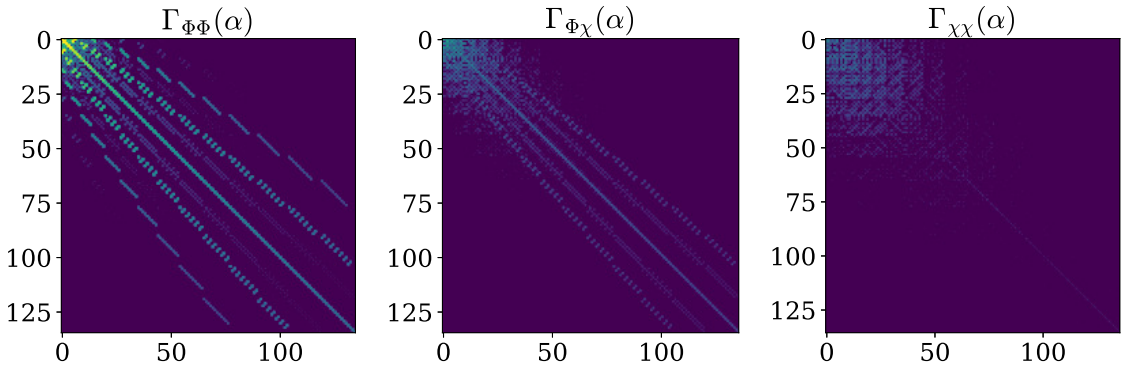

Figure 4.11: Angular covariance matrices between (from the left to the right): the phase on-axis and the phase at PAA, the log-amplitude on-axis and the phase at PAA, the log-amplitude on-axis and the log-amplitude at PAA.

we observe on both figures a good match between the theoretical error and the error computed from the data. Secondly, the phase variance is decreased in the estimated case with a total residual phase variance of 0.41 rad^2 compared with 0.78 rad^2 in the classical case. The estimator is also shown to particularly decrease the low order mode residual phase variances, decreasing the tip by more than 50% of its initial value, the tilt by 30% and the focus by 50%. This is of particular interest as the beam wander induced by the tip and tilt error is at the origin of the deeper fades, as shown in chapter 3, in section 3.5, when analyzing the LGS case performance.

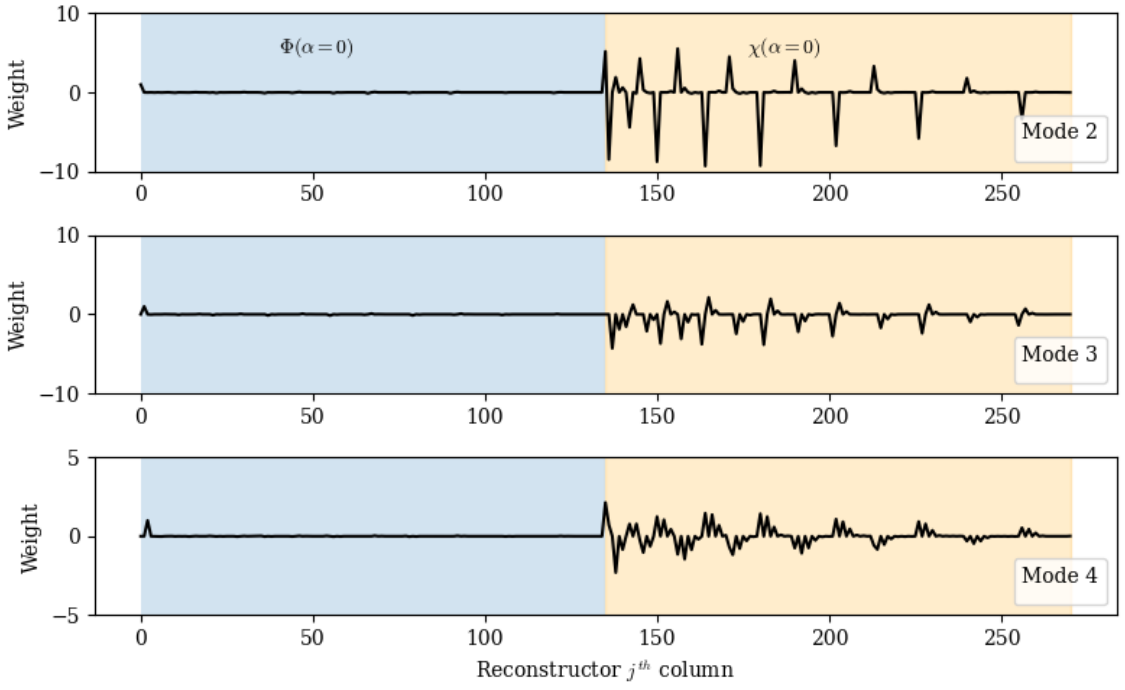

Figure 4.12: Three first rows of the reconstructor matrix, corresponding to the weight applied on the j^{th} component of the measurement vector to correct the i^{th} mode at point ahead angle.

We explain this gain by the fact that the addition of the log-amplitude to the measurement vector brings information on the perturbations occurring on the upper layer, where the anisoplanatism is generated. From the analysis of the covariance matrices that we de-

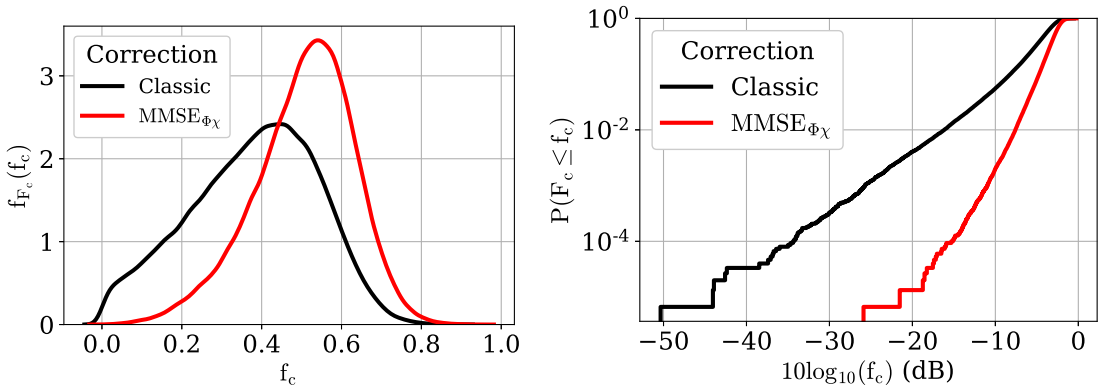

(a) (b)

Figure 4.13: Coupled flux statistics for MOSPAR 9090 at 30° elevation, D=60 cm and L0=20m. The two correction cases are depicted: classic in black, MMSE$_{\Phi\chi}$ in red.

pict in figure 4.11, although the cross-covariance matrix between the phase at point ahead angle and the log-amplitude on-axis shows weaker correlations than the phase angular covariances, it shows that the log-amplitude brings additional information to the estimation that is correlated to the quantity of interest.

To identify the source of information, we plot the three first rows of the reconstructor in figure 4.12, showing what are the modes from the measurement vector bringing information on the tip tilt and focus. Indeed, these plots corresponds to the weight that is applied to the j^{th} element of the measurement vector for the tip tilt and focus correction. We observe that the contribution is mainly provided by the log-amplitude measurement in every case.

4.4.2.2 Impact on the telecom performance

Statistical analysis

In this part, we evaluate the estimator impact on the statistics of the reciprocal coupled flux by computing 150 000 samples thanks to the pseudo-analytical model described in section 3.4, in order to obtain statistical representativity. In Fig. 4.13a, we plot the probability density function (PDF) of the coupled flux $f_{F_c}(f_c)$ function of f_c. We observe a higher mean, 0.5 compared with 0.37 in the MMSE case and classical case, respectively, and a decreased variance of the PDF (0.06 compared with 0.17 scintillation index). We also observe that the tail of the distribution is thinner, meaning that deep fades are less likely to occur. The behavior of the tail is also illustrated on the cumulative density function (CDF) plotted in Fig. 4.13b function of the threshold in dBs. We observe a gain at probability 10^{-3} of 13 dBs as well as an increased slope of the CDF, meaning that deep fades are less likely to occur.

Temporal analysis

To analyze the estimator effect on the temporal characteristics of the coupled flux, we use the E2E simulator depicted in section 3.2. We computed a 10 s time-series by using 5 different seeds, that is plotted in Fig. 4.14. We can observe that the MMSE$_{\Phi\chi}$ method allows to decrease the number, depth, and duration of fade. A deeper analysis of the estimator impact on the fading statistics is given in figure 4.16 and discussed later in this paragraph.

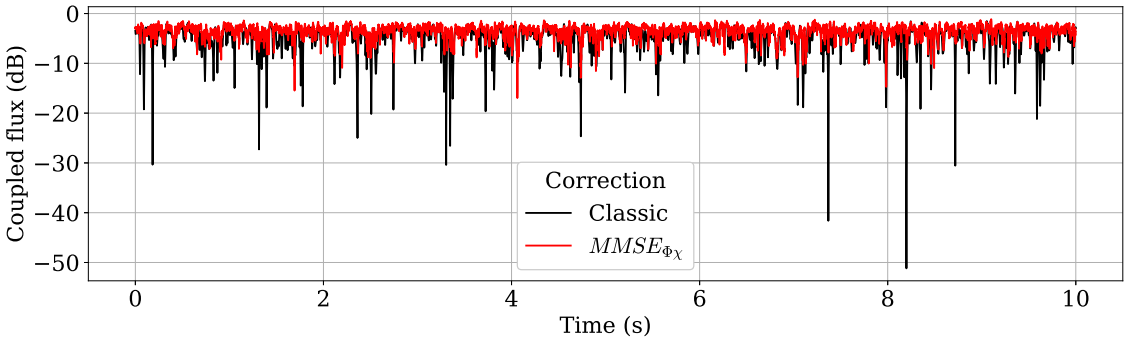

Figure 4.14: Time-series for the classical pre-compensated case and the $MMSE_{\Phi\chi}$ estimated case for the MOSPAR 9090 turbulence conditions.

Additionally, we analyze the temporal auto-correlation of the time-series in Fig. 4.15. We can observe that the $\text{MMSE}_{\Phi\chi}$ method allows to decrease the width of the temporal autocorrelation function, meaning that the coherence time of the signal is decreased. As we define the coherence time as the half width value of the autocorrelation function, this means that the coherence time is decreased. This is desirable as a shorter coherence time allows designing shorter interleavers. Especially, we note that the coherence time at mid-height decreases from 7.9 ms to 6 ms.

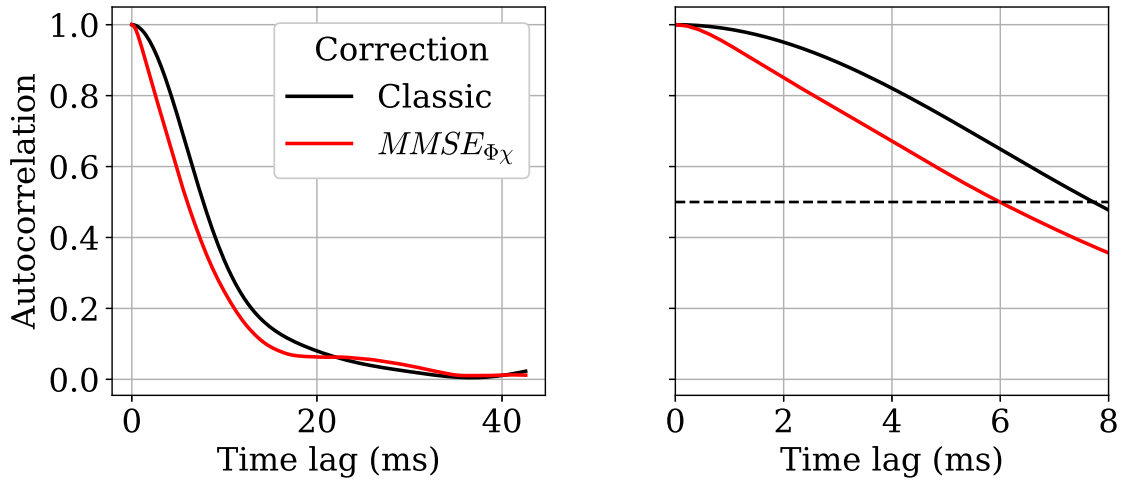

Figure 4.15: Temporal autocorrelation function (ACF) for the classical pre-compensation case and the $MMSE_{\Phi\chi}$ estimated case. On the right, zoom of the ACF for time lags from 0 to 8 ms.

Additionally, we study the statistics of the fades as these statistics will impact the design of the telecom reliability mechanisms such as the interleavers duration, or the re-synchronization frequency. Figure 4.16 depicts the mean fade time in ms and the fade frequency in Hz function of the coupled flux threshold, depicting the classical pre-compensation case in black and the $\text{MMSE}_{\Phi\chi}$ corrected case in red. In Fig. 4.16a, we observe that the mean fade time is decreased by more than 50% using the $\text{MMSE}_{\Phi\chi}$ method. Fig. 4.16b shows that the fade frequency is also decreased.

Finally, we plot the fade time distribution in figure 4.17, for three different thresholds. The thresholds are chosen around the detection threshold required for a $BER = 10^{-3}$ OOK communication at 25 Gbps. We observe in each case that the distribution of the fade duration is reduced to lower values in the MMSE case, and do not exceed 10 ms.

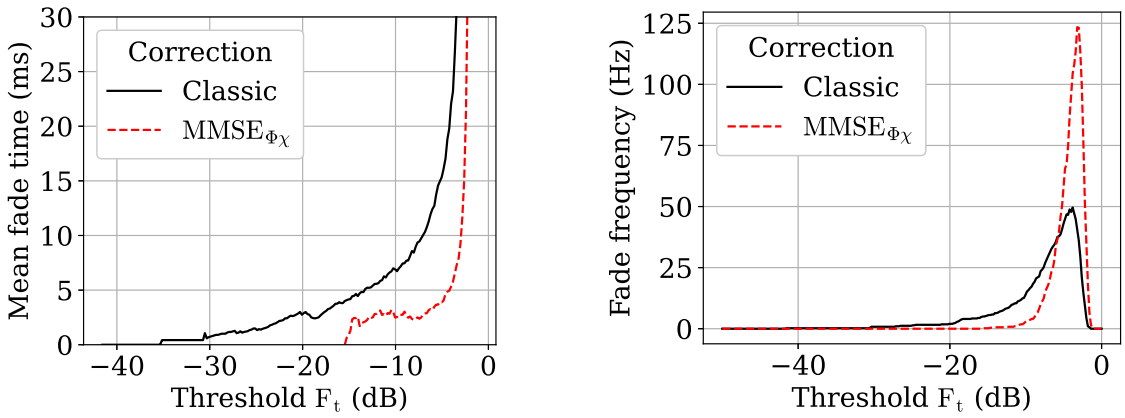

(a) (b)

Figure 4.16: Mean fade duration (a) and fade frequency (b) function of the coupled flux threshold F_t for the classical pre-compensation case and the $MMSE_{\Phi\chi}$ estimated case in the MOSPAR 9090 turbulence case.

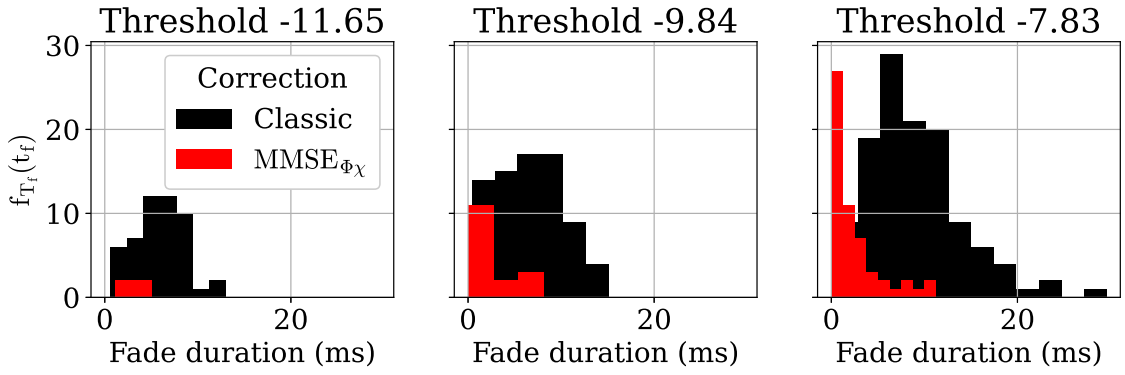

Figure 4.17: Fade duration distribution for 3 different arbitrary thresholds for the classical pre-compensation case and the $MMSE_{\Phi\chi}$ estimated case in the MOSPAR 9090 turbulence case.

4.4.2.3 Parametric evaluation of the gain

In this section, we study the gain of the estimator for different atmospheric conditions and system geometries. This sensitivity study can easily be done thanks to the pseudo-analytical model, allowing to systematically evaluate the gain on the coupled flux statistics.

Impact of the turbulence conditions

We start by evaluating the gain for different values of outer scale. In Fig. 4.18a and Fig. 4.18b, we plot the total MSE and the Tip and Tilt MSE, respectively, as a function of L_0 for the MOSPAR 9090 case. We depict on both graphs several MSE reduction key points. We observe a saturation of the absolute MSE for both correction methods around L_0=10 m. The reduction rate reaches 46.6% for the total MSE and 49.4% for the tip and tilt MSE around L_0=20 m, which is a typical value considered in the literature [181]. We can conclude that the proposed estimator provides a significant MSE reduction for all the outer scale considered values, with a greater reduction for large outer scales.

In Fig. 4.19, we plot the associated coupled flux CDF value at probability 10^{-3} in dB as a function of the outer scale as well as the gain brought by the proposed estimator. We can observe that this gain is comprised between 2.9 dB and 15.6 dB. Figure 4.18 and

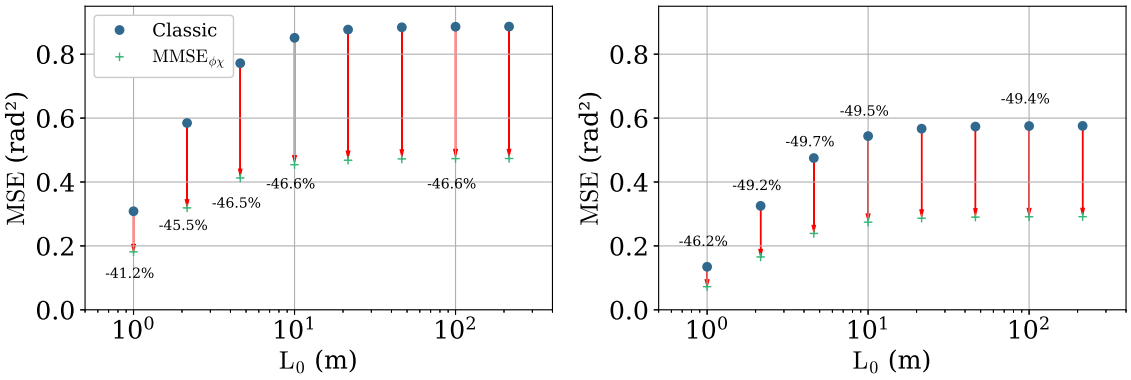

(a) Total residual phase variance

(b) Tip tilt

Figure 4.18: Red arrows correspond to the MSE reduction provided by the MMSE$_{\Phi\chi}$ method, with the reduction rate below the arrow. (a) Total MSE error over the AO corrected modes, (b) MSE error on tip and tilt.

Figure 4.19 also show that the outer scale strongly impacts the phase and signal statistics. However, the proposed estimator, by limiting the increase of the phase MSE also reduces the sensitivity to L_0. The range of the CDF value at probability 10^{-3} for an outer scale from 1 m to 200 m, is shown in Fig. 4.19 to span 8 dB for the proposed estimator whereas it spans 20 dB using the classical method. This illustrates the reduction of the losses dynamic.

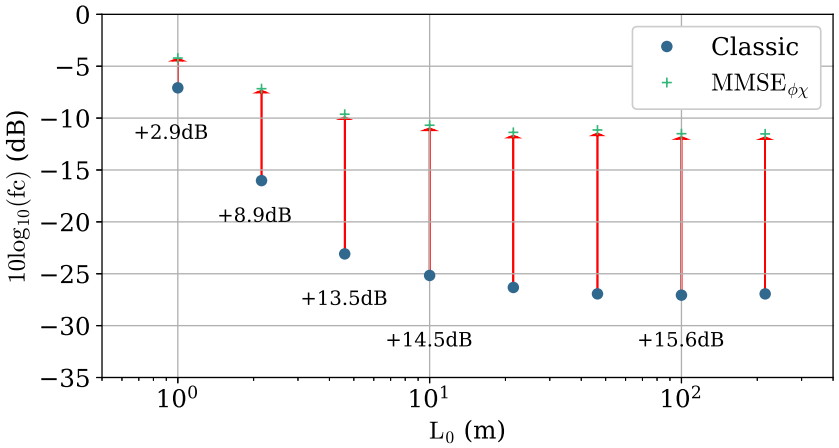

Figure 4.19: Absolute value of the CDF at $P(f_c \leq F_c) = 10^{-3}$ for the classical case (blue circles) and the MMSE$_{\Phi\chi}$ case (green crosses) versus L_0. Red arrows correspond to the gain at probability 10^{-3} on the CDF provided by the MMSE$_{\Phi\chi}$ method, with the gain value given below the arrow.

Furthermore, we study the sensitivity to the C_n^2 profile by varying the threshold of the MOSPAR XY for all the 25 profiles with $(X, Y) \in \{50, 60, 70, 80, 90\} \times \{50, 60, 70, 80, 90\}$. We recall the associated integrated parameters for a given θ_0 threshold and r_0 threshold in table 2.2, in the section 2.7.2 of chapter 2. We set L_0 to its earlier value of 20 m. In Fig. 4.20, we plot the MSE reduction gain as a function of θ_0, for different values of r_0.

In Fig. 4.20a and Fig. 4.20b we plot the total MSE and tip and tilt MSE, respectively, as a function of the anisoplanatic angle corresponding to the studied C_n^2 profile for different r_0 parameters. The results from the classical method and proposed estimator are represented by dots and crosses, respectively. The different colors depicts the different strengths of r_0.

We observe that the total MSE value is almost independent from r_0. This was an expected result as the anisoplanatic error is mainly driven by θ_0. The total MSE is reduced from 35 to 46% and the tip-tilt MSE from 38 to 49%. We can conclude that, stronger is the anisoplanatism, larger is the gain. Additionally, we notice a higher gain than expected for the case MOSPAR 5050. This can be interpreted by the fact that the estimator gain depends also on the C_n^2 profile structure and not only on the parameter θ_0.

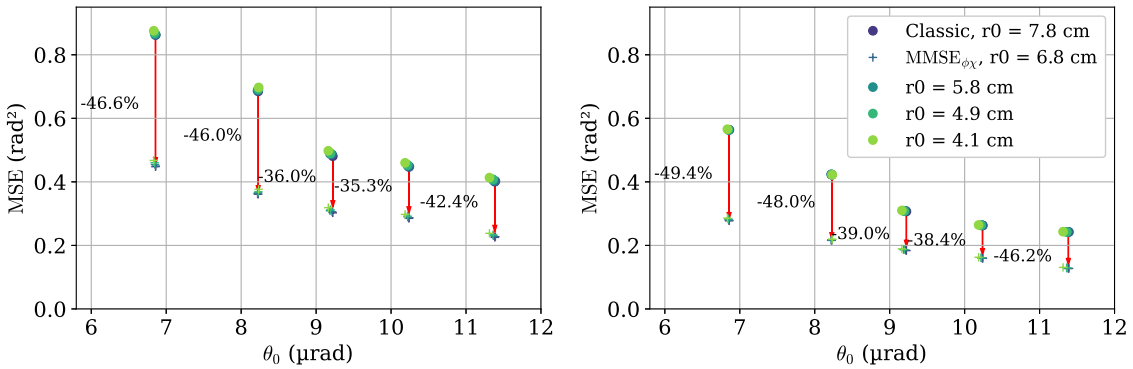

(a) Total residual phase variance

(b) Tip tilt

Figure 4.20: Absolute value of the MSE for the classical case (circles) and the MMSE$_{\Phi\chi}$ case (crosses) versus θ_0, for different r_0. Each color depicts a different r_0. Red arrows correspond to the MSE reduction provided by the MMSE$_{\Phi\chi}$ method, with the reduction value on its left.
(a) Total MSE error over the AO corrected modes.(b) MSE error on tip and tilt.

In Fig. 4.21, we plot the associated coupled flux threshold of the CDF at probability 10^{-3} as a function of the anisoplanatic angle corresponding to the considered C_n^2 profile. Similarly, we observe a quasi-null impact of the Fried parameter on the coupling attenuation value in both classical and MMSE$_{\Phi\chi}$ cases. We observe a gain from 5.5 to 15.8 dB provided by the new estimator. Thus, we can conclude that the estimator gain (in phase variance or in coupled flux), is almost insensitive to r_0, and increases with more severe anisoplanatic conditions.

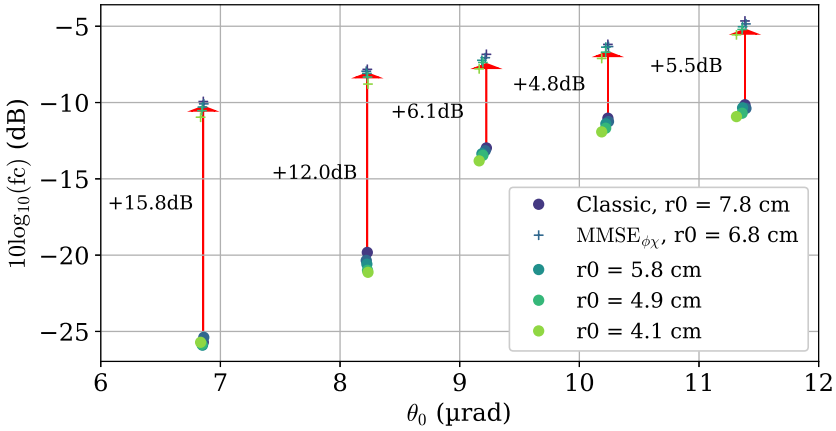

Figure 4.21: Absolute value of the CDF at $P(f_c \leq F_c) = 10^{-3}$ for the classical case (circles) and the MMSE$_{\Phi\chi}$ case (crosses) versus θ_0. Each color depicts a different r_0. Red arrows corresponds to the gain at probability 10^{-3} on the CDF provided by the MMSE$_{\Phi\chi}$ method, with the gain given on the left of the arrow.

Impact of the telescope diameter

We study the sensitivity of the estimation to the telescope diameter. Indeed, usually, in order to limit the fades, the tendency is to decrease the telescope diameter in order to limit the impact of the turbulence (by decreasing the factor $\frac{D}{r_0}$). However, in photon starving links such as the GEO Feeder link, there is an advantage to have a large telescope diameter in order to limit the geometrical losses that are conversely proportional to the square of the distance of the satellite.

We study the gain of the estimator based on phase and log-amplitude measurements for telescope diameters from 20 to 100 cm, in the MOSPAR 9090 turbulence conditions. Figure 4.22 depicts the modal residual phase variance for the classical case (black) and the pre-compensation based on the $MMSE_{\Phi\chi}$ phase estimation (red) for all the considered diameters. We observe that a gain starts to arise from a diameter of 30 cm, still on the low order modes. The absolute phase variance rises with the diameter, and the gain appears to grow with the diameter. This increase of the gain is also highlighted in Fig. 4.23 where we plot the total residual phase variance for the classical case and the estimated case in Fig. 4.23a, for two different outer scales, and the associated phase variance reduction in Fig. 4.23b. First, we can observe that while the anisoplanatic phase variance increases with the diameter, it seems to converge in the $MMSE_{\Phi\chi}$ case. We note as well as there is a gain, although small, for small diameter, around 10% for the 20 cm diameter case. We explain this gain increasing with the diameter as a performance increasing with the absolute value of anisoplanatism error. Additionally, the larger is the aperture diameter, the stronger will be the downlink and reciprocal uplink beam footprints correlations, as the portion of the turbulent volume seen by the two beam increases. This improves the performance of the estimator. Additionally, the reduction percentage is exactly the same for both outer scale. From this fact, we conclude that the estimation performance is insensitive to the outer scale.

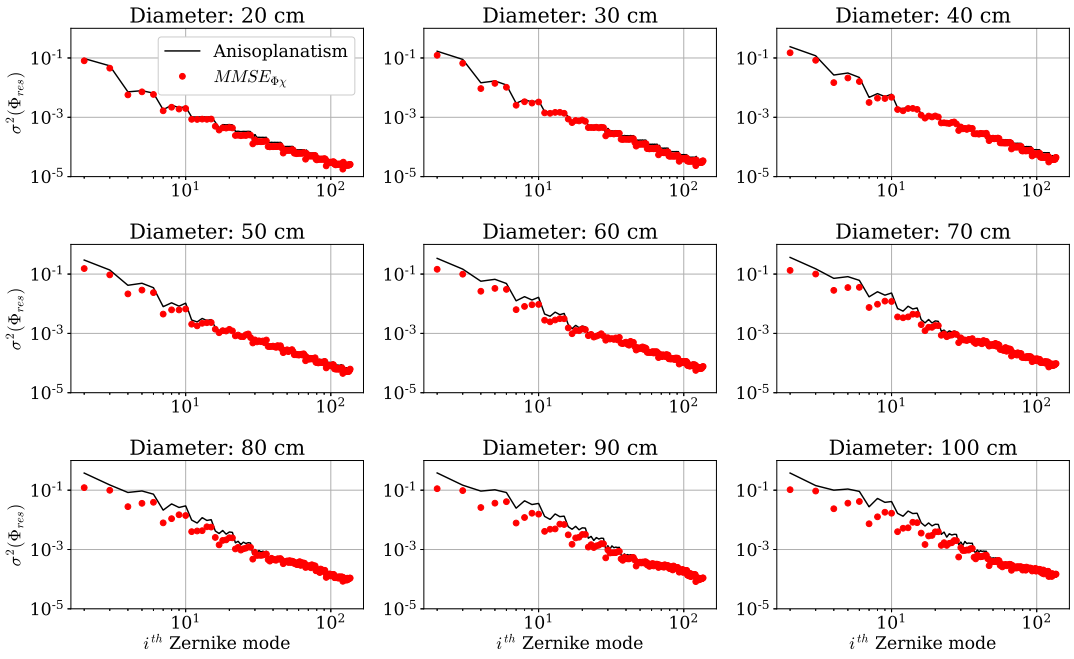

Figure 4.22: Modal residual phase variance function of the Zernike mode for the classical pre-compensation and the MMSE$_{\Phi\chi}$ method, for various telescope diameters from 20 to 100 cm.

To be able to state on the trade-off between turbulence losses and geometrical losses due

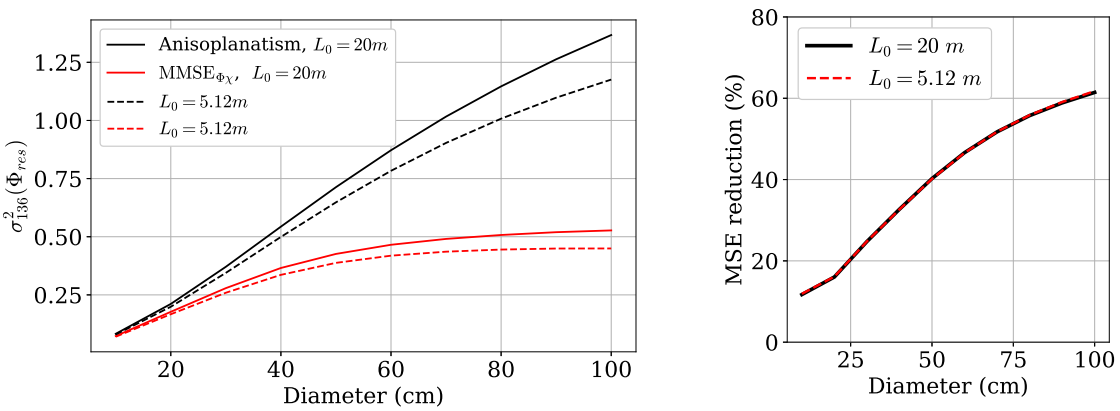

(a) Absolute residual phase variance

(b) Phase variance reduction

Figure 4.23: Total residual phase variance function of the telescope aperture diameter for the classical pre-compensation case and the $MMSE_{\Phi\chi}$ estimated case for two different outer scales.

to the size of the diameter, we study the impact of a growing diameter on the coupled flux statistics. First, we analyze the probability density function of the coupled flux impaired by the pre-compensation error in Fig. 4.24 (without the geometrical losses). We observe that, as the diameter becomes larger, the classical pre-compensation case PDF shifts toward the left, with a tail that becomes heavier. On the contrary, the shape of the PDF of the $MMSE_{\Phi\chi}$ estimated case stays quite stable (although presenting variance and mean value variations). We interpret this shape behavior as related to the tip-tilt absolute value.

Additionally, we study the cumulative density function by adding the geometrical losses, to study the gain at probability 10^{-3} by balancing the two effects (turbulence and geometrical losses). Figure 4.25a depicts the CDF of the turbulence losses added to the geometrical losses. Firstly, we observe that the $MMSE_{\Phi\chi}$ always bring a gain with respect to the classical case. This gain is illustrated in Fig. 4.25b, and can reach more than 20 dBs for the 1 m diameter case. Secondly, at probability 10^{-3}, the best performance is obtained by the larger diameter that provides a 15 dBs gain with respect to the 20 cm case without MMSE estimation. Indeed, the 20 cm case shows a small signal dynamic but is very impaired by the geometrical losses. Compared with the 1 m case with classical pre-compensation, it performs better because of the large signal dynamic of due to the atmospheric turbulence

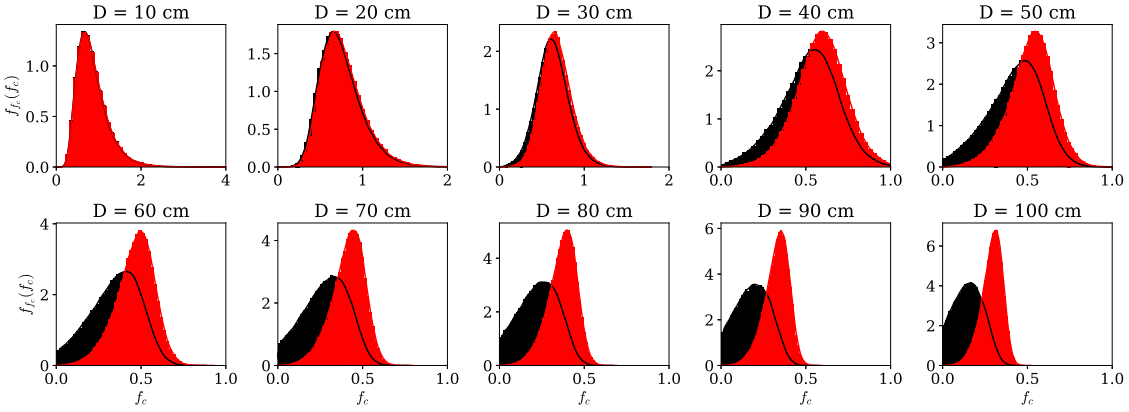

Figure 4.24: PDF for the classical pre-compensation case (black) and the $MMSE_{\Phi\chi}$ estimated case (red), for different aperture diameters, for the MOSPAR 9090 turbulence case.

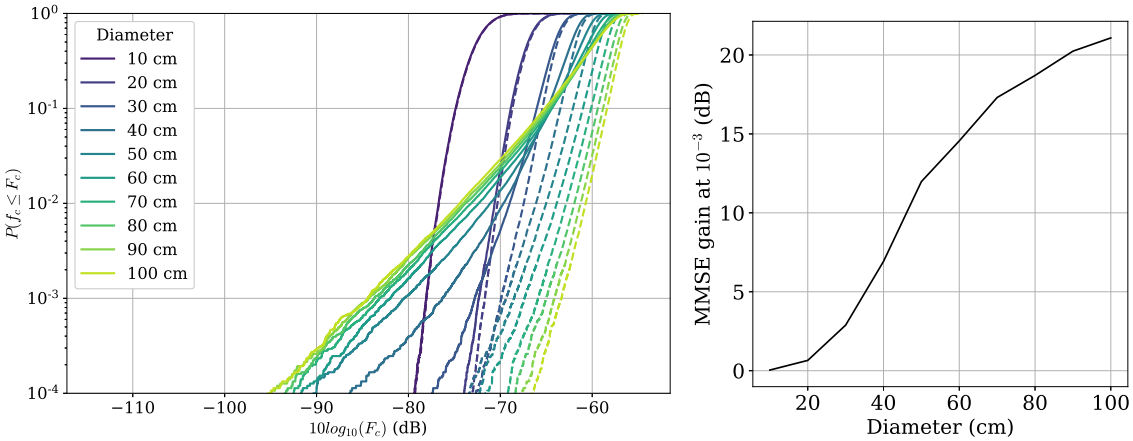

(a) CDF

(b) Gain at probability 10^{-3}

Figure 4.25: Cumulative density function of the coupled flux added to the geometrical losses for each diameter size, for the classical pre-compensation case (plain lines) and the $MMSE_{\Phi\chi}$ estimated case (dashed lines).

induces losses. However, once we estimate the phase with the $MMSE_{\Phi\chi}$ method, the signal dynamic is largely reduced, and we therefore benefit from lower geometrical losses of the 1 m case.

These results revisits the analysis of Conan [8] with our new correction strategy. The new MMSE estimator fully modifies the conclusions obtained in this earlier paper and clearly pushes towards larger aperture diameters. This should have a major impact on future OGS for Feeder links design choices.

4.5 Robustness of the estimator

In this section, we discuss the case of the estimation errors that can be induced when the estimator is computed with wrong priors. Indeed, in more realistic situations, some parameters used to compute the reconstructor such as the outer scale or the C_n^2 profile will be estimated with uncertainties. It is therefore of importance to compute the sensitivity of the estimator to the error that can be made in the estimation of these priors. We present a preliminary analysis of the estimation robustness in the following sections.

4.5.1 Estimation error formalism

To evaluate theoretically the phase error associated to a prior uncertainty, we introduce the following formalism. Here, we compute the error covariance matrix associated to an estimator whose priors are wrong. We define first the two reconstructors, the one associated to the good priors:

$$\mathbf{R}_{MMSE} = \mathbf{\Gamma}_{\Phi y_m}(\alpha)\mathbf{\Gamma}_{y_m y_m}(0)^{-1} \tag{4.23}$$

and the one associated to the erroneous priors:

$$\mathbf{R}'_{MMSE} = \mathbf{\Gamma}'_{\Phi y_m}(\alpha)\mathbf{\Gamma}'^{-1}_{y_m y_m}(0) \tag{4.24}$$

The reconstructor associated to the wrong priors can also be written as:

$$\mathbf{R}'_{MMSE} = \mathbf{R}_{MMSE} + \Delta\mathbf{R}. \tag{4.25}$$

We can show[1] that the error covariance matrix therefore reads:

$$\mathbf{\Gamma}'_{\Phi_{res}} = \mathbf{\Gamma}_{\Phi_{res}} + \Delta\mathbf{R}\mathbf{\Gamma}_{y_m y_m}(0)\Delta\mathbf{R}^T \tag{4.26}$$

which is the combination of the error covariance matrix computed for the true priors plus an additional term depending on the measurement autocovariance and of the difference between the two reconstructors.

In the following, we apply this formalism to errors made on the outer scale measurement and errors made on the C_n^2 profile reconstruction.

4.5.2 Sensitivity to outer scale errors

Typical L_0 values measured from the literature are around 20 m [181]. However, this parameter can be difficult to measure or estimate with accuracy, and impacts greatly the value of low order modes such as tip and tilt.

Therefore, we study the impact on the phase error of an estimator computed with the wrong knowledge of the outer scale. Typically, in the example taken, we suppose an infinite outer scale to compute the estimator, whereas the true value is finite and equals to $L_0 = 5.12\ m$. We also suppose a constant value of outer scale along the line of sight, for the sake of simplicity.

In figure 4.26, we plot the modal residual phase variance after phase estimation with wrong and true priors of the outer scale, function of the Zernike mode number, for the turbulence case MOSPAR 9090. On the left, we plot the phase variance obtained with the analytical model. The wrong prior case is the case where we compute the reconstructor for an infinite outer scale. We observe that there is almost no difference between the two modal spectrums. Additionally, the total phase variances are, for the case with true and wrong priors, equal to 0.418 and 0.419, respectively. We confirm this result by applying the estimators with true and wrong priors to the E2E data. We plot the modal residual phase variance from the data in the graph on the right. The residual phase variance computed from data is shown to follow the same behavior as the results obtained from the model. Therefore, we conclude that over-estimating the outer scale does not impact the estimator's performance and that the estimation of this parameter is not crucial to apply this estimation technique.

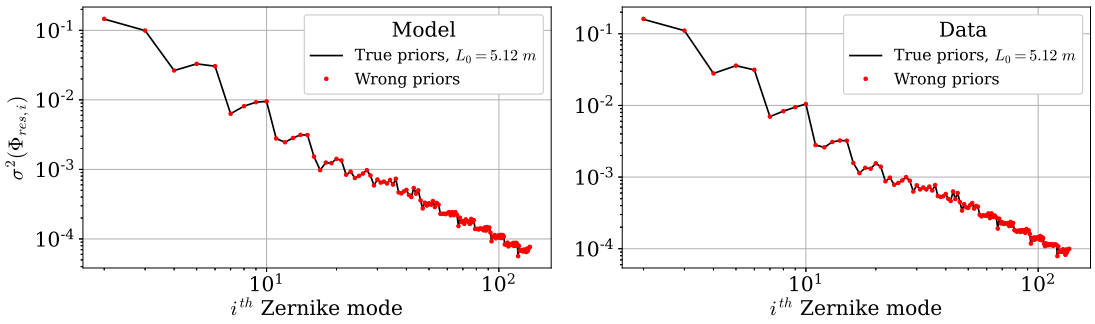

Figure 4.26: Modal residual phase variance computed: from the model on the left, from E2E data on the right, for the estimated case with true priors (in black), and wrong priors (in red).

[1] Formalism proposed by Jean-Marc Conan and Cyril Petit

4.5.3 Cn2 profile uncertainties

As the C_n^2 profile measurement is a prior essential to the computation of the estimator, we study the sensitivity to the profile inthis section. As a first evaluation, we compute the estimator performance by switching the MOSPAR profiles of different strength.

Therefore, we study the following cases: turbulent conditions MOSPAR 5050, 9090 and 9999, corrected with an estimator computed thanks to the profiles 5050, 9090 and 9999. Figure 4.27 depicts the resulting residual phase variance, where the black dots depict the case with true priors, and the blue stars and red crosses the cases with wrong priors on the profile. In the MOSPAR 5050 case, computing the variance with estimator calculated for tougher profiles, we observe that even with wrong priors, the phase variance is decreased with respect to the true phase variance. In the MOSPAR 9090 case, we observe an equivalent performance when the wrong profile to compute the estimator is stronger, and an increased phase variance on the high order modes when the wrong profile to compute the estimator is less severe, and no impact on the tip and tilt modes. This observation is confirmed in the MOSPAR 9999 case. We conclude that in the studied cases, the profile used to compute the estimator have few impact on the estimator performance.

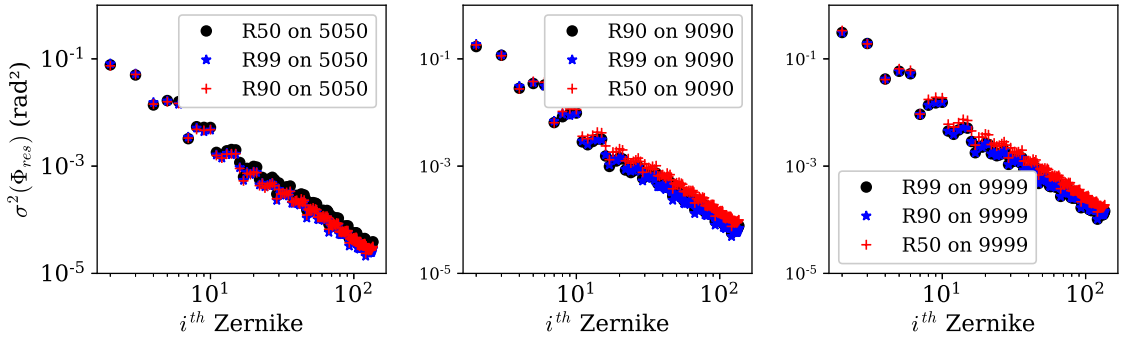

Figure 4.27: Analytical residual phase variance computed in three turbulence cases, with true and wrong priors on the profile.

To intend explaining this observation, we plot in figure 4.28, the value of the first rows of the three estimator, that we called R50, R90 and R99. The i^{th} row, corresponds to the weighting of the measurement vector to correct the mode of index $i+2$. For instance, we depict on the left the first row, corresponding to the tip correction, the second row in the center, corresponding to the tilt correction, and the third row corresponding to the focus correction. We observe in each case that the structure of the weights for the three estimators is very similar. It shows that the first modes of the measurement vector,

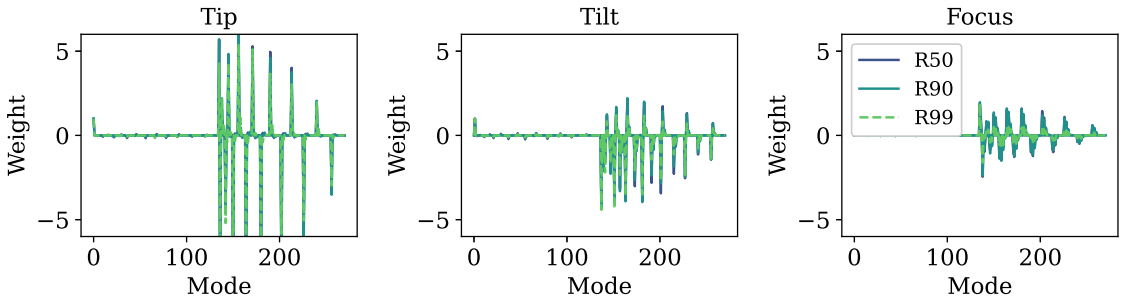

Figure 4.28: Three first rows of the estimator computed for the profiles MOSPAR 5050, 9090 and 9999.

corresponding to the phase information, brings very little information, and confirms that the information comes from the log-amplitude, regardless of the profile.

To conclude, the estimator seems robust to errors on the profile uncertainties. In future work, we will proceed to an actual profile reconstruction from the data, using state-of-the-art methods such as the SCO-SLIDAR method, to assess this robustness to profile uncertainties in scenarios close to experimental conditions.

4.6 Limits of the estimator

Previously, we evaluated the robustness of the estimator to errors due to uncertainties. It was shown that the estimator is resistant to such estimation errors. In this section, we explore the limits of the estimator. Indeed, this analytical estimator is constructed following some assumptions, whose most important one is the assumption of the turbulence to be within the Rytov regime. The perturbations are assumed to be most of the time within the Rytov regime, for the considered elevation. However, for some rarer turbulence conditions, this perturbation's strength can be beyond this regime. Therefore, it is of interest to study the estimator behavior at the limits or out of this regime. This will be studied in section 4.6.1. Additionally, we question the estimator efficiency for strong angular decorrelations in section 4.6.2. This angular decorrelation can be, in the GEO case, due to strong turbulence in high altitude layers. We extend the study to a more conceptual analysis, not concerning the GEO case, for varying PAA. This study is the first step toward studying different types of links, such as LEO optical uplinks.

4.6.1 Turbulence regime

In this section, we study the estimator performance in the limits of the Rytov regime. To this aim, we consider the following profile that is called **P2** and that is a CNES reference profile. The integrated parameters of the profile are given in table 4.1. We note that the Rytov variance is equal to 0.29, meaning that this profile is at the limit of the Rytov regime, as the Rytov regime is generally defined such that $\sigma^2_{\chi_R} \leq 0.3$. This is confirmed by the fact that we measure on the data a log-amplitude variance equal to 0.23, which differs from the theoretical value given in table 4.1. The phase and log-amplitude conditions are illustrated in figure 4.29. We can clearly observe a large dynamic of the phase and strong scintillation patterns on the log-amplitude.

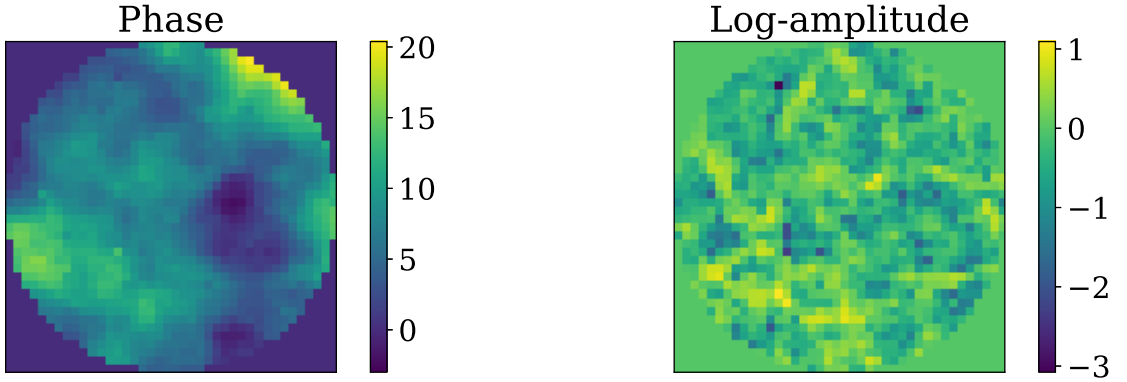

Figure 4.29: Example of phase and log-amplitude pattern of a complex field propagated from the satellite to the ground at the OGS telescope pupil, for the P2 atmospheric conditions.

r_0	θ_0	$\sigma^2_{\chi_R}$
3.3 cm	6.7 µrad	0.29

Table 4.1: Integrated parameters of the $P2$ C_n^2 turbulence profile.

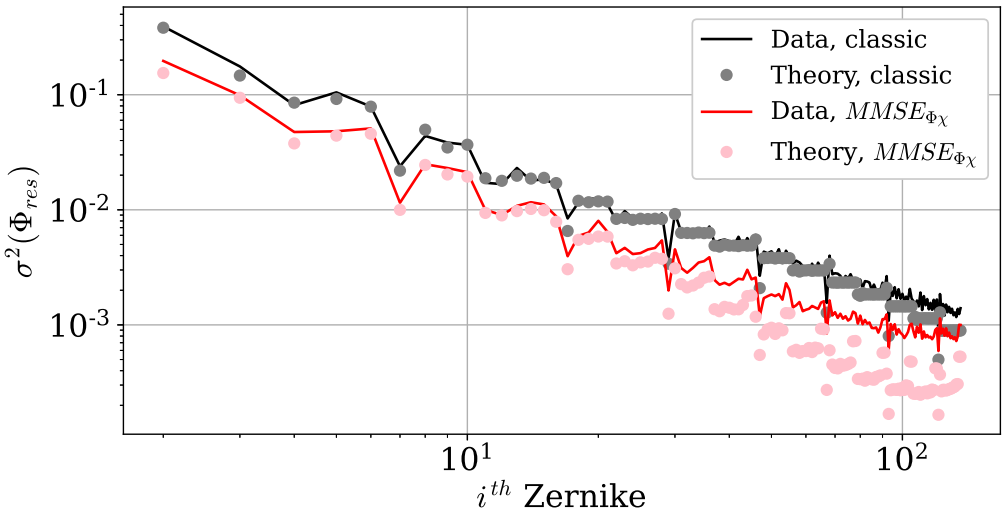

Figure 4.30: Modal residual phase variance both theoretical and computed from data, function of the Zernike mode, for the classical case and the $MMSE_{\Phi\chi}$ estimated case.

We plot in figure 4.30 the modal residual phase variance function of the Zernike mode, for the theoretical case (computed from analytical formulas), and the variance computed from the E2E data, for both the classical and $MMSE_{\Phi\chi}$ pre-compensations. We observe from the classical case that the theoretical anisoplanatic phase variance corresponds to the phase variance computed from data, with a small deviation arising for high-order modes. However, it is not the case for the $MMSE_{\Phi\chi}$ case, whose theoretical phase variances are significantly lower for the high-order modes than the variances obtained from the data. This could be explained by a larger inaccuracy of the analytical covariance between the phase and the log-amplitude and/or the autocovariance of the log-amplitude, which would lead to a suboptimal performance. However, although not optimal, the $MMSE_{\Phi\chi}$ estimator still brings significant gain on every mode, still greatly reducing the low order modes variance. The reduction of the high order mode variances is a second surprising observation. It is surprising because it is a behavior we do not observe for any other turbulence profile, where the $MMSE_{\Phi\chi}$ estimator only reduces the low order mode variances. We interpret this effect as resulting from a a measurement vector more informative due to stronger scintillation patterns. To conclude, even not optimal, the estimator still allows reducing the anisoplanatic phase variance (by 47 %) in the limit of the Rytov regime.

We also study the impact on the coupled flux statistics of this estimation. In figure 4.31 we plot the PDF (Fig. 4.31a) and CDF (Fig. 4.31b) of the coupled flux aboard the satellite for the classical and $MMSE_{\Phi\chi}$ estimated case in the $P2$ turbulence conditions. We observe on the PDF that the estimator allows improving the mean value of the signal and reducing a lot the occurrence probability of the deep fades. This behavior can be observed as well on the CDF, where the gain at probability 10^{-3} is equal to 13 dBs with respect to the classical case. For illustration purposes, we plot the associated time-series in figure 4.32, where we can observe the rise of the mean value and the diminution of the fade occurrences and depth.

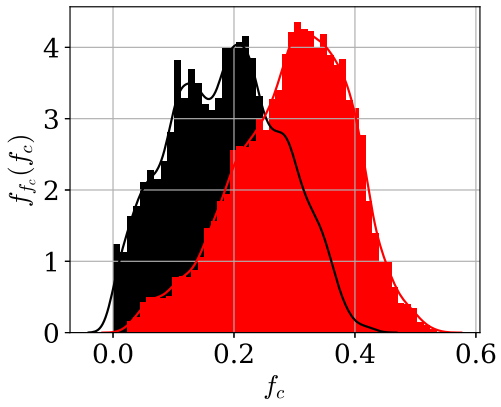

(a) PDF of the coupled flux f_c computed from E2E data

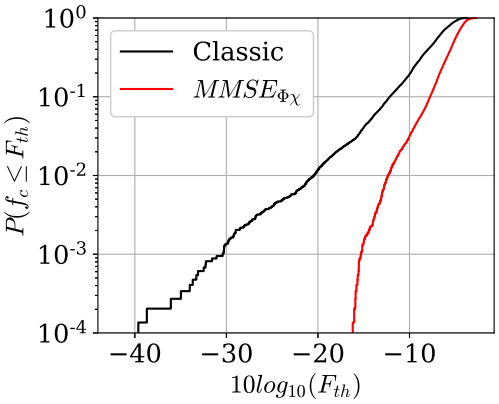

(b) CDF of the coupled flux f_c computed from E2E data

Figure 4.31: Coupled flux statistics for the classical and $MMSE_{\Phi\chi}$ estimated cases.

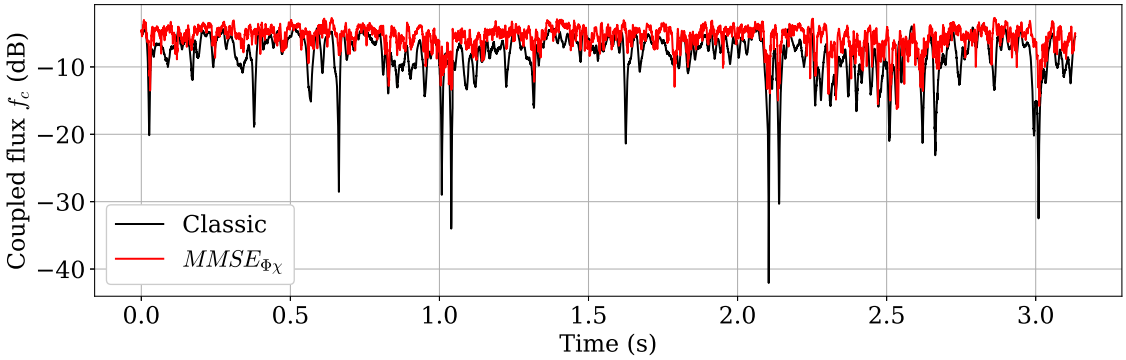

Figure 4.32: Timeseries of the coupled flux f_c for the classical pre-compensation case and the $MMSE_{\Phi\chi}$ estimated case, for the P2 turbulence conditions.

To conclude, we showed that the estimator was still efficient at the limit of the Rytov regime, still reducing effectively the phase error, and therefore inducing improvements in the coupled flux statistics and temporal characteristics. However, to produce these results, we used an optical field analysis framework, not using any wavefront sensor and phase reconstruction algorithm. Therefore, these results are to be considered with caution, given that phase errors can arise during the phase reconstruction in a real system in the moderate to strong scintillation regime.

4.6.2 Angular decorrelation

In this section, we explore the behavior of the estimator for strong angular decorrelations. These cases can occur for GEO-Feeder links with small anisoplanatic angles θ_0. More broadly, strong angular decorrelations occur for larger point-ahead angles. This scenario goes beyond GEO uplink cases, but is still interesting to understand the behavior of the estimator. Additionally, it raises the question of the applicability of the pre-compensation to optical LEO uplinks.

Larger turbulence angular decorrelation

We start by considering cases with stronger angular decorrelation. In that aim, we use the profile MOSPAR 9999, whose integrated parameters are given in table 2.2.

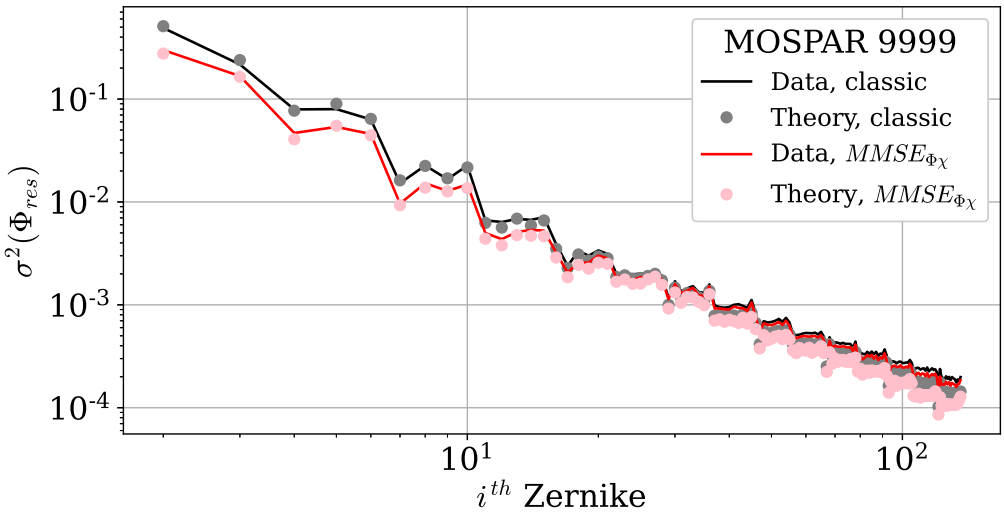

Figure 4.33: Modal residual phase variance both theoretical and computed from data, function of the Zernike mode, for the classical case and the $MMSE_{\Phi\chi}$ estimated case, for the MOSPAR 9999 turbulence conditions.

We plot the associated modal residual phase variance in figure 4.33, for the classical pre-compensation case and the $MMSE_{\Phi\chi}$ estimated case. The results obtained from the theory are depicted in dots, and the one computed from the E2E data in plain lines. We observe a good match between the variances computed from the data and the theoretical results. A slight deviation can be observed on the high-order modes, however, the impact of this difference is negligible on the performance. The estimator is shown to decrease the residual phase variance by 33%.

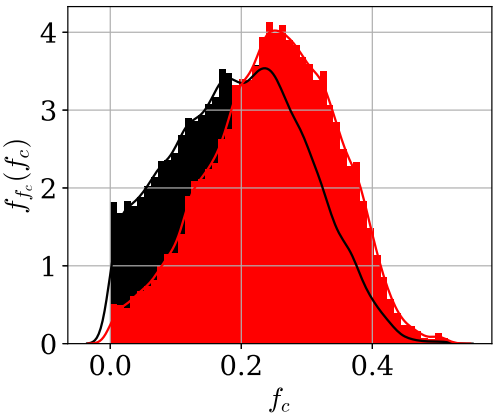

(a) PDF of the coupled flux f_c computed from E2E data

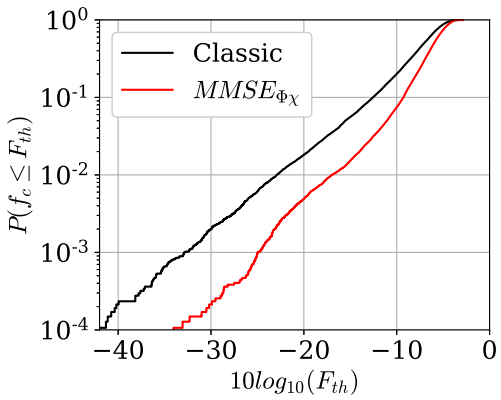

(b) CDF of the coupled flux f_c computed from E2E data

Figure 4.34: Coupled flux statistics for the classical and $MMSE_{\Phi\chi}$ estimated cases, for the MOSPAR 9999 turbulence conditions.

In figure 4.34 we plot the associated coupled flux statistics obtained from E2E data, for the classical and $MMSE_{\Phi\chi}$ cases. We can observe from the PDF of the coupled flux in Fig. 4.34a that the estimated case improves the shape of the PDF, shifting the mean and reducing the occurrence of deep fades. However, the statistics are still quite bad, with top coupled flux values that are limited to 0.4. This attenuation factor below 0.4 is limited

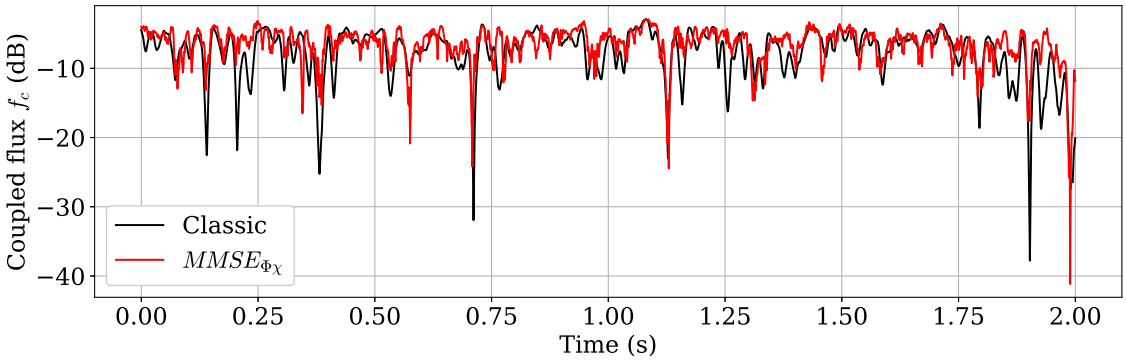

Figure 4.35: Timeseries of the coupled flux f_c for the classical pre-compensation case and the $MMSE_{\Phi\chi}$ estimated case, for the MOSPAR 9999 turbulence conditions.

by the fitting error that is large in these conditions, equal to 0.23 rad². Moreover, it is highlighted on the CDF in Fig. 4.34b that while still bringing a 10 dB gain at probability 10^{-3}, the performance obtained with the estimated case is quite bad. This is explained by the fact that, although reduced by a non-negligible percentage, the absolute residual phase variance of the estimated case is high and therefore the beam quality is impaired. Finally, we plot the associated timeseries in Fig. 4.35, we observe a small improvement of the temporal behavior of the $MMSE_{\Phi\chi}$ case, but not as large as the previous studied cases.

Larger PAA

Finally, we study the case of bidirectional links with larger PAA, as it can be the case for LEO links whose PAA can reach 50 μrad [171]. Except from the interest of applying the estimator to an existing case, studying the estimator performance for large to very large angles informs us on the behavior of the angular properties of the turbulent phase and amplitude. Therefore, we study and compare the gain for both $MMSE_{\Phi}$ and $MMSE_{\Phi\chi}$ for angle from 18.5μrad to several $mrads$. We perform this study for the MOSPAR 9090 case at 30° elevation. As this case is still Rytov, we only compute the theoretical phase variance and gains.

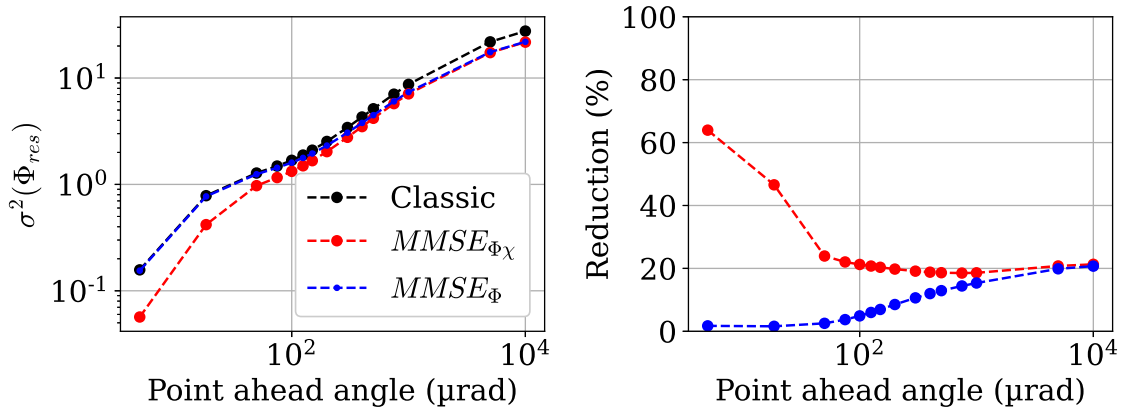

Figure 4.36: Total residual phase variance function of the point ahead angle for the classical, $MMSE_{\Phi}$ and $MMSE_{\Phi\chi}$ cases, for the MOSPAR 9090 turbulence conditions. On the left: absolute value, on the right, phase variance reduction with respect to the classical case.

We plot in Fig. 4.36 the total residual phase variance function of the point ahead angle,

for the classical, the $MMSE\Phi$ and the $MMSE_{\Phi\chi}$ cases in the MOSPAR 9090 turbulence conditions. First, we observe that the $MMSE_{\Phi\chi}$ case always brings a gain with respect to the classical case, even for wide angles, with a variance reduction decreasing from around 60% for small angles to a convergence around 20%. Secondly, it is interesting to comment on the behavior of the $MMSE_{\Phi}$ case. For small angles, this estimator brings no gain and, as the angle becomes larger, the phase variance performance converges toward the $MMSE_{\Phi\chi}$ estimator performance. This means that for wide angles, the log-amplitude does not bring information anymore on the phase perturbation. This can be explained as follows: as the angle becomes larger, the higher layers start to be decorrelated, and the information carried by the log-amplitude is progressively less and less informative. It would be interesting to study the evolution of the modes of log-amplitude, bringing the information to the estimation. We would expect this required resolution would be smaller with the increase of the angle, as larger speckles coming from higher layers would not be informative anymore, and smaller speckles induced by still correlated layers would still be informative.

To conclude, given the results commented above, we expect for cases such as LEO uplinks to be able to benefit as well from the phase estimation at point-ahead angle to enhance the pre-compensation. However, it is true that the absolute residual phase variance, even estimated, stays high for angles around 150 μrad. We will later, in chapter 5, study advanced techniques in order to further improve the phase estimation, that will be as well applicable to LEO uplinks.

4.7 Conclusion

Main results and conclusions

In this chapter, we presented a new method to optimize the pre-compensation phase at PAA for the GEO-Feeder link. This method, inspired from previous work, especially Whiteley's work, is a phase at PAA estimator, relying on phase and log-amplitude measurements and associated modal statistical priors. While the knowledge and ability to compute analytically the modal statistical priors allows computing the reconstructor matrix, the measurement vector is used to compute in real time the phase at PAA estimate. The novelty of this method lies in the exploitation of the on-axis log-amplitude measurements, which are freely available measurements at the OGS from the wavefront sensor that were not exploited before. These measurements inform on the perturbations from the high altitude turbulent layers at the origin of the anisoplanatism.

Therefore, after giving the MMSE estimator general formalism for any measurements, we specified the estimator for different measurements. We started by applying the state-of-the-art method from Whiteley, relying on on-axis phase measurements, to the telecom bidirectional link scenario. The evaluation of the MMSE estimator relying only on on-axis phase measurements, had never been done in this scenario, and we have shown it brings almost no improvement in terms of phase variance reduction. Then, we investigate an MMSE estimator based on phase and log-amplitude measurements, which is the main contribution of this chapter. We develop the required formulas to compute the analytical reconstructor in a modal formalism. This includes phase and log-amplitude autocovariances, and angular covariances. As it is less common to use the Zernike modal formalism to analyze the log-amplitude fluctuations, all formulas were not available in the literature, especially the angular cross-covariance between the phase and the log-amplitude. Therefore, we extended the formulas from the literature to compute fully analytically the estimator $MMSE\Phi\chi$. We showed that this estimator greatly reduced (by 30% and above) the phase

error for various atmospheric conditions and OGS geometries, with respect to the classical pre-compensation scheme suffering from the anisoplanatism error. This pre-compensation error reduction was shown, thanks to the reciprocal formalism, to greatly improve the statistics and temporal characteristics of the coupled flux aboard the satellite.

Finally, we discussed the estimator robustness uncertainties on the parameters needed to compute the statistical priors, such as the outer scale and the C_n^2 profile. The estimator performance was shown not to be sensitive to uncertainties on the outer scale, and barely sensitive to C_n^2 uncertainties. Additionally, we discussed the estimator performance in two types of extreme regimes that are strong perturbation regimes and strong angular decorrelations conditions. These regimes can concern optical links with GEO satellites, but, more importantly, are a first performance evaluation for scenarios of optical links with LEO satellites. We showed that, for the considered turbulent cases, in strong perturbation regimes, the analytical performance was deflecting from the performance obtained from the E2E data, however, we could still obtain a large reduction of the residual phase variance. This shows that even out of the regime of validity of the analytical estimator, it is still significantly improving the link performance. Concerning the strong angular decorrelation regimes, it was shown that the performance was degraded because there is less information to exploit. However, the gain was still interesting (above 30%).

Perspectives

From the work presented in this chapter, three questions arise. Firstly, we showed that the estimator reduced the pre-compensation error and therefore improved the coupled flux statistics. The first question is therefore: how does this improvement of the coupled flux statistics impact the telecommunication performance of the link ? Indeed, we wonder how these channel model improvement impacts the capacity of the link (maximum theoretical rate that can be achieved), and what is the effective data-rate that we can achieve on this link for a sufficiently low bit error rate. This consideration will be treated in chapter 7.

Additionally, we showed that the gains of the estimator were varying function of the atmospheric conditions, and started to be limited for strong angular decorrelation turbulence conditions. It is limited because the correlations between the physical quantities were starting to be weaker, but also because the absolute value of the phase variance was still very high. Therefore, a second question is: would it be possible to collect additional measurements that would bring further information and therefore improve the estimator performance, especially in strong angular decorrelation conditions ? This study, consisting in looking for additional measurements of various nature informative on the phase at PAA, will be the topic of chapter 5 and chapter 6.

Finally, a broader perspective is to go toward an experimental demonstration of this pre-compensation method at point-ahead angle in order to confirm the feasibility and efficiency of the method. Indeed, the performance that has been presented here can be considered as an upper limit of the performance one will get on a real system, as we neglected many system aspects in this study. An experimental demonstration would allow assessing the gains or the gap with the theoretical gains presented here. While this experimental demonstration is beyond the scope of this thesis, several technical points to elucidate have been identified. The first point of interest is to assess for the feasibility of the construction of the analytical estimator based on C_n^2 profile measurements. (model including noise ? or change of space ; slopes and intensity). The second point would be to develop a control law based on the MMSE phase estimation.

CHAPTER 5

Temporal statistics to model and optimize the pre-compensation phase at point-ahead angle

Contents

We presented in chapter 4 a new estimator relying on phase and log-amplitude measurements and statistical priors, allowing to decrease the pre-compensation phase error. These results showed that the log-amplitude from the downlink beam is informative on the phase perturbations at the origin of the anisoplanatism. These results were obtained neglecting the phase error induced by the AO loop delay.

In this chapter, we will explore the possibility to collect and use additional information from the downlink beam (phase and log-amplitude) in order to further improve the phase estimator at point-ahead angle performance. In particular, we study the gain that can be brought by past measurements of phase and log-amplitude in the estimation. It is the

occasion to introduce the temporal error in the model, that is induced by the AO loop delay.

In this aim, we develop a joint temporal-angular analytical framework in order to model the phase error in presence of temporal error and to optimize the phase estimator. Previously, we neglected the temporal error mentioned in section 2.4.3 that is induced by the AO loop delay. Doing so allowed to emphasis on the anisoplanatic error and on the estimator capacity to reduce this angular error. Here, in order to have a more realistic model, we introduce the formalism to model the temporal error together with the anisoplanatic error, on the ground to GEO link. We highlight that these two errors have to be modeled jointly, as they both results from phase error due to turbulence layer spatial variations. This joint modeling of temporal and anisoplanatism errors is not especially done in the literature [89]. We also study the impact of this temporal error on the estimation of the phase at point ahead angle for an estimator when the estimator neglects this error. As it is possible to model this temporal error, it is as well possible to use this formalism to optimize the estimator taking into account the delay between the instant of the measurements and the instant of correction, if wind information is available. Therefore, we study the gain brought by this estimator. Finally, we study the gain brought by an estimator accounting for several past measurements, in the aim to quantify the information brought by temporal measurements. It was already shown that such approach brings heavy gains in a downlink point of view, aiming only at correcting the temporal error induced by the loop delay, with phase only measurements, in slewing satellite scenarios [179, 182].

5.1 Temporal anisoplanatism

5.1.1 Principle

Within the hypothesis of Taylor frozen flow turbulence [90], stating that the temporal variation of the turbulence is induced by the displacement of the layer at the speed of the wind projection orthogonal to the line of sight, one can assimilate the turbulence temporal variations to spatial variations as mentioned in [183, 184]. Therefore, the phase delayed from Δt can be expressed as:

$$\Phi(\boldsymbol{r}, z, t - \Delta t) = \Phi(\boldsymbol{r} - \Delta t \cdot \boldsymbol{v}(z), z, t) \tag{5.1}$$

Therefore, the temporal correlations of the phase and the log-amplitude can be expressed thanks to the angular correlation formalism detailed in section 4.4.

This equivalence between the temporal and spatial shift of the wavefront is illustrated in figure 5.1 on one turbulent layer. In this figure, we represent the beam footprint at instant t in red and its associate position along the x axis on a single atmospheric layer at height z, which is taken as the reference position x_0. The previous beam footprint is represented in black with respect to the x component of the wind speed direction (in (a) the wind projection on the vector $\vec{x}$ is positive, in (b) negative). It results that the position of this previous beam footprint can be expressed as a spatial shift with respect to the beam footprint reference x_0, depending on the time delay, the wind norm and direction. By knowing the wind profile along the line of sight, this one layer shift can be extended to the multi layer model.

We presented above the concept of expressing the time variations of the turbulence as spatial variations, therefore allowing to express temporal covariances as spatial covariances. This idea can be extended to express the temporal variations of the phase at point-ahead angle. Indeed, we can jointly describe the temporal and angular phase variations as fol-

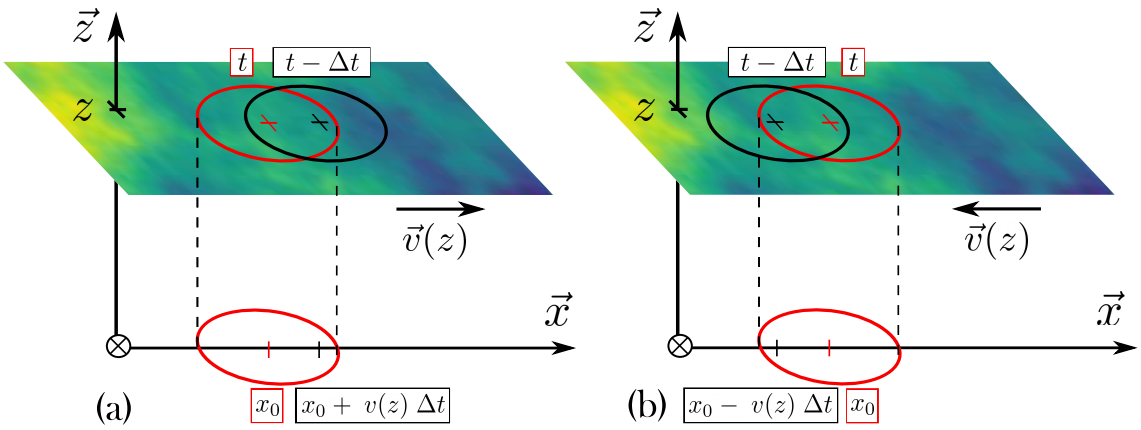

Figure 5.1: Illustration of the principle of temporal anisoplanatism within Taylor frozen flow hypothesis. (a) for a positive wind direction, (b) for a negative wind direction.

lowing:

$$\Phi(\mathbf{r}, t+\Delta t, \alpha_{PAA}) = \Phi(\mathbf{r} - \Delta t \cdot \boldsymbol{v}(z) + \alpha_{PAA} \cdot z \cdot \mathbf{e}_x, t, 0) \tag{5.2}$$

that is the wavefront at point-ahead angle ahead of time expressed function of the space shifted on-axis wavefront. In the following, for sake fo simplicity, we assume that the temporal and angular variations are along the x axis. This spatial shift is illustrated in figure 5.2 for a given wind direction along the x axis, where $v(z) \in \mathbb{R}$ is defined such as $v(z) > 0$, when the wind is in the $\vec{x}$ direction. On this scheme, the blue footprint is the on-axis ($\alpha = 0$) downlink beam footprint at the instant $t - \Delta t$, therefore in the past, that is the instant of the measurements. It is associated to the reference position x_0. The black footprint is the reciprocal uplink beam footprint at point-ahead angle at instant $t - \Delta t$, at position $x_0 + \alpha z$. The red footprint is the reciprocal uplink beam footprint at point-ahead angle at instant t, that we intend to correct. Its position with respect to the downlink beam footprint in the past is $x_0 + \alpha z + \vec{v}(z)\Delta t$.

Therefore, by expressing jointly these temporal-angular phase variations, we can describe the reciprocal pre-compensation residual phase statistics due to angular and temporal errors.

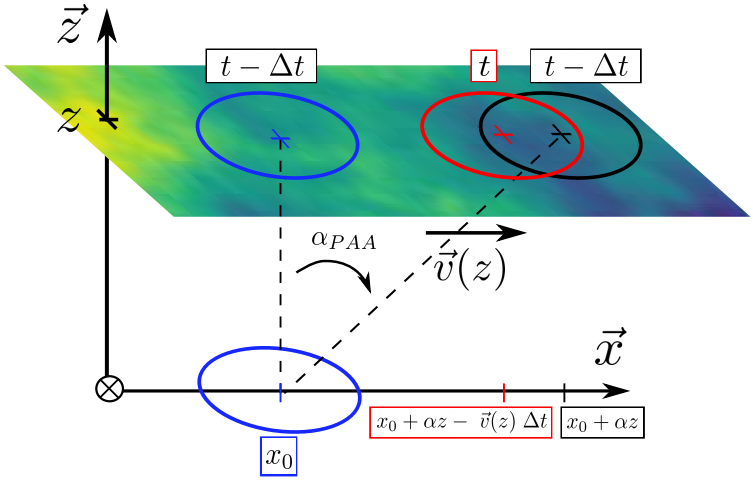

Figure 5.2: Representation of the principle of joint temporal and angular anisoplanatism for one layer with a wind vector in the direction of the point-ahead angle.

.

5.1.2 Analytical covariance matrix terms

To express the associated angular-temporal covariance matrices between the phase at point-ahead angle and the delayed measurements of the phase on-axis or between the phase at point-ahead angle and the delayed measurements of the log-amplitude on-axis, we can therefore apply the formulas described in section 4.4.1.2, by modifying Eq. 3.38 as:

$$d(z, \Delta\alpha, \Delta t) = \Delta\alpha \cdot z - \Delta t \cdot v(z) \tag{5.3}$$

where $\Delta \mathrm{t} = \mathrm{N}/\mathrm{f}_{\mathrm{samp}} = \mathrm{Nt}_{\mathrm{samp}}$ where f_{samp} is the sampling frequency of the AO loop and N is the number of frames corresponding to the AO loop delay, and $t_{samp} = 1/f_{samp}$. As defined earlier, $v(z)$ denotes the wind speed parallel to the $\vec{x}$ axis. We note that a positive time step $+\Delta t$ describes a covariance between a physical quantity from the past and a physical quantity in the future, and that a negative time step $-\Delta t$ describes the reverse (from future to the past). We highlight that the joint temporal-anisoplanatic phase error differs from the addition of both errors considered separately.In the following, the angular-temporal covariance matrices will be denoted as $\Gamma(\Delta\alpha, \Delta t)$.

5.2 Modeling the AO loop delay

In order to have a more realistic modeling of the adaptive optics system residual phase error, we include the temporal error induced by the AO loop delay in the AO error budget. The aim here is to study the impact of the estimation error that occurs when the estimator is computed without the knowledge of this temporal delay.

We consider an adaptive optics system whose correction is delayed by Δt. The resulting residual uplink reciprocal phase is expressed as:

$$\Phi_{res}(t) = \Phi_{PAA}(t) - \hat{\Phi}_{PAA}(t - \Delta t) \tag{5.4}$$

5.2.1 Impact on the classical pre-compensation

For the classical pre-compensation case, the phase error becomes:

$$\Phi_{res}(t) = \Phi_{PAA}(t) - \Phi_0(t - \Delta t) \tag{5.5}$$

and its error covariance matrix is then expressed as:

$$\Gamma_{res,delay} = 2\Gamma_{\Phi\Phi}(0,0) - \Gamma_{\Phi\Phi}(\Delta\alpha, \Delta t) - \Gamma_{\Phi\Phi}(\Delta\alpha, \Delta t)^T \tag{5.6}$$

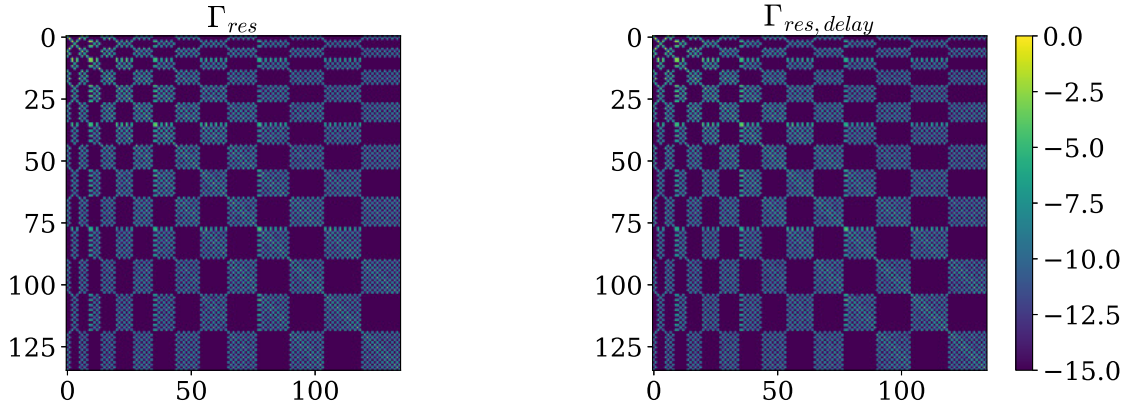

Figure 5.3: Comparison of the phase error covariance matrix without (left) and with (right) temporal error for the MOSPAR 9090 case with classical pre-compensation.

This new covariance matrix is illustrated in Fig. 5.3. We can observe, comparing the error covariance matrix without (on the left) or with (on the right) temporal error induced by the AO loop delay, that they are almost identical.

Figure 5.4 depicts the modal residual phase variance for the classical case without (in black) or with (in red) the temporal error induced by the AO loop delay. We compared the variances obtained analytically (plain lines) with the variances computed from the E2E data (dots). We emulated on the data the AO loop delay by shifting by two samples the phase to correct from its correction. First, we observe a very good accordance between the analytical results and the results obtained from the data. Secondly, we observe that the temporal delay increases the variance of the high order modes. However, we can see that this temporal error is negligible with respect to the anisoplanatic error. It is therefore expected to have very few impacts on the coupled flux statistics.

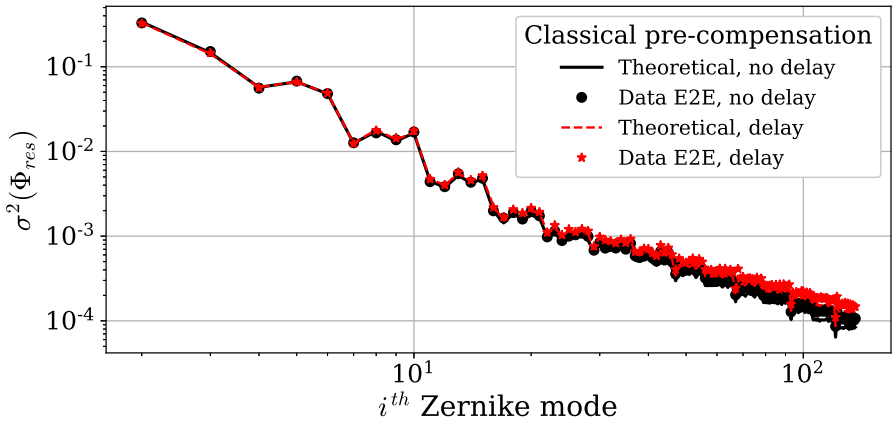

Figure 5.4: Modal residual phase variance function of the Zernike mode for the classical pre-compensation, computed analytically and from E2E data, with and without AO loop delay.

5.2.2 Estimation error induced by the AO loop delay

In the case of the MMSE$_{\Phi\chi}$ estimator described in section 4.4, the residual phase is expressed as:

$$\boldsymbol{\Phi}_{res}(t) = \boldsymbol{\Phi}_{PAA}(t) - \boldsymbol{R}_{MMSE_{\Phi\chi}} \boldsymbol{y}_m(t - \Delta t) \tag{5.7}$$

where the measurement vector $\boldsymbol{y}_m$ corresponds to the delayed phase and log-amplitude measurements on axis and where the reconstructor $\boldsymbol{R}_{MMSE_{\Phi\chi}}$ is computed not accounting for the time delay.

Therefore, the theoretical error covariance matrix obtained with an estimator not accoutning for the temporal delay can be expressed thanks to the formalism developed in section 4.5.1 as:

$$\boldsymbol{\Gamma}^{\mathbf{tempo,wrong}}_{\boldsymbol{\Phi}_{\mathbf{res}}} = \boldsymbol{\Gamma}^{\mathbf{tempo,true}}_{\boldsymbol{\Phi}_{\mathbf{res}}} + \boldsymbol{\Delta R \Gamma}_{\mathbf{y_m y_m}} \boldsymbol{\Delta R}^{\mathbf{T}} \tag{5.8}$$

where $\boldsymbol{\Gamma}^{\mathbf{tempo,wrong}}_{\boldsymbol{\Phi}_{\mathbf{res}}}$ is the phase error covariance matrix including the temporal and angular errors, $\boldsymbol{\Gamma}^{\mathbf{tempo,true}}_{\boldsymbol{\Phi}_{\mathbf{res}}}$ is the phase error covariance matrix with temporal error , when the estimator accounts for the temporal delay and $\boldsymbol{\Delta R}$ is defined as:

$$\boldsymbol{\Delta R} = \mathbf{R}_{MMSE_{\Phi\chi}} - \mathbf{R}^{tempo}_{MMSE_{\Phi\chi}}, \tag{5.9}$$

the difference between the reconstructor with wrong and good priors. The computation of $\mathbf{R}^{tempo}_{MMSE_{\Phi\chi}}$ will be explained later in section 5.3.

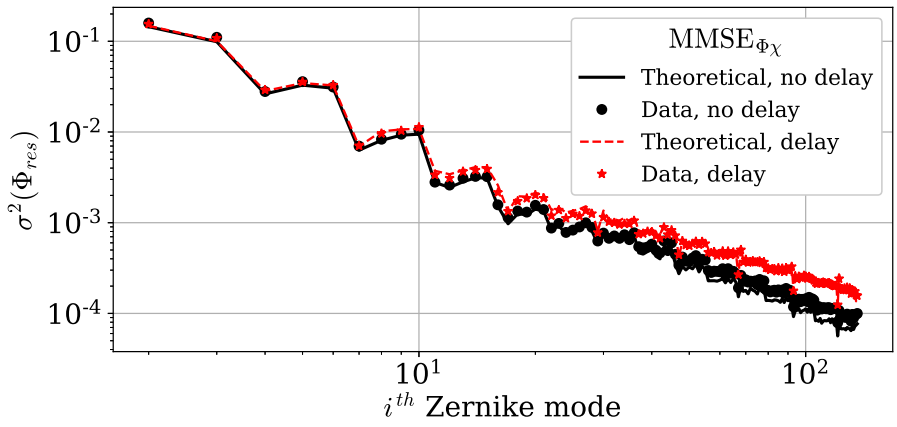

Figure 5.5: Modal residual phase variance function of the Zernike mode for the $MMSE_{\Phi\chi}$ with wrong priors, computed analytically and from data, with and without AO loop delay.

Figure 5.5 depicts the modal residual phase variance resulting from the $MMSE_{\Phi\chi}$ phase estimated method without (in black) or with (in red) the temporal error induced by the AO loop delay. The knowledge of the temporal delay is not taken into account in the estimator computation. We compare the variances obtained analytically (plain lines) with the variances computed from the E2E data (dots). First, we observe as for the classical pre-compensation case a good accordance between the theoretical variances and the variances computed from the data. A slight deviation can be observed for the high order modes variance that is interpreted to be due to numerical error. Secondly, the delay of correction is shown to increase the modal phase variance of the high order modes. However, it seems to have no impact on the tip and tilt estimation, we therefore expect the estimator to improve the fading statistics to be enhanced.

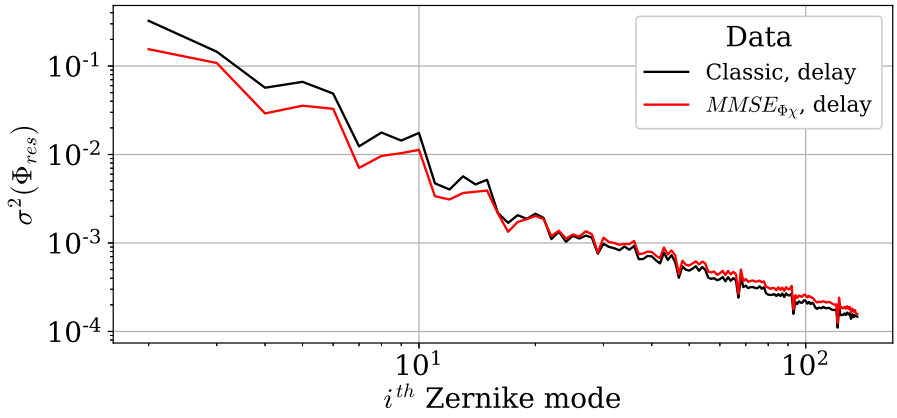

Figure 5.6: Modal residual phase variance function of the Zernike mode for the classical case and $MMSE_{\Phi\chi}$ with wrong priors case, computed from data, with an AO loop delay.

Finally, we compare in figure 5.6 the residual modal phase variance of the classical case compared to the MMSE estimated case with anisoplanatic and temporal error. We plot the variances obtained from the E2E data function of the Zernike mode number. We observe that the MMSE estimated case present a decreased variance for the low order modes and a higher variance for the high order modes in comparison with the classical case. As the low order modes are the most energetic and the modes at the origin of the fades, the estimator is still expected to perform well.

5.2.3 Impact on the coupled flux statistics

Here, we study the impact of the temporal error on the coupled flux statistics for the classical and the $MMSE_{\Phi\chi}$ pre-compensated cases. Figure 5.7 depicts the probability density function and the cumulative density function of the reciprocal uplink coupled flux in both cases, with and without AO loop delay. Considering the classical pre-compensation case, we observe that the temporal error due to the AO loop delay there has very few impacts on either the CDF (on the left) or the PDF. We notice a mean value of 0.36 for the classical case with or without delay, and 0.45 and 0.46 for the estimated case with or without delay. The normalized variance of the signal is not very affected as well, and is equal to 0.15 in the classical case and 0.06 in the estimated case. However, the temporal delay is shown to increase the tail of the MMSE estimated case CDF, and to shift its mean value. Despite this degraded performance, the MMSE estimator shows to still bring the same gain at probability 10^{-3}.

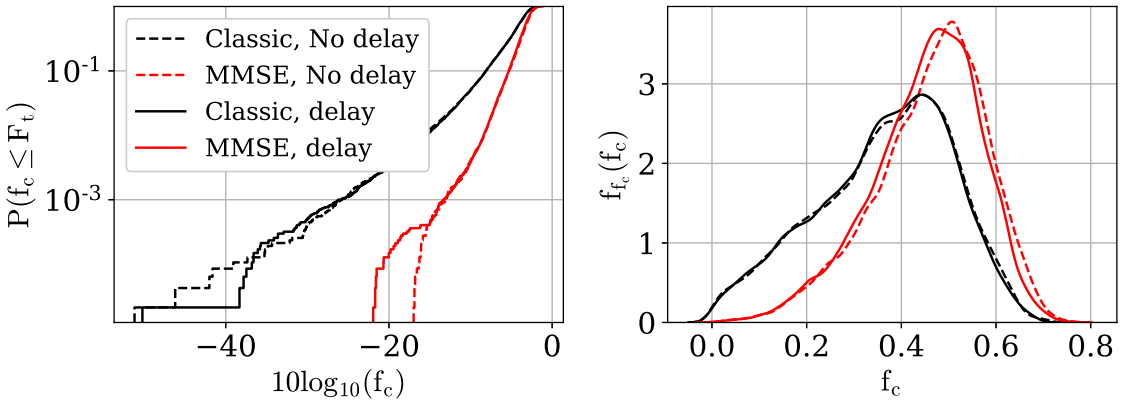

Figure 5.7: On the left, cumulative density function of the coupled flux function of the coupled flux threshold F_c in dBs. On the right, probability density function of the coupled flux. Both functions are plotted for the classical and MMSE case with and without delay.

5.3 Correction of the AO loop delay

We used previously the joint temporal and angular anisoplanatism formalism in order to express the error induced by the AO loop delay, in the classical pre-compensation and the MMSE estimated case, without accounting for the AO loop delay. This study relied on the expression of the analytical covariance matrix of the phase error induced by anisoplanatism and temporal error. Thanks to this formalism, we can also compute the MMSE estimator relying on the good priors, by taking into account the temporal delay of the AO loop in the computation of the estimator at PAA.

To compute the estimate $\hat{\mathbf{\Phi}}_{PAA}(t)$ at instant t, we define the new measurement vector as:

$$\boldsymbol{y}_m(t - 2 \cdot t_{samp}) = \left[\mathbf{\Phi}_0^T(t - 2 \cdot t_{samp}) \quad \boldsymbol{\chi}_0^T(t - 2 \cdot t_{samp})\right]^T \tag{5.10}$$

where t is instant of correction and $t - 2 \cdot t_{samp}$ is the instant of the measurements for an AO system with 2 frames delay.

The influence of the introduced time delay on the measurement vector has evidently no impact on the computation of the autocovariance matrix of the measurement vector. Conversely, the angular covariance matrix will now be computed as following:

$$\mathbf{\Gamma}_{\Phi_{\mathrm{y_m}}}(\alpha_{\mathrm{PAA}}, 2 \cdot \mathrm{t_{samp}}) = \left[\mathbf{\Gamma}_{\Phi\Phi}(\alpha_{\mathrm{PAA}}, 2 \cdot \mathrm{t_{samp}}) \quad \mathbf{\Gamma}_{\Phi\chi}(\alpha_{\mathrm{PAA}}, 2 \cdot \mathrm{t_{samp}})\right] \tag{5.11}$$

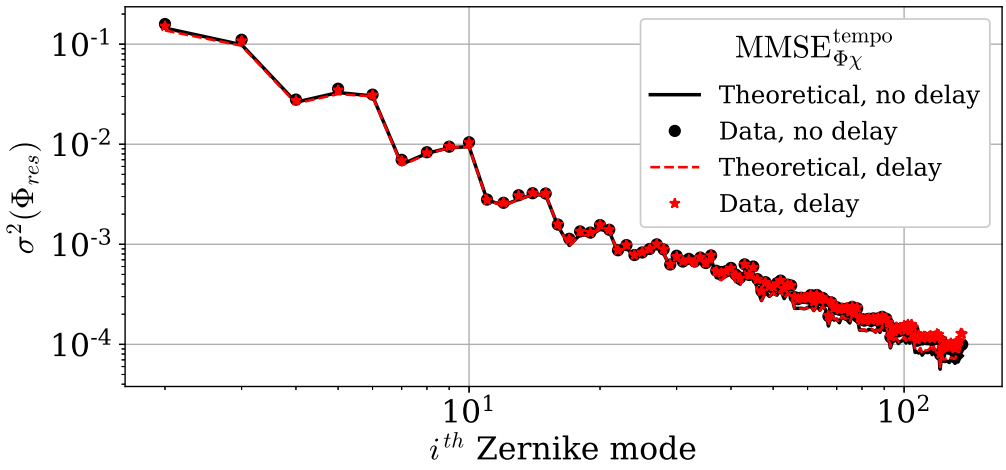

Figure 5.8: Modal residual phase variance function of the Zernike mode for the $MMSE^{tempo}_{\Phi\chi}$ with good priors, computed analytically and from data, with and without AO loop delay.

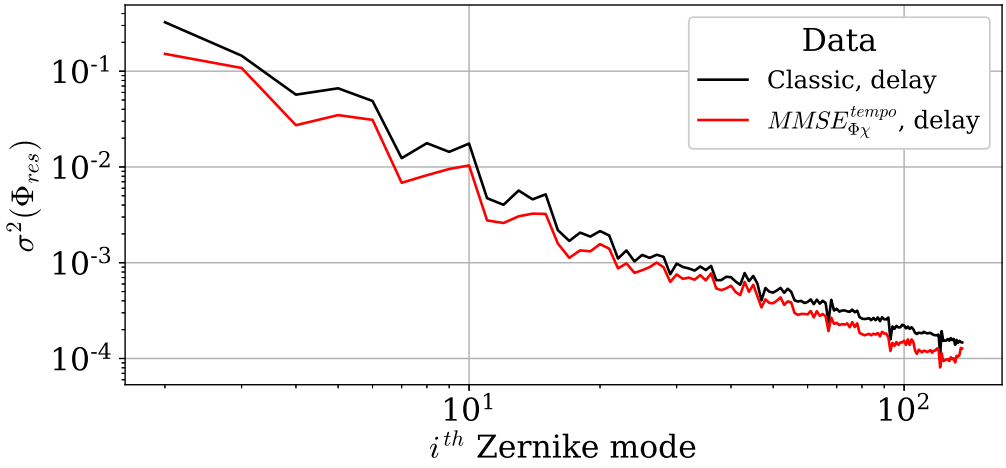

Figure 5.9: Modal residual phase variance function of the Zernike mode for the classical case and $MMSE_{\Phi\chi}$ with good priors case, computed from data, with an AO loop delay.

Therefore, one can compute the new reconstructor as described in section 4.4.

Figure 5.8 depicts the modal residual phase variance obtained with the new estimator $MMSE^{tempo}_{\Phi\chi}$ that is computed using the good priors (red), compared with the case without AO loop delay (black). This case differs from the case presented in section 5.2 because the estimator now account for the loop delay when there is one. We also plot the theoretical and obtained from E2E data phase variances. First, we still observe a good accordance between the theory and the E2E data. Secondly, we observe that the variances with or without delay are superimposed, meaning that the estimator has completely corrected the temporal error.

Figure 5.9 compares the modal residual phase variance computed from the data for the classical case with AO loop delay and the new estimated case, taking into account the temporal delay in the construction of the estimator. In this case, we observe that the $MMSE^{tempo}_{\Phi\chi}$ estimator decrease the variance of all the modes.

The resulting coupled flux statistics are depicted in figure 5.10. In this case, we can see both in the cumulative density function and the probability density function that the MMSE estimated case using the knowledge of the temporal priors in presence of AO loop

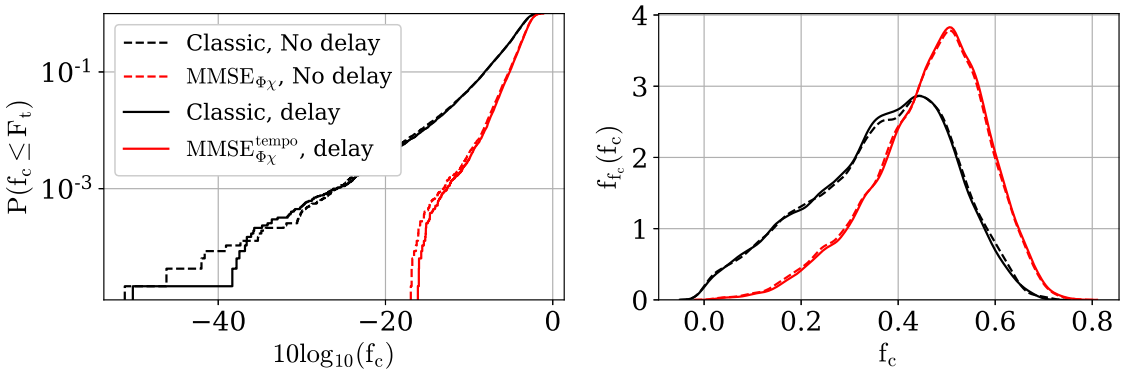

Figure 5.10: On the left, cumulative density function of the coupled flux function of the coupled flux threshold F_c in dBs. On the right, probability density function of the coupled flux. Both functions are plotted for the classical and $MMSE^{tempo}_{\Phi\chi}$ case with and without delay.

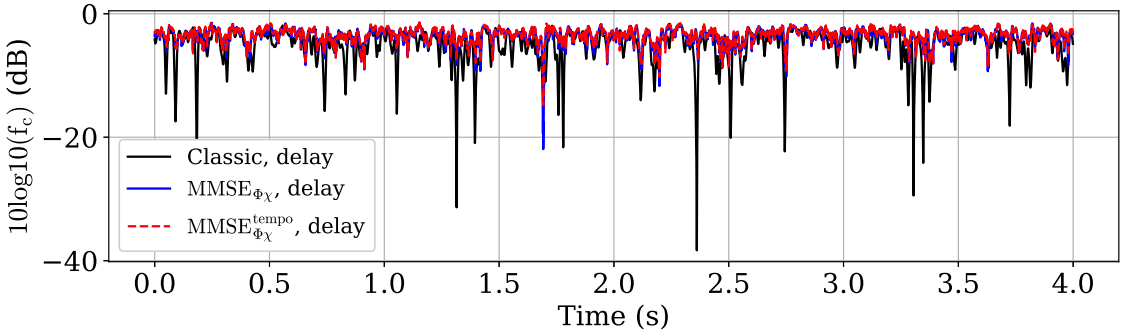

Figure 5.11: Coupled flux time series in dBs for the classical pre-compensation case with temporal error due to the AO loop delay (black), the $MMSE_{\Phi\chi}$ case with temporal error and the estimator not accounting for the delay in the priors (blue), and the $MMSE^{tempo}_{\Phi\chi}$ case with temporal error and the estimator accounting for the delay in the priors (red).

delay performs the same and even slightly better in the case of fading reduction than the case without AO loop delay.

Finally, we study the impact on the time series of the different estimation methods (with good or wrong priors and with an AO loop delay) in figure 5.11. We plot a sample of 4s time series. We observe that while the estimator $MMSE_{\Phi\chi}$ still suppresses many fades, some fades are persistent and are reduced by using the $MMSE^{tempo}_{\Phi\chi}$ estimator.

5.4 Estimation at N time steps

We previously showed that we can use the temporal statistical turbulence a priori in order to correct for the temporal error induced by the AO loop. To go further, we propose to use several phase and log-amplitude measurement time steps in the past in order to bring further information to the estimation. This idea of using several past time steps to estimate a wavefront can be found in the literature in the domain of predictive control in [179, 182], in order to correct for the downlink temporal error in the case of moving targets (slewing satellite for instance). However, the impact and gain of such an estimation using past measurements in order to estimate the uplink pre-compensation phase, mixing angular and temporal anisoplanatism and using log-amplitude correlations, has not yet been studied.

5.4.1 Analytical estimator

We define the new measurement vector as:

$$\boldsymbol{y}_m(t) = \left[\boldsymbol{\Phi}_0^T(t - 2 \cdot t_{samp}) \quad \boldsymbol{\chi}_0^T(t - 2 \cdot t_{samp})^T \quad \cdots \quad \boldsymbol{\Phi}_0^T(t - N \cdot t_{samp}) \quad \boldsymbol{\chi}_0^T(t - N \cdot t_{samp})\right]^T \tag{5.12}$$

with N-2 the number of selected past time steps used in the estimation.

As it is less direct than for the one-step estimation, we will fully describe the covariance and autocovariance matrices needed to compute the reconstructor.

The autocovariance of the measurement vector is expressed as follows:

$$\Gamma_{y_m y_m}(0) = \begin{pmatrix} \Gamma\Gamma_0(0) & \Gamma\Gamma_0(-1 * \Delta t) & \dots & \Gamma\Gamma_0(-(N-2) * \Delta t) \\ \Gamma\Gamma_0(1 * \Delta t) & \Gamma\Gamma_0(0) & \dots & \Gamma\Gamma_0(-(N-3) * \Delta t) \\ \vdots & \vdots & \ddots & \vdots \\ \Gamma\Gamma_0((N-2) * \Delta t) & \dots & \dots & \Gamma\Gamma_0(0) \end{pmatrix} \tag{5.13}$$

where we factorize:

$$\Gamma\Gamma_{\Delta\alpha=0}(\Delta t) = \begin{pmatrix} \Gamma_{\Phi\Phi}(\Delta\alpha, \Delta t) & \Gamma_{\Phi\chi}(\Delta\alpha, \Delta t) \\ \Gamma_{\chi\Phi}(\Delta\alpha, \Delta t) & \Gamma_{\chi\chi}(\Delta\alpha, \Delta t) \end{pmatrix} \tag{5.14}$$

Additionally, the covariance matrix is expressed as the combination of the following N-2 block matrices:

$$\Gamma_{\Phi y_m}(\alpha_{PAA}) = \begin{pmatrix} \Gamma\Gamma_{\alpha_{PAA}}(\Delta t) & \Gamma\Gamma_{\alpha_{PAA}}(-1 * \Delta t) & \dots & \Gamma\Gamma_{\alpha_{PAA}}(-N * \Delta t) \end{pmatrix} \tag{5.15}$$

where each block matrix is one entity corresponding to one time delay expressed as:

$$\Gamma\Gamma_{\Delta\alpha=\alpha_{PAA}}(\Delta t) = \begin{pmatrix} \Gamma_{\Phi\Phi}(\Delta\alpha, \Delta t) & \Gamma_{\Phi\chi}(\Delta\alpha, \Delta t) \end{pmatrix} \tag{5.16}$$

We note that the relative sign of the temporal and angle delay play an important role to compute the accurate estimator.

Thanks to these two covariance matrices, following equation 4.4 from section 4.2, one can compute the associated MMSE reconstructor.

5.4.2 Estimator performance

5.4.2.1 Residual phase variance

We study here the gain brought by the estimator taking into account N-2 time steps in the past. We study the cases of a measurement vector accounting for 1, 2 and 3 past time steps.

Figure 5.12 depicts the total residual phase variance on 135 modes (from 2 to 136) as well as the tip and tilt residual phase variance function of the number of time steps considered. We note the case of zero time step is the classical pre-compensation case (without estimation) and that the one time step case corresponds to the estimator of section 5.3. We observe that adding a second time step further decreases the residual phase variance by 62% with respect to the classical pre-compensation case. The tip and tilt variance is as well decreased. However, adding a third time step does not improve the estimation. This corroborates the results from [179], that highlights that the estimation converges for a two step measurements in the past.

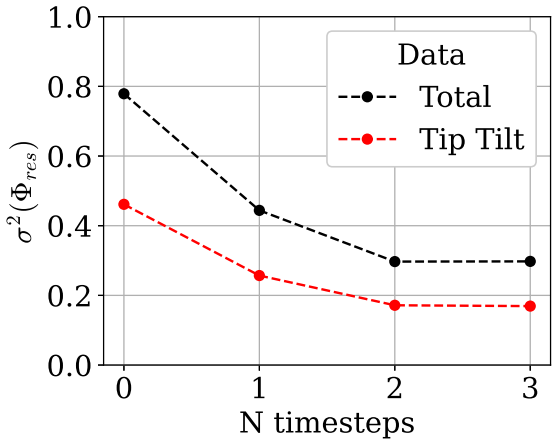

Figure 5.12: Total residual phase variance computed on data for the MOSPAR 9090 case at 30° elevation, function of the number of time steps considered in the estimation. The black curve represents the total over 135 Zernike modes, and the red curve the total of the tip and tilt variance. The case 0 time step corresponds to the classical pre-compensation.

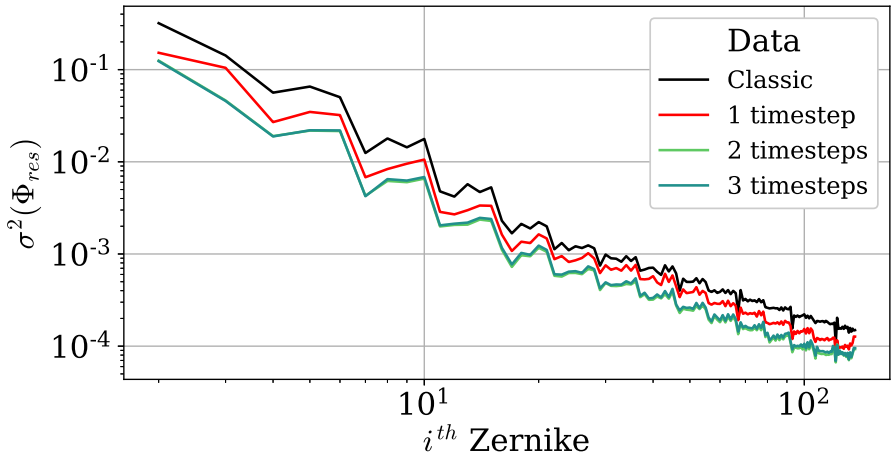

Figure 5.13: Modal residual phase variance function of the Zernike mode for the classical case with an AO loop delay and the several time steps estimated case with good priors, computed from data, for 1, 2 and 3 time steps.

We represent the associated modal spectrum computed from the E2E data in figure 5.13, function of the Zernike mode number, for the 4 case of correction (classic, 1, 2, and 3 time steps in the measurement vector). We observe that the 2 and 3 time steps spectrum curves are merged, showing that the third time step does not bring improvement to the estimation. Additionally, the second time step decrease the modal variance on all the modes, including the tip and tilt.

We plot in figure 5.14 the rows of the reconstructor using two time steps for the estimation, corresponding to the tip correction, the tilt correction and the $50th$ mode correction. The blue zones corresponds to the weighting brought by the phase projections on-axis measurements, while the orange/yellow zones corresponds to the weighting brought by the on-axis log-amplitude measurements. On the contrary to the reconstructor not accounting for temporal priors from chapter 4, we observe that the phase brings information, in addition to the log-amplitude. We notice that this is the case especially for the high orders' estimation.

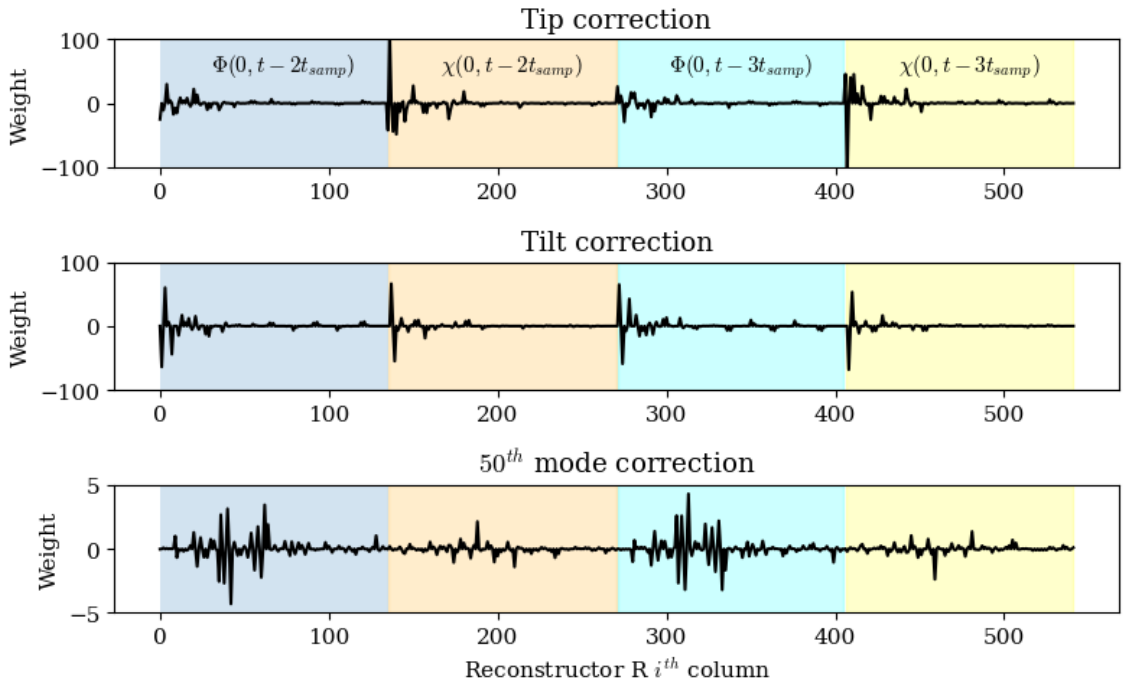

Figure 5.14: Rows 0, 1 and 48 of the reconstructor, corresponding to the weights applied to the measurement vector, in the two steps estimation case.

5.4.2.2 Impact on the coupled flux

The resulting coupled flux statistics are depicted in figure 5.15. In this case, we can see both in the cumulative density function and the probability density function that the MMSE estimated case computed from two and three previous time steps brings a significant gain, both reducing the tail of the CDF and improving the mean and variance of the PDF. The gain at probability 10^{-3} with respect to the classical case is now equal to 17 dBs. We note that, as expected, the estimated case with three time steps does not bring improvement with respect to the case estimated with two time steps.

Figure 5.16 depicts the associated time series for the classical case with AO loop delay (black), the estimated case with one previous time step (red), and the estimated case with two previous time steps (green). We did not plot the 3 time steps estimated case, as it is

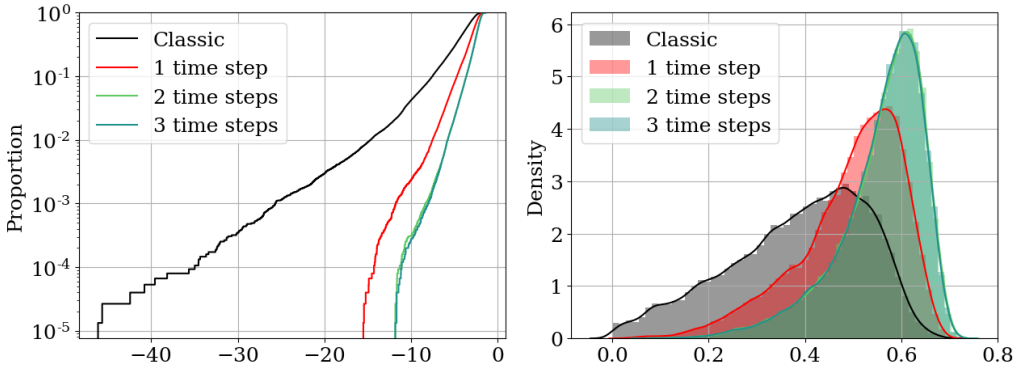

Figure 5.15: On the left, CDF of the coupled flux function of the coupled flux threshold F_c in dBs. On the right, PDF of the coupled flux. Both functions are plotted for the classical and $MMSE_{\Phi\chi}$ estimated case with 1, 2 and 3 previous time steps in the measurement vector.

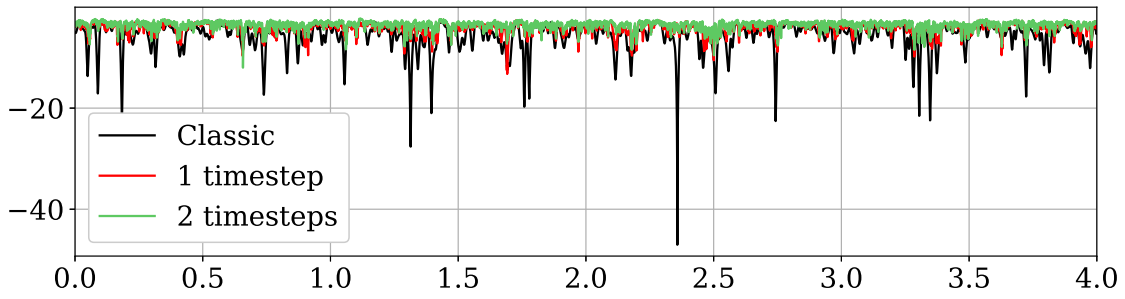

Figure 5.16: Coupled flux time series in dBs for the classical pre-compensation case with temporal error due to the AO loop delay (black), the $MMSE_{\Phi\chi}$ case with temporal error computed from one previous time step (red) and two previous time step (green).

shown to perform the same as the 2 time steps case. We observe that the two time steps case still reduces the number depth and duration of the fades of the signal.

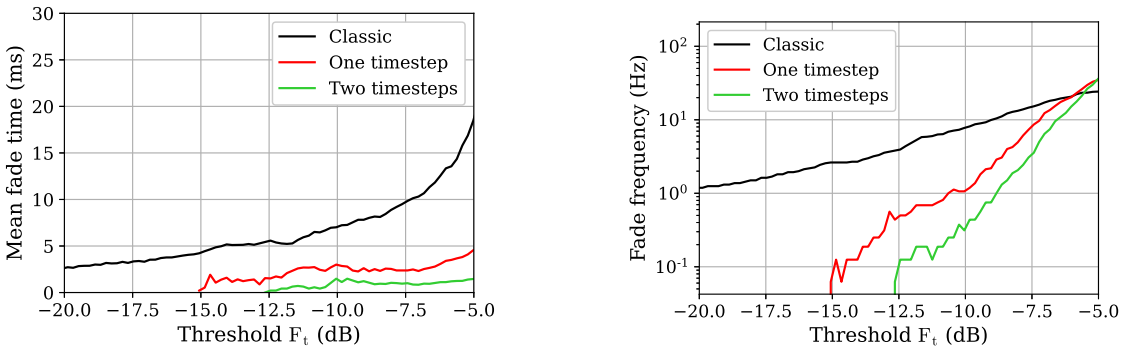

(a) Mean fade duration

(b)

Figure 5.17: Fade statistics for the classical pre-compensation, the one time step MMSE estimated and the two time steps MMSE estimated case. (a) Mean fade duration function of the coupled flux threshold. (b) Fade frequency function of the couple flux threshold.

Finally, to highlight the improvement on the signal temporal statistics, we plot in figure 5.17 the fade statistics of the signal, depicting on the left the mean fade duration and on the right the fade frequency, for the classical case, the one time step (red) and two time steps (green) estimation cases. We observe that the mean fade time is limited to 3 ms for a threshold between -10 dBs and -5 dBs for the two time steps estimated case, that is reduced with respect to the one time step estimated case (that is below 5 ms), and reduced with respect to the classical case with a mean fade time going from 7 to 20 ms in the same range. We also observe that the fades are less frequent for the two time steps estimated case for every value of the threshold.

5.4.3 Impact of wind speed and loop frequency on the performance

Previously, we presented the possibility to estimate the phase at point ahead angle based on several downlink phase and log-amplitude past measurements. It shows to greatly improve the performance of the link (both to decrease the residual phase variance and improve the coupled flux statistics). As mentioned, this estimator relies on temporal measurements, which depend on the turbulence dynamic behavior and the frequency of measurement acquisition and AO loop delay (whose duration varies with the loop frequency). Therefore,

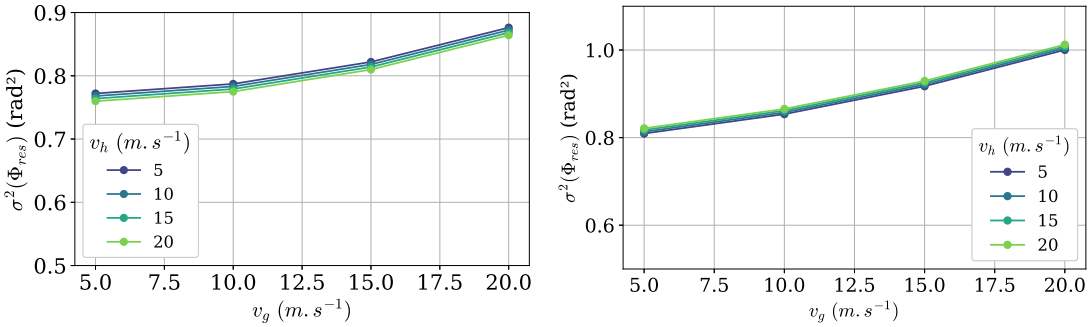

(a) Wind in the direction of the PAA

(b) Wind direction opposite to the PAA

Figure 5.19: Total residual phase variance function of the ground layer wind speed, for different tropopause wind speed, for the MOSPAR 9090 turbulence case, for the classical AO pre-compensation.

it seems important to study this estimator gain for several temporal behaviors of the turbulence led by the wind speed, within the Taylor Frozen flow turbulence hypothesis.

We recall that the wind is assumed to follow a Bufton wind profile, defined in section 2.2.3.1. This model depends on v_g the wind speed at the ground or low altitude and v_t the wind speed at the tropopause.

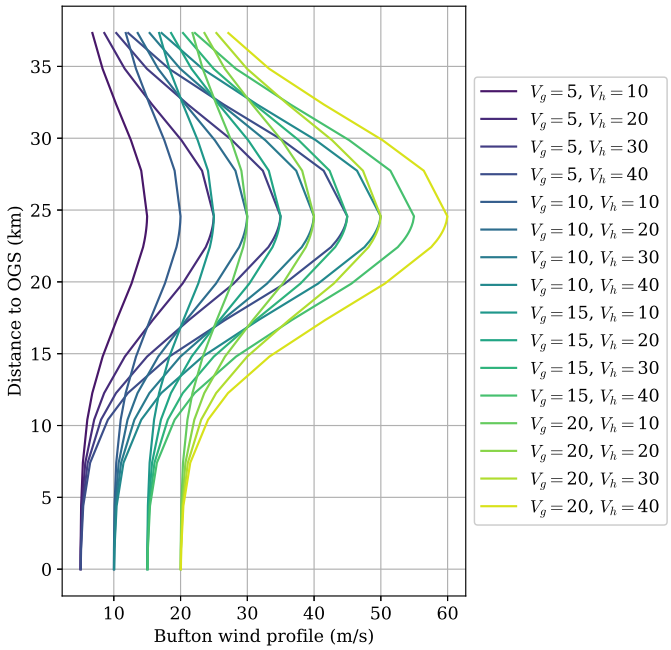

Figure 5.18: Bufton wind speed profile (m/s) function of the distance to the OGS on the line of sight, for different combinations of ground layer and tropopause wind speed.

We expect the tropopause wind speed to impact the anisoplanatic phase behavior and the ground layer wind speed to impact the absolute value of the phase. To study this hypothesis, we consider several couples $(v_g, v_t) \in \{5, 10, 15, 20\} \times \{10, 20, 30, 40\}$, with the associated Bufton wind profiles illustrated in figure 5.18.

We start by studying the impact of the wind speed on the anisoplanatic residual phase with temporal error. Figure 5.19a depicts the total residual phase variance computed on 136 Zernike modes function of the ground layers wind speed, for different tropopause wind

speeds (depicted in different colors), for $f_{samp} = 4700\ Hz$. First, we observe that the residual phase variance increases with the ground layer wind speed. This shows that the temporal error contribution to the phase variance is very sensitive to the ground layer turbulence. On the contrary, we observe that the higher is the wind at the tropopause, the lower is the residual phase variance, with however a tiny difference in absolute value. We explain this small gap in absolute value due to the low temporal error induced by higher layer turbulence (which is much weaker than ground layer turbulence).

Additionally, the increase of the residual phase variance with the decrease of the wind speed is related to the wind-speed direction. In the case of figure 5.19a, the wind speed is in the direction of the PAA. Hence, the distance between the beam footprint at PAA and the past downlink beam footprint is reduced, with respect to a case without temporal error. Consequently, the joint angular-temporal anisoplanatic error is smaller. We expect this behavior to be reversed in the case of a wind in the opposite direction. We plot in figure 5.19b the results obtained for an opposite wind direction. It is confirmed that the residual phase variance is higher for high tropopause wind speeds, resulting from more spaced beam footprints. Overall, we notice a larger residual variance, and a phase variance that increases with v_g, as in figure 5.19a.

Secondly, we study the estimator gain for the different wind conditions. We plot in figure 5.20 on the left the absolute value of the total residual phase variance function of the ground layer wind speed, for the different tropopause wind speeds (represented in different colors). The reduction gain is plotted on the right of the figure. The residual phase variance is computed for the classical pre-compensation case with temporal error (plain lines), the 1 time step (dashed lines), 2 time steps (dotted lines), and 3 time steps (dots) $MMSE_{\Phi\chi}$ pre-compensated cases. The classical pre-compensation case is the same as in figure 5.19a. First, we observe that whatever the phase estimation technique used, the residual phase variance is insensitive to the rise of the ground layer wind speed, on the contrary to the phase variance without phase estimation (classic). This means that the estimator accounting for temporal priors corrects for the temporal error induced by ground layers. Secondly, the estimator taking into account one time step has the same absolute residual phase variance (and reduction gain) for different tropopause wind-speed. However, by adding past measurements (2 or 3), we observe a greater estimator gain as the tropopause wind-speed increase. We interpret this behavior as the consequence of adding temporal measurements that inform the estimator on the temporal process of the turbulence, allowing therefore to improve the estimation. Finally, the best estimator gain is found to be obtained when both the ground and tropopause wind speeds are the highest,

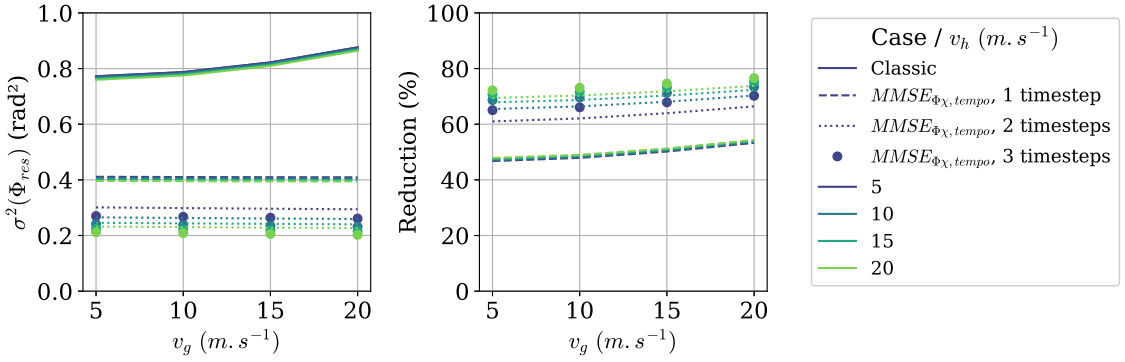

Figure 5.20: On the left, absolute residual phase variance function of the ground wind-speed, on the right, reduction gain function of the ground wind-speed, for several tropopause wind-speed, in the MOSPAR 9090 turbulence case. The wind direction is in the direction of the PAA.

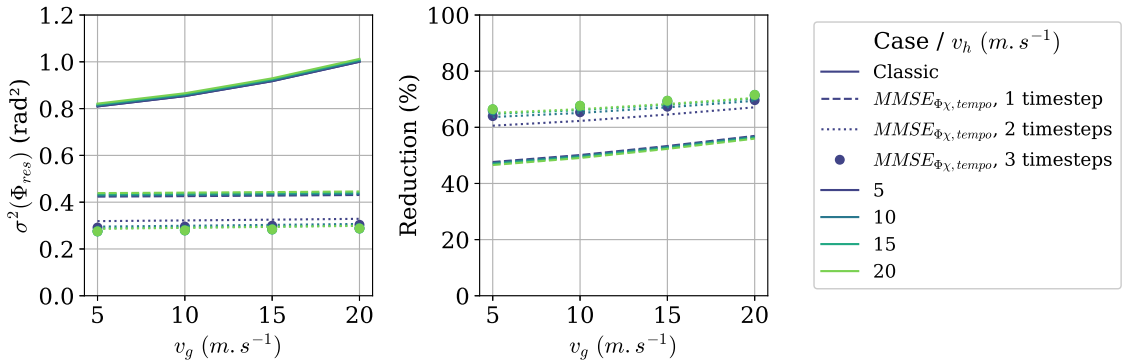

Figure 5.21: On the left, absolute residual phase variance function of the ground wind-speed, on the right, reduction gain function of the ground wind-speed, for several tropopause wind-speed, in the MOSPAR 9090 turbulence case. The wind direction is in the opposite direction from the PAA.

reaching more than 75% of residual phase reduction.

When studying the same curves in figure 5.21, for a wind direction at the opposite to the PAA, we observe in the same way, the same amount of phase reduction with respect to the one step estimation. We notice that in this scenario, the classical, and the one time step estimation pre-compensation errors are conversely affected by the wind direction, with an error (slightly) increasing with the tropopause wind speed increasing. However, when adding a second or a third time step in the estimation, this trend is reversed. In these cases, we also observe a smaller gain brought by several time steps in the estimation. This gain is also less sensitive to changes in the tropopause wind speed.

To conclude, we studied the impact of the wind speed strength and direction on the pre-compensation phase error variance. Focusing on the impact of the wind strength at the ground layers, we've shown that it mostly impacts the temporal error induced by the loop delay, and that the classical residual phase variance was increasing when v_g increases, whatever the wind direction. We've shown that this temporal error was compensated when using the phase estimator using one time step in the measurements. In this case, the residual phase variance is constant when v_g increases. Concerning the tropopause wind influence, we showed that the classical pre-compensation phase error was sensitive to the wind direction and norm. It is because the anisoplanatism error between the downlink beam footprint at instant $t-\Delta t$ and the uplink beam footprint at instant t in high altitude, are either closer or farther, function of the wind direction. This lead to reduce or increased angular error. The one step estimation method is shown to still be sensitive to this wind direction. However, the two and three steps estimation are less sensitive to this parameter. Overall, the gains are shown to reach, at best, nearly 80%, with a three steps estimation, when the wind is in the PAA direction, and that both the ground and tropopause wind speeds are high. We insist on the fact that this study only informs on the strength of the pre-compensation phase error impacted by the AO loop delay and the reduction of this error thanks to past measurements. However, it does not inform on the temporal evolution of the phase nor of the coupled flux. This evolution has been studied in [5] through numerical studies, showing that slower wind speeds led to longer fades. We also underline that the provided formalism allow computing the modal residual phase temporal autocorrelation function, and will be the topic of future developments.

5.5 Extension to the pre-compensated LEO uplink case

We've shown previously that using several past time steps in the measurement vector allowed greatly reducing the pre-compensation phase error in the GEO case. However, in order to apply this method, it is necessary to have measurements of the wind profile, in addition to C_n^2 profile measurements, which can be challenging. This is less challenging in LEO configurations, where the temporal effects are dominated by the slew rate of the satellite, which is deterministic. Therefore, in this section, we consider the ability of the method to improve a pre-compensation in the LEO case. The temporal priors are already exploited in the framework of LEO optical downlink optimal control, as studied in the thesis of Pablo Robles [185], in order to correct for the temporal delay induced by the loop delay. The LEO case presents several other differences with respect to the GEO case, that are:

- A link budget less constrained due to the distance of the LEO satellite that is much closer to the earth than the GEO satellite,
- A greater point-ahead angle that evolves with the elevation of the slewing satellite, therefore, a stronger anisoplanatism is expected, if a pre-compensation based on the downlink beam is applied,
- An AO link budget with a stronger contribution of the temporal error due to the slew rate of the satellite.

In the literature, because of the less constrained link budget and the strong anisoplanatism conditions, with point ahead angles in the order of 50 µrad, the choices to operate LEO optical uplinks has turned to OGS geometries with several small apertures without AO pre-compensation. This choice allows not being limited by phase distortions. Therefore, the questions we aim at answering in this section are:

- is there a gain in pre-compensating LEO uplinks with medium size emission apertures with respect to completely uncompensated uplinks with small apertures ?
- if there is a gain: is it possible to use the temporal estimation methods knowing only the slew-rate ?

Uplink pre-compensation for LEO links have been very few studied in the literature, however, recent studies from [171] and [186] concluded that it was beneficial to use a classical pre-compensation to improve the uplink link budget. Therefore, we build our study on these analyses, to investigate if estimated pre-compensation methods, using temporal priors, can further benefit the LEO uplink link budget and signal statistics.

5.5.1 LEO scenario considered

5.5.1.1 Link geometry

We consider a satellite at 400 km, when the satellite is at the zenith ($\Theta = 90°$), whose trajectory is assumed zenithal. We consider elevations from 20 to 90°. For a satellite at this distance, computing the orthogonal speed of the satellite $v_{sat,\perp}$, that is depicted in figure 5.22, we can compute the point-ahead angle per elevation. Both the distance, the orthogonal speed and resulting PAA are plot in figure 5.22. We observe that the satellite distance almost doubles for low elevations. As the elevation increases, the orthogonal speed of the satellite increases, reaching its maximum at zenith. As the PAA is linearly related to the orthogonal satellite speed, we also observe an increase of the PAA with respect to

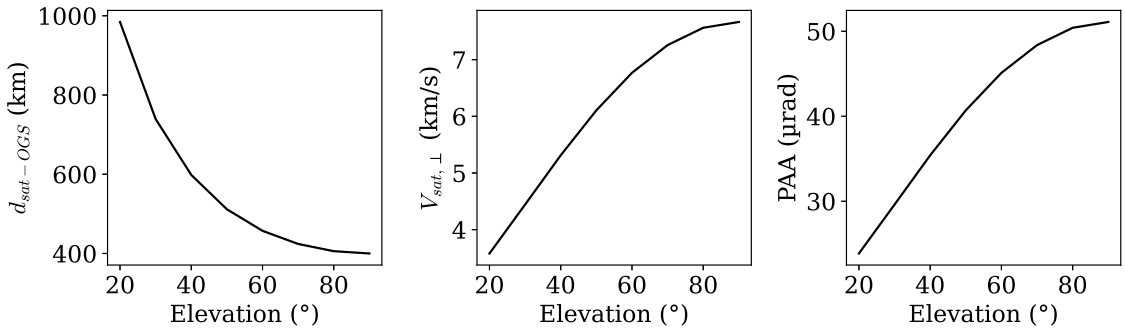

Figure 5.22: Satellite distance, orthogonal speed and point-ahead angle function of the elevation.

the elevation. It is minimum at 20° elevations, with a PAA of 23.86 µrad and maximum at 90° with a PAA of 51.09 µrad.

5.5.1.2 Turbulence conditions

We consider a turbulence profile MOSPAR 7575, whose anisoplanatic angle and Fried parameter have a 0.75 probability to be above the chosen value. This atmospheric profile integrated parameters are varying with the elevation, as the optical path within the layers increases with the elevation decreasing. The integrated parameters function of the elevation are plotted in figure 5.23. The Fried parameter r_0 is shown to evolve, from the lower elevation to the higher, between 4 cm and 8 cm, the anisoplanatic angle θ_0 from 4.6 to 25.6 µrad and the scintillation index from 0.1 to 0.01. It is interesting to comment on the respective evolution of the PAA with respect to the anisoplanatic angle. We also computed the fraction θ_{PAA}/θ_0. It is shown not to evolve much, and start increasing at low elevations, being equal to approximately 2 at zenith and 5 at 20° elevation. Therefore, the pre-compensation anisoplanatism is expected to be more degraded in the low elevations' regime. We also note that, whilst studying a link at low elevations, the scintillation conditions for the chosen C_n^2 profile still belong to the Rytov regime. Therefore, the developed analytical and pseudo-analytical models are still valid. Additionally, we consider a Bufton wind profile with $v_g = 10$ m/s and $v_t = 20$ m/s, as specified in section 2.7.2.

5.5.1.3 OGS geometry and AO sizing

The aim of using an AO pre-compensation is to correct for phase disturbances and, therefore, be able to take advantage of larger emission aperture diameter in order to benefit

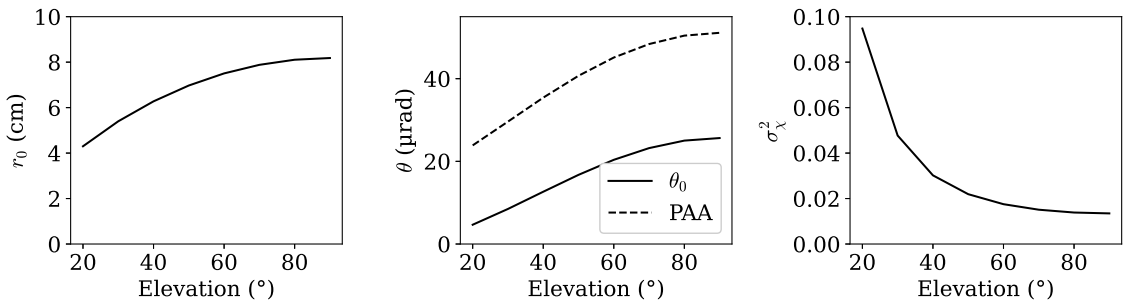

Figure 5.23: Atmospheric parameters function of the elevation. From the left to the right: Fried parameter, anisoplanatic angle, log-amplitude variance.

from the antenna gain. Therefore, we consider three emission aperture cases: a 40 cm Tx aperture for the pre-compensated cases, that we compare to 20 cm and 5 cm Tx aperture for uncompensated cases, that are cases where the signal is dominated by log-amplitude fluctuations, in the reciprocal point of view. The 40 cm case corresponds to the considered pre-compensated scenarios in [171, 186], while the 20 cm and 5 cm apertures corresponds to current uplink schemes, as the one used in the TBIRD NASA project, having four 7.5 cm apertures to operate the uplink at low data-rates [187].

At the satellite, we consider two different aperture diameters: a 20 cm case, which is within the range of considered apertures in [171, 186], and also consider a 2 cm aperture. This small diameter would be more suitable for uplinks with low-cost LEO satellites, as CubeSats, like the TBIRD's one [188].

For the AO design, we consider the number of modes used for the LEO downlink correction. We take the number of modes of the station FEELINGS, that aims at operating links with LEO satellites. Therefore, we keep 136 AO modes of correction. Still considering the FEELINGS design, we set the loop frequency at 4700 Hz.

5.5.2 Link budget before turbulence losses

We adapt the link budget from section 2.7.3 to the LEO case. Indeed, several parameters varies between the LEO and GEO case. First, the antenna gains need to be adapted for the new Tx and Rx aperture sizes. Secondly, the satellite distance and the length of the optical path changes with the elevation. Therefore, the losses induced by the free space atmospheric losses, varies with the satellite distance, and the absorption losses varies with the length of the optical path through the atmosphere. To compute the absorption variation, we apply the formula from [189], computing the absorption as $L_{abs}^{dB} = 10\log_{10}(a_{abs}^{1/\sin\Theta})$, where a_{abs} is the atmosphere transmission coefficient at zenith ($\Theta = 90$). We assume clear sky conditions and neglect scattering. The resulting losses function of the elevation are depicted in figure 5.24.

Contribution (zenith)	$D_{OGS} = 40\ cm$	$D_{OGS} = 20\ cm$	$D_{OGS} = 5\ cm$	unit
P_{Tx}	30	30	30	dBm
G_{Tx}	117.26	111.24	99.2	dB
G_{Rx} (D=25 cm/D=2 cm)	113.1/91.2	113.1/91.2	113.1/91.2	dB
a_{fso}	-250	-250	-250	dB
L_{abs}	-0.5	-0.5	-0.5	dB
a_{Tx}	-3	-3	-3	dB
a_{Rx}	-3	-3	-3	dB
$L_{pointing}$	-2	-2	-2	dB
Total before turbulence	1.86/-20.04	-4.14/-26.04	-16.2/-38.1	dBm
Required sensitivity (OOK)	-41	-41	-41	dBm
Link margin	3	3	3	dB
Link margin before turb	39.8/17.9	33.8/11.9	21.8/-0.1	dB

Table 5.1: Link budget for a LEO link for different Tx/Rx aperture sizes, at zenith.

The new link budget for the LEO case is given in table 5.1, with the new link margin before turbulence attenuation, for the same detection properties (25 Gbps OOK). We note that the link margin is in every case much higher than the one obtained in the GEO case,

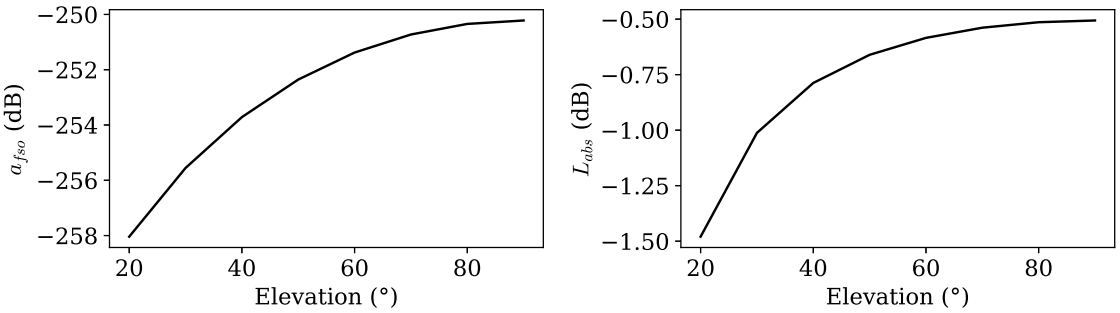

Figure 5.24: Evolution of the atmospheric absorption and the free-space losses function of the elevation.

except in the case of the Tx aperture of 5 cm and Rx aperture of 2 cm. Actually, the latter aperture' scenario is usually used in a multi-Tx scheme at much lower data-rates ($\sim$ kbps).

5.5.3 Impact of the pre-compensation

We study the impact of pre-compensating the LEO uplink in the 40 cm Tx aperture scenario. First, we analyze the anisoplanatic error induced by the classical pre-compensation. Secondly, as we aim to exploit the link temporal priors, we also study the ability to estimate the phase at point ahead angle for the different satellite elevations using several past time steps, in the case where the natural wind profile is known, and in the case where we only know about the satellite slew-rate. For every case, we account for the phase error induced by the AO loop delay.

5.5.3.1 Classical pre-compensation

Figure 5.25 depicts the modal residual phase variance for the classical pre-compensation case, that is affected by anisoplanatic and temporal errors, for each considered elevation. We observe the variance increasing while the elevation decreases. This behavior was expected, since the ratio θ_{PAA}/θ_0 increases when the elevation decreases.

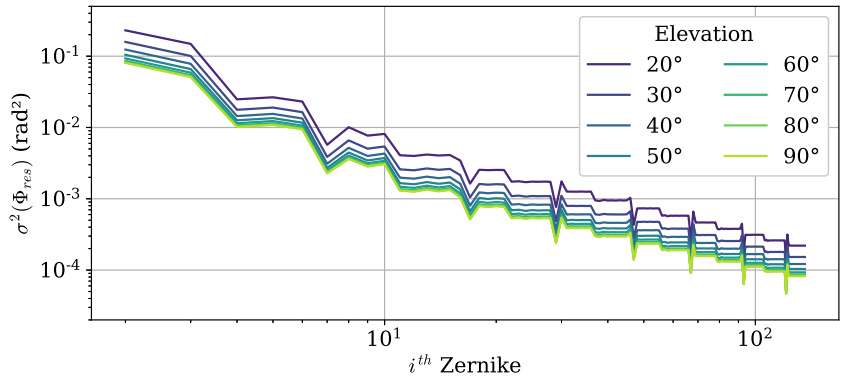

Figure 5.25: Modal residual phase variance function of the Zernike mode number, for the classical AO pre-compensation, for elevations from 20 to 90°.

We also compare the modal residual phase variance with anisoplanatic error and with or without temporal error on figure 5.26, in order to highlight the impact of the temporal

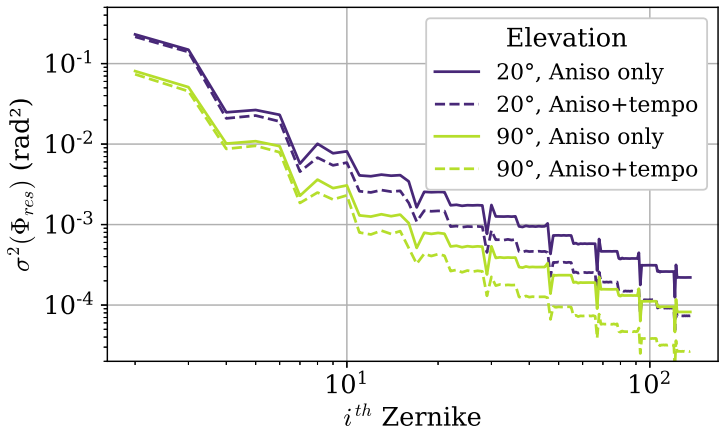

Figure 5.26: Modal residual phase variance function of the Zernike mode number, for the classical AO pre-compensation, for elevations from 20 to 90°. The plain line represents the joint anisoplanatic and temporal error, and the dashed lines the anisoplanatic only error.

error. We depict on this figure the case for the 20 and 90° elevation. We observe that the temporal error barely affects the tip and tilt error, and start increasing for modes higher than order 3, with a strong impact on high order modes. It also seems that the 90° case is more affected by the temporal error than the 20° elevation case. This is due to a higher slew rate, as the satellite orthogonal speed is maximum at 90° elevation.

5.5.3.2 With natural wind knowledge

We now apply the $MMSE_{\Phi\chi}$ estimator computed thanks to several time steps to the LEO scenario, as described in section 5.4, in order to decrease the pre-compensation phase error. In this section, we assume to be able to measure the natural wind profile and the C_n^2 profile, to compute the analytical estimator.

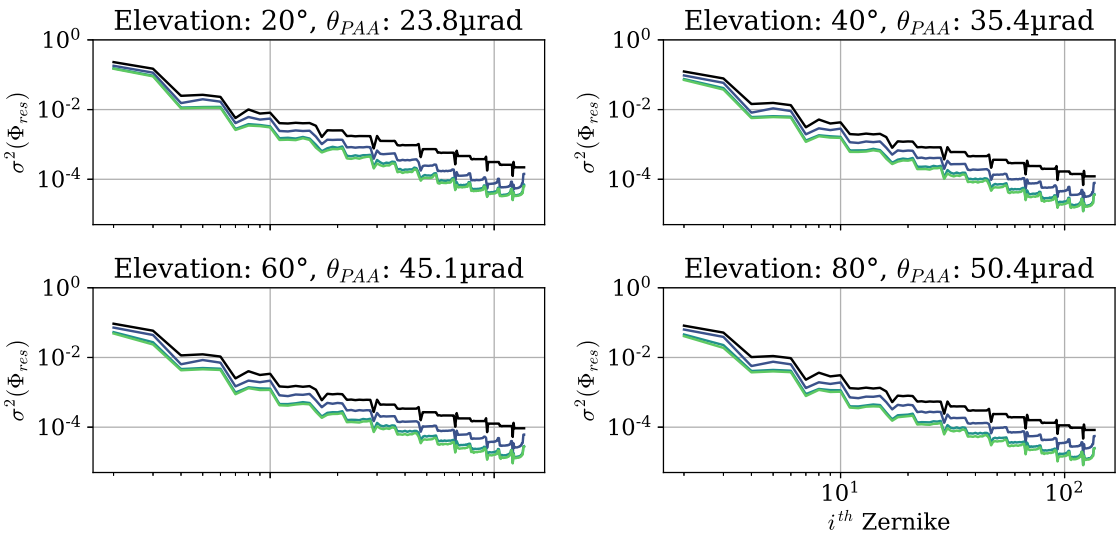

Figure 5.27: Modal residual phase variance computed for the elevations 20, 40, 60 and 80, for the following pre-compensation methods (from the darker to the lighter colors): classical, $MMSE_{tempo}$ using one, two and three past measurements and accounting for the AO loop delay.

We plot in figure 5.27 the modal residual phase variance for elevations 20, 40, 60 and

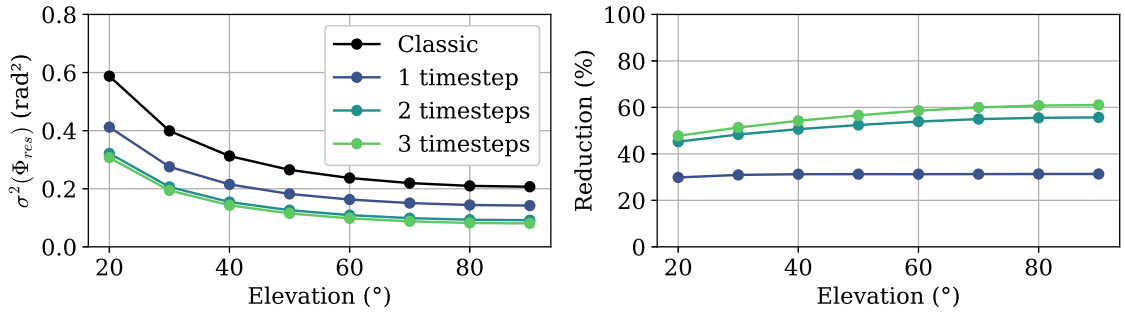

Figure 5.28: On the left: total residual phase variance computed on 136 modes function of the elevation, for the following pre-compensation methods (from the darker to the lighter colors): classical, $MMSE_{tempo}$ using one, two and three past measurements and accounting for the AO loop delay. On the right: gain with respect to the classical pre-compensation.

80°. We compare the results obtained with the classical pre-compensation, to the estimated cases with one, two, and three time steps. For every case, we observe a significant reduction brought by the one and two time steps estimation. However, the three time steps estimation brings few improvements to the phase variance reduction. Additionally, we observe a tip tilt reduction increasing with the elevation, when the ratio θ_{PAA}/θ_0 decreases. We interpret this behavior as an ability of the estimator to estimate the tip tilt when the angular decorrelation is not too large, as well as an ability to correct for the temporal error when the ground wind speed is slow.

We also compute the residual phase variance summed on 136 modes in figure 5.28. On the right, we depict the absolute value of the phase variance, and the reduction percentage with respect to the classical pre-compensation. We observe that the gain with the one-step estimation is equal to at least 30% and at best 33%. In the two steps case, the reduction gain is at least 45% and maximum 55% and, in the three steps, even weak with respect to the two steps scenario, we observe a reduction from 50% to 60% of the anisoplanatic phase variance. We conclude that using two or three past measurements of phase and log-amplitude improve the phase estimation for all elevations.

5.5.3.3 Without natural wind knowledge

As we want to explore the possibility not to use the knowledge of the wind profile, we compute the residual phase variance in the scenario where we only know the apparent wind of the satellite induced by the satellite slew-rate. Thus, we compute the residual phase error using the method introduced in section 4.5.1. This calculation takes into consideration the errors arising from the use of inaccurate prior information during the estimation process.

We plot in figure 5.29 the resulting modal residual phase variance, for the elevation case 90° on the top and 20° at the bottom, with the one-step estimation in blue on the left, and the two steps estimation in green on the right. The expected result with the true priors in plain lines, and the wrong priors in dashed lines. We observe in every case that the gain on the tip-tilt is conserved, and that the gain is reduced on the high order modes. We conclude that this estimator with wrong wind priors does not correct anymore for the temporal error, that is dominated by the perturbations close to the ground, where the natural wind is dominant with respect to the satellite apparent wind. Indeed, we illustrate the wind difference between the satellite apparent wind and the natural wind in figure 5.30, function of the distance to the OGS, where we plot in black the case at 20° elevation and in red the case at 90° elevation. When the curve values are positive, this means that the

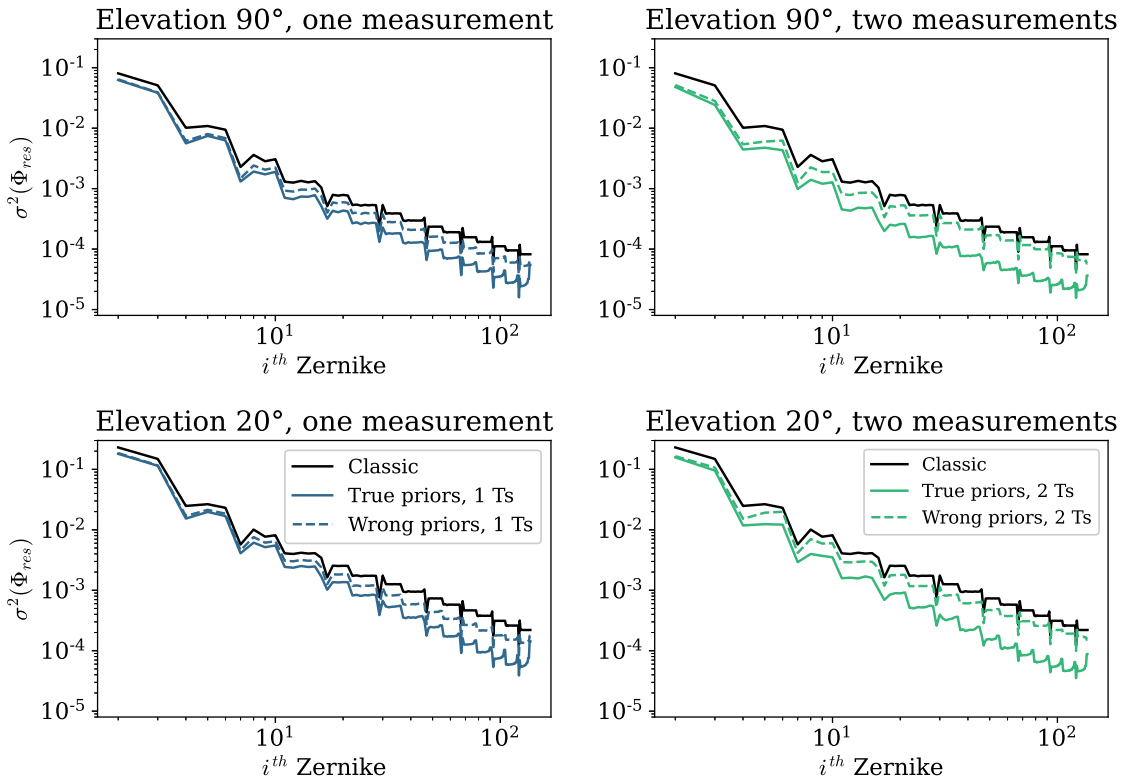

Figure 5.29: Comparison of the modal residual phase variance for an estimate with true (plain line) and wrong (dashed line) temporal priors, compared with the classical pre-compensation error, for the 90° (top) and 20° (bottom) elevation cases. The one step estimation is depicted in blue and the two step estimation in green.

apparent wind from the satellite is dominant, and conversely. We observe that the natural wind dominates within a larger distance in the 20° elevation case than the 90° elevation case, and that the wind difference is less important in absolute value, overall, even for higher elevations. This emphasis the observation that the slew rate priors are weaker in the 20° elevation case than in the 90° elevation case.

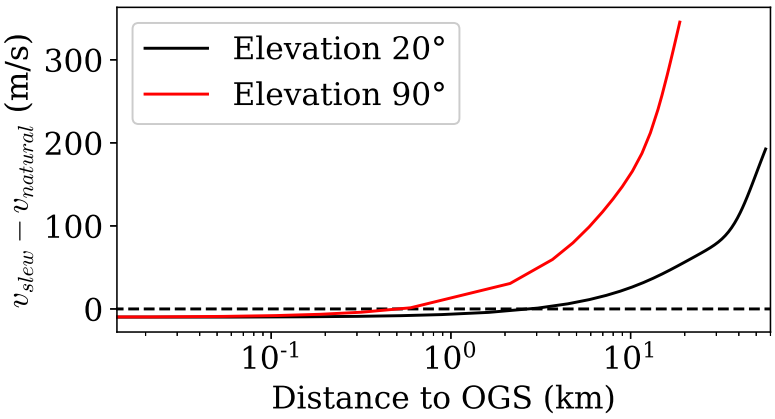

Figure 5.30: Difference between the apparent wind of the satellite and the natural wind function of the distance to the OGS, for elevation 20 (black) and 90 (red).

The last question to answer is: is this estimation with wrong temporal priors performs

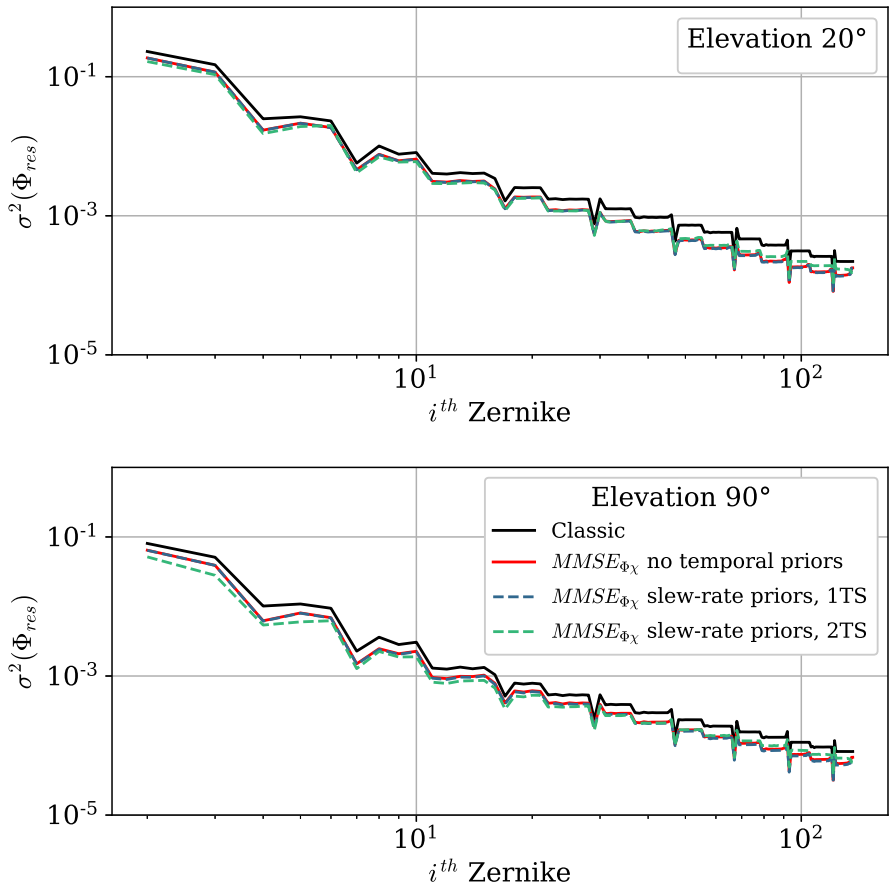

Figure 5.31: Comparison of the modal residual phase variance obtained with an estimator without temporal priors (red), and an estimate with only slew-rate priors, for one and two step estimation, in blue and green, respectively.

better than an estimator with no temporal priors at all. To elucidate this interrogation, we plot in figure 5.31 a comparison between the modal residual phase variance using no temporal priors ($MMSE_{\Phi_\chi}$ not aware of the AO loop delay, as described in section 5.2), and obtained with only slew rate priors. We also plot the classical AO phase error as a reference. For the 90° elevation case, at the bottom, we observe no improvement with the one step estimation with respect to the estimation using no temporal priors. However, a gain is observed for the two step estimation case, especially on the low order modes. In the 20° elevation case, no gain is observed for both one and two step estimation cases.

We conclude from these observations that knowing only the slew rate brings few improvements with respect to an estimation not using temporal priors, especially in cases at low elevation, that are the most perturbed cases, and the most affected by both anisoplanatism and temporal error. Indeed, the links at low elevation suffers from a tougher angular decorrelation between the uplink and the downlink beams, and are less dominated by the satellite apparent wind, whose orthogonal speed decreases with the elevation. However, an interesting gain can be obtained with two time steps estimation if one can retrieve the wind profile.

5.5.4 Coupled flux statistics

We now assume that we can retrieve the full wind profile, and consider the estimator case with true temporal priors. We study the resulting coupled flux distribution to study the gain brought by the temporal estimator on the link margin. We compare these statistics with the coupled flux distributions of the small diameters 20 and 5 cm, without phase compensation. We only study the losses induced by atmospheric turbulence.

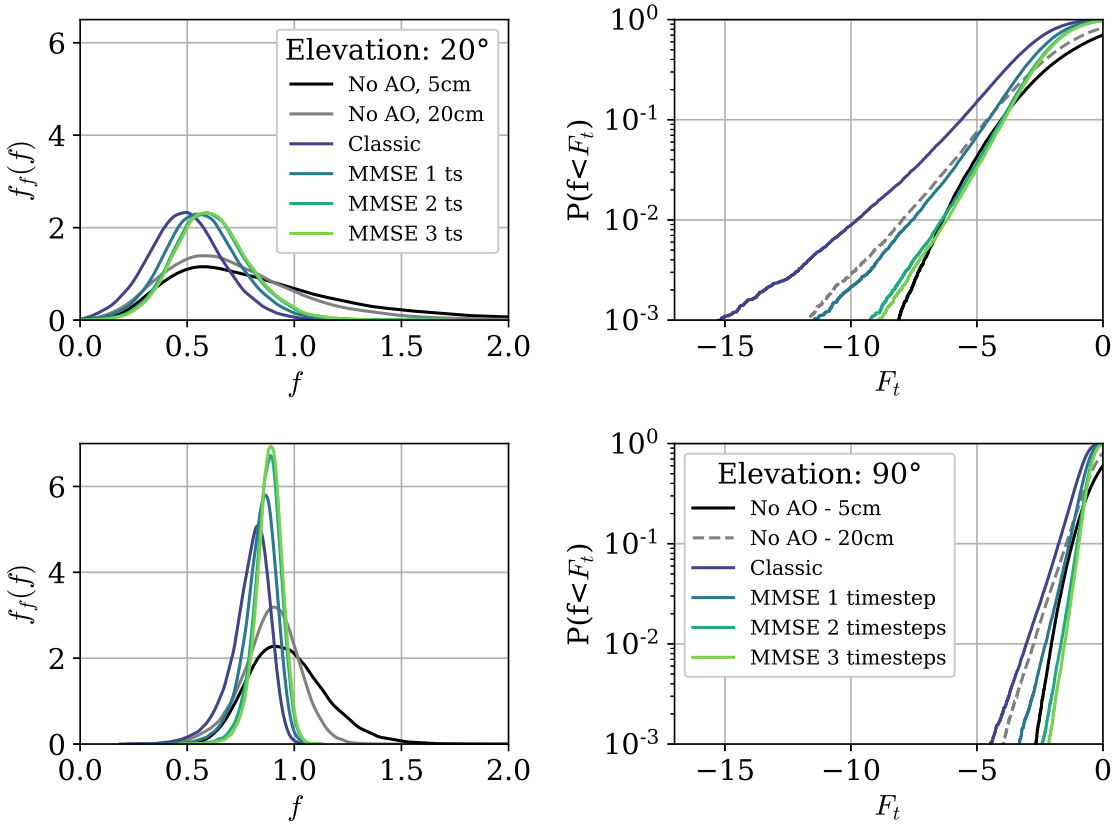

Figure 5.32: Comparison of PDF and CDF of the uncompensated cases for 5 and 20 cm Tx aperture diameter, with pre-compensated cases.

We plot in figure 5.32 the PDF (left) and CDF (right) for elevations 20 and 90°, for the following phase pre-compensations: classical, one, two, and three steps MMSE estimation. We also plot the statistics of the uncompensated cases for 5 and 20 cm Tx apertures, depicted in black and gray respectively. First, we observe, in accordance with the theory, that the uncompensated cases follows a log-normal distribution. We also observe that all pre-compensated cases have a decreased mean with respect to uncompensated cases, but also show to have a decreased signal variance. Analyzing the improvement brought by the estimator with temporal priors, the signal distribution is shown to be improved for each additional time step used, with a greater impact on the 90° elevation case. Considering the CDF at the threshold 10^{-3}, corresponding to an 99.9% availability, we observe in the 90° and 20° elevation cases, that bigger losses are obtained with the classical AO, followed by the uncompensated 20 cm case. The one step estimation is shown to perform better than the uncompensated case with a 20 cm aperture, but worst than the uncompensated case with 5 cm aperture. All the pre-compensation estimated with more than one step performs better in the 90° case than the no AO 5 cm aperture case. This trend is reversed in the 20° elevation. To conclude, the uncompensated case with a small aperture of 5 cm show

to limit the signal losses with respect to estimated cases. However, the estimated cases are shown to also limit the coupled flux fluctuations, which will be advantageous when adding the static losses from the link budget. Indeed, the gain on the geometrical losses obtained with a 40 cm telescope equals 6 and 18 dB with respect to the 20 cm and 2 cm Tx telescope apertures, respectively. Indeed, analyzing the CDF at probability 10^{-3} from figure 5.32, we clearly observe that all the MMSE pre-compensation methods outperform the no AO case with a 20 cm Tx aperture, and that the gap between this case and the classical pre-compensation case is below 6 dB, for the two considered elevations.

5.5.5 Conclusions on the LEO case

In this section we questioned the ability of an AO pre-compensation to improve the coupled flux statistics onboard the satellite for LEO uplinks, with respect to uncompensated links with small apertures, that are currently envisioned. Considering pre-compensated LEO uplinks with larger emission apertures allows indeed to benefit from greater antenna gains. We also studied the possibility to reduce the pre-compensation phase error using phase and log-amplitude past measurements. We also investigated the possibility to estimate the phase pre-compensation, relying only on the LEO link strong temporal priors that are due to the satellite apparent wind.

First, by establishing the link budget adapted to each elevation, we could show that using 40 cm apertures provides a 6 dB and 18 dB gain with respect to the 20 and 5 cm cases, taken as uncompensated uplink benchmarks, without turbulence losses. Secondly, before comparing the coupled flux statistics, we studied the pre-compensated phase error function of the elevation and the efficiency of phase estimation at PAA. We showed that the phase estimation relying on past measurements decreases the phase error, and that adding up to 3 past measurements improved the phase estimation. The phase estimation was shown to be less effective for low elevations where the ratio θ_{PAA}/θ_0 starts increasing. However, the residual phase variance in these regimes is decreased by 50% using three past measurements, against 30% using only one measurement. We also showed that only the slew rate information as a prior to compute the estimator was not sufficient to improve the phase estimation. Therefore, to use such methods, the metrology of both wind and C_n^2 profile is required.

Finally, studying the coupled flux statistics for a 99.9% availability threshold, adding up all the link budget terms, we showed that pre-compensation in general allows to provide improved link margins with respect to uncompensated links.

However, the implementation of such schemes opens new questions. As the phase estimation relies on C_n^2 profile metrology along the line of sight, we can wonder to what extent a single measurement at one elevation could be extrapolated to other elevations, or if several C_n^2 profiling would be required to be able applying these techniques. A study, from [190], compares measurements at different elevations with integrated parameters computed thanks to the theory from a profile measured at zenith and scaled at the given elevation, showing good agreements between measurements and theory starting from 20° elevation. Although it will be needed to further investigate this question for the phase estimation, this study results are encouraging.

The second challenge is the wind profiling and the robustness of the estimator to measured wind profiles, that is general to all the estimation tools based on temporal measurements that we presented.

5.6 Conclusion

Summary and main findings

Modeling temporal phase errors using spatial covariances, is not new and has already been used to model and estimate temporal downlink phase perturbations. We proposed, in this section, to fusion the phase angular anisoplanatism and temporal anisoplanatism formalism to jointly deal with temporal and anisoplanatic errors, and model the reciprocal pre-compensated uplink.

Thanks to this formalism, we could develop modeling tools, to model the phase error induced by the AO loop delay on the classical pre-compensation, as well as the estimation error induce by phase at point ahead angle with an estimator that is not aware of the AO loop delay. It was confirmed that the temporal error induced by the AO loop delay has few impact on the residual phase variance, nor on the coupled flux statistics, in both pre-compensation cases. It is also shown that the estimation error induced by the AO loop delay only affects high order modes.

Additionally, we used this formalism to estimate the phase at point-ahead angle, accounting for the AO loop delay and later introducing several past measurements in the estimation, to further decrease the pre-compensation phase error. Either using one, two or three past measurements was shown to greatly reduce the pre-compensation phase error. The additional information, especially on the tip and tilt, is shown to be issued from both the phase and amplitude on-axis, on the contrary to the estimation without temporal priors that mostly take advantage of the log-amplitude information. A second difference with the estimation without temporal priors, is that we now obtain a reduction of the low order and high order modes phase variances. Indeed, the former estimator was only reducing the pre-compensation error on the low order modes.

Finally, we applied the proposed estimation method using several past measurements in the LEO uplink case. As the satellite is slewing in this scenario, it provides deterministic temporal priors on the wind speed, due to the satellite apparent wind. The aim of this application was double. Firstly, we aimed at comparing the link availability using either a pre-compensation on a large emission aperture, or state-of the art methods using small apertures to mitigate the fades. Secondly, we explored the possibility to use only the deterministic temporal priors (and not the true priors requiring to measure the wind on the line of sight), to apply temporal phase estimation. We showed that the link availability was improved using large apertures and a pre-compensation (even classical), even though the correction was less efficient at low elevations. We showed that temporal phase estimation can bring an interesting gain on the link margin, even if the estimation efficiency is also reduced at low elevations. Finally, we showed that the knowledge of the slew rate was not sufficient to apply temporal phase estimation. Consequently, larger apertures with an AO pre-compensation, are interesting, even for LEO links, that can benefit from the additional link margin to reduce the emitted power requirements, or improve the data-rates, while enabling for coherent transmissions (on the contrary to classical multi-Tx schemes).

Perspectives

A first perspective concerns the modeling of the channel. We've shown that we could compute the modal temporal auto-correlation of the residual phase. A next step could be to use this auto-correlation function to produce time-series of residual phase Zernike coefficients, to obtain a temporal mode of the pseudo-analytical model. This would be a fast valuable tool for channel performance evaluation.

A second perspective is to demonstrate the feasibility of the temporal phase estimation using the phase and log-amplitude past measurements. Similarly to the "static" estimation presented in chapter 4, this method relies on C_n^2 profile measurements, and we need in addition information on the wind speed profile. Evaluate the robustness of the estimator on these two parameters would be a first step toward an experimental demonstration. Additionally, if interesting in applying the method to LEO uplinks, the question of the possibility to scale the C_n^2 and wind speed profiles for each of the elevations is a question that still needs to be answered.

CHAPTER 6

Spatial measurements and priors to optimize the pre-compensation phase at point-ahead angle

Contents

In the previous chapter, we used temporal measurements and statistical priors, using one or several time steps to improve the pre-compensation phase at point ahead angle. In this chapter, we study the ability of spatial measurements and priors, considering different OGS schemes, to further improve the uplink phase pre-compensation.

In section 6.1, we study the possibility to use several apertures to spatially capture additional information issued from the large downlink beam pattern on the ground. We also develop the associated analytical formalism to compute the reconstructor, and study several ground multi-aperture geometries. The main results from this section were presented in [191], and are extended to different aperture configurations.

In section 6.2, we study an optical ground station scheme aided by a laser guide star (LGS) and study the possibility to exploit the high order modes measurements from

the laser guide star at point-ahead angle jointly with the downlink beam measurements, in order to estimate the tip tilt and focus at PAA, that cannot be measured from the LGS. We also investigate the possibility to stabilize the laser guide star with this tip and tilt estimation. This results were presented during the COAT 2023 workshop and will be the topic of a peer-review paper in preparation.

Finally, in section 6.3, we synthesize the performance obtained using the different estimators from chapter 4 to 6 and conclude on the gain provided by phase estimation methods.

6.1 Addition of spatial measurements and priors in a multi-aperture OGS scheme

In section 5, we studied the gain brought by adding temporal past measurements in the measurement vector and the associated temporal a priori. In this section, we will explore the possibility of adding spatial measurements from additional apertures in order to enhance the estimation. We therefore consider in this section a multi-aperture optical ground station system. We specify that we negelect the temporal error induced by the AO loop delay in this section, to focus on the anisoplanatism reduction. However, the formalism could be easily extended to account for temporal effects.

6.1.1 State of the art

In this section, we study an estimator based on measurements from several apertures, therefore relying on the use of spatial phase and log-amplitude covariance matrices. Therefore, we start by reviewing state-of-the-art work relying on the use of these matrices, for turbulent beam analysis or AO correction. As such multi-aperture systems already exist, we also review the different schemes and concepts of multi-aperture systems from the literature. The interest is to study to what aim these systems are used for and with which geometry.

Use of spatial correlations to enhance AO correction

The formalism to compute phase angular covariances introduced by [157] is by definition relying on the computation of spatial covariances of the turbulence, considering covariances between spatially separated phase footprints for each layer of the turbulence. This formalism depends on the distance between the footprint that is denoted $d(z, \alpha)$ in section 4.4.1.2. In the work of Chassat, this distance parameter depends only on the distance induced by the angular or temporal shift between two optical paths for a single telescope receiver. This formalism is generalized in Takato and Yamaguchi's work [192] with the aim to use several apertures to measure the outer scale. It is also adopted in [193] to investigate the phase temporal properties induced by source and aperture motion by using this inter-aperture cross-correlation formalism, that is illustrated in figure 6.1 from the original scheme by Whiteley. The geometry of the considered system is represented in this scheme, depicting two different sources and two different apertures with the corresponding beam footprint at height z. He also uses this formalism to analyze the fringe visibility loss in interferometric systems due to anisoplanatism in [194].

Later on, this formalism was used, not only for phase correlation analysis but for phase correction enhancement, as illustrated in Whiteley's thesis [10], where Whiteley uses this formalism to estimate the correction phase of an interferometric system (with two distinct apertures), and enhance the performance of airborne laser systems with source and target

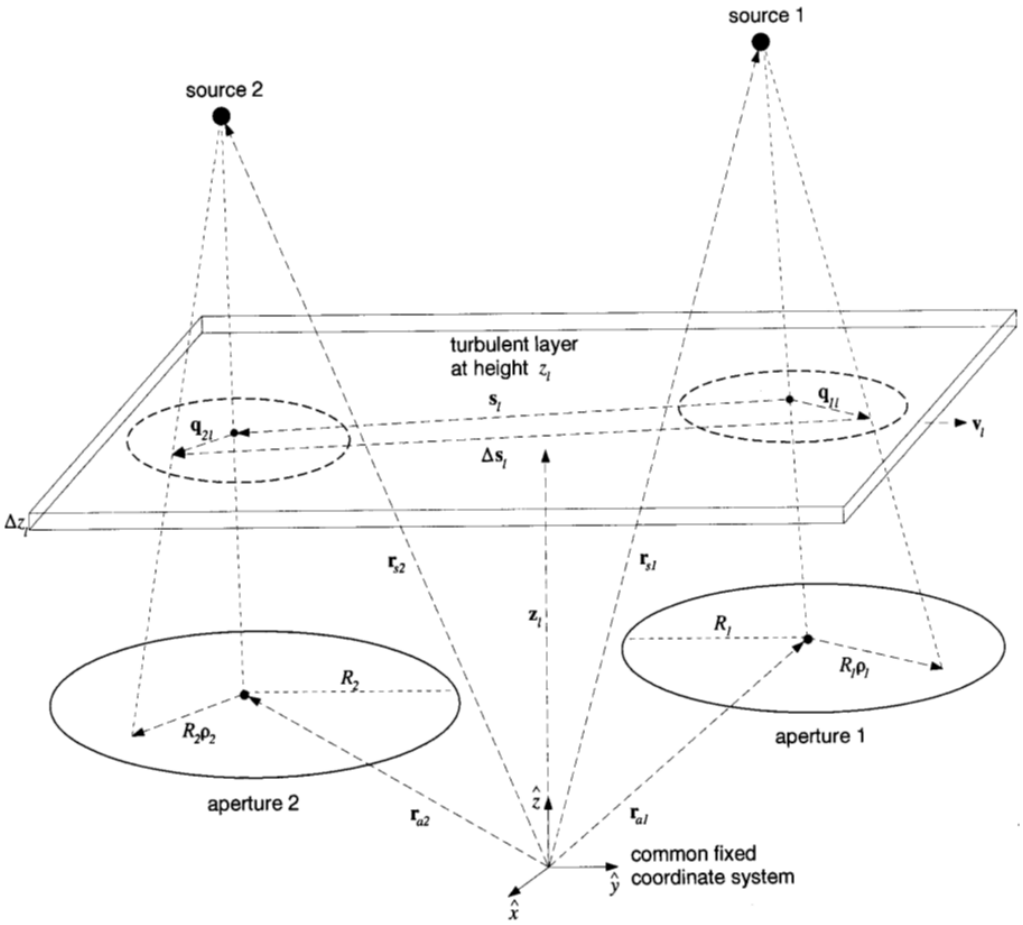

Figure 6.1: Scheme of two beam footprint patterns issued from two different sources and collected by two different apertures, considered in Whiteley's work for phase estimation [193]

motion. In this work, he uses optimal estimation corresponding to the MMSE estimation method.

As another example of systems using phase spatial correlations to enhance AO correction, we can cite the tomography adaptive optics (TAO) techniques used in astronomy [195, 196], where several guide stars (natural or laser guide stars) are used to probe the turbulent volume, and to reconstruct the wavefront to correct [197]. This approach uses several sources and one large aperture on the ground, specific to astronomy systems, in order to increase the angular resolution of the system. The system we propose that is illustrated in figure 6.2 on the right, compared with LTAO systems on the left, can be seen as a reversed tomographic system where we use only one bright source and several apertures on the ground to estimate the wavefront of one of the two apertures.

The principle of using several apertures to estimate turbulence perturbations is not new. It have been used for the parametrical identification of turbulence statistics. Among these techniques, we can cite the C_n^2 turbulence profile measurement and estimation techniques, such as the SCO-SLIDAR technique [198], that uses slopes and intensity measurements and correlations between the different sub-pupils of a Shack-Hartmann wavefront sensor (SH-WFS) in order to estimate the profile from a single source. However, this system scale is very different from the method we propose, using different apertures of size much bigger than the SH-WFS sub-pupils. The metric to optimize is also different.

To conclude, the modal phase spatial covariance analytical formalism exits in the liter-

ature, but was never used for ground to space link pre-compensation estimation. Additionally, in the framework of phase estimation, the use of the phase information from different pupils have been explored, but never using jointly phase and log-amplitude measurements from the different apertures. Therefore, we propose to develop the formalism here needed to compute a phase estimator at PAA relying on measurements from several apertures. Before detailing the estimator, we review the different schemes of multi-aperture ground station from the literature.

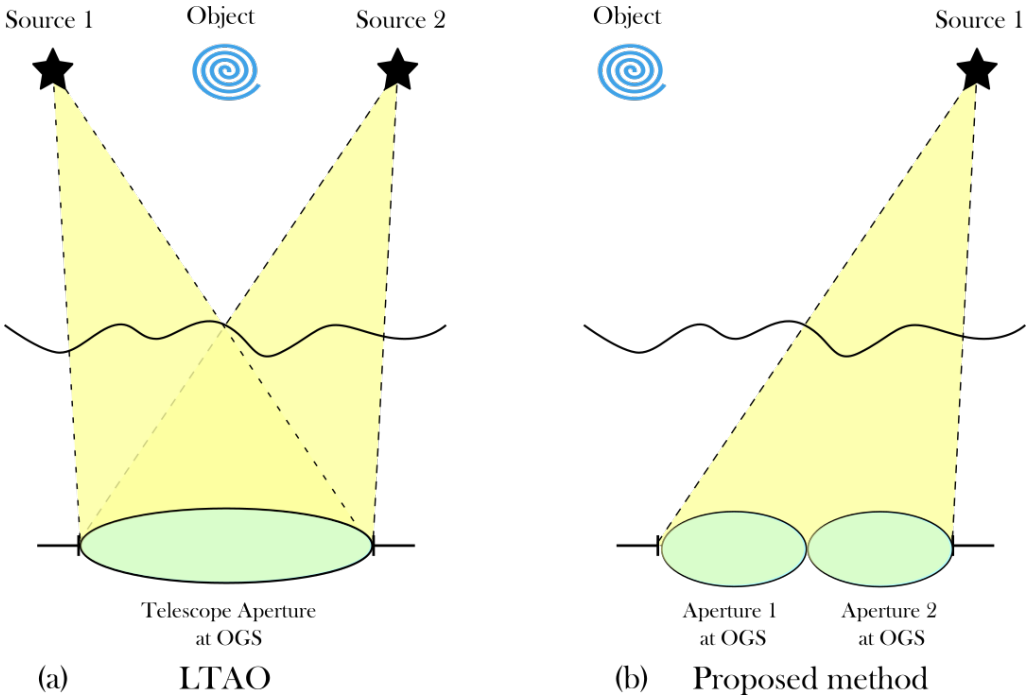

Figure 6.2: Comparison of a multi-source, one receiver concept used in astronomy in LTAO systems, versus a one source multi-receiver system proposed in the thesis.

Multi-aperture OGS in the literature

One can find in the literature concepts and experimental set-ups of multi-aperture optical ground stations. These systems have been conceived in order to exploit the spatial decorrelation of the turbulence and therefore apply spatial diversity concepts such as receiver diversity [199] in the downlink case, and transmitter diversity [200] concerning the uplink.

Receiver diversity. Using receiver diversity consists in sending information from one emitter, to N receivers. This scheme is called a SIMO (single-input multi-outputs) system. We can find such theoretical studies of such scheme for optical downlinks, that is supposed to be an alternative to AO corrected links. By receiving the beam on different apertures, the phase perturbations show to be decorrelated and therefore the coupled flux received on the different apertures are decorrelated as well. The simpler receiver diversity scheme is the signal averaging in reception, although not especially the optimal. Therefore, using optical or digital combining schemes, it is therefore possible to minimize the error probability of the detected information symbol, at a fixed SNR. These studies showed that this schemes improved the capacity of the downlink and minimized the outage probability [201, 202]. Experiments for satellite to ground links have not been reported yet. However, slant path elevation experiments have been reported in the scope of the VERTIGO experiment, showing link improvement after data post-processing [203].

Transmitter diversity. Using transmitter diversity consists in sending information from N emitters, to one receiver. This scheme is called a MISO (Multi-inputs single-output) system. Applying spatial diversity to ground to satellite links consists in emitting laser beams carrying copies or combination of information symbols through different apertures toward the satellite. As the beams propagate through different turbulent paths, they do not experience the same perturbations and the total received signal is an average of both single signals [204]. This technique allows averaging the fades. However, to average the fades in reception, the optical sum of the beams needs to be incoherent, to avoid destructive interferences in the satellite plane. One solution to achieve an incoherent sum at the satellite plane is to use different wavelengths on both apertures, at the cost of a decreased spectral efficiency. In order to be able to use the whole WDM spectrum on both apertures, and therefore, maximize the spectral efficiency and limit the system complexity, Fuchs proposed a scheme [133] called *Phase-Division in Bit-Time*. This scheme uses an additional phase modulation in order to mitigate the impact of spectral overlap between two apertures, and was experimentally demonstrated in the lab.

Experiments have been reported in the framework of ground to satellite or ground to moon links. During the experimental campaign, establishing links with Artemis in 2003, ground to satellite using delay lines to make the beams incoherent and 4 beams with a 4 to 30 cm beam waist diameter, have been reported [204, 205]. Uplinks were also conducted in 2014 in the framework of the LLCD demonstration, between the ground and the LADEE's payload, orbiting around the moon, by NASA [206]. In this experiment, a spectral shift was used to make the beams incoherent, and the system was composed 4×15 cm apertures. Additionally, a new OGS ground station, not yet in operation, called frogs [47], presents as well two apertures of 20 cm, planned for multi-aperture emission.

To conclude, using multi-aperture systems is already envisioned in the literature, therefore, such systems already exist for experimental demonstrations. In the first place, we will not limit the explored designs in this section to existing OGS designs, in order to explore the method full potential. However, the study being parametric, it will be possible to identify on the results the operating point associated to the different designs.

Proposed concept introduction

We've shown that the concept of using spatial measurement to estimate turbulence or phase perturbations can be found in the literature, as well as the associated formalism, yet not applied to pre-compensation at PAA optimization. Moreover, the idea of using multi-aperture OGS systems for GEO-Feeder link can also be found in the literature, but only in the aim to use either receiver or receiver diversity. However, the concept to use a second aperture or a portion of a larger aperture as a sensor to collect information in order to pre-compensate a large uplink has not been studied yet. Unlike the previous methods that aims at receiving or emitting a laser beam through decorrelated turbulence, we aim here at sensing a portion of the downlink beam spatially correlated with the uplink. We propose to study this scheme in the following section. We start by developing the estimator relying on spatially collected phase and log-amplitude measurements and statistical priors in a general N apertures case. Then, we study the performance of this estimator for different receiver configurations.

6.1.2 Multi-aperture system and principle

We consider a multi-aperture optical ground station scheme with one additional or several apertures positioned in the direction of the point-ahead angle in order to probe the relevant turbulent volume. The scheme is illustrated in figure 6.3, with the one aperture scheme represented on the left and the new multi-aperture scheme on the right. A part of the large downlink beam is illustrated on both schemes. This beam footprint size is equal to approximately 75 m for a GEO satellite with an onboard 25 cm telescope aperture. Therefore, by positioning the second aperture in the direction of the point ahead angle, we access to two on-axis probes (collected on apertures 1 and 2) for one oblique projection of the phase to estimate at PAA, on aperture 1. The measurements from aperture 2 are thus expected to bring information to the estimation.

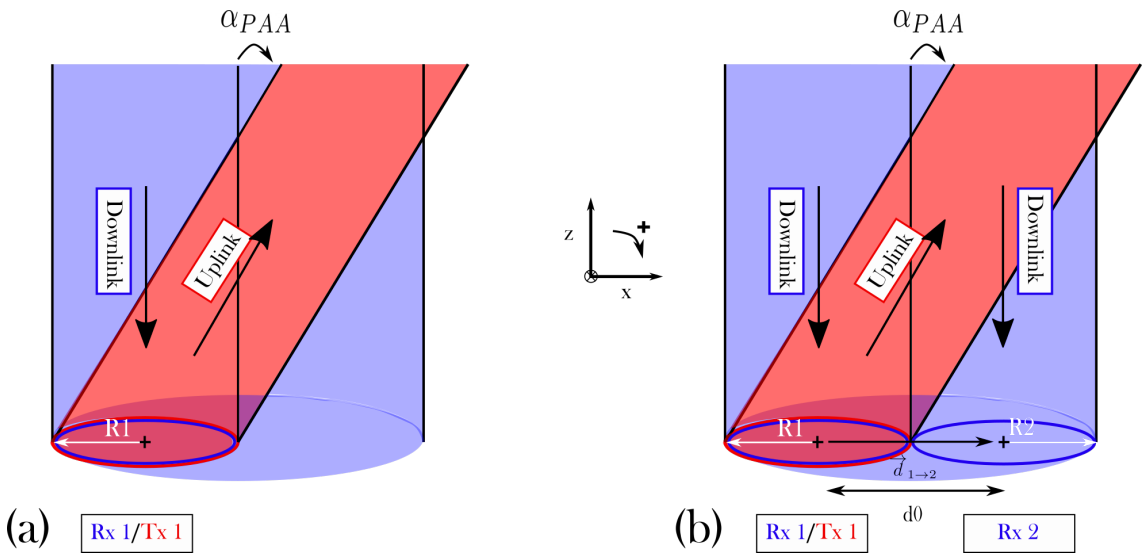

Figure 6.3: (a) One aperture optical ground station with the same aperture for downlink reception and uplink emission. (b) Two apertures optical ground station with the same aperture for downlink reception and uplink emission as Rx1/Tx1 and Rx2 used to sense an additional part of the large downlink beam.

If tuning the S1 and S2 coefficient depicted in equation 4.4.1.2, it is possible to study 2D complex arrangements in space. However, we limit the study to a 1D positioning of the apertures along the x-axis. We use the position of the center of the receiver 1 as the spatial coordinates references, denoted as $\vec{r_{c_1}} = (x_{c_1}, y_{c_1}, z_{c_1}) = (0, 0, 0)$. Therefore, the center coordinates of the second aperture are equal to $\vec{r_{c_2}} = (x_{c_2}, y_{c_2}, z_{c_2}) = (d_0, 0, 0)$. Moreover, we denote the radius of aperture 1 and aperture 2, $R_{tel,1}$ and $R_{tel,2}$, respectively. This system description can be generalized to N apertures. We depicted the system for two apertures, however, it can be generalized to N apertures.

The associated modal covariance matrices between the two physical quantities issued from aperture i and j of radius $R_{tel,i}$ and $R_{tel,j}$ separated by the oriented angle $\Delta\alpha$ and whose center on the ground are distant from $d_{j\to i}$ are denoted:

$$\mathbf{\Gamma}_{\Phi_i\Phi_j}(\Delta\alpha, \omega_{j,i}, d_{j\to i}), \quad \mathbf{\Gamma}_{\Phi_i\chi_j}(\Delta\alpha, \omega_{j,i}, d_{j\to i}), \quad \mathbf{\Gamma}_{\chi_i\chi_j}(\Delta\alpha, \omega_{j,i}, d_{j\to i}), \tag{6.1}$$

where $\omega_{j,i} = R_{tel,j}/R_{tel,i}$ and $d_{j\to i} = x_{c_i} - x_{c_j}$. For sake of readability, in the following, the indexes i and j will only be indicated on the parameters $\omega_{j,i}$ and $d_{j\to i}$ as for instance: $\mathbf{\Gamma}_{\Phi\Phi}(\Delta\alpha, \omega_{j,i}, d_{j\to i})$.

6.1.3 Spatial extension of the formalism

In this section, we develop the analytical formalism of the MMSE estimator using spatial phase and log-amplitude measurements and statistical priors for an N aperture system. We then explicit the estimator for the two-apertures case as an example by using the phase and log-amplitude measurements or only the log-amplitude measurement from the second aperture. The two apertures results have been presented in [191].

6.1.3.1 N-apertures MMSE formalism

We define the new measurement vector that is composed of the concatenation of the phase and log-amplitude measurements on N apertures, where we suppose z and y fixed to 0:

$$\boldsymbol{y}_m = \begin{bmatrix} \Phi_0(r=(0,0);R=R_{tel,1}) \\ \chi_0(r=(0,0);R=R_{tel,1}) \\ \Phi_0(r=(x_{c_2},0);R=R_{tel,2}) \\ \chi_0(r=(x_{c_2},0);R=R_{tel,2}) \\ \dots \\ \Phi(r=(x_{c_N},0);R=R_{tel,N}) \\ \chi(r=(x_{c_N},0);R=R_{tel,N}) \end{bmatrix}, \tag{6.2}$$

where $\boldsymbol{r}=(x_i,y_i)$ denotes the spatial coordinates of the center of the i^{th} aperture, where $\boldsymbol{r}=(0,0)$ denotes the coordinates of the emission aperture. Additionally, R_i is the radius of the i^{th} aperture. We neglect the temporal aspects in the first place to isolate the spatial contribution to the estimation.

Therefore, the autocovariance matrix and the covariance matrix necessary to the estimation can be written:

$$\boldsymbol{\Gamma}_{y_m y_m}(0) = \begin{bmatrix} \boldsymbol{\Gamma\Gamma}_0(\omega_{1,1},d_{1\to1}) & \boldsymbol{\Gamma\Gamma}_0(\omega_{2,1},d_{2\to1}) & \dots & \boldsymbol{\Gamma\Gamma}_0(\omega_{N,1},d_{N\to1}) \\ \boldsymbol{\Gamma\Gamma}_0(\omega_{1,2},d_{1\to2}) & \boldsymbol{\Gamma\Gamma}_0(\omega_{2,2},d_{2\to2}) & \dots & \boldsymbol{\Gamma\Gamma}_0(\omega_{N-1,2},d_{N-1\to2}) \\ \vdots & \vdots & \ddots & \vdots \\ \boldsymbol{\Gamma\Gamma}_0(\omega_{1,N},d_{1\to N}) & \dots & \dots & \boldsymbol{\Gamma\Gamma}_0(\omega_{N,N},d_{N\to N}) \end{bmatrix} \tag{6.3}$$

and

$$\boldsymbol{\Gamma}_{\Phi y_m}(\alpha) = \begin{bmatrix} \boldsymbol{\Gamma\Gamma}_\alpha(\omega_{1,1},d_{1\to1}) & \boldsymbol{\Gamma\Gamma}_\alpha(\omega_{2,1},d_{2\to1}) & \dots & \boldsymbol{\Gamma\Gamma}_\alpha(\omega_{N,1},d_{N\to1}) \end{bmatrix} \tag{6.4}$$

where

$$\boldsymbol{\Gamma\Gamma}_0(\omega_{j,i},d_{j\to i}) = \begin{bmatrix} \Gamma_{\Phi\Phi}(\Delta\alpha=0,\omega_{j,i},d_{j\to i}) & \Gamma_{\Phi\chi}(\Delta\alpha=0,\omega_{j,i},,d_{j\to i}) \\ \Gamma_{\chi\Phi}(\Delta\alpha=0,\omega_{j,i},d_{j\to i}) & \Gamma_{\chi\chi}(\Delta\alpha=0,\omega_{j,i},d_{j\to i}) \end{bmatrix} \tag{6.5}$$

and

$$\boldsymbol{\Gamma\Gamma}_\alpha(\omega_{j,i},d_{j\to i}) = \begin{bmatrix} \Gamma_{\Phi\Phi}(\Delta\alpha=\alpha,\omega_{j,i},d_{j\to i}) & \Gamma_{\Phi\chi}(\Delta\alpha=\alpha,\omega_{j,i},d_{j\to i}) \end{bmatrix} \tag{6.6}$$

The novelty here lies in the definition of an offset between the beam footprints in order to consider the adjacent aperture. It is introduced in the computation of the analytical covariance terms as:

$$d(z,\Delta\alpha,d_{j\to i}) = \Delta\alpha\cdot z + d_{j\to i} \tag{6.7}$$

We also introduced the beam portion necessary to compute the spatial covariance between two footprints of different radius. This term was already given in [120]. We compute this term by introducing $\omega_{j,i}$ in Eq. 4.19 as:

$$[\Gamma_{XY}(\Delta\alpha, \omega_{j,i}, d_{j\to i})]_{i,j} = \mathbb{E}[x_i y_j] - \mathbb{E}[x_i]\mathbb{E}[y_j] = 5.20K_{ij}\int_0^L dz C_n^2(z)\int_0^{+\infty} dk k^{\frac{-14}{3}} \\ J_{n_i+1}(k)J_{n_j+1}(k\omega_{j,i})F_{xy}\left(\frac{zk^2}{2k_0R_i^2}\right)\left(1+\frac{2\pi R_i}{L_0 k}^2\right)^{\frac{-11}{6}} \cdot \\ \left(\frac{S_1}{\omega_{j,i}}J_{m_1+m_2}(\frac{kd(z,\Delta\alpha,d_{j\to i})}{R_i}) + \frac{S_2}{\omega_{j,i}}J_{|m_1-m_2|}(\frac{kd(z,\Delta\alpha,d_{j\to i})}{R_i})\right) \quad (6.8)$$

6.1.3.2 Example of the 2-aperture estimator

In this section, we illustrate the above formalism in the two aperture case. As a first step, we take into account both phase and log-amplitude measurements from aperture 2 to compute the estimate. As a second step, we consider only the log-amplitude measurements from the second aperture, as it can alleviate the cost of the second system to only have an amplitude detector. These results were published in the article [191].

Phase and log-amplitude measurements on both apertures

We specify the measurement vector relying on phase and log-amplitude from two apertures as:

$$\mathbf{y}_m = \left[\mathbf{\Phi}_0^T(R_1,0) \quad \boldsymbol{\chi}_0^T(R_1,0) \quad \mathbf{\Phi}_0^T(R_2,d_{1\to 2}) \quad \boldsymbol{\chi}_0^T(R_2,d_{1\to 2})\right]^T, \quad (6.9)$$

where R_1, R_2 are aperture 1 (Rx/Tx) and 2 (Rx) radius respectively, and $d_{1\to 2} = R_1 + R_2$ is the distance separating the two pupil centers.

Therefore, by applying Eq. 6.4 and Eq. 6.3 for N=2, we can compute the angular covariance matrix and the autocovariance matrix as:

$$\mathbf{\Gamma}_{\Phi y_m}(\alpha_{PAA}) = \left[\mathbf{\Gamma\Gamma}_{\alpha_{PAA}}(\omega_{1,1},0) \quad \mathbf{\Gamma\Gamma}_{\alpha_{PAA}}(\omega_{2,1},d_{2\to 1})\right] \quad (6.10)$$

and

$$\mathbf{\Gamma}_{y_m y_m}(0) = \begin{bmatrix} \mathbf{\Gamma\Gamma}_0(\omega_{1,1},0) & \mathbf{\Gamma\Gamma}_0(\omega_{2,1},d_{2\to 1}) \\ \mathbf{\Gamma\Gamma}_0(\omega_{1,2},d_{1\to 2}) & \mathbf{\Gamma\Gamma}_0(\omega_{2,2},0) \end{bmatrix}, \quad (6.11)$$

where $d_{2\to 1} = -d_{1\to 2} = -(R_1 + R_2)$.

Log-amplitude only measurements from the second aperture

As it can alleviate the cost of the second detector, we also consider the scenario where we only measure the log-amplitude from the second aperture. In this case, the measurement vector is expressed as:

$$\mathbf{y}_m = \left[\mathbf{\Phi}_0^T(R_1,0) \quad \boldsymbol{\chi}_0^T(R_1,0) \quad \boldsymbol{\chi}_0^T(R_2,d_{1\to 2})\right]^T, \quad (6.12)$$

The associated angular covariance matrix is therefore expressed as:

$$\mathbf{\Gamma}_{\Phi y_m}(\alpha_{PAA}) = \left[\mathbf{\Gamma}_{\Phi\Phi}(\alpha_{PAA},\omega_{1,1},0) \quad \mathbf{\Gamma}_{\Phi\chi}(\alpha_{PAA},\omega_{1,1},0) \quad \mathbf{\Gamma}_{\Phi\chi}(\alpha_{PAA},\omega_{2,1},d_{2\to 1})\right] \quad (6.13)$$

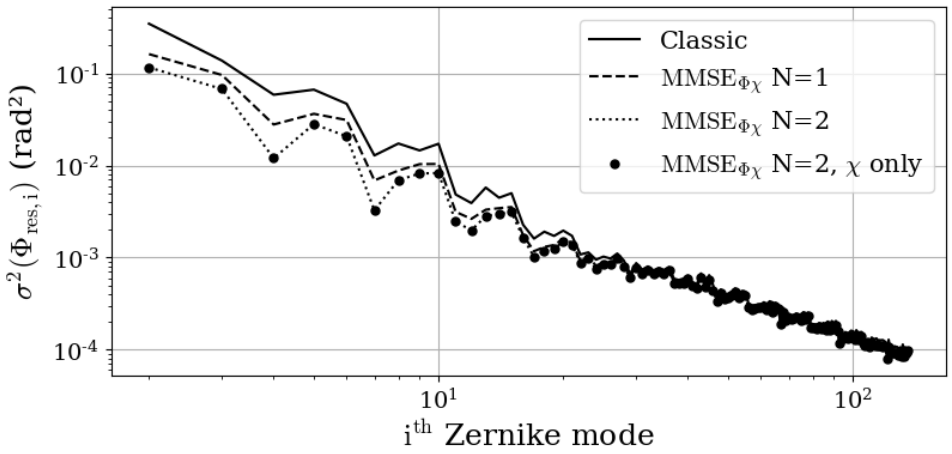

Figure 6.4: Residual phase variance function of the mode for the classical (solid line) and estimation methods using: one aperture (dashed line), two apertures (dotted line) and χ only from the 2^{nd} aperture (dots).

and the autocovariance matrix as:

$$\mathbf{\Gamma}_{y_m y_m}(0) = \begin{bmatrix} \mathbf{\Gamma}_{\Phi\Phi}(0,\omega_{1,1},0) & \mathbf{\Gamma}_{\Phi\chi}(0,\omega_{1,1},0) & \mathbf{\Gamma}_{\Phi\chi}(0,\omega_{2,1},d_{2\to1}) \\ \mathbf{\Gamma}_{\chi\Phi}(0,\omega_{1,1},0) & \mathbf{\Gamma}_{\chi\chi}(0,\omega_{1,1},0) & \mathbf{\Gamma}_{\chi\chi}(0,\omega_{2,1},d_{2\to1}) \\ \mathbf{\Gamma}_{\chi\Phi}(0,\omega_{1,2},d_{1\to2}) & \mathbf{\Gamma}_{\chi\chi}(0,\omega_{1,2},d_{1\to2}) & \mathbf{\Gamma}_{\chi\chi}(0,\omega_{2,2},0) \end{bmatrix} \tag{6.14}$$

6.1.4 Performance in a 2 aperture scheme

To evaluate the performance in a two aperture scheme, we start by considering two adjacent 60 cm apertures.

6.1.4.1 Phase variance reduction

Figure. 6.4 depicts the modal residual phase variance function of the considered Zernike mode for the classical method, the one aperture MMSE estimation method described in paragraph 4.4, the two aperture estimation method, and the two aperture method relying only on the log-amplitude measurement from the second aperture, computed for the MOSPAR 9090 case. We observe that the two aperture MMSE method performs better than both classical and one aperture estimation. In addition, similarly to the one aperture scheme, the two aperture scheme allows decreasing the variance of the low order modes, including the tip and tilt, decreased by 66 and 50%, respectively, the two modes that are at the origin of the beam wander in the satellite plane. Finally, the two aperture scheme relying only on log-amplitude measurements on the second aperture shows the same performance as the one using the phase and the log-amplitude. From these results, we can conclude that the log-amplitude measurement from the second aperture is the physical quantity that brings more information. This has the consequence to simplify the second system that only needs an amplitude detector instead of an additional wavefront sensor.

To specify the resolution requirements of the second amplitude detector, we study the impact, on the phase estimation, of N_{max} the maximum mode number of the second aperture log-amplitude measurement (third term of Eq. 6.12) expressed as:

$$\boldsymbol{\chi}_0^T(R_2,d_0) = \begin{pmatrix} b_1 & \dots & b_{N_{max}} \end{pmatrix} \tag{6.15}$$

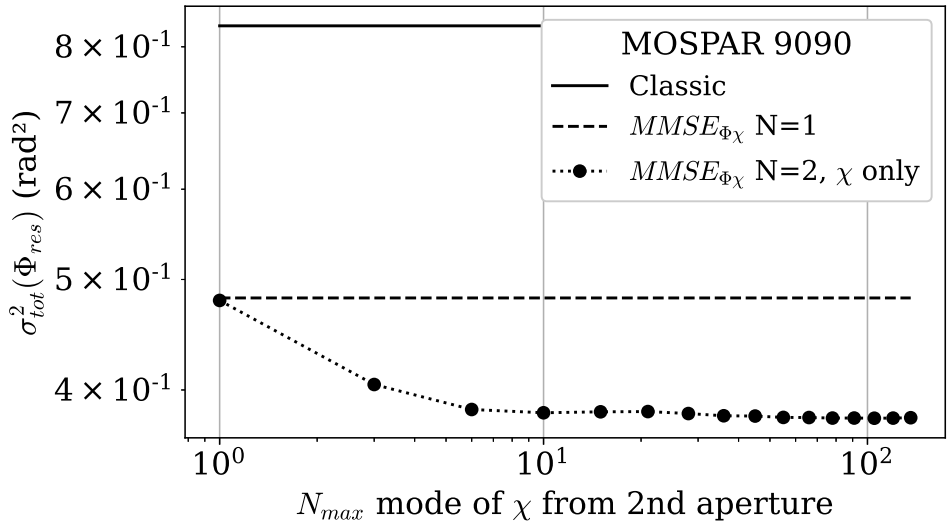

Figure 6.5: Total residual phase variance function of N_{max}, the maximum χ mode order from the 2^{nd} aperture used in the estimation, compared with the classical method (solid lines) and the one aperture estimation (dashed lines).

where $N_{max} \leq N_{AO}$ is the maximum Zernike mode order considered in the log-amplitude modal expansion.

We plot in figure. 6.5 the total residual phase variance, which is the sum of the modal phase variances, function of the log-amplitude resolution from the second aperture N_{max}. We consider the classical pre-compensation method, the one aperture MMSE estimation and the two aperture estimation corresponding to the measurement vector in Eq. 6.12. We observe that the total residual phase variance resulting from the two aperture method with varying resolution converges around $N_{max} = 10$ in the MOPSAR 9090 turbulence case. This convergence can be explained by the size of the on-axis downlink log-amplitude speckles that are proportional to the square-root of the distance to the aperture, meaning that the turbulence at the origin of the largest speckles is also the farthest from the aperture, where the uplink and downlink beam footprints are the more separated, and the anisoplanatism generated.

Finally, we present the modal reduction gain obtained from E2E data in figure 6.6,

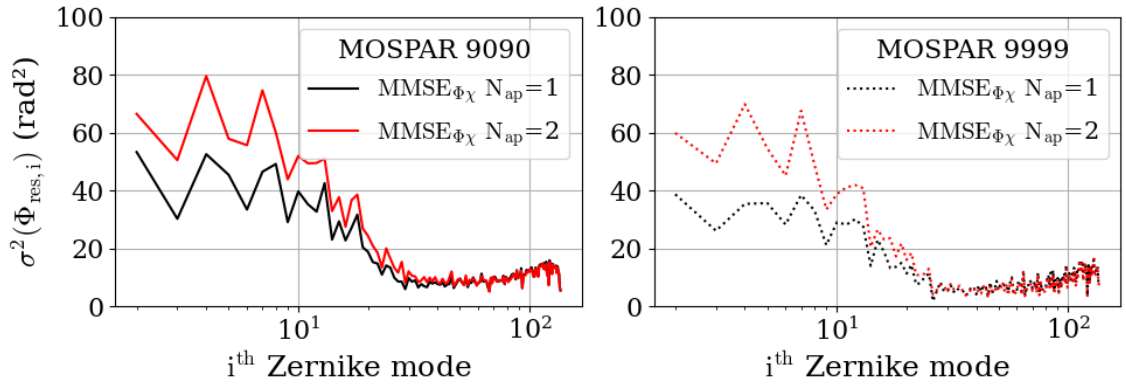

Figure 6.6: Reduction of the anisoplanatic modal phase variance brought by the: one aperture estimation (black), two aperture estimation with χ-only where $N_{max} = 36$ (red). On the left: MOSPAR 9090 turbulence case, MOSPAR 9999 on the right.

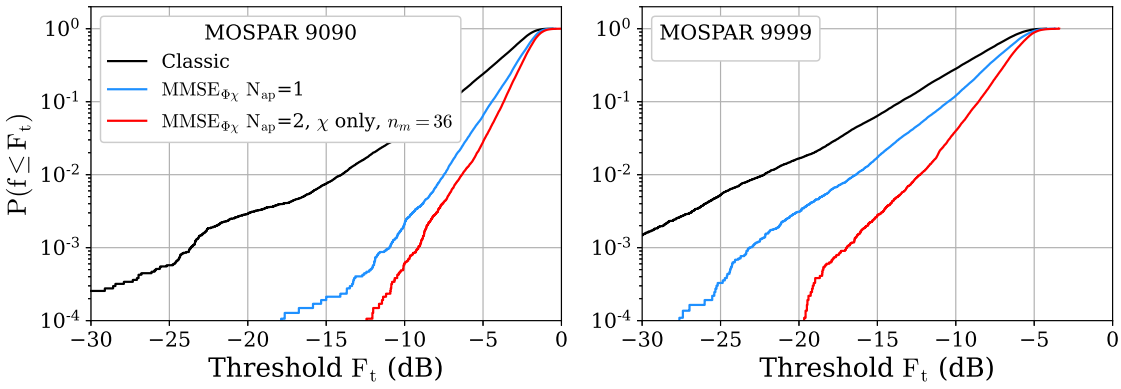

Figure 6.7: Coupled flux cumulative density function in the two turbulence conditions for the classical pre-compensation (black), one (blue) and two apertures with only low resolution χ ($N_{max} = 36$) measurement on the 2^{nd} aperture method (red).

on the MOSPAR 9090 and 9999 case, using only the low resolution measurements. The reduction is compared with the one aperture estimation results. In both turbulence cases, the gain is improved with respect to the one aperture estimation, on all the modes, reaching values above 50% for the five first modes that are also the most energetic.

To conclude, we showed that to improve the performance of the estimation, we only need a low resolution amplitude detector on the second aperture.

6.1.4.2 Impact on the coupled flux statistics

We compute E2E coupled flux time series in the turbulence cases MOSPAR 9090 and 9999 and compare the results obtained for the classical pre-compensation case (black), the one aperture (blue) and the two aperture estimation method with only the low resolution log-amplitude measurement from aperture 2 (red), where we select the resolution $N_{max} = 36$ to ensure convergence for both MOSPAR 9090 and 9999 cases. We computed 36545 samples.

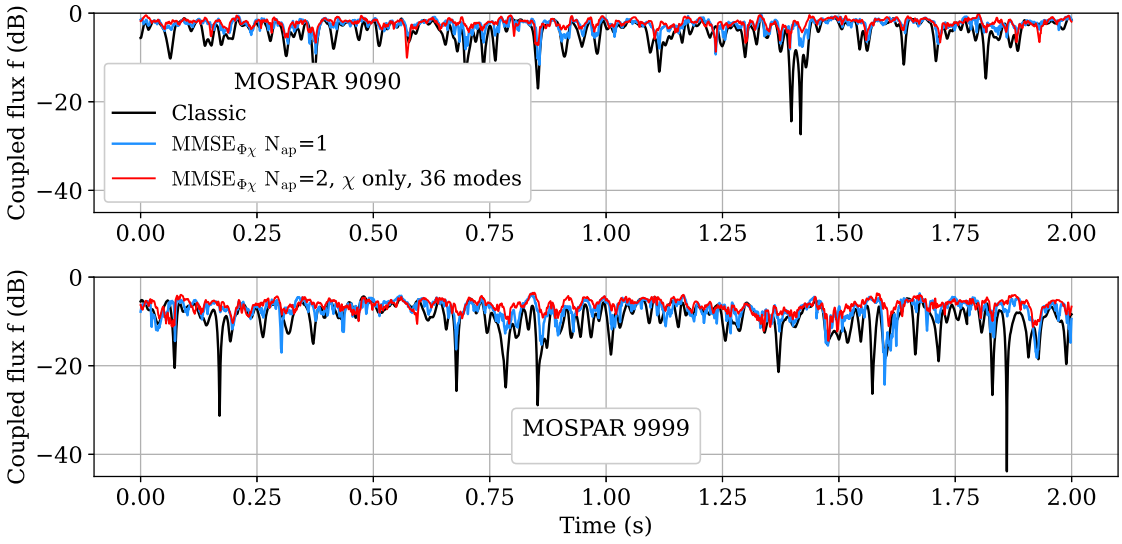

Figure 6.8: Coupled flux time series in the two turbulence conditions for the classical pre-compensation (black), one (blue) and two apertures with only low resolution χ measurement ($N_{max} = 36$) on the 2^{nd} aperture method (red).

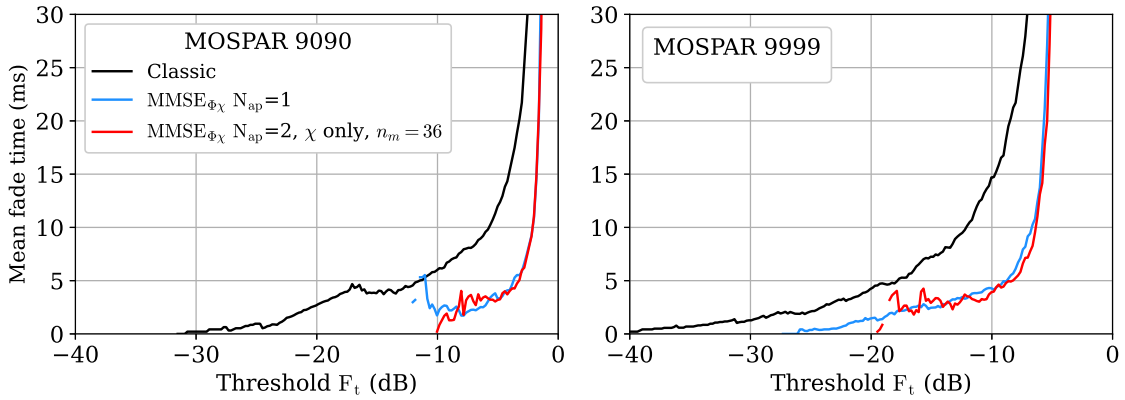

Figure 6.9: Mean fade time for the two turbulence conditions for the classical pre-compensation (black), one (blue) and two apertures with only low resolution χ measurement on the 2^{nd} aperture method (red).

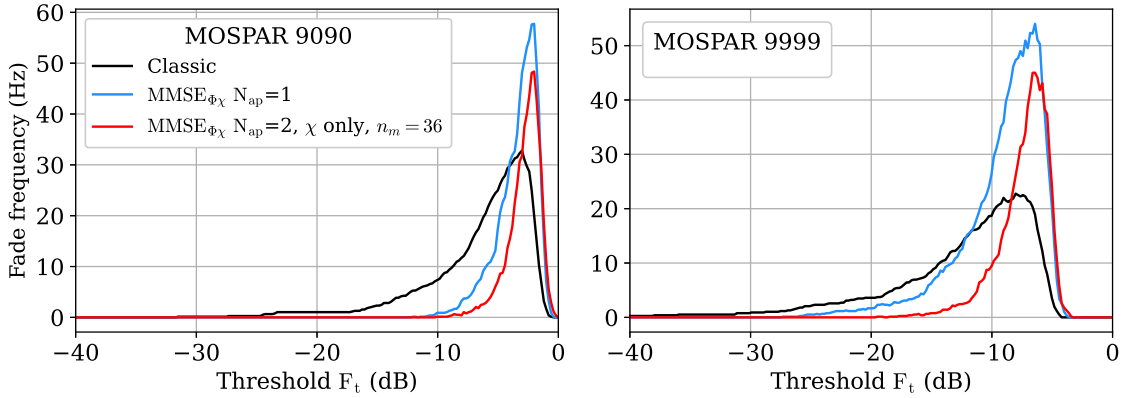

Figure 6.10: Fade frequency for the two turbulence conditions for the classical pre-compensation (black), one (blue) and two apertures with only low resolution χ measurement on the 2^{nd} aperture method (red).

Figure 6.7 depicts the cumulative density function of the signal function of the fading threshold F_t. The low resolution two aperture method brings a gain at probability 10^{-3} of 14.5 dB and 14.4 dB with respect to the classical pre-compensation, in the MOSPAR 9090 and 9999 cases, respectively. This method is also shown to be more robust to the stronger atmospheric turbulence conditions than the one aperture estimation, whose gain decreases to 8 dB, with respect to the classical pre-compensation, in the MOSPAR 9999 case. Concerning the link margin after turbulence, at the probability of 99.9%, the link margin of the link is equal to 2.5 dB, with respect to 0.73 in the one aperture estimation case, for the MOSPAR 9090 turbulence. However, for the MOSPAR 9999 turbulence case, the gain is still not sufficient to close the link budget with 99.9% availability. It is possible to close the link budget with a 98.9% availability rate in the two aperture scheme, compared to 93% and 82% for the one estimation and classical schemes, respectively.

We observe from the time series from Fig. 6.8 that all estimation methods reduce the length and depth of the fades in both turbulence conditions. Finally, the low resolution log-amplitude only method shows to perform better than the 1 aperture method.

Finally, Fig. 6.9 and Fig. 6.10 depict the mean fade time and the fade frequency function of the coupled flux threshold. It shows that the two aperture method does not reduce the mean fade time with respect to the one aperture estimation, but allows reducing the fade

frequency at a fixed threshold. As a result, by enhancing the temporal statistics of the signal, the two aperture estimation should allow relaxing the constraints on the design of the telecom reliability mechanisms.

6.1.4.3 Conclusion

To conclude, the two aperture estimation shows to improve the coupled flux performance in both atmospheric conditions, showing to have a greater impact in very severe atmospheric conditions. Hence, the addition of spatial information in the measurement vector, in the direction of the point-ahead angle, shows to make the telecommunication link more robust to tough atmospheric conditions. Additionally, we could show that only a low resolution amplitude measurement was necessary from the second aperture, to improve the performance. This can alleviate the cost of the two aperture system. We also showed that the mean fade duration was not affected by the new estimator, however, we showed that the fades were less frequent. This should benefit the design of the telecommunication system.

6.1.5 System geometry optimization

We've shown that using a two aperture scheme with two apertures of 60 cm, sensing the downlink complex field on two 60 cm apertures allowed, to greatly improve the coupled flux statistics and temporal characteristics of the uplink emitted by one of the apertures. In this section, we study the gain of the estimator by varying the following parameters:

- The radius of the second aperture,
- The distance between the two apertures,
- The number of apertures.

We note that the diameter of the emission aperture is fixed to $2R_1 = 60\ cm$.

6.1.5.1 Radius variation

We consider a second aperture with a varying diameter R_i from 5 cm to 60 cm, located next to the first aperture. The scheme of the system is depicted in figure 6.11 with an example of two different sizes for the second aperture. The principal aperture, emitting

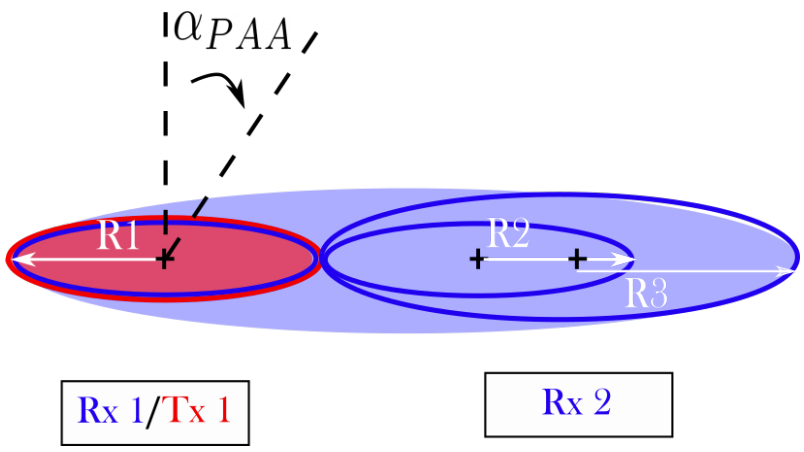

Figure 6.11: Two apertures scheme with a second joint aperture with varying diameter.

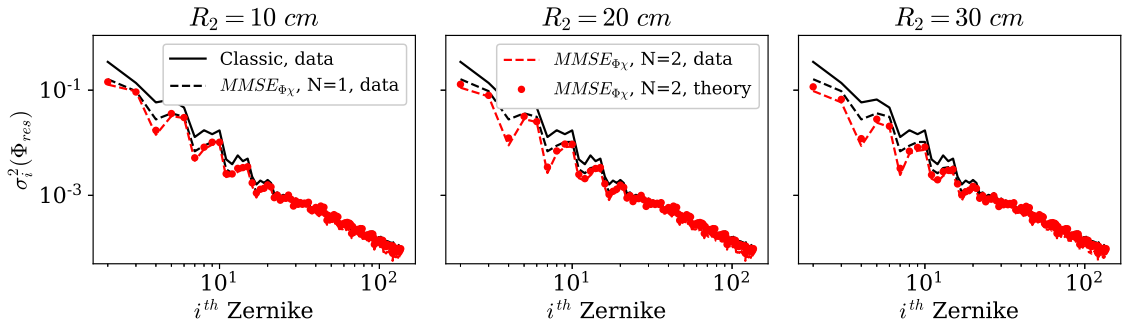

Figure 6.12: Modal residual spectrum computed from the E2E data on the pre-compensation cases: classic (black), one aperture estimation (black dashes), two aperture estimation (red dashes), with a varying aperture radius. The red dots depict the two aperture estimation from the theory.

the uplink, is depicted in red, and a part of the global downlink beam footprint in blue (which is much larger in reality).

By applying the general methodology presented in section 6.1.3.1, choosing $\omega_{2/1} = R_2/R_1$ and $d_{1\to2} = R_1 + R_2$, corresponding to adjacent apertures, we compute the analytical reconstructor $\mathbf{R}$. To validate the formulas, we compare in figure 6.12 the theoretical modal residual phase variance, obtained analytically, with the results obtained from the application of the analytical estimator to the E2E data. This validation is important to avoid obtaining aberrant results, which may be due to numerical calculation problems. Indeed, numerical errors can occur when calculating the autocovariance inversion, which may be ill-conditioned. In this figure, we plot three graphs, corresponding to estimated cases using an auxiliary aperture of diameter 20, 40 and 60 cm, from the left to the right. For each case, we plot from the E2E data: the anisoplanatic phase variance on the 136 modes, resulting from the classical pre-compensation and the results obtained with the one aperture estimation. Finally, we plot the results obtained in the two adjacent aperture scheme for the indicated radius, computed from data (dashed lines), and analytically (dots). For each diameter, we observe a good match between the theoretical error and the error computed from the data. To comment on the nature of the reduction for each diameter, we observe that a 20 cm aperture is not very effective to further reduce the tip and tilt, but participate in reducing the focus. The 40 cm and 60 cm aperture size show a

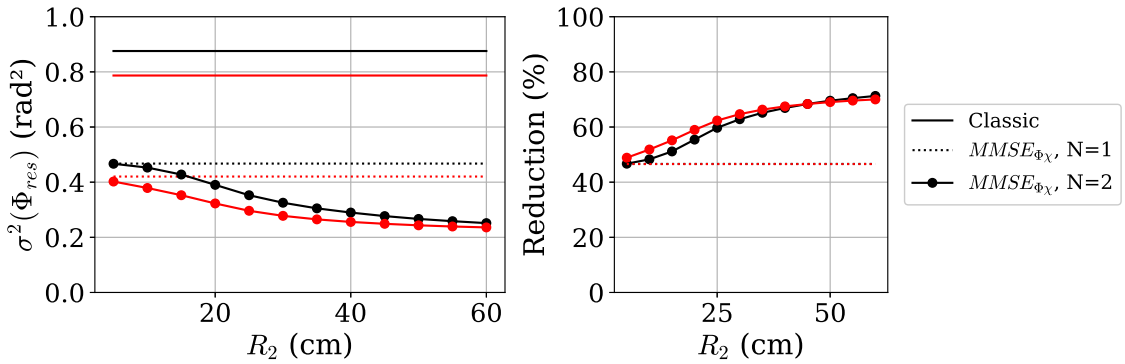

Figure 6.13: On the left: total residual phase variance function of the second aperture radius, depicted for two different outer scale values (20 m in black, 5.12 m in red), for the MOSPAR 9090 case. On the right: reduction of the total phase variance with respect to the classical pre-compensation error.

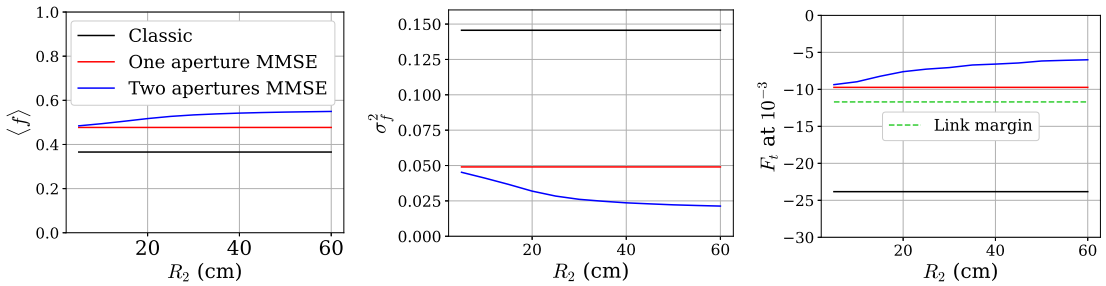

(a) Mean coupled flux (b) Coupled flux variance (c) f_t for $P(f \leq f_t) = 10^{-3}$

Figure 6.14: Mean, normalized variance and CDF value at 10^{-3} of the coupled flux f, function of the second aperture radius, for the MOSPAR 9090 turbulence case and an outer scale of 5.12 m, for the classical (black), one aperture (red), and two aperture estimation cases (blue).

significant tip and tilt reduction. An interpretation is that the width of the signal detected on the second aperture is of importance to collect information on the tip and tilt.

Figure 6.13, on the left, depicts the total residual phase variance on 136 modes in function of the radius of the second aperture, for two different outer scales (L0=20 m in black, and 5.12 m in red), computed for the MOSPAR 9090 turbulence case. The residual phase variance is shown to decrease with the radius increasing, and seems to converge for large diameter for both outer scale cases. On the right, we depict the reduction of the anisoplanatic phase variance, function of the aperture radius, for both outer scales, compared with the gain obtained with the one aperture estimation in dotted lines. The gain seems to converge to a reduction of 70% for very large apertures. It is also shown that adding a small aperture slightly increases the anisoplanatic reduction.

Thanks to the error covariance matrices, we computed coupled flux samples thanks to the Monte-Carlo method presented in chapter 3. We plot in figure 6.14 the mean and variance of the coupled flux function of the second aperture radius, for the MOSPAR 9090 turbulence case, for an outer scale of 5.12 m. We also plot the coupled flux threshold at probability 10^{-3} of the CDF function of the second aperture radius. We observe a

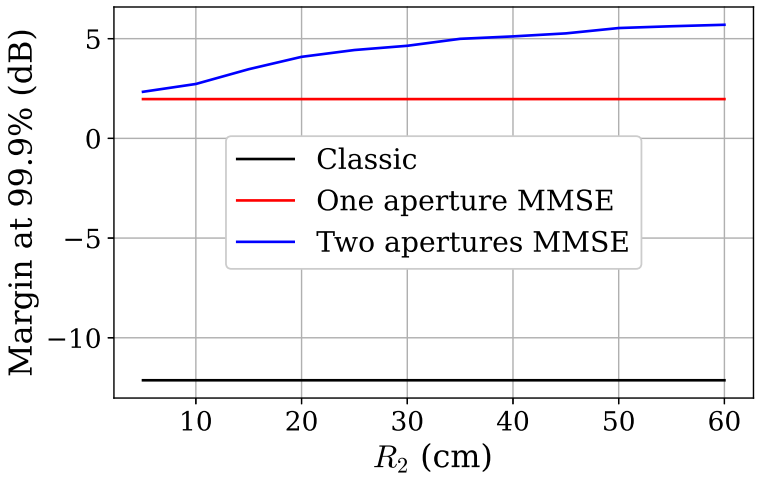

Figure 6.15: Link margin function of the radius in the MOSPAR 9090 case, with an outer scale of 5.12 m, for the pre:compensation cases: classical (black), one aperture (red) and two aperture estimation (blue).

gain of 0.05 of the mean value obtained for the largest second aperture, compared with

the one aperture method, and 0.15 compared with the classical pre-compensation scheme. Concerning the signal variance, it is at maximum reduced by two with respect to the one aperture case and divided by 6 with respect to the classical pre-compensation case. Finally, the reference coupled flux threshold is reduced by 4 dBs at maximum with respect to the one aperture case, and 19 dBs with respect to the classical case. We also observe that all the MMSE estimated cases are above the link margin (in green) defined with respect to the detection threshold for a 25 Gbps OOK communication link.

We plot the corresponding link margin at 99.9% availability in figure 6.15, function of the second aperture radius. We observe that adding a second aperture, even small, allows increasing the link margin, that is already positive thanks to the one aperture estimation. It reaches a maximum 6dB of additional link margin after turbulence.

6.1.5.2 Offset variation

In this section, we wonder if the best location for the second aperture is to be adjacent to the aperture 1, to collect the useful information for the estimation. Therefore, we vary the offset $d_{1\to2}$ with values greater than the sum of both aperture radius. Figure 6.16 illustrates the new apertures' configuration. The offset can be expressed as: $d_{1\to2} = R_1 + R_2 + d_0$, where d_0 is chosen to take values from 0 to 80 cm.

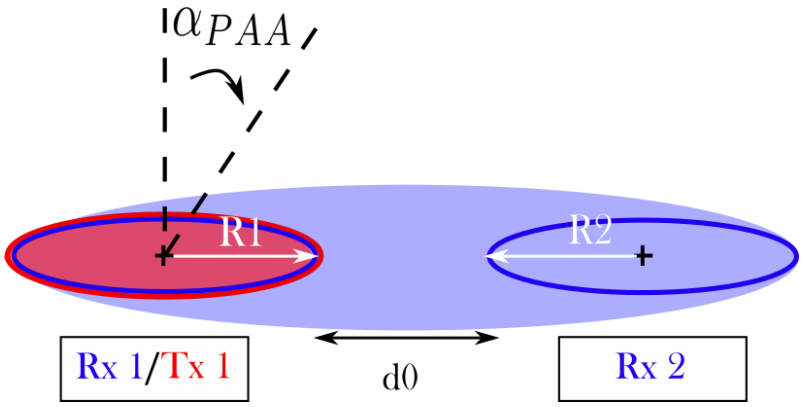

Figure 6.16: Two apertures scheme with varying offset between the two apertures.

We intuit that the angular decorrelation regime can have an impact on this location optimum. Therefore, to explore this hypothesis, we compute the estimator for the MOSPAR 9090 and 9999 case.

Figure 6.17 depicts the total residual phase variance function of the separation $d_{1\to2}$, for the two turbulence cases. It is plotted for varying second aperture radius. The results are compared to the one aperture estimation (red) and classical pre-compensation case (black). In the MOSPAR 9090 case, we observe that the minimums differ for each second aperture diameter. However, for the small apertures (of R_2=5 and 20 cm), the minimum is around the same value in each case, that is 45 cm. For larger apertures, the minimum is obtained when the apertures are adjacent.We also observe that for a large distance between each the two apertures the variance increases toward the value obtained with the one aperture estimator. This can be explained by a loss of correlation between the physical quantities, once the measurements are too far from the turbulence volume to sample.

We also plot in figure 6.18 the associated gain on the total phase residuals, obtained for each considered aperture 2 radii, function of the offset d_0 (not to confuse with the distance between the two aperture centers depicted in the figure 6.17). We plot the results for both turbulence cases. We also represented the results for the MOSPAR 9090 considering two

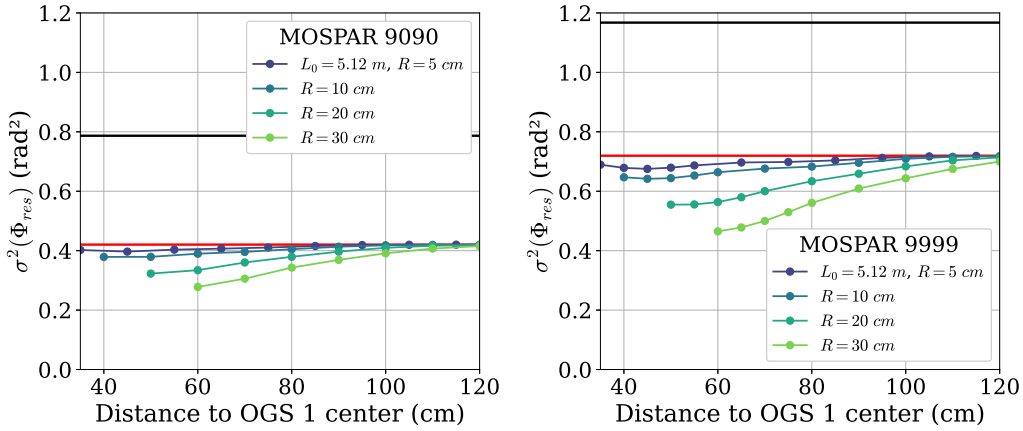

(a) MOSPAR 9090 case, $L_0 = 5.12\ m$ (b) MOSPAR 9999 case, $L_0 = 5.12\ m$

Figure 6.17: Total residual phase variance computed for different offsets between the two aperture centers, for several diameters, and two turbulence cases, compared with the classical (black) and one aperture estimation performance (red). The variance is plotted function of $d_{1\to2} = R_1 + R_2 + d_0$.

outer scales (5.12 in plain lines and 20 in dashed lines). First, we observe that for all radius cases, when the offset is large (greater than 60 cm), all reduction gain tends to the same value, that is the gain of the one aperture estimation. Secondly, we observe that the outer scale does not affect the gain. Finally, the gain is weaker in the MOSPAR 9999 case, showing the heavier angular decorrelation θ_0.

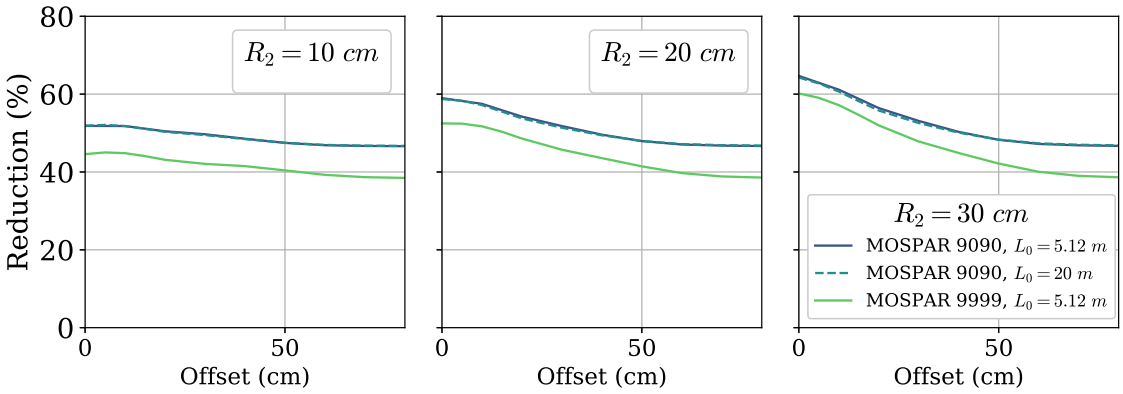

Figure 6.18: Reduction gain function of the offset d_0 between the two pupils, for different radii, and two turbulence cases.

As the behavior is similar as in the radius study, we don't compute the coupled flux and extrapolate that the behavior is similar, with a gain between 2.5 and 6 dB on the link margin.

6.1.5.3 N aperture scheme

Finally, we study the behavior of the estimator in an N aperture scheme. The idea is to explore the gain difference between the two 60 cm aperture scheme and several smaller pupils to sample the turbulent volume. Indeed, the system complexity and cost decreases with the addition of small aperture with respect to large apertures. The considered scheme is illustrated in figure 6.19

We compute the results for the MOSPAR 9090 case. Figure 6.20 plots the total residual

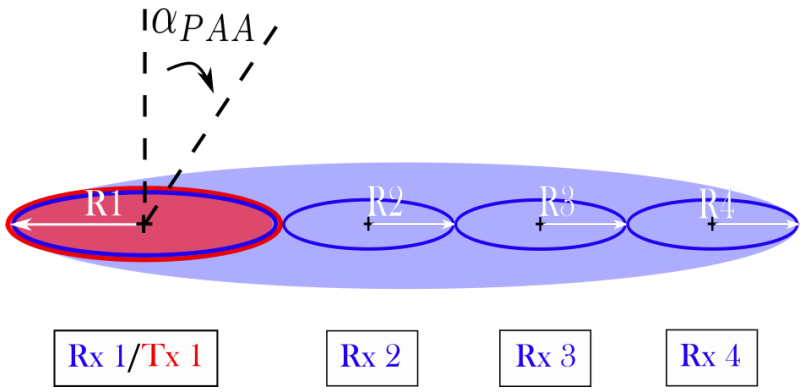

Figure 6.19: N apertures scheme, with the radii of the auxiliary apertures smaller than the principal aperture. In this case, $R_2 = R_3 = R_4$.

phase variance on 36 modes, to limit the computation time, with respect to the size of the auxiliary apertures' radius. The results are depicted for 1, 2, 3, 4 and 5 apertures, and for the classical pre-compensation error. The associated reduction gain is plot in figure 6.21. We observe in every cases that adding a third aperture participates in the reduction of the phase variance, with a reduction becoming smaller when the aperture is large, with respect to the two aperture reduction. Moreover, using 4 or 5 apertures do not reduce the phase variance with respect to a 3 aperture system, except in the case of the aperture of radius 5 and 10 cm. From this notice, we can conclude that there is a maximum distance, defined from the center of aperture 1, beyond which the measurements of the downlink beam are no longer informative on the phase at PAA.

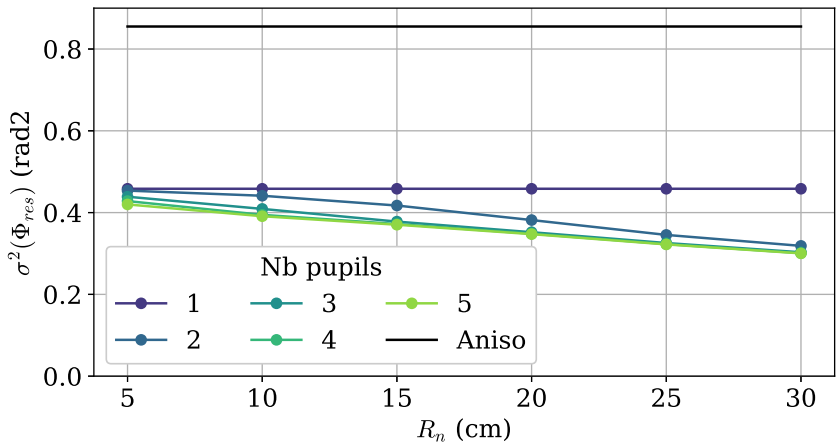

Figure 6.20: Total residual phase variance computed on 36 modes in the MOSPAR 9090 case for the outer scale of $L_0 = 5.12$ m, function of the apertures radii, for a variable number of apertures.

This corroborates the observations made in the cases with varying aperture and offset variation. Indeed, we observe for the small aperture case that adding apertures in the PAA direction does not decrease the total phase variance. However, adding several large apertures decrease the phase variance. This is explained by the fact that the small apertures do not sample the turbulence in the $\vec{y}$ axis. A perspective is therefore to study different spatial arrangements of small apertures sampling the space in the PAA direction until this maximum distance, in the $(\vec{x}, \vec{y})$ plane.

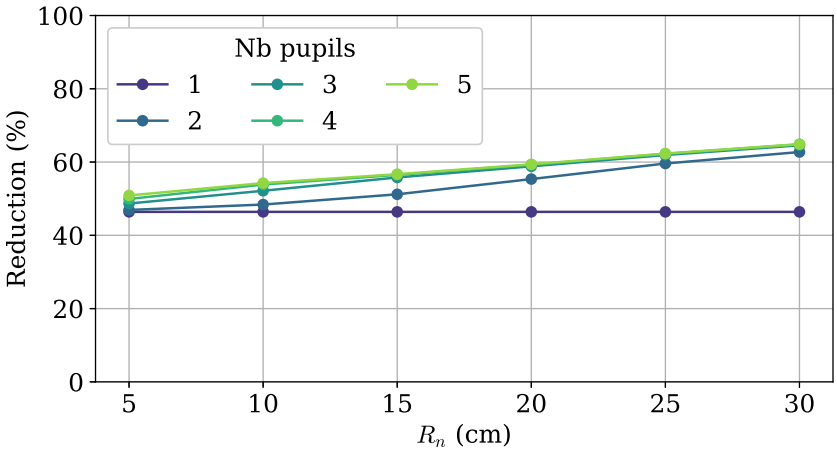

Figure 6.21: Total residual phase variance reduction with respect to the anisoplanatic phase variance, computed on 36 modes in the MOSPAR 9090 case for the outer scale of $L_0 = 5.12$ m, function of the apertures radii, for a variable number of apertures.

6.1.6 Conclusion and discussion

Conclusion and main findings

In this section, we proposed to use spatial information collected from several apertures to improve the phase estimation. On the contrary to classical multi-aperture schemes, aiming at obtaining uncorrelated signals, we exploit the uplink and downlink beam correlations.

To that aim, we present a general formalism to compute phase and log-amplitude angular modal covariances between N apertures, on the basis of existing work dealing with phase covariance between two separate apertures [157, 194]. The novelty is to extend the computation for the angular cross-correlation between the phase and the log-amplitude and the log-amplitude angular covariance. We exploited this formalism in order to compute a new phase estimator relying on phase and log-amplitude measurements from several apertures, proposing a new OGS scheme.

We applied this estimator to a two 60 cm apertures scheme. We showed that this new estimator was further reducing the low order modes of the reciprocal residual phase variance, hence reducing the pre-compensation error. We also showed that it was only required to use the log-amplitude information from the second aperture, with a low resolution, to reach the full performance using the phase and log-amplitude. Consequently, the coupled flux statistics were improved and shown to be more robust in very severe atmospheric conditions.

In order to understand better the nature of the spatial information useful to the estimation, we considered different aperture configurations, varying the aperture diameter, location, and number. The optimal studied scheme was shown to be a unique auxiliary aperture with a large diameter. It was shown that the width of the aperture sensing the signal was as important as the length, and that, due to the link geometry, there was a maximum distance from the first aperture until which the measurements were not adding information anymore. Knowing all these factors, a question that has not been treated, remains: would the gain be the same with several small apertures with an optimized arrangement in the $(\vec{x}, \vec{y})$ plane ? This question opens the perspectives that we enumerate in the following.

Perspectives

The study of the multi-aperture scheme has two aims. The first was to identify the source of useful information, that we explored in this section. The second is, knowing where the information is, to conceive a realistic and affordable OGS. Some multi-aperture OGS scheme already exists, even not in the purpose of being used for the phase estimation method. A first perspective could be, for a given existing OGS, to study potential gains in its geometry. The second is to propose new designs, realizable, by studying for instance the reachable gain with an arrangement of small apertures located next to the Tx pupil, covering the surface of interest. several ideas for potential designs are depicted in figure 6.22. This requires to extend the formalism to a 2D space analysis. This is possible in practice by adapting the coefficient S_1 and S_2 described in the table 3.1 and 3.2, that depends on Θ, the angle in the $(\vec{x}, \vec{y})$ plane between the axis co-linear with the PAA, and a rotated coordinate system in the same 2D plane. By jointly tuning Θ, the offset d_0 and the auxiliaries' aperture radii R_n, one can study such system. Another configuration that

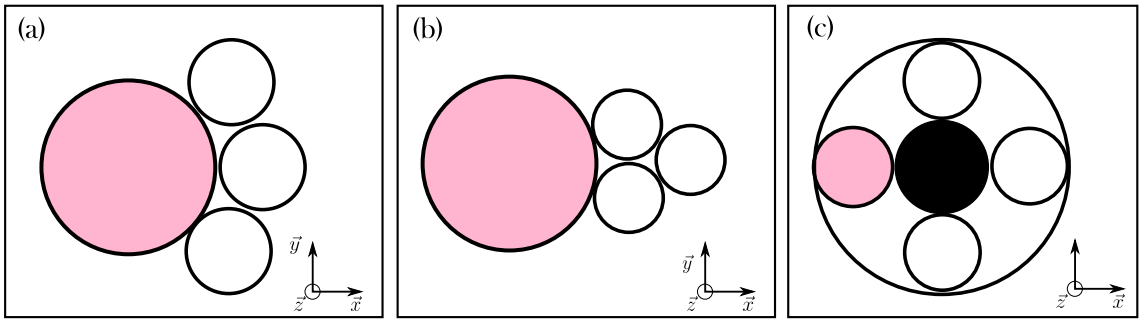

Figure 6.22: Proposition of multi-aperture scheme configurations.
(a) The cat paw, (b) the chick, (c) the daisy.

we didn't study that could be of interest in the case of confounded pupils, with a large aperture of measurements and a smaller pupil of emission included in the larger pupil.

A second perspective is to use this formalism for modeling. We used the proposed formalism for the estimation of the reciprocal phase at PAA. We could also use this formalism to numerically simulate thanks to pseudo-analytic models, either multi-Rx downlink schemes, or reciprocal multi-Tx channels.

Finally, we can wonder, knowing that we retrieve additional information with auxiliary apertures, if these measurements could be as well exploited for C_n^2 metrology purposes.

6.2 Addition of modal measurements and priors in an OGS scheme aided by a laser guide star system

In previous sections, we studied the gain brought by adding temporal and spatial information from the downlink beam to the estimation. Finally, we consider a last system based on an optical ground station aided by a laser guide star system at point ahead angle. We study the ability to enhance the estimation by incorporating the high order measurements from the laser guide star at PAA combined with downlink beam measurements in order to estimate the tip tilt and focus at PAA, modes that cannot be measured from the LGS.

We start in section 6.2.1 by presenting laser guide star state-of-the-art technologies and current challenges in the use of LGS for ground to GEO satellite systems, in particular tip tilt and focus retrieval issues. In section 6.2.2, we present the considered system and the hypothesis taken to model the LGS based correction. In section 6.2.3, we present a new method to estimate the tip tilt and focus from measurements on the on-axis downlink and from the LGS high order modes measurements. We evaluate the estimation performance in a perfect LGS configuration. Finally, we discuss, in section 6.2.4, the impact on the estimation when considering measurements from a more realistic LGS system.

6.2.1 State of the art

As mentioned in section 4.1, laser guide star systems are of interest for GEO Feeder link adaptive optics pre-compensation, as they can provide wavefront measurements from the direction of interest, that is the point-ahead angle direction.

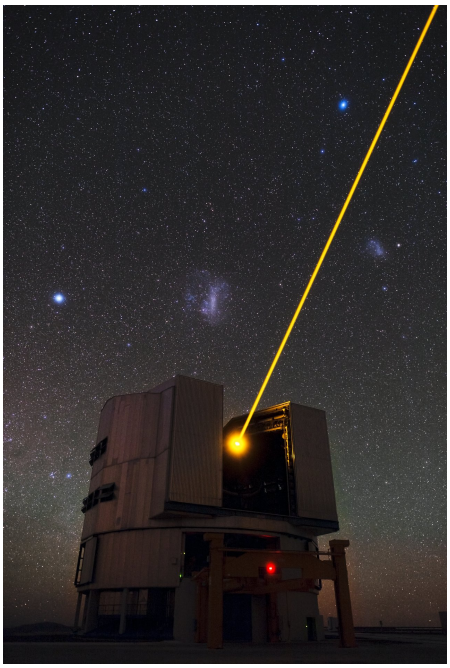

(a) Credit: ESO/B. Tafreshi (twanight.org)

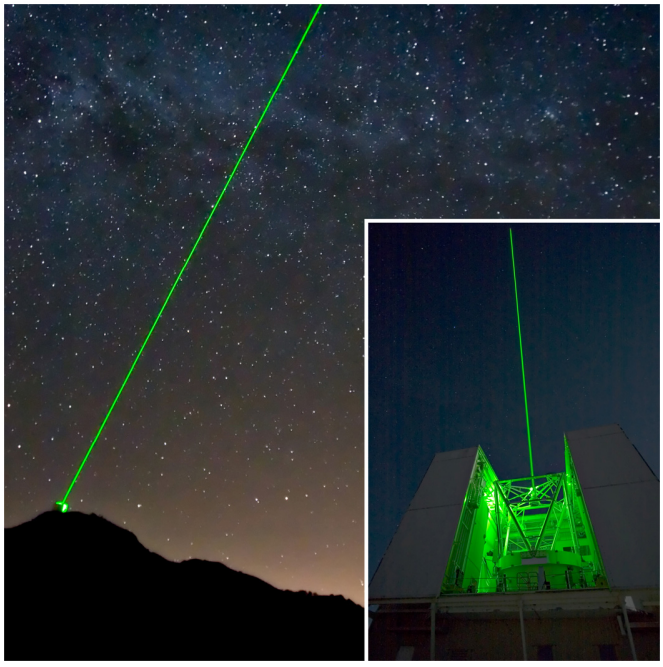

(b) Images courtesy Thomas Stalcup.

Figure 6.23: Illustration of (a) a sodium LGS at ESO, (b) a Rayleigh LGS at the 6.5m MMT (formerly the multiple-mirror telescope) in southern Arizona.

We can find two types of laser guide star in the literature, the Rayleigh laser guide star and the sodium laser guide star. The Rayleigh laser guide star uses a laser beam at 351 nm, and relies on the Rayleigh scattering from lower atmosphere layers (20 to 35 km) [207].

As for the sodium guide stars, they rely on a laser beacon at 589 nm exciting the sodium layer of the atmosphere located in the mesosphere at heights from 80 to 100 km [208, 209]. The two type of LGS are illustrated in figure 6.23.

We can find two types of configuration to retrieve LGS measurements: bistatic and monostatic configurations. In the articles of Ragazzoni, the emitter of the LGS is called the projector, and the telescope is the measurement aperture [210]. In the bistatic scheme, the LGS is sent from the auxiliary telescope and received on the main telescope that measures the perturbation. In the monostatic configuration, the LGS is sent and measured from the same telescope aperture. It is technically more challenging to implement, but the monostatic configuration provides an LGS of smaller width than using bi-static schemes, as illustrated in figure 6.24. The monostatic vs. bistatic scheme been also investigated and quantified in the scope of the ALASCA project [3, 211, 212], which is a European project for the demonstration of GEO-Feeder links aided by LGS.

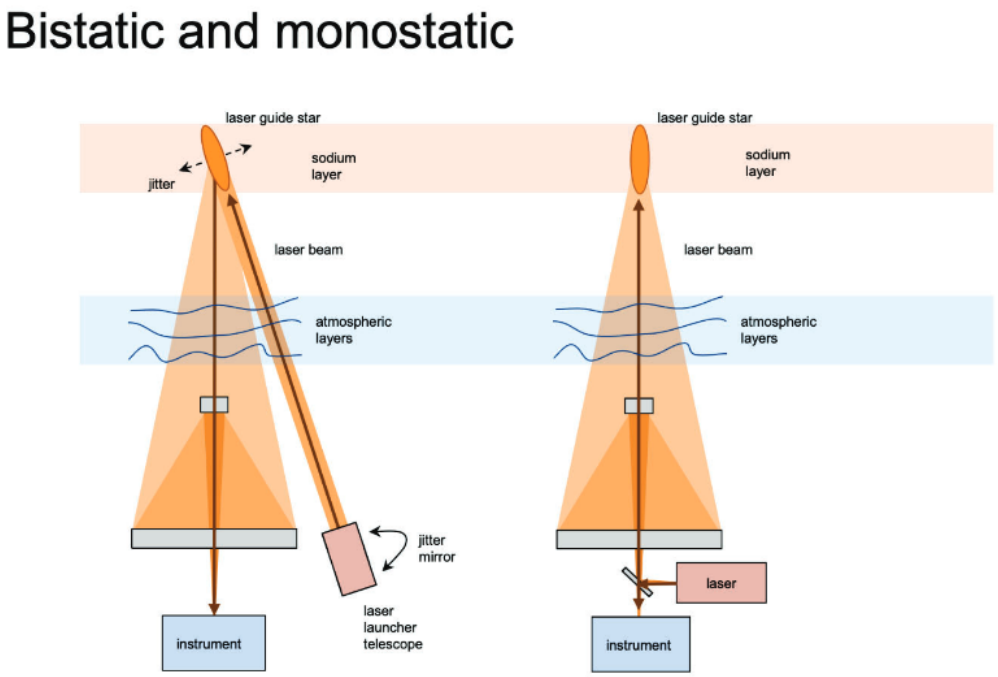

Figure 6.24: Refaire un schéma. Credits: [3]

These systems currently suffer from tip and tilt and focus indetermination. The focus indetermination is caused by fluctuations of the sodium density in the 3D sodium layer, resulting in measurement errors on the focus. As for the tip and tilt indetermination, it arises because both emitted and returning photons from the LGS experience identical deflection on the outward and return paths. This has two consequences: first, the impossibility to measure the tip and tilt, secondly, this introduces a pointing error due to the impossibility to stabilize the laser guide star, inducing error measurement of the high order modes.

The tip and tilt retrieval has been the object of numerous scientific investigations. A first idea from Ragazzoni was to exploit multiple auxiliary telescopes or multiple projectors in order to retrieve the tilt [210, 213]. He also proposed in a monostatic scheme to use the propagation delays of laser pulses in order to retrieve the absolute tip-tilt [169]. Noelia Martinez also proposed to retrieve the tip tilt from the monitoring of the fluctuations of the illuminated sodium anisotropies, using a plenoptic camera [170]. There are also investigations on the use of polychromatic guide stars in order to exploit the path differences taken by photons at different wavelengths, allowing measuring differential tilts [214, 215].

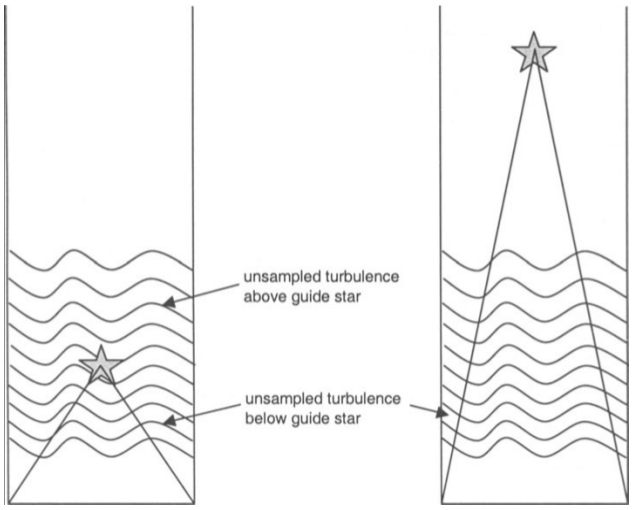

Figure 6.25: Cone effect illustrated for: on the left, Rayleigh LGS, on the right, sodium LGS. Credit:[217]

The main concerns on the polychromatic LGS feasibility for telecom systems is the return flux SNR, that is strongly related to the spot size in the mesosphere, the aperture diameter and the integration time in reception [216]. These parameters can be favorable in an astronomical case, but are less favorable for FSO system geometries.

In this section, we propose a new alternative for tip-tilt-focus retrieval, that suits telecom OGS geometries. We presented in this manuscript a method already improving the tip tilt and focus at PAA, relying only on the downlink beam measurements. We introduce an extension of this method, relying on the downlink beam measurements and the high order measurements from the laser guide star, in order to estimate the tip tilt and focus at PAA. Earlier work, by Whiteley [177], consider using high-order measurements from an LGS or NGS in order to estimate the tip and tilt of an off-axis object. However, our scheme differs, as we consider having a first beacon at angle reference 0 (that is the downlink), accompanied by an LGS off-axis. Such method could also be used to stabilize the LGS, using an LGS pre-compensation, therefore enhancing the accuracy of the high order measurements.

To explain this new method, we start in section 6.2.2 by presenting the considered system and LGS scheme used in this study. In section 6.2.3, we present the analytical formalism used for the estimation for a perfect LGS case, meaning that we assume it provides perfect high order measurements. We also present the results issued from the new method on the tip til and focus reduction, and its impact on the coupled flux statistics. Finally, in section 6.2.4, we consider the impact on the measurements of a more realistic system, and discuss the impact on the estimation in this case.

6.2.2 System and hypothesis

For this study, we consider a monostatic sodium LGS. This system allows limiting the width of the excited sodium structure that is sensed by the telescope. The sodium LGS is emitted in the direction of the point-ahead angle. Therefore, we assume it gives access to the measurements of three quantities: the downlink phase on-axis $\Phi(0, \mathbf{r})$, the downlink log-amplitude on-axis $\chi(0, \mathbf{r})$ and the LGS phase high orders at PAA $\Phi_{HO}(\alpha_{PAA}, \mathbf{r})$, with $\mathbf{r}$ the spatial coordinates defined over the pupil. The downlink optical path is represented in blue in figure 6.26, the uplink in red, and the LGS, located on the optical axis at point-ahead angle, in green.

As we consider a Sodium LGS and a small aperture (with respect to astronomical cases), we assume that the cone effect can be neglected. The cone effect is the phase error induced by the conical projection of the wavefront instead of a cylindrical projection. It is illustrated in figure 6.25.

We neglect in the first place temporal effects, in particular the temporal error induced by the loop delay, for both the LGS and the downlink measurements.

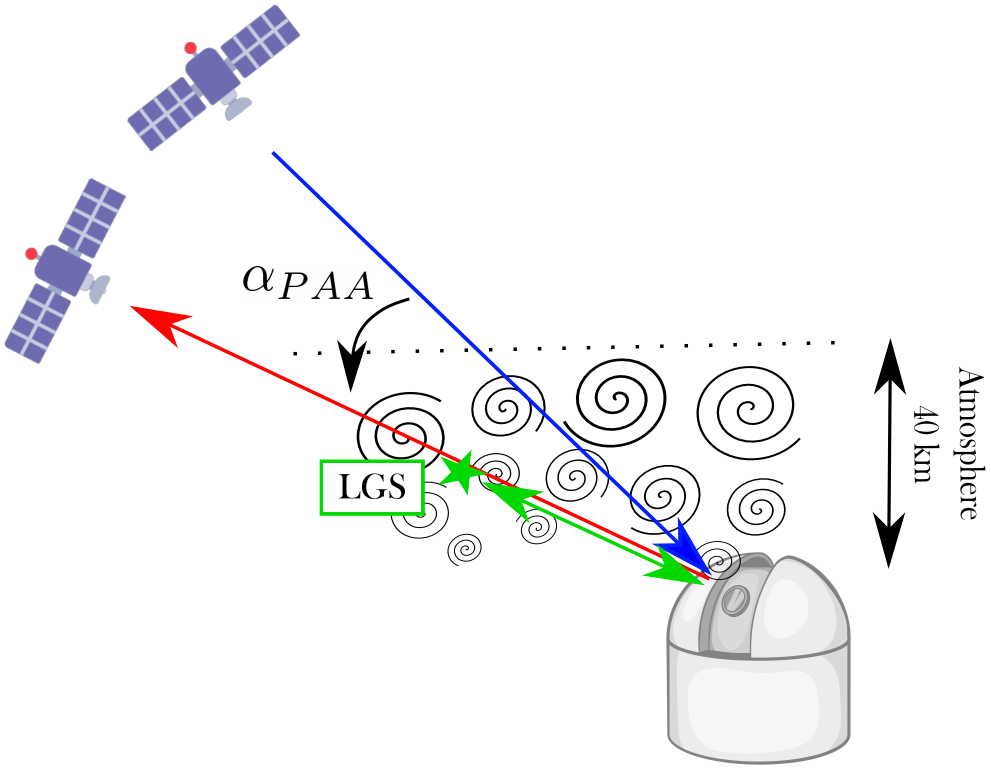

Figure 6.26: Scheme of the GEO-Feeder link aided by an LGS system, located on the axis at point-ahead angle. The downlink is depicted in blue, the uplink in red and the LGS in green.

6.2.3 Perfect LGS case

In order to study the ultimate gain achievable thanks to the estimation method relying on both downlink phase and amplitude and LGS high order phase measurements and statistical a priori. In reality, the LGS has a finite width, that implies that the measurements are made over an extended source. Therefore, as the scintillation is averaged over the extended source, we assume that we only can measure the phase from the LGS source. Also, if not stabilized, the LGS spot wanders as it is also affected by tip and tilt. However, we first assume the LGS system to be punctual and stabilized in the sky.

As a direct consequence of the LGS idealization, we assume to obtain perfect measurements of the high order modes of the phase at point-ahead angle. Secondly, as these modes are perfectly measured from the LGS, they are considered to be also perfectly corrected on the pre-compensated uplink. Therefore, we focus the study on the estimation of the tip, tilt and focus at point-ahead angle.

6.2.3.1 Theoretical estimator

In order to develop the phase estimator, we define the new error criterion as:

$$\mathbf{e} = \mathbf{\Phi}_{res,TTF} = \mathbf{\Phi}_{PAA,TTF} - \mathbf{R}\mathbf{y}_m \tag{6.16}$$

where

$$\mathbf{\Phi}_{PAA,TTF} = \begin{bmatrix} a_2^\alpha & a_3^\alpha & a_4^\alpha \end{bmatrix}^T \tag{6.17}$$

as we only aim at estimating the tip tilt and focus at point-ahead angle. The terms a_i^α depicts the projections of the phase at point-ahead angle onto the i^{th} Zernike mode.

We define the new measurement vector as:

$$\mathbf{y}_m = \begin{bmatrix} \mathbf{\Phi}_0^T & \chi_0^T & \mathbf{\Phi}_{\alpha,HO}^T \end{bmatrix} \tag{6.18}$$

where the high order of the phase at point ahead angle are described as:

$$\mathbf{\Phi}_{\alpha,HO}^T = \begin{bmatrix} a_5^\alpha & \dots & a_{N_{AO}}^\alpha \end{bmatrix}^T \tag{6.19}$$

Thanks to this new error criterion and measurement vector, we can derive the MMSE reconstructor by defining the covariance matrix between the tip-tilt-focus at point-ahead angle and the measurement vector and the autocovariance of the measurement vector.

The covariance matrix between the tip-tilt-focus at point-ahead angle and the measurement vector is computed as:

$$\mathbf{\Gamma}_{\Phi_{TTF}y_m}(\alpha) = \begin{bmatrix} \mathbf{\Gamma}_{\Phi_{TTF}\Phi}(\alpha) & \mathbf{\Gamma}_{\Phi_{TTF}\chi}(\alpha) & \mathbf{\Gamma}_{\Phi_{TTF}\Phi_{HO}}(0) \end{bmatrix} \tag{6.20}$$

where $\mathbf{\Gamma}_{\Phi_{TTF}y_m}(\alpha) \in \mathbb{R}^{3\times((N_{AO}-1)+N_{AO}+(N_{AO}-4))}$.

Moreover, we define the autocovariance of the measurement vector as:

$$\mathbf{\Gamma}_{y_m y_m}(0) = \begin{bmatrix} \mathbf{\Gamma}_{\Phi\Phi}(0) & \mathbf{\Gamma}_{\Phi\chi}(0) & \mathbf{\Gamma}_{\Phi\Phi_{HO}}(\alpha) \\ \mathbf{\Gamma}_{\chi\Phi}(0) & \mathbf{\Gamma}_{\chi\chi}(0) & \mathbf{\Gamma}_{\chi\Phi_{HO}}(\alpha) \\ \mathbf{\Gamma}_{\Phi_{HO}\Phi}(\alpha) & \mathbf{\Gamma}_{\Phi_{HO}\chi}(\alpha) & \mathbf{\Gamma}_{\Phi_{HO}\Phi_{HO}}(0) \end{bmatrix} \tag{6.21}$$

where $\mathbf{\Gamma}_{y_m y_m}(\alpha) \in \mathbb{R}^{((N_{AO}-1)+N_{AO}+(N_{AO}-4))\times((N_{AO}-1)+N_{AO}+(N_{AO}-4))}$.

Knowing the two covariance matrices, and applying Eq. 4.4, we can compute the MMSE estimator, that we name: $MMSE_{\Phi\chi,LGS}$

6.2.3.2 Performance analysis

In this section, we present the performance of the estimator developed above. First, we detail the benchmark cases used to compare the new estimator results and then present the results obtained with the new tip tilt and focus estimator.

Benchmark cases

We compare the results obtained with the $\text{MMSE}_{\Phi\chi,\text{LGS}}$ method to two classes of methods: the methods not aided and aided by an LGS system. Concerning systems not aided by an LGS system, we consider the classical pre-compensated case and the $\text{MMSE}_{\Phi\chi}$ case from chapter 4. In these cases, the residual phase variance is distributed over all the Zernike modes, as illustrated in black and blue dots on figure 6.27.

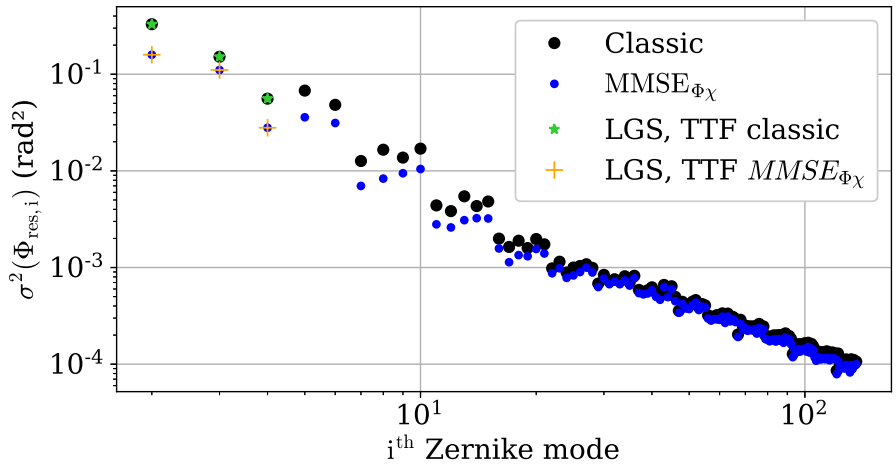

Figure 6.27: Modal residual phase variance function of the Zernike mode for the all the benchmark cases computed from E2E data.

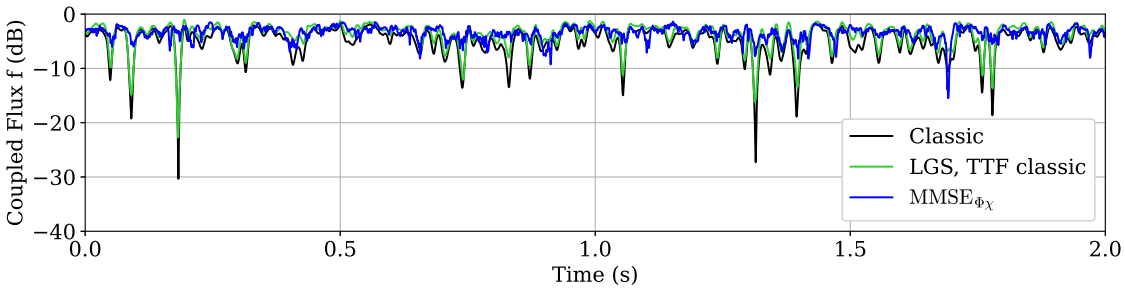

Figure 6.28: Coupled flux time series for all the benchmark cases.

As for the method aided by an LGS system we consider the LGS method with a tip tilt and focus corrected with the downlink tip tilt and focus, that we call LGS-1, that was already modeled in chapter 3, and the LGS method with a tip tilt and focus corrected with the tip tilt and focus estimated with the $MMSE_{\Phi\chi}$ method, that we call LGS-2. We denote in the graphs LGS-1 as LGS, TTF classic and LGS-2 as LGS, TTF $MMSE_{\Phi\chi}$, for sake of clarity. Because we neglect the temporal error and consider a perfect LGS system, we assume in these cases the high order modes to be perfectly corrected. Therefore, the modal residual phase variance corresponds to the green and orange stars from figure 6.27. We highlight that the results corresponding to the LGS-2 case are new, however we consider them as benchmark as they correspond only to the naive concatenation of the LGS-1 method and the $MMSE_{\Phi\chi}$ method without further computation.

The coupled flux associated with the benchmark cases is depicted in figure 6.28. We can already observe that the signal associated with the LGS-1 correction case depicted in green still presents long and deep fades, whereas the $MMSE_{\Phi\chi}$ case erases most of the fades. The first conclusion is that the system without LGS but with MMSE phase estimation leads to better coupled flux statistics than the LGS system with anisoplanatic tip-tilt and focus. We also illustrate in figure 6.29 the comparison between the coupled flux obtained with the LGS-1 and LGS-2 correction. A clear reduction of the fades is observed using the LGS-2 method, that limits the pre-compensation error on the tip-tilt and focus.

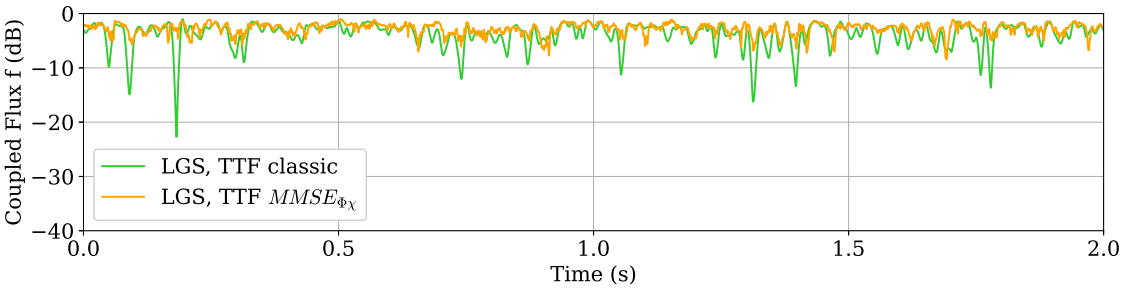

Figure 6.29: Coupled flux time series for the LGS-1 = LGS, TTF classic and LGS-2=LGS, TTF $MMSE_{\Phi\chi}$ cases.

Tip tilt and focus reduction

In this section, we present the results obtained with the new estimator $\text{MMSE}_{\Phi\chi,\text{LGS}}$ relying on the off-axis LGS phase high order modes, downlink phase and log-amplitude measurements and statistical priors. In figure 6.30, we plot the on the left the absolute value of the residual phase variance of the tip, the tilt, and the focus for the classical case (in black), the $MMSE_{\Phi\chi}$ case (in blue), and the $\text{MMSE}_{\Phi\chi,\text{LGS}}$ case in red, for the MOSPAR 9090 atmospheric turbulence conditions. We observe that the $\text{MMSE}_{\Phi\chi,\text{LGS}}$ further decreases the residual phase variance of these modes. This gain is highlighted in the figure on the right where we observe that the tip-tilt and focus are reduced by 70%, 50%,and 80% with respect to the classical case. This gain is higher than for the $\text{MMSE}_{\Phi\chi}$ without LGS.

We also plot in figure 6.31 the tip tilt and focus reduction in the MOSPAR 9999 case. In these turbulence conditions, the tip tilt and focus are shown to be higher than in the MOSPAR 9090 case. Both methods, $MMSE_{\Phi\chi}$ and $MMSE_{\Phi\chi,LGS}$, show to reduce the tip tilt and focus values, with a reduced efficiency than in the MOSPAR 9090 case. However, the reduction is still high, reducing the tip variance by 60%, the tilt value by 50% and the focus value by 70%. This results in an absolute value of these modes that is below 0.22 rad^2. We recall that the absolute values of the tip and the tilt are important, as it is related to the beam wandering around the satellite pupil.

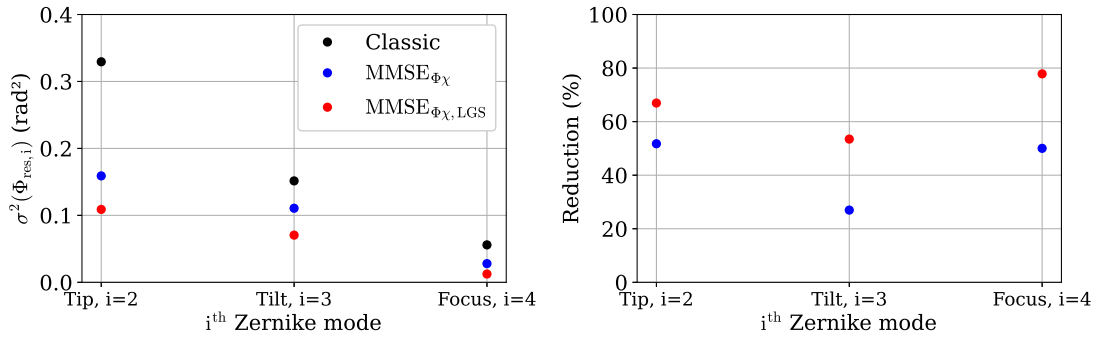

Figure 6.30: Tip tilt and focus residual phase variance for the classical pre-compensation, the $MMSE_{\Phi\chi}$ case and the new estimated $MMSE_{\Phi\chi,LGS}$ case, in the **MOSPAR 9090** conditions. The absolute value of the residual phase is depicted on the left and the reduction gain on the right.

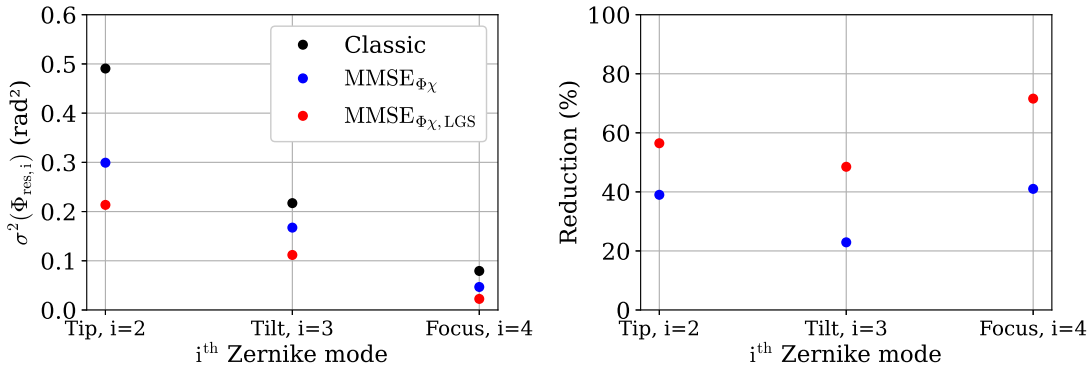

Figure 6.31: Tip tilt and focus residual phase variance for the classical pre-compensation, the $MMSE_{\Phi\chi}$ case and the new estimated $MMSE_{\Phi\chi,LGS}$ case, in the **MOSPAR 9999** conditions. The absolute value of the residual phase is depicted on the left and the reduction gain on the right.

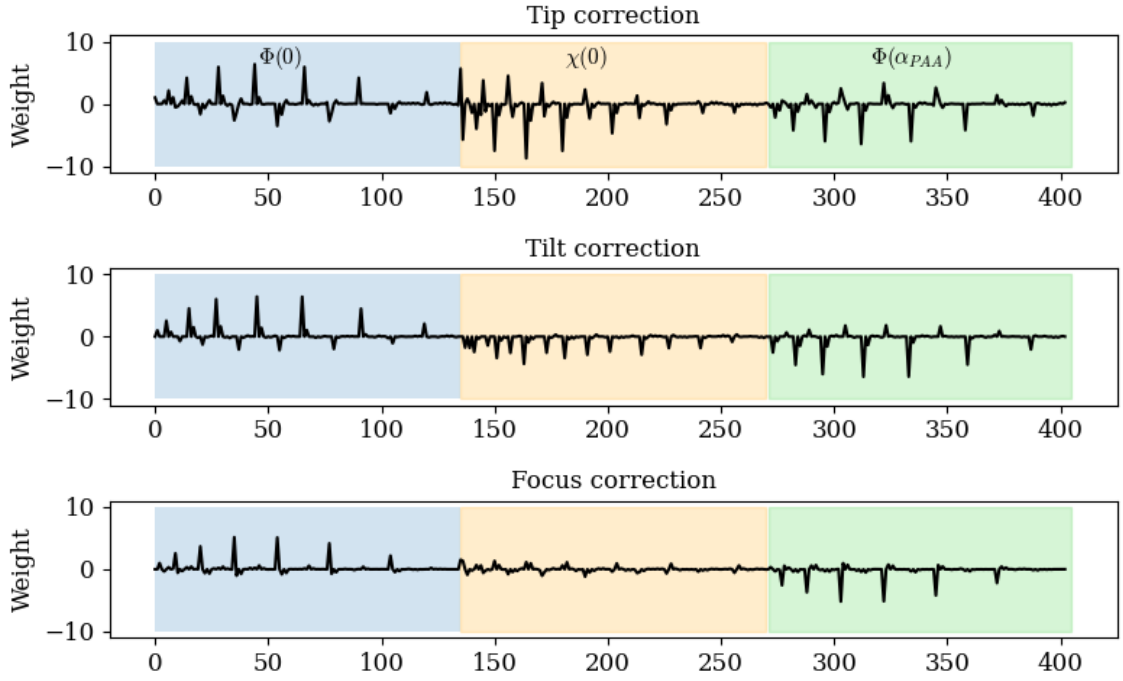

Figure 6.32: Weight of the j^{th} columns of the LGS reconstructor, applied to the j^{th} component of the measurement vector.

We also plot in figure 6.32 the weight of the reconstructor applied to the j^{th} component of the measurement, for the tip, tilt and focus correction. We observe in this case that every type of physical quantity is useful in the estimation. We interpret the fact that even the phase on-axis allows for an improvement, on the contrary to the one aperture only estimation, because the joint measurement of phase on-axis and off-axis is more informative than using only the on-axis phase measurement.

Impact on the coupled flux statistics

We plot in figure 6.33 the cumulative density function of the coupled flux function of the coupled flux threshold F_t obtained with the classical pre-compensation (black), the

$MMSE_{\Phi\chi}$ method (blue), the LGS-1 method (green), the LGS-2 method (orange) and the $MMSE_{\Phi\chi,LGS}$ method (red), for the two turbulence cases, MOSPAR 9090 on figure 6.33a and MOSPAR 9999 on figure 6.33b. First, we observe, as noticed in figure 6.28, that the method $MMSE_{\Phi\chi}$ performs better than the LGS-1 method (with a tip tilt and focus correction issued from the downlink). Secondly, analyzing the methods using a laser guide star, the $MMSE_{\Phi\chi,LGS}$ outperforms the other strategies for both turbulence cases. In particular, the new estimator $MMSE_{\Phi\chi,LGS}$ provides a 19 dB gain with respect to the classical case in the MOSPAR 9090 turbulence conditions and a 20 dB gain in the MOSPAR 9999 turbulence conditions, at probability 10^{-3}. All the gains with respect to the classical case are depicted in table 6.1. As a conclusion, the new estimation method allows reducing the probability of occurrence of deep fades.

	Without LGS	With LGS		
Case	$MMSE_{\Phi\chi}$	LGS-1	LGS-2	$MMSE_{\Phi\chi,LGS}$
Gain at 10^{-3}, MOSPAR 9090	13 dB	5 dB	16 dB	19 dB
Gain at 10^{-3}, MOSPAR 9999	8 dB	4 dB	13 dB	18 dB

Table 6.1: Gain on the cumulative density function at probability 10^{-3} with respect to the classical pre-compensation case, in dBs.

To go further, we analyze the probability density function of the coupled flux in figure 6.34 for the four benchmark cases and the new estimated case $MMSE_{\Phi\chi,LGS}$. We observe that the LGS-1 case has the effect of improving the mean value of the coupled flux, but does not reduce the variance of the signal, whereas all the cases with an estimated tip tilt and focus shows an increased mean but also decreased variance. Indeed, we report scintillation indexes (normalized by the mean variance) equals to: 0.15, 0.11, 0.06, 0.05, 0.02 and 0.26, 0.21, 0.15, 0.12, 0.07, for the case MOSPAR 9090 and 9999 and for the classical, LGS-1, $MMSE_{\Phi\chi}$, LGS-2, and $MMSE_{\Phi\chi,LGS}$, respectively.

In figure 6.35, we plot the link margin after turbulence losses for all the considered AO pre-compensation cases, function of the link availability threshold, for the MOSPAR 9090 and 9999 cases. In the MOSPAR 9090 conditions, we observe that we can reach a 97% availability with the classical pre-compensation case, 98.5% with the LGS-1 technique, 99.8% with the $MMSE_{\Phi\chi}$ method, 99.97% with the LGS-2 method, and 100% with the $MMSE_{\Phi\chi,LGS}$ method. We conclude that all MMSE based techniques considerably improve the availability threshold in the MOSPAR 9090 case, with the last introduced

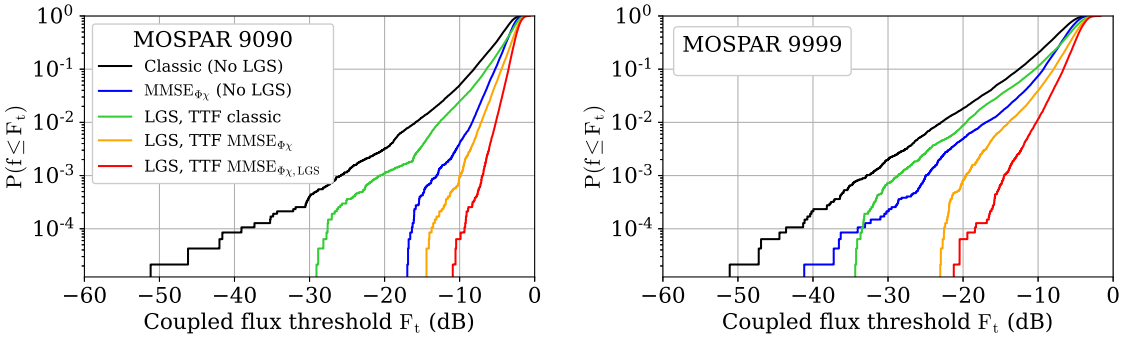

(a) MOSPAR 9090

(b) MOSPAR 9999

Figure 6.33: Cumulative density function (CDF) function of the coupled flux threshold F_t for the four benchmark cases and the new method $MMSE_{\Phi\chi,LGS}$.

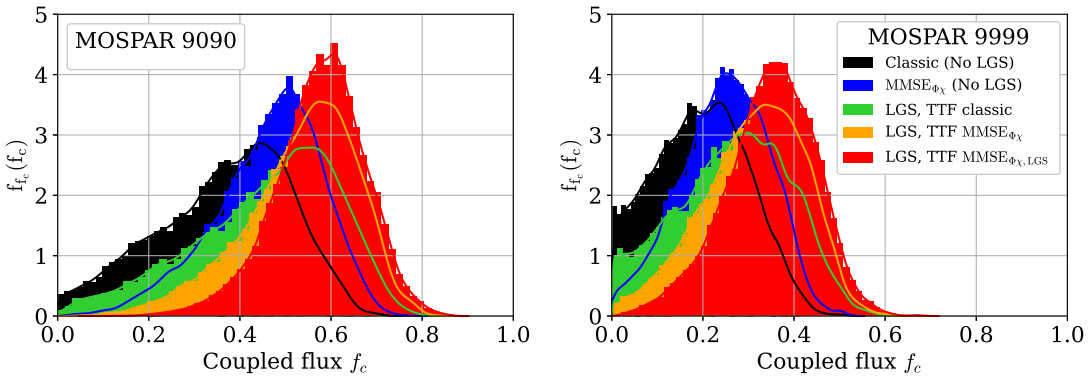

Figure 6.34: Probability density function (PDF) function of the coupled flux f_c for the four benchmark cases and the new method $MMSE_{\Phi\chi,LGS}$.

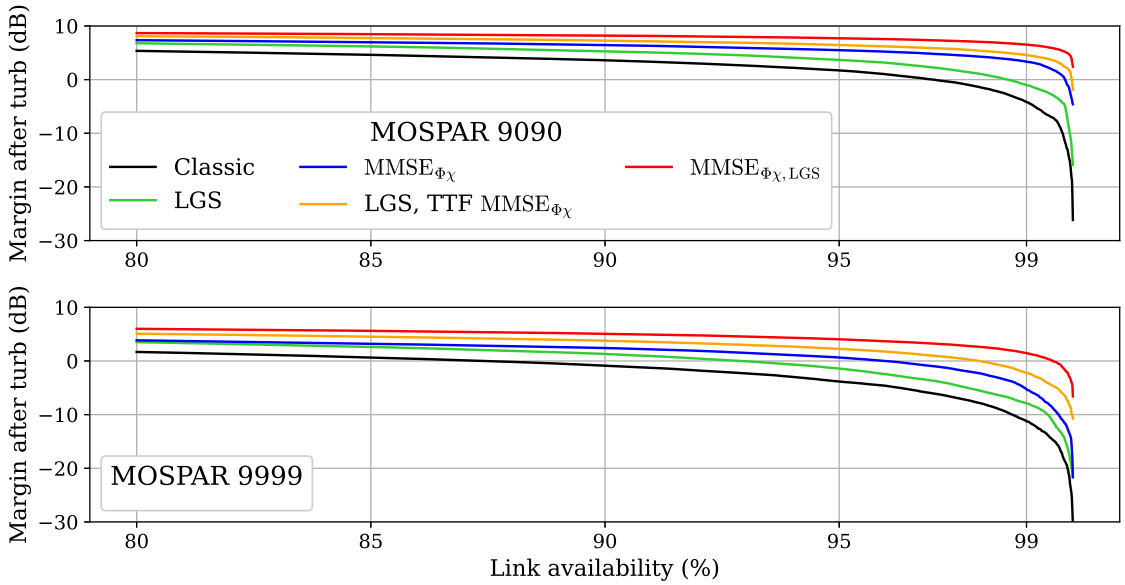

Figure 6.35: Margin after turbulence for all pre-compensation case, function of the link availability threshold, for the MOSPAR 9090 (top) and 9999 (bottom) cases.

technique ensuring a 100% reliable communication at 25 Gbps. Considering the MOSPAR 9999 case, the availability threshold decrease to 87% in the classical case, 93% for the LGS-1 case, 96% with the $MMSE_{\Phi\chi}$ method, 98% for the LGS-2 method and 99.6% in the $MMSE_{\Phi\chi,LGS}$ method. Once again, the link reliability is considerably improved with the new proposed technique.

Finally, we study the impact of this new estimator on the temporal properties of the coupled flux. Figure 6.36 depicts two 2 s time series for both MOSPAR 9090 and MOSPAR 9999 turbulence cases. We observe that in both conditions, the new estimated method decreases the number, duration, and depth of the fades with respect to the benchmark cases depicted.

This is highlighted in figure 6.37 and figure 6.38 where we plot the mean fade time and the fade frequency function of the coupled flux threshold in both turbulence cases, computed from 10 s of data. In figure 6.37, we observe that the new estimated case allows to further reduce the mean fade time with respect to every other methods. We notice in

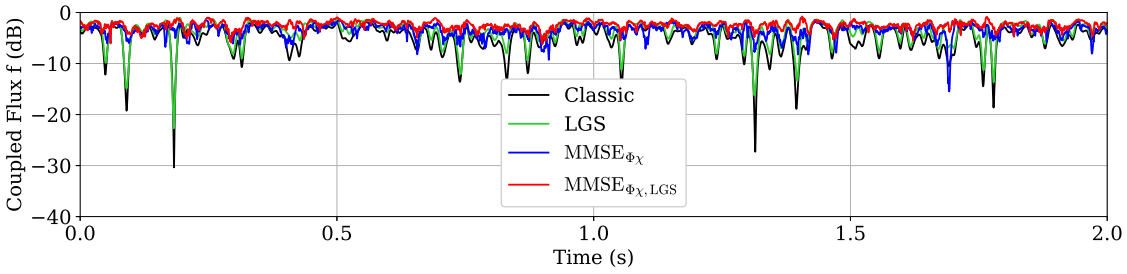

(a) MOSPAR 9090

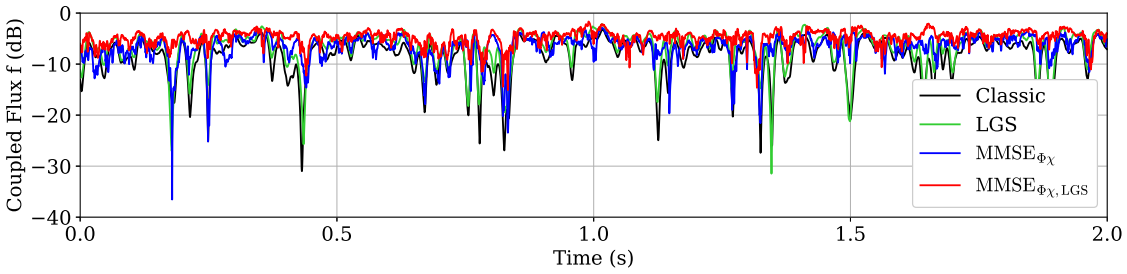

(b) MOSPAR 9999

Figure 6.36: Coupled flux time series for all the benchmark cases and the new $MMSE_{\Phi\chi,LGS}$ estimated case for two turbulence conditions.

the MOSPAR 9090 case that the fade's mean duration is comprised between 1 and 2.5 ms for a threshold from -10 to -5 dBs, whereas, in the same range, the $MMSE_{\Phi\chi}$ case average fade duration is comprised between 2.5 and 5 ms, between 7 and 12.5 ms in the LGS-1 case and 7.5 and 20 ms for the classical case. The same tendency is observed for the MOSPAR 9999 case. We also analyze the fade frequency in figure 6.38 function of the coupled flux threshold, plotted in a logarithmic scale. We observe that the new method reduces by almost a decade the fade frequency with respect to every other methods.

Conclusion

In this section, we've presented two novel methods that rely on a system aided by LGS sensing and compared their performance to the case of the literature, and the $MMSE_{\Phi\chi}$ method presented in chapter 4.

The first method is the method called LGS-2, and that uses the technique from chapter 4 to pre-compensated the tip tilt and focus of the uplink at PAA, and pre-compensates the rest of the high order modes thanks to the LGS at PAA measurements. Improving the tip tilt and focus estimation was already shown to improve the coupled flux statistics, outperforming the LGS-1 case, because of the improved tip tilt and focus correction, and also outperforming the $MMSE_{\Phi\chi}$ case, because of the total correction of the high order modes, within the scenario hypothesis.

The second method, that is at the heart of our new proposition, is to combine the measurements from the on-axis downlink beam and the LGS at PAA high order phase measurements, in order to further improve the tip tilt and focus estimation. This method is shown to outperform every other methods, bringing a high reduction of the pre-compensation phase error on the tip tilt and focus. It results in further improved coupled flux statistics, providing a 18 dB gain at probability 10^{-3} on the CDF with respect to classical pre-compensation, and a 14 dB gain with respect to the LGS-1 method. The fading statistics are also improved, showing a mean fade duration limited to 2 ms for fades at the detection

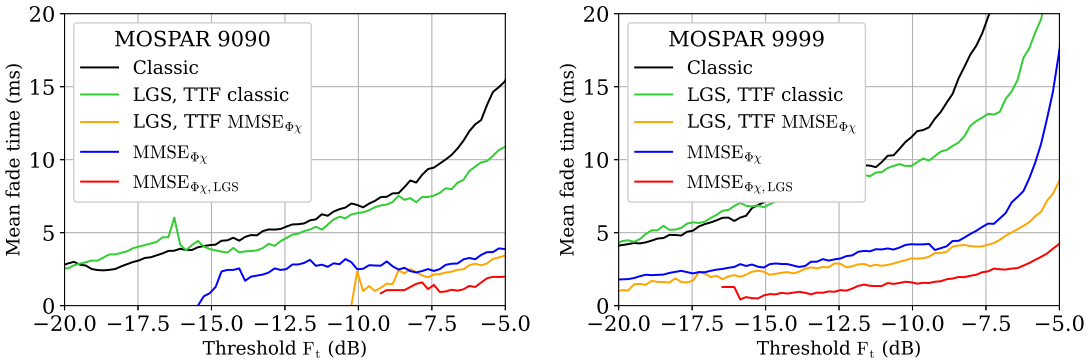

(a) (b)

Figure 6.37: Mean fade time function of the coupled flux threshold for all the benchmark cases and the new $MMSE_{\Phi\chi,LGS}$ estimated case for two turbulence conditions.

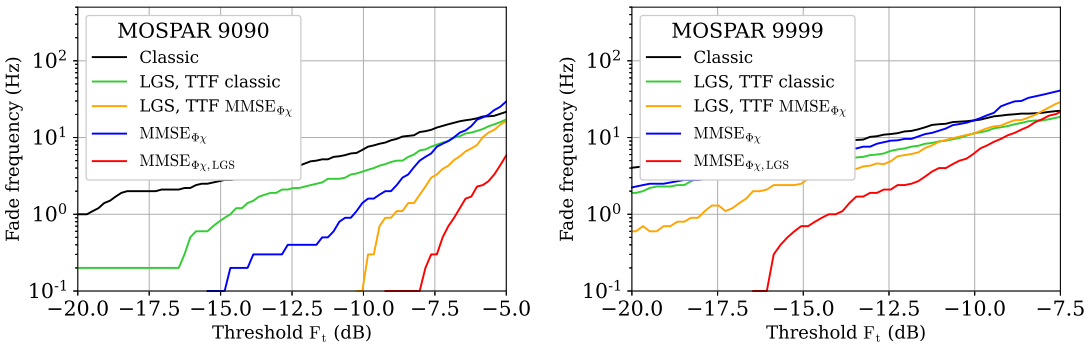

(a) (b)

Figure 6.38: Fade frequency function of the coupled flux threshold for all the benchmark cases and the new $MMSE_{\Phi\chi,LGS}$ estimated case for two turbulence conditions.

threshold of -11.7 dBs, with respect to fades duration of 10 ms in the classical and LGS-1 cases, in the tougher atmospheric turbulence case. On the other hand, in the MOSPAR 9090 case, there are no fades any more below the detection threshold.

However, the presented results corresponds to an LGS system that is idealized, and would therefore correspond to an upper bound of the achievable performance. The system is idealized for three reasons. We assumed a static LGS in the sky, located at PAA, whereas in reality, if no pre-compensation is applied to the LGS, the beam uplink LGS beam suffers from the same issue as our communication link, that is, the beam wander. In a realistic case, the high order measurements are not perfect, as the phase measured from the LGS is issued from a spot wandering in the sky. Secondly, we considered a perfect punctual spot generated by the LGS. In reality, although reduced by the monostatic nature of the LGS, the spot has a finite size. Therefore, the measurements of the LGS phase are performed on an extended source of a given width. This can also induce errors on the off-axis phase high order measurements. Finally, we neglected the noise on the LGS measurements. Although it can be neglected on the downlink beam measurements, that are done in a high flux regime, it is less true for the LGS measurements.

In the following, we propose to question the effect of the beam wander on the estimation of the tip tilt and focus.

6.2.4 Imperfect LGS case

We now consider a more realistic LGS model, and question the ability to estimate the tip tilt and focus for an imperfect LGS system. We investigate more deeply the impact of the lack of stabilization of the LGS on the tip tilt and focus estimation.

6.2.4.1 LGS stabilization

As mentioned before, the LGS system is subject to the same optical effects as the data communication uplink. An effect that can be detrimental to the retrieval of the correct high order measurements is the LGS lack of stabilization induced by the beam wander. Indeed, due to the tip and tilt induced by the turbulent atmosphere, the LGS spot wanders around the optical axis at PAA. Therefore, the photons back-propagated to the ground are issued from a location randomly moving around the optical path at PAA.

In this study, we will assume that the LGS is at minimum pre-compensated by the tip tilt from the downlink beam tip and tilt, that will already limit the beam wander.

The aim is therefore to evaluate the error on the high order modes induced by the LGS beam wander, and the impact of this error on the tip tilt and focus estimation.

6.2.4.2 Model of the unstabilized LGS

To model the measurement error on the phase high order modes of the LGS, we operate a static study, computing the angular spot deviation in the sky function of the residual tip of the pre-compensated LGS. This angular spot deviation is computed in a one dimensional study. We compute the angular deviation for the tip value at 3σ, in the turbulence conditions MOSPAR 9090. As the tip variance is larger than the tilt variance, the angular deviation considering only the tip induced displacement should provide a worst case scenario.

The relationship between the residual tip standard deviation at 3σ and the mispointing on sky is computed as:

$$\Delta\alpha = \frac{4\lambda}{2\pi D_{tel}} 3\sigma_{a_2} \tag{6.22}$$

We consider both the case where the LGS is pre-compensated by the tip and tilt issued from the downlink beacon, and the case where it is pre-compensated by the estimated $MMSE_{\Phi\chi}$ method. The tip variance at 3σ for both scenario, in the MOSPAR 9090 case, are given in table 6.2. The resulting LGS mispointing at 3σ for a 60 cm telescope diameter is also given. It results, in the LGS pre-compensated by the classical method, in a 1.71 µrad mispointing error and 0.73 µrad mispointing error in the $MMSE_{\Phi\chi}$ pre-compensated case.

	Tip value a_2 at $3\sigma_{a_2}$(rad)	$\Delta\alpha$ (µrad)
Classic	1.71	2.81
$MMSE_{\Phi\chi}$	1.17	1.92

Table 6.2: Angular mispointing at 3σ induced by the imperfect LGS stabilization, for the turbulence case MOSPAR 9090.

6.2.4.3 Impact of the lack of stabilization on the estimation

Having calculated the mispointing at 3σ, we compute the error on the estimation induced by phase high order measurements issued from $\alpha_{PAA} \pm \Delta\alpha$.

In this case, we are interested in quantifying the deviation to the perfect measurement error, of an estimated phase computed from $\alpha + \Delta\alpha$ phase high order measurements, with an estimator assuming that the measurements comes from the axis α.

In this scenario, the deviation from the perfect pre-compensation phase error writes as:

$$\Delta\mathbf{\Gamma}_{res} = \mathbf{\Gamma}_{res,perfect} - \mathbf{\Gamma}_{res,imperfect} \tag{6.23}$$

where $\mathbf{\Gamma}_{res,perfect}$ is the error covariance matrix computed as in section 6.2.3.1 and $\mathbf{\Gamma}_{res,imperfect}$ is the error covariance matrix computed from measurements of the LGS issued from $\alpha_{PAA} \pm \Delta\alpha$, with an estimator assuming measurements issued from α_{PAA}. To compute $\mathbf{\Gamma}_{res,imperfect}$, we use the formalism presented in section 4.5. Following this methodology, we define the true reconstructor as the reconstructor obtained with the measurements of the off-axis phase high order modes at $\alpha_{PAA} \pm \Delta\alpha$ to estimate the phase at α_{PAA}. The LGS measurements used to compute $\mathbf{R}$ corresponds to the actual location of the LGS. Therefore, we define the reconstructor as:

$$\mathbf{R}_{MMSE,LGS,true} = \mathbf{\Gamma}_{\Phi_{TTF}y'_m}(\alpha)\mathbf{\Gamma}_{y'_m y'_m}(0) \tag{6.24}$$

where y'_m is defined as:

$$\mathbf{y}'_m = \left(a_2^0, ...a_{N_{AO}}^0, b_1^0, ..., b_{N_{AO}}^0, a_5^{\alpha\pm\Delta\alpha}, ..., a_{N_{AO}}^{\alpha\pm\Delta\alpha}\right) \tag{6.25}$$

and the reconstructor with wrong angular priors (assuming an LGS high order modes measurement at α_{PAA}):

$$\mathbf{R}'_{MMSE,LGS} = \mathbf{\Gamma}_{\Phi_{TTF}y_m}(\alpha_{PAA})\mathbf{\Gamma}_{y_m y_m}(0) \tag{6.26}$$

where y_m is equal to:

$$\mathbf{y}_m = \left(a_2^0, ...a_{N_{AO}}^0, b_1^0, ..., b_{N_{AO}}^0, a_5^{\alpha}, ..., a_{N_{AO}}^{\alpha}\right) \tag{6.27}$$

Applying Eq. 4.26, we obtain the following residual phase covariance estimation error:

$$\mathbf{\Gamma}_{res,imperfect} = \mathbf{\Gamma}_{res,LGS,true} + \Delta\mathbf{R}\Gamma_{y'_m y'_m}(0)\Delta\mathbf{R}^T \tag{6.28}$$

where $\Delta\mathbf{R} = \mathbf{R}_{MMSE,LGS} - \mathbf{R}_{MMSE,LGS,true}$.

We plot the performance deviation in figure 6.39, in absolute value. Looking at the angular range at 3σ from table 6.2, we note that the error deviation from the imperfect measurements of high order modes is on the order of 10^{-2} rad^2 in absolute value, for the angular mispointings below 3 µrad. We conclude that the impact of the imperfect measurement of high order modes of the LGS induced by the lack of LGS stabilization is negligible.

6.2.4.4 Conclusion and perspectives

As a conclusion, using jointly LGS measurements and downlink measurements in the estimation brings a great reduction of the tip tilt and focus error. We also showed that the estimation error induced by the lack of stabilization of the LGS was negligible. However, we still need to evaluate the impact of the measurement on the extended source and the impact of the noise on the estimation. This will be done in future work.

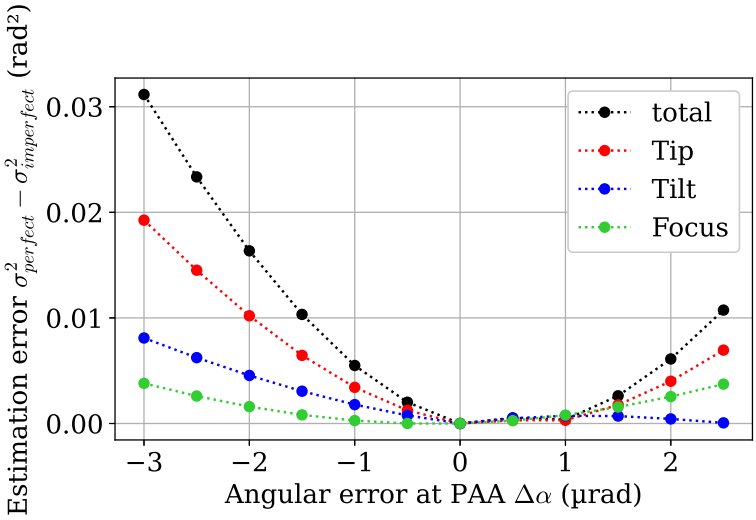

Figure 6.39: Estimation error deviation from phase estimation error using perfect LGS measurements ($\mathbf{\Gamma}_{perfect} - \mathbf{\Gamma}_{imperfect}$).

6.3 Synthesis and conclusion

Finally, we conclude this chapter, and all chapters dealing with phase estimation at point-ahead angle, by synthesizing the performance of the different methods developed and discussing on further potential of estimation methods. We also discuss their limits and challenges in perspective of future experimental demonstration.

6.3.1 Synthesis: performance comparison of the different phase estimators at PAA

We synthesize the results obtained with the different estimators developed in chapters 4, chapter 5 and chapter 6. For this comparison, we use the turbulence case MOSPAR 9090. We also note that for a fair comparison, we neglect the AO loop delay.

We start by comparing the residual phase variance associated to each method in figure 6.40.

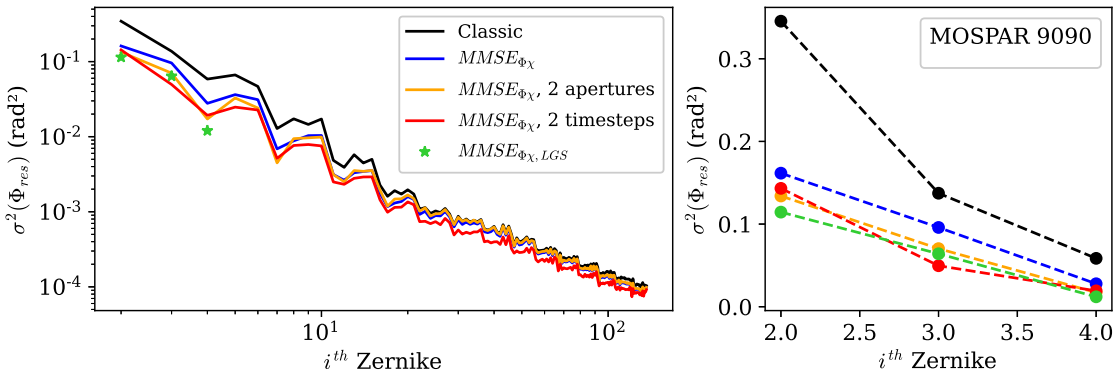

Figure 6.40: Pre-compensation residual phase variance in the MOSPAR 9090 turbulence case, for the phase AO correction: classic (black), $MMSE_{\Phi\chi}$ (blue), 2 apertures estimation case, 2 time steps estimation case and the $MMSE_{\Phi\chi,LGS}$ method. On the left: plotted on 136 modes, on the right: only tip tilt and focus.

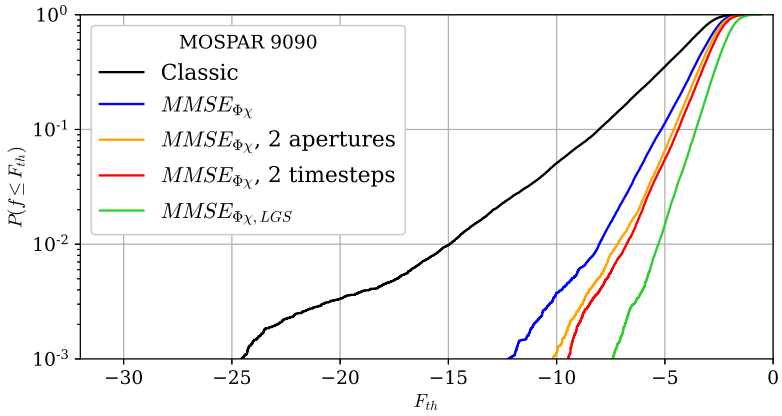

Figure 6.41: Cumulative density function for all estimated cases, for the MOSPAR 9090 case.

On the left, the residual phase is plotted for 136 modes. We observe that the method, using two time steps of phase and log-amplitude in the estimation, is the only one allowing decreasing the high order modes. We also observe that the two apertures estimation allows decreasing the low order modes with respect to the $MMSE_{\Phi\chi}$ method, but brings less improvement than the two time steps estimation on the low order modes. When analyzing the methods' performance on the tip tilt and focus estimation, it is shown that the tip is better estimated by the $MMSE_{\Phi\chi,LGS}$ method, followed by the 2 apertures estimation method, the 2 time steps method and the $MMSE_{\Phi\chi}$ method. It is worth noticing that spatial estimation methods (LGS and two apertures) are the methods reducing the most the tip, that is the mode the most affected by the anisoplanatism. We explain this gain by the incorporation in the estimation of information in the direction of the PAA, allowing to exploit correlations to correct the modes that are the most affected by the orientation of the link. We also note that the tip behavior is different. In this case, the two time step estimation performs better. This shows that spatial and temporal estimation benefit from different information that impacts differently the estimation. Finally, we also observe that for all methods, except the two time steps estimation method, the tip-tilt-focus curve seems linear. Given this analysis, we expect the LGS method to better reduce the fades and improve the coupled flux quality.

This is confirmed by analyzing the coupled flux statistics, whose CDF is plotted in figure 6.41. We observe that all cases brings significant gain with respect to the classical case. The 2 aperture and 2 time steps cases are shown to perform similarly. However, it is the LGS based estimation that performs the best. The slope of the LGS based estimation is similar to the two apertures and two time steps estimation, however, the mean value of the LGS based estimation is better, shifting the curve toward 0. From these observations, we conclude that the low-order modes reduction improves the slope of the CDF (an improved slope is a steeper slope), meaning that it reduces the signal variance, whereas the high order modes reduction improves the signal mean, bringing a gain that shifts the curve toward the low attenuations values. There is therefore an interest, as in the LGS case, to both improve the low order modes estimation and correct the high order modes.

Finally, we analyze the temporal characteristics of the coupled flux obtained with the different methods. As an illustration, we plot all time-series in figure 6.42. Globally, all methods allow erasing the deep fades. For a quantitative analysis, we plot the mean fade duration and the fade frequency with respect to the coupled flux threshold in figure 6.43. We observe that the two aperture estimation does not decrease the mean fade duration with respect to the $MMSE_{\Phi\chi}$ method, but reduces the fade frequency. Considering the

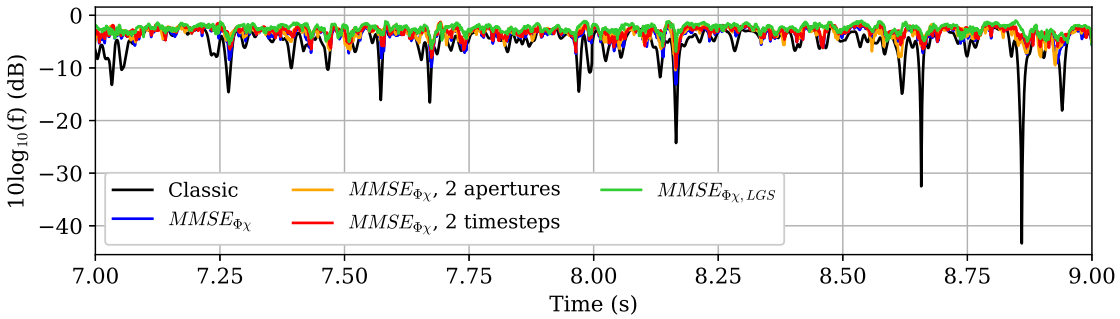

Figure 6.42: Time-series for all estimated cases, for the MOSPAR 9090 case.

behavior of the methods correcting high order modes, they seem to follow the same behavior but shifted toward zero, once again as a consequence of the increased signal average value. Analyzing the fade frequency, the fades are shown to be more frequent in the two time steps estimated case than the two aperture estimated case. We conclude that in this case, the fades are more frequent but shorter. This might be due to the less effective tip reduction of the two time steps estimation case. Finally, the LGS estimated case and temporal estimated cases have the same fade frequency behavior, but shifted toward zero. We conclude that the low order modes reduction, especially the tip that is very energetic, allows reducing the fade frequency. Additionally, correcting the high order modes provides an additional gain on the fade statistics, that shifts the curves toward zero with respect to the threshold.

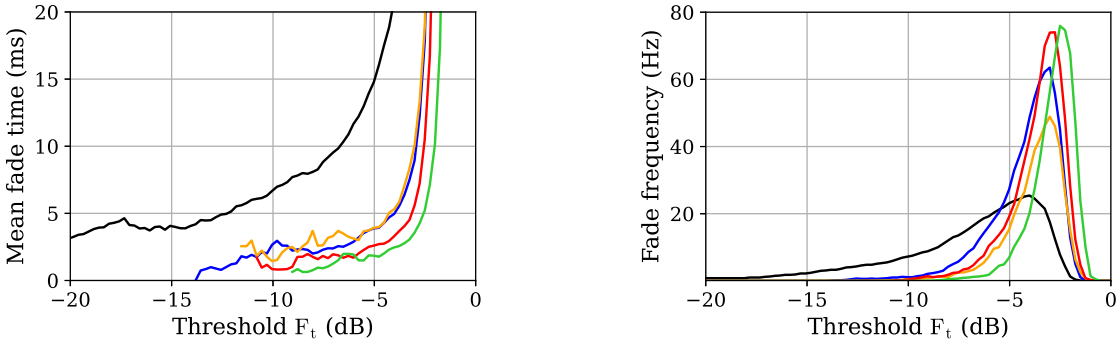

(a) Mean fade time

(b) Fade frequency

Figure 6.43: Fading statistics for all estimation methods, for the MOSPAR 9090 case.

In figure 6.44, we plot the temporal autocorrelation function obtained from the different channels, in the MOSPAR 9090 turbulence case. Compared with the width at half maximum of the classical pre-compensated case, equals to 7.3 ms, we obtain a lag of 6.3 ms, 5.5 ms, 5.5 ms and 4.6 ms obtained with the two apertures method, the $MMSE_{\Phi\chi}$ method, $MMSE_{\Phi\chi,LGS}$ method and the two time steps estimation method, respectively. We note that the two time steps estimation method outperforms all other methods. This should benefit to the interleaving process.

To conclude, we showed that the **different types of measurements** and priors were bringing **gains of different nature**, and that these two categories of priors can be separated in temporal and spatial priors. The spatial priors are shown to impact only the low order modes, with an increased efficiency to correct the modes that are more affected by the link orientation, whereas the temporal priors allow for correcting all the modes,

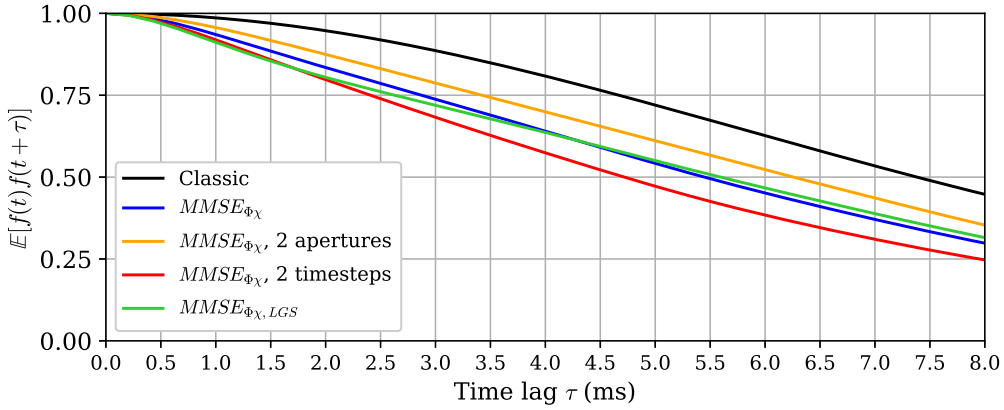

Figure 6.44: Temporal autocorrelation function of the coupled flux, function of the time lag τ, for all the pre-compensation methods, in the MOSPAR 9090 case.

but with less efficiency on the tip reduction. We also showed that different reductions of these modes have different impact on the coupled flux and fading statistics. The low order modes reduction participates in reducing the signal variance, whereas the high order modes reduction improves the average value of the signal.

From these observations, two natural questions arise:

- given that each method is associated to a different system of different complexity, what would be the easier method to implement to obtain a trade-off between the performance and the cost/complexity of the associated system ? and what is the complexity of the systems required to measure the priors ? (such as the wind profile or the C_n^2 profile)

- knowing that spatial and temporal measurements and priors bring different information, what would be the ultimate performance combining both temporal and spatial measurements ?

We start by answering the second question in the next section.

6.3.2 Synthesis: Combination of estimation techniques

We combine the estimation methods using temporal and spatial measurements and priors. In this part, due to lack of time, we calculated the estimator directly from covariance and autocovariance matrices computed from the E2E data, in order to illustrate the concept. As our database is composed of 5 seeds of 9400 samples, we computed the estimator using the 4 first seeds, to reach statistical convergence, and applied the estimator to the set of data corresponding to the last seed. This estimator could however be computed analytically applying the formalism presented in the thesis.

We illustrate the potential of combining different estimation techniques by combining an estimation relying on several past measurements on two apertures. The same principle could be applied to the LGS system.

Temporal and multi-aperture measurement and statistical priors

We combine measurements taken from several apertures at different time steps. We consider two past measurements of phase and log-amplitude on two 60 cm apertures. We compute the estimated pre-compensation phase and the associated coupled flux in the

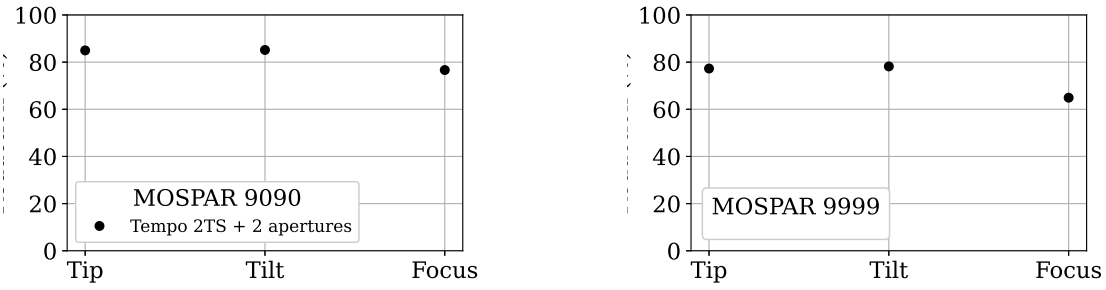

(a) MOSPAR 9090 (b) MOSPAR 9999

Figure 6.45: Residual phase variance reduction for the tip tilt and focus for the estimation method combining temporal and multi-aperture measurements.

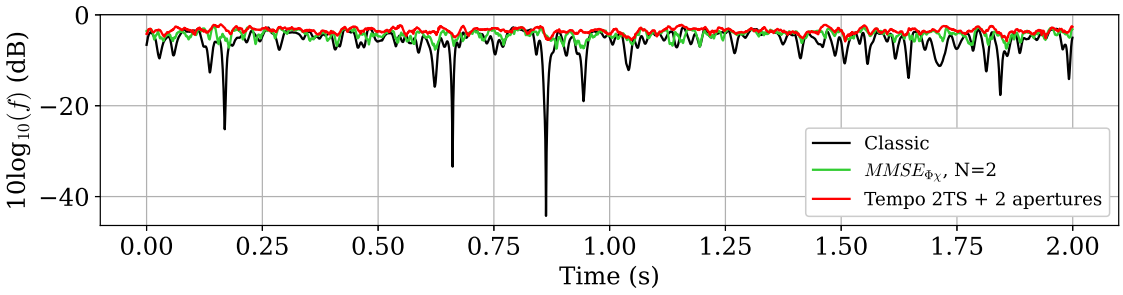

Figure 6.46: Time-series of the coupled flux pre-compensated by AO for the methods: classic (black), two aperture estimation (green), combined two-aperture and two time steps estimation (red), in the MOSPAR 9090 case.

MOSPAR 9090 and MOSPAR 9999 case, to evaluate the robustness of the estimator to greater angular decorrelation regimes.

We plot, in figure 6.45, the residual phase variance reduction percentage for the tip tilt and focus in the MOSPAR 9090 and 9999 case. We observe gains that we have never observed before, above 80% in the MOSPAR 9090 case and around 79% in the MOSPAR 9999 case. We plot the associated time-series in figure 6.46 and figure 6.47. In both cases, the estimation method combining the temporal and spatial measurements and priors is more robust, erasing more fades. The improvement is even more noticeable in the MOSPAR 9999 case, where the two aperture estimation case was not correcting every fade, that are now limited by the combined estimation.

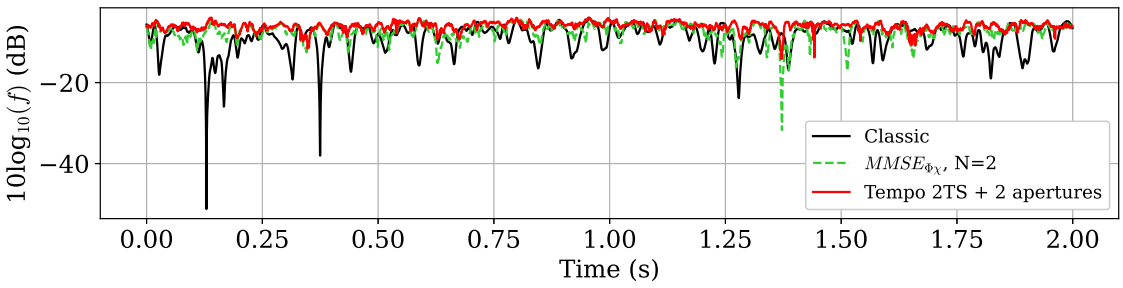

Figure 6.47: Time-series of the coupled flux pre-compensated by AO for the methods: classic (black), two aperture estimation (green), combined two-aperture and two time steps estimation (red), in the MOSPAR 9999 case.

We conclude that, combining spatial and temporal estimation methods provides a larger gain on the pre-compensation phase error reduction, allowing to make the link more reliable in very severe atmospheric conditions. We believe that such methods could allow extending the link availability for every OGS, and, by improving the overall link budget and statistics of the received SNR onboard the satellite, allow for unlocking reliable high data rates transmissions. The latter assumption still needs to be confirmed.

6.4 Conclusion and perspectives

In the last three chapters, we studied the estimation of the phase at point ahead angle using a minimum-mean-square error estimator based on measurements available at the optical ground station. We developped the MMSE estimation in four flavors, modifying the measurement vector. We used the phase and log-amplitude measurements, the phase and log-amplitude past measurements or collected on several apertures or from an LGS, to improve the phase estimation at PAA. Both spatial and temporal measurements improve the estimation, and also show to bring complementary information.

The next natural step is therefore to confirm these gains and assessing for the feasibility of each method by undertaking experimental demonstration of the different proposed methods. They are all associated to different cost and implementation complexities, however some experimental challenges are common to all methods, such as the impact of the C_n^2 metrology on the estimation.

A second perspective is to evaluate the telecommunication performance obtained on each of these channels. This is the topic of the next chapter.

CHAPTER 7

Optimization of the telecom transmission chain

Contents

7.1 Introduction

Previously, we modeled and improved the AO pre-compensated channel statistics. To evaluate the channel performance and gain brought by the different methods, we compared the gains on the signal CDF and the margin with respect to a given detection threshold.

In this chapter, we abandon these metrics at a precise threshold corresponding to a certain transmission rate, and evaluate the channel transmission limits, that are defined as the channel capacity. As the coupled flux onboard the satellite is a random variable, the channel capacity itself is a random variable that needs to be modeled and characterized. To serve future developments, in particular digital communication systems optimization, we also explore the analytical modeling of the coupled flux statistics.

Therefore, we start in this chapter, in section 7.2 by evaluating the AO pre-compensated channel capacity, for the classical pre-compensation and for the developed estimated pre-compensation phase developed in this thesis, that are summarized in section 7.3. We evaluate this capacity in presence or not of an interleaver, to study if the proposed estimators allow for a reduction of the interleaver size. Indeed, reducing the interleaver size

is at stake to reduce the system complexity onboard the satellite, and to minimize the latency of the link. Finally, in 7.4, we present preliminary results on the development of the analytical AO pre-compensated ground to GEO channel. In this study, we continue using the reciprocal modeling point-of-view, in order to take advantage of existing models accounting for AO correction.

7.2 Theoretical transmission limits of the channel

7.2.1 Capacity definition

7.2.1.1 General definition

The capacity is defined as the maximal quantity of information that can be reliably transmitted over a communication channel. Indeed, as stated by the noisy coding theorem of Shannon [218], if the communication rate that we denote R is strictly below the capacity $\mathcal{C}$, it is possible to communicate discrete data (digital information) nearly error-free. The capacity is defined as units of information per unit of time.

We compute the capacity as follows. Let $X \in \mathcal{X}$ and $Y \in \mathcal{Y}$ be two random variables, from the alphabet $\mathcal{X}$ and $\mathcal{Y}$, characterized by the probability laws p_X and p_y. X is the emitted symbol and Y the received symbol after propagation through the channel. The capacity is defined as:

$$\mathcal{C} = \max_{p_X(x)} I(X;Y) \tag{7.1}$$

where $I(X;Y)$ is the mutual information between the two random variables. It quantifies the dependence between the two variables. It is computed as:

$$I(X;Y) = H(X) - H(X|Y) = H(Y) - H(Y|X) \tag{7.2}$$

where $H(X)$ is the entropy of the random variable X and $H(X|Y)$ is the conditional entropy.

The variables' entropy and conditional entropy are defined, in the case of discrete random variable (whose alphabet is discrete and finite), as:

$$H(X) = -\sum_{x \in \mathcal{X}} p(X = x) \log_2(p(X = x)) \tag{7.3}$$

and

$$H(X|Y) = -\sum_{y \in \mathcal{Y}} p_Y(y) H(X|Y = y) \tag{7.4}$$

These entropies calculation can be extended to continuous random variable. In this case, the entropy is called differential entropy.

7.2.1.2 AWGN channel capacity

We recall that the AWGN channel is defined as:

$$y = x + \omega \tag{7.5}$$

where $x \in \mathcal{X}$ is the emitted symbol, $\omega \in \mathbb{R}$ is an additive white Gaussian noise following the law $\mathcal{N}(0, N_0/2)$. Therefore, the received symbol $y \in \mathbb{R}$.

Assuming a memoryless channel, the capacity of the AWGN channel is shown to be maximized for a continuous random variable X whose probability function is Gaussian. In this case, the capacity, also known as the Shannon capacity, writes as:

$$\mathcal{C}_{AWGN} = \frac{1}{2} \log_2(1 + SNR^{lin}) \tag{7.6}$$

where the SNR^{lin} is the linear electrical SNR defined as the ratio of the received electrical power P over the noise power N_0.

In the case of bandwidth limited channels, following the Shannon-Hartley theorem [219], the capacity becomes:

$$\mathcal{C}_{AWGN,BL} = B\log_2(1 + \frac{P}{N_0 B}) \tag{7.7}$$

where B is the signal electrical bandwidth.

In the case where the alphabet of the input symbols X is discrete, following a uniform distribution, the mutual information, writes as:

$$I(X;Y) = \sum_{x\in\mathcal{X}} \int dy P_X(x) f_{Y|X}(y|x) \log_2 \left(\frac{f_{Y|X}(y|x)}{\sum_{x\in\mathcal{X}} P_X(x) f_{Y|X}(y|x)} \right) \tag{7.8}$$

where, P_X is the probability law of X, following a uniform distribution over $\mathcal{X}$ (for instance $\mathcal{X} = \{-1, 1\}$ in the BPSK case), and $f_{Y|X}(y|x)$ is the probability density function of a Gaussian variable, centered on the X value.

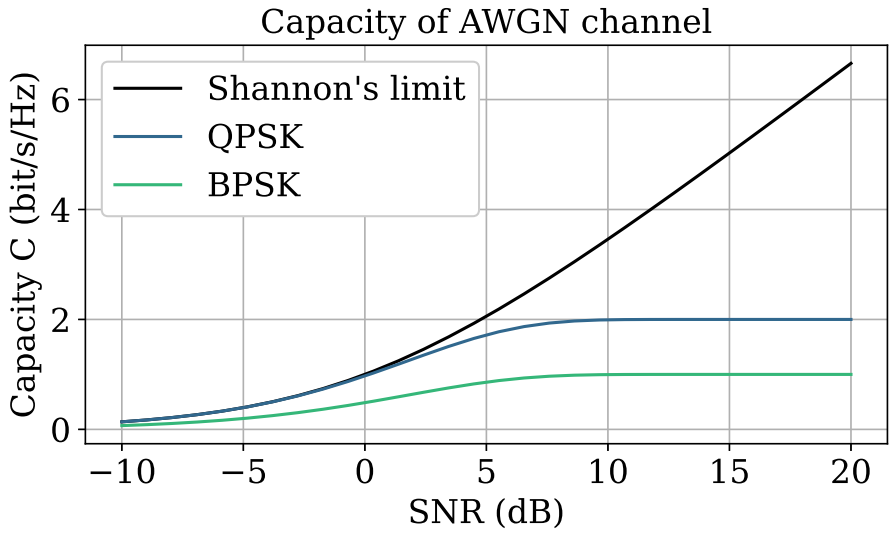

Figure 7.1: AWGN channel capacity function of the SNR.

We illustrate the bandwidth limited Shannon's capacity and the mutual information in the BPSK and QPSK case in figure 7.1. The capacity is expressed in information bits per second and per Hertz (as we normalized the capacity by the signal bandwidth). We observe that, while the Shannon's capacity keeps increasing as the SNR increases, the DPSK and QPSK mutual information saturates. This is due to the limited spectral efficency. For instance, for BPSK, at maximum 1 information bit can be sent, and for the QPSK case 2 information bits. We also note a gap between the mutual information of the QPSK and DPSK schemes with respect to the Shannon's capacity. This gap is induced by the nature of the random variable X that is discrete and follows a uniform law. Constellation shaping aims at closing this gap by tuning the discrete distribution of X.

7.2.1.3 Capacity of fading channels

We presented above the case of the AWGN channel that is only impaired by the channel noise and depends on the received power per symbol, that we considered constant. However, in the case of the turbulent ground to satellite optical link, the received symbols are

affected by random attenuations from the turbulent channel. In this case, the channel is called a **fading channel**, and the capacity behavior depends on the statistical law of the attenuation factor denoted h in the general case.

We define the fading channel as:

$$y = hx + \omega \tag{7.9}$$

where x and y are the emitted and received signals. The symbol x energy is normalized to 1, and the noise power is denoted N_0. For the atmospheric perturbed channel, $h = \sqrt{f_{atmo}}$.

The instantaneous capacity of the fading channel is defined as:

$$\mathcal{C}_{fading} = B\log_2(1 + f_{atmo}SNR^{lin}) \tag{7.10}$$

As f_{atmo} is a random variable, the capacity is also a random variable. Hence, the capacity characterization needs to be statistical. There are two commonly used metrics to characterize fading channels: the ergodic capacity and the outage capacity.

The ergodic capacity is defined as the average of the instantaneous capacity, as

$$\mathcal{C}_{ergo} = \mathbb{E}[C(f_{atmo})] \tag{7.11}$$

It is therefore the maximum achievable rate in average. The use of the ergodic capacity is relevant for fast fading channels (channel coherence time T_c is lower than the symbol rate), whose symbol samples' will experience several fades. However, in the case of a slow fading channel (channel coherence time is much greater than the symbols' duration), the capacity can fell below the ergodic capacity for a long time, therefore not ensuring an error free transmission.

The outage probability characterizes slow fading channels. As specified by the noisy channel coding theorem, if the rate $\mathcal{R} < \mathcal{C}$, there exists a code such that the transmission is error free. The reciprocal implication of the theorem is that, if the capacity $\mathcal{C} < \mathcal{R}$, there is no code at this rate such that the transmission is error-free. In the case of the slow fading channel, as the capacity is a random variable, for a fixed rate, there is a non-zero probability that the capacity fells below the rate. In this case, the link is said in outage. The outage probability is therefore defined as:

$$p_{outage} = Pr(\mathcal{C}(f_{atmo}) < \mathcal{R}) = Pr(\log_2(1 + f_{atmo}SNR^{lin}) < \mathcal{R}) \tag{7.12}$$

where we particularized the outage probability to the turbulent channel case.

Finally, as a derivative of the outage capacity, we define the ϵ-outage capacity, that is the capacity defined such that the outage probability is equal to ϵ. The classical value taken by ϵ is 10^{-3}.

7.2.2 Capacity of the pre-compensated ground to GEO link

Having defined the capacity, we now compute the capacity of the AO pre-compensated ground to GEO satellite optical link. We consider a one subcarrier channel, with a transmission over one polarization.

7.2.2.1 Capacity of the ground to GEO optical link without turbulence

As a benchmark, we consider the optical uplink without turbulence losses, with fixed emitted power equals to 50 W. In this scenario, the channel corresponds to an AWGN channel, whose capacity is determined with respect to the received SNR. This SNR, for a

fixed link budget, will only vary with the symbol rate, as the electrical SNR per symbol decreases when the symbol rate increases.

As explained in section 1.3.7, the electrical SNR can be defined as:

$$SNR^{dB} = OSNR^{dB} - 10\log_{10}\left(\frac{B}{12.5 * 1e9}\right) \tag{7.13}$$

where B is the signal electrical bandwidth, equals to $B = 2D_b$, where D_s is the symbol rate.

For the evaluation of the capacity, we choose the OSNR given the hypothesis from section 2.7.3. We recall, within these hypotheses, that the power received onboard the satellite equals $-25.1\ dBm$, and, after amplification, the $OSNR^{dB} = 28.9\ dB$. This OSNR is computed for an emitted power of 50 W.

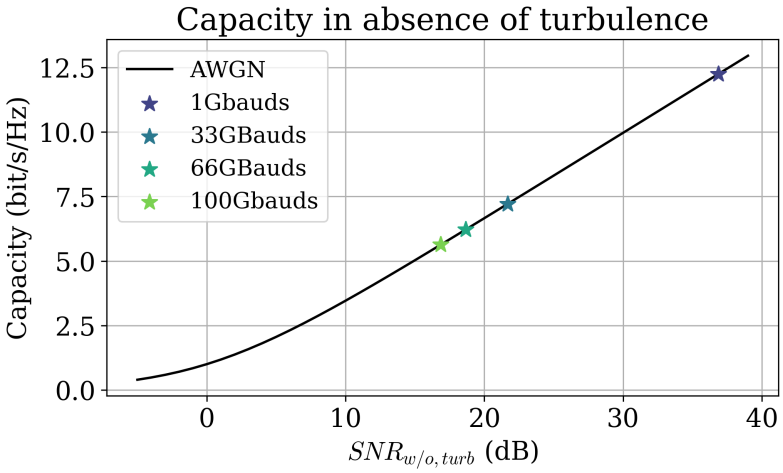

Figure 7.2: AWGN channel function of the SNR. The SNR corresponding to the link budget are plot for different Gbaud/s.

In figure 7.2, we plot the capacity function of the SNR, and highlight the SNR affected by the atmospheric channel static losses values for the baud rates 1 Gbaud/s, 33 Gbaud/s, 66 Gbaud/s and 100 Gbaud/s. The resulting SNR equals to 36.8 dB, 21.6 dB, 18.6 dB and 16.8 dB.

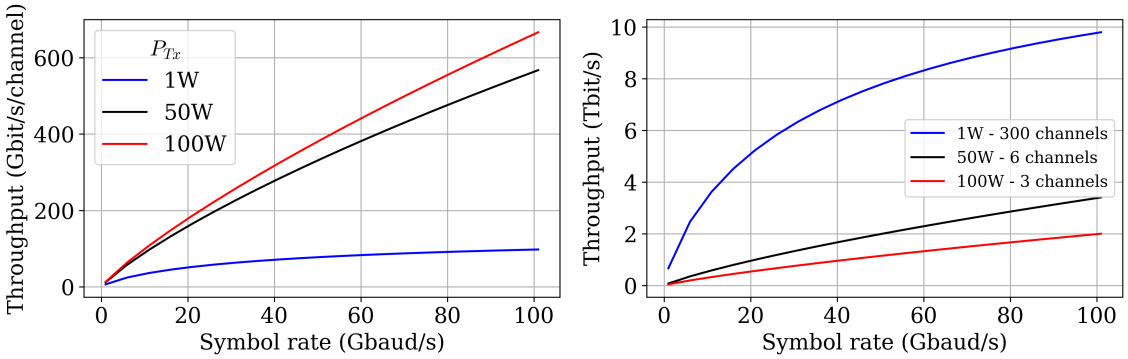

Figure 7.3: Capacity function of the baud-rate, for different emitted power. On the left, the capacity is expressed in Gbit/s/channel, and in Gbit/s on the right.

We finally compute in figure 7.3 the capacity function of the Baud-rate for different emitted power. We plot on the left the capacity in Gbit/s/Hz for the emitted power 1 W,

50 W and 100 W. We observe that with emitted power in the range of 50 and 100 W, we can reach data-rates as high as 600 Gbit/s/Hz. Now, we consider on the left the capacity in bit/s by multiplying the capacity by the number of channels. This number of channels is limited by the power constraints of 300 W over one link [27]. Therefore, we consider 300 channels when emitting 1 W, 6 channels when emitting 50 W and 3 channels when emitting 100 W. We observe that the more favorable case is the scenario using 300 channels with $P_{Tx} = 1$ W. We note that in this scenario, considering an 11.4 THz wide optical bandwidth, the baud-rate using 300 channels is limited to 38 Gbaud/s.

In the following, we introduce the impact of the attenuation of the atmospheric turbulence in the capacity evaluation.

7.2.2.2 Capacity of the AO pre-compensated uplink channel

We now study the capacity of the pre-compensated uplink channel, where we apply the classical pre-compensation. We consider the turbulence cases 9090 and 9999. To compute the capacity, we apply the fading channel capacity from equation 7.10, normalized by the bandwidth, where the coefficient f_{atmo} is extracted from the E2E time-series. We still neglect the temporal error induced by the AO loop delay.

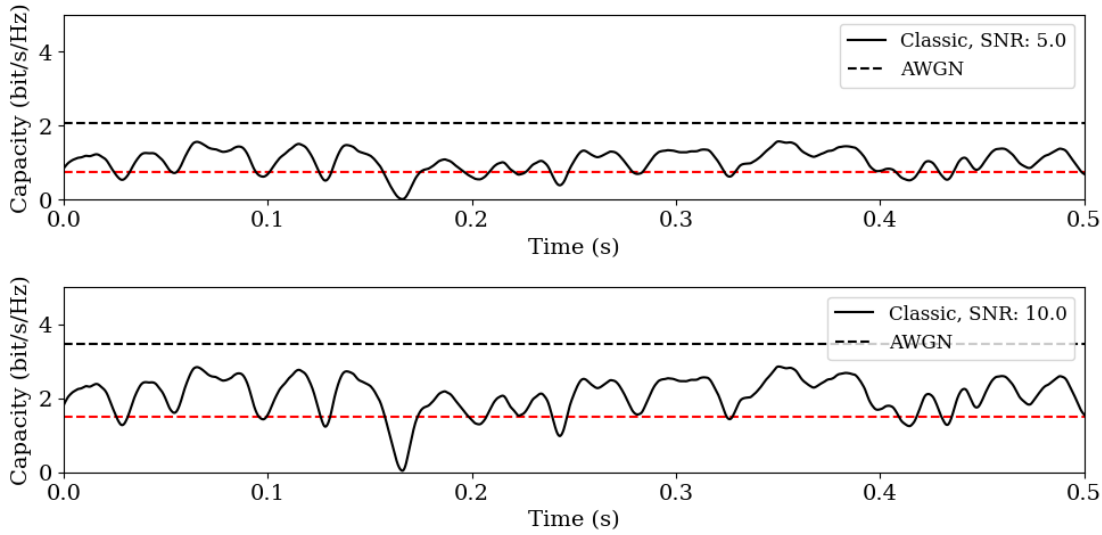

Figure 7.4: Capacity time-series of the uplink pre-compensated channel, with classical pre-compensation, in the MOSPAR 9090 case. The AWGN capacity is represented in black dashes, and the rate threshold in red dashes.

We start by illustrating the random capacity function of the time in figure 7.4, in the MOSPAR 9090 turbulence scenario, for a 0.5 s sample. In this figure, we plot the capacity for a 5 dB SNR on the top and 10 dB at the bottom, compared with the associated AWGN capacity, without atmospheric disturbances, in black dashes. We also depict in red dashes a rate threshold of 0.75 in the SNR=5 dB case, and 1.5 in the SNR=10 dB case, in order to illustrate the outages. In practice, the rate 0.75 could correspond to a FEC rate 3/4 in a one level-modulation scheme, or 3/8 in a two-level modulation scheme, and the 1.5 rate a 3/4 rate in a two-level modulation scheme (QPSK for instance). We observe that for the chosen thresholds, there is one or several outages of several milliseconds.

We study the link reliability thanks to the outage probability in figure 7.5, where we plot p_{outage} function of the SNR, for the two turbulence cases and the rates 0.7 and 1.5 depicted earlier. In this case, we observe that for reaching a 99.9% reliability threshold,

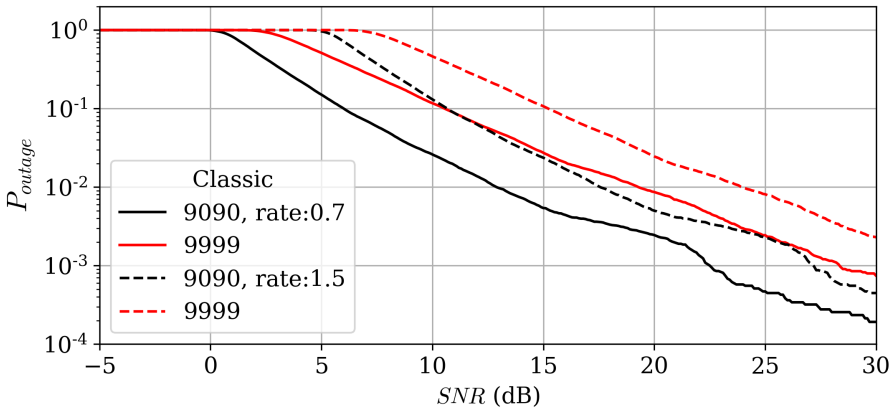

Figure 7.5: Outage probability function of the SNR, for the MOSPAR 9090 case (black) and 9999 (red), for the rates 0.5 (plain lines) and 1.5 (dashed lines).

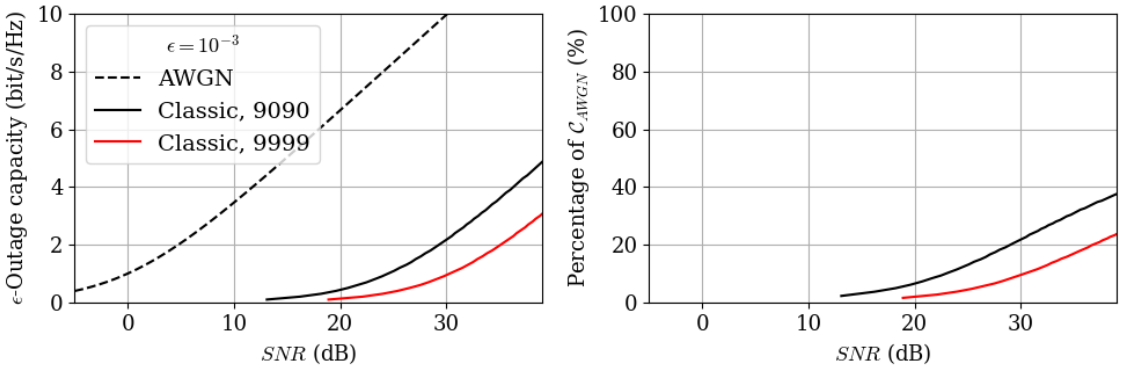

Figure 7.6: ϵ-outage capacity in the MOSPAR 9090 (black) and 9999 (red) cases, in absolute value on the left and in AWGN capacity percentage on the right.

corresponding to an outage threshold of 10^{-3}, for a 0.7 rate, the SNR should be at least equal to 22 dB in the MOSPAR 9090 case and 27 dB in the MOSPAR 9999 case.

Finally, by retrieving the values at probability 10^{-3} on the outage probability for several rates and SNRs, we plot the ϵ-outage capacity in figure 7.6, function of the SNR, for a $\epsilon = 10^{-3}$. We plot on the right the absolute value of the ϵ-outage capacity, and the percentage of the AWGN capacity on the right, for the classical pre-compensation in the 9090 and 9999 turbulence conditions. We observe that it is impossible to communicate with this reliability level, even at low rates, if the SNR is below 12 dB. We observe, for instance for a rate equal to 2, a minimum of 20 dB loss, with respect to the AWGN channel. Additionally, in the best case, at high SNR (30 dB), we can only achieve 40% of the AWGN capacity. We observe in the MOSPAR 9090 case a capacity loss of 99% to 60% in the SNR range 12 to 40 dB, and 99% to 75% in the MOSPAR 9999 case, in the SNR range from 19 to 40 dB.

To conclude, the capacity of the classical AO pre-compensated channel is very impaired by the atmospheric turbulence. To have a reliable transmission, it is necessary to have a high SNR.

7.2.2.3 Capacity gain with advanced pre-compensation techniques

In the following, we quantify the capacity improvement brought by the different estimation methods proposed in the manuscript, with respect to the classical AO pre-compensation

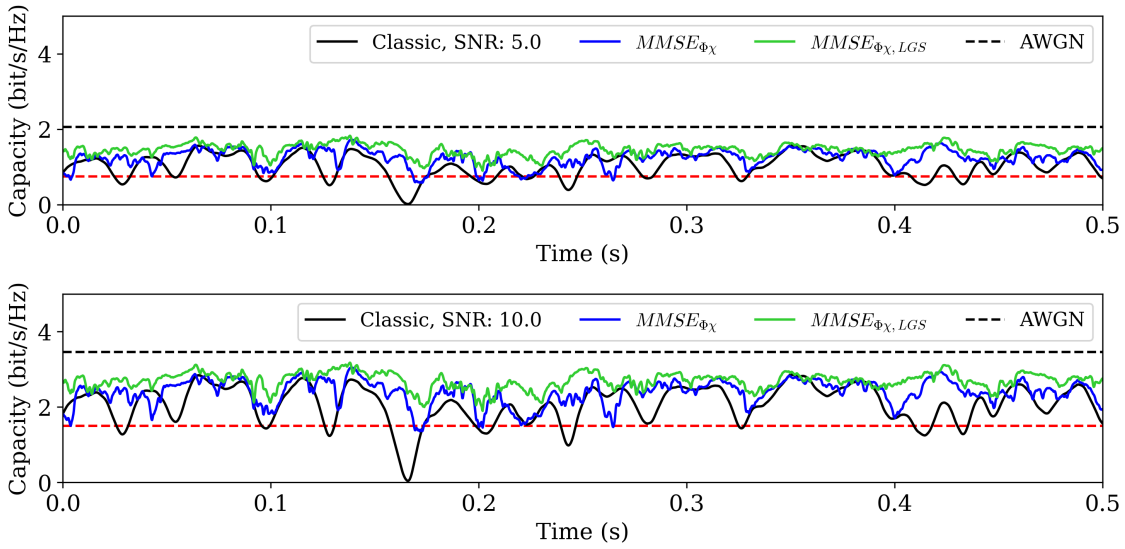

Figure 7.7: Capacity time-series of the uplink pre-compensated channel, with classical pre-compensation, and the estimated pre-compensations $MMSE_{\Phi_\chi}$ and $MMSE_{\Phi_\chi,LGS}$, in the MOSPAR 9090 case.

method.

In figure 7.7, we plot the capacity time-series for the classical, $MMSE_{\Phi_\chi}$ and $MMSE_{\Phi_\chi,LGS}$ AO correction cases, in the MOSPAR 9090 turbulence case. On the top and at the bottom, the capacity is depicted for the SNR = 5 dB, resp. 10 dB, and we also show the rate threshold 0.75, resp. 1.5, in red dashes. For both couples of SNR and rate, we observe now that the capacity obtained with estimated correction are almost always above the given rate threshold. The outages are therefore limited with respect to the classical pre-compensation. Additionally, the capacity issued from the estimated method $MMSE_{\Phi_\chi,LGS}$ shows to be closer to the AWGN channel capacity. We will prove these two latter observations, rather qualitative for the moment, in the following.

We analyze the gain provided by the advanced methods on the outage probability in figure 7.8. We plot the outage probability for the rate 0.7 on the left and 1.5 on the right. We observe at probability 10^{-3}, that the proposed methods bring a 15 to 18 dBs gains, which corresponds to the same gains that we observed on the compared CDF of the different signals. This means that using the advanced pre-compensation methods allows reaching the reliability threshold of 99.9% for less power received onboard the satellite. The power requirements could be relaxed.

To analyze the gain on the capacity that can be obtained for the reliability threshold of 10^{-3}, we plot the ϵ-outage capacity function of the SNR in figure 7.9. We observe on the absolute value of the ϵ-outage capacity on the left, that the advanced pre-compensation methods, allows to reliably communicate starting from a received SNR of 5 dB in the $MMSE_{\Phi_\chi}$ method and -1 dB for the $MMSE_{\Phi_\chi,LGS}$ method. Additionally, the SNR gap between the classical pre-compensated capacity and the AWGN capacity is more than half reduced using any of the estimation methods. Concerning the capacity gain, that is depicted on the right, we observe that all estimation methods allows decreasing the capacity losses. For instance, at SNR 10 dB, it is impossible to reliably communicate using the classical AO pre-compensation, whereas the $MMSE_{\Phi_\chi}$ method allows reaching 20% of the AWGN capacity, the methods using spatial and temporal measurements reach a 30% percentage of C_{AWGN} and the LGS based method more than 40%. At SNR 20 dB, the classical method allows to reliably communicate with rates below to 9% of the capacity (that

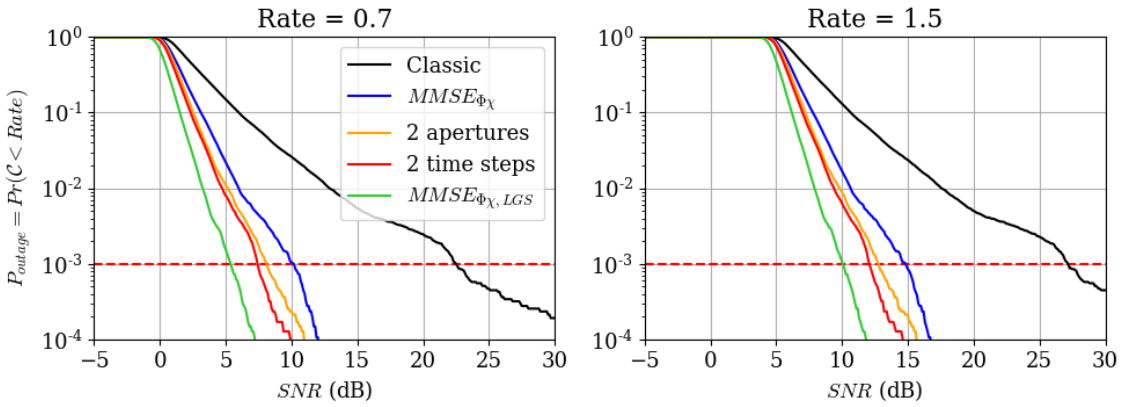

Figure 7.8: Outage probability for all pre-compensation methods, for the rates 0.7 on the left and 1.5 on the right, in the MOSPAR 9090 turbulence case.

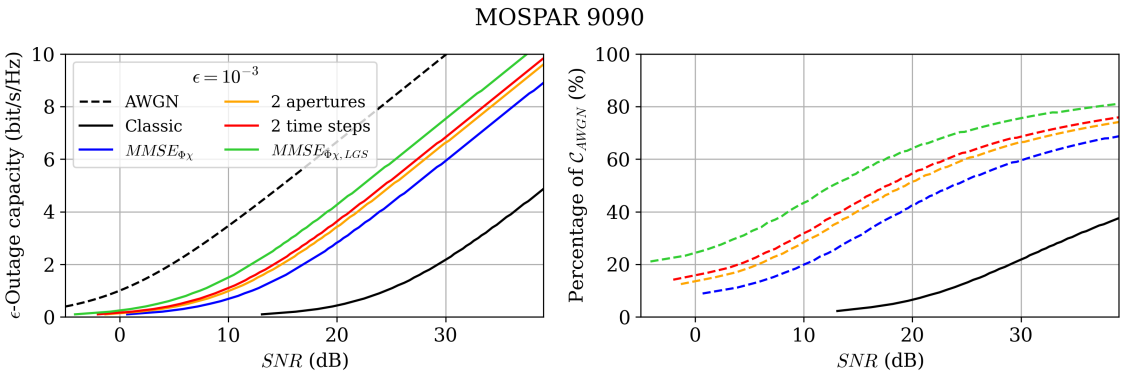

Figure 7.9: ϵ-outage probability for all pre-compensation methods, in the MOSPAR 9090 turbulence case.

is equal to 0.63 bit/second/Hz), whereas the $MMSE_{\Phi\chi}$, the 2 apertures based method, the 2 time steps method and the LGS based methods, allows communicating respectively at rates below to 42%, 50%, 55% and 65% of the AWGN capacity (equals to rates below 2.94, 3.5, 3.85 and 4.55 bit/second/Hz). This means that we can expect communicating with high order modulations in these SNR regimes when using advanced phase estimation methods.

We also analyze the same ϵ-outage capacity in the tougher turbulence regime MOSPAR 9999, in figure 7.10, in order to analyze the pre-compensation methods' robustness to the high angular decorrelation regime. We observe in this case that the capacity of all the correction methods is degraded. For a SNR of 10 dBs, it is not possible to communicate reliably with the classical method and the $MMSE_{\Phi\chi}$ methods. For the temporal based method, the 2 aperture method and the LGS based method, it is possible to reliably communicate with rate below 1bit/second/Hz. The corresponding percentage of achieved AWGN capacity decreases to 5%,11% and 20% for the temporal, two apertures and LGS based methods, respectively. For a 20 dB SNR, We observe that in this case, the two aperture estimation capacity is improved with respect to the two time step estimated case, whose performance was reversed in the MOSPAR 9090 case.

Finally, we comment in figure 7.11 the capacity sensitivity to the turbulence atmospheric conditions, for each pre-compensated channel. We plot the relative capacity loss, defined as the capacity loss between the e-outage capacity in the MOSPAR 9090 case and

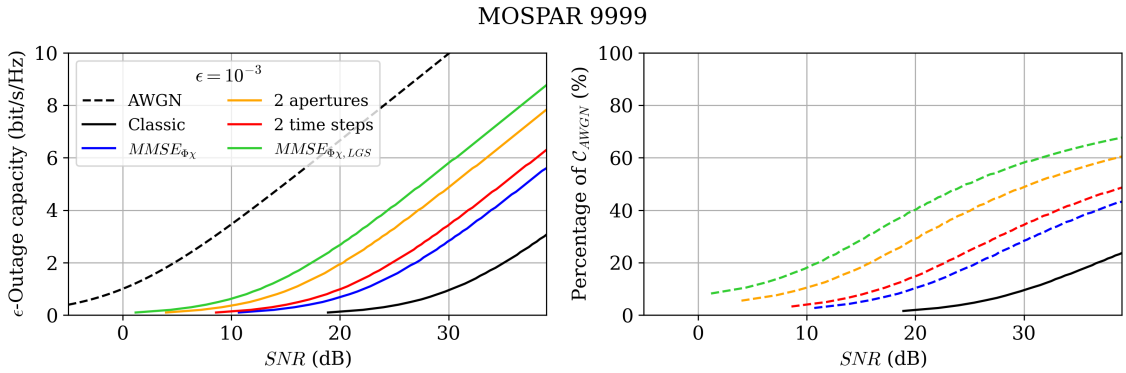

Figure 7.10: ϵ-outage probability for all pre-compensation methods, in the MOSPAR 9090 turbulence case.

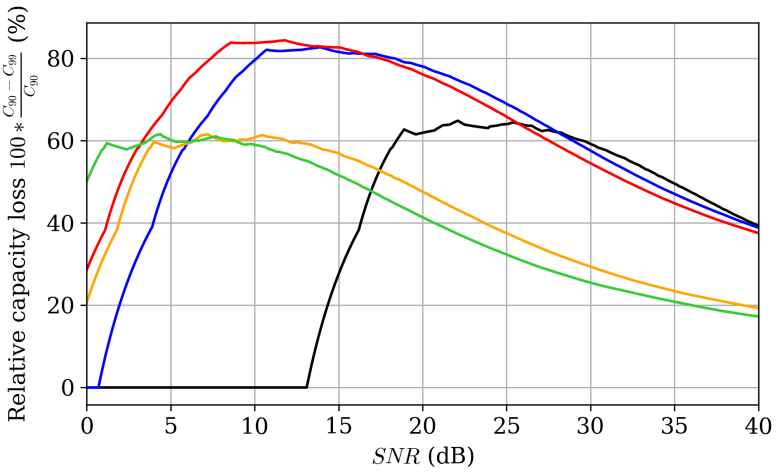

Figure 7.11: Relative ϵ-capacity loss between the two turbulence conditions, for all the pre-compensation methods.

the MOSPAR 9999 case: $\frac{C_{9090} - C_{9999}}{C_{9090}} * 100$. Therefore, a high capacity loss means that the pre-compensation method lose its efficiency in tougher turbulence conditions. We observe that the $MMSE_{\Phi_\chi}$ and the two time steps estimation methods present higher capacity losses than the other methods, showing a loss of performance in more severe angular decorrelation conditions. However, their capacity loss curve are shifted to the low SNR values compared to the classical pre-compensation method. This illustrates that these methods allows to communicate reliably at lower SNR than the classical pre-compensation method. Finally, the two apertures estimated case and the LGS estimated case conserve a capacity loss maximum comparable to the classical pre-compensation method. It shows that these methods are less sensitive to the increase of the angular decorrelation of the turbulence. To conclude, the developed advanced pre-compensation methods allows improving the ϵ-outage capacity of the ground to GEO satellite channel, that is the rate limit to ensure a reliable transmission. Function of the applied pre-compensation method, lower SNR are required to communicate at a same rate (up to 18 dB lower). We also showed that the LGS based method and the two aperture based method were less sensitive to the change of atmospheric conditions.

7.2.3 Impact of interleaving on the uplink fading channel

7.2.3.1 Capacity of fading channel with interleaving

Interleaving consist in randomizing the fadings of the channel to enable FEC correction. An example of the interleaving process is given in figure 7.12. It is illustrated in a very simplistic scenario, where the four bits of the codeword 3 are lost due to the fade. After interleaving the bits, there is only one bit by codeword that is lost, allowing for the decoding. In this example, L corresponds to the number of bits in the codeword. Hence, the sub-channel l is composed of all the l^{th} bits of each codeword. In this case, the fade occurs during one codeword. However, in our case, the signal fades will affect many codewords, and this principle can be generalized to a larger number of bits or symbols.

By applying a channel interleaver, we can now express the capacity averaged over each sample of the sub-channel, that is the channel from sample 0 to L as:

$$C_{int} = \frac{1}{L}\sum_{l=1}^{L} \log_2(1 + h_l^2 SNR^{lin}) \text{ bit/s/Hz} \tag{7.14}$$

Hence, the outage probability of the averaged channel is equal to:

$$p_{outage,div} = Pr(C_{int} < R) \tag{7.15}$$

In the following, we study the ϵ-outage capacity for sub-channels spaced by the number of samples corresponding to the interleaver duration, of milliseconds order. We evaluate the ability of the new pre-compensated channels to reduce the interleaver duration.

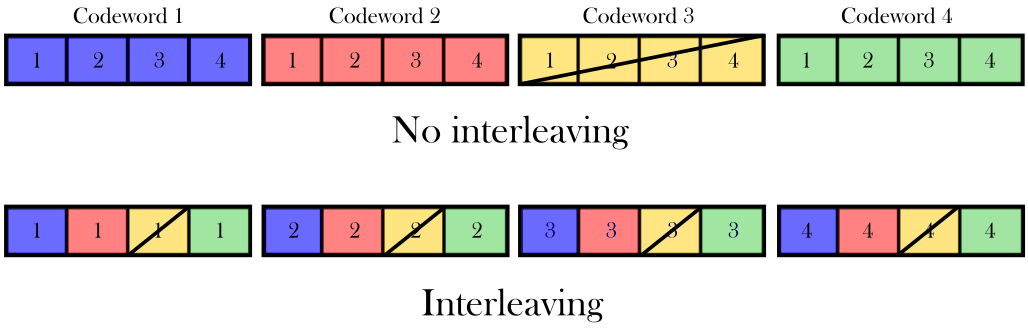

Figure 7.12: Principle of interleaving for fading channels.

7.2.3.2 Impact on the AO pre-compensated uplink channels

To evaluate the interleaving impact on the different AO pre-compensated uplink channels, we average the capacity by a sliding window whose size is equal to the interleaver size.

We give an example in figure 7.13 of the capacity of the channel with classical AO correction averaged over 50 and 150 ms long sub-channels, corresponding respectively to 135 and 705 channel samples, with a channel sampling rate of 4700 Hz. It corresponds to the size of the interleaver. With the interleaver duration increasing, we observe a reduction of the fades of the corresponding channel.

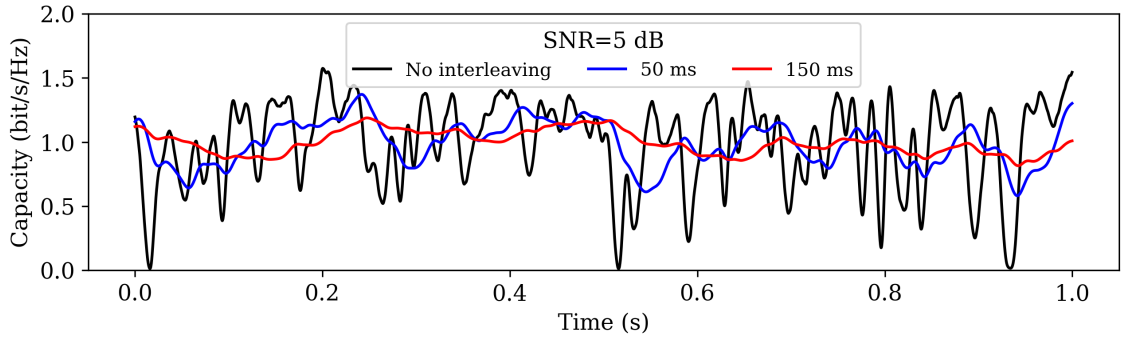

Figure 7.13: Capacity function of the time for the time-averaged channel for 0, 50 and 150 ms interleaver duration. Example in the case of the classical AO pre-compensation, in the MOSPAR 9090 case.

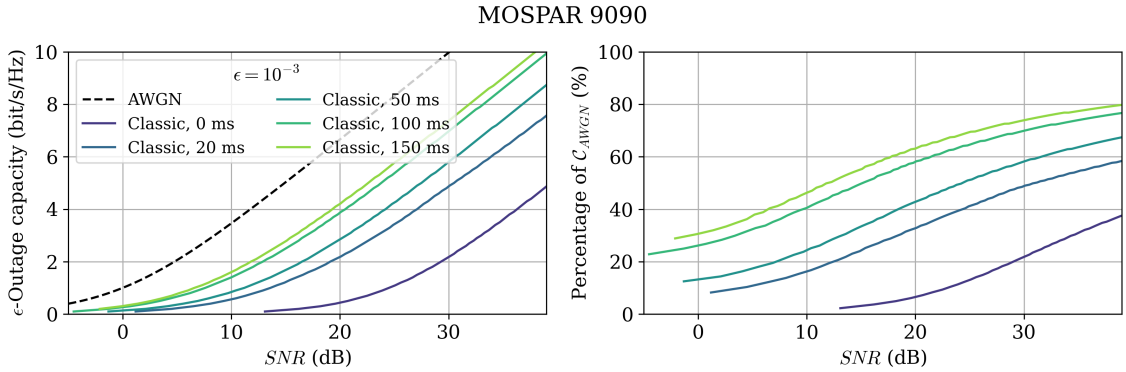

Figure 7.14: On the left: ϵ-outage capacity for the classical pre-compensation in the MOSPAR 9090 case, function of the SNR, computed for several time-averaged channels. On the right, AWGN capacity percentage function of the SNR.

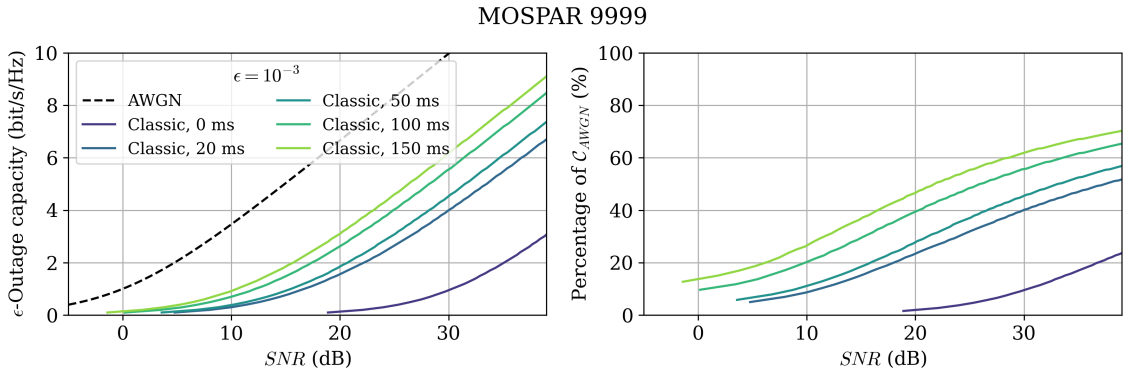

Figure 7.15: On the left: ϵ-outage capacity for the classical pre-compensation in the MOSPAR 9999 case, function of the SNR, computed for several time-averaged channels. On the right, AWGN capacity percentage function of the SNR.

We start by analyzing the interleaving impact on the ϵ-outage capacity for the channel corresponding to the classical AO pre-compensation. We plot in figure 7.14 the ϵ-outage capacity for the interleaver durations 0, 20, 50, 100 and 150 ms in the MOSPAR 9090 case, compared with the AWGN channel capacity. The absolute value of the capacity is plot on the left, and the AWGN capacity percentage achieved on the right. We observe that a 20 ms interleaver brings a large gain with respect to the non-interleaved channel.

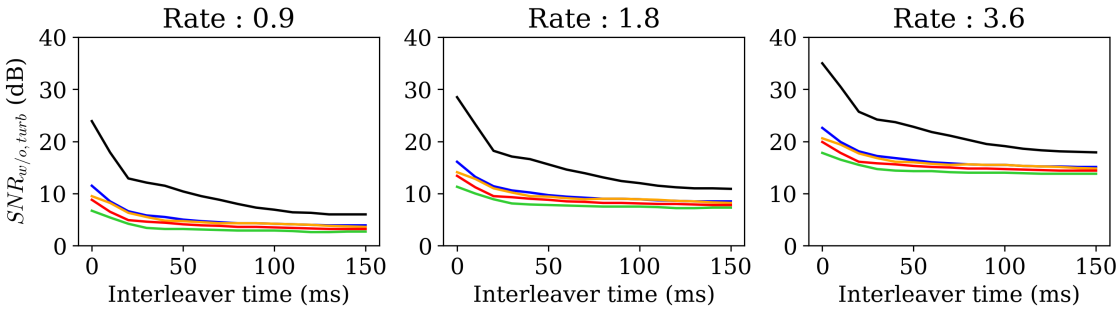

(a) MOSPAR 9090

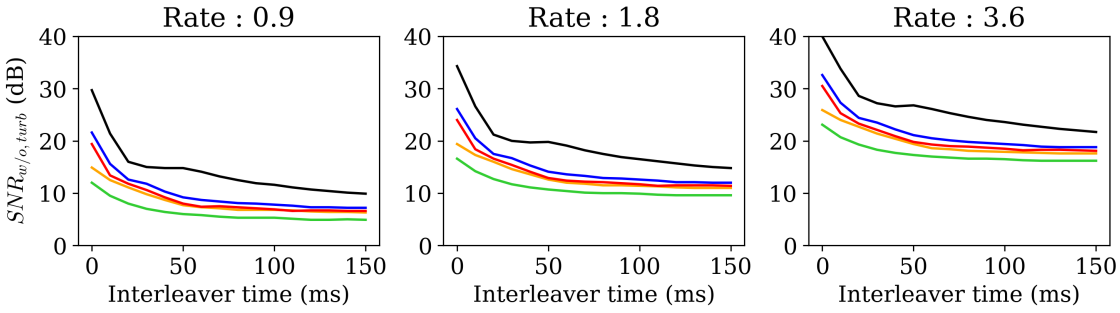

(b) MOSPAR 9999

Figure 7.16: Required SNR from the ϵ-outage capacity achieved for a given rate, for the different channels averaged over the given time window, corresponding to the interleaver duration.

For instance, for a capacity equal to 2 bit/s/Hz, we observe a gain of 10 dB with a 20 ms interleaver, and 13 dB, 17 dB and 18 dB for 50, 100 and 150 ms interleavers, respectively. We notice that the higher gain, of 18 dB is approximately equal to the gain on the ϵ-outage probability obtained with the LGS based estimation method without interleaving. When analyzing the same curve for the turbulence case MOSPAR 9999 in figure 7.15, we observe that it is no longer true, and that the classical pre-compensated case with 150 ms interleaver performs better than the estimated case based on LGS measurements. We conclude that, in each case, the interleaving process improves the channel capacity.

We generalize these results to each channel. In order to emphasize on the interleaver duration reduction brought by the advanced MMSE channels, we first plot in figure 7.16, for a fixed rate, the SNR required to obtain an outage probability of 10^{-3}, function of the interleaver duration. We plot the results in the MOSPAR 9090 turbulence case in figure 7.16a and in the MOSPAR 9999 turbulence case in figure 7.16b, for the rates 0.9, 1.8 and 3.6. For the channel with classical AO pre-compensation (black), we observe a slow decrease of the SNR that seems reaching an asymptotic value for interleaver duration above 150 ms for both turbulence case. In the case of the advanced estimated method, in the MOSPAR 9090 case, we observe a faster convergence toward the asymptotic SNR value, that is reach from 50 ms in the $MMSE_{\Phi\chi}$ method and the two aperture estimation method, and 20 ms for the estimation methods based on two time steps and LGS measurements. In the MOSPAR 9999 case, the convergence is slower, reached for 60 ms in the $MMSE_{\Phi\chi}$ method, the two aperture estimation method and the two time steps estimation method, while it is reached for 40 ms in the LGS based estimated method.

Finally, we compare the rate improvement, for a different SNR values function of the interleaver duration, in figure 7.17. We evaluate the achievable rate for an outage equal to 10^{-3}, in the MOSPAR 9090 case 7.17a and MOSPAR 9999 in figure 7.17b. In the same way, we observe a faster convergence of the advanced estimated methods to an asymptotic

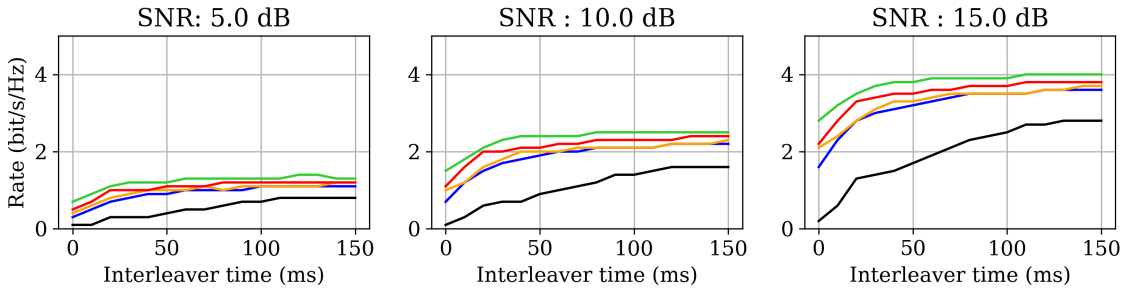

(a) MOSPAR 9090

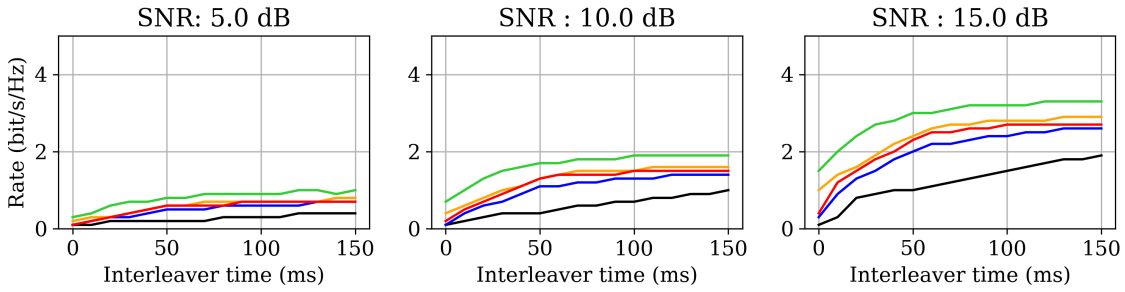

(b) MOSPAR 9999

Figure 7.17: Rate from the ϵ-outage capacity achieved for a given SNR, for the different channels averaged over the given time window, corresponding to the interleaver duration.

rate value, with respect to the classical AO pre-compensation. When considering a SNR of 5 dB, the asymptotic rate is above 1 for all advanced pre-compensation methods in the MOSPAR 9090 case. However, every method fells below the rate 1 in the MOSPAR 9999 condition. For a SNR of 10 dB, the capacity rate reaches values above 2 for the advanced methods for interleaver durations above 70 ms in the MOSPAR 9090 case, whereas the rate obtained with the classical method stays below 2 bit/s/Hz even for 150 ms long interleavers. The rate is also decreased in the MOSPAR 9999 case, but we still observe an important gain brought by the advanced pre-compensation methods. The same trend is observed for the SNR of 15 dB.

To conclude, adding a channel interleaver is shown to improve the ϵ-outage capacity for $\epsilon = 10^{-3}$, in every AO pre-compensated case. The pre-compensation methods developed in the thesis are shown to require shorter interleavers in order to reach the asymptotic capacity value, that is also improved with respect to the classical AO pre-compensation channel. This interleaver value depends on the considered method and on the turbulence conditions. The LGS based method shows the best capacity improvement at short interleaver durations.

7.3 E2E telecom transmission

We present preliminary results on the BER performance numerical assessment with a complete transmission chain. These results allow assessing the observed trends on the theoretical transmission limits from the last section.

7.3.1 Transmission chain

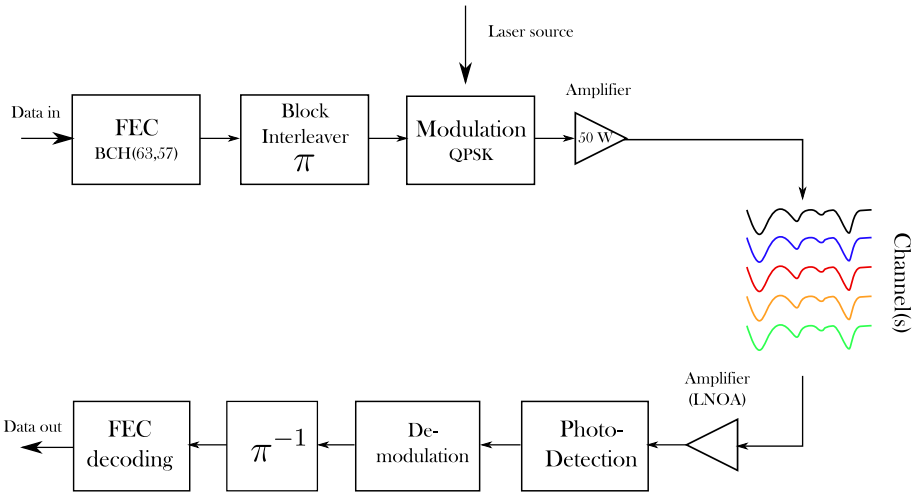

Figure 7.18: Considered E2E transmission chain in the numerical assessment of the BER for the AO ground to satellite pre-compensated channel.

For this numerical end-to-end simulation of the Bit-error-rate, applying FEC, we consider the following transmission chain depicted in figure 7.18. The data is sent to the FEC encoder, that encodes the bits with a BCH(63,57) code, that corresponds to a code rate $r_c = 0.9$. We chose a short FEC code, to have low complex simulation, easy to run. This FEC code is used in the literature to protect data over FSO channels [220]. The data is then interleaved by a 30 ms interleaver. It is short with respect to current interleavers duration that are considered [5], however, this choice limited the chain numerical complexity. The interleaved data is then mapped into QPSK constellation symbols, mapped to an electrical signal modulating the continuous laser source. After amplification, the 50 W signal propagates through the channel. In practice, we apply the static and dynamic losses from the 5 considered channels, corresponding to each of the methods. After applying the channel coefficients, the received signal onboard the satellite is amplified with a LNOA of noise figure $NF = 4\ dB$. The signal is filtered, detected and the symbols are demodulated. In this case, we assume that the channel state is known at the receiver, as the channel evolution is very slow with respect to the symbol rate. We also assume a perfect carrier synchronization at the receiver for the QPSK coherent detection. The detected symbols, unmapped to bits, are de-interleaved and decoded, with a hard decision decoding. The BER is computed after FEC decoding.

Because the sampling rate of the temporal series is equal to $f_{samp} = 4700Hz$, at 1 Gbaud and for an interleaver of 30 ms, it was required to simulate $N = \frac{D_b N_{samp}}{f_{samp}}$. It results in a simulation of 60 million of bits, which is too complex to run. Therefore, the simulation could only be done on a limited number of channel samples, and couldn't see all the channel fadings. A lack of convergence may be observed, however the expected behaviors are observable.

7.3.2 Bit error rate comparison

We consider the MOSPAR 9090 turbulence case and a transmission at 1Gbaud/s, for a QPSK modulation. We plot the BER function of the SNR obtained without interleaving in figure 7.19, for all the classical pre-compensation method, and every estimated pre-compensation phase proposed in this thesis. We underline that the computation complexity was very large, and that each point is averaged over 100 channel coefficients. We observe that the two timesteps result deviates from the other pre-compensation methods. This can be explained by a lack of convergence, as this method affects more temporal statistics of the channel (not the same fades at the same place). Observing the other channels, we note that they all perform better than the classical pre-compensation method, with gains up to 2 dBs when considering the best performance, that is brought by the 2 apertures method. From a broader perspective, the two methods that brings the best gains are the LGS aided method and the two aperture method, which corroborate the trend observed on the capacity in section 7.2.2.3. We note that we didn't perform any particular code optimization, as the aim was to obtain a first performance assessment.

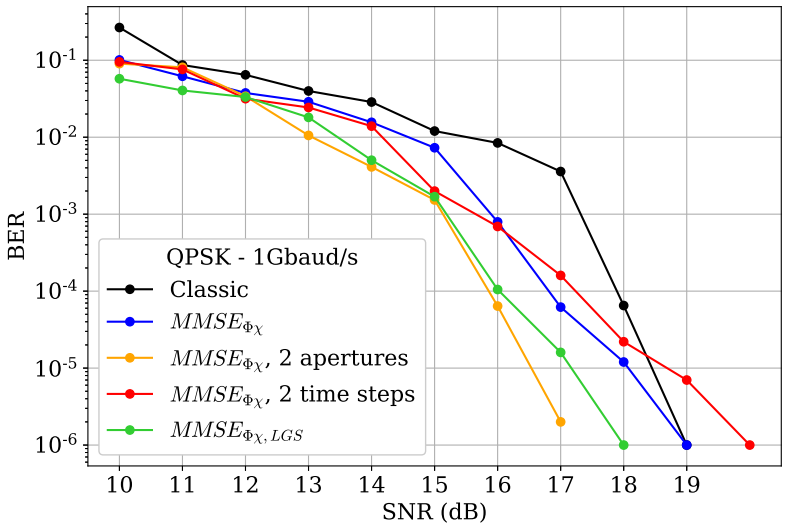

Figure 7.19: BER after FEC BCH(63,57) without interleaving for QPSK modulation at 1 Gbaud/s.

Figure 7.20 depicts the BER function of the SNR obtained with a 30 ms channel interleaver, for the QPSK modulation at 1 Gbaud/s. In this case, the estimated case using two time-steps is very improved by the interleaving process. This can be due to the fact that it reduces the coherence time of the coupled flux much more than the other methods. The classical pre-compensation also shows an SNR gain of 0.5 dB at probability 10^{-6} due to the interleaver. The $MMSE_{\Phi\chi}$ performance however is decreased, and the better performance are still obtained with the LGS and the two apertures methods.

Finally, we take a closer look at the gain brought by the interleaver on each channel in figure 7.21. We observe that the channel that benefits the most from the interleaver, is the channel with the two time steps estimated phase (in red), with 2 dB gain at $Pe = 1e-6$. This is a behavior that was also observed on the channel capacity. At the same probability, all other pre-compensation methods show a 0.5 db gain thanks to the use of the interleaver. To confirm these results, it is planned to perform the simulation on more channel coefficients.

To conclude, even if the gains are smaller than the one observed on the theoretical capacity, the performance trend is confirmed, with phase estimation methods using spatial

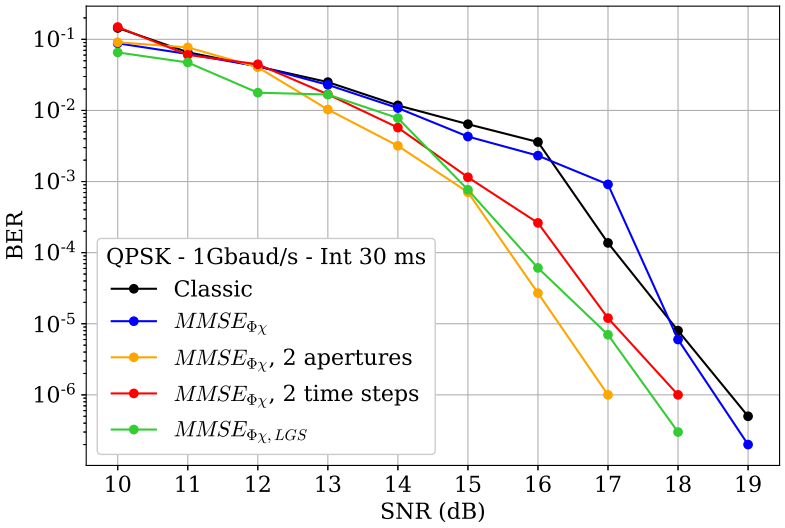

Figure 7.20: BER after FEC BCH(63,57) with 30 ms interleaving for QPSK modulation at 1 Gbaud/s.

measurements that outperform the classical pre-compensation methods. We also observe the same sensitivity to the interleaving process of the phase estimation using temporal measurements. As this work is a first glance on the telecommunication performance allowed by the phase estimation methods, we intend in the future to make these results more reliable by averaging the results on more channel samples. We also intend to evaluate the performance for different codes, code-rate, and interleaver duration. A broader study could consist in evaluating other modulation formats, and data-rates.

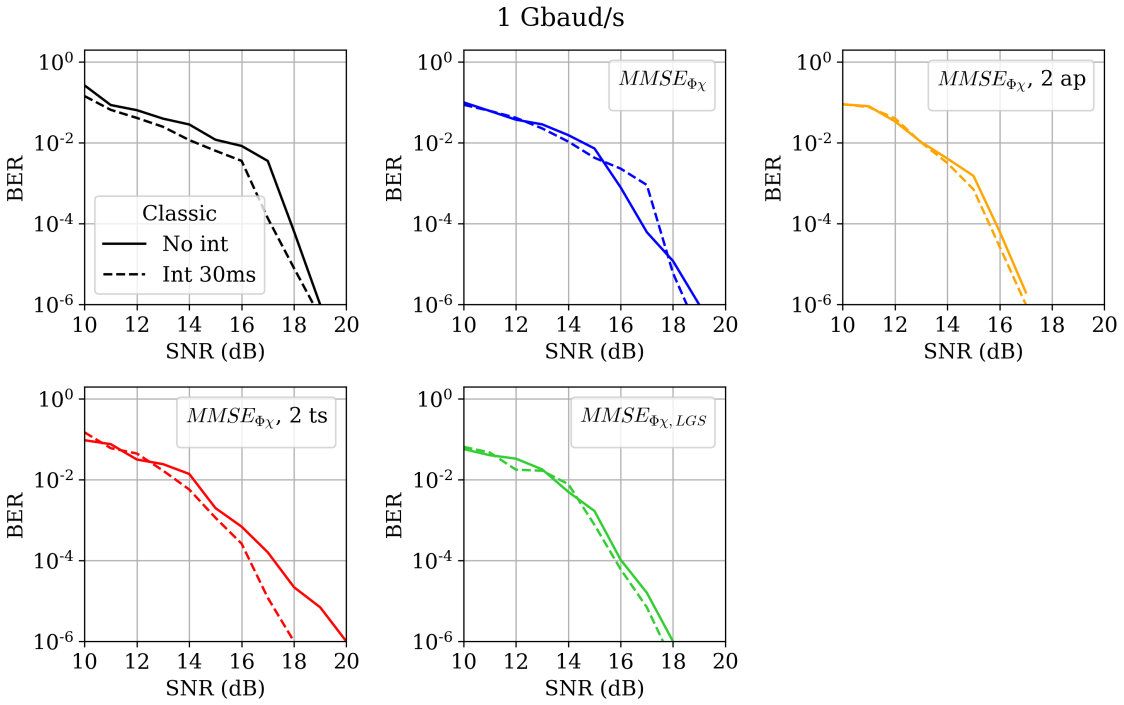

Figure 7.21: Sensitivity of the BER to the 30 ms interleaver for each channel, at 1 Gbaud/s.

7.4 Analytical channel model development

In the previous section, we showed that using the advanced pre-compensation methods allowed to improve the channel statistics, therefore enhancing the communication capabilities (achievable data-rate and reliability). To optimize the digital signal processing of the telecommunication link, it is required to characterize the channel statistics. Until this part, this channel characterization was done numerically. However, if one wants to adapt and optimize the digital processing parameters, a statistical model is required. This model can also allow to explore the channel limits with respect to the atmospheric conditions and AO performance. Our aim is therefore to develop the AO pre-compensated uplink analytical channel model, whose parameters depend on the residual phase statistics that are already known.

As described in chapter 2, section 2.3.5, analytical models have been developed applying Rytov methods to Gaussian beams [98, 105], however, it is not convenient to model the impact of a pre-compensation in this formalism. Therefore, we continue to adopt the reciprocal formalism in order to model the reciprocal uplink. This allows to rely on existing work considering downlink plane waves corrected by adaptive optics.

Therefore, we consider the statistics of the reciprocal uplink, and we focus on the contribution to the coupling related to the phase ρ_Φ. We recall that we assumed in chapter 3 that the coupled flux equals to:

$$f = \rho_\chi \rho_\Phi \tag{7.16}$$

where the phase and the log-amplitude contribution to the coupled flux were assumed independent and where the log-amplitude contribution to the coupling follows log-normal statistics. We also recall that the reciprocal coupled flux consist in coupling the back propagated reception mode of the satellite to the emission mode of the laser at the OGS, as explained in chapter 3.

In this section, we start by presenting state-of-the-art models, for the uncorrected and AO corrected downlinks. We also discuss the validity of these models in the reciprocal uplink with partial AO correction. The more relevant development with respect to our objective is the study of Canuet considering the modeling of the phase contribution to the coupling efficiency in presence of a partial adaptive optics correction, in the downlink scenario. We summarize the main results of his study and discuss its applicability to the reciprocal uplink with anisoplanatic phase residuals. Finally, we consider different anisoplanatic regimes and explore the potential models in these regimes.

7.4.1 State of the art of statistical models

We can find several types of analytical models describing the analytical coupled flux to an optical system in the literature. Many models were developed in the framework of FSO horizontal links, not especially considering phase compensation. These models consider the collection of the flux on a captor, with no specific needs to amplify the signal in reception, therefore to couple it to a single mode fiber. This results in a characterization of the received intensity fluctuation rather than the coupling efficiency to a SMF, impaired by phase effects. However, whether to describe the received field behavior or to draw inspiration from the methods used, it is useful to be aware of these models. Other models were developed to account for an AO correction in reception, considering perfect AO correction. In the same way, these models do not correspond to our scenario, but we still describe them to look for analogies with our case. Finally, we can find in the literature the model of the downlink coupled flux with partial AO correction, which was the topic of the thesis of Canuet [165]. However, with respect to this model, our scenario differs in the strength of the residual

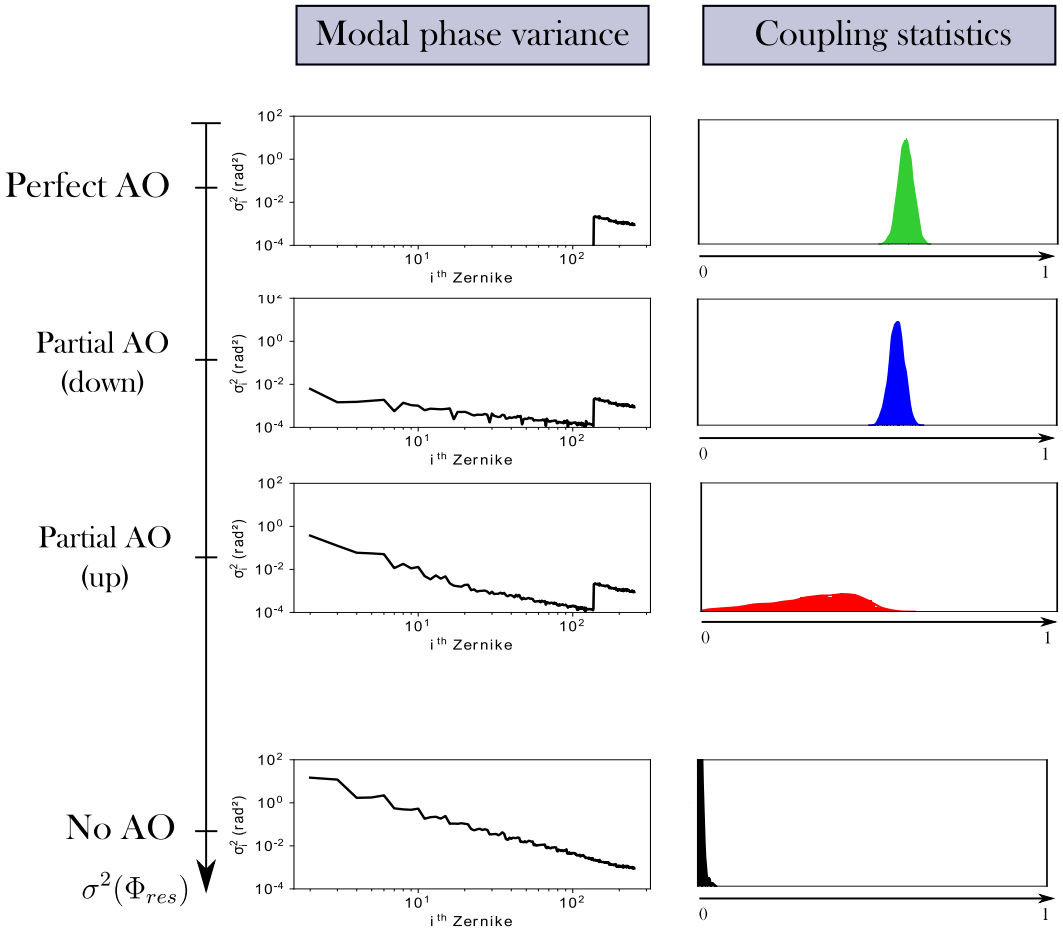

Figure 7.22: Summary of the coupled flux statistics, obtained with E2E simulations, function of the quality of the AO correction. It is computed in the MOSPAR 9090 turbulence case.

phase that we encounter,since in our uplink case, the link suffers from anisoplanatic phase error.

Therefore, to present this literature review, we classify the channels in function of the quality of the AO correction, hence, function of the value of residual phase variance. A summary of the coupled flux behavior function of the AO correction quality is presented in figure 7.22. In this figure, we plot the phase residual modal variance on the left for each regime, and the resulting coupled flux PDF on the right. We observe a change of behavior of the signal PDF, with the increase of the residual phase variance. This section intends to explain the relationship between a given modal spectrum and the signal PDF behavior.

No AO

Many models have been proposed to describe the resulting intensity from optical propagation through a turbulent medium without any phase correction [221]. The choice of models depends on the turbulence strength. Lognormal models have been shown to describe the received intensity in the weak to moderate turbulence regime [106]. In the stronger turbulence regime, the gamma-gamma model is widely used [222]. As discussed in section 2.3.5, the gamma-gamma model aims to represent the impact of intensity fluctuations as the modulation of the intensity induced by small and large-scale eddies. When considering aperture-averaged intensity statistics, the exponentiated Weibull distribution

has been shown to offer an accurate fit [223]. It's worth noting that the development of this model was not conducted analytically and relies on empirical fitting of the signal probability density function. However, all these models provide a description of intensity statistics, and not the coupling efficiency to a SMF that is very impaired by phase disturbances, in addition to amplitude distortions. In fact, all these models concern horizontal FSO links, which do not necessarily require optical amplification, hence a coupling to a single mode fiber.

Perfect AO correction

Another family of models concerns the models of incident turbulent optical fields perfectly corrected. The perfect correction is applied to modes 2 to N_{AO}. Two methods are used in the literature to analytically develop statistical models in this scenario.

The first method is the phasors technique, developed originally by Goodman [94], considering a speckled regime (when the point spread function of the beam in the focal plane lose its spatial coherence). It is applied to the perfect AO corrected link by Belmonte and Kahn [224]. This method consists in separating the real and imaginary part of the complex field and to transform the overlap integral on a finite sum of phasors over N cells, supposedly independent, as follows:

$$\alpha_r \propto \exp(\overline{\chi}) \sum_{i=0}^{N_{cells}} \exp(\chi_k - \overline{\chi_k}) \cos(\Phi_k) \tag{7.17}$$

$$\alpha_i \propto \exp(\overline{\chi}) \sum_{i=0}^{N_{cells}} \exp(\chi_k - \overline{\chi_k}) \sin(\Phi_k) \tag{7.18}$$

where α_r and α_i are the real and imaginary parts of the complex coupling, $\exp(\chi_k)$ and Φ_k are the module and argument of the N_{cells} phasors. Within the assumption that the N_{cells} being large and that the phasors arguments Φ_k are independents, the two sums can be expressed as joint Gaussian variables. This expression allows developing the statistics of the coupled flux module that is shown to follow a modified Ricean probability. However, this is not the case for the reciprocal classical anisoplanatic uplink. We show in figure 7.23 the histogram of the real and imaginary parts of the complex coupling issued from our E2E reciprocal database, for an uncorrected case (black), a perfect AO correction of the tip and tilt modes (blue), the perfect AO correction of 9 modes (green), and in the classical pre-compensation case under anisoplanatic residual phase (red), in the MOSPAR 9090

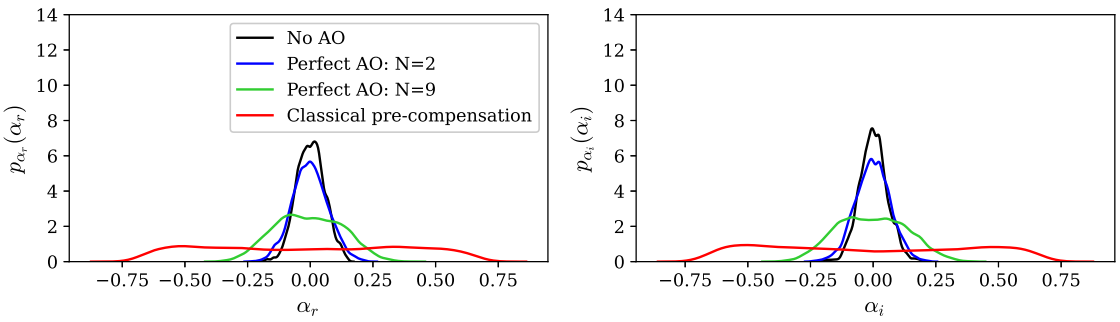

Figure 7.23: Distribution of the real and imaginary part of the complex coupling for an uncorrected optical link (black), a link with tip and tilt perfect correction (blue), a link with a perfect correction of the 9 first Zernike modes (green) and for the reciprocal uplink with classical pre-compensation (red), in the MOSPAR 9090 turbulence case.

turbulence case. We highlight that we neglect the log-amplitude fluctuations. It is shown in our case that the uncorrected case and the case perfectly corrected until 2 modes are Gaussian. It is not anymore true for 9 perfectly corrected modes and in the reciprocal uplink case with classical pre-compensation. We can explain this difference by the fact that the phasors are not independent, due to the strong low order residual affecting the wavefront.

A second method to model the links with perfect AO correction is employed in [225]. This method involves approximating the coupled flux using the instantaneous Strehl ratio, with the condition that the Strehl ratio is larger than 0.1. The statistics of the residual phase variance are also developed using the perfectly corrected phase structure function, providing an analytical expression for the first term that depends on the number of independent phase cells, denoted as N_{cells}. Both the number of cells and the residual phase variance are used to compute the parameters of the probability distribution for the instantaneous residual phase, which follows a gamma distribution.

These two last methods do not directly apply to our scenario. However, it is interesting to understand the methods used and the underlying approximations to develop the uplink model.

Partial AO correction

The last family of methods involves partial adaptive optics correction (not perfect). The downlink coupled flux, corrected by adaptive optics, has been studied in the thesis of Lucien Canuet. In his work, the residual phase variance is affected by weak residuals issued from the AO system, such as fitting, temporal, and aliasing errors. The developments he made led to an analytical model expression with no closed form, depending on the modal residual phase variance of the system. In the following, we will recall his developments and explore their applicability to the reciprocal uplink scenario.

7.4.2 Application of the downlink development in presence of partial AO correction to the reciprocal uplink

7.4.2.1 Modele principle

To describe the downlink channel model with partial AO correction from [116], we start by giving the problem notations. In his work, Canuet defines a new scalar product as:

$$\langle X|Y\rangle_{W_0} = \int\int W_0(\mathbf{r})X(\mathbf{r})Y(\mathbf{r})^* d^2\mathbf{r} \tag{7.19}$$

where $W_0(\mathbf{r}) = M_0(\mathbf{r})P(\mathbf{r})$ where $P(\mathbf{r})$ is the aperture mask and $M_0(\mathbf{r})$ is the Gaussian mode of the single mode fiber expressed in the pupil plane. He also defines the spatial normalized average and variance as:

$$\langle X\rangle_{W_0} = \frac{\langle X|1\rangle_{W_0}}{\langle 1|1\rangle_{W_0}} \tag{7.20}$$

$$\sigma^2_{W_0}(X) = \left\langle X^2\right\rangle_{W_0} - \langle X\rangle^2_{W_0} \tag{7.21}$$

Within these notations, it is shown that the complex coupling of the complex perturbed field $\Psi(\mathbf{r}) = A_0 \exp(j\Phi_{res}(\mathbf{r}))$ with the Gaussian mode, normalized by the complex coupling of a plane wave $\Psi_0(\mathbf{r}) = A_0$, is expressed as:

$$\frac{\Omega}{\Omega_0} = \frac{\langle\Psi|M_0\rangle_P}{\sqrt{\langle\Psi|\Psi\rangle_P \langle M_0|M_0\rangle_P}} \frac{\sqrt{\langle\Psi_0|\Psi_0\rangle_P \langle M_0|M_0\rangle_P}}{\langle\Psi_0|M_0\rangle_P} = \langle\exp(j\Phi_{res})\rangle_{W_0} \tag{7.22}$$

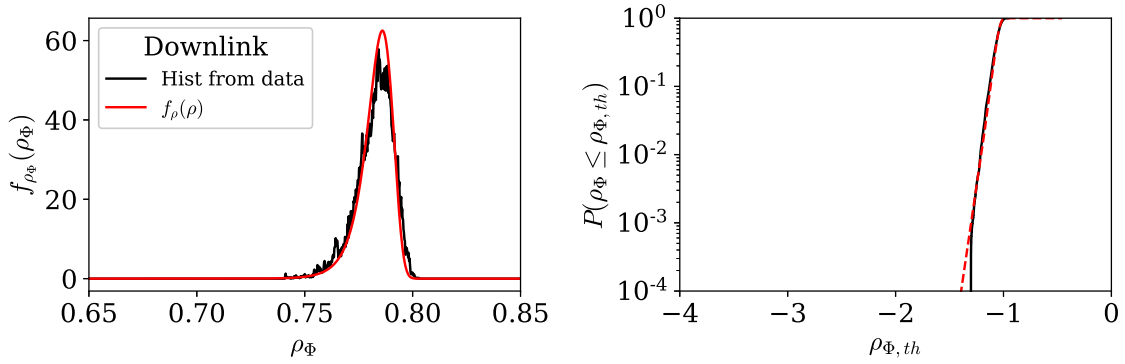

Figure 7.24: Comparison of the analytical distribution from [116] with the downlink histogram from E2E data, in the AO partial correction case, with very weak phase residuals, in the MOSPAR 9090 turbulence scenario.

He shows that this expression can be transformed as:

$$\frac{\Omega}{\Omega_0} = \exp\left(\langle j\Phi_{res}\rangle_{W_0}\right) \sum_{k=0}^{\infty} \frac{\left\langle j^k(\Phi_{res} - \langle\Phi_{res}\rangle_{W_0})^k\right\rangle_{W_0}}{k!} \tag{7.23}$$

which corresponds to the sum of the moment of the residual phase, that writes as:

$$\frac{\Omega}{\Omega_0} = \exp\left(\langle j\Phi_{res}\rangle_{W_0}\right) \exp\left(-\sigma^2_{W_0}(\Phi_{res})/2\right) \tag{7.24}$$

under the assumption of Gaussian phase.

Therefore:

$$\frac{\rho}{\rho_0} = \exp\left(-\sigma^2_{W_0}(\Phi_{res})\right) = \exp\left(-\sum_{i=2}^{N} c_i^2\right) \tag{7.25}$$

where $(c_2, ..., c_N) = \mathbf{M}^{-1}(a_2, ..., a_N)^T$, where $\mathbf{M}$ is the transition matrix from the Zernike space to the W_0 space. The computation of this matrix can be found in [116].

The component of the phase projections vector following a Gaussian distribution, by linearity, the projections in the W_0 space follows also a Gaussian distribution. Denoting $z = \sum_{i=2}^{N} c_i^2$, the author shows that the distribution of z is equal to:

$$p_z(z) = \frac{1}{\pi} \int_0^{\infty} \frac{\cos\left(\sum_{i=2}^{N} \alpha \arctan(\beta_i u) - zu\right)}{\prod_{i=2}^{N} \left(1 + u^2\beta_i^2\right)^{\alpha/2}} du \tag{7.26}$$

where $\beta_i = 2\sigma_{b_i}$ and $\alpha = 0.5$. The distribution of ρ, after Jacobian transformation, is shown to be:

$$p_{\rho_\Phi}(\rho_\Phi) = \frac{1}{\rho_\Phi} p_z\left(\log\left(\frac{\rho_0}{\rho_\Phi}\right)\right) \tag{7.27}$$

where we recall that ρ_0 is the coupled flux of a plane wave with the SMF Gaussian mode.

We computed numerically the proposed integral and compared to an empirical histogram of a downlink case issued from our E2E numerical data. The result is plot in figure 7.24 and shows a good agreement between the model and the data histogram in the downlink corrected turbulence regime.

7.4.2.2 Application to the reciprocal uplink

The main assumption of the model of Canuet, is to assume a Gaussian spatial distribution of the phase over the telescope aperture. We plot the histogram of the phase distribution in the downlink case and the reciprocal uplink case under classical pre-compensation in figure 7.25. We observe that the phase distribution in the downlink corrected case is quasi-Gaussian, whereas it is no more Gaussian in the reciprocal uplink case. This is explained by the presence of strong low order phase residuals.

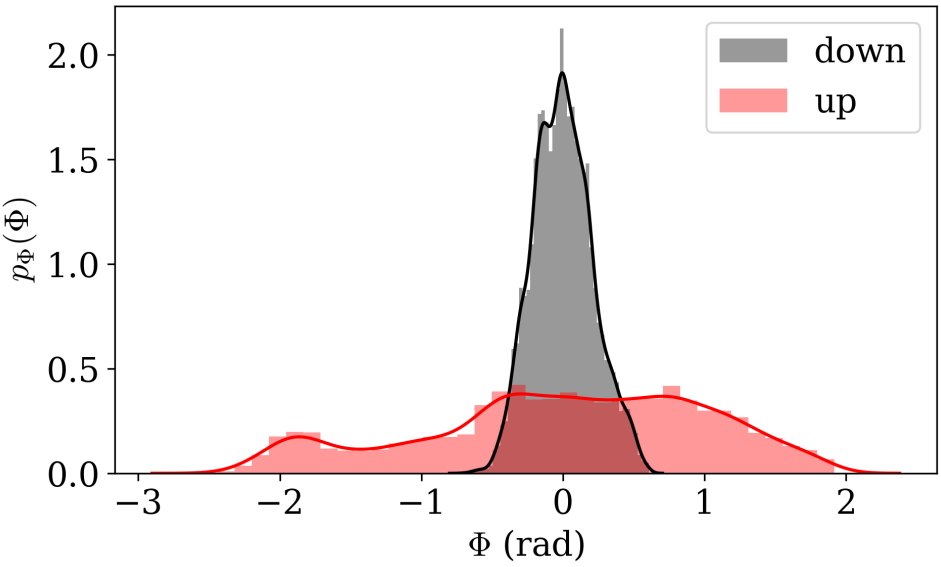

Figure 7.25: Spatial phase distribution for the downlink with weak phase residuals (in black) and the reciprocal uplink with classic pre-compensation with anisoplanatic phase residuals (red), from a unique complex field sample.

To see the limits of the downlink model when applied to the uplink, we plot its PDF and CDF, along with empirical PDF and CDF obtained from the E2E time-series computed over 47000 samples (equivalent to 10 s of data), for the classical pre-compensation, the $MMSE_{\Phi\chi}$ and the $MMSE_{\Phi\chi,LGS}$ correction cases, in figure 7.26. We observe that for the classical pre-compensation, a large mismatch between the model and statistics from the data appears, especially on the CDF tail. The model fails to represent the statistics of deep fades. This matches the observations made in [225], whose condition to approximate the coupled flux as an equivalent of the instantaneous Strehl ratio, that we define as $\rho_{approx}(t) \propto \exp\left(-\sigma^2_{W_0}(\Phi_{res})\right)$, is for the instantaneous Strehl to be greater than 0.1. In the $MMSE_{\Phi\chi}$ case, we still observe a deviation concerning the deep fade statistics. The model is shown to perform better in the $MMSE_{\Phi\chi,LGS}$ case, whose phase residuals are very weak with respect to the two other cases.

To study the impact of the tip-tilt on the coupling, we numerically compute the coupling for fields: with anisoplanatism error on every mode, with perfect tip-tilt correction and anisoplanatism on all the other modes, and with only tip-tilt anisoplanatism. We plot the resulting CDFs in figure 7.27. We compare the CDFs of the exact numerical coupling with the one issued from the approximation Eq. 7.25. We observe from the plot in the middle, corresponding to the case with perfect tip-tilt correction, that the approximated coupled flux fits perfectly the CDF obtained from data. However, when the residual phase is only affected by the tip-tilt, we still observe a large deviation between the CDF obtained with the approximation with respect to the one obtained from the data. This confirms that the

residual tip and tilt is at the origin of the deviation from the downlink statistical model.

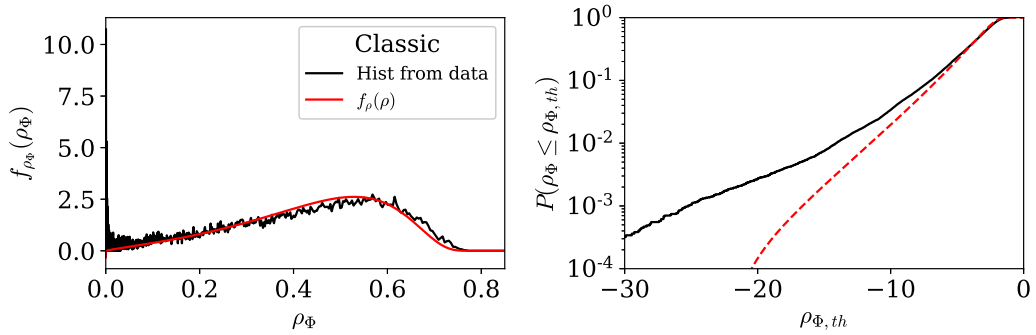

(a) Classical pre-compensation

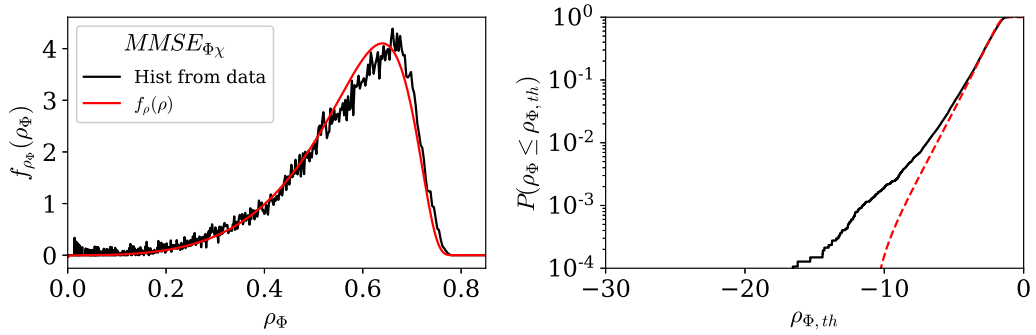

(b) $MMSE_{\Phi\chi}$ pre-compensation

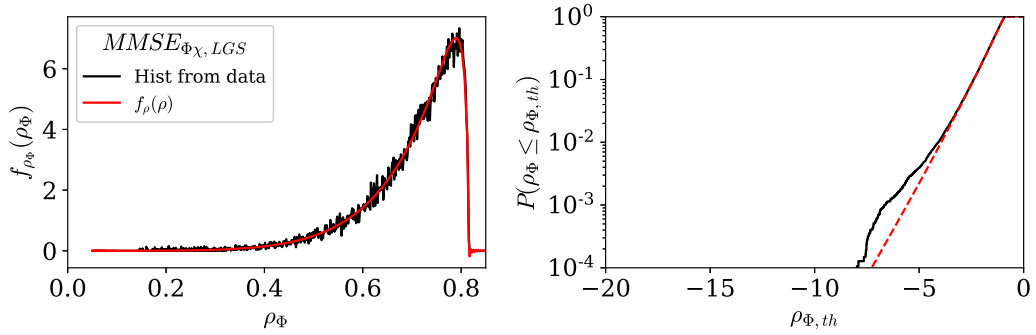

(c) $MMSE_{\Phi\chi,LGS}$ pre-compensation

Figure 7.26: Comparison of the analytical distribution from [116] with the reciprocal uplink histograms from E2E data, for different pre-compensations, in the MOSPAR 9090 turbulence scenario.

We can conclude that the statistical model developed for the downlink with a good partial AO correction, does not apply systematically to the reciprocal uplink case. It can be applied if the phase residuals are weak, and especially if the residual tip and tilt are weak. Indeed, we've shown that strong tip and tilt residuals are modifying the spatial statistics of the phase averaged by the pupil and that the downlink model is accurate when the tip and tilt modes are perfectly corrected.

From these observations, two questions arise:

1. what is the tip-tilt variance threshold and the total residual variance threshold until which the downlink model can be applied ?

2. how to model the tip-tilt impact on the coupled flux?

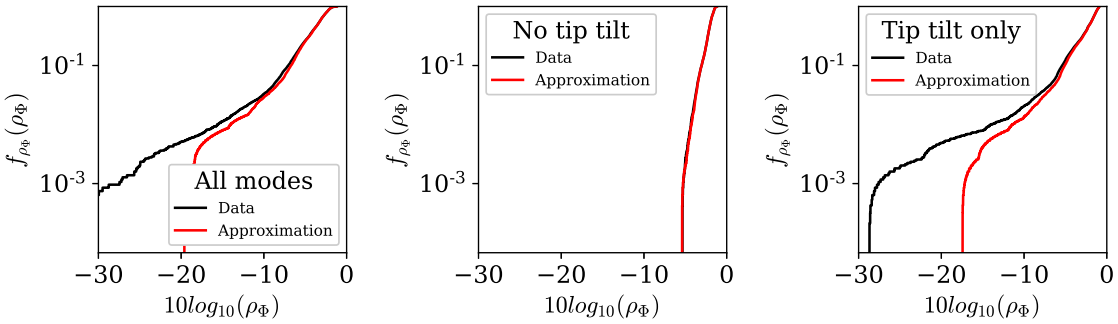

Figure 7.27: CDF of the coupled flux, for different AO correction. On the left: classical correction on all the modes. In the center: perfect tip-tilt correction, classical correction on the other modes. On the right: perfect high orders correction, classical correction on the tip and tilt. The results are shown in the MOSPAR 9090 turbulence case.

7.4.3 Reciprocal uplink statistical channel model

7.4.3.1 Statistical channel model in weak/moderate residual tip tilt conditions

First, we consider a regime with a weak residual tip tilt. This corresponds to a case of very good AO correction, that can occurs when the anisoplanatic angle is not too small, or in a case of good tip tilt estimation.

The first question we want to answer is to question 1. To give a first element of answer, we conduct an initial numerical experiment.

Experiment: tip tilt variance threshold determination.

To determine the tip tilt spatial variance threshold until which the approximation stands, we compute the numerical coupling and the coupling approximated in the case where:

1. We impose static tip and tilt values a_2 and a_3,
2. We keep the variable high orders from the Zernike mode 4 to 136, from the MOSPAR 9090 case,

where, for simplification, we take $a_2 = a_3 \in [0, 2]$. The resulting phases do not especially correspond to physical ones but allows studying the sensitivity of the coupling to the tip and tilt.

We plot the comparison between the CDF of the exact coupling (black) and the approximated coupling (red) in figure 7.28, for the different values of tip and tilt, in the

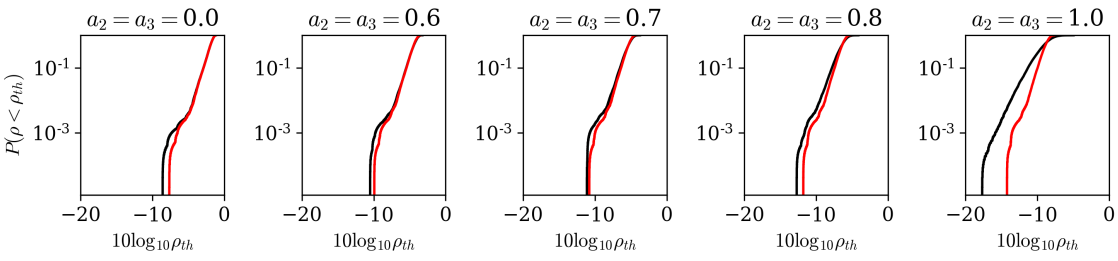

Figure 7.28: Comparison of the exact and approximated coupled flux. The black curve depicts the exact coupling, and the red curve the coupling approximation. It is computed for a fixed tip and tilt value, and varying high order modes, in the MOSPAR 9090 turbulence case.

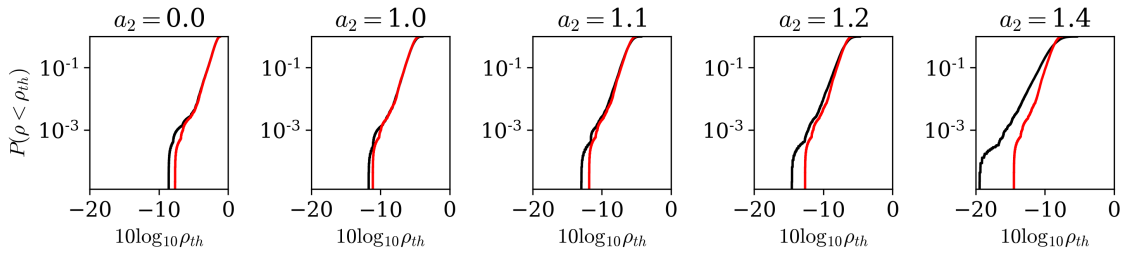

Figure 7.29: Comparison of the exact (black) and approximated coupled flux (red). It is computed for a fixed tip, a null tilt value, and varying high order modes, in the MOSPAR 9090 turbulence case.

MOSPAR 9090 case. First, we observe a CDF tail whose value increases with the tip and tilt variance. We also observe a constant offset of approximately 2 dBs when considering the tail of the CDF. It is due to the residual focus. This offset is constant until the value of the tip and tilt exceed 0.7 radian. This corresponds to a tip and tilt combined spatial variance approximately below one.

Having a condition on the sum, we also empirically study if there is a condition on the individual variance of each mode. To that aim, we consider a 1 dimensional case where the tip is equal to zero and the tilt varies between 0 and 2. We plot the results in figure 7.29. In this case, we observe that the approximation (modulo the 2 dB induced by the focus), applies until the tip value equals to 1.

We conclude that the condition for the approximation to holds, is that the instantaneous value of $\sqrt{(a_2^2 + a_3^2)}$ must be below 1.

Validation on the available database

We verify this observation on the weak turbulence strength scenarios. For the purpose of this study, we add the profiles MOSPAR 1010, 2020 and 3030 to the existing database, whose integrated parameters and tip-tilt residual phase variance are given in table 7.1. We compute the residual phase variance in the classical pre-compensation case and $MMSE_{\Phi\chi}$ estimated case, thanks to the pseudo-analytical model.

	MOSPAR 1010	MOSPAR 2020	MOSPAR 3030	MOSPAR 5050
θ_0	17.76 µrad	15.15 µrad	14.35 µrad	11.36 µrad
r_0	16.32 cm	12.73 cm	10.6 cm	7.86 cm
Classic : $3\sigma_{Tip}/3\sigma_{Tilt}$	0.75/0.50 rad	0.88/0.58 rad	0.92/0.60 rad	1.14/0.74 rad
MMSE : $3\sigma_{Tip}/3\sigma_{Tilt}$	0.52/0.41 rad	0.59/0.48 rad	0.64/0.50 rad	0.77/0.61 rad

Table 7.1: Table of the integrated parameters for the profiles MOSPAR 1010, 2020, 3030 and 5050.

We plot the CDF for the turbulence cases MOSPAR 1010, 2020, 3030 and 5050 in figure 7.30, for the classical pre-compensation case. We compute the exact numerical coupling, in black and the coupling approximation, in red. We observe that the approximation fits the exact coupling for the three weaker MOSPAR profiles. For the MOSPAR 5050 turbulence conditions, the value at 3 sigmas of the tip equals $1.14 > 1$, as shown in table 7.1, which corroborates our initial observation.

We also plot the results for the $MMSE_{\Phi\chi}$ method, in the same turbulence conditions, in figure 7.31. In this case, we observe a perfect match between the exact coupling and the coupling approximation. We also note, from table 7.1, that none of the tip or tilt value at 3 sigmas in this scenario is above one.

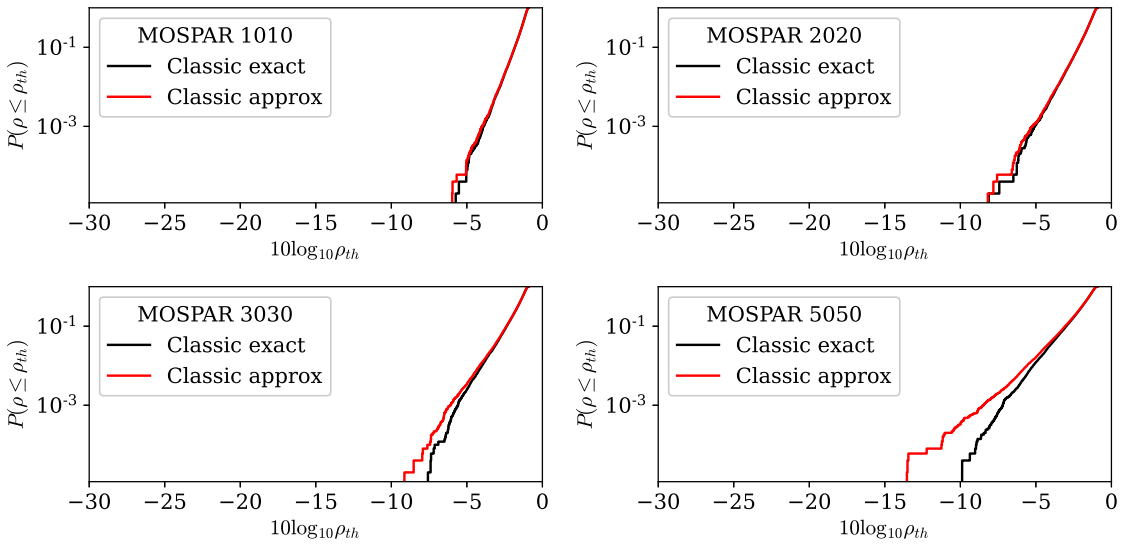

Figure 7.30: Comparison of the exact and approximated coupled flux CDF function of the coupled flux threshold, for the classical pre-compensation, in the MOSPAR 1010, 2020, 3030 and 5050 conditions.

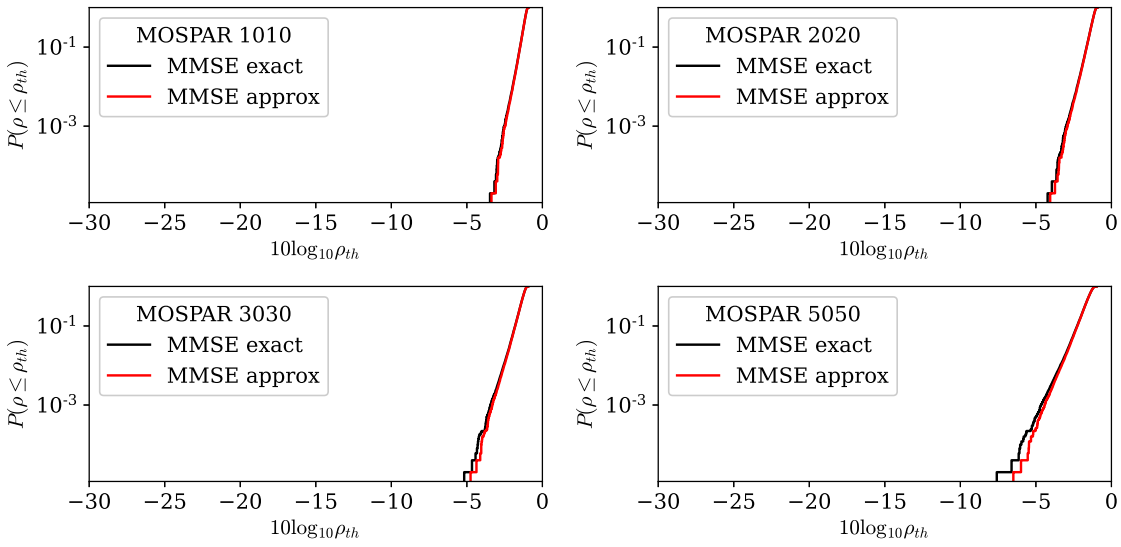

Figure 7.31: Comparison of the exact and approximated coupled flux CDF function of the coupled flux threshold, for the $MMSE_{\Phi_\chi}$ method, in the MOSPAR 1010, 2020, 3030 and 5050 conditions.

Simplification of the existing model

When the approximation of equation 7.25 meets the condition to be applied to the reciprocal uplink, we can approximate the law as a log-gamma distribution [226]. Indeed, by denoting:

$$z = \sum_{i=2}^{N} c_i^2 \tag{7.28}$$

as $\forall i$, c_i is a centered Gaussian variable of variance σ_i^2, c_i^2 is therefore a χ^2 random variable, that is a special case of Gamma random variable of parameters $k = 1/2$, $\theta = 2\sigma_i^2$. Hence, as

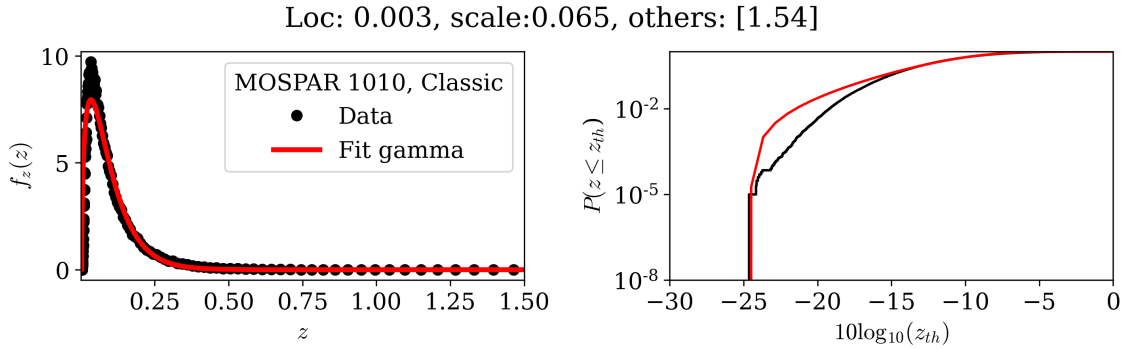

Figure 7.32: Statistics of $z = \sum_{i=2}^{N_{AO}} c_i^2$, fitted as a Gamma distribution, in the MOSPAR 1010 case, for the classical pre-compensation.

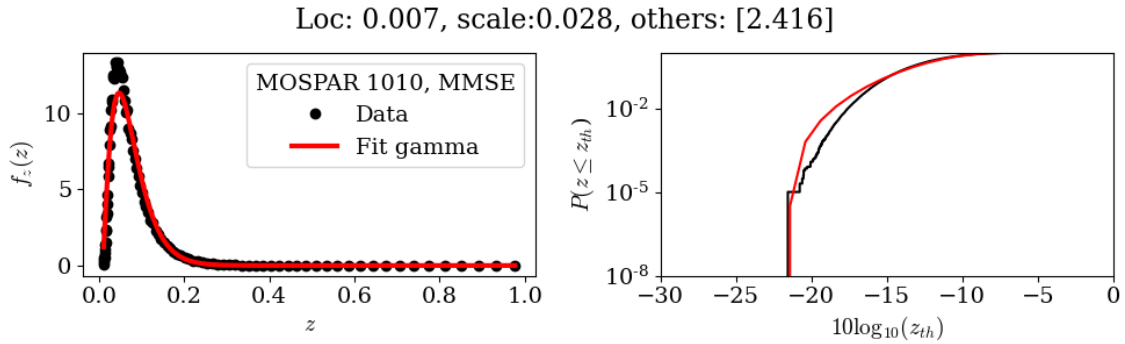

Figure 7.33: Statistics of $z = \sum_{i=2}^{N_{AO}} c_i^2$, fitted as a Gamma distribution, in the MOSPAR 1010 case, for the classical pre-compensation.

a sum of Gamma random variable of same shapes and different scales, we can approximate z distribution as a Gamma random variable.

We plot in figure 7.32 the fit of z with the gamma distribution, for the profiles MOSPAR 1010, for the classical pre-compensation. The same graph is plotted in 7.33 for the MMSE pre-compensation case. We observe that it does not completely fit the CDF. In fact, as z is composed of a sum of Gamma random variable with the same shape but different variances. Indeed, each Gamma parameters depend on each Zernike mode individual variance, that decreases exponentially with the radial order. This sum of Gamma RV with different parameters produce the bumps we observe on the signal statistics. We also fit the probability of z for the same profile in the MMSE pre-compensated case.

Therefore, as the coupling is approximated as the exponential of $-z$, it can be approximated by the log-gamma distribution. We plot the fit of the coupled flux in figures 7.34 and 7.35, in the MOSPAR 1010 case and in the classical and $MMSE_{\Phi_\chi}$ pre-compensation cases, respectively. We observe a good fit between the empirical distribution and the fit both on the CDF and PDF. However, we note that the tail of the CDF diverges, especially in the classical pre-compensation case.

To conclude, we showed that until a given value of tip and tilt variance, the approximation to model the downlink with partial AO correction developed by Canuet stands. Under these conditions, the coupled flux statistics can be modeled as a log gamma distribution. It is convenient to approximate this distribution to exploit its results, as there is no closed form for the PDF found in [116]. Future work should consist in making the link between the residual phase variance values and the log-gamma PDF parameters.

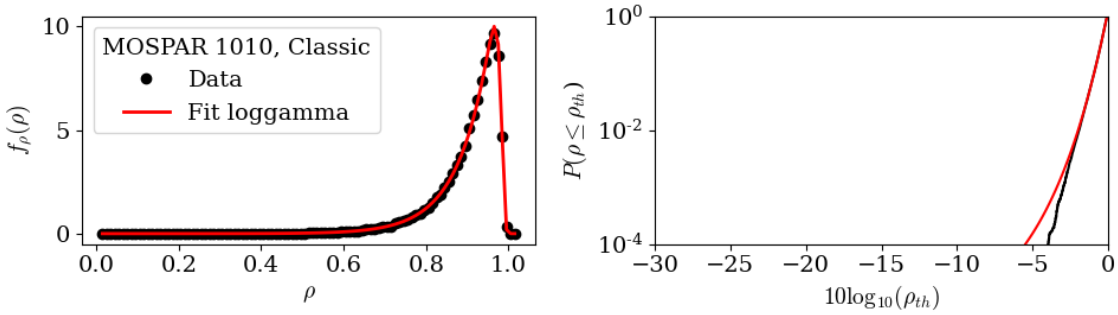

Figure 7.34: Statistics of ρ_ϕ, fitted as a loggamma distribution, in the MOSPAR 1010 case, for the classical pre-compensation.

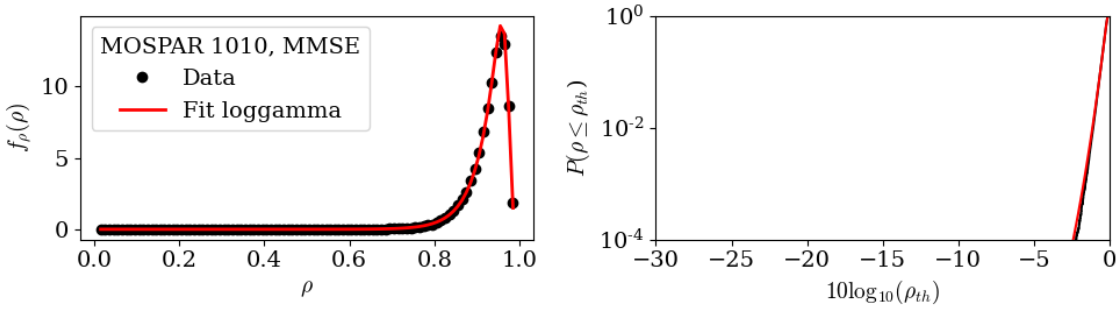

Figure 7.35: Statistics of ρ_ϕ, fitted as a loggamma distribution, in the MOSPAR 1010 case, for the $MMSE_{\Phi\chi}$ pre-compensation.

7.4.3.2 Exploration of models in the strong residual tip-tilt regime

Previously, we have shown that the downlink model with partial AO correction can be used when the tip or tilt variances doesn't exceed 0.16 rad^2. We now explore the regime beyond this value, that can be assimilated to the named *beam wander regime* from the literature. Indeed, strong residual tip tilt in the reciprocal point of view would, in the conventional sens of modeling, induce the beam to wander in the satellite plane.

We start by presenting the coupled flux E2E time series in the MOSPAR 9090 case, compared to the coupling approximation, in order to emphasize on the instants when the approximation fails to represent the fades. We plot the time series in figure 7.36, where the exact coupling is depicted in black and the approximation from Eq. 7.25 in red dashes. We observe that the signal global behavior is well approximated, except at given instants, when the fades are deep. We focus our attention on two fades that are denoted **fading 1** and **fading 2**.

Considering these two fades, we explore the exact coupling value function of the tip and tilt values, normalized by the coupling approximation when $a_2 = a_3 = 0$. By exploring all the tip and tilt combinations from -4 to 4, we obtain the surface maps depicted in figure 7.37. In these maps, we observe a quasi Gaussian shape of coupling function of the tip and tilt values. However, we also observe that it is asymmetrical. This means that a couple of (a_2, a_3) will not give the same coupling, function of their signs. This shape can be interpreted by the fact that the instantaneous point spread function, in the focal plane, is not a symmetrical pattern due to the anisoplanatism error and the presence of energetic high order Zernike modes. Therefore, by modifying the tip and tilt, it is equivalent in the focal plane to compute the coupling between the fiber single mode whose center moves along the PSF shape. This explains the correlation between the tip-tilt and the high order

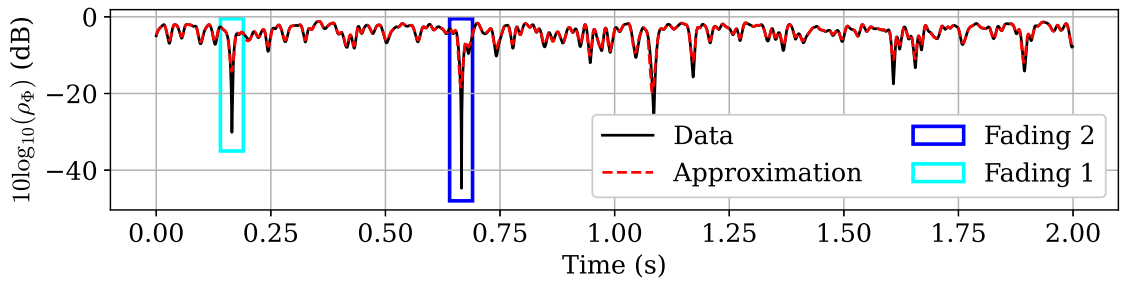

Figure 7.36: Time-serie for the coupled flux for the classical pre-compensation, computed from the E2E data and approximated by Eq. 7.25.

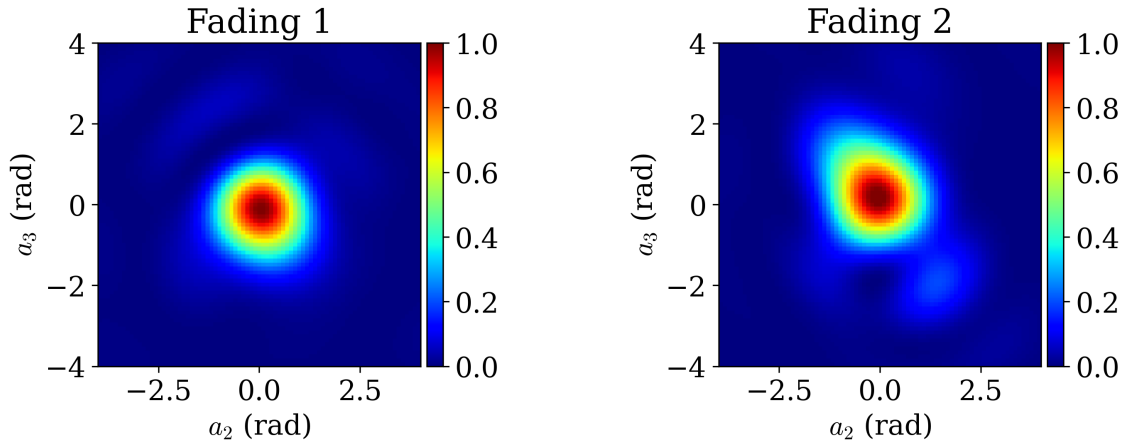

Figure 7.37: Color map of the normalized coupling of the fades 1 and 2, function of the tip and tilt values. The sum of the square of the high order modes is equal to 0.30 rad² for the fading 1 and 0.61 rad² for the fading 2.

modes, that was highlighted in chapter 2, when refining the pseudo-analytic model.

We also observe the impact of the tip and tilt not in a fade, for two samples of the time series, in figure 7.38. We observe that the color map is also unstructured for the fade 12, with also observable asymmetries. In this case, the spatial variance of the high orders is equal to 0.80 rad². In the sample 64 case, we observe a quasi-symmetric shape, and the spatial variance of the high orders equals to 0.25 rad². We conclude that the instantaneous value of the high order modes affects the coupling value with a non-symmetric impact that depends on the tip and tilt value. We interpret this phenomenon as the results of the high order modes changing the shape of the diffraction pattern in the focal plane of the optical system, that is also non-symmetrical.

To analyze the interaction between the value of the high order modes and the tip tilt value, we plot in figure **??** the time series of the value of $a_2^2 + a_3^2$ and the sum of the square of the high order modes. We observe that when the tip tilt is increasing, most of the time, the high order value decreases. This is due to anti-correlations in the modal covariance matrix between the tip tilt and the coma aberrations. This explains that, even if the high order modes are energetic, and modify the PSF structure, as the tip and tilt are weak (below one, therefore concentrated in the orange zone from the color maps showed, for instance, in figure 7.38), therefore the approximation stands. However, in the case of a fade, the sum of the square tip tilt is high, and the coupling value is in the halo that is unstructured and whose shape has not been calculated.

From these observations, we conclude that:

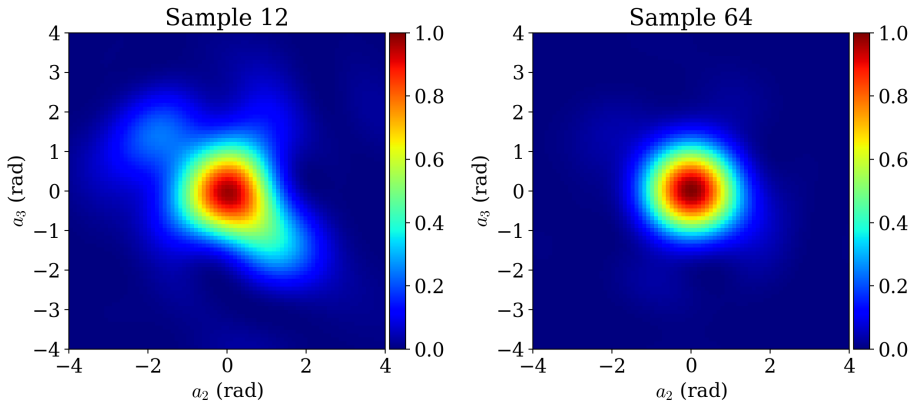

(a) Not in a fade, the sum of the square of the high orders equals to 0.80 rad².

(b) Not in a fade, the sum of the square of the high orders equals to 0.25 rad².

Figure 7.38: Normalized coupling function of the tip and tilt value, not in a fade (samples 12 and 64 corresponding to the instants 0.002 s and 0.013 s).

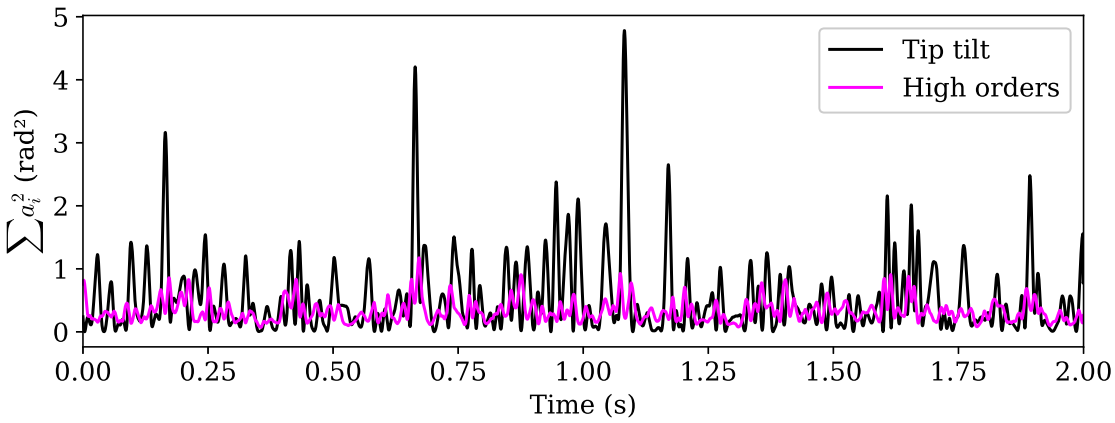

Figure 7.39: Sum of the square of the tip tilt coefficients and high order Zernike coefficients, function of the time.

- When considering a sample not in a fade, the tip, and tilt value is moderate (below one in absolute value). For some occurrences, we observe an intensity pattern in the focal plane that shows to be asymmetrical. However, this does not impact the coupling if the tip and tilt are weak.

- In a fade, the coupling is impacted as it is found that the signal overlapped with the Gaussian mode is shifted and corresponds to the part of the Halo of the turbulent PSF.

- We also show that the high order sum tends to decrease when the sum of the tip and tilt increases, and conversely.

- We also empirically set the limit of the approximated regime to a tip and tilt variance equal to one.

From these observations, we develop a new methodology to account for the reciprocal uplink modeling in the presence of strong tip and tilt residuals.

Proposed method

We showed earlier that there were two different regimes function of the sum of the squared tip and tilt. Therefore, we propose to develop the statistics of ρ_ϕ using the conditional signal probability function of the tip and tilt value. Therefore, we can write that:

$$P(\rho_\Phi) = P(\rho_\Phi|\sqrt{a_2^2+a_3^2} \leq 1)P(\sqrt{a_2^2+a_3^2}) \leq 1) + P(\rho_\Phi|\sqrt{a_2^2+a_3^2} > 1)P(\sqrt{a_2^2+a_3^2} > 1). \tag{7.29}$$

Already, we know that a_2 and a_3 follow a centered Gaussian distribution, therefore, the probability of $X = a_2^2 + a_3^2$ is a Gamma random variable, whose parameters have to be developed and therefore, $Z = \sqrt{X}$ follows a Nakagami distribution. Therefore, $P(\sqrt{a_2^2+a_3^2} \leq 1)$ can be developed as the CDF evaluated in 1 of the Nakagami distribution. Following the development in section 7.4.3.1, we assume that $P(\rho_\Phi|\sqrt{a_2^2+a_3^2} \leq 1)$ follows a log gamma distribution.

Lastly, we need to determine the coupled flux when $\sqrt{a_2^2+a_3^2} > 1$ is higher than the threshold 1. To develop the complex coupling term, we first assume that $\Phi_{res,TT} >> \Phi_{res,HO}$. Therefore, it yields:

$$\Omega_\Phi = \int_0^1 \int_0^{2\pi} \exp\left(i\Phi_{res}(r,\theta)\right) M_0(r) r d\theta dr \approx \int_0^1 \int_0^{2\pi} \exp\left(i\Phi_{res,TT}(r,\theta)\right) M_0(r) r d\theta dr \tag{7.30}$$

where we recall that $M_0(\mathbf{r})$ is the Gaussian mode expressed in the pupil plane, with the waist $\omega_0 = D/2.2$. Since the spatial phase is equal to the tip and tilt contribution, we develop these terms as:

$$\Phi_{res,tt}(r,\theta) = 2ra_2 \sin(\theta) + 2ra_3 \cos(\theta) \tag{7.31}$$

That can be simplified as:

$$\Phi_{res,tt}(r,\theta) = 2r\sqrt{a_2^2+a_3^2} \sin(\theta + \arctan(a_3/a_2)) \tag{7.32}$$

Denoting $A = \sqrt{a_2^2+a_3^2}$ and $B = \arctan(a_3/a_2)$, we obtain:

$$\Omega_\Phi = \sqrt{\frac{2}{\pi\omega_0^2}} \int_0^1 \int_0^{2\pi} \exp\left(i2Ar\sin(\theta+B)\right) \exp\left(-2r^2/\omega_0^2\right) r d\theta dr \tag{7.33}$$

We compute this integral over θ. Knowing the Bessel J_0 properties [227], it yields:

$$\Omega_\Phi = 2\pi\sqrt{\frac{2}{\pi\omega_0^2}} \int_0^1 J_0(2Ar) \exp\left(-r^2/\omega_0^2\right) r dr = \frac{2\pi}{4A^2}\sqrt{\frac{2}{\pi\omega_0^2}} \int_0^{2A} J_0(X) \exp\left(-X^2/(4A^2\omega_0^2)\right) X dX \tag{7.34}$$

that is obtained with the change of variable $X = 2Ar$. To compute this integral, we use the Bessel series expansion of the Bessel J_0:

$$J_0(r) = \sum_{i=0}^{\infty} \frac{(-1/4)^i r^{2i}}{i!\Gamma(1+i)} \tag{7.35}$$

Therefore:

$$\Omega_\Phi = \frac{2\pi}{4A^2}\sqrt{\frac{2}{\pi\omega_0^2}} \sum_{i=0}^{\infty} \frac{(-1/4)^i}{i!\Gamma(1+i)} \int_0^{2A} X^{2i} \exp\left(-X^2/(4A^2\omega_0^2)\right) X dX \tag{7.36}$$

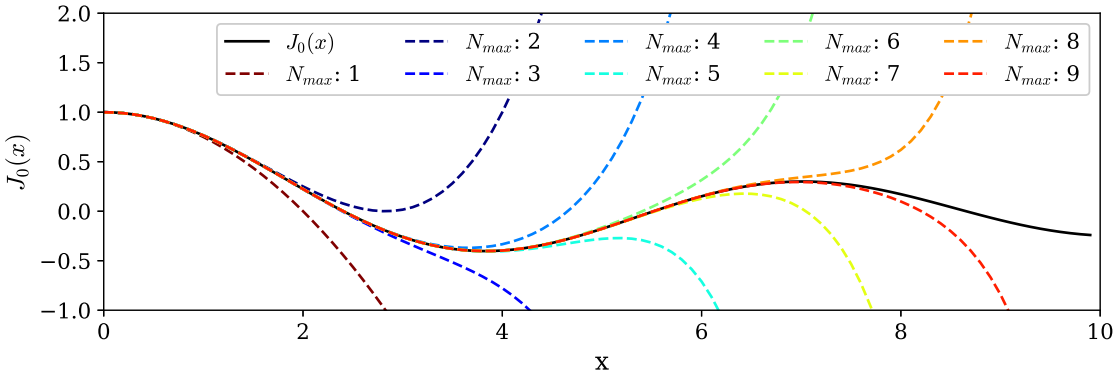

Figure 7.40: Bessel of order 0 function of x and its series approximation truncated for different truncation values.

that we simplify as:

$$\Omega_\Phi = \sum_{i=0}^{\infty} \frac{C(i)}{A^2} \int_0^{2A} X^{2i} \exp\left(-X^2/(4A^2\omega_0^2)\right) X dX \tag{7.37}$$

where $C(i) = \frac{2\pi}{4}\sqrt{\frac{2}{\pi\omega_0^2}}\frac{(-1/4)^i}{i!\Gamma(1+i)}$. The following integral can therefore be linearized and computed.

To compute this integral, we truncate the series of the Bessel function of order 0 to its N^{th} term that is to determine. We recall that the Bessel is evaluated in the integral from 0 to $2A$, where $2A = 2\sqrt{a_2^2 + a_3^2}$. We plot in figure 7.40 the Bessel function of order 0 and its series approximations truncated at the index N.

To determine until which index N the sum needs to be considered, we plot the PDF of $2\sqrt{a_2^2 + a_3^2}$ for different atmospheric conditions and different AO corrections in figure 7.41. We observe that the extreme values of the distribution varies function of the considered turbulence and AO correction case. For instance, in the worst considered case, that is the MOSPAR 9090 case with classical AO correction, the extreme values reach the values of 4. This means that the integral needs to be approximated until $N = 5$. We also observe bumps on the different PDFs that approximately corresponds to the number of terms that needs to be considered in the sum.

Consequently, developing the i^{th} term of the integral, it yields:

$$\int_0^{2A} X^{2i+1} \exp\left(-\frac{X^2}{(2A)^2\omega_0^2}\right) dX = 2^{1+2i} A^{2+2i} \left(\omega_0^2\right)^{1+i} \left(\Gamma(1+i) - \Gamma\left(1+i, \frac{1}{\omega_0^2}\right)\right) \tag{7.38}$$

Therefore, we can express the integral as:

$$\Omega_\Phi = \sum_{i=0}^{N} C'(i)(A^2)^i, \tag{7.39}$$

that is a polynomial of order N evaluated in $A^2 = a_2^2 + a_3^2$, where $C'(i)$ simplifies as:

$$C'(i) = \sqrt{2\pi\omega_0^2}\frac{(-1)^i}{i!\Gamma(1+i)} \left(\omega_0^2\right)^i \left(\Gamma(1+i) - \Gamma\left(1+i, \frac{1}{\omega_0^2}\right)\right) \tag{7.40}$$

Finally, the complex coupling, in this case, is real and is equal to a polynomial of order N, evaluated in $a_2^2 + a_3^2$. The resulting coupling efficiency is therefore obtained as:

$$\rho_\phi = |\Omega_\phi|^2 \tag{7.41}$$

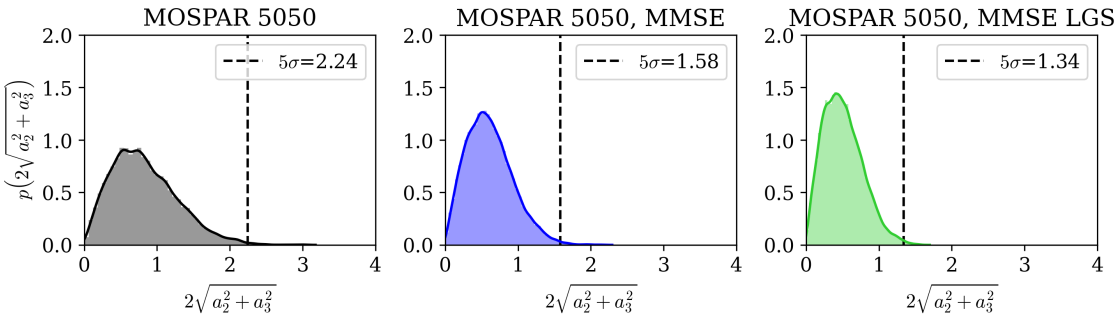

(a) MOSPAR 5050

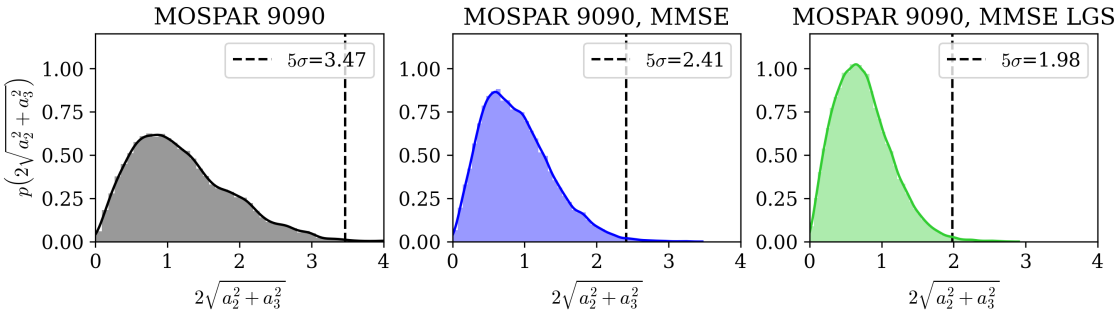

(b) MOSPAR 9090

Figure 7.41: Statistics of $2\sqrt{a_2^2+a_3^2}$

whose polynomial maximum order is equal to $2N$.

Knowing that $a_2^2+a_3^2$ follows a Gamma distribution, the probability law of the phase contribution to the coupling is therefore the distribution of the sum of Gamma random variable with exponent q. We know from the literature that: if X is a Gamma random variable, hence X^q follows a generalized gamma distribution. As a sum of generalized gamma random variable, we expect the coupling to be approximated as a generalized gamma distribution.

Recalling the equation from Eq. 7.29:

$$P(\rho_\Phi) = P(\rho_\Phi|\sqrt{a_2^2+a_3^2} \leq 1)P(\sqrt{a_2^2+a_3^2} \leq 1) + P(\rho_\Phi|\sqrt{a_2^2+a_3^2} > 1)P(\sqrt{a_2^2+a_3^2} > 1). \tag{7.42}$$

we now know the probability law of the conditional variables $\rho_\Phi|\sqrt{a_2^2+a_3^2}^2 \leq 1$ and $\rho_\Phi|\sqrt{a_2^2+a_3^2} > 1$. Following the preceding method, the coupled flux contribution to the coupling ρ_ϕ can be modeled as the sum of a log-gamma and a generalized gamma random variables. As the generalized gamma distribution family comprises most of the gamma distributions, we conjecture that the total distribution follows also a generalized gamma distribution.

We fit in figure 7.42 our E2E data in the case MOSPAR 9090 for three different correction cases, with the generalized gamma distribution. We observe for the Classical precompensation and the $MMSE_{\phi\chi}$ correction a good match between the PDF and CDF obtained from data and the fitted generalized gamma distribution. In the classical precompensated case, we observe different bumps on the PDF, that can reflect the nature of the coupling to follow a sum of distributions. In the case of the $MMSE_{\phi\chi,LGS}$, in figure 7.42c, as we assume the high orders to null, the contribution to the coupling is exactly equal to the PDF developed in the high tip-tilt regime. Therefore, we fit the term $1-\rho_{\Phi,MMSE,LGS}$ as the first term of the polynomial equals to 1. We observe a good match

between the empirical PDF and CDF, and the fitted distribution.

To conclude, in our approach, we calculated the distribution of the coupling when it is dominated by the tip and the tilt value, in order to compute the missing term allowing to compute a composite statistical law of ρ_ϕ. To compute this distribution, we assumed the instantaneous tip and tilt values to be large, and that we also approximated the Bessel function J_0 to an order that is relative to the term $\sqrt{a_2^2 + a_3^2}$ extreme values. The found probability law is a generalized gamma function, whose parameters link to the modal phase variance remains to determine. This will be the objective of future work.

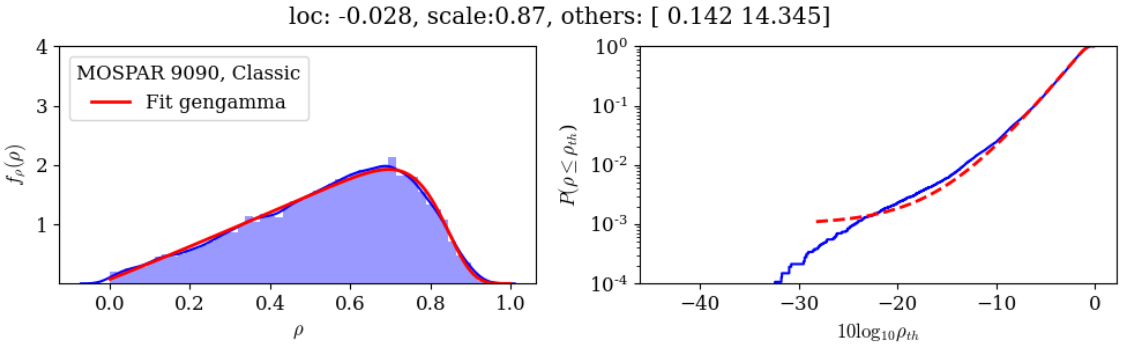

(a) Classical pre-compensation, fit of ρ_ϕ.

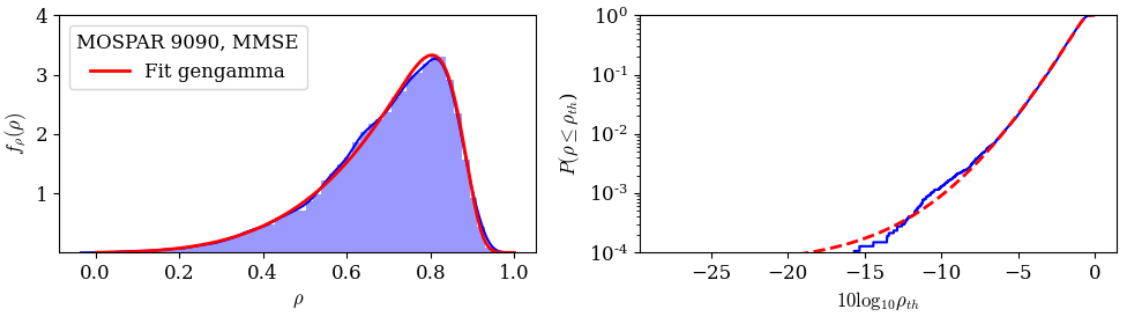

(b) $MMSE_{\Phi\chi}$ pre-compensation, fit of ρ_ϕ.

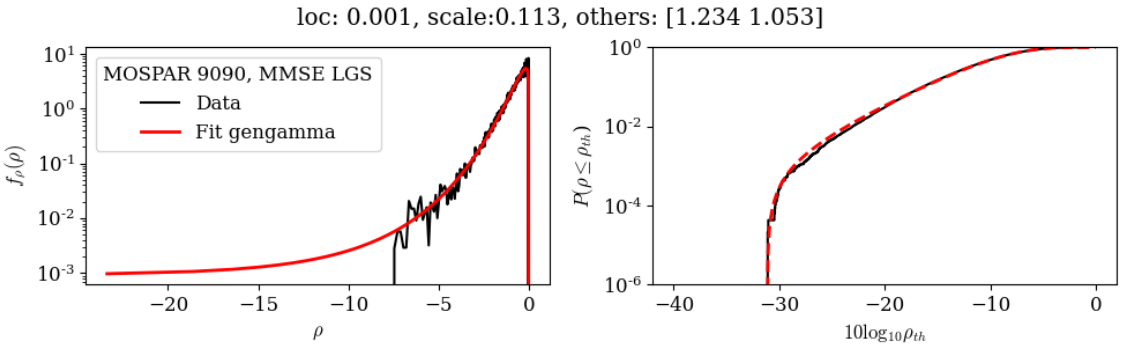

(c) $MMSE_{\Phi\chi,LGS}$ pre-compensation, fit of $1 - \rho_\phi$.

Figure 7.42: Fit of the PDF and CDF from the data with the generalized gamma distribution, in the MOSPAR 9090 case.

7.5 Conclusion

Main findings

To summarize, in this chapter, we evaluated the capacity of the channel corresponding to the ground to GEO channel pre-compensated by AO, thanks to the estimated pre-compensation phase presented in the thesis. In particular, we evaluated the ϵ-outage capacity that is more suitable to evaluate fading channels capacities. We've shown that every developed pre-compensation method allows improving the channel capacity, with respect to the state-of-the-art classical pre-compensation, for a reliability threshold of 10^{-3}. We also showed that adding a channel interleaver was improving the capacity of every channel. Also, some pre-compensation methods showed greater gains than the other for short interleaver duration, such as the one relying on several time steps measurements. This is due to the property of this estimator to further reduce the coherence time of the channel with respect to other methods.

In section 7.3, we performed a numerical transmission in a QPSK format at 1 Gbaud/s, with a BCH FEC encoding added to a 30 ms encoder. Although not averaged over any fading occurrences, the presented results confirm the trend observed on the capacity. However, the gains are lower than the one from the theoretical capacity. This is expected as the coding scheme was not especially optimized, and as there are always losses between theoretical and gains obtained on real systems.

Finally, in section 7.4, we presented our work on the development of the AO pre-compensated ground-to-GEO statistical channel model. After describing the different models from the literature, we verify if the different developed models hypothesis stands for the reciprocal AO corrected uplink scenario. We emphasized on the model developed by Canuet [116], and explore its validity in the reciprocal uplink scenario. We show that this model is valid as long as the residual tip-tilt is weak. We empirically characterize the instantaneous value required for this model to stand. We show that the sum of the square tip and tilt value needs to be below 1 rad^2. As the previous model has no closed form, we propose an equivalent simplified model that is a Gamma distribution. Finally, we explore the regime where the tip tilt residuals are strong. We propose a method, relying on conditional probabilities, to develop the coupling term statistics. We show that the distribution is equal to a weighted sum of a log gamma distribution and a second distribution, that we show to be a generalized gamma distribution.

Perspectives

Many preliminary results were presented in this chapter. For short term perspectives, the E2E numerical transmission needs to be consolidated and evaluated for different coding schemes and chain scenarios (different modulation schemes or interleaver size), in order to assess the gains obtained with the advanced pre-compensation methods.

Concerning the channel model, we presented and fitted the laws in different residual tip-tilt regimes. These findings need to be combined to validate the total distribution that was intuited, and we need to pursue the developments in order to link the law parameters to the residual phase variances, that characterize the quality of the AO correction.

As a broader perspective, having an analytical channel model, will allow developing the theoretical transmission bounds of the channel function of the AO correction quality. Therefore, this direct link between the correction parameter and the coupled signal statistics at the OGS, that can be computed thanks to a measured C_n^2 profile, can allow further optimization of the digital processing system.

Conclusions and perspectives

Conclusions

The establishment of a globalized space network can benefit from the use of optical links between the ground and satellites. In this context, the GEO Feeder uplink is a link foreseen to exchange data between the earth and the satellite at data-rates of several Tbps. The link current data-rates and reliability is limited by the atmospheric turbulence. Hence, we recall that the question we aimed at answering in this thesis was:

How can we ensure reliable communication at high data rates over the pre-compensated ground-to-GEO satellite optical fading channel?

To answer this question, we emphasized on the assessment of the pre-compensated by adaptive optics link performance using state-of-the-art methods, and on its improvement using now optical strategies. In particular, we studied the optimization of the pre-compensation phase at point-ahead angle using different source of information (or measurements) available at the optical ground station. Finally, we studied the statistics of the AO pre-compensated ground to GEO link, in order to pave the way for future optimization of the digital signal processing systems. We summarize the main conclusions of this thesis as follows.

Reciprocal channel model and link performance using state-of-the-art methods

We started the thesis by introducing and demonstrating the reciprocity principle, that we use all along the thesis to model the AO pre-compensated ground to GEO satellite link. This principle is used to model the pre-compensation phase errors and the coupled flux onboard the satellite. We illustrate the strength of this formalism by characterizing the performance of our benchmark links, for various OGS configuration and turbulence conditions. These benchmarks are the links pre-compensated with the AO correction of the on-axis downlink, that we called classical pre-compensation, or aided by an LGS. We showed that the coupled flux is very impaired when the pre-compensation phase suffers from large residual tip-tilt. In these cases, when the angular decorrelation of the turbulence is large, therefore when the anisoplanatic angle is small, the coupled flux issued from both methods undergoes long and deep fades. It was therefore emphasized that improving the tip-tilt pre-compensation was essential to improve the coupled flux statistics.

To improve the coupled flux statistics and increase the power link margin for a threshold of 99.9% availability, we proposed to optimize the pre-compensation phase at PAA.

Advanced pre-compensation methods

On the basis of Whiteley's work, we developed the formalism of a general linear and modal MMSE phase estimator, applicable to any kind of measurements. This estimator

construction relies on the computation of angular covariance matrices between the phase at PAA and the physical quantities that compose the measurement vector.

At the root of the methods proposed in the thesis lies the idea of using jointly the phase and the log-amplitude measurements from the on-axis downlink. Indeed, the on axis log-amplitude informs on the perturbations from the atmosphere upper layers, where the anisoplanatism is generated. We developed the MMSE estimator based on these measurements, by extending the covariance formulas from the literature, based on Chassat's and Mahé's work, to obtain all the covariances necessary to the estimator construction. This estimator is shown to greatly reduce the phase error, especially the tip and tilt phase error, which results in signal statistic improvements. Indeed, applying the phase estimate to the pre-compensation shows to reduce the fade number depth and duration. We highlight that we systematically validated the analytical and pseudo-analytical results on the E2E data.

Based on this idea, we developed three additional estimators, relying on different type of measurements, that comprises: temporal past measurements of phase and log-amplitude, phase and log-amplitude collected on several apertures in a multi aperture OGS scheme, and phase and log-amplitude collected from the on-axis downlink, combined with phase high order measurements obtained with LGS wavefront sensing. We showed that:

- In general: a large amount of the useful information is comprised in the on axis log-amplitude measurement.
- When using past measurements, the phase is also informative on the perturbation at PAA, as the phase temporal correlations are stronger than the phase angular correlations. Using temporal measurements in presence of phase temporal error induced by the AO loop delay, corrects for this temporal error. Adding 3 past measurements and no more further decreases the phase error (both the low orders and high orders), resulting in a coupled flux improvement of 16 dBs in severe turbulence condition.
- Using spatial information, collected on several apertures in the direction of the PAA, also decreases the pre-compensation phase error. This method shows to be more robust to high turbulence angular decorrelation. We also showed that in a two apertures scheme, only an additional low resolution amplitude measurement from the second aperture was required. The gains on the coupled flux statistics are improved by 15 dB on the CDF at probability 10^{-3}.
- In a system aided by an LGS, the best gains are obtained, since the tip tilt and focus reduction error is equivalent or better than the one obtained in the multi-aperture scheme, and that we benefit from an almost perfect correction of all the other modes. In this case, the gains on the coupled flux statistics are improved by 19 dB on the CDF at probability 10^{-3}.
- Temporally and spatially collected measurements show to bring complementary information that, if combined, results in a very robust correction in very severe turbulence conditions.

In addition, we developed a formalism to test the robustness of the estimator, and applied it to question its robustness to C_n^2 profile uncertainties. We also questioned the efficiency of the estimator in limit regimes.

Telecommunication performance

Once the different phase estimator constructed and assessed, we evaluated the telecommunication performance of the channels, especially the channel capacity, which is the channel

theoretical transmission limit. We showed that the different estimators allowed for improving the channel capacity with respect to state-of-the-art methods, especially the ϵ-outage capacity, for $\epsilon = 10^{-3}$, that characterizes the capacity that can be achieved in a fading channel with a reliability threshold of 99.9%. We also showed that the new developed channels allowed decreasing the required interleaver duration. This should allow decreasing the complexity of the telecommunication receiver onboard the satellite, as well as reduce the link latency.

We also presented preliminary results on the validation of an E2E transmission, using a QPSK modulation at 1 Gbaud/s, and a FEC correction using a BCH code of code rate 0.9 and a 30 ms interleaver. Although the gain provided by the different methods was decreased, the tendencies observed on the capacity results were confirmed. The channel using a pre-compensation estimated from two apertures measurements showed the best performance, and the time estimated pre-compensation channel showed the best improvement thanks to the interleaving process.

Channel modeling

Finally, we presented our work on the statistical modeling of the reciprocal ground to satellite channel corrected by adaptive optics. Statistical models have been developed to model the uplink Gaussian beam propagation from the ground to the satellite. However, evaluating the impact of an adaptive optics pre-compensation in this framework is difficult. Therefore, we took the reciprocal point of view to revisit existing models while taking advantage of developments made for downlink corrected links. This framework also allowed to account for developments made in astronomy characterizing anisoplanatic effects.

We showed that most of the state-of-the-art models had strong assumptions on the phase spatial statistics that are not especially true for an anisoplanatic link in the presence of phase low order residuals over a finite aperture, such as strong tip and tilt residuals. We also explored in details the applicability of the model developed by Canuet, that is a statistical characterization of the coupled flux for a downlink corrected by adaptive optics, with a good AO correction. We showed that this model could be applied if the tip and tilt phase residuals are weak. We empirically characterized the tip and tilt value threshold under which this model is applicable.

Knowing that, we presented preliminary results on the general reciprocal uplink statistical model. We proposed a new composite approach that account for the signal statistics both within the weak tip and tilt regime and beyond this regime. As the missing piece was the characterization of the signal statistics in the strong residual tip and tilt regime, we proposed a development of the complex coupling equation, neglecting the high orders with respect to the tip and tilt value in this regime. In this case, we developed an approximation of the coupling efficiency and from this equation, we showed that it was following a generalized gamma distribution. We confirmed this preliminary result by fitting the data with the generalized Gamma distribution, which showed to match the data.

Perspectives

From the work presented in this thesis, we can identify the following perspectives:

Advanced pre-compensation methods

The main perspective concerning the development of the advanced pre-compensation methods is the experimental demonstration of these methods feasibility and efficiency. As the use of the phase and log-amplitude from the downlink beam is at the heart of all the new strategies, the first step is to experimentally demonstrate the $MMSE_{\Phi\chi}$ approach, that covers experimental challenges common for every other methods. We note that the use of phase and log-amplitude measurements is already used in the metrology domain [228].

- $MMSE_{\Phi\chi}$ experimental demonstration

To demonstrate the feasibility of this method, two main points need to be addressed. Firstly, the feasibility of computing the reconstructor by retrieving C_n^2 profile measurements. This has already been done using Shack-Hartmann data in [228], and further used during the FEEDELIO experimental campaign [89]. Further questions arise concerning the reconstructor computation thanks to turbulence measurements. For an optimal computation, what resolution is needed ? what instruments should we use ? dedicated metrology instruments or reconstruction from AO telemetry data ? what should be the refresh time of the C_n^2 profile measurements ? Are some layers more important to measure from others ? All these questions open a new panel of research topics.

Secondly, the implementation of an AO control loop controlling a second DM to implement either the total uplink correction, either a differential correction, with a common path correction applied on a DM correcting both the downlink and part of the uplink phase disturbances. Additionally, it was shown that the term describing the downlink amplitude averaged by the pupil has an important role in the estimation. This term is not centered by nature, on the contrary to the measured phase modes. Therefore, careful photometric calibrations will be required, in order to re-center the pumping term before the applying the reconstructor on the measurements. We note also that the computation time of the reconstructor will need to be optimized.

- Demonstration of methods relying on spatial measurements

Once the basic block being the demonstration of the $MMSE_{\Phi\chi}$ is demonstrated, we can envision to test for advanced techniques. Considering the techniques using spatial measurements, some systems are already implemented (LGS or multi-aperture systems), and could be used to test the estimation techniques.

The challenges using spatial measurements are different, and are more related to aspect as measurement synchronization, or the system optimization in order to design affordable systems (in the multi-aperture case for instance). In the LGS case, further numerical simulations should be done with less assumptions on the LGS system, in order to assess the feasibility of this method, before experimental demonstration.

- Demonstration of methods relying on temporal measurements

In the case of application of methods relying on temporal measurements, it is needed to retrieve, in addition to the C_n^2 profile, the wind profile. Some methods analyzing scintillation spatio-temporal spectrum exists in the literature [229, 230]. Techniques of this kind would need to be tested in order to assess for the feasibility of these methods. It could be tested on links with LEO satellites, reducing the need for wind metrology to ground wind measurements.

Channel modeling

Concerning the channel modeling perspective, we can divide it into the numerical modeling perspectives and the analytical modeling perspectives.

- Numerical modeling

On the one hand, we used and refined a pseudo-analytical model based on the modal phase variance statistics. On the other hand, we developed the formalism required to compute the modal residual phase temporal auto-correlation. A future objective would be to use this analytical characterization of the residual phase temporal autocorrelation to develop a temporal pseudo-analytical tool. Such tool will be useful to quickly emulate time-series, that are needed for telecommunication evaluation in presence of interleaving.

Additionally, the multi-aperture spatial covariance formalism developed can also be used to model the coupled flux in a multi-emitter ground to GEO link.

- Statistical modeling

We presented in this thesis preliminary results concerning the channel model leading to a parametric generalized gamma model. However, the computation to link the distribution parameters to the residual phase variances still needs to be made. Future work will consist in finalizing the analysis to obtain the complete channel model. In the same way, we empirically determined a value that separates the weak and strong residual tip-tilt regimes. This threshold will also need to be analytically proven.

Communication system optimization

We also presented preliminary results concerning the E2E telecommunication performance evaluation over the different proposed channels. First, these results need to be consolidated, and secondly, more parameters can be explored to determine what is the ultimate performance and data-rate we can achieve on the ground to GEO link.

Such model would allow computing the theoretical bounds of the channel whatever the turbulence conditions and the adaptive optics system performance.

Turbulence conditions monitoring

All the proposed optimization methods depends on the turbulence conditions. To carry out this study, we used a given database of turbulence conditions. Further studies should study the impact of the atmospheric conditions measured on larger and more representative databases, that corresponds to the atmospheric conditions of future OGS sites. Recent studies provided global models of atmospheric parameters [231, 232]. Also, the prediction of optical links availability given limited number of parameters is an active field of research, already applied to the downlink [117], and could be extended to the evaluation and prediction of uplinks availability. Such tools would benefit the telecommunication network management.

Application to other fields

Finally, the advanced pre-compensation methods developed have been applied to the use case of uplink optical high data rate communication. However, the telecommunication with GEO satellites field is not the only one that can benefit from an uplink improved optical signal. First, as already discussed in this thesis, the estimated pre-compensation techniques could be applied to other types of telecommunication links, such as LEO links.

Enabling high data rate LEO uplink could unlock new types of internet network structures. Additionally, these uplink pre-compensated link could benefit the field of quantum communication. Indeed, some quantum communication key distribution protocols, rely on the transmission of a key from the ground to a GEO or LEO satellite, and could benefit from the channel statistics enhancement. Finally, a last application that could benefit from the channel improvement is the satellite time and frequency transfer.

APPENDIX A

Résumé en Français

A.1 Introduction et contexte

Dans un contexte de besoins numériques croissants, les réseaux de télécommunication satellitaires sont amenés à complémenter les infrastructures terrestres existantes. Un internet satellitaire permettrait de couvrir des zones peu connectées actuellement par manque d'infrastructures fibrées dont l'installation est coûteuse. Le rôle du satellite en orbite geostationnaire (GEO) est de redistribuer au reste du réseau satellitaire l'information issue du réseau terrestre. Le lien de la terre vers le satellite GEO doit donc transporter de la donnée à de très hauts débits. Les technologies optiques sont de très bons candidats pour atteindre ces débits, du fait de la large bande passante disponible (11.4 THz). Ces faisceaux optiques sont aussi moins divergents, ce qui augmente la sécurité intrinsèque de la liaison et permet de s'affranchir d'un système d'allocation de fréquences (système mis en place pour les communications satellitaires RF).

Cependant, ces liens optiques sol-satellite sont fortement affectés par le blocage du signal en présence de nuages et par l'atténuation du signal induite par la turbulence atmosphérique. Tandis que la multiplication de sites d'installation de stations sol optiques vise à s'affranchir des problèmes de couverture nuageuse, des systèmes, tels que l'optique adaptative, permettent de limiter l'impact de la turbulence atmosphérique. Ces systèmes reposent sur la mesure et la correction en temps réel de la phase de l'onde perturbée par l'atmosphère, permettant de réduire de plus d'un facteur 1000 l'atténuation du signal,

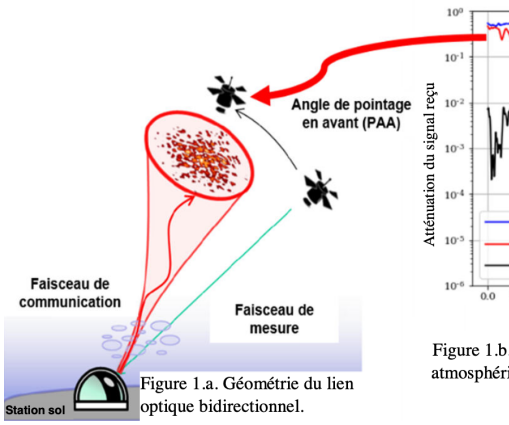

Figure 1.a. Géométrie du lien optique bidirectionnel.

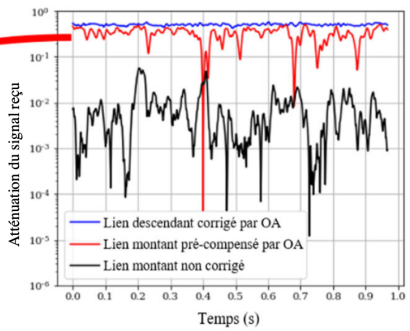

Figure 1.b. Atténuation du signal induit par la turbulence atmosphérique pour des liens montant et descendant avec ou sans correction par OA.

Figure A.1: Illustration de la géométrie du lien GEO Feeder et de l'impact de la turbulence sur le flux couplé à bord du satellite.

comme illustré en figure 1.b. par le passage du signal atténué en noir à celui en bleu. Dans le cas du lien montant, auquel je m'intéresse, la technique envisagée est de pré-compenser la phase de l'onde émise par optique adaptative depuis la station sol, avec une correction basée sur la mesure issue du lien descendant. Cependant, du fait d'un angle de pointage en avant entre les liens montants et descendants, illustré Fig.1a., les trajets et donc les perturbations rencontrées par les faisceaux montant et descendant ne sont pas les mêmes. Il en résulte que la pré-compensation à l'état de l'art ne réduit pas aussi efficacement les atténuations du signal que sur le lien descendant. Par conséquent, de profondes et longues atténuations et donc des pertes d'information subsistent, comme illustré par le signal atténué en rouge en figure 1.b.

L'objectif de ma thèse est d'optimiser la phase de pré-compensation par optique adaptative, et de quantifier les gains apportés par les nouvelles méthodes développées au système de télécommunication. Cette optimisation doit permettre de fiabiliser la transmission d'information du sol vers le satellite GEO, tout en assurant un haut débit et en tenant compte des contraintes du système telles qu'une capacité de calcul limitée à bord du satellite, une puissance émise depuis la station sol limitée ainsi qu'une latence du lien à limiter pour répondre aux standards des télécommunications.

A.2 Méthodologie

Afin d'étudier l'impact de la pré-compensation par optique adaptative sur la performance du système de télécommunication, j'ai dû modéliser l'atténuation du signal reçu à bord du satellite, puis caractériser la performance télécom à l'aide des métriques appropriées.

L'originalité de la méthode de modélisation choisie réside dans l'utilisation d'un formalisme réciproque, que nous avons vérifié expérimentalement. Cette approche permet d'accéder à l'erreur de phase de pré-compensation à l'origine des atténuations du signal. En utilisant ce principe, j'ai pu adapter les outils de simulation numérique existants, dits "de bout-en-bout", pour modéliser cette erreur de phase et l'atténuation du signal associée. J'ai aussi pu utiliser des approches "pseudo-analytiques", reposant sur la connaissance des statistiques de l'onde après propagation, permettant d'obtenir un grand nombre d'échantillons de coefficients d'atténuation tout en s'abstrayant de l'étape de propagation numérique, qui est coûteuse en temps de calcul. J'ai pu améliorer ces outils pseudo-analytiques en montrant l'importance de la prise en compte de corrélations statistique de la phase.

De plus, pour évaluer la performance télécom, j'ai étudié la ϵ-capacité, soit le débit maximal théorique, par unité de fréquence, pouvant être atteint avec un seuil de fiabilité 1-ϵ. Nous choisissons un seuil de fiabilité à 99.9%, soit $\epsilon = 10^{-3}$.

A.3 Principaux résultats

Durant ma thèse, j'ai pu développer quatre techniques d'estimation de phase au pointage en avant, dénotée Φ_{PAA}. J'ai pu évaluer le gain apporté par ces méthodes sur la ϵ-capacité, définie ci-dessus, par rapport aux méthodes de l'état de l'art, notamment la pré-compensation dite classique, reposant sur l'application de la correction mesurée sur le lien descendant, sur axe.

La première méthode[1], dont le principe est au cœur de toutes les méthodes qui suivent, consiste à exploiter les mesures de phase et d'amplitude du faisceau descendant pour développer un estimateur de la phase de pré-compensation au pointage en avant, Φ_{PAA}. Cet estimateur est construit en utilisant une approche MMSE (minimisation de l'erreur

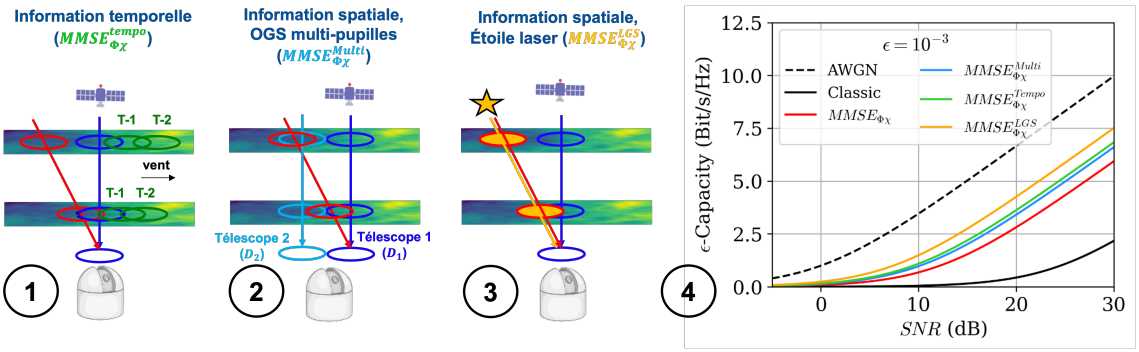

Figure A.2: En 1,2,3: schéma de principe des différentes sources d'information utilisées dans les méthodes 2,3 et 4, pour l'estimation de la phase de pré-compensation (phase résultante du faisceau hors-axe en rouge).En 4: ϵ-capacité associée aux différentes méthodes proposée, comparées à la pre-compensation classique (traits pleins noirs), méthode de l'état de l'art, et au canal AWGN (tirets noir), qui est la borne supérieure de la capacité. Ces résultats sont obtenus en condition de forte turbulence.

quadratique moyenne), dont le calcul repose sur la connaissance d'a priori statistiques de la turbulence. La nouveauté de la méthode consiste à utiliser les mesures d'amplitude du lien descendant, apportant de l'information sur les perturbations atmosphériques ayant lieu en haute altitude, là où la majeure partie de l'erreur de phase est générée. Nous avons pu montrer que cette méthode réduit l'erreur de phase MSE de 30%, réduisant ainsi les fluctuations du signal reçu à bord du satellite, ainsi que la durée des atténuations, réduite de moitié aux seuils de détection considérés. Son application permet donc d'améliorer la fiabilité de la transmission du lien GEO Feeder et d'atteindre des débits plus élevés.

La seconde méthode, illustrée en figure A.2.1., repose sur une estimation de Φ_{PAA} en utilisant plusieurs mesures passées de phase et d'amplitude du lien descendant, en utilisant l'approche MMSE. L'ajout de mesures et d'a priori temporels permet d'améliorer davantage la statistique du signal reçu. Cette méthode permet également de diminuer notablement le temps de cohérence du canal, ce qui est bénéfique pour la réduction de la longueur des entrelaceurs (mécanisme de fiabilisation de l'information par moyennage temporel). Cette réduction permet de réduire la complexité du système de réception à bord du satellite.

La troisième méthode[2], illustrée en figure A.2.2., repose sur une estimation de Φ_{PAA} en utilisant plusieurs mesures de phase et d'amplitude du lien descendant, collectées par plusieurs télescopes situés dans la direction du pointage en avant. En effet, du fait de la distance du satellite GEO (38000 km), l'empreinte au sol du faisceau descendant est beaucoup plus large (∼100 m) que la portion mesurée par le télescope (60 cm). L'idée est d'utiliser ces fuites de faisceau pour obtenir une deuxième mesure spatiale, permettant d'améliorer l'estimation de phase. J'ai pu montrer que seule la mesure d'amplitude sur le deuxième télescope suffisait à améliorer l'estimation, ce qui simplifie la conception du système additionnel. Cette méthode fiabilise le lien, notamment dans des cas de très forte turbulence qui limitent l'apport de la première méthode.

La quatrième méthode, illustrée en figure A.2.3., repose sur une estimation de Φ_{PAA} en utilisant conjointement les mesures de phase et d'amplitude du lien descendant, et les mesures issues d'une étoile laser, au pointage en avant. Cette méthode fusionne la technique d'étoile laser avec celle de l'estimation de phase MMSE, en utilisant les mesures de phase accessibles via l'étoile laser et celles de phase et d'amplitude issues du lien descendant pour estimer les modes de tip, tilt et focus. En effet, ces modes ne peuvent pas être mesurés par l'étoile laser. Cette méthode procure les meilleures performances, au prix d'un système

[1][Lognoné-OpticsExpress-2022, doi: https://doi.org/10.1364/OE.476328]
[2][Lognoné-OpticsLetters-2023, doi: https://doi.org/10.1364/OL.495200]

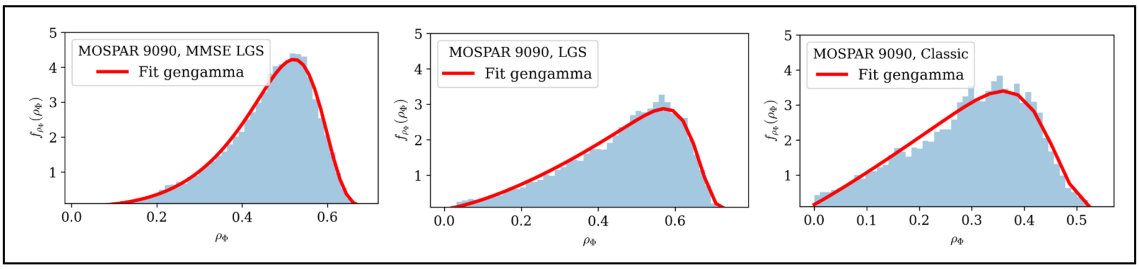

Figure A.3: Histogramme normalisé de l'atténuation du signal reçu à bord du satellite, induite par la turbulence atmosphérique, pour trois méthodes de pré-compensation différentes. En rouge, fit de la loi de probabilité Gamma généralisée.

d'étoile laser auxiliaire qui représente un coût supplémentaire.

Les travaux proposés permettent d'identifier et exploiter les sources d'information disponibles et utiles à l'estimation de la phase de pré-compensation au pointage en avant. On illustre en figure A.2.4. le gain en ϵ-capacité apporté par les différentes méthodes développées, par rapport à la pré-compensation classique, représentée en noir, en condition de forte turbulence. Pour un rapport signal sur bruit (SNR) de 17 dB, correspondant au point de fonctionnement selon nos hypothèses sur le bilan de puissance, la ϵ-capacité est multipliée d'un facteur 8 à 14, selon la méthode utilisée. Nous avons aussi pu montrer que chacune de ces méthodes permet de relaxer la durée des entrelaceurs utilisés pour l'encodage du signal d'information, réduisant ainsi la complexité du système à bord du satellite.

Cette évaluation de la limite de transmission théorique a pu être complétée par une première évaluation de performance par simulation numérique d'une chaîne de transmission complète, avec codage et entrelacement des bits d'information. La réalisation de ces travaux s'est faite en collaboration avec la start-up MIMOPT. Cette simulation a permis de valider les tendances observées sur la capacité théorique.

Finalement, j'ai pu travailler durant cette thèse au **développement d'un modèle de canal statistique**. En effet, la connaissance de la statistique du signal reçu est essentielle pour optimiser les systèmes de télécommunication. J'ai pu montrer, en exploitant la méthode de réciprocité, que la statistique du lien montant pré-compensé, avec de forts résidus de phase, se distinguait de la statistique des canaux connus de la littérature (liens optiques en espace libre non corrigés ou liens descendants très bien corrigés). J'ai également pu montrer, en proposant une méthode originale de calcul analytique du flux couplé, que le signal considéré suit une loi Gamma généralisée, comme illustré en figure A.3.

A.4 Conclusion et perspectives

Pour établir un réseau internet satellitaire, il est essentiel de pouvoir communiquer du sol vers le satellite GEO à de très hauts débits. Dans cette thèse, nous avons pu montrer que, étant donné les contraintes de puissance du lien, la capacité du lien optique pre-compensé à l'état de l'art est limitée. Nous avons pu proposer 4 méthodes d'estimation de phase de pre-compensation, permettant de réduire les pertes de signal à bord du satellite, améliorant ainsi la capacité du canal optique sol-satellite. En effet, on observe une réduction de la puissance nécessaire, à capacité égale, jusqu'à 17 dB, en conditions de forte turbulence. Ainsi, l'optimisation du canal optique turbulent permet d'atteindre les débits requis pour ces liaisons (plusieurs Terabits par seconde), dans de nombreuses conditions de turbulence, tout en limitant la complexité du système à bord du satellite. Nous avons aussi pu montrer que ces méthodes peuvent s'appliquer aux liaisons montantes avec des satellites en orbite basse

(LEO), dont la géométrie est plus contraignante (angle de pointage en avant plus large). La possibilité de communiquer du sol vers un satellite LEO à de très hauts débits, permet d'envisager de nouvelles architectures de réseau internet satellitaire, plus optimisées. De plus, pour atteindre cette capacité théorique, une optimisation du système numérique est nécessaire. Nous avons également pu dans cette thèse, en utilisant l'approche réciproque, montrer que la statistique des pertes de signal induites par la turbulence atmosphérique du lien montant pré-compensé, suit une loi Gamma généralisée, dont les paramètres dépendent des conditions de turbulence, et de la qualité de la correction par optique adaptative. Lorsque les paramètres de cette loi seront développés, la connaissance de cet état du canal permettra d'optimiser le traitement numérique aux conditions atmosphériques rencontrées.

La suite naturelle de ces travaux est de démontrer expérimentalement l'efficacité des estimateurs de phase de pre-compensation. En effet, le calcul des estimateurs proposés repose sur la connaissance d'a priori statistiques de la turbulence. Plusieurs méthodes existent pour mesurer ces a priori. Il s'agira de démontrer la performance de ces nouvelles pre-compensations en utilisant les méthodes de métrologie de turbulence existantes. Il faudra aussi valider expérimentalement les modèles statistiques de pertes atmosphériques développés. Finalement, une fois que les paramètres du modèle statistique du canal pré-compensé seront développés, il faudra optimiser le traitement du signal d'information, afin d'atteindre la capacité théorique du canal.

Au-delà des retombées de ces travaux sur l'implémentation de réseaux internet satellitaires futurs, la maîtrise de la pré-compensation au pointage en avant ouvre la porte à de nouvelles applications telles que la dissémination de clés quantiques (QKD) pour des communications sécurisées utilisant de nouveaux protocoles basés sur des liens montant (twin-field) ou encore l'application à la désorbitation de débris spatiaux, ou le transferts de temps-fréquences, utilisés dans les systèmes de positionnement.

Bibliography

[1] Robert K Tyson. "Adaptive optics and ground-to-space laser communications". In: *Applied optics* 35.19 (1996), pp. 3640–3646.

[2] François Rigaut and Eric Gendron. "Laser guide star in adaptive optics : the tilt determination problem". In: *Astronomy and Astrophysics* 261 (1992), pp. 677–684.

[3] Roberto Biasi, Domenico Bonaccini Calia, Mauro Centrone, Martin Enderlein, Marco Faccini, Ollie J Farley, Daniele Gallieni, D Gooding, Pierre Haguenauer, Petr Janout, et al. "ALASCA: the ESA Laser Guide Star Adaptive Optics Optical Feeder Link demonstrator facility". In: *International Conference on Space Optics—ICSO 2022*. Vol. 12777. SPIE. 2023, pp. 2219–2236.

[4] Perrine Lognoné, Jean-Marc Conan, Ghaya Rekaya, and Nicolas Védrenne. "Phase estimation at the point-ahead angle for AO pre-compensated ground to GEO satellite telecoms". In: *Optics Express* 31.3 (2023), pp. 3441–3458.

[5] Daniel Romero Arrieta, Sylvain Almonacil, Jean-Marc Conan, Laurie Paillier, Eric Dutisseuil, Sébastien Bigo, Jérémie Renaudier, and Rajiv Boddeda. "Proof-of-Concept Real-Time Implementation of Interleavers for Optical Satellite Links". In: *Journal of Lightwave Technology* (2023).

[6] Jeffrey H Shapiro and Andrew L Puryear. "Reciprocity-enhanced optical communication through atmospheric turbulence—Part I: Reciprocity proofs and far-field power transfer optimization". In: *Journal of Optical Communications and Networking* 4.12 (2012), pp. 947–954.

[7] Clélia Robert, Jean-Marc Conan, Vincent Michau, Jean-Baptiste Renard, Claude Robert, and Francis Dalaudier. "Retrieving parameters of the anisotropic refractive index fluctuations spectrum in the stratosphere from balloon-borne observations of stellar scintillation". In: *J. Opt. Soc. Am. A* 25.2 (Feb. 2008), pp. 379–393. URL: http://opg.optica.org/josaa/abstract.cfm?URI=josaa-25-2-379.

[8] Jean-Marc Conan, Aurélie Montmerle-Bonnefois, Nicolas Védrenne, Caroline B Lim, Cyril Petit, Vincent Michau, Marie-Thérèse Velluet, Jean-François Sauvage, Serge Meimon, Clélia Robert, Joseph Montri, Francis Mendez, Philippe Perrault, Géraldine Artaud, and Bouchra Benammar. "Adaptive Optics for GEO-Feeder Links: from Performance Analysis via Reciprocity Based Models to Experimental Demonstration". In: *Workshop Communications and Observations through Atmospheric Turbulence: characterization and mitigation (COAT)*. 2019. URL: https://hal.archives-ouvertes.fr/hal-03206080.

[9] O. J. D. Farley, M. J. Townson, and J. Osborn. "FAST: Fourier domain adaptive optics simulation tool for bidirectional ground-space optical links through atmospheric turbulence". In: *Opt. Express* 30.13 (June 2022). URL: http://opg.optica.org/oe/abstract.cfm?URI=oe-30-13-23050.

[10] Matthew R Whiteley, Byron M Welsh, and Michael C Roggemann. "Optimal modal wave-front compensation for anisoplanatism in adaptive optics". In: *JOSA A* 15.8 (1998), pp. 2097–2106.

[11] ITU. *Global connectivity report 2022*. https://www.itu.int/itu-d/reports/statistics/2022/05/29/gcr-chapter-1/. 2022.

[12] Harald Hauschildt, Carlo Elia, Hermann Ludwig Moeller, Wael El-Dali, Tomas Navarro, Maria Guta, Silvia Mezzasoma, and Josep Perdigues. "HydRON: High throughput optical network". In: *2019 IEEE International Conference on Space Optical Systems and Applications (ICSOS)*. IEEE. 2019, pp. 1–6.

[13] TSFI. *Telecom sans frontiere website*. https://www.tsfi.org/fr. 2023.

[14] Verizon. *Monthly IP Latency Data*. https://www.verizon.com/business/terms/latency/. 2023.

[15] H. Kotake, Y. Abe, T. Fuse, and M. Toyoshima. "System architecture of adaptive optical satellite network for various communication services". In: *38th International Communications Satellite Systems Conference (ICSSC 2021)*. Vol. 2021. 2021, pp. 84–88.

[16] Alberto Carrasco-Casado and Ramon Mata-Calvo. "Space optical links for communication networks". In: *Springer Handbook of Optical Networks*. Springer, 2020, pp. 1057–1103.

[17] Guray Acar, Daniel Arapoglou, Emiliano Re, Angelo Altamura, Alberto Mengali, Wael El-Dali, Monica Politano, Christopher Vasko, Haraldt Hauschildt, Josep Perdigues, Vincenzo Schena, Luca Rodio, Alberto Pandolfi, Peter Schwaderer, Garima Pandey, Ian Petersen, Joern Streppel, and Klaus Schoenherr. "HydRON Vision: preparation towards a flight demonstration ". In: *International Conference on Space Optics — ICSO 2022*. Ed. by Kyriaki Minoglou, Nikos Karafolas, and Bruno Cugny. Vol. 12777. International Society for Optics and Photonics. SPIE, 2023, 127773W. URL: https://doi.org/10.1117/12.2690569.

[18] In Keun Son and Shiwen Mao. "A survey of free space optical networks". In: *Digital communications and networks* 3.2 (2017), pp. 67–77.

[19] Amar Mody and Eva Gonzalez. "An operator's view: The medium-term feasibility of an optical feeder link for VHTS". In: *2017 IEEE International Conference on Space Optical Systems and Applications (ICSOS)*. 2017, pp. 278–285.

[20] ESA. https://artes.esa.int/projects/qvfeed. 2017.

[21] ESA. https://artes.esa.int/projects/qvfeed-0. 2022.

[22] ESA. https://artes.esa.int/news/first-wband-transmission-space. 2021.

[23] ESA. https://artes.esa.int/projects/wcube. 2018.

[24] Jussi Säily, Janne Kuhno, Joel Flavio, Michel Schmidt, Eveline Greschitz, Karin Plimon, Laura Manoliu, Luis Cupido, et al. "First results from the W-CUBE mission: CubeSat-based characterization of wave propagation of W-band and Q-band signals". In: *1st Space Microwave Week*. ESA/ESTEC. 2023.

[25] Hamid Hemmati. *Near-earth laser communications*. Vol. 1. CRC press, 2020.

[26] Thomas Plank, Erich Leitgeb, Pirmin Pezzei, and Zabih Ghassemlooy. "Wavelength-selection for high data rate Free Space Optics (FSO) in next generation wireless communications". In: *2012 17th European Conference on Networks and Optical Communications*. 2012, pp. 1–5.

[27] Rajiv Boddeda, Daniel Romero Arrieta, Sylvain Almonacil, Jérémie Renaudier, and Sébastien Bigo. "Achievable Capacity of Geostationary-Ground Optical Links". In: *Journal of Lightwave Technology* (2023).

[28] Christian Fuchs, Sylvain Poulenard, Nicolas Perlot, Jerome Riedi, and Josep Perdigues. "Optimization and throughput estimation of optical ground networks for LEO-downlinks, GEO-feeder links and GEO-relays". In: *Free-Space Laser Communication and Atmospheric Propagation XXIX*. Vol. 10096. SPIE. 2017, pp. 298–307.

[29] Bouchra Benammar, Louis Pericart, Géraldine Artaud, and Frédéric Lacoste. "Optical Ground Network Diversity Analysis for Free Space Optical Communications". In: *2019 IEEE International Conference on Space Optical Systems and Applications (ICSOS)*. IEEE. 2019, pp. 1–6.

[30] Shkelzen Cakaj, Bexhet Kamo, Vladi Koliçi, and Olimpjon Shurdi. "The Range and Horizon Plane Simulation for Ground Stations of Low Earth Orbiting (LEO) Satellites." In: *Int. J. Commun. Netw. Syst. Sci.* 4.9 (2011), pp. 585–589.

[31] Ronald R Parenti. "Adaptive optics for astronomy". In: *Lincoln laboratory journal* 5.1 (1992), pp. 93–114.

[32] Gérard Maral, Michel Bousquet, and Zhili Sun. *Satellite communications systems: systems, techniques and technology*. John Wiley & Sons, 2020.

[33] Nicolas Védrenne, Cyril Petit, A. Montmerle-Bonnefois, C. B. Lim, J.-M. Conan, L. Paillier, M.-T. Velluet, K. Caillault, F. Gustave, A. Durecu, V. Michau, F. Cassaing, S. Meimon, and J. Montri. "Performance analysis of an adaptive optics based optical feeder link ground station". In: *International Conference on Space Optics — ICSO 2020*. Vol. SPIE 11852, 1185219. 2020. URL: https://doi.org/10.1117/12.2599232.

[34] Bernard J Klein and John J Degnan. "Optical antenna gain. 1: Transmitting antennas". In: *Applied optics* 13.9 (1974), pp. 2134–2141.

[35] John J Degnan and Bernard J Klein. "Optical antenna gain. 2: Receiving antennas". In: *Applied optics* 13.10 (1974), pp. 2397–2401.

[36] Francis Bennet, Kate Ferguson, Ken Grant, Ed Kruzins, Nicholas Rattenbury, and Sascha Schediwy. "An Australia/New Zealand optical communications ground station network for next generation satellite communications". In: *Free-Space Laser Communications XXXII*. Vol. 11272. SPIE. 2020, p. 1127202.

[37] Paolo Villoresi, Fabrizio Tamburini, Markus Aspelmeyer, Thomas Jennewein, Rupert Ursin, Claudio Pernechele, Giuseppe Bianco, Anton Zeilinger, and Cesare Barbieri. "Space-to-ground quantum communication using an optical ground station: a feasibility study". In: *Quantum Communications and Quantum Imaging II*. Vol. 5551. SPIE. 2004, pp. 113–120.

[38] Arnaud Le Kernec, Lucien Canuet, Anaëlle Maho, Michel Sotom, Daniel Matter, Laurent Francou, James Edmunds, Matthew Welch, Efstratios Kehayas, Nicolas Perlot, et al. "The H2020 VERTIGO project towards tbit/s optical feeder links". In: *International Conference on Space Optics—ICSO 2020*. Vol. 11852. SPIE. 2021, pp. 508–519.

[39] WT Roberts, D Antsos, A Croonquist, S Piazzolla, LC Roberts Jr, V Garkanian, T Trinh, MW Wright, R Rogalin, J Wu, et al. "Overview of ground station 1 of the NASA space communications and navigation program". In: *Free-Space Laser Communication and Atmospheric Propagation XXVIII*. Vol. 9739. SPIE. 2016, pp. 82–99.

[40] David J Israel, Bernard L Edwards, and John W Staren. "Laser Communications Relay Demonstration (LCRD) update and the path towards optical relay operations". In: *2017 IEEE Aerospace Conference*. IEEE. 2017, pp. 1–6.

[41] Robert E Lafon, Yingxin Bai, Armen Caroglanian, James Dailey, Nikki Desch, Howard Garon, Steve Hall, Ron Miller, Dan Paulson, Haleh Safavi, et al. "Current status of NASA's Low-Cost Optical Terminal (LCOT) at Goddard Space Flight Center". In: *Free-Space Laser Communications XXXV*. Vol. 12413. SPIE. 2023, pp. 238–254.

[42] Zoran Sodnik, Christoph Voland, Josep Perdigues, Edgar Fischer, Klaus Kudielka, and Reinhard Czichy. "Optical feeder-link between ESA's optical ground station and Alphasat". In: *International Conference on Space Optics—ICSO 2020*. Vol. 11852. SPIE. 2021, pp. 520–526.

[43] J Perdigues, Z Sodnik, H Hauschildt, P Sarasa, M Witting, P Biller, C Baumgaertel, K Saucke, C Rochow, D Troendle, et al. "ESA's OGS upgrades for EDRS: Development status". In: *2017 IEEE International Conference on Space Optical Systems and Applications (ICSOS)*. IEEE. 2017, pp. 89–98.

[44] Hideaki Kotake, Yuma Abe, Yasuhiro Takahashi, Takuya Okura, Tetsuharu Fuse, Yohei Sato, Takamasa Itahashi, Shiro Yamakawa, and Morio Toyoshima. "First experimental demonstration of optical feeder link by using the optical data relay satellite LUCAS". In: *International Conference on Space Optics—ICSO 2022*. Vol. 12777. SPIE. 2023, pp. 364–374.

[45] C Fuchs, F Moll, J Poliak, A Reeves, and C Schmidt. "Optical satellite links at DLR". In: *Free-Space Laser Communications XXXV*. Vol. 12413. SPIE. 2023, pp. 34–41.

[46] A Bonnefois, C Petit, JM Conan, A Durecu, F Gustave, C Lim, J Montri, L Paillier, P Perrault, MT Velluet, et al. "FEELINGS, ONERA's optical ground terminal for AO pre-compensated GEO feeder links demonstration". In: *International Conference on Space Optics—ICSO 2022*. Vol. 12777. SPIE. 2023, pp. 740–749.

[47] Sylvain Poulenard, Thomas Anfray, Michael Crosnier, Jean-Frédéric Chouteau, Jordane Thouras, Charles-Ugo Piat, Jean-Adrien Vernhes, Laurent Coret, Walid Atitallah, Alassane Dupuy, et al. "10 Gbauds digital optical link and analog link from/to geostationary satellite". In: *International Conference on Space Optics—ICSO 2022*. Vol. 12777. SPIE. 2023, pp. 384–397.

[48] Arnaud Le Kernec, Lucien Canuet, Anaëlle Maho, Michel Sotom, D Matter, and L Francou. "Optical feeder links for high throughput satellites and the H2020 VERTIGO project". In: *COAT-2019-workshop (Communications and Observations through Atmospheric Turbulence: characterization and mitigation)*. 2019.

[49] Ricardo Barrios, Svilen Dimitrov, Ramon Mata-Calvo, and Dirk Giggenbach. "Link budget assessment for GEO feeder links based on optical technology". In: *International Journal of Satellite Communications and Networking* 39.2 (2021), pp. 160–177.

[50] Ramon Mata Calvo, Dirk Giggenbach, Alessandro Le Pera, Juraj Poliak, Ricardo Barrios, and Svilen Dimitrov. "Optical feeder links for very high throughput satellites-System perspectives". In: *KA and Broadband communication conference*. 2015.

[51] Pham Tien Dat, Abdemoula Bekkali, Kamugisha Kazaura, Kazuhiko Wakamori, Toshiji Suzuki, Mitsuji Matsumoto, Takeshi Higashino, Katsutoshi Tsukamoto, and Shozo Komaki. "Studies on characterizing the transmission of RF signals over a turbulent FSO link". In: *Optics express* 17.10 (2009), pp. 7731–7743.

[52] Katsutoshi Tsukamoto, Takeshi Higashino, Takuya Nakamura, Koichi Takahashi, Yuji Aburakawa, Shozo Komaki, Kazuhiko Wakamori, Toshiji Suzuki, Kamugisha Kazaura, Alam Mohammad Shah, et al. "Development of radio on free space optics system for ubiquitous wireless". In: *PIERS online* 4.1 (2008), pp. 96–100.

[53] K Saucke, R Mahn, P Martin Pimentel, F Heine, R Mata-Calvo, J Surof, Ricardo Barrios, A Reeves, H Bischl, H Brandt, et al. "Three years of optical satellite to ground links with the T-AOGS: data transmission and characterization of atmospheric conditions". In: *International Conference on Space Optics—ICSO 2018*. Vol. 11180. SPIE. 2019, pp. 525–534.

[54] Bernie Edwards, Trisha Randazzo, Nidhin Babu, Kendall Murphy, Shane Albright, Nick Cummings, Javier Ocasio-Perez, William Potter, Russell Roder, Sharon A Zehner, et al. "Challenges, lessons learned, and methodologies from the LCRD optical communication system AI&T". In: *2022 IEEE International Conference on Space Optical Systems and Applications (ICSOS)*. IEEE. 2022, pp. 22–31.

[55] Paul Berceau, Stéphane Angibault, Adrien Barbet, Jean Claude Barthes, Damien Blattes, Nicolas de Guembecker, Raphael Fidanza, Emilie Gary, Vincent Lefftz, Thibault Marduel, et al. "Space optical instrument for GEO-Ground laser communications". In: *International Conference on Space Optics—ICSO 2022*. Vol. 12777. SPIE. 2023, pp. 1317–1327.

[56] John R Barry. "Low-density parity-check codes". In: *Georgia Institute of Technology* 5 (2001), pp. 1–20.

[57] Donald M Cornwell. "NASA's optical communications program for 2017 and beyond". In: *2017 IEEE International Conference on Space Optical Systems and Applications (ICSOS)*. IEEE. 2017, pp. 10–14.

[58] Géraldine Artaud, Jean-Frederic Chouteau, Lyonel Barthe, Benjamin Gadat, Thomas Anfray, Sylvain Poulenard, Alain Dominique Thomas, and Alain Quentel. "Design and validation of a new coding and synchronization layer for space optical communications". In: *International Conference on Space Optics—ICSO 2022*. Vol. 12777. SPIE. 2023, pp. 2055–2068.

[59] Zhen Qu and Ivan B Djordjevic. "On the probabilistic shaping and geometric shaping in optical communication systems". In: *IEEE Access* 7 (2019), pp. 21454–21464.

[60] VINCENT BILLAULT, SIMON LEVEQUE, ANAËLLE MAHO, MATTHEW WELCH, JÉRÔME BOURDERIONNET, ERIC LALLIER, MICHEL SOTOM, ARNAUD LE KERNEC, and ARNAUD BRIGNON. "Optical coherent combining of high power optical amplifiers for free space optical communications". In: (2023).

[61] Laurie Paillier. "Architecture de récepteur cohérent pour les liens optiques satellite-sol avec optique adaptative". PhD thesis. Institut polytechnique de Paris, 2020.

[62] Bob Chomycz. *Planning fiber optics networks*. McGraw-Hill Education, 2009.

[63] Afxendios Tychopoulos, Odysseas Koufopavlou, and Ioannis Tomkos. "FEC in optical communications-A tutorial overview on the evolution of architectures and the future prospects of outband and inband FEC for optical communications". In: *IEEE Circuits and Devices Magazine* 22.6 (2006), pp. 79–86.

[64] Bernard Roy, Sylvain Poulenard, Svilen Dimitrov, Ricardo Barrios, Dirk Giggenbach, Arnaud Le Kernec, and Michel Sotom. "Optical feeder links for high throughput satellites". In: *2015 IEEE International Conference on Space Optical Systems and Applications (ICSOS)*. IEEE. 2015, pp. 1–6.

[65] Andrey Nikolaevich Kolmogorov. "The local structure of turbulence in incompressible viscous fluid for very large Reynolds". In: *Numbers. In Dokl. Akad. Nauk SSSR* 30 (1941), p. 301.

[66] Alexander Mikhailovich Obukhov et al. "Structure of the temperature field in a turbulent flow". In: *Izv. Akad. Nauk SSSR, Ser. Geogr. Geofiz* 13.1 (1949), pp. 58–69.

[67] Stanley Corrsin. "On the spectrum of isotropic temperature fluctuations in an isotropic turbulence". In: *Journal of Applied Physics* 22.4 (1951), pp. 469–473.

[68] V. I. Tatarski, R. A. Silverman, and Nicholas Chako. "Wave Propagation in a Turbulent Medium". In: *Physics Today* 14.12 (Jan. 1961), p. 46.

[69] RE Hufnagel. "Variations of atmospheric turbulence. Digest of technical papers". In: *Topical meeting on optical propagation through turbulence, university of Colorado, Boulder, CO*. 1974.

[70] Frédéric Mahé. "Application d'un modèle atmosphérique à l'étude des fluctuations d'indice de réfraction dans la couche limite: influence de la scintillation sur l'analyse de front d'onde". PhD thesis. Nice, 2000.

[71] John L Green, Kenneth S Gage, and Thomas E Van Zandt. "Atmospheric measurements by VHF pulsed Doppler radar". In: *IEEE Transactions on Geoscience Electronics* 17.4 (1979), pp. 262–280.

[72] Gennaro H Crescenti. "A look back on two decades of Doppler sodar comparison studies". In: *Bulletin of the American Meteorological society* 78.4 (1997), pp. 651–674.

[73] Chloé Sauvage, Clélia Robert, Laurent M Mugnier, J-M Conan, J-M Cohard, K-L Nguyen, Mark Irvine, and J-P Lagouarde. "Near ground horizontal high resolution Cn2 profiling from Shack–Hartmann slopeand scintillation data". In: *Applied optics* 60.34 (2021), pp. 10499–10519.

[74] Arun K Majumdar. "Free-space laser communication performance in the atmospheric channel". In: *Journal of Optical and Fiber Communications Reports* 2.4 (2005), pp. 345–396.

[75] Robert E Hufnagel. "Propagation through atmospheric turbulence". In: *The Infrared Handbook* 6 (1978), pp. 1–56.

[76] George C Valley. "Isoplanatic degradation of tilt correction and short-term imaging systems". In: *Applied Optics* 19.4 (1980), pp. 574–577.

[77] Jack L Bufton. "Comparison of vertical profile turbulence structure with stellar observations". In: *Applied optics* 12.8 (1973), pp. 1785–1793.

[78] David L Fried. "Optical resolution through a randomly inhomogeneous medium for very long and very short exposures". In: *JOSA* 56.10 (1966), pp. 1372–1379.

[79] F Roddier, JM Gilli, and G Lund. "On the origin of speckle boiling and its effects in stellar speckle interferometry". In: *Journal of Optics* 13.5 (1982), p. 263.

[80] David L Fried. "Anisoplanatism in adaptive optics". In: *JOSA* 72.1 (1982), pp. 52–61.

[81] François Roddier. "V the effects of atmospheric turbulence in optical astronomy". In: *Progress in optics*. Vol. 19. Elsevier, 1981, pp. 281–376.

[82] Valerian Ilich Tatarski. *Wave propagation in a turbulent medium*. Courier Dover Publications, 1961.

[83] Valerian Ilitch Tatarskii. "The effects of the turbulent atmosphere on wave propagation". In: *Jerusalem: Israel Program for Scientific Translations, 1971* (1971).

[84] Robert W Lee and Jeffrey C Harp. "Weak scattering in random media, with applications to remote probing". In: *Proceedings of the IEEE* 57.4 (1969), pp. 375–406.

[85] Stanley M Flatté, Guang-Yu Wang, and Jan Martin. "Irradiance variance of optical waves through atmospheric turbulence by numerical simulation and comparison with experiment". In: *JOSA A* 10.11 (1993), pp. 2363–2370.

[86] Stanley M Flatté, Charles Bracher, and Guang-Yu Wang. "Probability-density functions of irradiance for waves in atmospheric turbulence calculated by numerical simulation". In: *JOSA A* 11.7 (1994), pp. 2080–2092.

[87] JM Martin and Stanley M Flatté. "Intensity images and statistics from numerical simulation of wave propagation in 3-D random media". In: *Applied Optics* 27.11 (1988), pp. 2111–2126.

[88] Nicolas Védrenne, JM Conan, MT Velluet, M Sechaud, M Toyoshima, H Takenaka, A Guérin, and F Lacoste. "Turbulence effects on bi-directional ground-to-satellite laser communication systems". In: *Proc. Int. Conf. Sp. Opt. Syst. Appl.* Vol. 12. 2012.

[89] Aurélie Montmerle-Bonnefois, Marie-Thérése Velluet, Mahawa Cissé, Caroline B Lim, Jean-Marc Conan, Cyril Petit, Jean-François Sauvage, Serge Meimon, Philippe Perrault, Joseph Montri, et al. "Feasibility demonstration of AO pre-compensation for GEO feeder links in a relevant environment". In: *Optics Express* 30.26 (2022), pp. 47179–47198.

[90] Geoffrey Ingram Taylor. "The spectrum of turbulence". In: *Proceedings of the Royal Society of London. Series A-Mathematical and Physical Sciences* 164.919 (1938), pp. 476–490.

[91] WP Brown. "Validity of the Rytov approximation in optical propagation calculations". In: *JOSA* 56.8 (1966), pp. 1045–1052.

[92] Ronald L Fante. "Electromagnetic beam propagation in turbulent media". In: *Proceedings of the IEEE* 63.12 (1975), pp. 1669–1692.

[93] Richard J Sasiela. *Electromagnetic wave propagation in turbulence: evaluation and application of Mellin transforms*. Vol. 18. Springer Science & Business Media, 2012.

[94] Joseph W Goodman. *Statistical optics*. John Wiley & Sons, 2015.

[95] David L Fried. "Aperture averaging of scintillation". In: *JOSA* 57.2 (1967), pp. 169–175.

[96] Frederic Mahé, Vincent Michau, Gerard Rousset, and Jean-Marc Conan. "Scintillation effects on wavefront sensing in the Rytov regime". In: *Propagation and Imaging through the Atmosphere IV*. Vol. SPIE 4125, 77-86. 2000. URL: https://doi.org/10.1117/12.409307.

[97] Robert J. Noll. "Zernike polynomials and atmospheric turbulence". In: *J. Opt. Soc. Am.* 66.3 (Mar. 1976), pp. 207–211. URL: http://opg.optica.org/abstract.cfm?URI=josa-66-3-207.

[98] Larry C Andrews, Ronald L Phillips, Richard J Sasiela, and Ronald R Parenti. "Strehl ratio and scintillation theory for uplink Gaussian-beam waves: beam wander effects". In: *Optical Engineering* 45.7 (2006), pp. 076001–076001.

[99] Noah Schwartz. "Précompensation des effets de la turbulence par optique adaptative: application aux liaisons optiques en espace libre". PhD thesis. Université Nice Sophia Antipolis, 2009.

[100] Adrien-Richard Camboulives. "Atmospheric turbulence effects mitigation for a ground to geostationary satellite optical link : impact on the ground terminal architecture". PhD thesis. Université Paris Saclay, Dec. 2017. URL: https://tel.archives-ouvertes.fr/tel-02185130.

[101] LC Andrews, RL Phillips, and PT Yu. "Optical scintillations and fade statistics for a satellite-communication system". In: *applied optics* 34.33 (1995), pp. 7742–7751.

[102] Kamran Kiasaleh. "On the probability density function of signal intensity in free-space optical communications systems impaired by pointing jitter and turbulence". In: *Optical Engineering* 33.11 (1994), pp. 3748–3757.

[103] Gary J Baker. "Gaussian beam weak scintillation: low-order turbulence effects and applicability of the Rytov method". In: *JOSA A* 23.2 (2006), pp. 395–417.

[104] Federico Dios, Juan Antonio Rubio, Alejandro Rodriguez, and Adolfo Comeron. "Scintillation and beam-wander analysis in an optical ground station-satellite uplink". In: *Applied optics* 43.19 (2004), pp. 3866–3873.

[105] A-R Camboulives, M-T Velluet, S Poulenard, L Saint-Antonin, and V Michau. "Statistical and temporal irradiance fluctuations modeling for a ground-to-geostationary satellite optical link". In: *Applied optics* 57.4 (2018), pp. 709–721.

[106] MA Al-Habash, Larry C Andrews, and Ronald L Phillips. "Mathematical model for the irradiance probability density function of a laser beam propagating through turbulent media". In: *Optical engineering* 40.8 (2001), pp. 1554–1562.

[107] Romain Fétick. "Traitement d'image en optique adaptative: estimation paramétrique de la réponse impulsionnelle et déconvolution". PhD thesis. Aix Marseille Université, 2020.

[108] Alix Yan, Laurent M Mugnier, Jean-François Giovannelli, Romain Fétick, and Cyril Petit. "Extending AMIRAL's blind deconvolution of adaptive optics corrected images with Markov chain Monte Carlo methods". In: *Adaptive Optics Systems VIII*. Vol. 12185. SPIE. 2022, pp. 1190–1200.

[109] Thierry Fusco and Jean-Marc Conan. "On-and off-axis statistical behavior of adaptive-optics-corrected short-exposure Strehl ratio". In: *JOSA A* 21.7 (2004), pp. 1277–1289.

[110] Roland V Shack. "Production and use of a lenticular Hartmann screen". In: *Spring Meeting of Optical Society of America, 1971*. Vol. 656. 1971.

[111] Gerard Rousset. "Wave-front sensors". In: *Adaptive optics in astronomy* 1 (1999), p. 91.

[112] Roberto Ragazzoni. "Pupil plane wavefront sensing with an oscillating prism". In: *Journal of modern optics* 43.2 (1996), pp. 289–293.

[113] Simone Esposito, Orla Feeney, and Armando Riccardi. "Laboratory test of a pyramid wavefront sensor". In: *Adaptive Optical Systems Technology*. Vol. 4007. SPIE. 2000, pp. 416–422.

[114] P-Y Madec. "Overview of deformable mirror technologies for adaptive optics and astronomy". In: *Adaptive Optics Systems III*. Vol. 8447. SPIE. 2012, pp. 22–39.

[115] Brent L Ellerbroek, Charles Van Loan, Nikos P Pitsianis, and Robert J Plemmons. "Optimizing closed-loop adaptive-optics performance with use of multiple control bandwidths". In: *JOSA A* 11.11 (1994), pp. 2871–2886.

[116] Lucien Canuet, Nicolas Védrenne, Jean-Marc Conan, Cyril Petit, Geraldine Artaud, Angelique Rissons, and Jerome Lacan. "Statistical properties of single-mode fiber coupling of satellite-to-ground laser links partially corrected by adaptive optics". In: *J. Opt. Soc. Am. A* 35.1 (Jan. 2018), pp. 148–162. URL: https://opg.optica.org/josaa/abstract.cfm?URI=josaa-35-1-148.

[117] Emile Klotz, Sidonie Lefebvre, Nicolas Vedrenne, Christian Musso, Sylvain Poulenard, and Thierry Fusco. "Assessment of adaptive optics-corrected optical links statistics from integrated turbulence parameters through a Gaussian process metamodel". In: *International Journal of Satellite Communications and Networking* (2023).

[118] Jeffrey H Shapiro. "Reciprocity of the turbulent atmosphere". In: *JOSA* 61.4 (1971), pp. 492–495.

[119] J Stone, PH Hu, SP Mills, and S Ma. "Anisoplanatic effects in finite-aperture optical systems". In: *JOSA A* 11.1 (1994), pp. 347–357.

[120] F. Chassat, G. Rousset, and J. Primot. "Theoretical And Experimental Evaluation Of Isoplanatic Patch Size For Adaptive Optics". In: *Active Telescope Systems*. Vol. SPIE 1114, 14-22. 1989. URL: https://doi.org/10.1117/12.960805.

[121] T Fusco, J-M Conan, LM Mugnier, V Michau, and G Rousset. "Characterization of adaptive optics point spread function for anisoplanatic imaging. Application to stellar field deconvolution". In: *Astronomy and Astrophysics Supplement Series* 142.1 (2000), pp. 149–156.

[122] David L Fried, Glenn A Tyler, and OPTICAL SCIENCES CO PLACENTIA CA. "Strategic Laser Communications Uplink Analysis". In: *Interim Report* (1981).

[123] Robert K Tyson. "Bit-error rate for free-space adaptive optics laser communications". In: *JOSA A* 19.4 (2002), pp. 753–758.

[124] Noelia Martinez. "Atmospheric Pre-Compensation of Ground-to-Space Communications with Adaptive Optics: Past, Present and Future—A Field Review". In: *Photonics*. Vol. 10. 7. MDPI. 2023, p. 858.

[125] Nina Leonhard, René Berlich, Stefano Minardi, Alexander Barth, Steffen Mauch, Jacopo Mocci, Matthias Goy, Michael Appelfelder, Erik Beckert, and Claudia Reinlein. "Real-time adaptive optics testbed to investigate point-ahead angle in precompensation of Earth-to-GEO optical communication". In: *Optics express* 24.12 (2016), pp. 13157–13172.

[126] Aoife Brady, René Berlich, Nina Leonhard, Teresa Kopf, Paul Böttner, Ramona Eberhardt, and Claudia Reinlein. "Experimental validation of phase-only pre-compensation over 494 m free-space propagation". In: *Optics letters* 42.14 (2017), pp. 2679–2682.

[127] Aoife Brady, Conrad Rössler, Nina Leonhard, Marlies Gier, Paul Böttner, Ramona Eberhardt, Andreas Tünnermann, and Claudia Reinlein. "Validation of precompensation under point-ahead-angle in a 1 km free-space propagation experiment". In: *Optics Express* 27.13 (2019), pp. 17840–17850.

[128] Rudolf Saathof, Remco den Breeje, Wimar Klop, Niek Doelman, Thijs Moens, Michael Gruber, Tjeerd Russchenberg, Federico Pettazzi, Jet Human, Ramon Mata Calvo, Juraj Poliak, Ricardo Barrios, Mathias Richerzhagen, and Ivan Ferrario. "Pre-correction adaptive optics performance for a 10 km laser link". In: *Free-Space Laser Communications XXXI*. Vol. SPIE 10910, 109101H. 2019. URL: https://doi.org/10.1117/12.2506849.

[129] A Montmerle Bonnefois, J-M Conan, Cyril Petit, CB Lim, V Michau, S Meimon, P Perrault, F Mendez, B Fleury, J Montri, et al. "Adaptive optics pre-compensation for GEO feeder links: the FEEDELIO experiment". In: *International Conference on Space Optics—ICSO 2018*. Vol. 11180. SPIE. 2019, pp. 889–896.

[130] Nicolas Védrenne, Jean-Marc Conan, Aurélie Bonnefois, Cyril Petit, Marie-Thérèse Velluet, and Vincent Michau. "Adaptive optics pre-compensation for GEO feeder links: Towards an experimental demonstration". In: *2017 IEEE International Conference on Space Optical Systems and Applications (ICSOS)*. IEEE. 2017, pp. 77–81.

[131] Don M Boroson, Joseph J Scozzafava, Daniel V Murphy, Bryan S Robinson, and MIT Lincoln. "The lunar laser communications demonstration (LLCD)". In: *2009 Third IEEE International Conference on Space Mission Challenges for Information Technology*. IEEE. 2009, pp. 23–28.

[132] Jean-Marc Conan and Aurélie Montmerle-Bonnefois. *Turbulence mitigation strategies for Ground-GEO uplinks: adaptive optics pre-compensation on single aperture versus multi-aperture diversity*. COAT 2023 workshop presentation, Durham. 2023.

[133] Christian Fuchs, Dirk Giggenbach, Ramon Mata Calvo, and Werner Rosenkranz. "Transmitter diversity with phase-division applied to optical geo feeder links". In: *IEEE Photonics Technology Letters* 33.11 (2021), pp. 541–544.

[134] C Willem Korevaar, Rudolf Saathof, Tara van Abkoude, and Niek Doelman. "Latency-constrained fading mitigation for coherent optical feeder links based on space-time-frequency coding". In: *International Conference on Space Optics—ICSO 2022*. Vol. 12777. SPIE. 2023, pp. 2069–2080.

[135] Deborah E Tjin-Tham-Sjin, Cynthia Y Young, and Larry C Andrews. "Temporal broadening of ultrashort space-time Gaussian pulses with applications in laser satellite communication". In: *Free-Space Laser Communication Technologies X*. Vol. 3266. SPIE. 1998, pp. 231–240.

[136] Larry C Andrews and Ronald L Phillips. "Laser beam propagation through random media". In: *Laser Beam Propagation Through Random Media: Second Edition* (2005).

[137] Kerry Mudge, Bradley Clare, Elisa Jager, Vladimir Devrelis, Francis Bennet, Michael Copeland, Nicholas Herrald, Ian Price, Gottfried Lechner, Jeewani Kodithuwakkuge, Joseph Magarelli, Dharmapriya Bandara, Christopher Peck, Monique Hollick, Paul Alvino, Peter Camp-Smith, Barbara Szumylo, Agam Raj, and Kenneth Grant. "DSTG Laser Satellite Communications -Current Activities and Future Outlook". In: *IEEE International Conference on Space Optical Systems and Applications (ICSOS)*. 2022, pp. 17–21.

[138] Cyril Petit, Aurélie Montmerle-Bonnefois, Jean-Marc Conan, Anne Durecu, François Gustave, Caroline Lim, Joseph Montri, Laurie Paillier, Philippe Perrault, Marie-Thérèse Velluet, Jean-Baptiste Volatier, and Nicolas Védrenne. "FEELINGS : the ONERA optical ground station for Geo Feeder links demonstration". In: *IEEE International Conference on Space Optical Systems and Applications (ICSOS)*. 2022, pp. 255–260.

[139] Dimitar Kolev, Koichi Shiratama, Alberto Carrasco-Casado, Yoshihiko Saito, Yasushi Munemasa, Junichi Nakazono, Phuc V. Trinh, Hideaki Kotake, Hiroo Kunimori, Toshihiro Kubooka, Tetsuharu Fuse, and Morio Toyoshima. "Status Update on Laser Communication Activities in NICT". In: *IEEE International Conference on Space Optical Systems and Applications (ICSOS)*. 2022, pp. 36–39.

[140] Alberto Mengali, Charilaos I Kourogiorgas, Nikolaos K Lyras, Bhavani Shankar Mysore Rama Rao, Farbod Kayhan, Athanasios D Panagopoulos, Thomas Bäumer, and Konstantinos Liolis. "Ground-to-GEO optical feeder links for very high throughput satellite networks: Accent on diversity techniques". In: *International Journal of Satellite Communications and Networking* (2020).

[141] Zoran Sodnik, Josep Perdigues Armengol, Reinhard H. Czichy, and Rolf Meyer. "Adaptive optics and ESA's optical ground station". In: *Free-Space Laser Communications IX*. Vol. SPIE 7464, 746406. 2009. URL: https://doi.org/10.1117/12.826163.

[142] Edgar Fischer, Thomas Berkefeld, Mikael Feriencik, Marco Feriencik, Volker Kaltenbach, Dirk Soltau, Bernhard Wandernoth, Reinhard Czichy, Jens Kunde, Karen Saucke, Frank Heine, Mark Gregory, Christoph Seiter, and Hartmut Kampfner. "Development, integration and test of a transportable adaptive optical ground station". In: *IEEE International Conference on Space Optical Systems and Applications (ICSOS)*. 2015, pp. 1–6.

[143] J Osborn, R W Wilson, M Sarazin, T Butterley, A Chacón, F Derie, O J D Farley, X Haubois, D Laidlaw, M LeLouarn, E Masciadri, J Milli, J Navarrete, and M J Townson. "Optical turbulence profiling with Stereo-SCIDAR for VLT and ELT". In: *Monthly Notices of the Royal Astronomical Society* 478.1 (Apr. 2018). eprint: https://academic.oup.com/mnras/article-pdf/478/1/825/25698645/sty1070.pdf. URL: https://doi.org/10.1093/mnras/sty1070.

[144] Detlev Sprung and Erik Sucher. "Characterization of optical turbulence at the solar observatory at the Mount Teide, Tenerife". In: *Remote Sensing of Clouds and the Atmosphere XVIII; and Optics in Atmospheric Propagation and Adaptive Systems XVI*. Vol. SPIE 8890, 889015. 2013. URL: https://doi.org/10.1117/12.2032744.

[145] Aurélie Montmerle-Bonnefois, Marie-Thérèse Velluet, Mahawa Cissé, Caroline B. Lim, Jean-Marc Conan, Cyril Petit, Jean-François Sauvage, Serge Meimon, Philippe Perrault, Francis Mendez, Bruno Fleury, Joseph Montri, Vincent Michau, and Nicolas Védrenne. "First feasibility demonstration of AO pre-compensation for GEO feeder links in a relevant environment". In: *Opt. Express* (2022). to be published.

[146] RF Lutomirski and HT Yura. "Propagation of a finite optical beam in an inhomogeneous medium". In: *Applied Optics* 10.7 (1971), pp. 1652–1658.

[147] Jeffrey H. Shapiro and Andrew L. Puryear. "Reciprocity-Enhanced Optical Communication Through Atmospheric Turbulence — Part I: Reciprocity Proofs and Far-Field Power Transfer Optimization". In: *J. Opt. Commun. Netw.* 4.12 (Dec. 2012), pp. 947–954. URL: http://opg.optica.org/jocn/abstract.cfm?URI=jocn-4-12-947.

[148] Andrew L Puryear, Jeffrey H Shapiro, and Ronald R Parenti. "Reciprocity-enhanced optical communication through atmospheric turbulence—Part II: Communication architectures and performance". In: *Journal of Optical Communications and Networking* 5.8 (2013), pp. 888–900.

[149] Clélia Robert, Jean-Marc Conan, and Peter Wolf. "Impact of turbulence on high-precision ground-satellite frequency transfer with two-way coherent optical links". In: *Phys. Rev. A* 93 (3 Mar. 2016), p. 033860. URL: https://link.aps.org/doi/10.1103/PhysRevA.93.033860.

[150] Perrine Lognoné, Aurélie Montmerle Bonnefois, Jean-Marc Conan, Laurie Paillier, Cyril Petit, Caroline B Lim, Serge Meimon, Joseph Montri, Jean-François Sauvage, and Nicolas Védrenne. "New results from the 2021 feedelio experiment-a focus on reciprocity". In: *2022 IEEE International Conference on Space Optical Systems and Applications (ICSOS)*. IEEE. 2022, pp. 261–266.

[151] Dirk Giggenbach, William Cowley, Ken Grant, and Nicolas Perlot. "Experimental verification of the limits of optical channel intensity reciprocity". In: *Appl. Opt.* 51.16 (June 2012), pp. 3145–3152. URL: http://opg.optica.org/ao/abstract.cfm?URI=ao-51-16-3145.

[152] Ronald R. Parenti, Jeffrey M. Roth, Jeffrey H. Shapiro, Frederick G. Walther, and Joseph A. Greco. "Experimental observations of channel reciprocity in single-mode free-space optical links". In: *Opt. Express* 20.19 (Oct. 2012), pp. 21635–21644. URL: http://opg.optica.org/oe/abstract.cfm?URI=oe-20-19-21635.

[153] Swaminathan Parthasarathy, Dirk Giggenbach, Christian Fuchs, Ramon Mata-Calvo, Ricardo Barrios, and Andreas Kirstaedter. "Verification of Channel Reciprocity in Long-Range Turbulent FSO Links". In: *Photonic Networks; 19th ITG-Symposium*. 2018, pp. 1–6.

[154] Nicolas Védrenne, Jean-Marc Conan, Aurélie Bonnefois, Cyril Petit, Marie-Thérèse Velluet, and Vincent Michau. "Adaptive optics pre-compensation for GEO feeder links: Towards an experimental demonstration". In: *IEEE International Conference on Space Optical Systems and Applications (ICSOS)*. 2017, pp. 79–81.

[155] A. Montmerle Bonnefois, J. -M. Conan, C. Petit, C. B. Lim, V. Michau, S. Meimon, P. Perrault, F. Mendez, B. Fleury, J. Montri, and N. Védrenne. "Adaptive optics pre-compensation for GEO feeder links: the FEEDELIO experiment". In: *International Conference on Space Optics — ICSO 2018*. Ed. by Zoran Sodnik, Nikos Karafolas, and Bruno Cugny. Vol. 11180. International Society for Optics and Photonics. SPIE, 2019, pp. 889–896. URL: https://doi.org/10.1117/12.2536003.

[156] Karl Pearson. "Note on Regression and Inheritance in the Case of Two Parents". In: *Proceedings of the Royal Society of London Series I* 58 (Jan. 1895), pp. 240–242.

[157] Francois Chassat. "Optical propagation through atmospheric turbulence. Model analysis of anisoplanatism and application to adaptive optics". PhD thesis. Office National d'Etudes et de Recherche Aerospatiale, France, Nov. 1992.

[158] N. Védrenne, J.-M. Conan, C. Petit, and V. Michau. "Adaptive optics for high data rate satellite to ground laser link". In: *Free-Space Laser Communication and Atmospheric Propagation XXVIII*. Vol. SPIE 9739, 97390E. 2016. URL: https://doi.org/10.1117/12.2218213.

[159] Perrine Lognoné, Jean-Marc Conan, Laurie Paillier, Nicolas Védrenne, and Ghaya Rekaya. "Channel model of a ground to satellite optical link pre-compensated by adaptive optics". In: *Signal Processing in Photonic Communications*. Optica Publishing Group. 2022, SpTu3G–3.

[160] Nicolas Perlot. "Turbulence-induced fading probability in coherent optical communication through the atmosphere". In: *Applied optics* 46.29 (2007).

[161] Frédéric Mahé. "Application d'un modèle atmosphérique à l'étude des fluctuations d'indice de réfraction dans la couche limite : influence de la scintillation sur l'analyse de front d'onde". PhD thesis. 2000. URL: http://www.theses.fr/2000NICE5404.

[162] Richard J Sasiela. "Basic Equations for Wave Propagation in Turbulence". In: *Electromagnetic Wave Propagation in Turbulence*. Springer, 1994, pp. 19–46.

[163] Jean-Marc Conan. "Etude de la correction partielle en optique adaptative". PhD thesis. Paris 11, 1994. URL: http://www.theses.fr/1994PA112450.

[164] F. Roddier. *Adaptive Optics in Astronomy*. Cambridge University Press, 1999.

[165] Lucien Canuet. "Fiabilisation des transmissions optiques satellite-sol". 2018ESAE0005. PhD thesis. 2018. URL: http://www.theses.fr/2018ESAE0005/document.

[166] Robert K. Tyson. "Adaptive optics and ground-to-space laser communications". In: *Appl. Opt.* 35.19 (1996), pp. 3640–3646. URL: http://opg.optica.org/ao/abstract.cfm?URI=ao-35-19-3640.

[167] Renaud Foy, Michel Tallon, Herbert W Friedman, Andre Baranne, Francois Biraben, Gilbert Grynberg, Miska Le Louarn, Alain Denis Petit, Jean-Marc Weulersse, Arnold Migus, et al. "Polychromatic guide star". In: *High-Power Laser Ablation*. Vol. 3343. SPIE. 1998, pp. 194–204.

[168] S Esposito, R Ragazzoni, A Riccardi, Créidhe O'Sullivan, N Ageorges, M Redfern, and R Davies. "Absolute tilt from a laser guide star: a first experiment". In: *Experimental Astronomy* 10 (2000), pp. 135–145.

[169] Roberto Ragazzoni. "Propagation delay of a laser beacon as a tool to retrieve absolute tilt measurements". In: *The Astrophysical Journal* 465.1 (1996), p. L73.

[170] Noelia Martinez and Luis Fernando Rodriguez Ramos. "The use of sodium layer density anisotropies to fully measure the atmospheric turbulence, including tip-tilt, focus, and higher order aberrations". In: *Adaptive Optics Systems VII*. Vol. 11448. SPIE. 2020, pp. 446–455.

[171] James Osborn, Matthew J. Townson, Ollie J. D. Farley, Andrew Reeves, and Ramon Mata Calvo. "Adaptive Optics pre-compensated laser uplink to LEO and GEO". In: *Opt. Express* 29.4 (Feb. 2021), pp. 6113–6132. URL: http://opg.optica.org/oe/abstract.cfm?URI=oe-29-4-6113.

[172] Steven M Kay. *Fundamentals of statistical signal processing: estimation theory*. Prentice-Hall, Inc., 1993.

[173] Thierry Fusco, Jean-Marc Conan, Gérard Rousset, Laurent Marc Mugnier, and Vincent Michau. "Optimal wave-front reconstruction strategies for multiconjugate adaptive optics". In: *JOSA A* 18.10 (2001), pp. 2527–2538.

[174] Benoit Neichel, Thierry Fusco, and Jean-Marc Conan. "Tomographic reconstruction for wide-field adaptive optics systems: Fourier domain analysis and fundamental limitations". In: *JOSA A* 26.1 (2009), pp. 219–235.

[175] Lèonard Prengère, Caroline Kulcsár, and Henri-François Raynaud. "Zonal-based high-performance control in adaptive optics systems with application to astronomy and satellite tracking". In: *JOSA A* 37.7 (2020), pp. 1083–1099.

[176] Matthew Raymond Whiteley. *Optimal atmospheric compensation for anisoplanatism in adaptive-optical systems*. Air Force Institute of Technology, 1998.

[177] Matthew R Whiteley, Byron M Welsh, and Michael C Roggemann. "Incorporating higher-order modal measurements in tilt estimation: natural and laser guide star applications". In: *Applied optics* 37.36 (1998), pp. 8287–8296.

[178] Fabrice Vidal, Eric Gendron, and Gérard Rousset. "Tomography approach for multi-object adaptive optics". In: *JOSA A* 27.11 (2010), A253–A264.

[179] Jean-Marc Conan, Cyril Petit, Pablo Robles, and Perrine Lognoné. *Turbulence temporal prediction performance assessment for adaptive optics: application to observation of, and space-ground optical links with, LEO satellites*. 2023.

[180] Matthew R. Whiteley, Byron M. Welsh, and Michael C. Roggemann. "Optimal modal wave-front compensation for anisoplanatism in adaptive optics". In: *J. Opt. Soc. Am. A* 15.8 (Aug. 1998). URL: http://www.osapublishing.org/josaa/abstract.cfm?URI=josaa-15-8-2097.

[181] Aziz Ziad. "Review of the outer scale of the atmospheric turbulence". In: *Adaptive Optics Systems V*. Vol. SPIE 9909, 99091K. 2016. URL: https://doi.org/10.1117/12.2231375.

[182] Pablo Robles, Cyril Petit, Jean-Marc Conan, Bouchra Benammar, and Benoit Neichel. "Predictive adaptive optics for satellite tracking applications: optical communications and satellite observation". In: *Adaptive Optics Systems VIII*. Vol. 12185. SPIE. 2022, pp. 917–931.

[183] David L Fried. "Varieties of isoplanatism". In: *Imaging through the Atmosphere*. Vol. 75. SPIE. 1976, pp. 20–29.

[184] Richard J Sasiela. "Strehl ratios with various types of anisoplanatism". In: *JOSA A* 9.8 (1992), pp. 1398–1405.

[185] Pablo Robles. "Adaptive Optics for LEO-to-Ground Optical Communication: Modeling, Optimization, and Experiment". PhD thesis. Aix Marseille Université, 2023.

[186] Shane Walsh and Sascha Schediwy. "Adaptive optics LEO uplink pre-compensation with finite spatial modes". In: *Optics Letters* 48.4 (2023), pp. 880–883.

[187] Sabino Piazzolla, William T Roberts, Joseph Kovalik, Michael Peng, Vachik Garkanian, Christine Chen, William Buehlman, Mark Brewer, Gerardo Ortiz, Kittrin Matthews, et al. "Ground station for terabyte infrared delivery (TBIRD)". In: *Free-Space Laser Communications XXXV*. Vol. 12413. SPIE. 2023, pp. 280–295.

[188] Curt M Schieler, Kathleen M Riesing, Andrew J Horvath, Bryan C Bilyeu, Jesse S Chang, Ajay S Garg, Jade P Wang, and Bryan S Robinson. "200 Gbps TBIRD CubeSat downlink: pre-flight test results". In: *Free-Space Laser Communications XXXIV*. Vol. 11993. SPIE. 2022, pp. 200–206.

[189] Dirk Giggenbach, Marcus T Knopp, and Christian Fuchs. "Link budget calculation in optical LEO satellite downlinks with on/off-keying and large signal divergence: A simplified methodology". In: *International Journal of Satellite Communications and Networking* (2023).

[190] Lily Westerby-Griffin, James Osborn, Ollie JD Farley, Ryan Griffiths, and Gordon D Love. "Atmospheric optical turbulence measurements at varying elevation angles". In: *Free-Space Laser Communications XXXV*. Vol. 12413. SPIE. 2023, pp. 412–414.

[191] Perrine Lognoné, Jean-Marc Conan, Ghaya Rekaya, Laurie Paillier, and Nicolas Védrenne. "Two-aperture measurements for GEO-feeder adaptive optics pre-compensation optimization". In: *Optics Letters* 48.17 (2023), pp. 4550–4553.

[192] Naruhisa Takato and Ichirou Yamaguchi. "Spatial correlation of Zernike phase-expansion coefficients for atmospheric turbulence with finite outer scale". In: *JOSA A* 12.5 (1995), pp. 958–963.

[193] Matthew R Whiteley, Michael C Roggemann, and Byron M Welsh. "Temporal properties of the Zernike expansion coefficients of turbulence-induced phase aberrations for aperture and source motion". In: *JOSA A* 15.4 (1998), pp. 993–1005.

[194] Matthew R Whiteley, Byron M Welsh, and Michael C Roggemann. "Effect of modal atmospheric compensation on angular anisoplanatism in optical interferometric imaging". In: *Adaptive Optical System Technologies*. Vol. 3353. SPIE. 1998, pp. 177–188.

[195] M Tallon and R Foy. "Adaptive telescope with laser probe-Isoplanatism and cone effect". In: *Astronomy and Astrophysics (ISSN 0004-6361), vol. 235, no. 1-2, Aug. 1990, p. 549-557.* 235 (1990), pp. 549–557.

[196] Roberto Ragazzoni, Enrico Marchetti, and Gianpaolo Valente. "Adaptive-optics corrections available for the whole sky". In: *Nature* 403.6765 (2000), pp. 54–56.

[197] Thierry Fusco, Jean-Marc Conan, Gérard Rousset, Laurent Marc Mugnier, and Vincent Michau. "Optimal wave-front reconstruction strategies for multiconjugate adaptive optics". In: *J. Opt. Soc. Am. A* 18.10 (Oct. 2001), pp. 2527–2538. URL: https://opg.optica.org/josaa/abstract.cfm?URI=josaa-18-10-2527.

[198] Nicolas Védrenne, Vincent Michau, Clélia Robert, and Jean-Marc Conan. "C n 2 profile measurement from Shack-Hartmann data". In: *Optics letters* 32.18 (2007), pp. 2659–2661.

[199] Anjitha Viswanath, Virander Kumar Jain, and Subrat Kar. "Reduction in transmitter power requirement for earth-to-satellite and satellite-to-earth free space optical links with spatial diversity". In: *Optical and Quantum Electronics* 50 (2018), pp. 1–20.

[200] Juraj Poliak, Dirk Giggenbach, Florian Moll, Fabian Rein, Christian Fuchs, and Ramon Mata Calvo. "Terabit-throughput GEO satellite optical feeder link testbed". In: *2015 13th International Conference on Telecommunications (ConTEL)*. IEEE. 2015, pp. 1–5.

[201] Jing Ma, Kangning Li, Liying Tan, Siyuan Yu, and Yubin Cao. "Performance analysis of satellite-to-ground downlink coherent optical communications with spatial diversity over Gamma–Gamma atmospheric turbulence". In: *Applied optics* 54.25 (2015), pp. 7575–7585.

[202] Aniceto Belmonte and Joseph M Kahn. "Capacity of coherent free-space optical links using diversity-combining techniques". In: *Optics express* 17.15 (2009), pp. 12601–12611.

[203] Nicolas Perlot, Peter Hanne, Abraham Johst, Marcel Rothe, Bill Antonio Bernhardt, Anagnostis Paraskevopoulos, and Ronald Freund. "18km bidirectional free-space optical link with multi-aperture antenna and DWDM SFP+ transceivers (VERTIGO project)". In: *Free-Space Laser Communications XXXV*. Vol. 12413. SPIE. 2023, pp. 255–261.

[204] Ramon Mata Calvo, Peter Becker, Dirk Giggenbach, Florian Moll, Malte Schwarzer, Martin Hinz, and Zoran Sodnik. "Transmitter diversity verification on ARTEMIS geostationary satellite". In: *Free-Space Laser Communication and Atmospheric Propagation XXVI*. Vol. 8971. SPIE. 2014, pp. 24–37.

[205] Adolfo Comeron, Federico Dios, Alejandro Rodriguez, Juan Antonio Rubio, Marcos Reyes, and Angel Alonso. "Modeling of power fluctuations induced by refractive turbulence in a multiple-beam ground-to-satellite optical uplink". In: *Free-Space Laser Communications V*. Vol. 5892. SPIE. 2005, pp. 196–205.

[206] Don M Boroson, Bryan S Robinson, Daniel V Murphy, Dennis A Burianek, Farzana Khatri, Joseph M Kovalik, Zoran Sodnik, and Donald M Cornwell. "Overview and results of the lunar laser communication demonstration". In: *Free-Space Laser Communication and Atmospheric Propagation XXVI*. Vol. 8971. SPIE. 2014, pp. 213–223.

[207] Laird A. Thompson. "Rayleigh laser guide stars for extremely large telescopes". In: *Adaptive Optical System Technologies II*. Ed. by Peter L. Wizinowich and Domenico Bonaccini. Vol. 4839. International Society for Optics and Photonics. SPIE, 2003, pp. 1175–1181. URL: https://doi.org/10.1117/12.459066.

[208] Laird A. Thompson and Scott W. Teare. "Rayleigh Laser Guide Star Systems: Application to the University of Illinois Seeing Improvement System". In: *Publications of the Astronomical Society of the Pacific* 114.799 (Aug. 2002), p. 1029. URL: https://dx.doi.org/10.1086/342043.

[209] D. Bonaccini Calia, Y. Feng, W. Hackenberg, R. Holzlöhner, L. Taylor, and S. Lewis. "Laser Development for Sodium Laser Guide Stars at ESO". In: *The Messenger* 139 (Mar. 2010), pp. 12–19.

[210] Roberto Ragazzoni, S Esposito, and E Marchetti. "Auxiliary telescopes for the absolute tip–tilt determination of a laser guide star". In: *Monthly Notices of the Royal Astronomical Society* 276.1 (1995), pp. L76–L78.

[211] Domenico Bonaccini Calia, James Osborn, Pierre Haguenauer, Marcos Reyes, David Alaluf, Mauro Centrone, Noelia Martinez Rey, David R Jenkins, Petr Janout, Marco Faccini, et al. "CaNaPy: LGS-AO experimental facility for visible wavelengths". In: *Adaptive Optics Systems VIII*. Vol. 12185. SPIE. 2022, p. 121857L.

[212] Noelia Martinez Rey, Guido Agapito, Alfio Puglisi, Domenico Bonaccini Calia, Pierre Haguenauer, James Osborn, Matthew Townson, Mauro Centrone, Marco Faccini, David Alaluf, et al. "Simulating CaNaPy performance with PASSATA: bistatic versus monostatic laser propagation." In: *Adaptive Optics Systems VIII*. Vol. 12185. SPIE. 2022, 121852Y.

[213] Roberto Ragazzoni. "Absolute tip-tilt determination with laser beacons." In: *Astronomy and Astrophysics* 305 (1996), p. L13.

[214] R Foy, A Migus, F Biraben, G Grynberg, PR McCullough, and M Tallon. "The polychromatic artificial sodium star: a new concept for correcting the atmospheric tilt." In: *Astronomy and Astrophysics Supplement, v. 111, p. 569* 111 (1995), p. 569.

[215] Renaud Foy, Jean-Paul Pique, Alain Denis Petit, Patrick Chevrou, Vincent Michau, Gilbert Grynberg, Arnold Migus, Nancy Ageorges, Veronique Bellanger, Francois Biraben, et al. "Polychromatic guide star: feasibility study". In: *High-Power Laser Ablation III*. Vol. 4065. SPIE. 2000, pp. 312–323.

[216] Hugues Guillet de Chatellus, Jean-Paul Pique, and Ioana Cristina Moldovan. "Return flux budget of polychromatic laser guide stars". In: *JOSA A* 25.2 (2008), pp. 400–415.

[217] R Foy. "The cone effect". In: *Laser Guide Star Adaptive Optics for Astronomy* (2000), pp. 107–123.

[218] Claude Elwood Shannon. "Communication in the presence of noise". In: *Proceedings of the IRE* 37.1 (1949).

[219] Claude Elwood Shannon. "A mathematical theory of communication". In: *The Bell system technical journal* 27.3 (1948), pp. 379–423.

[220] Sylvain Poulenard, Benjamin Gadat, Lyonel Barthe, and Ronald Garzón-Bohórquez. "Protection schemes for optical communication between optical ground station and a satellite". In: *COAT-2019-workshop (Communications and Observations through Atmospheric Turbulence: characterization and mitigation)*. 2019.

[221] S Magidi and A Jabeena. "Free space optics, channel models and hybrid modulation schemes: A review". In: *Wireless Personal Communications* 119.4 (2021), pp. 2951–2974.

[222] Murat Uysal and Jing Li. "Error rate performance of coded free-space optical links over gamma-gamma turbulence". In: *2004 IEEE international conference on communications (IEEE Cat. No. 04CH37577)*. Vol. 6. IEEE. 2004, pp. 3331–3335.

[223] Ricardo Barrios and Federico Dios. "Exponentiated Weibull distribution family under aperture averaging for Gaussian beam waves". In: *Optics express* 20.12 (2012), pp. 13055–13064.

[224] Aniceto Belmonte and Joseph M Kahn. "Performance of synchronous optical receivers using atmospheric compensation techniques". In: *Optics express* 16.18 (2008), pp. 14151–14162.

[225] Italo Toselli and Szymon Gladysz. "Effectiveness of adaptive optics for coherent laser communications in atmospheric turbulence". In: *Environmental Effects on Light Propagation and Adaptive Systems V*. Vol. 12266. SPIE. 2022, pp. 44–50.

[226] Jerry F Lawless. "Inference in the generalized gamma and log gamma distributions". In: *Technometrics* 22.3 (1980), pp. 409–419.

[227] Frank Bowman. *Introduction to Bessel functions*. Courier Corporation, 2012.

[228] Nicolas Védrenne, Vincent Michau, Clélia Robert, and Jean-Marc Conan. "Cn2 profile measurement from Shack-Hartmann data". In: *Opt. Lett.* 32.18 (Oct. 2007). URL: http://opg.optica.org/ol/abstract.cfm?URI=ol-32-18-2659.

[229] Miao Yu and Mikhail A Vorontsov. "Remote sensing of atmospheric wind profiles using spatio-temporal intensity information and wavefront sensor information". In: *Sensors for Harsh Environments II*. Vol. 5998. SPIE. 2005, pp. 55–66.

[230] VA Banakh, DA Marakasov, and MA Vorontsov. "Cross-wind profiling based on the scattered wave scintillations in a telescope focus". In: *Applied Optics* 46.33 (2007), pp. 8104–8117.

[231] S Basu, J Osborn, P He, and AW DeMarco. “Mesoscale modelling of optical turbulence in the atmosphere: the need for ultrahigh vertical grid resolution”. In: *Monthly Notices of the Royal Astronomical Society* 497.2 (2020), pp. 2302–2308.

[232] James Osborn, Jean-Edouard Communal, and Frédéric Jabet. “Global atmospheric turbulence forecasting for free-space optical communications”. In: *Free-Space Laser Communications XXXV*. Vol. 12413. SPIE. 2023, pp. 365–379.

ECOLE
DOCTORALE

Titre : Optimisation des Liens Télécom Sol-GEO Haut-Débit à l'aide de Stratégies Optiques et Numériques

Mots clés : Optique adaptative, Communications optiques, télécommunications satellitaires, anisoplanétisme.

Résumé : Dans un contexte de besoins numériques croissants, les communications optiques par satellite, complémentaires aux infrastructures terrestres, permettraient d'échanger des données du sol vers l'espace à des débits de l'ordre du térabit par seconde. L'une des principales limitations de ces liaisons optiques est la perturbation du champ complexe lors de sa propagation dans l'atmosphère. Du fait de ces perturbations, le flux couplé à bord du satellite fluctue fortement, entrainant de longs et profonds évanouissements du signal, qui dégradent le signal d'information. Plusieurs solutions existent pour atténuer ces pertes d'information. Des moyens physiques, tels que l'utilisation d'une correction par optique adaptative (OA), permettent minimiser les pertes de couplage, tandis que les techniques numériques permettent d'améliorer la fiabilité des informations grâce au codage et à l'entrelacement. Ces techniques ont été appliquées à la liaison descendante dans des travaux antérieurs. Concernant le lien montant, la technique envisagée est la pré-compensation par OA. Cependant, du fait de la géométrie du lien, comme le lien montant et descendant sont séparés par l'angle de pointage en avant, cette pré-compensation, identique à celle du lien descendant, est sous-optimale. Par conséquent, des évanouissements profonds et longs du signal persistent.

Dans cette thèse, nous concevons de nouvelles méthodes pour optimiser la phase de pré-compensation au pointage en avant, améliorant ainsi les statistiques du canal. La conception et l'évaluation de ces méthodes reposent sur un formalisme réciproque qui permet une description de l'erreur de pré-compensation et du flux couplé associé. Pour optimiser la phase de pré-compensation au pointage en avant, nous développons quatre méthodes qui exploitent les informations obtenues à partir des mesures disponibles au sein de la station terrestre optique. Toutes ces méthodes permettent de réduire considérablement l'erreur de pré-compensation et donc d'améliorer les statistiques du flux couplé à bord du satellite. De plus, nous évaluons les performances de télécommunication des liaisons utilisant les méthodes de pré-compensation développées. Enfin, nous développons un modèle statistique de canal de la liaison pré-compensée par optique adaptative.

Title : Optimization of High Data Rate Ground to Satellite Links Pre-compensated by Adaptive Optics

Keywords : Adaptive optics, Optical communications, Satellite communications, Anisoplanatism.

Abstract : In a context of growing digital needs, optical satellite communications serve as a complementary tool to existing terrestrial communication infrastructures. Establishing optical links with GEO-stationary satellites would enable data exchange at rates on the order of Terabits per second between Earth and space. One of the primary limitations this optical link is the disturbance of the optical wave during its propagation through the atmosphere. The effect of atmospheric turbulence results in spatiotemporal fluctuations in the phase and amplitude of this wave. This translates into a highly disturbed beam with speckles evolving over time in the satellite's plane. Consequently, the coupled flux onboard the satellite fluctuates significantly, leading to long and deep signal fades that degrade the information signal.

Solutions exist to mitigate these information losses. Physical means, such as adaptive optics, can minimize coupling losses, while digital techniques can enhance information reliability through coding and interleaving. These techniques have been applied to the downlink in previous works (Lucien Canuet). Concerning the uplink, the envisioned optical technique is the pre-compensation by adaptive optics. However, due to the geometry of the link, where the optical up and downlink path are separated by a point-ahead angle, this pre-compensation identical to the downlink AO correction is currently suboptimal. As a result, deep and long signal fades persist.

In this thesis, we have designed new methods to optimize the pre-compensation phase at the point-ahead angle, thereby improving the channel statistics. These methods design and evaluation rely on a reciprocal formalism that allows for an analytical description of the pre-compensation phase error and associated coupled flux. To optimize the pre-compensation phase at the point-ahead angle, we have developed four methods that exploit information obtained from available measurements at the optical ground station. All the proposed methods show to greatly reduce the pre-compensation phase error and therefore improve the statistics of the coupled flux aboard the satellite. Additionally, we evaluate the telecommunication performance of the links using the developed pre-compensation methods. Finally, we develop the statistical channel model of the AO pre-compensated link.

Institut Polytechnique de Paris
91120 Palaiseau, France